



Exploring Silver-Pyrimidine Chemistry and the Controlled Assembly of M-DNA Systems

Liam Mistry

A thesis submitted in partial fulfilment of the requirements for the award of

Doctor of Philosophy

School of Natural & Environmental Sciences

(Chemistry)

Newcastle University, Newcastle upon Tyne, UK

Submitted: October 2020

Supervisors – Prof Andrew Houlton*, Dr Ben Horrocks

and Dr Nick Wright

Abstract of the Dissertation

Exploring Silver-Pyrimidine Chemistry and the Controlled Assembly of M-DNA Systems

Liam Mistry

The body of work discussed within this thesis focuses on silver-pyrimidine chemistry traditionally found between a mismatched cytosine-cytosine (C-C) DNA base-pair.

Three examples of $[\text{Ag}^{\text{I}}\text{-bis}(\text{N}^3\text{-cytosine})]^+$ were prepared and structurally characterised by single crystal X-ray diffraction: *cisoidal*- $[\text{Ag}^{\text{I}}\text{-(N}^3\text{-cytosine)}_2][\text{NO}_3]$ (**C_{bent}**), *transoidal*- $[\text{Ag}^{\text{I}}\text{-(N}^3\text{-cytosine)}_2][\text{NO}_3]\cdot\text{H}_2\text{O}$ (**T_{bent}**) and *transoidal*- $[\text{Ag}^{\text{I}}\text{-(N}^3\text{-cytosine)}_2][\text{PF}_6]\cdot 2\text{H}_2\text{O}$ (**T_{linear}**). All three compounds displayed the typical $\text{N}^3\text{-Ag}^{\text{I}}\text{-N}^3$ coordination motif with variable geometries including, *cisoidal/transoidal* (**C/T**) and bent/linear base arrangements. Collectively, they represent three of five possible combination of these parameters. Density-Functional theory calculations showed the global minimum conformation to be the bent-*transoidal* arrangement; the entire series being **T_{bent}** > **T_{linear}** > **C_{linear}** > **C_{bent}**.

$[\text{Ag}^{\text{I}}\text{-bis}(\text{N}^3\text{-cytidine})][\text{NO}_3]$ was prepared and structurally characterised by single crystal X-ray diffraction techniques and revealed to show the expected linear $\text{N}^3\text{-Ag}^{\text{I}}\text{-N}^3$ coordination. The resulting *bis*-nucleoside (ribose form) complexes spontaneously stacked inline to produce a helical arrangement (right-handed) analogous to DNA (approximately 10-bp per rotation). In solution, a significant change in the circular dichroism profile was observed compared to cytidine_(aq) and was associated with the formation of helical structure. The helix is stabilised by hydrogen bonding between adjacent exocyclic $\text{N}^4\cdots\text{O}^2$ groups of the ligands, argentophilic and hydrophilic interactions. The silver ions positioned down the central core are sufficiently close, with $\text{Ag}\cdots\text{Ag}$ distances of approximately 3.0 Å for argentophilic interactions. Despite having $\text{Ag}\cdots\text{Ag}$ distances <5% of the metallic radii, the material displayed electrically insulating properties, likely due to a large bandgap (2.5 eV). Furthermore, when prepared in an alcoholic solvent (MeOH and EtOH) the corresponding silver complex produced a sample-spanning homogenous gel. A rheological study showed an entangled network with thixotropic (self-healing) properties.

$[\text{Ag}^{\text{I}}\text{-bis}(\text{N}^3\text{-2'-deoxycytidine})][\text{NO}_3]$ was prepared and structurally characterised by single crystal X-ray diffraction to show a similar helical arrangement to its ribose counterpart. However, the deoxy analogue possessed a left-handed (LH) rotation to the helix. Interestingly, the CD changes previously associated with a helical structure were similar for both the ribose (RH) and deoxy (LH) compounds. Atomic force microscopy imaging of the complex drop-cast from an aqueous solution on to a silicon wafer showed coiled fibres 10 nm in height. Individual coils could be followed into larger aligned assemblies or bundles before merging with the

crystal lattice. These images hold an insight into the mechanisms of crystal growth for polymeric systems.

Two solvates of the nucleotide complex $[\text{Ag}^{\text{I}}-(\text{N}^3, \text{O}^2\text{-cytidine-5'-monophosphate})]$ (Cmp) were prepared and structurally characterised by single crystal X-ray diffraction; *cis*- $[\text{Ag}^{\text{I}}-(\text{N}^3, \text{O}^2\text{-Cmp})][\text{NO}_3]\cdot\text{H}_2\text{O}$ and *cis*- $[\text{Ag}^{\text{I}}-(\text{N}^3, \text{O}^2\text{-Cmp})][\text{NO}_3]\cdot\text{MeOH}$. A one-to-one stoichiometry extends the repertoire of metal coordination sites of cytosine to include the exocyclic O^2 acceptor group. This mode of coordination ($\text{N}^3\text{-Ag}^{\text{I}}\text{-O}^2$) leads to a polymeric array where the Ag^{I} ions “zigzag” down the crystal lattice axis. This configuration means the $\text{Ag}\cdots\text{Ag}$ distances are short, at 2.9 Å. Furthermore, both compounds exist as 3D coordination polymers owing to a third coordination $\text{Ag-O}^{\text{7'}}$ from a phosphodiester group of an adjacent complex. Attempts were made to access and isolate single Ag-chains from crystalline material by mechanical exfoliation techniques. Sonication (in hexane) yielded a uniform distribution of 2D flakes that were 3.0 nm in height. Powder X-ray diffraction results suggested that the cleavage likely occurred at the $\text{Ag-O}^{\text{7'}}$ position resulting in flakes with a bilayer of Ag-chains running perpendicular to the substrate in the [101] direction.

Cytosine rich oligonucleotides were investigated as a controlled method of accessing stabilised few atom metallic clusters or particles. Oligonucleotides were designed with a non-binding central region, which allowed folding into a hairpin type secondary structure facilitated by C-Ag-C coordination. A novel approach to controlled metal ion capture was investigated. A focus was placed on loop and stem optimisation utilising mass spectroscopy, circular dichroism and isothermal titration calorimetry techniques. It was discovered that oligos required central non-binding looped regions of at least two units to retain sufficient flexibility for the folding of the oligo. The abilities to capture or populate the free mismatched cytosine-cytosine mediation-sites with Ag^+ decreased as the length and number of mismatched C-C sites increased. This was due to increased conformational flexibility and cooperativity effects. We were able to maximise the Ag^+ occupancy for oligonucleotides with six or less C-C mismatched sites.

Acknowledgements

I am truly thankful to Professor Andrew Houlton and Dr Benjamin Horrocks for seeing potential in me a little over three-years back, enough to offer the chance to write this thesis. I've learnt and grown under their guidance, which have made me not only a better scientist; but a better person. I'd also like to thank Dr Nick G. Wright for help with my scholarship funding making this all possible.

To my family; Jay, Vas & Sandra Mistry, I cannot begin to express how grateful I forever will be for the unwavering support and encouragement they've shown me. It's been a long journey since I first decided to go back into education those nine years ago, but they've always stood behind me providing moral and emotional support through it all.

With a special mention to a couple of close friends, Jake Musselle-Sexton, Brandon Peterson, Oliver Glenister, Dominic Barns, Willian Searle, Patrick Higgs, Eva Gougoula and Cheney Leung who have always been there as close friends. I'd like to thank them for their unwavering support and abilities to raise my spirit when I needed it.

Last, but most importantly, I'd like to show my appreciation to an amazing Swede, Linnéa Husén. Her incredible support and inspirational attitude helped immeasurably; Tack så mycket, du är verkligen speciell!

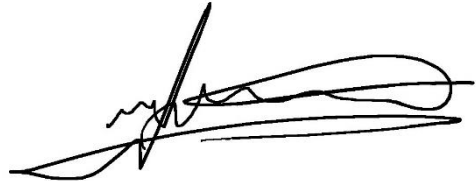
I'd like to make special mention to several individuals who went above and beyond while aiding or collaborating with this research in some form. From Durham university who gave us access time and time again to their instrumentation; Dr Jackie Mosely and Christopher A. Whitmore. Within the Bedson building, Dr Osama El-Zubir, Dr Gema Dura, Dr Mike Probert, Dr Paul G. Waddell, Prof. William Clegg, Dr Maggie White, Racheal Dack and Joao Victor De Souza Cunha.

And finally, and by no means least, to everyone in the Nanoscience corridor... It was great to work alongside you all over the past three-years.

Thank you all for your support and encouragement!

Declaration

Except where specific references have been made to other sources, the work in this thesis is the original work of the author. It has not been submitted, in whole or in part, for any other degree. Certain results have already been published in peer review journals.

A handwritten signature in black ink, consisting of several fluid, overlapping strokes that form a stylized representation of the author's name.

Liam Mistry

Table of Content

Chapter 1.	M-DNA - A Review of Silver-Pyrimidine Chemistry and its Applications towards Nanomaterials of the Future. Pages 8 – 58
Chapter 2.	<i>Transoid</i> and <i>Cisoid</i> Conformations in Silver-Mediated Cytosine Base Pairs. Hydrogen-Bonding Dictates Argentophilic Interactions in the Solid-State. Pages 59 – 96
Chapter 3.	“Metallo-DNA” – Ag ^I -Mediated Supramolecular Duplex with Self-Healing Gelatinous Properties. Pages 97 – 127
Chapter 4.	Metallo-DNA: Left- vs. Right-Handed Helical Rotation in the Solid-State for Ag ^I -Mediated Supramolecular Duplexes. Pages 128 – 156
Chapter 5.	Accessing One-Dimensional Argentophilic Arrays Base on N-Ag ^I -O Bond Formation: Single Crystal to Molecular-Sheet Transformation. Pages 157 – 175
Chapter 6.	Ag _n ^I -Oligonucleotide Systems: Controlled Metal-ion Capture within a Hairpin. Pages 176 – 229
Chapter 7.	Conclusions and Outlook. Pages 230 – 233
Chapter 8.	Experimental Detail. Pages 234 – 243
Appendix.	Chapter 2 (S1), Page 246 – 260 Chapter 3 (S2), Page 261 – 281 Chapter 6 (S3), Page 282 - 333

Abbreviations

°C	Degrees Celsius	l	Litre
1D	One Dimension	M	Molar
2D	Two Dimensional	m/z	Mass/Charge
3D	Three Dimensional	M-DNA	Metallo Deoxy Ribose Nucleic Acid
A	Adenosine	mg	Milligrams
Å	Angstrom	MHz	Mega-Hertz
AFM	Atomic Force Microscopy	ml	Millilitre
Ag-Ag	Silver-Silver argentophilic bonding	mM	Millimolar
AOT	Diocetyl Sodium Sulfosuccinate	mmol	millimole
aq	Aqueous	Mp	Melting-point
C	Cytosine	NC	Nanocluster
CD	Circular Dichroism	NCs	Nanoclusters
Cmp	Cytidine-5'-monophosphate	nM	Nano-molar
Cyt	Cytidine	NMR	Nuclear Magnetic Resonance
d	doublet (NMR)	NP	Nanoparticle
DCmp	2'-Deoxy-Cytidine-5'-monophosphate	NPs	Nanoparticles
DCyt	2'-Deoxycytidine	PXRD	Powder X-ray Diffraction
dd	doublet of doublets (NMR)	RNA	Ribonucleic Acid
DNA	Deoxyribose Nucleic Acid	ss-DNA	Single-stranded Deoxyribose Nucleic Acid
ds-DNA	Double-stranded Deoxyribose Nucleic Acid	T	Thymine
equiv.	Equivalent	t	Triplet (NMR)
ESI-MS	Electrospray Ionisation Mass Spectrometry	TSP	Trimethylsilylpropanoic acid
FTIR	Fourier Transform Infrared Spectrometer	U	Uracil
g	Grams	UV	Ultraviolet
G	Guanosine	XRD	X-ray Diffraction
Hz	Hertz	λ-DNA	Lambda-Deoxyribose Nucleic Acid
IMS	Ion Mobility Spectrometry	μl	Microliter
IMS-MS	Ion Mobility Spectrometry-Mass Spectrometry	μM	Micromolar
IR	Infrared		

Chapter 1.

M-DNA - A Review of Silver-Pyrimidine Chemistry and its Applications towards Nanomaterials of the Future.

Table of Contents

1.1. DNA and its Application in Nanotechnology	10
1.2. DNA – Structure and Function	10
1.3. The Synthesis of Oligonucleotides.....	14
1.4. The Sequence Dependent Structures and Conformations of DNA	17
1.5. M-DNA – Silver-Pyrimidine Chemistry	19
1.6. Ag-Pyrimidine Interaction.....	21
1.7. Ag-Nucleobase (Cytosine) Complexes	23
1.8. Ag-Nucleoside (Cytidine) Complexes	28
1.9. Ag-Nucleotide (Cytidine-5'-Monophosphate) Complexes	29
1.10. Ag-Oligonucleotide Complexes.....	30
1.11. Application of M-DNA Systems Based on Silver-Pyrimidine Coordination...	35
1.12. Nanoparticles or Clusters	35
1.13. Molecular Wires	38
1.14. Conclusions	40
1.15. Scope for Investigation	40

1.1. DNA and its Application in Nanotechnology

How small can we fabricate materials? For many years we have developed progressively better solutions and technologies addressing this question.¹ Whilst there is no obvious answer or boundary to our limitations or ingenuity, it has become clear that the biological world is far more adept. Many biological entities (e.g. amino acids, DNA and proteins) have self-organisation and self-assembly capabilities which are unequalled, yet they lack the functionality required for them to realise applications outside of their biological domain (*i.e.* molecular wire, sensors and drug-delivery).^{2,3} Fortunately, we can introduce functionality (optical, catalytic, electrical, magnetic) by addition of certain transition metals.^{2–6} DNA in particular seems well-suited for this purpose, as it readily binds to a wide range of metal ions whilst offering a large scope of versatility in its construction.^{4,6} To today, several groups have utilised DNA as scaffolds in the “bottom-up”⁷ construction of nano-scale materials including, nanoparticles/clusters^{8–12}, nanowires^{12–15} and molecular sensors^{5,16–18}. The remarkable advances made in synthetic techniques have made DNA’s use practical for many material scientists.¹⁹ The work conducted within this thesis addresses the well-known, yet poorly understood, specific interactions between Ag^I ions and DNA (specifically, interactions with cytosine); discovered only 18 years ago.²⁰

1.2. DNA – Structure and Function

Deoxyribose nucleic acid or DNA is the key building block to all discovered life to date. Its primary role within a biological cell is storage, transcription and expression of large amounts of encoded genetic information.²¹

The structure of DNA exists in many secondary forms but its principle physiological conformation was initially well described by the American biologist James Watson and English physicist Francis Crick in 1953 (**Figure 1.1**).²² They described a double-helix or duplex existing as two independent ridged anti-parallel polymeric strands (oligonucleotide) bound along a common fibre axis by hydrogen bonding between nucleic monomers (analogous to a twisted-ladder structure). The inherent chirality of duplexed DNA enables the formation of supercoiled helical structures under torsional stress. This feature allows for gene regulation and organisation allowing for translation or transcription events.²¹

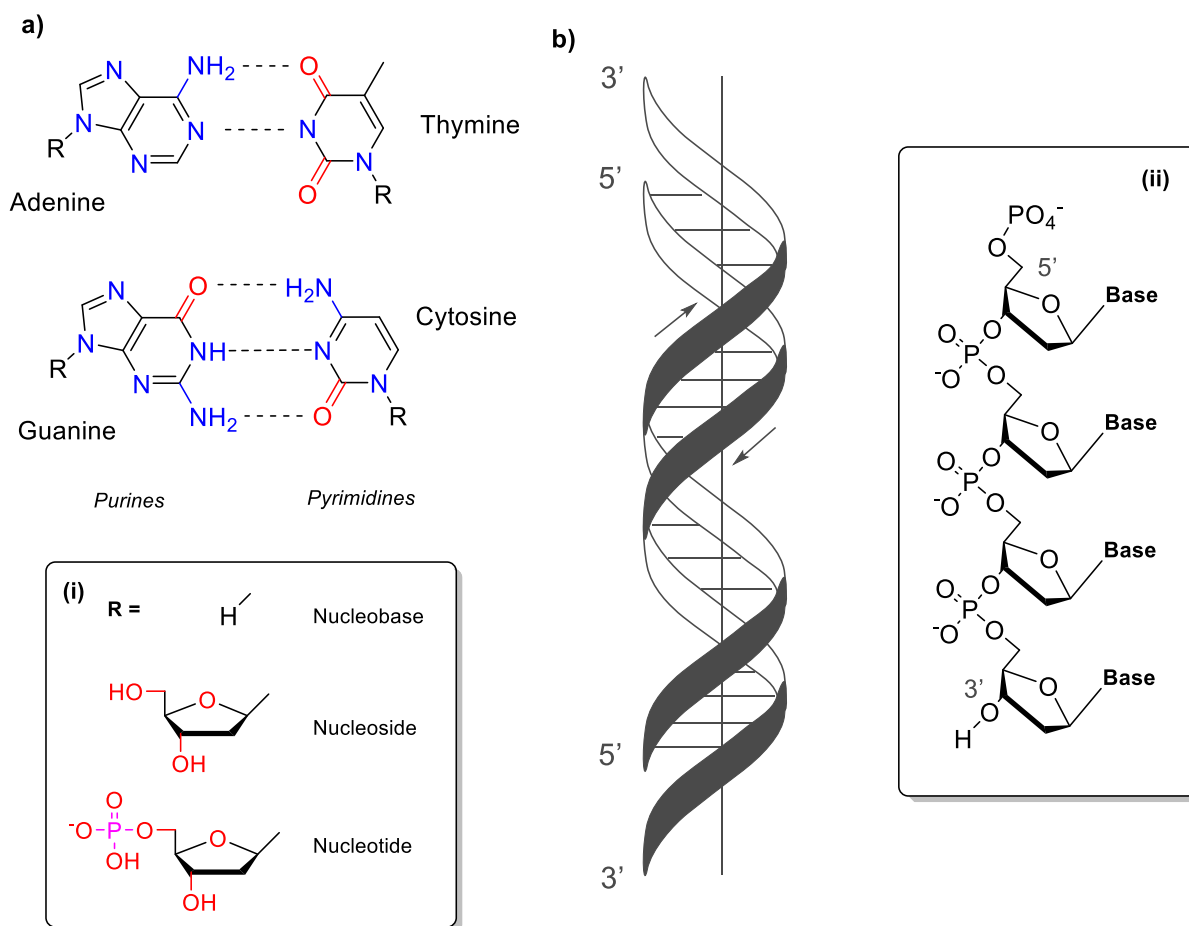


Figure 1.1 a) Illustrations of the purine-pyrimidine base-pairing (A-T and G-C) (Inset (i) R group differences between nucleobase, -side and -tide classifications) and b) A DNA duplex as proposed in the 1953 publication by Watson and Crick (Inset (ii) oligonucleotide backbone construction).²²

The monomers or nucleotides are comprised of a nucleobase and backbone linker consisting of five-carbon sugar sub-unit (2'-deoxyribose) and phosphodiester group.^{21–23} Nucleobases of DNA, of which there are four main types, can be split into two main groups, purines (adenine (A) and guanine (G)) and pyrimidines (thymine (T) and cytosine (C)).²¹ The dominant base tautomeric forms give rise to the well-established Watson-Crick dinucleotide hydrogen bonding interactions between adenine-thymine (A-T) and cytosine-guanine (C-G) base-pairing. Due to the complementarity of these two base sets, there exists a natural 1:1 ratio of pyrimidines vs. purines, which has

* Thymine (T) is replaced with uracil (U) within RNA

become known as Chargaff's rule.²⁴ From a chemist's point of view, DNA is an elegant pairing between a keto base (purine) with an amino base (pyrimidine). Two and three H-bonds exist between A-T and C-G respectively; as seen in **Figure 1.1**. For an A-T pairing, H-bonds exist across the endocyclic secondary and tertiary N^3 amines and exocyclic N^4 donor and O^4 acceptor. A C-G pairing has an additional N^2 - O^2 H-bond.

The ordering or sequence of base-pairs is obviously fundamental to the storage of genetic information, site-specific recognition (proteins and enzymes) and structural morphology of DNA. The genetic code is read linearly and in runs of three base-pairs (termed a codon); from a specific start codon.²¹ The information encoded within DNA affords sequence dependent physicochemical properties (*i.e.* structural rigidity and abilities to strand separate).²¹ DNA has naturally led to exploration by many scientists as a means of depositing and storing man-made digital information. The storage capacity of DNA has been theorised at 1.28 petabytes per gram or 1.8 bits of data per nucleotide.²⁵ The storage capacity is only limited by the length of DNA. Having many thousands of replicates of encoded DNA information ensures the reliability of the information retrieval against corruption. However, the downfall of such methods of information storage is the speed at which information can be accessed or written using the technologies currently available. DNA specific enzymes, such as polymerase, have been measured to have a working rate of approximately 50 nucleotide base-pairs per second.²⁶

The insights gained into the fundamentals of genetics over the past 60 years have gained a staggering amount of momentum and have since allowed for the plethora of genetic advances. The discovery of various DNA structures which have been visualised with alternative morphologies have been well characterised since the now famous 1953 publication by Watson & Crick.²⁷ B-DNA, A-DNA, and Z-DNA are all polymeric structures that exist as a double helices (**Figure 1.2**).²⁷ These can each be imagined as a simple straight ladder. Ribonucleic acid (RNA) typically differs itself from DNA as it tends to exist as a base-paired folded single strand polymer; double-stranded sequences have however been observed. The crucial physical and chemical differences in the biological properties of DNA therefore depend on their base sequence.

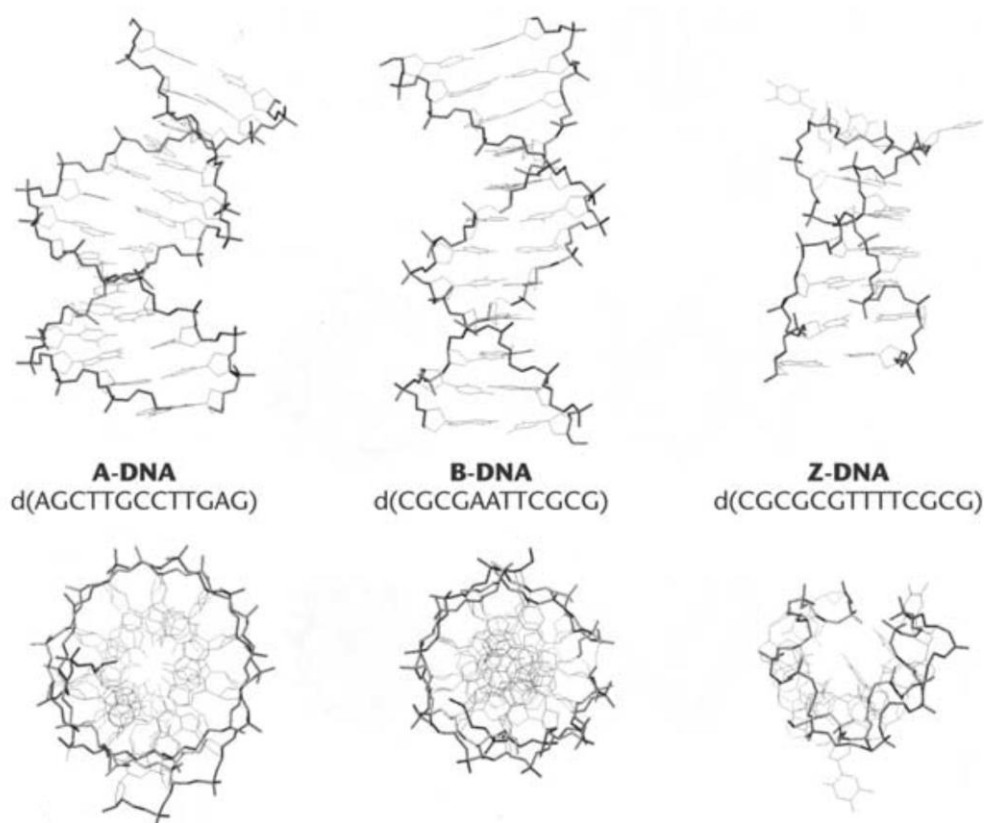


Figure 1.2 Top and side on views of crystal structures of A-, B- and Z-DNA.²⁸

**Reproduced with the permission of John Wiley and Sons.*

The most common and well described conformation of DNA is the B-form. The structure exists as a linear right-handed intertwined double-helix (1.9 nm dia.) with a complete rotation every 3.4 nm (antiparallel confirmation) around a common helical axis, approximately ten base-pairs (36° rotation per base-pair). This is also referred to as a plectonemic coil. Major and minor grooves exist along the duplex, enabling sequence specific protein interactions. The grooves allow gaps for protein-nucleobases back-end interactions.²³

A-form DNA exists as a right-handed helix (1.9 nm dia.) with a complete rotation every 11 base-pairs (33° rotation per base-pair). The major differences between A- and B-form DNA exist in the conformation or pucker of the sugar group (**Figure 1.3**). A-form DNA exists in a C^{3'}-endo (*syn*- base orientation) conformation, whilst B-form exists in a C^{2'}-endo (*anti*- base orientation).²⁹ This has the effect of reducing the distances between adjacent nucleotides in A-form DNA by approximately one Angstrom when compared to B-form. A second major difference is the positioning of bases within the

helical core. In B-form the bases are central to the helical axis, however, in A-form they are displaced towards the major grooves, resulting in a ribbon-like helix with a more open core.

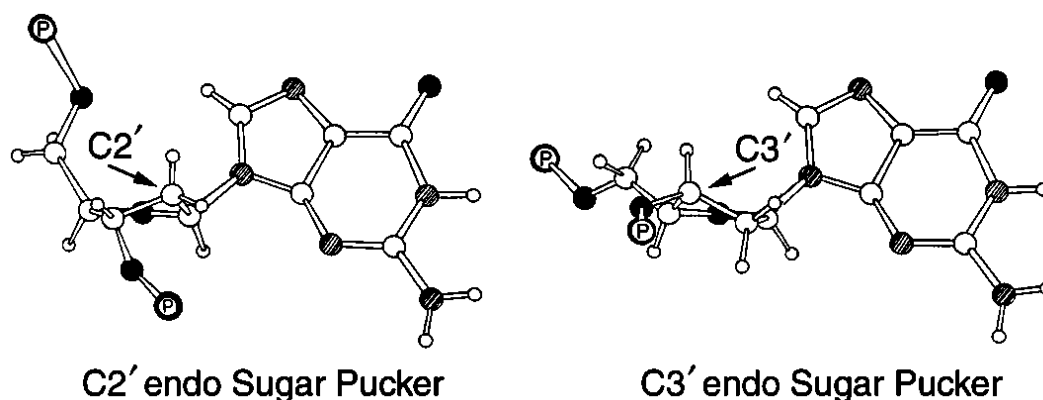


Figure 1.3 Guanosine (deoxy) displaying a C2' (LHS) and C3' (RHS) endo sugar pucker conformations found in B- and A-forms of DNA respectively.²⁹ *Reproduced with the permission of Springer Nature.

Z-form DNA exists as a significantly different left-handed helix (1.9 nm dia.) with a complete rotation every 12 base-pairs (30° rotation per base-pair). The helix has a pronounced “zig-zag” pattern, hence the Z- conformational assignment. Interestingly, small portions of DNA within a cell can exist in this Z-form by having runs of alternating GCGCGC sequences. This is due to G-nucleotide have a different conformation when compared to traditional B-form DNA. Guanine (G) is in the *Syn*-conformation due to the C3'-endo sugar pucker.²⁹ To accommodate the out of centre G-base position the structure distorts to allow H-bonding with its complementary adjacent C-base partner.

Ribonucleic acid (RNA) is similar to DNA in many ways, however its biological role involves the coding, decoding, regulation and expression of genes. Its most pronounced difference from DNA is uracil (U) in place of thymine (T). RNA primarily exists as a single stranded molecule, however, double stranded regions caused by back folding are similar to A-form geometries.

1.3. The Synthesis of Oligonucleotides

Synthesis of oligonucleotides has become widely automated over the past few decades. For most applications, very small quantities are required, usually 40 nmol

scale or lower, however larger scales (synthesis of multi-kilograms) are achieved using solid-phase synthesis. These solid-phase methods were originally pioneered by Marvin Caruthers in the early '80s and has since become the industry standard for oligonucleotide preparation.^{†19,30} The phosphoramidite oligonucleotide synthesis occurs with sequential growth in the 3' to 5' direction from a solid-support, where each cycle or solvent wash adds one additional nucleotide unit to the sequence. The phosphoramidite oligonucleotide synthesis cycle consists of six steps outlined in **Figure 1.4** below attached to a solid support.

The oligonucleotide synthesis begins with detritylation of the support-bound 3'-nucleoside. The first chosen unit protected nucleic unit (A, C, G or T) at the 3'-end comes pre-attached to a resin support with a 5'-(4,4'-dimethoxytrityl) (DMT) protecting group. DMT prevents polymerisation during resin functionalisation. Protecting group therefore must be removed prior to oligo-synthesis; removal involves trichloroacetic acid as an acid catalysed detritylation.

Following detritylation, the support-bound nucleoside is ready to couple with the next nucleic unit (**step-1**) added as a nucleoside phosphoramidite monomer (in excess). The phosphoramidite monomer is first activated using a tetrazole catalyst which displaces the protonated diisopropylamino group generating an ideal leaving group which is easily displaced by the 5'-hydroxyl group of the support-bound nucleoside, the newly formed phosphorus-oxygen bond generates a support-bound phosphite trimer. This process is remarkably efficient with reasonable yields of around 99.5%, however any remaining unreacted 5'-hydroxyl groups left unchecked could potentially react in following coupling cycles leading to a mutation or base-free unit in the desired oligo. To prevent this from occurring, **step-2** introduced a "capping" step to block any remaining 5'-hydroxyl groups. A mixture of acetic anhydride and N-methylimidazole (NMI) dissolved in tetrahydrofuran produces an electrophilic mixture which rapidly acetylates alcohols rendering any 5'-hydroxyl groups inert to subsequent reactions. At this stage small quantities of pyridine are added to maintain a basic pH.

The newly created phosphite-triester (P^{III}) formed during step-1 is relatively unstable to acids and therefore requires oxidation during **step-3** using iodine (in the presence

[†] Not to be confused with the 1984 Nobel prize winner Bruce Merrifield's method, which also relies on solid-phase chemical synthesis developed in the 1960's.

of water and pyridine) to produce a stabilised (P^V) species. The resulting phosphotriester is now analogous to that of a DNA-backbone. The 2-cyanoethyl group prevents any undesirable reactions from occurring during subsequent synthesis cycles. **Step-4** repeats the detritylation (deprotection of the DTM) at the 5'-end of the newly added nucleoside so that subsequent additions can occur. At this stage, Steps-1-4 are repeated until the desired oligonucleotide sequence is achieved.

Step-5 involves the removal or cleavage of the oligonucleotide from the resin support at the 3'-end is achieved using ester hydrolysis using ammonium hydroxide. Heat is finally applied in **step-6** to the now ammonia-dissolved oligonucleotide to remove the protecting groups from the heterocyclic bases and/or phosphate groups. High performance liquid chromatography (HPLC) techniques are generally used in a final purification step.

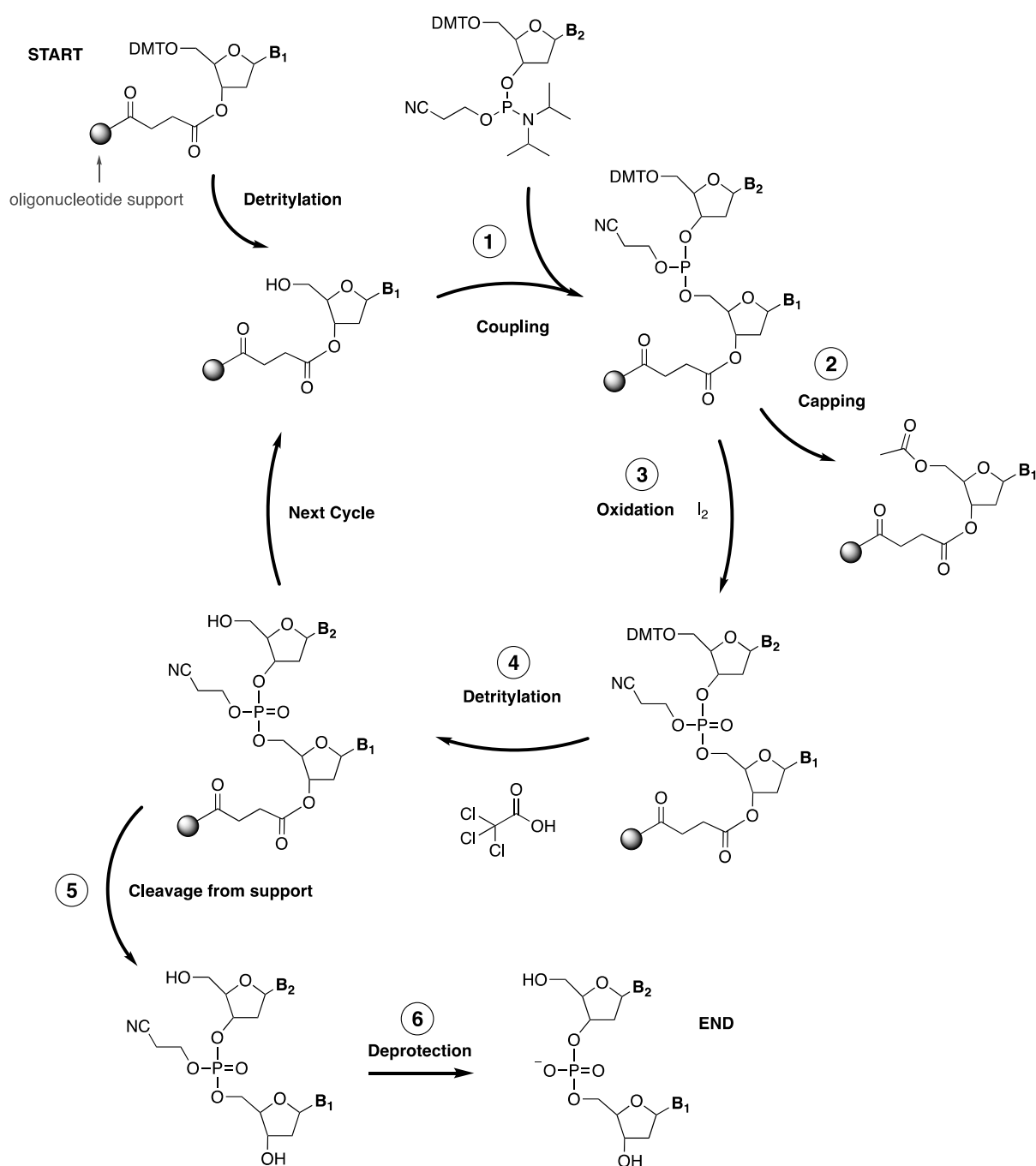


Figure 1.4 The phosphoramidite method of oligonucleotide synthesis (DMT, 4,4'-dimethoxytrityl and NC, cyanoethyl protecting groups).^{19,30}

1.4. The Sequence Dependent Structures and Conformations of DNA

The sequence dependant structures of both DNA and RNA have led to the discovery of several secondary structures. These include cruciform, H-DNA (triplex-DNA),³¹ G4-DNA (quadruplex),^{32,33} origami,^{34–37} hairpin,^{38–41} dumbbell^{42–44} and slipped strand DNA⁴⁵ (**Figure 1.5**).⁴⁰

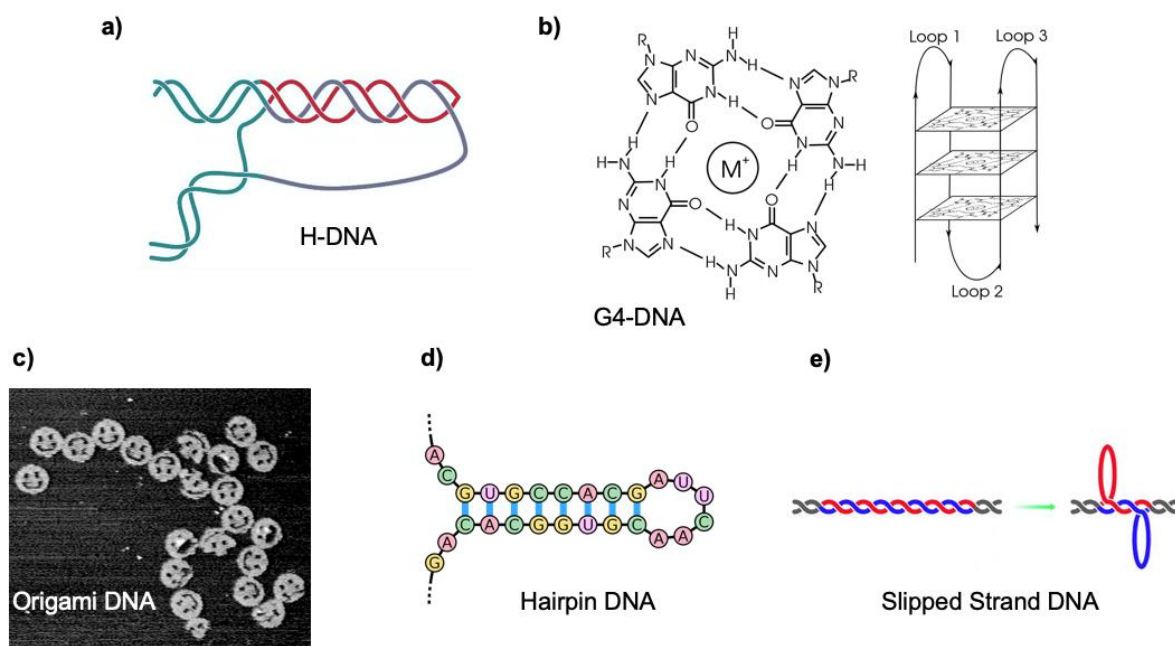


Figure 1.5 Examples of secondary DNA structures; a) H-DNA (triplex DNA),³¹ b) G4-DNA (quadruplex),^{32,33} c) origami DNA,^{34–37} d) hairpin^{38–41} and e) slipped strand DNA⁴⁵.

Of these, hairpin (also known as Stem-Loops) are particularly interesting due to their potential applications in numerous auto-assembly based⁴¹ or encapsulation type situations. A hairpin is a short secondary structure generated from the folding of single nucleic acid strand and consists of a base-paired stem and a loop with unpaired nucleotide bases.³⁹ A hairpin loop forms when two regions of the same nucleic single-strand (complementary when read in opposite directions) base-pair or hybridise to form a double helix which ends in an unpaired loop. The resulting secondary structure has been thought to be key to a number of biological mechanisms found in nature, *e.g.* gene expression⁴⁶ and regulation⁴⁷, ribozymes (RNA enzymes) and messenger-RNA.³⁹ Several studies have confirmed their existence by spectroscopic and calorimetric means. Metal-induced folding of DNA into hairpin structures has long been postulated to be an effective method of heavy-metal-ion encapsulation towards sensing, logic gates or nanoscale materials construction.^{41,48–54}

1.5. M-DNA – Silver-Pyrimidine Chemistry

Metal Ions are critical to many biological and chemical processes. Over the past few decades, the use of DNA-based routes towards nanomaterials have been actively pursued. While the main biological purpose of DNA is genetic storage of information, its chemical structure lends itself towards a plethora of metal binding possibilities.⁵⁵ This is achieved by either the phosphate backbone or nucleobase subunits. DNA possesses many remarkable traits, such as being highly stable, cost-effective and easily modified. DNA is therefore a fitting tool for the development of nanotechnology or materials. Numerous examples exist of metal-ions being used to functionalise DNA → M-DNA (metallo-DNA) giving them conductive^{56–64}, magnetic⁶² or luminescent^{65,66} properties. Transition metals in particular occupy a large proportion of the elements present on the periodic table and are of great analytical importance. Many transition metals can readily lose their bound water ligand for inner-sphere coordination, resulting in a high binding affinity for DNA.⁵⁵ Many non-specific interactions between DNA and transition metal ions have been studied by a variety of techniques showing a preference towards nucleobase binding rather than the phosphate backbone. The general affinity for divalent metal cations follows: $\text{Hg}^{\text{II}} > \text{Cu}^{\text{II}} > \text{Cd}^{\text{II}} > \text{Mn}^{\text{II}} > \text{Ni}^{\text{II}} > \text{Co}^{\text{II}} > \text{Fe}^{\text{II}}$ and $\text{Au}^{\text{I}} \approx \text{Ag}^{\text{I}}$ for monovalent cations.^{55,67} Such M-DNA systems have extensively been investigated towards the development of nanoscale materials; *i.e.* heavy metal sensors,^{55,68–70} nanowires,^{13,56,71} nanoparticles or clusters^{72–77}.

Metal-nucleobase interactions have been studied for the past 70 years, since divalent mercury cations (Hg^{II}) were found to coordinate strongly with thymine-rich polynucleotides.^{78,79} The discovery initially saw little impact owing to the inherent toxicity of mercury ions limiting its application. In 2002 Tanaka *et al.* demonstrated that silver ions possessed similar characteristics, allowing for coordinated across a C-C (C: cytosine) pyrimidine mismatch within a DNA duplex.²⁰ Their work demonstrated the exchange of natural G-C Watson-Crick type base-pair with a mismatched C-C pairing capable of coordinating across a silver ion ($\text{C-Ag}^{\text{I}}\text{-C}$).^{20,80} Unlike many naturally found metal counterions (K^+ , Na^+ and Mg^{2+}) which preferentially bind to the negatively charged phosphate backbone, Ag^{I} and Hg^{II} bind to the endocyclic *N*-donors of the heterocyclic bases. In a metal-mediated base-pair, the hydrogen bonds across a canonical base pair are formally exchanged by coordinate bonds across a metal-ion within the duplex.⁸¹ The reduced size of pyrimidines when compared to purines allows for a gap (4.4 Å), large enough for a single Ag^{I} and Hg^{II} ion to be selectively

incorporated into the core of helix.^{78,82,83} Other transition metal ions have since been reported to have similar interactions with DNA, such as U-Pt^{II}-U⁸⁴ and C-Zn^{II}-G⁸⁵. The term bio-coordination have since been used to describe these types of metal-nucleobase interaction.⁸⁶

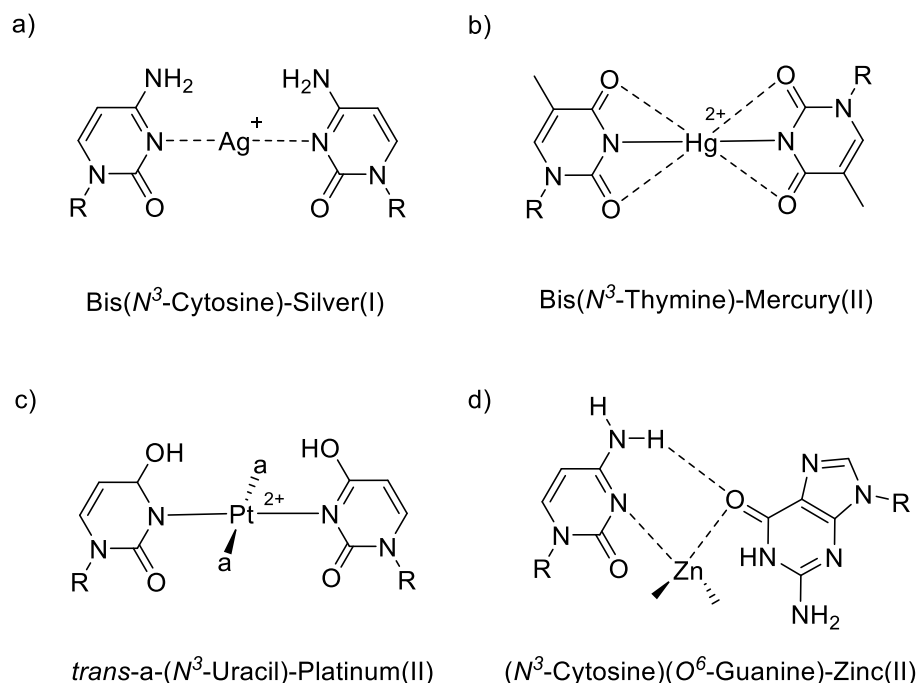


Figure 1.6 Examples of metal mediated/modified base pairs; a) C-Ag^I-C, b) T-Hg^{II}-T, c) U-Pt^{II}-U and d) C-Zn^{II}-G.⁸⁷

These particular types of metal-nucleobase interactions can be further sub-categorised into metal mediated or metal modified base pairs (**Figure 1.7**).⁸⁷ The former is observed by insertion of a metal ion between a non-interacting mis-pair or base surrogate pair (*i.e.* C-Ag^I-C and T-Hg^{II}-T). The latter occurs between a hydrogen bonded base pair. (*i.e.* G-C, A-T or A-U). The term metal modified base pair has been further extended to include larger metal-nucleobase aggregates such as triplets and quartet complexes.⁸⁷

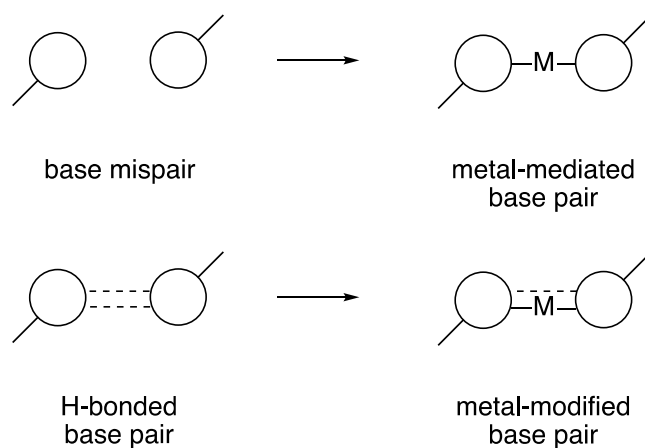


Figure 1.7 Metal mediated (top) vs. metal modified (bottom) base pair.⁸⁷

1.6. Ag-Pyrimidine Interaction

The discovery of these inner-duplex coordination modes, again, initially saw little impact, yet over the past decade has experienced a renaissance within the scientific community.^{4,6,87–90} Applications in materials science, biotechnology and analytical sensors became viable as costs associated with oligonucleotide synthesis reduced. Recent efforts to structurally characterise Ag^I-DNA systems have since led to the discovery of several new coordination partners beyond just the traditional C^{N3}-Ag-C^{N3} coordination motif. The scope of natural nucleobase coordination partners of Ag^I now includes; C^{O2}-Ag-C^{N3}, C^{N3}-Ag-A^{N6}, T^{N3}-Ag-T^{N3}, U^{N3}-Ag-U^{N3}, G^{N3}-Ag-G^{N3} and G^{N3}-Ag-C^{N3} (**Figure 1.8**).^{82,86–94}

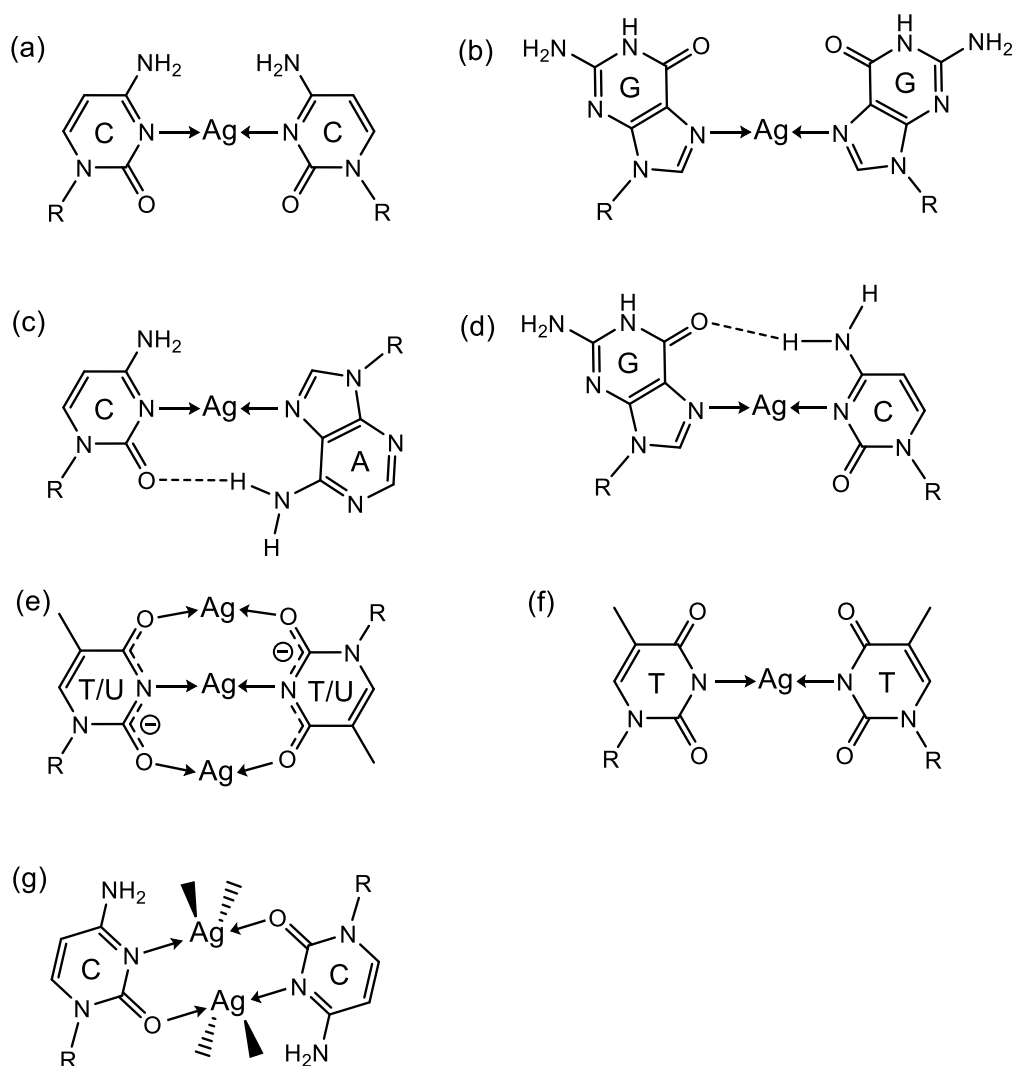


Figure 1.8 Examples of metal mediated/modified silver(I)-nucleobase complexes in R/DNA (a⁸⁷, b⁹¹, c⁹², d⁹³, e⁹⁴, f⁹⁴ and g⁹⁵).^{92,96–99}

*N*¹-blocked cytosine predominantly occurs in the amino oxo tautomer form as in DNA. Other rare tautomers exist and are associated with mispairing or mutagenesis within the nucleus of a cell. Metal binding sites (*N*¹-substituted) include O², *N*³, *N*⁴ and C⁵. Binding at the *N*⁴ and C⁵ positions requires the loss of a proton which can occur. Aqueous Ag⁺ cations are very weakly acidic (pK_a 11.9), which means they cannot readily deprotonate nucleobases and are therefore expected to bind through the loss of aqua ligands with unprotonated donor sites.⁸⁷ This feature is reflected in the highly specific *N*³ binding motif with cytosine. Relatively little is known about these mechanisms, nevertheless it is likely that electrophilic attack of the metal ion occurs and subsequent formation of *N*³ bound silver-cytosine complex (**Figure 1.9**). The role of the aqua ligands remains unclear, with some speculating the existence of a third Ag⁺-OH₂ interaction or ligand stabilising role.⁹²

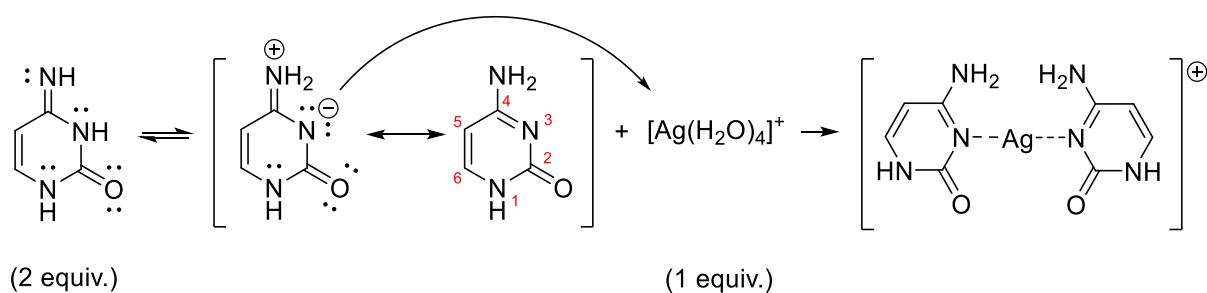


Figure 1.9 A theorised mechanism towards the formation of the $[\text{Ag}^{\text{I}}-(\text{N}^3\text{-cytosine})_2]$ coordination complex.

The coordination between the N^3 -donor of cytosine and silver ions is further understood by considering Hard and Soft Acid and Bases (HSAB) principle. Ag^+ is regarded as a soft-acid, due to its large ionic radius (>90 pm), low positive charge, completely filled atomic orbitals in its valence shell with low energy LUMOs. In contrast the N^3 amino group is an intermediate-base, with a large radius (>170 pm), highly polarizable and low energy HOMO. The alternative coordination sites N^1 , O^2 and N^4 are harder-bases when compared to N^3 . Therefore, to satisfy the soft-acid to soft-base binding principles Ag would tend towards the softer N^3 group when forming a covalent complex.

1.7. Ag-Nucleobase (Cytosine) Complexes

The earliest example of a “modified” metal-mediated base pair was discovered to exist by X-ray diffraction in the solid state between silver ions and an alkylated cytosine base, specifically 1-methylcytosine, was published in 1979 by Marzilli & Kistenmacher.⁹⁵ Surprisingly, the metal mediation observed did not exclusive show coordination to the amino N^3 donor site, but, involved the exocyclic O^2 acceptor (**Figure 1.10**). The inclusion of the carbonyl coordination ($\text{O}^2\text{-Ag-}\text{N}^3$) allowed for a 1:1 stoichiometry forming eight-membered macrocyclic dimers, $[\text{Ag}^{\text{I}}\text{-(1-Methylcytosine)}(\text{NO}_2)]_2$. The $\text{Ag}\cdots\text{Ag}$ distances are 3.34 Å within the dimer, and 3.64 Å to the nearest neighbour, generating a “zig-zagged” run of metal-ions or “pillars” through the crystal lattice. The ligands or bases of the dimers are offset by 1.4 Å in height but are coplanar.

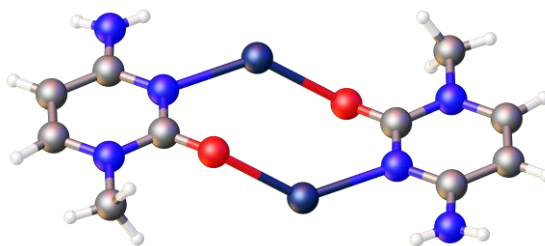


Figure 1.10 Molecular structure for $[\text{Ag}^{\text{I}}-(\text{N}^3\text{-1MeC})]_2$ showing a dimer within the unit cell (P_1). NO_3 anions removed for clarity.⁹⁵

By changing the stoichiometry from 1:1 to 2:1 (ligand to metal ratio) Frontera and Galindo *et al.* have since both demonstrated a fundamental change in the binding mode from N^3, O^2 ($\text{N}^3\text{-Ag}^{\text{I}}\text{-O}^2$) to purely N^3 ($\text{N}^3\text{-Ag}^{\text{I}}\text{-N}^3$).¹⁰⁰ This binding, for obvious reasons, is a more appropriate mimic to that of natural C-rich or C-homo M-DNA.

The second example of silver N^3 -bound to a modified nucleobase which was recently published by the Frontera group, demonstrates another helical structure involves the $\text{C}^*\text{-Ag-C}^*$ (C^* : N^3 -methylcytosine) binding motif (**Figure 1.11**).¹⁰⁰ The *bis*-complexes form a right-handed helix (35.7°) very similar to that of natural DNA ($\sim 36.0^\circ$). This is one of only two known modified nucleobase system (synthetically manufactured) to express a helical disposition upon metal-binding. The tendency to form a double helix in the absence of a sugar (ribose or deoxy-) or phosphate group is intriguing. The $\text{Ag}\cdots\text{Ag}$ distances are very short, ranging between $2.9 - 3.0 \text{ \AA}$, varying slightly down the long unit cell *c*-axis. The bases adopt a *cisoidal* arrangement allowing for π - π interactions. The twisted orientation of bases allows for diagonal intermolecular hydrogen bonding to occur between the carbonyl (O^2) and amino (N^4) groups of neighbouring complexes above and below. These synergistically (inner-helix) stabilising interactions allow for the formation of a double helical structure analogous to that of natural DNA.

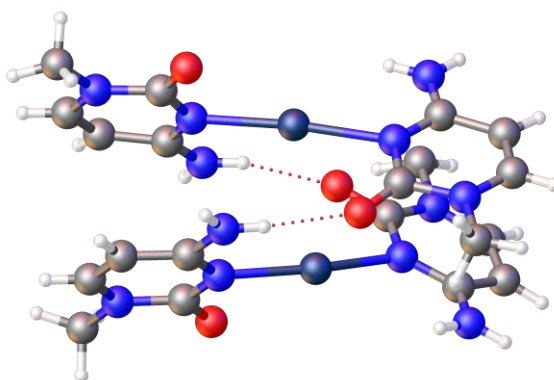


Figure 1.11 Molecular structure for $[\text{Ag}^{\text{I}}-(N^3\text{-1MeC})_2]$ showing two instances of the C- Ag^+ -C complexes stacked and stabilised through intramolecular $O^2\text{-H-}N^4$ hydrogen bonding and $\text{Ag}\cdots\text{Ag}$ argentophilic interactions.¹⁰⁰

The Terrón & Frontera group found a consecutive stacks of $\text{C}^*\text{-Ag-C}^*$ (C^* : N^1 -hexylcytosine) bound through N^3 -coordinations at the expected 2:1 (ligand-to-metal) stoichiometry gave $[\text{Ag}^{\text{I}}-(N^1\text{-hexylcytosine})_2]^+$ in the solid state (**Figure 1.12**).⁸⁶ By extending the modified alkylated site to a hexyl substituent, very little about the fundamental helix changes, as perhaps could be expected. The monomeric *bis*-complex ($\text{C}^*\text{-Ag-C}^*$) units stack to form a double helix analogue the previously mentioned $[\text{Ag}-(1\text{MeC})_2]^+$ complex. Both right- and left-handed helical senses ($\sim 33^\circ$) are observed in the solid-state. $\text{Ag}\cdots\text{Ag}$ distances are fairly unremarkable at 3.1 Å. The solid-state helical assembly is driven by alternating intramolecular hydrogen bonding between the exocyclic O^2 acceptor and the N^4 donor sites of neighbouring complex ions. This method of interaction orientates the ligands to be near perpendicular across the metal ion centre. The alkylated nucleobases show an identical tendency to orientate in a *cisoidal* geometry relative to their adjacent coordination partner.

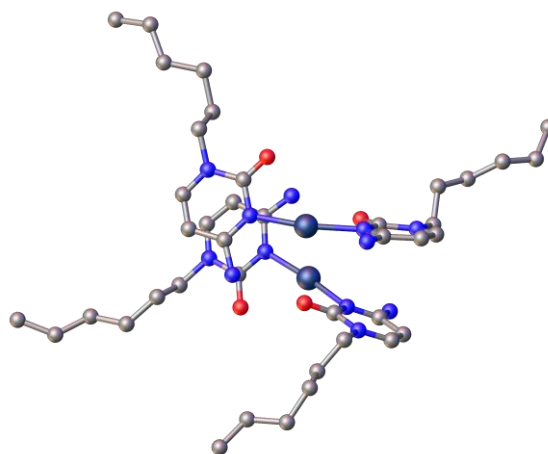


Figure 1.12 Molecular structure for $[\text{Ag}^{\text{I}}-(\text{N}^3-(\text{N}^1\text{-hexylcytosine})_2)]$ showing two instances of the C-Ag⁺-C complexes stacked and stabilised through intramolecular O²-H-N⁴ hydrogen bonding and Ag...Ag argentophilic interactions.¹⁰¹

A third example, published in 1992 by Menzer, Sabat and Lippert describes the structure of a silver-nucleobase complex involving methyl derivatives of both cytosine (1-methylcytosine) and adenine (9-methyladenine) to form $[\text{Ag}^{\text{I}}-(1\text{-MeC}^{\text{N}^3})(9\text{-MeA}^{\text{N}^7})]$ (**Figure 1.13**). The central coordinating silver cation binds strongly across the endocyclic N³ position of cytosine and N⁷ of adenine, with distances of 2.13 and 2.12 Å respectively. This arrangement allows the ligands to be nearly coplanar, granting an intramolecular H-bond between O² (MeC) and N⁶ (MeA) (3.05 Å). A stabilising eight-membered macrocycle is formed. It's interesting to note that the purine adopted a reversed Hoogsteen type conformation, which allows the N⁶ of the MeA and O² of MeC to interact while retaining a near linear 180° coordination geometry across silver cation centre above (166°). It is conceivable that $\text{Ag}^{\text{I}}-(\text{N}^3\text{-MeA})$ could be possible forming a complementary hydrogen bonded arrangement, however the N⁶-O² interactions would lead to a bent conformation across the N-Ag-N coordination. This crystallographic example further illustrates the affinity for silver to coordinate at the N³-site of cytosine, whilst expanding repertoire of nucleobases-silver interactions.

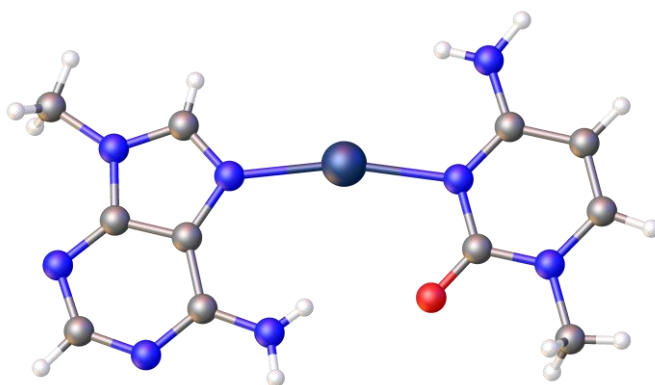


Figure 1.13 Molecular structure for [Ag^I-(1-MeC^{N3})(9-MeA^{N7})].¹⁰²

Until very recently, any reports of natural nucleobase-silver complex were surprisingly absent from the literature given the current surge of interest surrounding metal DNA and its synthetic derivatives. In many ways that is understandable, given that modified analogues were often far easier to grow single crystals for structural characterisation using X-ray diffraction.

Despite the lack of structural clarity surrounding unmodified, C-Ag^I-C, silver-cytosine complexes outside of a duplex, numerous computational and spectroscopic studies have been produced in attempts to address this short-coming. Lopez-Acevedo *et al.* used DFT-based quantum mechanics/molecular mechanics methods in the gas-phase to interrogate the structure and H-bonding within a silver-cytosine tetramer; consisting of two closely positioned *N*³ bound C-Ag^I-C complex ions.¹⁰³ By changing the Ag...Ag distances between 2.8 – 4.4 Å they observed both inter- and intra-molecular hydrogen bonding across the adjacent *N*⁴ and *O*² groups respectively. This simulation predicts that the closely arranged complex ions (with distances around 2.8 Å) could stack to form a series of 1D chains within the solid state supported by stabilizing intermolecular H-bonding, as observed in the modified [Ag^I-(*N*³-1MeC)₂] complex. However, if the metal-metal distances are greater, the stabilising H-bonding occurs intramolecularly. This would likely form independent complex ions in the solid state. These simulations use the assumption that the *transoidal* orientation, not *cisoidal*, has the lowest energy ground state as calculated previously by the co-author Gwinn *et al.* (**Figure 1.14**).⁹¹

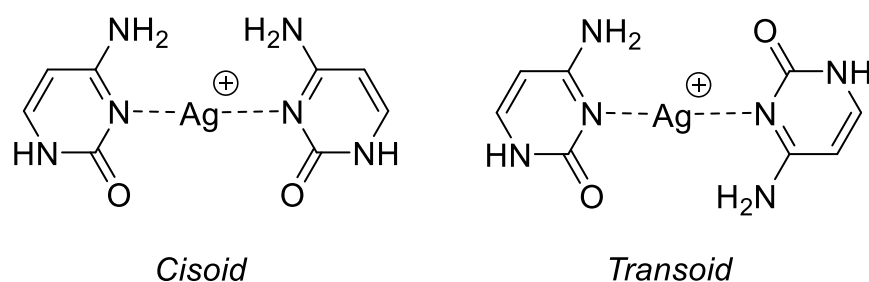


Figure 1.14 *Cisoidal* (*Cis*) and *transoidal* (*Trans*) structural variations of linearly flanking N^3 -bound cytosine bases about a central silver(I) ion.

Ono *et al.* conducted a comprehensive determination of the base pair arrangement for a silver(I) mediated cytosine-cytosine base pair using $^1\text{H}/^{15}\text{N}/^{109}\text{Ag}$ NMR spectroscopy in solution.¹⁰⁴ Their results showed, particularly those from the ^{15}N experiments, that the triplet resonances of the exocyclic N^4 heteroatoms in a C-Ag-C complex existed as an amino group ($-\text{NH}_2$). No isomerization and/or N^4 -Ag coordination was found to occur. At the time of publication, these findings directly discredited Wang *et al.*,¹⁰⁵ who proposed an alternative binding motif involving metal coordination at both the N^3 and O^2 sites based on UV-melting curves (**Figure 1.15**).

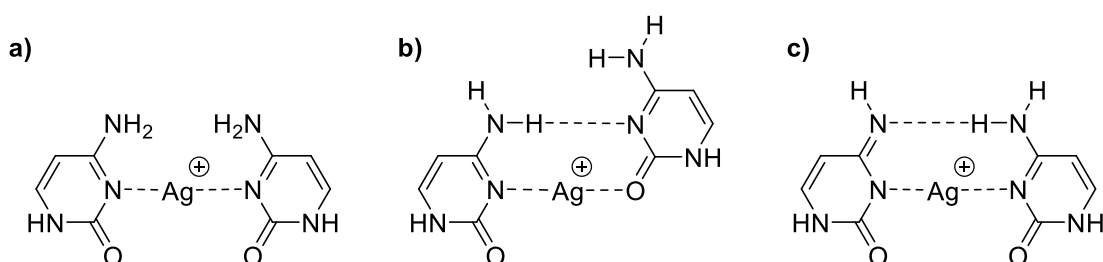


Figure 1.15 a) Structure of C-Ag^I-C with a N^3 -*Cisoidal* arrangement of the complex ion. b) The proposed structure by Wang *et al.* displaying N^3 , O^2 coordination to the central metal ion.¹⁰⁵ c) The most probable isomerized (deprotonated) structure for a N^3 -*cisoidal* silver-cytosine complex ion.¹⁰⁴

1.8. Ag-Nucleoside (Cytidine) Complexes

To date, no silver-cytidine (nucleoside) complexes have been crystallographically characterised outside of the work conducted in this thesis. It is speculative to assume a similar N^3 binding mode would exist, given the preference for such interactions as a *bis*-complex discussed previously.

1.9. Ag-Nucleotide (Cytidine-5'-Monophosphate) Complexes

Cytidine-5'-monophosphate (CMP) has little literature presence as a coordinating ligand, however, it has typically generated polymeric coordination complexes.^{106–109} It has also been noted to be a good supramolecular inducer of chirality.^{106–108} Terrón & Frontera recently reported the first crystallographic structure in the solid state for a silver(I) complex coordinated to the natural ribose nucleotide; CMP (CCDC no. 1562883).¹¹⁰ A 1:1 stoichiometry allows for the coordination of the Ag^+ to CMP *via* both the N^3 and O^2 heteroatoms of flanking cytosine ligands and $O^{7'}$ of the phosphate group from a neighbouring complex (**Figure 1.16**). In many ways, the N-, O- binding motif is reminiscent of the very early base-modified example, $[\text{Ag}^I-(N^3\text{-1MeC})]_2$ discussed earlier. The interconnectivity of the phosphate forms a 3D coordination polymer composed of continuous “zig-zag” runs or pillars of silver ion chains permeating down the *c*-axis, [100] (**Figure 1.17**). The $\text{Ag}\cdots\text{Ag}$ distances are remarkably short at 2.99 Å suggesting argentophilic interaction. Adjacent nucleobases have a plane twist of approximately 90° when looking along the *b*-axis as a consequence of the short Ag^+-Ag^+ distances. The ribose sugar group exists in a 3'-*endo* 'N'-twist conformation. Its chiral metal-organic framework (MOF) or crystal lattice yields further interesting solid-state properties, such as large channels or pores which incorporate solvent into the interior.

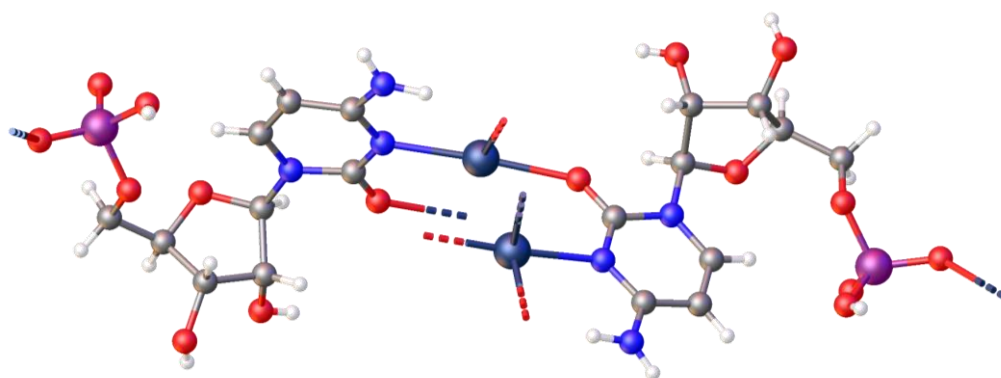


Figure 1.16 Molecular structure for $[\text{Ag}^I-N^3,O^2\text{-Cmp}]$ focusing on the interactions between the endocyclic N^3 donor and exocyclic O^2 acceptor with Ag^+ ($O^2\text{-Ag}^+-N^3$).¹¹⁰

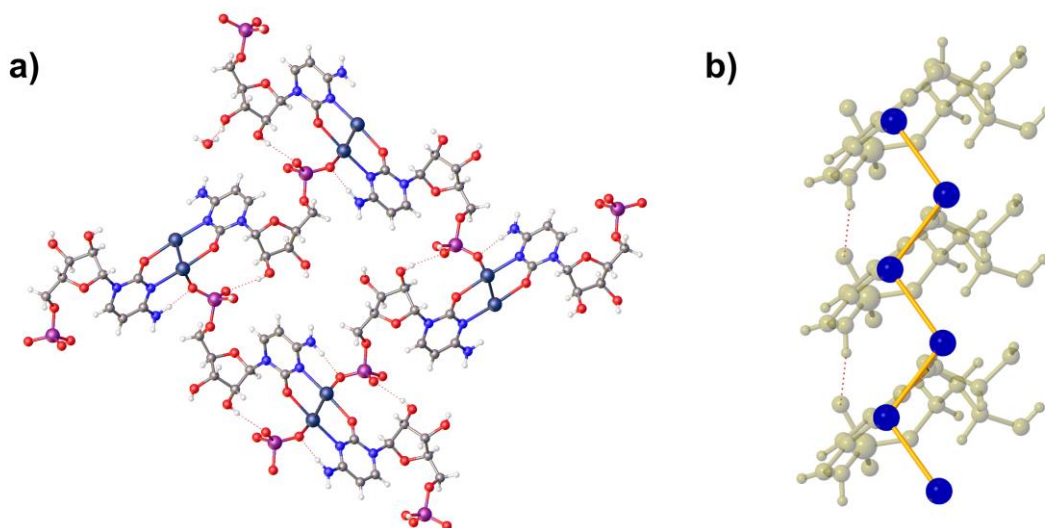


Figure 1.17 a) Top down [100] packing and b) side-sectional view of $[\text{Ag}^{\text{I}}\text{-N}^3, \text{O}^{2-}\text{Cmp}]$ highlighting the contiguous silver ion “zig-zag” 1D pillars within the crystal lattice.¹¹⁰

The weaker $\text{Ag}^+ \text{-O}^{7'}$ phosphate coordination critical for the three-dimensional lattice assembly could be susceptible to cleavage (by chemical or mechanical means), allowing access to lower one- or two- dimensional architecture. Access to molecular sheets or fibres bearing continuous runs of 1D silver chains could yield novel material properties.

1.10. Ag-Oligonucleotide Complexes

The second crystallographically determined structure from a single crystal involving natural metallo-base pair across pyrimidine bases C-Ag-C was formed within RNA.¹¹¹ Kondo *et al.* used a dodecamer $r(5'\text{GGACU}[\text{dC}^{\text{Br}}]\text{GACUCC}_3')$ (dC^{Br} = 5'-bromo-2'-deoxycytosine) (Bold = metal-mediation C-C mismatched sites) designed to be a self-complementary duplex containing two mismatched cytosine-cytosine base pairs (**Figure 1.18**). The dodecamer has modified $^{\text{Br}}\text{C}$ units at the fifth position to avoid phase issues during crystallisation, *i.e.* the loss of information during high-resolution diffraction of the crystal ($<1.2 \text{ \AA}$). Metal-mediation of the silver(I) ions occurs between these two mismatched sites generating the familiar linear ($177\text{-}180^\circ$) *bis*-coordination across the silver(I) ion. Both instances display *cisoidal* coplanar orientation with Ag-N^3

distances of 2.2 – 2.3 Å. The propeller twist angles of the two metallated sites is relatively large (-27 – -29°), compared with that of naturally duplexed A-form RNA (-12°).

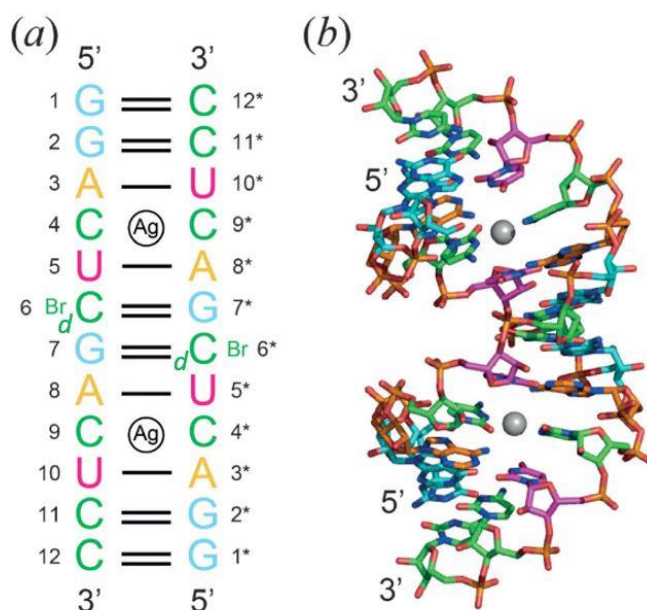


Figure 1.18 The secondary (a) and crystal structure of the silver-mediated RNA (A-form) duplex. The helix features two C-Ag-C coordination modes which do not interrupt the conical Watson-Crick base pair hybridisation.¹¹¹ *Reproduced with the permission of John Wiley and Sons.

Following the publication of the metal-mediated RNA structure, Kondo *et al.*⁹⁹ successfully determined the structure for a short dodecamer DNA hybrid duplex (Right-handed antiparallel, B-form) bearing a continuous one-dimensional array of uninterrupted silver ions in-place of the core Watson-Crick base pairing (**Figure 1.19**).⁹⁹ Ag-Ag distances are between 3.1 – 3.4 Å (average 3.2 Å). Unlike any of the previous C-Ag-C examples, they have demonstrated a range of alternative coordination modes; G-Ag-G, G-Ag-C and T-Ag-T. The binding types described here open up the range of possibilities for Ag-mediated systems. The authors went to some length to describe this system as a molecular wire without sufficient cause. The contiguous array of closely aligned silver ions along the helical axis was thought to allow electron transport, analogous to a wire, however such properties have yet to be experimentally tested.

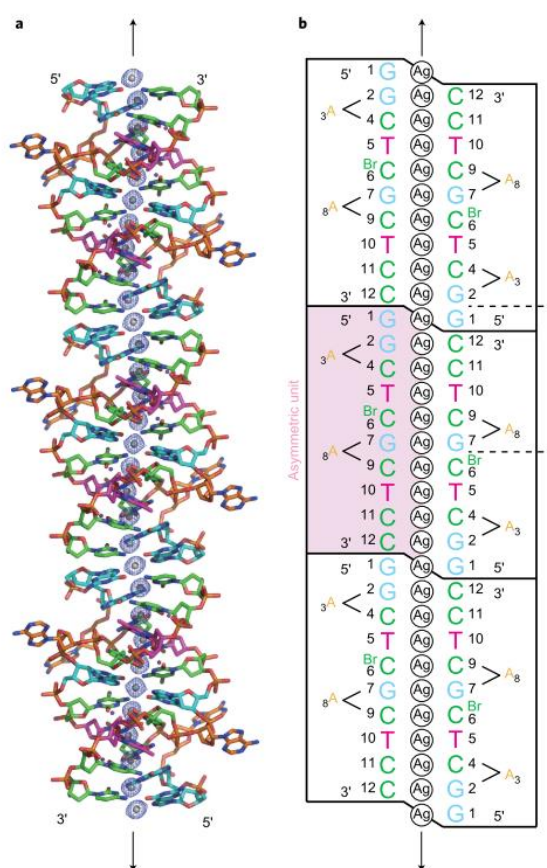


Figure 1.19 The crystal (a) and secondary (b) structure of the silver-mediated DNA $d(\text{GGACT}(\text{BrC})\text{GACTCC})$ forming a B-form duplex. The helix features an uninterrupted array of silver ions down the c-axis, [100]. Metal-mediation is observed across C-C, G-G, G-C and T-T base pairs.⁹⁹ *Reproduced with the permission of Springer Nature.

Despite the high level of interest in silver-oligonucleotide systems, examples with crystallographically determined structures are few. This is due to in part the dynamic irregularity of DNA leading to high entropy, which is not conducive to regular alignment within a lattice necessary for the formation a crystal. Fortunately, many other spectroscopic methods (CD and ESI-MS) have become well established tools for the analysis of bonding events when forming M-DNA. One such example, by Dickson *et al.*, has shown the capture of silver ions within a short homo-C oligonucleotide, $d\text{C}_{12}$.¹¹² Their investigation focused on a homo-C 12mer ($d\text{C}_{12}$) oligonucleotide that readily coordinates with a 6:1 addition of Ag^+ in an aqueous solution. Their results conclude

that interactions between the two occur, as observed by multiple new species in the MS correlating to 2 - 7 bound Ag^+ per oligo (**Figure 1.20**).

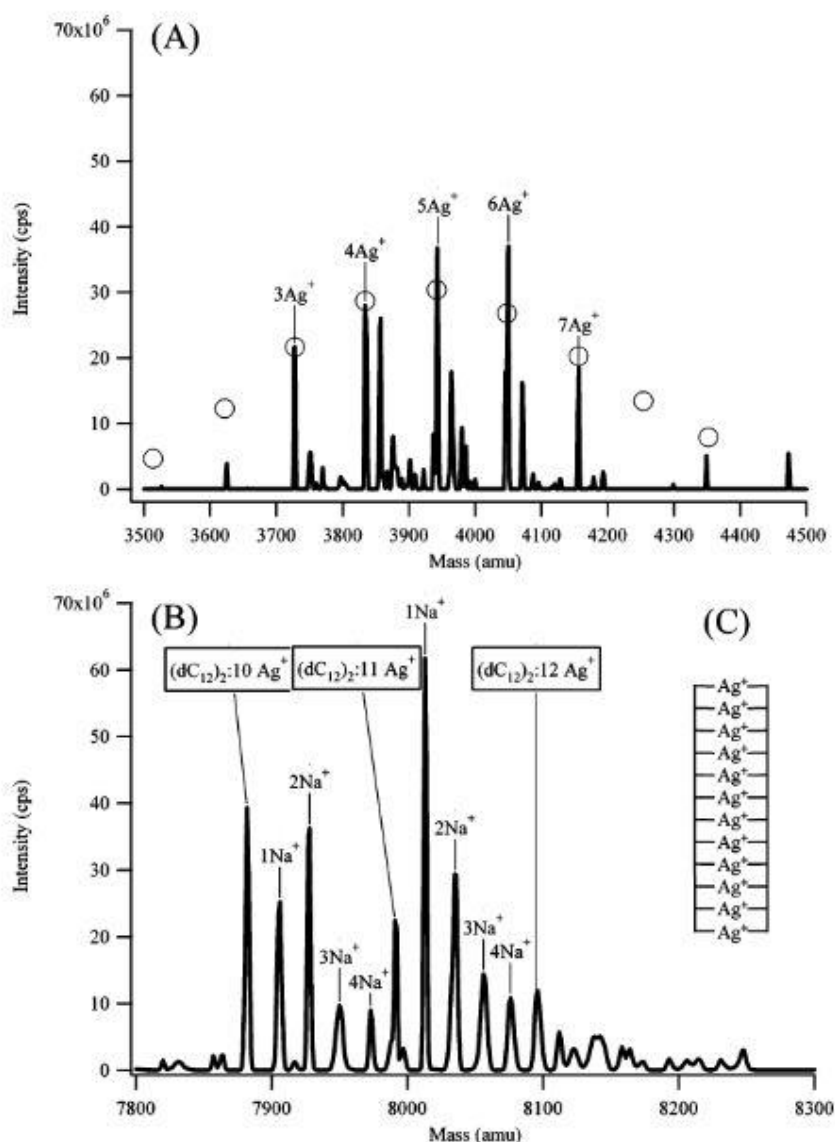


Figure 1.20 ESI-MS data directly from Dickson's publication showing the formation of multiple species relating to (a) $\text{Ag}^+_n:\text{dC}_{12}$ complex in solution and (b) $\text{Ag}^+_n:(\text{dC}_{12})_2$ forming duplexed M-DNA species. The Na^+ adducts are stabilized by the high negative charge density of the phosphodiester backbone (inset (c) illustrates a metal-mediated ladder of the M-DNA system).¹¹² *Reproduced with the permission of ACS Publications.

In summary, such direct techniques can readily detail interactions between the oligomer and metal ion. Based off these findings, we can further expand the range of and complexity of oligo substrates as demonstrated by the authors.⁹ It is plausible that the species observed in **Figure 1.20** formed a hairpin loop structure; in keeping with a

2:1 C-Ag stoichiometry. Unfortunately, the structural details were not probed further. Calorimetry experiments (e.g. Isothermal titration calorimetry) would be able to quantify Ag^I-C binding events and therefore be able to deduce if a single bonding/coordination event occurred *versus* two; as expected in the C-Ag⁺-C *bis*-complexation. A frame of reference would be required to quantify the amount of energy liberated or absorbed for a single Ag-C coordination event. From this, the number of coordination events per oligo could be used to determine the exact quantity of bonds per Ag⁺. Two binding events per oligo (2:1) would be indicative of a hairpin; the oligo folds to form a loop which facilitates the second C-Ag⁺-C interaction. If the measured enthalpy of the system only represented a single coordination per oligo, the system would be 1:1, and therefore single site coordination. A single coordination would not be conducive towards hairpin formation.

Dickson *et al.* made use of these Ag⁺:dC₁₂ complexes by subsequently chemically reducing the metal ions using BH₄⁻, yielding silver nanoparticles/clusters as evident from the number of transitions in the fluorescence and absorption spectra (typically observed in the range 200 and 400 nm). Various other research groups have used this approach to obtain stabilised few atom nano-clusters (NCs) or -particles (NPs). Recently, the Dickson group has published crystallographic evidence of silver nanocluster (NC) formation, templated on a DNA scaffold. Fluorescent Ag₈ clusters were stabilised upon a multistrand mismatched DNA scaffold (sequence: AACCCC or A₂C₄) yielding [(A₂C₄)₂Ag₈] (**Figure 1.21**).¹¹³ The crystal describes a short duplex or double stranded structure with two different metal-binding regions, the first involves three metal mediated C-Ag-C sites bound through the expected endocyclic N³ heteroatoms and the second region is composed of a rarely observed N,O bonding motif. The silver ions, which are found as a linear run when bound across cytosine ligands (2:1 ratio), changes to adopt a “zig-zag” arrangement (1:1 ratio) as they approach and coordinated between adenosine (A) sites. Binding alternates between the exocyclic N⁶ and endocyclic N¹ donors. Ag...Ag distances within the adenosine region are shorter than found between cytosine bases, at ~2.9 Å vs. ~3.1-3.4 Å. Fluorescence is observed from the crystal when excited at 405 nm. Emission shift from blue to green upon chemical- or photo-reduction yielding a ~100-fold increase in emission intensity owed to NC formation. The stability and structural features described by DNA-templation offer an intriguing route towards highly emissive biomolecules-metallocluster systems.

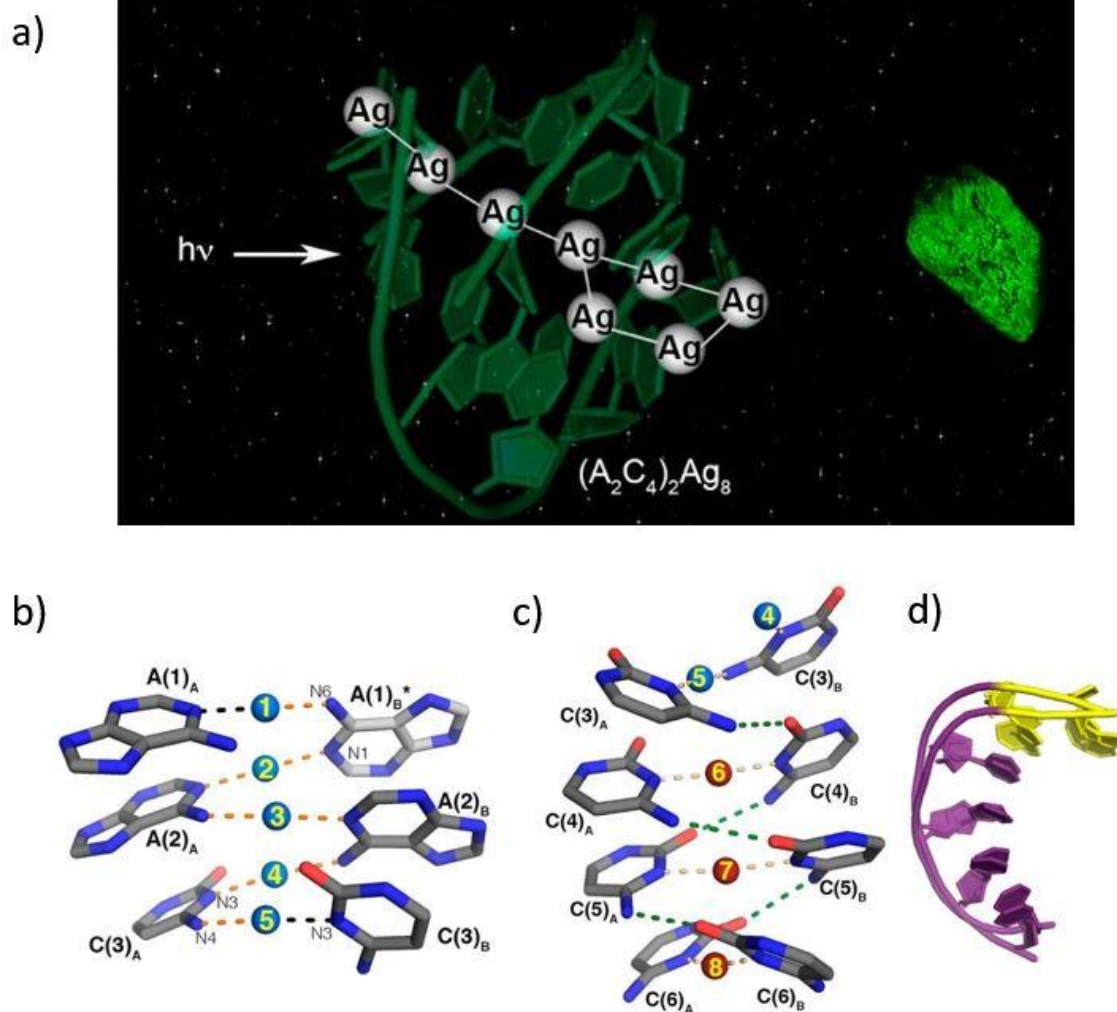


Figure 1.21 a) The crystal and structure of Dickson's fluorescent Ag_8 clusters templated upon a multistrand mismatched DNA scaffold yielding $[(\text{A}_2\text{C}_4)_2\text{Ag}_8]$. The b) adenosine and c) cytosine silver binding regions. d) The DNA-host conformation dictated by the silver interactions.¹¹³ *Reproduced with the permission of ACS Publications.

1.11. Application of M-DNA Systems Based on Silver-Pyrimidine Coordination

1.12. Nanoparticles or Clusters

Nanoparticles (NPs) are zero-dimensional particulates with core sizes ranging from 10-100 nm and have attracted a huge amount of attention over the past decade due to substantial size-dependent differences *versus* their bulk counterparts.^{114,115} Bulk

metals are excellent conductors, due to the freely delocalised electrons in the conductance band. NPs have been shown to display intense colour, due to their surface plasmon resonance caused by the collective oscillation of the conductance electrons interacting with light. Their size dependent properties give them a diverse portfolio of potential applications in nanoscale catalysis⁷⁶, data storage, molecular imaging¹¹⁶, biosensors, drug delivery⁷⁶ and nanomedicine.^{73,114,115,117}

Sub 1 nm particles consisting of several to tens of atoms or molecules are called nanoclusters (NCs), quantum clusters/dots (QCs/QDs) or metal clusters.^{76,118} At these size-regimes the electronic levels are discrete as they possess sizes comparable to the Fermi wavelength.¹¹⁵ The electrons of metal atoms are confined in molecular dimensions allowing for molecular or single atom like energy gaps compared to the continuous band experienced by bulk material (**Figure 1.22**). Its these discrete energy levels that allow for electronic transitions lead to strong photoluminescent due to quantum confinement effects, differentiating them from their larger NP (nanoparticle) counterparts. This is due to the loss of their size-related plasmonic properties. The loss of the plasmon resonance is due to the discrete level structure. If there is a discrete level structure, the valence electrons are no longer in a metallic state.¹¹⁵

Discrete molecular-like electronic transitions, size-dependent photophysical properties (luminescence) and in some cases magnetism have generated a wide array of interest in the synthesis of atomically precise cluster with a high monodispersity. The catalytic properties of clusters, both supported and unsupported, have been extensively explored.^{118–121} A range of noble metals (ruthenium, rhodium, palladium, silver, osmium, iridium, platinum and gold) have been investigated including their alloys. The size regime of NCs however, presents a unique challenge for chemists as they are far more difficult to synthesis and characterise when compared to their larger NP counterparts.

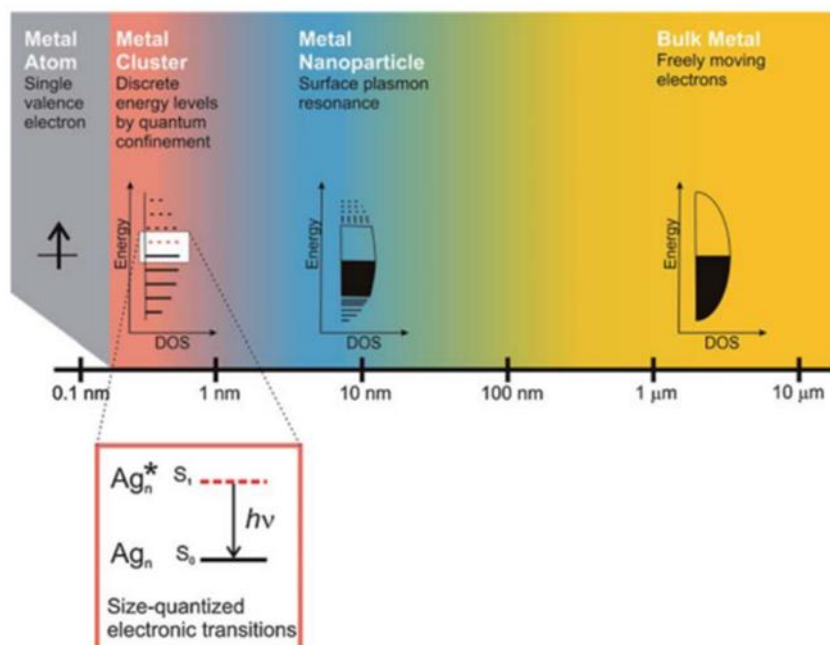


Figure 1.22 Size effects on metals, showing continuous bands of energy levels for bulk and nanoparticles, discrete energy levels for nanoclusters which bridge the gap between single atoms and nanoparticles allowing interactions with light by electronic transmission.¹²² *Reproduced with the permission of Springer Science + Business Media.

Several protocols exist for the synthesis of NCs with the aim of controlling cluster size, shape or functionality. Methods usually fall into two categories, bottom-up or top-down.^{76,118} A traditional bottom-up technique, known as the Brust-Schiffrin method, by Brust *et al.* use a two-phase synthesis (org/aq) utilizing a phase transfer agent moving the metal ion precursor into organic phase generating thiol capped nanoparticle.¹²³ Alternative bottom-up methods usually rely on wet chemistry methods reducing a metal-ions in the presence of ligands to achieve clusters, which incorporate: radiolytic, electrochemical, microwave assisted, microemulsion, solid state, sonochemical, photoreduction and template-based routes.⁷⁶ Top-down methods rely on the manipulation of bulk materials, *i.e.* ligand-exchange or etching from larger NPs.⁷⁶

Various methods have been used to stabilize NCs that include monolayers (Thiol capped, oxide layers),^{115,123–126} scaffolds (Dendrimers, polymers, short molecules, DNA, proteins and peptides)^{8,10,16,122,127–129} and microemulsions^{130–134}. DNA in particular has been shown to be a very effective scaffold due to the unique relationship observed through metal-mediation. The ability to design and build oligonucleotides

using “bottom-up” assembly techniques affords the opportunity to package atomically precise numbers of atoms.¹¹² Microemulsions have become a very attractive method of maintaining NCs in solution as they offer a physical barrier against aggregation of the particles.

It's those highly sensitive dimensional properties that give nanoclusters the ability to be tuned effectively by their core size. Dickson *et al.* generated a series of Ag-NCs encapsulated in single-stranded DNA (ss-DNA) that when reduced, generated a range of controlled Ag-NCs sizes which exhibited IR, red, green, blue and UV emissions.^{11,135} Bigioni *et al.* demonstrated how absorption was linked to particle core size in gold and silver bound nanoclusters with glutathione ligands using electrophoresis to separate bands containing “magic-numbers” of atoms.¹³⁶ Magic-number theory was developed to explain the tendency (narrow size distribution) and stability for certain cluster sizes.^{136,137} A reduction in a clusters surface energy exist more for certain sizes of cluster than those with semi-stabilized magic numbers (also known as the Jellium model^{138,139}), therefore a larger number of these clusters persist in a in solution.^{76,115,140} Without further stabilization those NCs tend to aggregate irreversibly which reduces their individual surface energies. Those larger aggregates with stabilised energies form NPs or bulk material. One interesting method of avoiding this would be to isolate the newly formed NPs within a microemulsion.¹³⁴

1.13. Molecular Wires

Molecular wires or nanowires (NWs) are a highly active area of research due to their potential application as electrically conducting (including semi-conducting and insulating)^{12,14,15,56,62,141,142}, sensing^{5,77} or biomedical materials of the future.^{5,14} From both an academic and industrial perspective such one-dimensional (1D) materials offer unique properties of value. To date, examples of molecular wires exist using Silver (Ag), Gold (Au), Copper (Cu), Zinc (Zn), Platinum (Pt), Palladium (Pd), Ruthenium (Ru) ions.⁵⁶

NWs offer several properties owed to their dimensions, such as a high surface-to-volume ratios (S/V), tunability and ease of preparation. Their finite or quantum size effects present a basis for the investigation and exploration of novel and interesting phenomena in physics, chemistry, biology and material science. Their large S/V can often be found to offer superior sensing abilities that those found by traditional chemical

surface techniques.¹⁴³ Furthermore, a tuneable bandgap has been observed for materials small enough to induce quantum confinement. Unfortunately, this has often been somewhat out of reach for many NWs as their dimensions are often too large in achieving quantum confinement.

Two distinct classes of M-DNA molecular wire exist; Outer-helix and Inner-Helix (**Figure 1.23**). The nomenclature effectively describes the interaction site between the metal-ions and DNA.

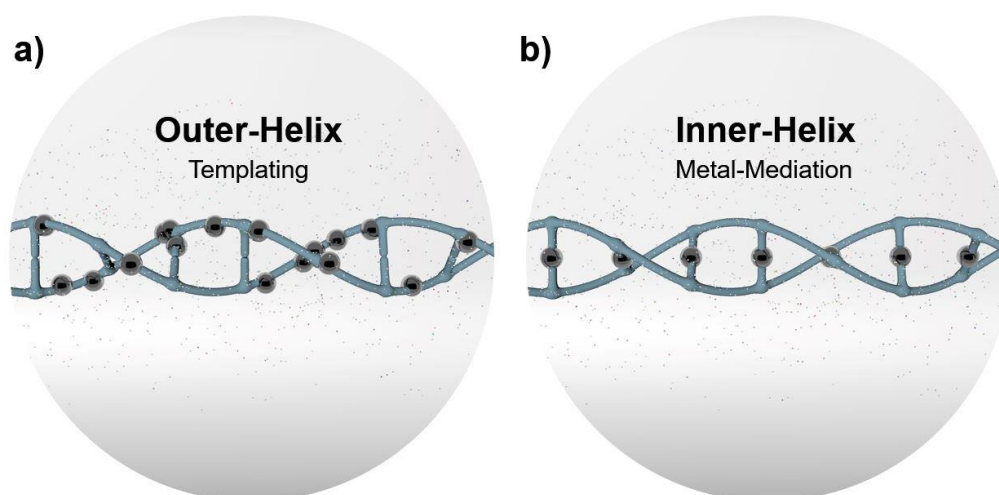


Figure 1.23 Methods of constructing M-DNA; a) Templating (a truly conductive nanowire would possess a more complete coating of metallic particles than is illustrated) vs. b) metal-mediation or molecular wire.

Outer-helix molecular wires are usually the result of metal-ions binding to the surface or grooves around a DNA scaffold. These methods have also been described as templating. Interactions can occur directly or indirectly through hydrogen bonding of the coordinating water molecules surrounding the structure.¹⁴⁴ Alternatively, direct coordination with bases *via* the major helical grooves (*i.e.* *cis-platin*¹⁴⁵) or with the phosphodiester backbone.¹⁴⁴ Braun *et al.* first described the successful templating of silver onto a DNA scaffold generating conducting nanowires that are 12 μm long and 100 nm wide. A three-step method was employed involving the selective localization of Ag^+ ions, Ag^+/Na^+ ion exchange and finally formation of the Ag^+ of the complex between the DNA and ions. Subsequently, Richter *et al.* and Ford *et al.* have published

work concerned with the metallization of DNA with palladium and platinum generating nanowires using templating methods very similar method to those described.^{14,142}

Inner-helix molecular wires are generated through coordination bonds within the axial core of DNA replacing the base pair hydrogen bonding interactions with metal-mediation or metal-modified base pairing. Functionalising the core of DNA with a continuous core of metal ions that are surrounded by π -stacked nucleobase units stabilised by a sugar-phosphodiester backbone has become of particular interest due to their precise composition and atom efficiency. It has been proposed that the argentophilic interactions between axially adjacent metal ions can lead to the compression of inter-pair bonding lengths from 3.4 to 3.3 Å of B-form DNA.⁷⁸ The proximity generated by the attractive interaction between adjacent silver cations has led to speculation of their electron transport credentials.⁷⁸ To date, no evidence exists of conductivity from such functionalised DNA species with continuous silver ion core despite two examples being identified.⁹⁹

1.14. Conclusions

This introductory chapter has described the key examples of silver-pyrimidine chemistry following a survey of current and past literature. The materials and structures discussed all share a unique affinity with Ag^+ , making them ideal model systems for future M-DNA or nanomaterial applications. The use and scope of silver as a metal-mediator has been explored across a range of cytosine analogues, highlighting its preference to bind linearly across two endocyclic *N*-donor sites ($\text{C-Ag}^{\text{I}}\text{-C}$) generally forming *bis*-complexes.

1.15. Scope for Investigation

Whilst there exists several well-developed systems utilising the established $\text{C-Ag}^{\text{I}}\text{-C}$ silver-DNA interaction outlined within this chapter, there are some concepts or variations that are yet to be explored. Despite the resurgence of interest in silver-pyrimidine chemistry, virtually all of the fundamental cytosine derived structures based on natural DNA are notably absent from the literature or crystallography databases. It seems prudent first to address these shortcomings. The structural details and nuances may help design alternative M-DNA systems.

The aim of manufacturing molecular wire with self-assembly characteristics would be remarkable. To date, most molecular wires possessing conductive properties are based upon a multi-step templating approach upon a non-conductive DNA scaffold. By utilizing the highly specific silver-cytosine interactions, a molecular wire could be achieved with in a single step.

Furthermore, the secondary structures of DNA offer a diversity of structural traits applicable towards the fabrication of nanostructures. Hairpin loops for example, have been designed as methods of accessing discrete metal packets of known quantity suitable for controlled bottom-up nanocluster formation. Many of these examples describe metal-coordination at a C-rich loop-region, yet the stem-region is equally capable.

References

- (1) Kelly, M. J. Intrinsic Top-down Unmanufacturability. *Nanotechnology* **2011**, 22 (24), 5–8. <https://doi.org/10.1088/0957-4484/22/24/245303>.
- (2) Sigel, A.; Sigel, H.; Sigel, R. K. O. *Metal Ions in Life Sciences*; Springer: Zurich, Switzerland, 2005; Vol. 10. <https://doi.org/10.1017/CBO9781107415324.004>.
- (3) Yan, Y.; Zhang, J.; Ren, L.; Tang, C. Metal-Containing and Related Polymers for Biomedical Applications. *Chem. Soc. Rev.* **2016**, 45 (19), 5232–5263. <https://doi.org/10.1039/c6cs00026f>.
- (4) Ono, A.; Torigoe, H.; Tanaka, Y.; Okamoto, I. Binding of Metal Ions by Pyrimidine Base Pairs in DNA Duplexes. *Chem. Soc. Rev.* **2011**, 40 (12), 5855–5866. <https://doi.org/10.1039/c1cs15149e>.
- (5) Ramgir, N. S.; Yang, Y.; Zacharias, M. Nanowire-Based Sensors. *Small* **2010**, 6 (16), 1705–1722. <https://doi.org/10.1002/sml.201000972>.
- (6) Houlton, A. New Aspects of Metal - Nucleobase Chemistry. *Adv. Inorg. Chem.* **2002**, 53, 87–158.
- (7) Peng, Z.; Liu, H. Bottom-up Nanofabrication Using DNA Nanostructures. *Chem. Mater.* **2016**, 28 (4), 1012–1021. <https://doi.org/10.1021/acs.chemmater.5b04218>.
- (8) Copp, S. M.; Schultz, D. E.; Swasey, S.; Gwinn, E. G. Atomically Precise Arrays of Fluorescent Silver Clusters: A Modular Approach for Metal Cluster Photonics on DNA Nanostructures. *ACS Nano* **2015**, 9 (3), 2303–2310. <https://doi.org/10.1021/nn506322q>.
- (9) Petty, J. T.; Zheng, J.; Hud, N. V.; Dickson, R. M. DNA-Templated Ag Nanocluster Formation. *J. Am. Chem. Soc.* **2004**, 126 (16), 5207–5212. <https://doi.org/10.1021/ja031931o>.
- (10) Sengupta, B.; Corley, C.; Cobb, K.; Saracino, A.; Jockusch, S. DNA Scaffolded Silver Clusters: A Critical Study. *Molecules* **2016**, 21 (2), 1–15. <https://doi.org/10.3390/molecules21020216>.

- (11) Hsiang, J.-C.; Antoku, Y.; Gonzalez, J. I.; Richards, C. I.; Dickson, R. M.; Vosch, T. Strongly Emissive Individual DNA-Encapsulated Ag Nanoclusters as Single-Molecule Fluorophores. *Proc. Natl. Acad. Sci.* **2007**, *104* (31), 12616–12621. <https://doi.org/10.1073/pnas.0610677104>.
- (12) Dong, L.; Hollis, T.; Connolly, B. A.; Wright, N. G.; Horrocks, B. R.; Houlton, A. DNA-Templated Semiconductor Nanoparticle Chains and Wires. *Adv. Mater.* **2007**, *19* (13), 1748–1751. <https://doi.org/10.1002/adma.200602543>.
- (13) Watson, S. M. D.; Pike, A. R.; Pate, J.; Houlton, A.; Horrocks, B. R. DNA-Templated Nanowires: Morphology and Electrical Conductivity. *Nanoscale* **2014**, *6* (8), 4027–4037. <https://doi.org/10.1039/c3nr06767j>.
- (14) Stoltenberg, R. M.; Woolley, A. T. DNA-Templated Nanowire Fabrication. *Biomed. Microdevices* **2004**, *6* (2), 105–111. <https://doi.org/10.1023/B:BMMD.0000031746.46801.7d>.
- (15) Braun, E.; Eichen, Y.; Sivan, U.; Ben-Yoseph, G. DNA-Templated Assembly and Electrode Attachment of a Conducting Silver Wire. *Nature* **1998**, *391* (6669), 775–778. <https://doi.org/10.1038/35826>.
- (16) Guo, W.; Yuan, J.; Dong, Q.; Wang, E. Highly Sequence-Dependent Formation of Fluorescent Silver Nanoclusters in Hybridized DNA Duplexes for Single Nucleotide Mutation Identification. *J. Am. Chem. Soc.* **2010**, *132* (3), 932–934. <https://doi.org/10.1021/ja907075s>.
- (17) Park, S.; Choi, S.; Yu, J. DNA-Encapsulated Silver Nanodots as Ratiometric Luminescent Probes for Hypochlorite Detection. *Nanoscale Res. Lett.* **2014**, *9* (1), 1–7. <https://doi.org/10.1186/1556-276X-9-129>.
- (18) Yeh, H. C.; Sharma, J.; Han, J. J.; Martinez, J. S.; Werner, J. H. A DNA-Silver Nanocluster Probe That Fluoresces upon Hybridization. *Nano Lett.* **2010**, *10* (8), 3106–3110. <https://doi.org/10.1021/nl101773c>.
- (19) Hughes, R. A.; Ellington, A. D. Synthetic DNA Synthesis and Assembly: Putting the Synthetic in Synthetic Biology. *Cold Spring Harb. Perspect. Biol.* **2017**, *9* (1), 1–18. <https://doi.org/10.1101/cshperspect.a023812>.

- (20) Tanaka, K.; Yamada, Y.; Shionoya, M. Formation of Silver(I)-Mediated DNA Duplex and Triplex through an Alternative Base Pair of Pyridine Nucleobases. *J. Am. Chem. Soc.* **2002**, *124* (30), 8802–8803. <https://doi.org/10.1021/ja020510o>.
- (21) Sinden, R. R. DNA Structure and Function. *DNA Struct. Funct.* **2012**, *282*, 1–398. <https://doi.org/10.1016/C2009-0-02451-9>.
- (22) J. D. Watson, F. H. C. C. A Structure for Deoxyribose Nucleic Acid. *Mol. Struct. Nucleic Acids* **1953**, *171* (4356), 737–738.
- (23) Wing, R.; Drew, H.; Takano, T.; Broka, C.; Tanaka, S.; Itakura, K.; Dickerson, R. E. Crystal Structure Analysis of a Complete Turn of B-DNA. *Nature* **1980**, *287* (5784), 755–758. <https://doi.org/10.1038/287755a0>.
- (24) Chargraff, E.; Lipshitz, R.; Green, C.; Hodes, M. E. Of the Desoxyribonucleic Salmon Sperm*. *J. Biol. Chem.* **1951**, *192*, 223–230.
- (25) Church, G. M.; Gao, Y.; Kosuri, S. Next-Generation Digital Information Storage in DNA. *Science* (80-.). **2012**, *337* (6102), 1628. <https://doi.org/10.1126/science.1226355>.
- (26) Schwartz, J. J.; Quake, S. R. Single Molecule Measurement of the “Speed Limit” of DNA Polymerase. *Proc. Natl. Acad. Sci. U. S. A.* **2009**, *106* (48), 20294–20299. <https://doi.org/10.1073/pnas.0907404106>.
- (27) Arnott, S. Historical Article: DNA Polymorphism and the Early History of the Double Helix. *Trends Biochem. Sci.* **2006**, *31* (6), 349–354. <https://doi.org/10.1016/j.tibs.2006.04.004>.
- (28) Ussery, D. W. DNA Structure: A-, B- and Z-DNA Helix Families. *Encycl. Life Sci.* **2002**, No. 1998, 1–7. <https://doi.org/10.1038/npg.els.0003122>.
- (29) Rich, A. The Double Helix: A Tale of Two Puckers. *Nat. Struct. Biol.* **2003**, *10* (4), 247–249. <https://doi.org/10.1038/nsb0403-247>.
- (30) Caruthers, M. H.; McBride, L. J.; Bracco, L. P.; Dubendorff, J. W. Studies on Nucleotide Chemistry 15. Synthesis of Oligodeoxynucleotides Using Amidine Protected Nucleosides. *Nucleosides and Nucleotides* **1985**, *4* (1–2), 95–105. <https://doi.org/10.1080/07328318508077833>.

- (31) Jain, A.; Wang, G.; Vasquez, K. M. DNA Triple Helices: Biological Consequences and Therapeutic Potential. *Biochimie* **2008**, *90* (8), 1117–1130. <https://doi.org/10.1016/j.biochi.2008.02.011.DNA>.
- (32) Keniry, M. A. Quadruplex Structures in Nucleic Acids. *Biopolymers* **2001**, *3* (56), 123–146.
- (33) Johnson, A. T.; Schlegel, M. K.; Meggers, E.; Essen, L. O.; Wiest, O. On the Structure and Dynamics of Duplex GNA. *J. Org. Chem.* **2011**, *76* (19), 7964–7974. <https://doi.org/10.1021/jo201469b>.
- (34) Chen, J.; Seeman, N. C. Synthesis from DNA of a Molecule with the Connectivity of a Cube. *Jacquier, A. Dujon, B. Biochim.* **1987**, *50* (April), 133–139.
- (35) Seeman, N. C. Nucleic Acid Junctions and Lattices. *J. Theor. Biol.* **1982**, *99* (2), 237–247. [https://doi.org/10.1016/0022-5193\(82\)90002-9](https://doi.org/10.1016/0022-5193(82)90002-9).
- (36) Zheng, J.; Birktoft, J. J.; Chen, Y.; Wang, T.; Sha, R.; Constantinou, P. E.; Ginell, S. L.; Mao, C.; Seeman, N. C. From Molecular to Macroscopic via the Rational Design of a Self-Assembled 3D DNA Crystal. *Nature* **2009**, *461* (7260), 74–77. <https://doi.org/10.1038/nature08274>.
- (37) Seeman, N. C. Nanotechnology and the Double Helix. *Sci. Am.* **2004**, *290* (6), 64–75. <https://doi.org/10.1038/scientificamerican0604-64>.
- (38) Lah, J.; Seručnik, M.; Vesnaver, G. Influence of a Hairpin Loop on the Thermodynamic Stability of a DNA Oligomer. *J. Nucleic Acids* **2011**, *2011*, 1–9. <https://doi.org/10.4061/2011/513910>.
- (39) Swadling, J. B.; Ishii, K.; Tahara, T.; Kitao, A. Origins of Biological Function in DNA and RNA Hairpin Loop Motifs from Replica Exchange Molecular Dynamics Simulation. *Phys. Chem. Chem. Phys.* **2018**, *20* (5), 2990–3001. <https://doi.org/10.1039/c7cp06355e>.
- (40) Bikard, D.; Loot, C.; Baharoglu, Z.; Mazel, D. Folded DNA in Action: Hairpin Formation and Biological Functions in Prokaryotes. *Microbiol. Mol. Biol. Rev.* **2010**, *74* (4), 570–588. <https://doi.org/10.1128/mmbr.00026-10>.
- (41) Green, S. J.; Lubrich, D.; Turberfield, A. J. DNA Hairpins: Fuel for Autonomous

- DNA Devices. *Biophys. J.* **2006**, *91* (8), 2966–2975. <https://doi.org/10.1529/biophysj.106.084681>.
- (42) Erie, D.; Olson, W.; Jones, R.; Breslauer, K.; Sinha, N. A Dumbbell-Shaped, Double-Hairpin Structure of DNA: A Thermodynamic Investigation. *Biochemistry* **1987**, *26* (22), 7150–7159. <https://doi.org/10.1021/bi00396a042>.
- (43) Yu, H.; Jiang, X.; Tan, K. T.; Hang, L.; Patzel, V. Efficient Production of Superior Dumbbell-Shaped DNA Minimal Vectors for Small Hairpin RNA Expression. *Nucleic Acids Res.* **2015**, *43* (18). <https://doi.org/10.1093/nar/gkv583>.
- (44) Jiang, X.; Yu, H.; Teo, C. R.; Tan, G. S. X.; Goh, S. C.; Patel, P.; Chua, Y. K.; Hameed, N. B. S.; Bertoletti, A.; Patzel, V. Advanced Design of Dumbbell-Shaped Genetic Minimal Vectors Improves Non-Coding and Coding RNA Expression. *Mol. Ther.* **2016**, *24* (9), 1581–1591. <https://doi.org/10.1038/mt.2016.138>.
- (45) Sinden, R. R.; Pytlos-Sinden, M. J.; Potaman, V. N. Slipped Strand DNA Structures. *Front. Biosci.* **2007**, *12* (13), 4788–4799. <https://doi.org/10.2741/2427>.
- (46) Xodo, L. E.; Manzini, G.; Quadrifoglio, F.; Van Der Marel, G.; van Boom, J. DNA Hairpin Loops in Solution. Correlation between Primary Structure, Thermostability and Reactivity with Single-Strand-Specific Nuclease from Mung Bean. *Nucleic Acids Res.* **1991**, *19* (7), 1505–1511. <https://doi.org/10.1093/nar/19.7.1505>.
- (47) Rentzeperis, D.; Alessi, K.; Marky, L. A. Thermodynamics of DNA Hairpins: Contribution of Loop Size to Hairpin Stability and Ethidium Binding. *Nucleic Acids Res.* **1993**, *21* (11), 2683–2689. <https://doi.org/10.1093/nar/21.11.2683>.
- (48) Xiao, Y.; Wu, Z.; Wong, K. Y.; Liu, Z. Hairpin DNA Probes Based on Target-Induced in Situ Generation of Luminescent Silver Nanoclusters. *Chem. Commun.* **2014**, *50* (37), 4849–4852. <https://doi.org/10.1039/c4cc01154f>.
- (49) Jash, B.; Müller, J. Metal-Mediated Base Pairs: From Characterization to Application. *Chem. - A Eur. J.* **2017**, *23* (68), 17166–17178. <https://doi.org/10.1002/chem.201703518>.

- (50) Hartenstine, M. J.; Goodman, M. F.; Petruska, J. Base Stacking and Even/Odd Behavior of Hairpin Loops in DNA Triplet Repeat Slippage and Expansion with DNA Polymerase. *J. Biol. Chem.* **2000**, 275 (24), 18382–18390. <https://doi.org/10.1074/jbc.275.24.18382>.
- (51) Kim, S.; Gang, J. The Detection of a Mismatched DNA by Using Hairpin DNA-Templated Silver Nanoclusters. *Anal. Biochem.* **2018**, 549, 171–173. <https://doi.org/10.1016/j.ab.2018.03.026>.
- (52) Velazquez, L. R.; Dunn, D. G.; Gwinn, E. G.; Kuchnir, D. DNA Hairpins with Poly-C Loops Stabilize Four Types of Fluorescent Ag Nanoclusters. *DNA Seq.* **2009**, 113 (11), 1–15.
- (53) Xiao, Y.; Wu, Z.; Wong, K. Y.; Liu, Z. Hairpin DNA Probes Based on Target-Induced in Situ Generation of Luminescent Silver Nanoclusters. *Chem. Commun.* **2014**, 50 (37), 4849–4852. <https://doi.org/10.1039/c4cc01154f>.
- (54) Zhang, J.; Li, C.; Zhi, X.; Ramón, G. A.; Liu, Y.; Zhang, C.; Pan, F.; Cui, D. Hairpin DNA-Templated Silver Nanoclusters as Novel Beacons in Strand Displacement Amplification for MicroRNA Detection. *Anal. Chem.* **2016**, 88 (2), 1294–1302. <https://doi.org/10.1021/acs.analchem.5b03729>.
- (55) Zhou, W.; Saran, R.; Liu, J. Metal Sensing by DNA. *Chem. Rev.* **2017**, 117 (12), 8272–8325. <https://doi.org/10.1021/acs.chemrev.7b00063>.
- (56) Watson, S. M. D.; Pike, A. R.; Pate, J.; Houlton, A.; Horrocks, B. R. DNA-Templated Nanowires: Morphology and Electrical Conductivity. *Nanoscale* **2014**, 6 (8), 4027–4037. <https://doi.org/10.1039/c3nr06767j>.
- (57) Pate, J.; Zamora, F.; Watson, S. M. D.; Wright, N. G.; Horrocks, B. R.; Houlton, A. Solution-Based DNA-Templating of Sub-10 Nm Conductive Copper Nanowires. *J. Mater. Chem. C* **2014**, 2 (43), 9265–9273. <https://doi.org/10.1039/c4tc01632g>.
- (58) Kim, H. J.; Roh, Y.; Hong, B. Selective Formation of a Latticed Nanostructure with the Precise Alignment of DNA-Templated Gold Nanowires. *Langmuir* **2010**, 26 (23), 18315–18319. <https://doi.org/10.1021/la101086h>.

- (59) Plaschke, J.; Schackert, H. K.; Pompe, W.; Richter, J.; Kirsch, R.; Mertig, M.; Seidel, R. Nanoscale Palladium Metallization of DNA. *Adv. Mater.* **2002**, *12* (7), 507–510. [https://doi.org/10.1002/\(sici\)1521-4095\(200004\)12:7<507::aid-adma507>3.0.co;2-g](https://doi.org/10.1002/(sici)1521-4095(200004)12:7<507::aid-adma507>3.0.co;2-g).
- (60) Richter, J.; Pompe, W.; Mönch, I.; Schackert, H. K.; Mertig, M. Construction of Highly Conductive Nanowires on a DNA Template. *Appl. Phys. Lett.* **2002**, *78* (4), 536–538. <https://doi.org/10.1063/1.1338967>.
- (61) Kundu, S.; Liang, H. Electrically Conductive Gold Nanowires on DNA Scaffolds. *Biosensing II* **2009**, 7397 (18), 73970W. <https://doi.org/10.1117/12.827233>.
- (62) Watson, S. M. D.; Mohamed, H. D. A.; Horrocks, B. R.; Houlton, A. Electrically Conductive Magnetic Nanowires Using an Electrochemical DNA-Templating Route. *Nanoscale* **2013**, *5* (12), 5349–5359. <https://doi.org/10.1039/c3nr00716b>.
- (63) Braun, E.; Eichen, Y.; Sivan, U.; Ben-Yoseph, G. DNA-Templated Assembly and Electrode Attachment of a Conducting Silver Wire. *Nature* **1998**, *391* (6669), 775–778. <https://doi.org/10.1038/35826>.
- (64) Houlton, A.; Pike, A. R.; Angel Galindo, M.; Horrocks, B. R. DNA-Based Routes to Semiconducting Nanomaterials. *Chem. Commun.* **2009**, *14*, 1797–1806. <https://doi.org/10.1039/b818456a>.
- (65) Yuan, Z.; Chen, Y. C.; Li, H. W.; Chang, H. T. Fluorescent Silver Nanoclusters Stabilized by DNA Scaffolds. *Chem. Commun.* **2014**, *50* (69), 9800–9815. <https://doi.org/10.1039/c4cc02981j>.
- (66) Högele, A.; Pardatscher, G.; Liedl, T.; Roller, E.-M.; Schreiber, R.; Govorov, A. O.; Fan, Z.; Kuzyk, A.; Simmel, F. C. DNA-Based Self-Assembly of Chiral Plasmonic Nanostructures with Tailored Optical Response. *Nature* **2012**, *483* (7389), 311–314. <https://doi.org/10.1038/nature10889>.
- (67) Müller, J. Functional Metal Ions in Nucleic Acids. *Metallomics* **2010**, *2* (5), 318–327. <https://doi.org/10.1039/c000429d>.
- (68) Zhu, G.; Zhang, C. Y. Functional Nucleic Acid-Based Sensors for Heavy Metal

Ion Assays. *Analyst* **2014**, *139* (24), 6326–6342.
<https://doi.org/10.1039/c4an01069h>.

- (69) Zhou, Y.; Tang, L.; Zeng, G.; Zhang, C.; Zhang, Y.; Xie, X. Current Progress in Biosensors for Heavy Metal Ions Based on DNAzymes/DNA Molecules Functionalized Nanostructures: A Review. *Sensors Actuators, B Chem.* **2016**, *223*, 280–294. <https://doi.org/10.1016/j.snb.2015.09.090>.
- (70) Sun, C.; Ou, X.; Cheng, Y.; Zhai, T.; Liu, B.; Lou, X.; Xia, F. Coordination-Induced Structural Changes of DNA-Based Optical and Electrochemical Sensors for Metal Ions Detection. *Dalt. Trans.* **2019**, *48* (18), 5879–5891. <https://doi.org/10.1039/c8dt04733b>.
- (71) Tang, Y.; He, W.; Wang, S.; Tao, Z.; Cheng, L. One Step Synthesis of Silver Nanowires Used in Preparation of Conductive Silver Paste. *J. Mater. Sci. Mater. Electron.* **2014**, *25* (7), 2929–2933. <https://doi.org/10.1007/s10854-014-1961-8>.
- (72) Lu, Y.; Chen, W. Sub-Nanometre Sized Metal Clusters: From Synthetic Challenges to the Unique Property Discoveries. *Chem. Soc. Rev.* **2012**, *41* (9), 3594–3623. <https://doi.org/10.1039/c2cs15325d>.
- (73) Murray, R. W. Nanoelectrochemistry: Metal Nanoparticles, Nanoelectrodes, and Nanopores. *Chem. Rev.* **2008**, *108* (7), 2688–2720. <https://doi.org/10.1021/cr068077e>.
- (74) Choi, S.; Dickson, R. M.; Yu, J. Developing Luminescent Silver Nanodots for Biological Applications. *Chem. Soc. Rev.* **2012**, *41* (5), 1867–1891. <https://doi.org/10.1039/c1cs15226b>.
- (75) Choi, S.; Dickson, R. M.; Yu, J. Developing Luminescent Silver Nanodots for Biological Applications. *Chem. Soc. Rev.* **2012**, *41* (5), 1867–1891. <https://doi.org/10.1039/c1cs15226b>.
- (76) Mathew, A.; Pradeep, T. Noble Metal Clusters: Applications in Energy, Environment, and Biology. *Part. Part. Syst. Charact.* **2014**, *31* (10), 1017–1053. <https://doi.org/10.1002/ppsc.201400033>.
- (77) Ras, R. H. A. Advanced Fluorescence Reporters in Chemistry and Biology III.

Adv. Fluoresc. Reporters Chem. Biol. **II** **2011**, *113*, 307–332.
<https://doi.org/10.1007/978-3-642-18035-4>.

- (78) Vecchioni, S.; Capece, M. C.; Toomey, E.; Nguyen, L.; Ray, A.; Greenberg, A.; Fujishima, K.; Urbina, J.; Paulino-Lima, I. G.; Pinheiro, V.; et al. Construction and Characterization of Metal Ion-Containing DNA Nanowires for Synthetic Biology and Nanotechnology. *Sci. Rep.* **2019**, *9* (1), 1–15.
<https://doi.org/10.1038/s41598-019-43316-1>.
- (79) Yamane, T.; Davidson, N. On the Complexing of Desoxyribonucleic Acid (DNA) by Mercuric Ion. *J. Am. Chem. Soc.* **1961**, *83* (12), 2599–2607.
<https://doi.org/10.1021/ja01473a001>.
- (80) Miyake, Y.; Togashi, H.; Tashiro, M.; Yamaguchi, H.; Oda, S.; Kudo, M.; Tanaka, Y.; Kondo, Y.; Sawa, R.; Fujimoto, T.; et al. MercuryII-Mediated Formation of Thymine-HgII-Thymine Base Pairs in DNA Duplexes. *J. Am. Chem. Soc.* **2006**, *128* (7), 2172–2173. <https://doi.org/10.1021/ja056354d>.
- (81) Müller, J. Nucleic Acid Duplexes with Metal-Mediated Base Pairs and Their Structures. *Coord. Chem. Rev.* **2019**, *393*, 37–47.
<https://doi.org/10.1016/j.ccr.2019.05.007>.
- (82) Liu, X.; Guo, G. C.; Fu, M. L.; Liu, X. H.; Wang, M. S.; Huang, J. S. Three Novel Silver Complexes with Ligand-Unsupported Argentophilic Interactions and Their Luminescent Properties. *Inorg. Chem.* **2006**, *45* (9), 3679–3685.
<https://doi.org/10.1021/ic0601539>.
- (83) Yamaguchi, H.; Šebera, J.; Kondo, J.; Oda, S.; Komuro, T.; Kawamura, T.; Dairaku, T.; Kondo, Y.; Okamoto, I.; Ono, A.; et al. The Structure of Metallo-DNA with Consecutive Thymine-Hg II -Thymine Base Pairs Explains Positive Entropy for the Metallo Base Pair Formation. *Nucleic Acids Res.* **2014**, *42* (6), 4094–4099. <https://doi.org/10.1093/nar/gkt1344>.
- (84) Schöllhorn, H.; Thewalt, U.; Lippert, B. Metal-Stabilized Rare Tautomers of Nucleobases. 2. 2-Oxo-4-Hydroxo Form of Uracil: Crystal Structures and Solution Behavior of Two Platinum(II) Complexes Containing Iminol Tautomers of 1-Methyluracil. *J. Am. Chem. Soc.* **1989**, *111* (18), 7213–7221.
<https://doi.org/10.1021/ja00200a048>.

- (85) Fusch, E. C.; Lippert, B. $[Zn_3(OH)_2(1\text{-MeC-N}_3)_5(1\text{-MeC-O}_2)_3]^{4+}$ ($1\text{-MeC} = 1\text{-Methylcytosine}$): Structural Model for DNA Cross-Linking and DNA Rewinding by Zn(II)? *J. Am. Chem. Soc.* **1994**, *116*, 7204–7209.
- (86) Terrón, A.; Moreno-Vachiano, B.; Bauzá, A.; García-Raso, A.; Fiol, J. J.; Barceló-Oliver, M.; Molins, E.; Frontera, A. X-Ray Crystal Structure of a Metalled Double-Helix Generated by Infinite and Consecutive $C^*-AgI-C^*$ ($C^*:N1\text{-Hexylcytosine}$) Base Pairs through Argentophilic and Hydrogen Bond Interactions. *Chem. - A Eur. J.* **2017**, *23* (9), 2103–2108. <https://doi.org/10.1002/chem.201604331>.
- (87) Lippert, B.; Sanz Miguel, P. J. The Renaissance of Metal-Pyrimidine Nucleobase Coordination Chemistry. *Acc. Chem. Res.* **2016**, *49* (8), 1537–1545. <https://doi.org/10.1021/acs.accounts.6b00253>.
- (88) Müller, J. Metal-Ion-Mediated Base Pairs in Nucleic Acids. *Eur. J. Inorg. Chem.* **2008**, No. 24, 3749–3763. <https://doi.org/10.1002/ejic.200800301>.
- (89) Müller, J. Chemistry: Metals Line up for DNA. *Nature* **2006**, *444* (7120), 698. <https://doi.org/10.1038/444698a>.
- (90) Wagenknecht, H. A. Metal-Mediated DNA Base Pairing and Metal Arrays in Artificial DNA: Towards New Nanodevices. *Angew. Chemie - Int. Ed.* **2003**, *42* (28), 3204–3206. <https://doi.org/10.1002/anie.200301661>.
- (91) Swasey, S. M.; Leal, L. E.; Lopez-Acevedo, O.; Pavlovich, J.; Gwinn, E. G. Silver (I) as DNA Glue: Ag^+ -Mediated Guanine Pairing Revealed by Removing Watson-Crick Constraints. *Sci. Rep.* **2015**, *5* (April), 1–9. <https://doi.org/10.1038/srep10163>.
- (92) Menzer, S.; Sabat, M.; Lippert, B. $Ag(I)$ Modified Base Pairs Involving Complementary (G, C) and Noncomplementary (A, C) Nucleobases. On the Possible Structural Role of Aqua Ligands in Metal-Modified Nucleobase Pairs. *J. Am. Chem. Soc.* **1992**, *114* (12), 4644–4649. <https://doi.org/10.1021/ja00038a030>.
- (93) Ishii, T.; Araki, N.; Wilson, A. W.; Jyo, A.; Ihara, T. Silver Ion Unusually Stabilizes the Structure of a Parallel-Motif DNA Triplex. *J. Am. Chem. Soc.* **2009**, *131* (11), 3826–3827. <https://doi.org/10.1021/ja809702n>.

- (94) France, G.; Beauchamp, A. Model Compounds for the Interaction of Silver(I) with Polyuridine. Crystal Structure of a 1:1 Silver Complex with 1-Methylthymine. *J. Am. Chem. Soc.* **1979**, *101* (21), 6260–6263. <https://doi.org/10.1021/ja00515a017>.
- (95) Kistenmacher, T. J.; Rossi, M.; Marzilli, L. G. Crystal and Molecular Structure of (Nitrate)(1-Methylcytosine)Silver(I): An Unusual Cross-Linked Polymer Containing a Heavy Metal and a Modified Nucleic Acid Constituent. *Inorg. Chem.* **1979**, *18* (2), 240–244. <https://doi.org/10.1021/ic50192a007>.
- (96) Lippert, B.; Sanz Miguel, P. J. The Renaissance of Metal-Pyrimidine Nucleobase Coordination Chemistry. *Acc. Chem. Res.* **2016**, *49* (8), 1537–1545. <https://doi.org/10.1021/acs.accounts.6b00253>.
- (97) Liu, H.; Shen, F.; Haruehanroengra, P.; Yao, Q.; Cheng, Y.; Chen, Y.; Yang, C.; Zhang, J.; Wu, B.; Luo, Q.; et al. A DNA Structure Containing AgI-Mediated G:G and C:C Base Pairs. *Angew. Chemie - Int. Ed.* **2017**, *56* (32), 9430–9434. <https://doi.org/10.1002/anie.201704891>.
- (98) Wada, S.; Ono, A.; Nakagawa, O.; Aotani, M.; Funai, T.; Miyazaki, Y.; Urata, H.; Torigoe, H.; Yamaguchi, E. AgI Ion Mediated Formation of a C-A Mismatch by DNA Polymerases. *Angew. Chemie Int. Ed.* **2012**, *51* (26), 6464–6466. <https://doi.org/10.1002/anie.201109191>.
- (99) Kondo, J.; Tada, Y.; Dairaku, T.; Hattori, Y.; Saneyoshi, H.; Ono, A.; Tanaka, Y. A Metallo-DNA Nanowire with Uninterrupted One-Dimensional Silver Array. *Nat. Chem.* **2017**, *9* (10), 956–960. <https://doi.org/10.1038/nchem.2808>.
- (100) Linares, F.; García-Fernández, E.; López-Garzón, F. J.; Domingo-García, M.; Orte, A.; Rodríguez-Diéguez, A.; Galindo, M. A. Multifunctional Behavior of Molecules Comprising Stacked Cytosine-AgI-Cytosine Base Pairs; Towards Conducting and Photoluminescence Silver-DNA Nanowires. *Chem. Sci.* **2019**, *10* (4), 1126–1137. <https://doi.org/10.1039/c8sc04036b>.
- (101) Terrón, A.; Moreno-Vachiano, B.; Bauzá, A.; García-Raso, A.; Fiol, J. J.; Barceló-Oliver, M.; Molins, E.; Frontera, A. X-Ray Crystal Structure of a Metalled Double-Helix Generated by Infinite and Consecutive C*-AgI-C* (C*:N1-Hexylcytosine) Base Pairs through Argentophilic and Hydrogen Bond Interactions. *Chem. - A*

Eur. J. **2017**, 23 (9), 2103–2108. <https://doi.org/10.1002/chem.201604331>.

- (102) Menzer, S.; Sabat, M.; Lippert, B. Ag(I) Modified Base Pairs Involving Complementary (G, C) and Noncomplementary (A, C) Nucleobases. On the Possible Structural Role of Aqua Ligands in Metal-Modified Nucleobase Pairs. *J. Am. Chem. Soc.* **1992**, 114 (12), 4644–4649. <https://doi.org/10.1021/ja00038a030>.
- (103) Espinosa Leal, L. A.; Karpenko, A.; Swasey, S.; Gwinn, E. G.; Rojas-Cervellera, V.; Rovira, C.; Lopez-Acevedo, O. The Role of Hydrogen Bonds in the Stabilization of Silver-Mediated Cytosine Tetramers. *J. Phys. Chem. Lett.* **2015**, 6 (20), 4061–4066. <https://doi.org/10.1021/acs.jpcllett.5b01864>.
- (104) Sychrovský, V.; Dairaku, T.; Okamoto, I.; Ono, A.; Yamanaka, D.; Šebera, J.; Furuita, K.; Nakashima, K.; Kondo, J.; Sato, H.; et al. Structure Determination of an Ag I -Mediated Cytosine-Cytosine Base Pair within DNA Duplex in Solution with 1 H/ 15 N/ 109 Ag NMR Spectroscopy . *Chem. - A Eur. J.* **2016**, 22 (37), 13028–13031. <https://doi.org/10.1002/chem.201603048>.
- (105) Wang, Y.; Ritzo, B.; Gu, L. Q. Silver(I) Ions Modulate the Stability of DNA Duplexes Containing Cytosine, Methylcytosine and Hydroxymethylcytosine at Different Salt Concentrations. *RSC Adv.* **2015**, 5 (4), 2655–2658. <https://doi.org/10.1039/c4ra14490b>.
- (106) Zhou, P.; Yao, J. F.; Sheng, C. F.; Li, H. A Continuing Tale of Chirality: Metal Coordination Extended Axial Chirality of 4,4'-Bipy to 1D Infinite Chain under Cooperation of a Nucleotide Ligand. *CrystEngComm* **2013**, 15 (42), 8430–8436. <https://doi.org/10.1039/c3ce40977e>.
- (107) Aoki, K. X-Ray Crystal Structures of the Ternary Complexes [Cd(5'-UMP)(Dpa)(H₂O)] & (5'-UMP= Uridine 5'-Phosphate,; Dpa=2,2' -Dipyridylamine): Metal Ion Bridged Stacking between Nucleotide Bases and Aromatic Ainine Rings, and [Cu(5'-CMP)(Dpa)(H₂O)] (5'-CMP=cytidine 5. *J. Chem. Soc.* **1979**, 625 (6), 589–591.
- (108) Marino, N.; Armentano, D.; Pardo, E.; Vallejo, J.; Neve, F.; Di Donna, L.; De Munno, G. Homochiral Self-Assembly of Biocoordination Polymers: Anion-Triggered Helicity and Absolute Configuration Inversion. *Chem. Sci.* **2015**, 6 (7),

4300–4305. <https://doi.org/10.1039/c5sc01089f>.

- (109) Marino, N.; Armentano, D.; Zanchini, C.; De Munno, G. Ca²⁺ Metal Ion Adducts with Cytosine, Cytidine and Cytidine 5'-Monophosphate: A Comprehensive Study of Calcium Reactivity towards Building Units of Nucleic Acids. *CrystEngComm* **2014**, *16* (35), 8286–8296. <https://doi.org/10.1039/c4ce00511b>.
- (110) Terrón, A.; Tomàs, L.; Bauzá, A.; García-Raso, A.; Fiol, J. J.; Molins, E.; Frontera, A. The First X-Ray Structure of a Silver-Nucleotide Complex: Interaction of Ion Ag(i) with Cytidine-5'-Monophosphate. *CrystEngComm* **2017**, *19* (39), 5830–5834. <https://doi.org/10.1039/c7ce01400g>.
- (111) Kondo, J.; Tada, Y.; Dairaku, T.; Saneyoshi, H.; Okamoto, I.; Tanaka, Y.; Ono, A. High-Resolution Crystal Structure of a Silver(I)-RNA Hybrid Duplex Containing Watson-Crick-like C-Silver(I)-C Metallo-Base Pairs. *Angew. Chemie - Int. Ed.* **2015**, *54* (45), 13323–13326. <https://doi.org/10.1002/anie.201507894>.
- (112) Ritchie, C. M.; Johnsen, K. R.; Kiser, J. R.; Antoku, Y.; Dickson, R. M.; Petty, J. T. Ag Nanocluster Formation Using a Cytosine Oligonucleotide Template. *J. Phys. Chem. C* **2007**, *111* (1), 175–181. <https://doi.org/10.1021/jp0648487>.
- (113) Huard, D. J. E.; Demissie, A.; Kim, D.; Lewis, D.; Dickson, R. M.; Petty, J. T.; Lieberman, R. L. Atomic Structure of a Fluorescent Ag₈ Cluster Templated by a Multistranded DNA Scaffold. *J. Am. Chem. Soc.* **2019**, *141* (29), 11465–11470. <https://doi.org/10.1021/jacs.8b12203>.
- (114) Khan, I.; Saeed, K.; Khan, I. Nanoparticles: Properties, Applications and Toxicities. *Arab. J. Chem.* **2019**, *12* (7), 908–931. <https://doi.org/10.1016/j.arabjc.2017.05.011>.
- (115) Jin, R.; Zeng, C.; Zhou, M.; Chen, Y. Atomically Precise Colloidal Metal Nanoclusters and Nanoparticles: Fundamentals and Opportunities. *Chem. Rev.* **2016**, *116* (18), 10346–10413. <https://doi.org/10.1021/acs.chemrev.5b00703>.
- (116) Smith, B. R.; Gambhir, S. S. Nanomaterials for in Vivo Imaging. *Chem. Rev.* **2017**, *117* (3), 901–986. <https://doi.org/10.1021/acs.chemrev.6b00073>.
- (117) Piepenbrock, M. O. M.; Clarke, N.; Steed, J. W. Rheology and Silver

Nanoparticle Templating in a Bis(Urea) Silver Metallogel. *Soft Matter* **2011**, 7 (6), 2412–2418. <https://doi.org/10.1039/c0sm00647e>.

- (118) Aiken, J. D.; Finke, R. G. A Review of Modern Transition-Metal Nanoclusters: Their Synthesis, Characterization, and Applications in Catalysis. *J. Mol. Catal. A Chem.* **1999**, 145 (1–2), 1–44. [https://doi.org/10.1016/S1381-1169\(99\)00098-9](https://doi.org/10.1016/S1381-1169(99)00098-9).
- (119) Dong, X. Y.; Gao, Z. W.; Yang, K. F.; Zhang, W. Q.; Xu, L. W. Nanosilver as a New Generation of Silver Catalysts in Organic Transformations for Efficient Synthesis of Fine Chemicals. *Catal. Sci. Technol.* **2015**, 5 (5), 2554–2574. <https://doi.org/10.1039/c5cy00285k>.
- (120) Kudaibergenov, S. E.; Tatykhanova, G. S.; Selenova, B. S. Polymer Protected and Gel Immobilized Gold and Silver Nanoparticles in Catalysis. *J. Inorg. Organomet. Polym. Mater.* **2016**, 26 (6), 1198–1211. <https://doi.org/10.1007/s10904-016-0373-z>.
- (121) Qiao, Z. A.; Zhang, P.; Chai, S. H.; Chi, M.; Veith, G. M.; Gallego, N. C.; Kidder, M.; Dai, S. Lab-in-a-Shell: Encapsulating Metal Clusters for Size Sieving Catalysis. *J. Am. Chem. Soc.* **2014**, 136 (32), 11260–11263. <https://doi.org/10.1021/ja505903r>.
- (122) Díez, I.; Ras, R. H. A. Fluorescent Silver Nanoclusters. *Nanoscale*. 2011, pp 1963–1970. <https://doi.org/10.1039/c1nr00006c>.
- (123) Rama, S.; Perala, K.; Kumar, S. Supporting Information for : On the Mechanism of Metal Nanoparticle Synthesis in Brust-Schiffrin Method. *Langmuir* **2013**, 29, 9863–9873.
- (124) Brust, M.; Walker, M.; Bethell, D.; Schiffrin, D. J.; Whyman, R. Synthesis of Thiol-Derivatized Gold Nanoparticles In. *J. Chem. Soc. Chem. Commun.* **1994**, No. 7, 801–802. <https://doi.org/10.1039/C39940000801>.
- (125) Yuan, X.; Setyawati, M. I.; Tan, A. S.; Ong, C. N.; Leong, D. T.; Xie, J. Highly Luminescent Silver Nanoclusters with Tunable Emissions: Cyclic Reduction-Decomposition Synthesis and Antimicrobial Properties. *NPG Asia Mater.* **2013**, 5 (2), e39-8. <https://doi.org/10.1038/am.2013.3>.

- (126) Perala, S. R. K.; Kumar, S. On the Mechanism of Metal Nanoparticle Synthesis in the Brust-Schiffrin Method. *Langmuir* **2013**, *29* (31), 9863–9873. <https://doi.org/10.1021/la401604q>.
- (127) Richards, C. I.; Choi, S.; Hsiang, J. C.; Antoku, Y.; Vosch, T.; Bongiorno, A.; Tzeng, Y. L.; Dickson, R. M. Oligonucleotide-Stabilized Ag Nanocluster Fluorophores. *J. Am. Chem. Soc.* **2008**, *130* (15), 5038–5039. <https://doi.org/10.1021/ja8005644>.
- (128) Gwinn, E.; Schultz, D.; Copp, S.; Swasey, S. DNA-Protected Silver Clusters for Nanophotonics. *Nanomaterials* **2015**, *5* (1), 180–207. <https://doi.org/10.3390/nano5010180>.
- (129) Medintz, I. L.; Uyeda, T. H.; Goldman, E. R.; Mattoussi, H. Quantum Dot Bioconjugates for Imaging, Labelling and Sensing. *Nat. Mater.* **2005**, *4*, 435–446. <https://doi.org/10.1038/nmat1390>.
- (130) Solanki, J. N.; Murthy, Z. V. P. Controlled Size Silver Nanoparticles Synthesis with Water-in-Oil Microemulsion Method: A Topical Review. *Ind. Eng. Chem. Res.* **2011**, *50* (22), 12311–12323. <https://doi.org/10.1021/ie201649x>.
- (131) Ledo-Suárez, A.; Rivas, J.; Rodríguez-Abreu, C. F.; Rodríguez, M. J.; Pastor, E.; Hernández-Creus, A.; Oseroff, S. B.; López-Quintela, M. A. Facile Synthesis of Stable Subnanosized Silver Clusters in Microemulsions. *Angew. Chemie - Int. Ed.* **2007**, *46* (46), 8823–8827. <https://doi.org/10.1002/anie.200702427>.
- (132) Langevin, D.; Guillot, S.; Espinosa, G.; Raspaud, E.; Swami, A.; Boué, F. Confinement of DNA in Water-in-Oil Microemulsions. *Langmuir* **2008**, *24* (20), 11828–11833. <https://doi.org/10.1021/la802233e>.
- (133) Solans, C.; Civera, C.; Boutonnet, M.; Sanchez-Dominguez, M.; Okoli, C.; Kuttuva, G. R.; Järås, S. Comparison and Functionalization Study of Microemulsion-Prepared Magnetic Iron Oxide Nanoparticles. *Langmuir* **2012**, *28* (22), 8479–8485. <https://doi.org/10.1021/la300599q>.
- (134) Solanki, J. N.; Murthy, Z. V. P. Controlled Size Silver Nanoparticles Synthesis with Water-in-Oil Microemulsion Method: A Topical Review. *Ind. Eng. Chem. Res.* **2011**, *50* (22), 12311–12323. <https://doi.org/10.1021/ie201649x>.

- (135) Zheng, J.; Nicovich, P. R.; Dickson, R. M. Highly Fluorescent Noble-Metal Quantum Dots. *Annu. Rev. Phys. Chem.* **2006**, *58* (1), 409–431. <https://doi.org/10.1146/annurev.physchem.58.032806.104546>.
- (136) Kumar, S.; Bolan, M. D.; Bigioni, T. P. Glutathione-Stabilized Magic-Number Silver Cluster Compounds. *J. Am. Chem. Soc.* **2010**, *132* (38), 13141–13143. <https://doi.org/10.1021/ja105836b>.
- (137) Copp, S. M.; Schultz, D.; Swasey, S.; Pavlovich, J.; Debord, M.; Chiu, A.; Olsson, K.; Gwinn, E. Magic Numbers in DNA-Stabilized Fluorescent Silver Clusters Lead to Magic Colors. *J. Phys. Chem. Lett.* **2014**, *5* (6), 959–963. <https://doi.org/10.1021/jz500146q>.
- (138) Brack, M. The Physics of Simple Metal Clusters: Self-Consistent Jellium Model and Semiclassical Approaches. *Rev. Mod. Phys.* **1993**, *65* (3), 677–732. <https://doi.org/10.1103/RevModPhys.65.677>.
- (139) Polozkov, R. G.; Ivanov, V. K.; Verkhovtsev, A. V.; Korol, A. V.; Solov'yov, A. V. New Applications of the Jellium Model for the Study of Atomic Clusters. *J. Phys. Conf. Ser.* **2013**, *438* (1), 012009–012020. <https://doi.org/10.1088/1742-6596/438/1/012009>.
- (140) Kumar, S.; Bolan, M. D.; Bigioni, T. P. Glutathione-Stabilized Magic-Number Silver Cluster Compounds. *J. Am. Chem. Soc.* **2010**, *132* (38), 13141–13143. <https://doi.org/10.1021/ja105836b>.
- (141) Abbasi, N. M.; Yu, H.; Wang, L.; Zain-UI-Abdin; Amer, W. A.; Akram, M.; Khalid, H.; Chen, Y.; Saleem, M.; Sun, R.; et al. Preparation of Silver Nanowires and Their Application in Conducting Polymer Nanocomposites. *Mater. Chem. Phys.* **2015**, *166*, 1–15. <https://doi.org/10.1016/j.matchemphys.2015.08.056>.
- (142) Houlton, A.; Watson, S. M. D. DNA-Based Nanowires. Towards Bottom-up Nanoscale Electronics. *Annu. Reports Prog. Chem. - Sect. A* **2011**, *107*, 21–42. <https://doi.org/10.1039/c1ic90017j>.
- (143) Swager, T. M. The Molecular Wire Approach to Sensory Signal Amplification. *Acc. Chem. Res.* **1998**, *31* (5), 201–207. <https://doi.org/10.1021/ar9600502>.

- (144) Anastassopoulou, J. Metal-DNA Interactions. *J. Mol. Struct.* **2003**, 651–653, 19–26. [https://doi.org/10.1016/S0022-2860\(02\)00625-7](https://doi.org/10.1016/S0022-2860(02)00625-7).
- (145) Dasari, S.; Bernard Tchounwou, P. Cisplatin in Cancer Therapy: Molecular Mechanisms of Action. *Eur. J. Pharmacol.* **2014**, 740, 364–378. <https://doi.org/10.1016/j.ejphar.2014.07.025>.

Chapter 2.

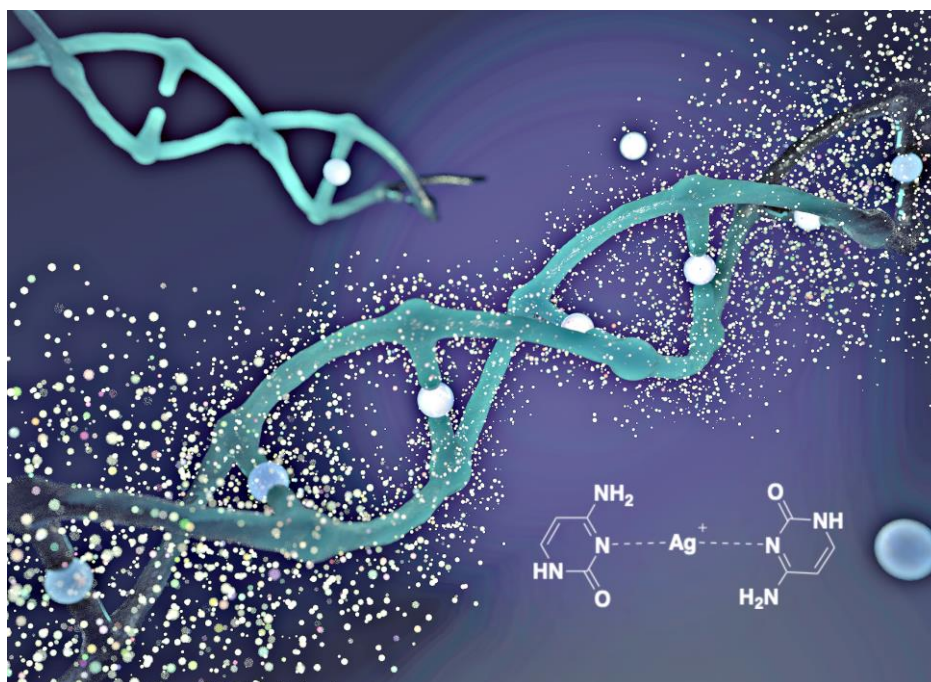
Transoid and *Cisoid* conformations in silver-mediated cytosine base pairs. Hydrogen-bonding dictates argentophilic interactions in the solid-state.

This chapter is based upon the following publication:

Liam Mistry, Paul G. Waddell, Nick G. Wright, Benjamin R. Horrocks, Andrew Houlton*, *Inorg. Chem.* 2019, **58**, 19, 13346 – 13352

2.1. Introduction

In recent years the interactions between silver(I)-ions and DNA have been of particular interest; thought to offer a highly-selective bottom-up route towards the development of functional biomolecular entities (**Scheme 2.1**), a promising avenue towards the construction of complex functional nanoarchitectures.^{1–5} Several reviews have commented on their potential applications as biosensors for metal ions,^{6–9} single-nucleotide-polymorphism (SNP) detectors,¹⁰ heavy-metal trappers, nanomachines,¹¹ molecular wires,^{12–17} uniform nanoclusters formation^{18–21} and logic gates^{22–24, 25,26}



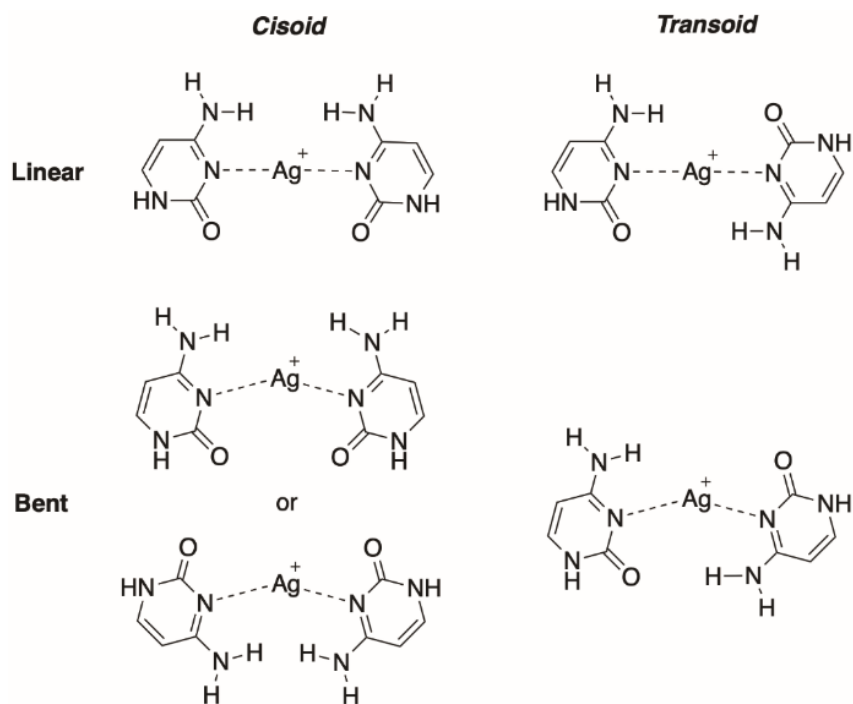
Scheme 2.1 A depiction of M-DNA with a molecular diagram of the C-Ag⁺-C coordination (C: cytosine).

Essential to these is the formation of the metal-mediated base pairs, C-Ag⁺-C. The binding of Ag⁺ to DNA was one of the earliest metal-ion nucleic acid interactions to be investigated. Even from those initial studies, it was recognised to display sequence specificity with nucleobase sites.^{2–4,27} Since then, the Ag⁺-N³ coordination has since become well-established as a basis for metal-mediation across cytosine mis-pairs in DNA.^{25,28,29} The d¹⁰ electronic configuration of silver has shown a tendency towards lower coordination numbers, often highly-linear (~180°). Recent studies have focused this binding motif towards the generation of 1D materials.^{30,31} The physico-chemical modifications observed in the metalation of DNA → M-DNA, extends their functional repertoire.

This pairing has recently been characterized using high resolution X-ray diffraction of single crystals describing a range of natural and modified alkylated-nucleobases (see *chapter 1, introduction*).^{17,32} Furthermore, several oligonucleotide sequences have been characterised that display a wider range of additional coordination motifs, including: G-Ag⁺-G, G-Ag⁺-C, T-Ag⁺-T and ^{Br}C-Ag⁺-C (^{Br}C - 5-bromo-2'-deoxycytidine).³³⁻³⁵

In principle, there are only two conformations possible for the C-Ag⁺-C base-pair, *Cisoid* (**C**) and *Transoid* (**T**) (**Scheme 2.2**). The *transoidal* arrangement is often cited as preferred due to its complementary positioning of the hydrogen-bond donor-acceptor sites.^{25,36} However, typical bonding distances between the two respective groups is too large at ca. 4.5 Å, for formal H-bonding. In fact, crystallographically characterised examples of this type of coordination motif are exclusively *cisoidal*. However, a notable is the lack of co-planarity exists between the ligands.^{13,36,37}

Two-coordinate Ag⁺ are not confined to purely linear geometries e.g. *bis*-(6-phenyl-1,3,5-triazine-2,4-diamine)-silver(I) nitrate,³⁸ *bis*-(2-amino-3-methylpyridine-*N*)-silver(I) nitrate,³⁹ and *bis*-[2-(1-phenylethyl)quinolato]silver(I) percholate⁴⁰ (Note: the defined linear geometry is N-Ag-N >160°). In relaxing this conformational constraint, numerous possibilities open up based on permutations of bent geometry and **C** or **T** arrangements. These are illustrated in **Scheme 2.2** as being **C**_{linear}; **T**_{linear}; **C**_{bent-OO}; **T**_{bent}; **C**_{bent-NN}.



Scheme 2.2 Structural variations for the metal-mediated $[C-Ag-C]^+$ base-pair based on permutations of linear/bent coordination geometry and *cisoid* (**C**)/*transoid* (**T**) conformation. These are short-handed as, from, left-right, top-bottom; **C**_{linear}, **T**_{linear}, **C**_{bent-OO}, **T**_{bent} and **C**_{bent-NN}.

In this chapter, we sought to prepare and structurally characterise examples of the recognised Ag^+ -mediated base-pair displaying as several alternative conformations. In particular, we hoped to obtain examples of the theoretically (*vide infra*) preferred, *transoidal* conformation. We chose to use the natural nucleobase, cytosine, as the ligand with a range of common silver salts ($AgNO_3$, $AgBF_4$ and $AgPF_6$) using a range of crystallisation techniques. At the start of this investigation, there were no crystallographically characterized examples of this particular coordination motif containing the unmodified nucleobase.

2.2. Results & Discussion

Herein, we report three $[\text{Ag}^{\text{I}}\text{-(cytosine)}_2]$ compounds isolated and structurally characterised for the first time in the solid-state. The compounds displayed marked differences in their molecular and intermolecular structures when compared to those alkylated^{13,36} or modified Ag^+ -mediated systems. Examples of both *cisoid* and *transoid* orientations stabilised in the solid-state through intramolecular base-pairing are shown. Furthermore, there is a notable absence of argentophilic chain formation within the single crystal, something which has dominated the intermolecular interactions of these derivatives.

The compounds were prepared by the reaction of cytosine (2 equiv.) with the corresponding silver salt (1 equiv.) in water under standard laboratory conditions (273 K, 100 kPa). Crystalline solid material suitable for single X-ray diffraction was produced using a range of techniques, evaporation, layering (without a buffer layer) and vapour diffusion using acetonitrile as the antisolvent. A simplistic mechanism was proposed below to explain the reaction (**Figure 2.1**). The Lewis base or tertiary (3°) N^3 amine of the cytosine ligand donates its lone-pair to the silver-ion or Lewis acid displacing the counter anion, forming an acid-base adduct; $\text{N-Ag}^{\text{I}}\text{-N}$. The N^3 nitrogen has the highest basicity ($3^\circ > 2^\circ > 1^\circ$, $N^3 > N^1 > N^4$), as electron donation from the conjugated system increases the nitrogen's lone-pair availability to coordinate.

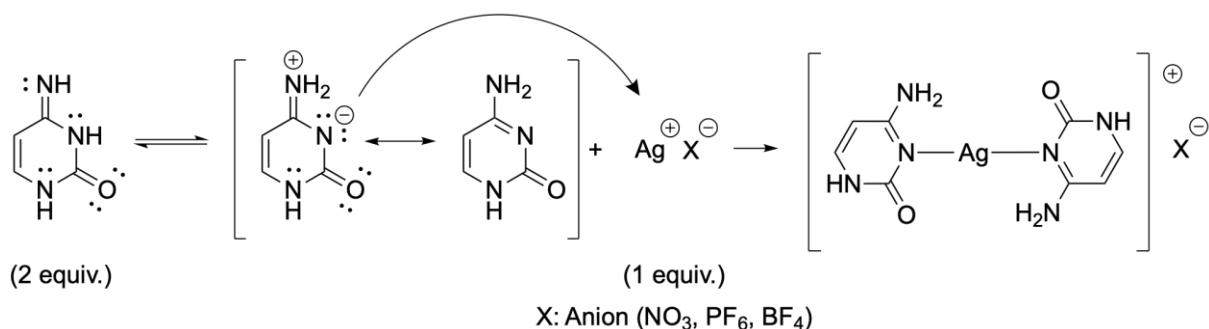


Figure 2.1 A proposed mechanism towards the formation of *bis*- $[\text{Ag}^{\text{I}}\text{-(}N^3\text{-Cytosine)}_2]^+$.

Compounds **1** – **3** were characterised by single X-ray diffraction as: *Cis*- $[\text{Ag}^{\text{I}}(N^3\text{-cytosine)}_2][\text{NO}_3]$, **1**; *Trans*- $[\text{Ag}^{\text{I}}(N^3\text{-cytosine)}_2][\text{NO}_3]\cdot\text{H}_2\text{O}$, **2** and *Trans*- $[\text{Ag}^{\text{I}}(N^3\text{-cytosine)}_2][\text{PF}_6]\cdot 2\text{H}_2\text{O}$, **3**. **Figure 2.2** depict their complex cations including any associated solvent motifs. All three complexes exist as the suspected Ag^+ *bis*-species

($N = 2$) retaining silver's preference for low coordination numbers. Binding occurs exclusively through the N^3 -heteroatom donor following HSAB theory. Interestingly, those solvent motifs dictate the bent/linear geometries and *cisoid* or *transoid* orientation of the ligands.

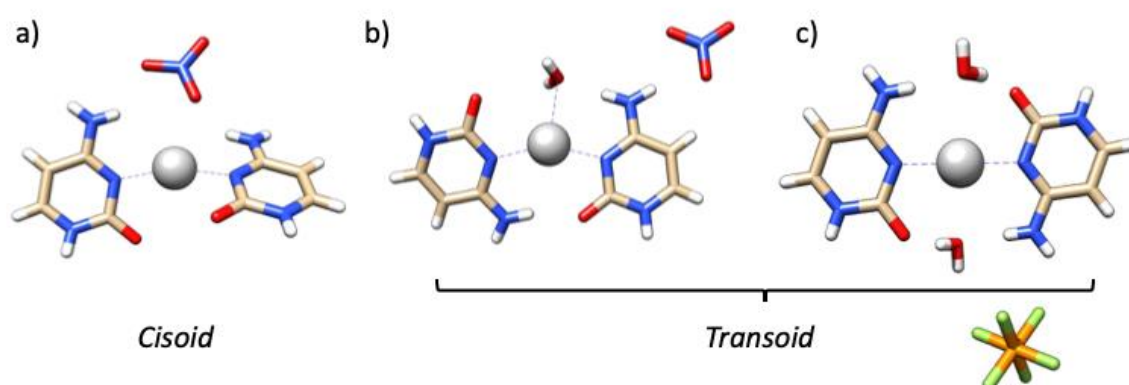


Figure 2.2 Three silver-cytosine conformations found to exist *via* single X-ray diffraction: a) *Cisoid*-[Ag^I-(N^3 -cytosine)₂][NO₃], (**1**); b) *Transoid*-[Ag^I-(N^3 -cytosine)₂][NO₃]-H₂O, (**2**) and c) *Transoid*-[Ag^I-(N^3 -cytosine)₂][PF₆]-2H₂O, (**3**). (Legend: silver – Ag⁺, blue – N, red – O, beige – C and white – H, orange – P, green – F).

Cisoid-[Ag^I-(N^3 -Cytosine)₂]⁺[NO₃]⁻, **1** (**Figure 2.3**), was prepared in an aqueous solution of cytosine and silver nitrate at a ligand-to-metal-ion ratio of 2:1. The solution was kept at room temperature avoiding exposure to ambient light where possible. Crystals were encouraged to form from a saturated solution within a closed system; yielding colourless crystals of **1** after 7 days. The complex exists in a *cisoid*-bent (**C_{bent}**) conformation bound through the expected N^3 -Ag- N^3 sites (bend angle – 158.79(10)°, N^3 -Ag distance: 2.170(3) and 2.173(3) Å). The base-plane twist angle is 13.90(12)°, likely due to the repulsion between carbonyl groups O² and O^{2'} caused by the accommodation of a nitrate anion above the metal-ion.

The disordered nitrate counter-anion exists in close-proximity to the silver-ion with the shortest O...Ag distance being 2.667(1) Å. For comparison, AgNO₃ in the solid state possess five Ag-O bonds, with distances of 2.482 – 2.588 and 2.448 – 2.579 Å in the orthorhombic⁴¹ and trigonal⁴² phases respectively. The longer distances between the metal-ion and nitrate in complex **1** indicate a weak interaction, further supported by a shift in the FTIR N-O stretch.

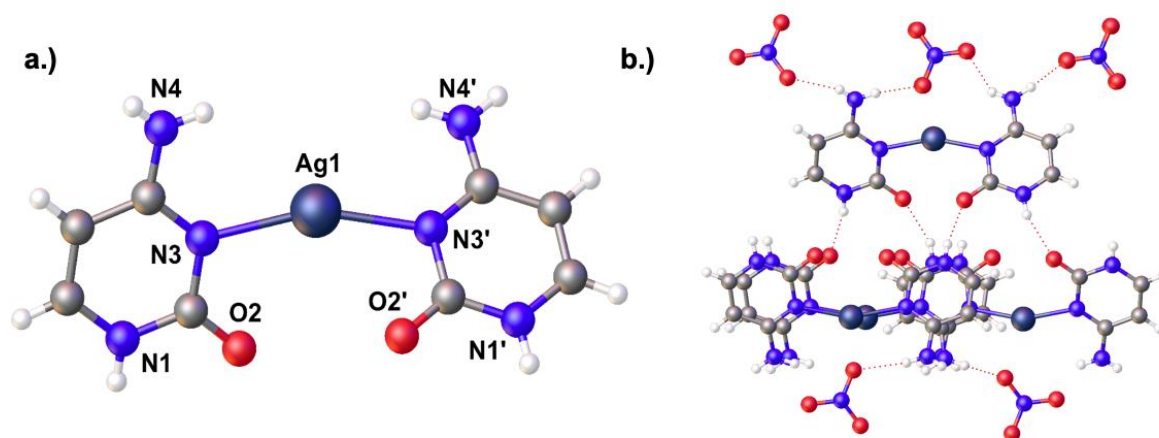


Figure 2.3 The complex cation **1**, *cisoid*-[Ag^I(*N*³-cytosine)₂]⁺[NO₃]⁻, a.) The molecular structure with atomic assignments and b.) hydrogen bonding interactions in the solid-state structure (100).

Further analysis into the packing of **1** reveals the fundamental lattice intermolecular interactions and stacking behaviour (**Figure 2.3**). Existing within the crystal are just two discrete intermolecular hydrogen-bonding exchanges along the b/c-axis. The first being between the *N*1-O2 sites of neighbouring cytosine ligands, “back-to-back”, misaligned slightly to allow shorter interaction distances. The second existing across the counter-anion, *N*⁴-H...NO₃...*N*^{4'} or *N*⁴, involving only the exocyclic primary (1°) amines. A subsequent layer or string of nitrate anions exists between each “back-to-back” double layer of bis-complexes. Exploring the stacking behaviour down the a-axis shows a distance and offset between planes (which interestingly are co-planar) of 3.268(4) and 1.359(7) Å, indicating that no π stacking effects are present, often commonly discussed as a stacking feature in the solid phase for interactions of this type.

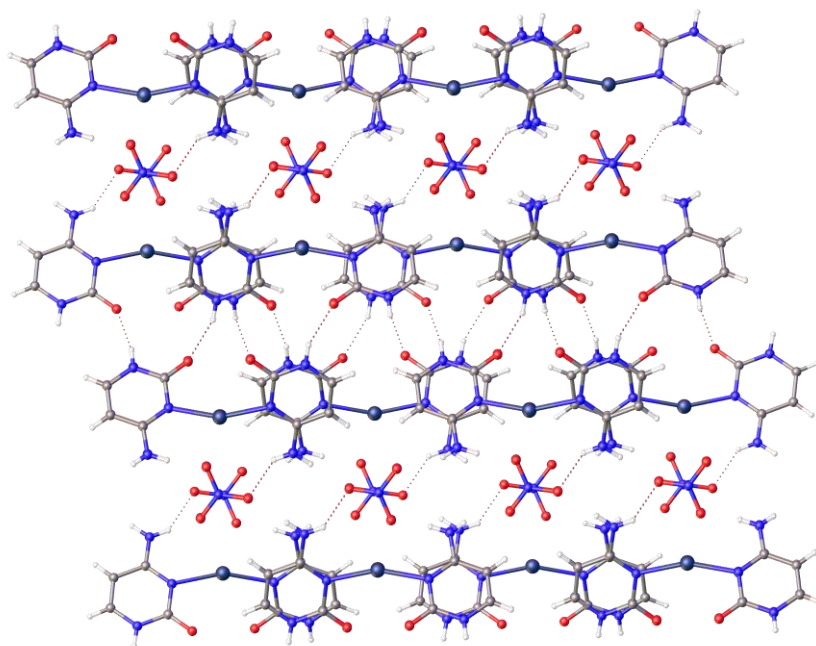


Figure 2.4 A packed view into the crystal structure of **1** looking down the *c*-axis showing the intermolecular hydrogen bonding interactions and resultant layers (note: the counter anions located between the layers are NO₃⁻).

Transoid-[Ag^I(*N*³-Cytosine)₂]⁺[NO₃]⁻·H₂O, **2** (**Figure 2.5**), was prepared in an aqueous solution of cytosine and silver nitrate at a ligand-to-metal-ion ratio of 2:1. The solution was kept at room temperature avoiding exposure to ambient light where possible. Crystals were encouraged to form using a layered approach with acetonitrile (MeCN) as the antisolvent; yielding colourless crystals of **2** after 14 days. Unlike **1**, complex **2** exist in a *transoid* conformation with a N-Ag-N bend angle of 151.2°. A small twist angle between cytosine ring planes (15.5(2)°), which allows for the exocyclic substituent groups to exist closely enough to allow intramolecular *N*⁴-H...O2' hydrogen bonding (2.929(8) Å). While such interactions are considered stabilising, this is the first example of such an interaction to be confirmed crystallographically, and this is only possible with the reduction of the N-Ag-N angle. The bent confirmation in-turn leads to a widening across the second set of exocyclic substituents (*N*^{4'}-O2, 5.712(8) Å); the large distance allows for the capture of a single water motif. The positioning of the solvent motif essentially bridges the gap, providing a H-bonding partner (*N*⁴-H...OH₂, 1.94(6) Å) (O2...H-OH, 2.98(10) Å) to the forming an eight-membered macrocycle.

The proximity between the metal-ion and water molecule ($\text{Ag}^+ \cdots \text{OH}_2$, 2.577(5) Å), possibly infers the existence of the $\text{Ag}^+ \cdots \text{OH}_2$ coordination. The coordination between the metal-ion and solvent motif in this fashion will be discussed later in this chapter with analysis of the Cambridge Crystallographic Data Centre (CCDC) database, comparing **2** and **3** against similar structures bearing solvent ligands adjacent to a N-Ag-N coordination.

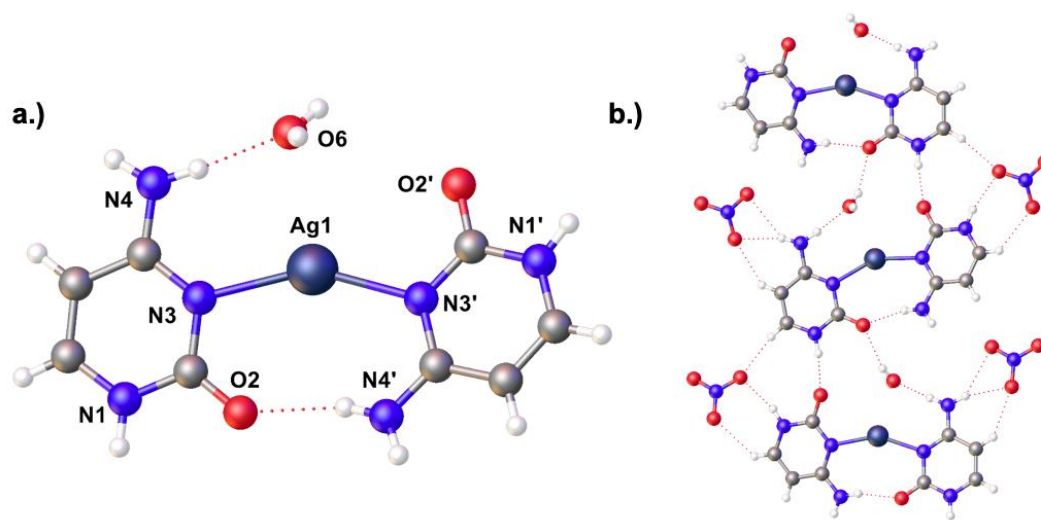


Figure 2.5 The complex cation *transoid*- $[\text{Ag}^{\text{I}}(\text{N}^3\text{-cytosine})_2 \cdot \text{H}_2\text{O}]^+ [\text{NO}_3]^-$, **2**; a.) The molecular structure with atomic assignments and b.) hydrogen bonding interactions in the solid-state structure.

Packing of the unit cell reveals how the single crystal lattice of **2** is assembled. Four primary interactions exist; $\text{O}^{2'} \cdots \text{H}_2\text{O}$ (2.10(11) Å), $\text{N}^{1'} \cdots \text{O}^{2'}$ (2.767(7) Å), $\text{N}^{1'} \cdots \text{NO}_3$ (3.049(8) Å) and $\text{N}^{4'} \cdots \text{NO}_3$ (2.902(8) Å) (**Figure 2.6**). Interestingly, in this symmetry generated view, the solvent motif more clearly shows to act as an intermolecular H-bonding bridge across two neighbouring complexes, $\text{N}^{4'} \cdots \text{H}_2\text{O} \cdots \text{O}^{2'}$. This arrangement allows for a second strong intermolecular hydrogen-bonding between $\text{O}^{2'} \cdots \text{N}^{1'}$. Exploring the stacking behaviour down the *a*-axis shows a distance and offset between planes (which are again are co-planar) of 3.56438(8) and 1.315(13) Å, indicating that no π stacking effects are present akin to complex **1**.

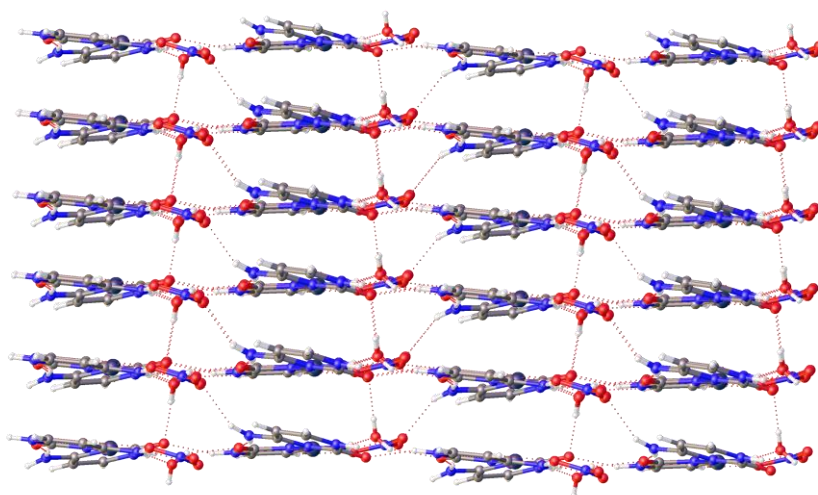


Figure 2.6 A packed view into the crystal structure of **2** looking down the *b*-axis showing the intermolecular hydrogen bonding interactions and resultant layers.

Transoid-[Ag^I(*N*³-Cytosine)₂]⁺[PF₆]⁻·2H₂O, **3** (**Figure 2.7**), was prepared in an aqueous solution of cytosine and silver hexafluorophosphate at a ligand-to-metal-ion ratio of 2:1. The solution was kept at room temperature avoiding exposure to ambient light where possible. Crystals were encouraged to form in a vapour diffusion set-up with acetonitrile (MeCN) as the miscible antisolvent; yielding colourless crystals of **3** after 21 days. Unlike the previous example described above the metal-ion occupies a centre of symmetry and therefore the Ag-*N*³ bonding lengths are equivalent at 2.166(1) Å with a linear N-Ag-N bond angle of 180°. The complex organises into a *transoidal* conformation as a direct consequence. The nucleobase-ligands are not entirely coplanar, angled at approximately 10° with respect to the coordination plane. Two water molecules decorate the complex above and below the metal-ion (1.918(6) Å) providing an ideal bridge across the exocyclic *N*⁴-donor (*N*⁴-H...OH₂, 2.945(2) Å) and O²-acceptor (O²...H-OH, 2.749(2) Å) of the flanking ligands. The *transoid* arrangement provides an ideal arrangement towards the capture of water molecules as seen here. As expected with a linear confirmation, the distances across the *N*⁴-O² sites are too distant (4.4321(17) Å) for hydrogen bonding to realistically occur between these groups.

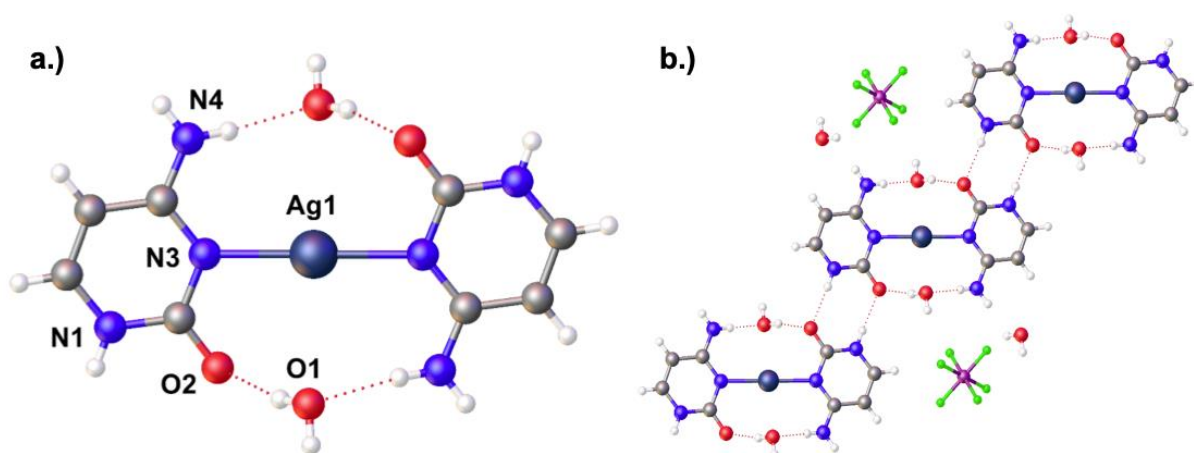


Figure 2.7 The complex cation *transoid*-[Ag^I(*N*³-cytosine)₂·2H₂O]⁺[PF₆]⁻, **3**; a.) The molecular structure with atomic assignments and b.) hydrogen bonding interactions in the solid-state structure.

Packing of the unit cell reveals how the single crystal lattice of **3** is assembled. Four primary interactions exist; O^{2'}...H₂O (2.7498(15) Å), N⁴...H₂O (2.945(2) Å) and two instances of N¹...O² (2.8002(16) Å) (**Figure 2.8**). Interestingly, in this symmetry generated view, the solvent motif more clearly shows to act as an intramolecular H-bonding bridge across a single complex ion, N⁴-H₂O-O^{2'}. Exploring the stacking behaviour down the *a*-axis shows a distance and offset between planes (which are again are co-planar) of 5.7355(1) or 4.2342(11) Å, indicating that no π stacking effects are present akin to complex **1** and **2**. The PF₆ anions do not have any clear interactions with the complex cations, existing between the spaces. The closest possible interaction is 3.0315(17) Å to an exocyclic N⁴ donor.

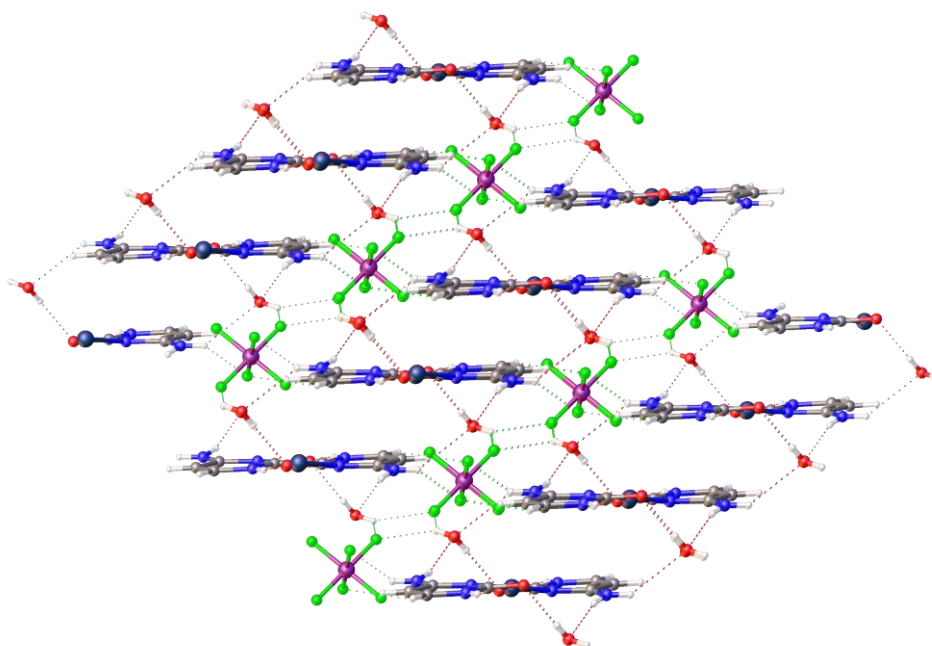


Figure 2.8 A packed view into the crystal structure of **3** looking down the *a*-axis showing the intermolecular hydrogen bonding interactions and resultant layers.

The solvent motif observed in complexes **2** and **3** have been speculated to have a stabilising role in the metal-mediation of nucleic acids (**Figure 2.9**). The position and distances suggest a bridging role across the N^4 -donor and O^2 -acceptor of both bent and linear geometries. However, the location and distances to the metal-ion must be considered. A comprehensive search through the Cambridge Structural Database (CSD) using Conquest for Ag-OH₂ occurrences revealed an average coordination distance of 2.462 ± 0.154 Å ($n = 618$). Including the N-Ag-N coordination with the Ag-OH₂ query gave an average distance of 2.547 ± 0.128 Å ($n = 269$). The distances between the central metal-ion and solvent motif for complexes **2** and **3** are 2.577(5) and 3.2192(12) Å respectively. The long distances in complex **3** suggest a purely bridging role; showing a weak affinity for the metal-ion.

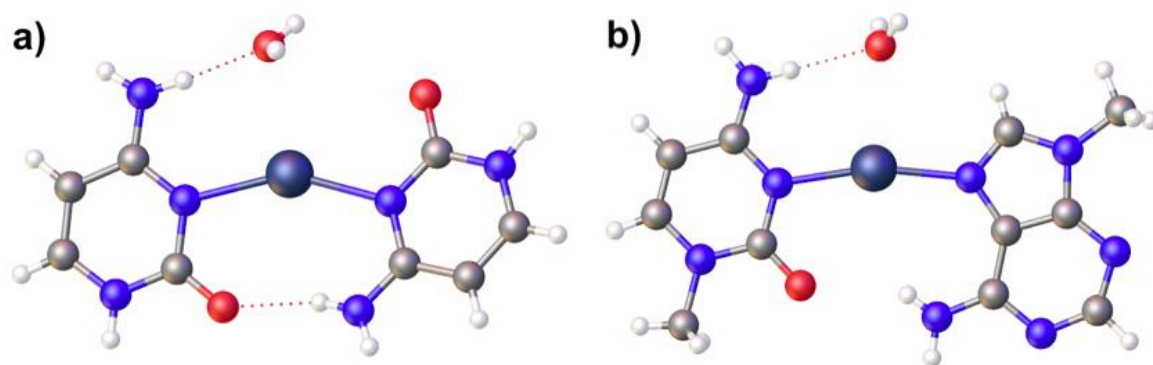


Figure 2.9 Comparison of the molecular cation of complex **2** and $[\text{Ag}^{\text{I}}-(N^3\text{-1-methylcytosine})(N^7\text{-9-methyladenosine})\text{H}_2\text{O}]^+$ highlighting the hydrogen bonding of the water molecules.

DFT calculations of all possible conformations were performed both constrained and unconstrained as a method of establishing the relative stabilities of the various conformations (performed using Gaussian 09 with the B3LYP functional and LanL2DZ basis-set processed).[‡] In principle, several different conformational arrangements are possible (ignoring twist-angles across ligands) for this coordination motif, based on combinations of linear/bent coordination geometries and *cisoid/transoid* orientations of the ligands (**Figure 2.10**). The transoid arrangement is often considered preferential due to the complementary positioning of the hydrogen bonding donor (N^4) and acceptor sites (O^2). However, for linear geometries the distances between those respective groups is too large, at $>4.0 \text{ \AA}$, for any interactions to be considered. Interestingly, to date for the several examples that currently exist of this coordination motif, it is the *cisoid* confirmation that has been generally observed.

[‡] The DFT calculations did not include explicit water molecules as shown in complexes **2** and **3**.

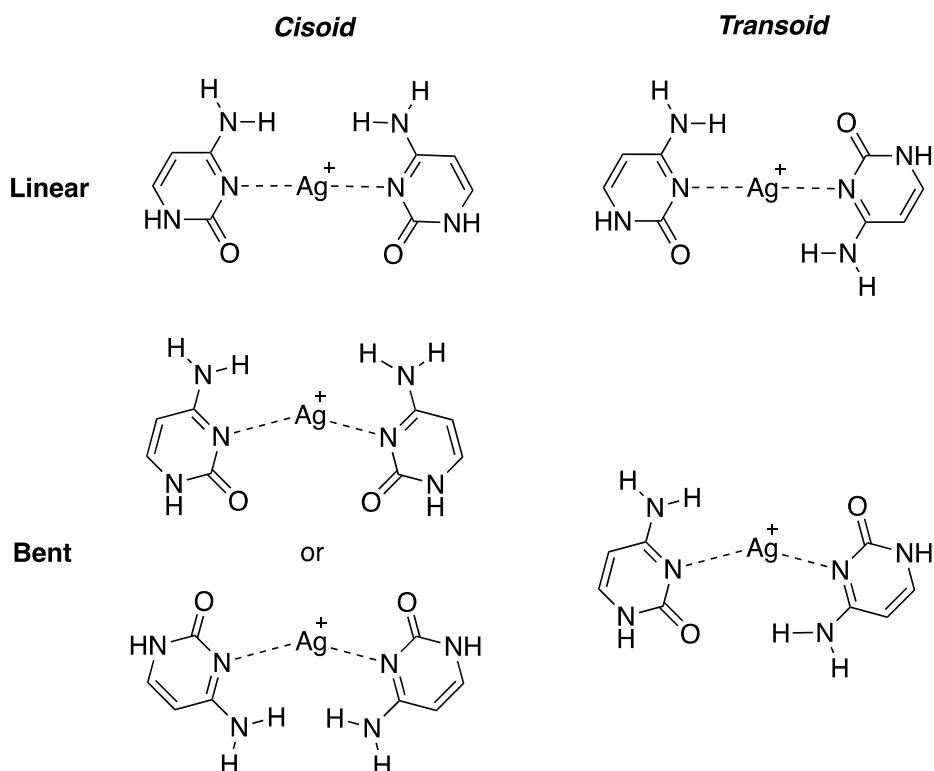


Figure 2.10 An illustration of the five possible confirmations of *bis*-[Ag^I-(N³-Cytosine)₂]⁺ in the solid state; Bent vs. Linear and *cisoid* vs. *transoid*.

Calculations of the *transoid*-bent (T_{bent}) geometry were obtained from an unconstrained relaxation (energy minimisation) of the C-Ag^I-C complex and was found to possess the lowest structural energy. This minimised geometry is due to the stabilising $O^2 \cdots H-N^4$ intramolecular hydrogen-bonding event (**Figure 2.11**). Constraining the N-Ag-N model geometry to a linear (180°) angle, preventing those groups from having any significant interactions, therefore reduces the overall stability of the complex. The relative stability sequence with the permutations, *cisoid* (C)/*transoid* (T) vs. bent/linear is; $T_{\text{bent}} > T_{\text{linear}} > C_{\text{linear}} > C_{\text{bent}}$. Interestingly, only examples of C_{linear} have been crystallographically characterised to date.

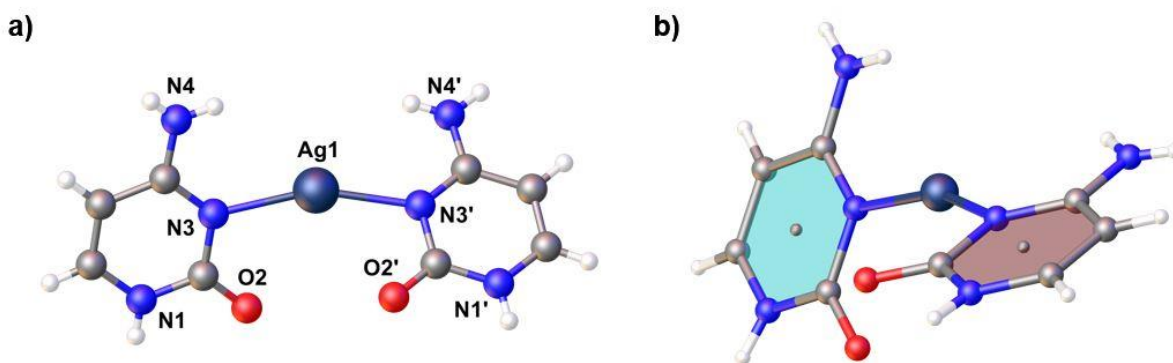


Figure 2.11 Two views of the complex cation of 1, highlighting the bent and twisted cisoidal conformation of the cytosine ligands.

Figure 2.12 shows how the inter-plane twist angle, θ , between cytosine ligands effects the energy of the complex. As often assumed, the *transoidal* conformation, T_{linear} ($\theta = 0^\circ$), is most stable. A steady destabilisation is observed as θ increases from 0 - 180° . In contrast, C_{linear} is indicated as the least stable, ($\theta = 180^\circ$).

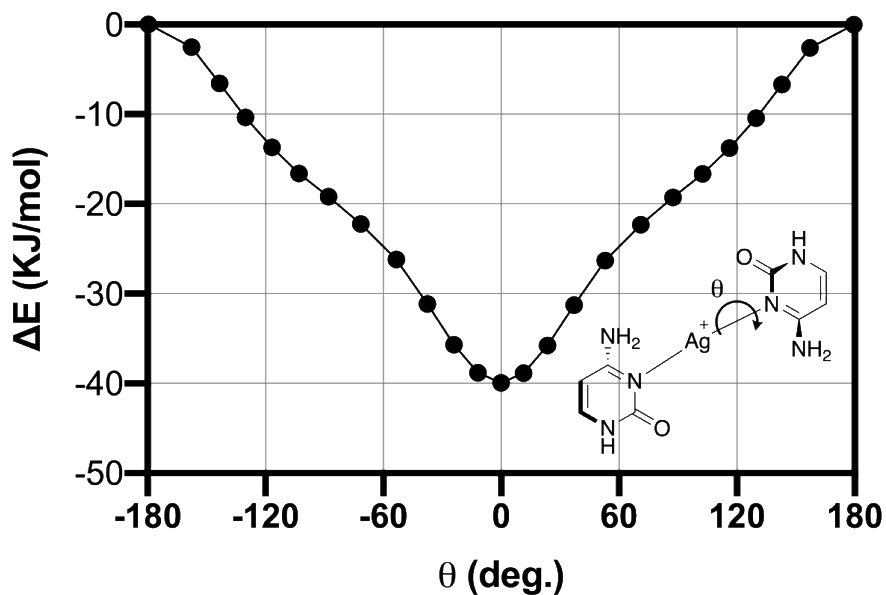


Figure 2.12 Calculated change in energy (ΔE , KJ mol $^{-1}$) against dihedral angle, θ , between the ligands for $[Ag^I-bis-(N^3-cytosine)]^+$ with a linear N-Ag-N coordination (180°) and set bond lengths of 2.175 Å. *Transoidal* conformation corresponds to $\theta = 0^\circ$ and *cisoidal* as $\pm 180^\circ$.

With the flanking cytosine ligands constrained to be co-planar, the relative stabilities for the four possible conformations shown in **Scheme 2.2** is: **T_{bent}** > **T_{linear}** > **C_{linear}** > **C_{bent}**. For the bent *cisoid* (**C_{bent}**) arrangement, two distinct types can be produced depending the N-Ag-N bond angle. If they are brought closer, by a change in the N-Ag-N angle, the O² (**C_{bent-oo}**) or N⁴ (**C_{bent-NN}**) sites can H-bond. **Figure 2.13** shows that compressing this angle towards the exocyclic amino groups has a more rapidly destabilizing effect than bringing the oxygen sites together. To date, for crystallographically characterized small molecule complexes the range of N-Ag-N angles ranges 148 - 177° in [Ag^I(N³-1MeC)₂],⁴³ 164 - 173° in [Ag^I(N³-1HexC)₂],³² and 169 - 177° in [Ag^I(N³-cytidine)₂]⁴⁴ though in these examples the ligands are significantly twisted with respect to one another.

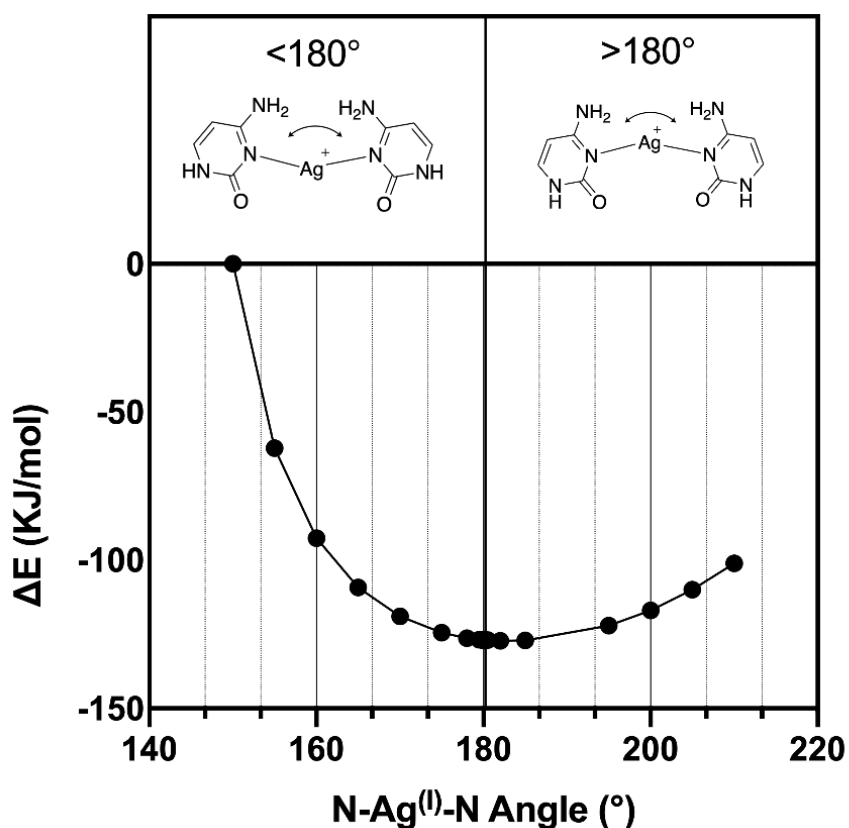


Figure 2.13 Change in energy (ΔE , KJ mol⁻¹) for the *cis*-[Ag^I-(cytosine)₂]⁺ complex as a function of N-Ag⁺-N bond angle. Angles >180° are **C_{bent-oo}** type while angles <180° are **C_{bent-NN}**. Ag⁺-N bond lengths were fixed at 2.175 Å and dihedral angle between ligands is equal to 0°; *i.e.* co-planar ligands.

Two-coordinate N-Ag-N systems; however common, are not exclusively confined to linear geometries ($>170^\circ$). A comprehensive study of the Cambridge Crystallography Structural Database (CCSD) using ConQuest (Version 2.0.0) coupled with the analysis features of Mercury (Version 4.0.0) yielded approximately one-hundred examples found at the time of writing with N-Ag-N angles between $140 - 160^\circ$.

Fourier transform infrared (FTIR) spectroscopy studies have previously been used to assess the binding properties between Ag^I and R/DNA of various types.^{13,45,46} Despite several experimental reports assessing m-R/DNA structures, reports of simple Ag^I -cytosine are rather scarce, however, several comprehensive studies exist assigning vibrations of the nucleobase cytosine and its tautomers.^{47–49} The lack of experimental literature is likely due to the limited effect of a single exocyclic bound heavy atom motif on the molecular vibrations, bending and stretching of the ligand (*See appendix for table of assigned FTIR peaks*).

Cytosine (4-amino-2(1H)-pyrimidinone or 4-amino-2-hydroxypyrimidine) predominantly exists as the amino-oxo or -keto tautomer, however five other minor tautomeric species exist (**Figure 2.14**).^{50–53} These structures have been studied both experimentally and computationally by DFT methods measuring the vibrations associated with FTIR. The findings of this investigation offering a viable comparison for assignments of complexes **1-3**. Interestingly, of these five minor tautomers studied the enol is the only species with a greater stability than the keto when isolated in the solid state; making it highly prevalent in the study of cytosine tautomerism.

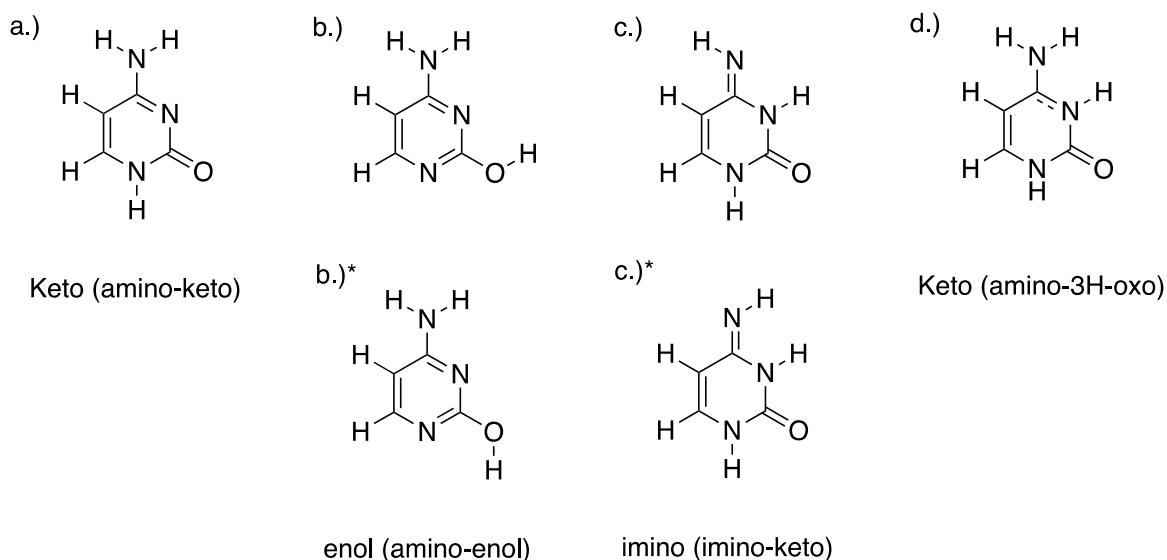


Figure 2.14 The six tautomers of cytosine; a.) keto, b.) enol, c.) imino-keto and d.) 3H-oxo.^{50–53}

To validate DFT results which showed an energetic preference towards a *transoidal* conformation in solution, a prepared aqueous solution of $[\text{Ag}-(\text{cytosine})_2]$ was rapidly freeze-dried and analysed by PXRD techniques. The act of rapidly freeze drying the material removes its ability to organise into an aligned lattice. **Figure 2.15** shows the experimental pattern acquired using this technique vs. the calculated pattern for the lowest energy state calculated, represented by the single crystal of **2**. The two patterns when overlapped shared many similar Bragg peaks indicative of a global *transoidal* complex ion conformation. These results demonstrate that the most likely conformation of the $[\text{Ag}^I-(\text{cytosine})_2]$ complex in solution is *transoidal*, in agreement with calculated in **Figure 2.12**. However, the conformation has been shown to subsequently alter depending on its crystallisation environment.

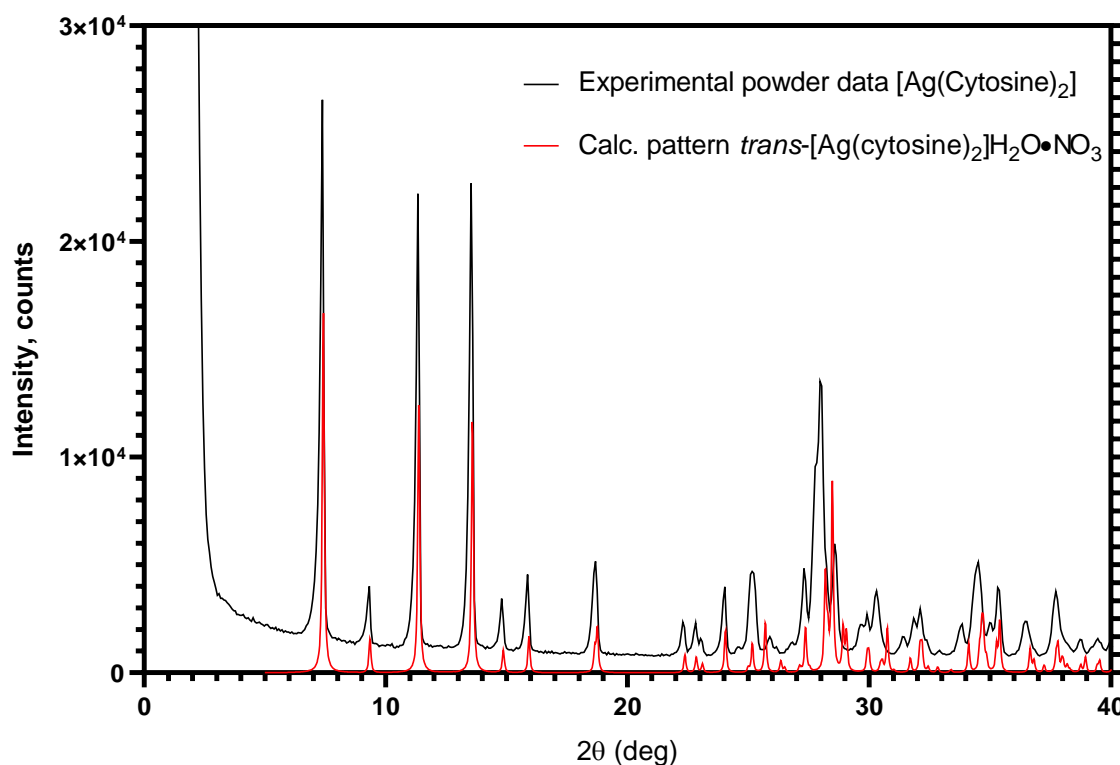


Figure 2.15 PXRD patterns acquired for $[\text{Ag}^{\text{I}}\text{-(Cytosine)}_2]$ prepared by freeze-drying techniques vs. a calculated pattern of $\text{trans-}[\text{Ag}^{\text{I}}\text{-(cytosine)}_2]\cdot\text{H}_2\text{O}\cdot\text{NO}_3$ from the single crystal data gained for **2**.

A satisfactory interpretation of the FTIR data for complexes **1** - **3** were made possible by computational and experimental studies of cytosine and cytidine (**Figure 2.16**).^{47–49,54} Small differences in the FTIR spectra around 1600 cm^{-1} for all three complexes were most notable, and were associated with the O^2 carbonyl of the cytosine ligand. The characteristic signals relating to the N^1 and N^4 positions were also slightly altered when compared to their parent ligand. A shift to lower wavenumbers and peak broadening is indicative of H-bonding interactions. However, direct evidence attributed to the newly formed $\text{N}^3\text{-Ag}^{\text{I}}$ coordination could not be easily linked to a new or existing characteristic vibrational difference. Similarities found within the solid states for complexes **1** - **3** *versus* cytosine was found to cause ambiguity.

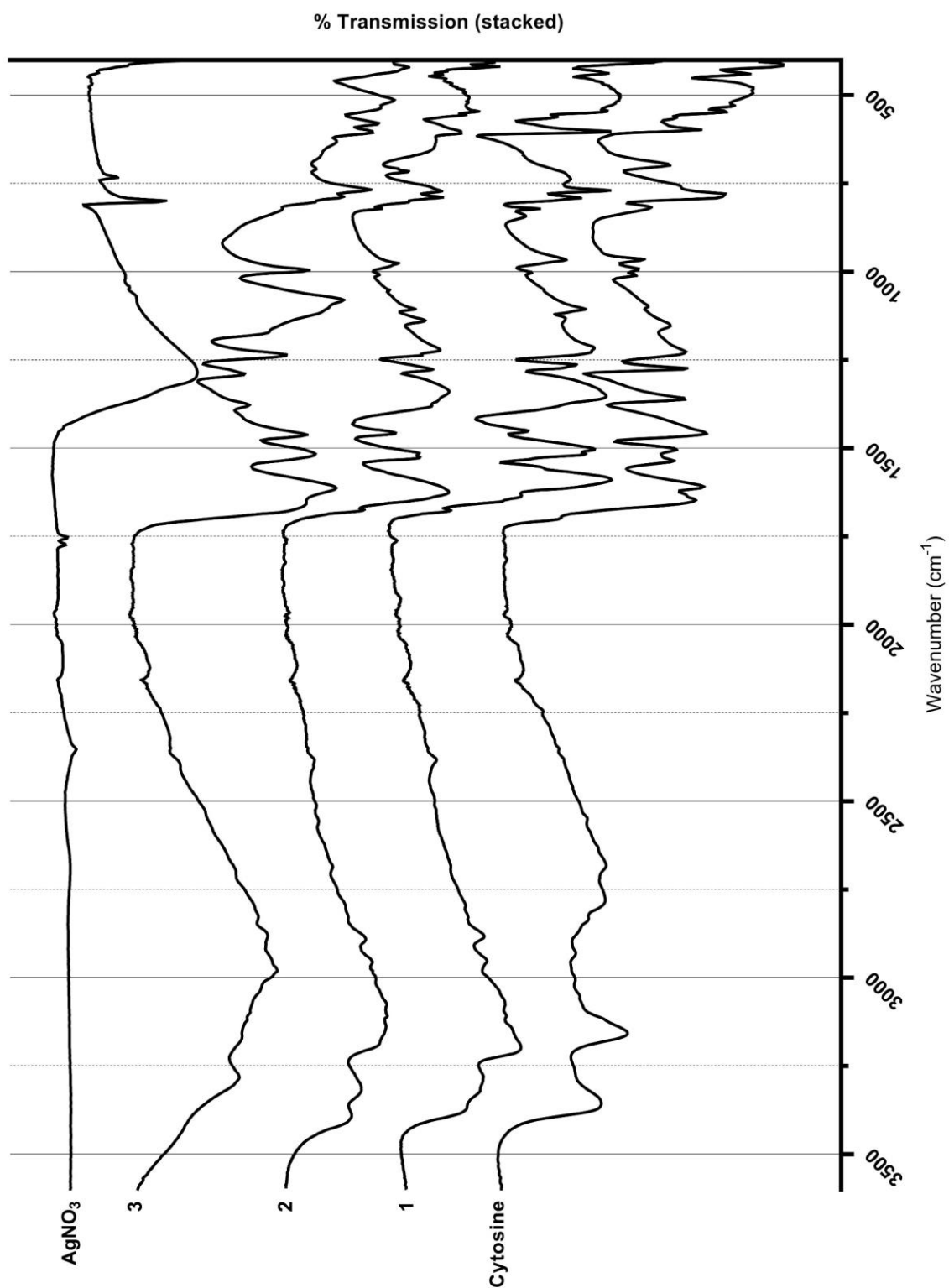


Figure 2.16 Stacked experimental FTIR spectra of cytosine, complexes 1 – 3 and silver nitrate.

To illustrate the differences in the intramolecular binding of cytosine within the solid-state (without a coordinating metal-ion) The Cambridge Crystallographic Database (CCDC) was interrogated. Eleven structures were identified as polymorphs of the natural nucleobase cytosine, eight of which were hydrates; two representative examples are shown below (**Figure 2.17**). The intermolecular hydrogen bonding within all polymorphs were alike; N^1-N^3 , O^2-N^4 and $O^2-H_2O-N^4$ present in the hydrate. The loss of only the N^1-N^3 interaction would be expected compared against complexes **1** – **3**. However, many of the intermolecular interactions useful in IR characterisation are indistinguishable spectroscopically when compared to complexes **1** – **3**.

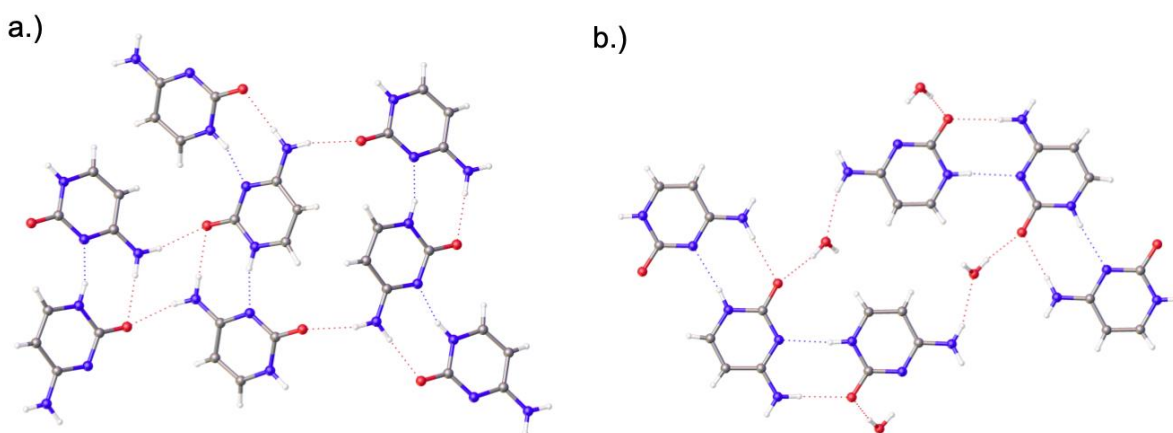


Figure 2.17 Packing diagrams displaying the hydrogen bonding interactions in the solid-state for a.) cytosine (CYTSIN) and b.) cytosine-monohydrate (CYTOSM).

Electrospray-Ionisation-Mass Spectrometry (ESI-MS) was used as a qualitative technique to confirm the presence of the *bis*-[Ag^I-(*N*³-Cytosine)₂]⁺ complex in aqueous solution. The expected C-Ag^I-C complex was observed as a [M]⁺ ion using ESI-MS (direct injection, positive ion mode) at 328.9986 m/z (**Figure 2.18**). Isotope patterns, splitting and masses aligned well with the theoretical values calculated for a 1:2 Ag^I-cytosine complex derived from the crystal structures; Calc. C₈H₁₀AgN₆O₂, [M]⁺, 328.9916 m/z (monoisotopic mass). Peak separation of 1.0 m/z suggests a species bearing a plus one charge, which was achieved by the metal ion without the loss of a proton. Silver possess two unique stable isotopes, ¹⁰⁷Ag (328.9986 m/z) and ¹⁰⁹Ag (330.9939 m/z) with ¹⁰⁷Ag being slightly more abundant (51.839%). The calculated

mass ($\text{C}_8\text{H}_{10}\text{AgN}_6\text{O}_2$; Calc. 328.99 m/z) and isotope pattern matched those of the experimental spectra in both positive and negative-ion modes.

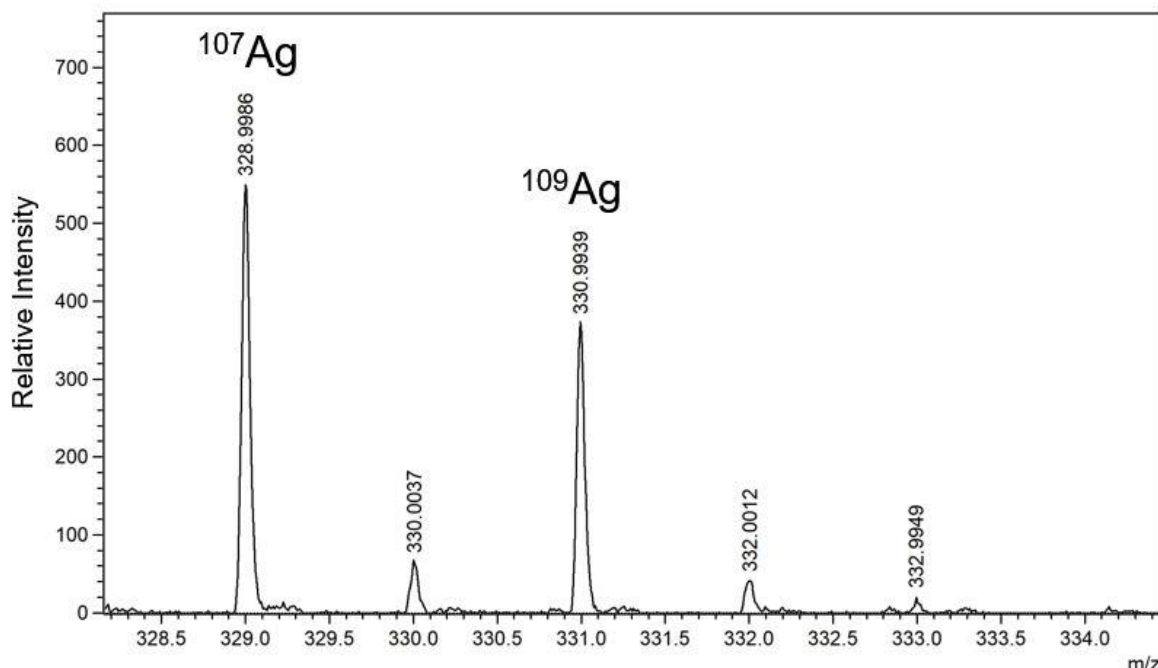


Figure 2.18 ESI-MS (positive ion mode) of an aqueous solution of $[\text{Ag}^{\text{I}}-(\text{cytosine})_2]^+$ ($\text{C}_8\text{H}_{10}\text{AgN}_6\text{O}_2$, $[\text{M}]_{\text{Calc.}}$: 328.9916 m/z). The two naturally stable isotopes of silver (^{107}Ag and ^{109}Ag) can be observed at 328.9986 and 330.9939 m/z.

Spectroscopic UV-Vis data was analysed for cytosine_(aq) and Ag^{I} -cytosine_(aq) at the expected 2:1 metal-to-ligand ratio. No changes were observed in either position or intensity of the absorption band (**Figure 2.19**). This is due to the main chromophore, cytosine, largely remaining unchanged when coordinated through the Lewis base N^3 -donor to Ag^+ or Lewis acid. Furthermore, the selection rule with forbidden d-d transitions would also help explain the observations. The formation of a peak around 400 nm was expectedly observed following chemical reduction of Ag^+ to its elemental Ag^0 state. This was achieved by the addition of sodium borohydride (NaBH_4^+) causing a rather dramatic and instantaneous formation of silver-nanoparticles (AgNPs) seen as a black precipitated.

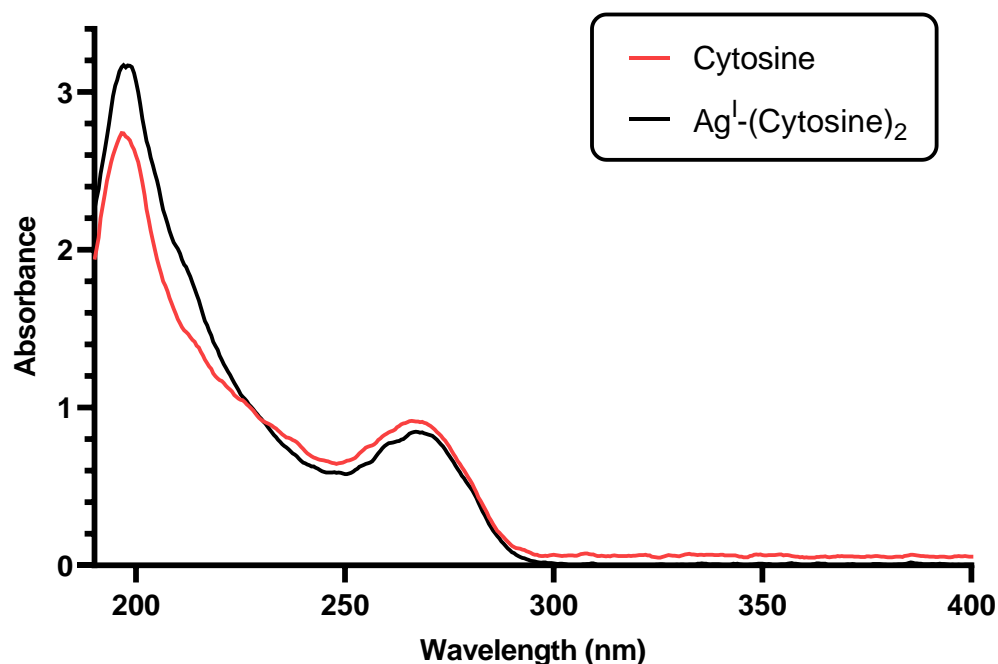


Figure 2.19 UV-vis data of the parent ligand cytosine (red-line) and following the addition of silver nitrate at a ligand-to-metal ratio of 2:1.

To further interrogate the structure and binding modes isothermal titration calorimetry (ITC) was used as a method of thermal quantification of bonding events in solution. The amount of heat liberated (exothermic (-)) or absorbed (endothermic (+)) as the reaction proceeds can be quantified as coordination events. The heat changes are typically very small, sub-millionths of a degree, but are universal and can be detected. The number of coordination events can be thermally quantified using a known titrant concentration. This method of analysis assumes that the only interaction occurs between Ag⁺ and cytosine at the expected *N*³ site. The heat of solvation, dilution effects and drift are accounted for during prior control experiments. Once the titration is complete the raw data showing individual injection peaks are converted into a wiseman plot for examination.⁵⁵ An appropriate binding model is chosen, and the isotherm is fitted to give binding enthalpies (ΔH), association constant (K_a) and stoichiometry (n). For simple chemical systems, as we have shown here, these values can be readily calculated from the plot. The binding enthalpy, ΔH , is typically the difference in energy between the major peak and baseline, association constant, K_a , is the steady gradient from that peak and stoichiometry, n , is the molar ratio position at the mid-point along that slope.

A concentrated solution of AgNO_3 (5.0 mM) was titrated against cytosine (0.1 mM) held at 25°C gave a clear sigmodal isotherm (**Figure 2.20**). The negative peaks indicate an exothermic reaction, releasing $-2.74 \text{ KJ mol}^{-1}$ (-655.5 cal/mol) of energy (ΔH). The total number of available sites or molar ratio gave $n = 0.5$, in agreement with a 2:1 reaction ligand-to-metal stoichiometry observed in the single crystal.

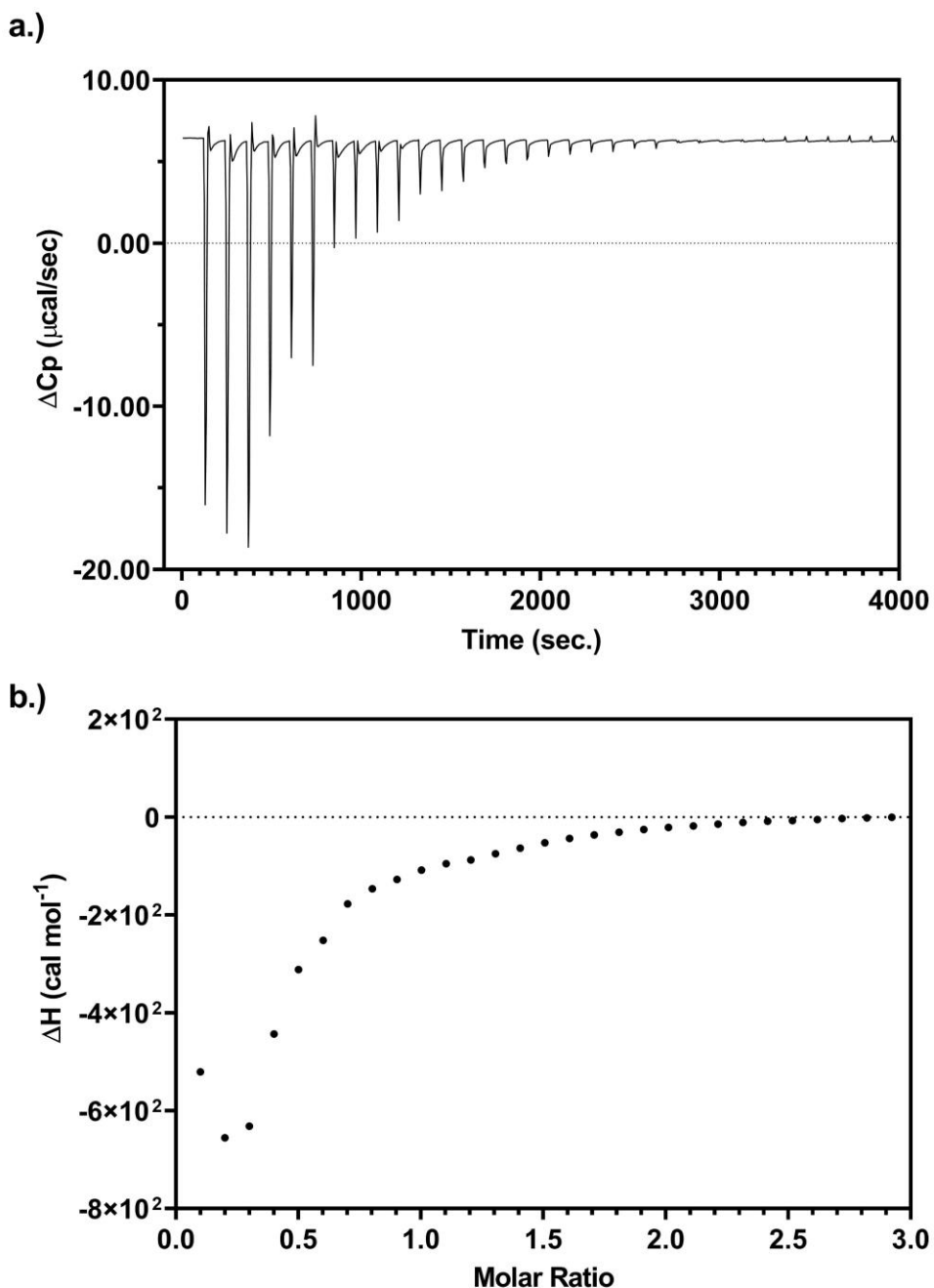
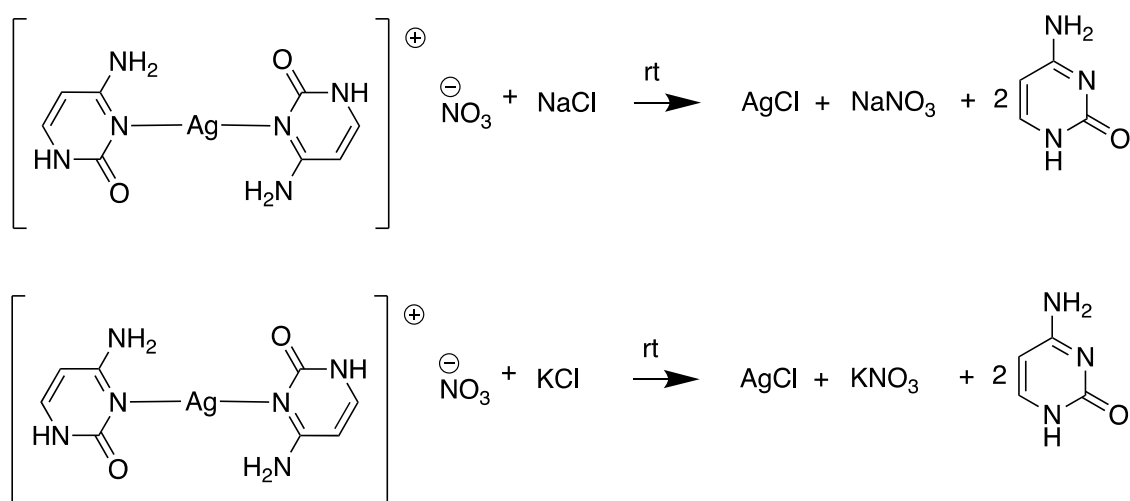


Figure 2.20 a.) Isothermal titration calorimetry (ITC) data recorded by titrating Ag^+ ions against cytosine (40-injections with time intervals of 120 seconds per injection)

shown as the change in heat capacity, ΔC_p). b.) Integrated peaks as a Wiseman plot presenting binding isotherms (ΔH) vs. molar ratio.[§]

Ligand Transformation Experiment

In an exercise to establish the reversibility of the N^3 -Ag bond a simple ligand transformation experiment was carried out. Sodium or potassium chloride was added to an aqueous solution bearing $[Ag^I-(Cytosine)_2]^+\cdot NO_3^-$. By offering a more labile anion to the silver-ion we expected to see ligand exchange (**Scheme 2.3**). The colourless solutions showed a rapid and spontaneous formation of AgCl as a white precipitate at room temperature. This solid was subsequently filtered off and confirmed to be AgCl *via* FTIR spectroscopy (see supporting information). The facile precipitation of AgCl allowed me to conclude that the Ag-cytosine complexation reaction was reversible.



Scheme 2.3 Ligand transformation experiment, exchanging cytosine for chloride anions.

[§] ITC data only accounted for dilution effects (*i.e.* volume change) as a background (water-into-water).

Mechanical Synthesis of $[\text{Ag}^{\text{I}}-(\text{N}^3\text{-Cytosine})_2]$

Mechanical synthesis or mechano-synthesis methods has been around since the early fourteenth century, primarily used for increasing the effectiveness of gunpowder when finely ground down.⁵⁶ More commonly today employed in the fabrication of super-alloys or nanocrystalline materials. The mechanical milling process provides a way of mixing or combining solids, usually in powder form, down to an atomic level while remaining in a solid state.^{56–58}

The common laboratory-based approach involves the use of high energy ball milling process which has since established itself as a viable solid-state dry-synthesis processing route. Initially, this method was developed for the mixture of new alloy composites in a homogenous state.^{57–60} More recently, mechano-methods have found their way into synthetic⁶¹ and nanomaterial chemistry⁵⁶. This approach to synthesis is defined as “*a method in which the reaction outcome is determined by the use of mechanical constraints to direct reactive molecules to specific molecular sites*”.

Herein we describe the mechano-synthesis of C-Ag^I-C *bis*-complex in the absence of solvent. The milled material was subsequently analysed by FTIR and PXRD techniques. Cytosine (2 equiv.) and silver nitrate (1 equiv.) were placed within a high-energy ball-mill (14 Hz) for a total of five hours. At each one-hour interval samples (ca. 10 mg) were taken for real-time analysis.

The spectroscopic data collected at one-hour time intervals showed an evolution of the material as it underwent mechanical milling. The changes of the spectra after five-hours are similar to those observed for complexes **1-3**. Small differences in the peak position around 1600 cm⁻¹ were most notable, associated with the O² carbonyl of the cytosine ligand. The characteristic signals relating to the N¹ and N⁴ positions were also

slightly changed when compared to their parent ligand over time. A shift to lower wavenumbers and peak broadening is indicative of changes occurring of the H-bonding interactions. This is most noticeable broadening can be seen of peaks at higher wavelengths, between 3000 – 3500 cm^{-1} .

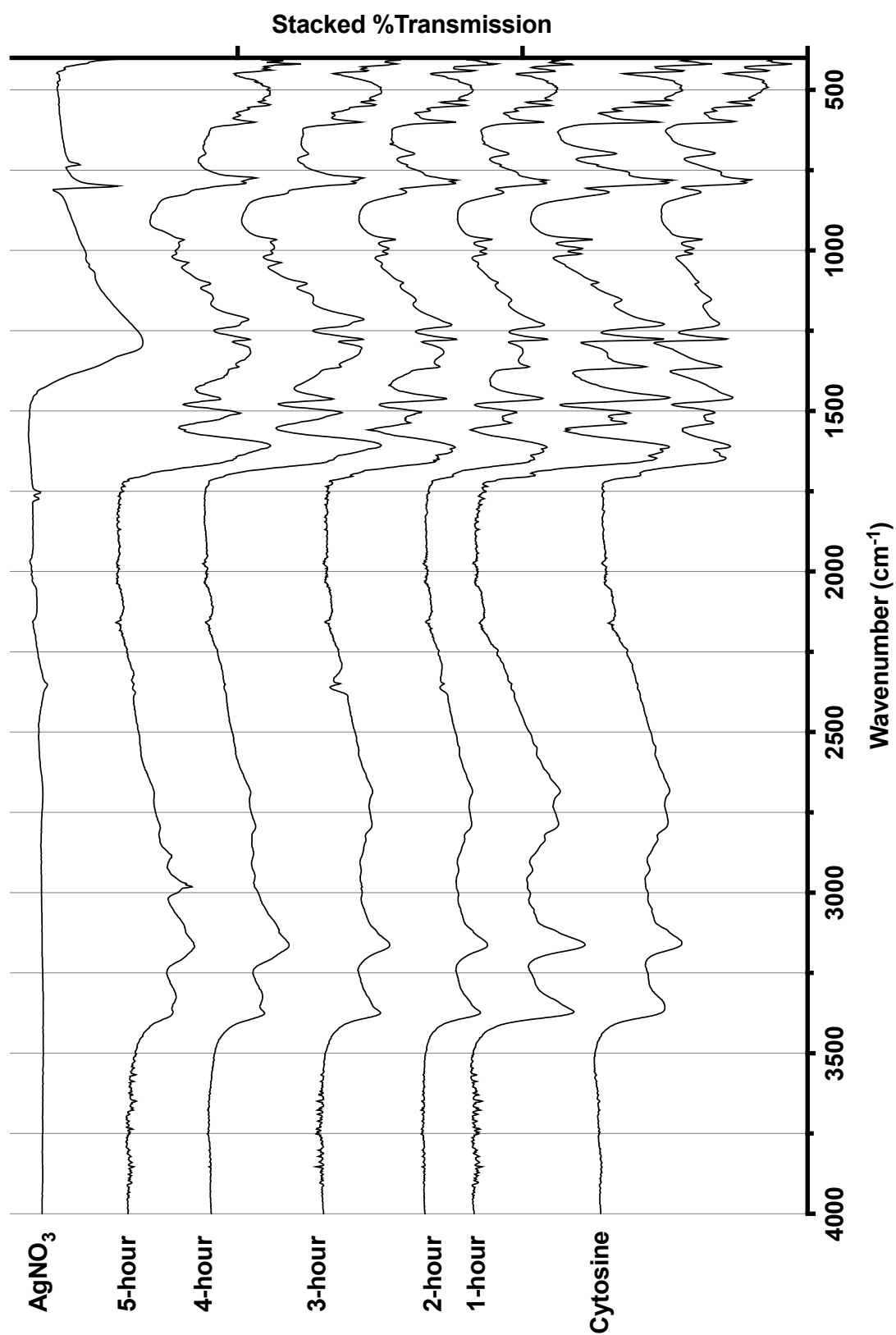


Figure 2.21 Stacked FTIR data following mechanical milling of cytosine and silver nitrate at a 2:1 ratio over five-hours.

The powder x-ray diffraction (PXRD) data collected for material following five-hours of milling can be seen in **Figure 2.22**. The experimental patterns collected after five hours of milling were unsurprisingly amorphous in nature and lacked clarity. Nevertheless, four major Bragg peaks were identified at 7.42, 11.04, 13.64 and 28.08° that showed good fit against the calculated pattern for compound **2**. Moreover, the patterns analysed of the milled material shared no similar characteristics to either of its starting reagents, cytosine or silver nitrate. This indicated a reaction of the two rather than a mixture had occurred during the milling process. These results indicate that complex **2** is favoured when not confined within a regular lattice framework as in a single crystal.

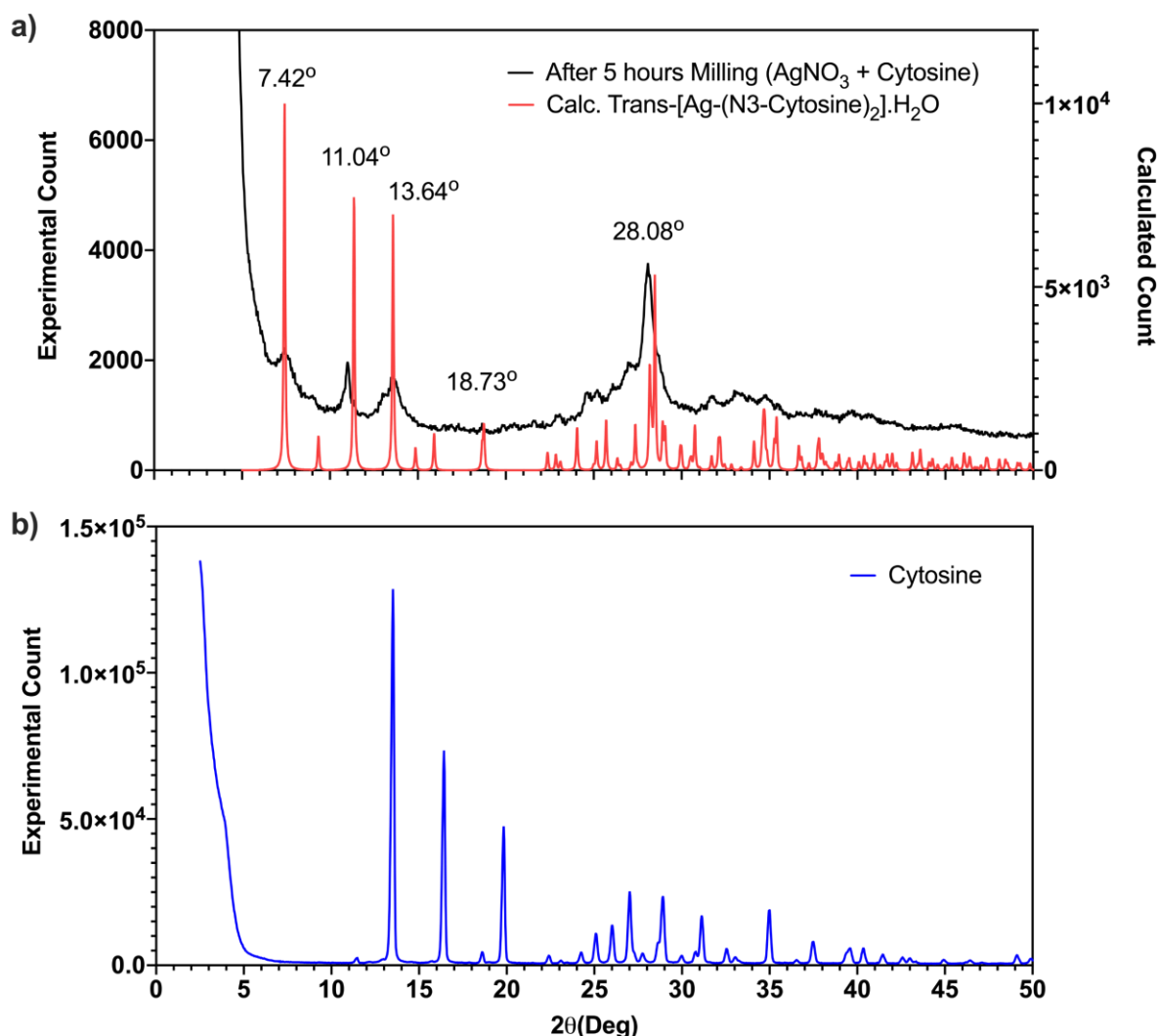


Figure 2.22 PXRD data for (a.) material milled for 5 hours (silver nitrate (1 equiv.) + cytosine (2 equiv.)), Black-line) *versus* a calculated pattern for **2** (red-line) and (b.) experimental powder pattern for cytosine (blue-line).

To further validate this, cytosine was milled for five-hours showing a decrease in peak intensity and slight increase in background noise compared to the starting pattern (See supporting information).

2.3. Conclusions

For the first time since its discovery of the highly selective C-Ag-C metal-mediation over 70 years ago, we have isolated and structurally characterised a series of simple silver-cytosine complexes by X-ray diffraction of single crystals. By using a judicious choice of silver-salts and crystallisation techniques it has been possible to isolate a series of $[\text{Ag}-(\text{N}^3\text{-Cytosine})_2]^+$ complexes; displaying several *bis*-conformations, *cisoid/transoid*, bent and linear geometry combinations. Predominantly, the *cisoid* conformation had been observed in oligonucleotide structures previously, with essentially linear N-Ag-N coordination geometries. The dramatically different hydrogen-bonding patterns in these compounds has shown dependence on the presence of solvent in the *transoidal* orientation, allowing for macrocyclic solvent bridge across the exocyclic heteroatom donor N^4 and acceptors O^2 . In their absence the distance across these two H-bonding partners is too large for intermolecular interactions to occur.

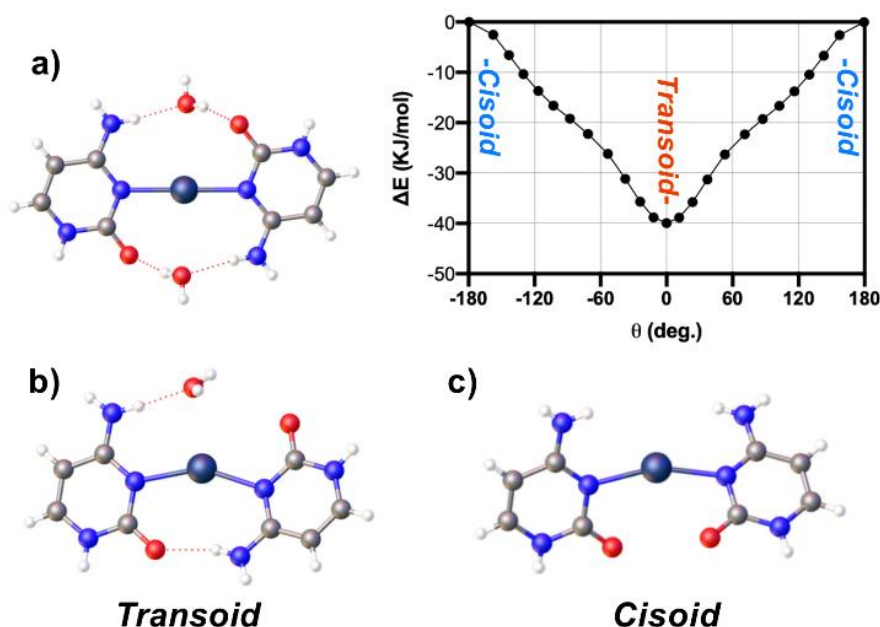


Figure 2.23 Three crystallographically characterised C-Ag^I-C *bis*-complexes displaying both *cisoid/transoid*, bent/linear geometries. Inset shows the energies of different isomers calculated by DFT. The N-Ag-N dihedral angle, θ , between the

ligands of a linear coordination were sampled through a complete rotation of 360° (Transoid conformation corresponds to $\theta = 0^\circ$; cisoid to $\pm 180^\circ$).

Critically, the foundation and understanding we have gained by fully characterising the most basic natural metal-mediated silver-pyrimidine system is a critical component in any further chapters discussed in this body of work. It has been shown that the bis- $[(Ag^I-(Cytosine)_2)]$ complex can exist as either *cisoid* or *transoid* in the solid-state. It is however likely that the more stable *transoidal* conformation exists in solution, as demonstrated by DFT and PXRD studies.

2.4. References

- (1) Yamane, T.; Davidson, N. On the Complexing of Deoxyribonucleic Acid by Silver(I). *BBA - Biochim. Biophys. Acta* **1962**, 55 (5), 609–621. [https://doi.org/10.1016/0006-3002\(62\)90839-9](https://doi.org/10.1016/0006-3002(62)90839-9).
- (2) Gillen, K.; Jensen, R.; Davidson, N. Binding of Silver Ion by Adenine and Substituted Adenines. *J. Am. Chem. Soc.* **1964**, 86 (14), 2792–2796. <https://doi.org/10.1021/ja01068a008>.
- (3) Dattagupta, N.; Crothers, D. M. Solution Structural Studies of Ag(I)-DNA Complex. *Nucleic Acids Res.* **1981**, 9 (12), 2971–2985.
- (4) Lippert, B.; Sanz Miguel, P. J. The Renaissance of Metal-Pyrimidine Nucleobase Coordination Chemistry. *Acc. Chem. Res.* **2016**, 49 (8), 1537–1545. <https://doi.org/10.1021/acs.accounts.6b00253>.
- (5) Clever, G. H.; Kaul, C.; Carell, T. DNA-Metal Base Pairs. *Angew. Chemie - Int. Ed.* **2007**, 46 (33), 6226–6236. <https://doi.org/10.1002/anie.200701185>.
- (6) Li, Y.; Yuan, J.; Xu, Z. A Sensitive Fluorescence Biosensor for Silver Ions (Ag^+) Detection Based on C-Ag⁺-C Structure and Exonuclease III-Assisted Dual-Recycling Amplification. *J. Anal. Methods Chem.* **2019**, 2019, 1–8. <https://doi.org/10.1155/2019/3712032>.
- (7) Kim, J. H.; Kim, K. B.; Park, J. S.; Min, N. Single Cytosine-Based Electrochemical Biosensor for Low-Cost Detection of Silver Ions. *Sensors Actuators, B Chem.* **2017**, 245, 741–746. <https://doi.org/10.1016/j.snb.2017.01.181>.

- (8) Luo, Y. Functional Nucleic Acid Based Biosensors for Noble Metal Ion Detection. In *Functional Nucleic Acid Based Biosensors for Food Safety Detection*; Springer Singapore: Singapore, 2018; pp 161–183. https://doi.org/10.1007/978-981-10-8219-1_6.
- (9) Wu, Y.; Lai, R. Y. A Reagentless DNA-Based Electrochemical Silver(I) Sensor for Real Time Detection of Ag(I) — the Effect of Probe Sequence and Orientation on Sensor Response. *Biotechnol J.* **2016**, *11* (6), 788–796. <https://doi.org/10.1002/biot.201500428.A>.
- (10) Guo, X.; Seela, F. Anomeric 2'-Deoxycytidines and Silver Ions: Hybrid Base Pairs with Greatly Enhanced Stability and Efficient DNA Mismatch Detection with α -DC. *Chem. - A Eur. J.* **2017**, *23* (49), 11776–11779. <https://doi.org/10.1002/chem.201703017>.
- (11) Chen, X.; Karpenko, A.; Lopez-Acevedo, O. Silver-Mediated Double Helix: Structural Parameters for a Robust DNA Building Block. *ACS Omega* **2017**, *2* (10), 7343–7348. <https://doi.org/10.1021/acsomega.7b01089>.
- (12) Kondo, J.; Tada, Y.; Dairaku, T.; Hattori, Y.; Saneyoshi, H.; Ono, A.; Tanaka, Y. A Metallo-DNA Nanowire with Uninterrupted One-Dimensional Silver Array. *Nat. Chem.* **2017**, *9* (10), 956–960. <https://doi.org/10.1038/nchem.2808>.
- (13) Linares, F.; García-Fernández, E.; López-Garzón, F. J.; Domingo-García, M.; Orte, A.; Rodríguez-Diéguez, A.; Galindo, M. A. Multifunctional Behavior of Molecules Comprising Stacked Cytosine-Ag-Cytosine Base Pairs; Towards Conducting and Photoluminescence Silver-DNA Nanowires. *Chem. Sci.* **2019**, *10* (4), 1126–1137. <https://doi.org/10.1039/c8sc04036b>.
- (14) Bhalla, V.; Bajpai, R. P.; Bharadwaj, L. M. DNA Electronics. *EMBO Rep.* **2003**, *4* (5).
- (15) Toomey, E.; Xu, J.; Vecchioni, S.; Rothschild, L.; Wind, S.; Fernandes, G. E. Comparison of Canonical versus Silver(I)-Mediated Base-Pairing on Single Molecule Conductance in Polycytosine DsDNA. *J. Phys. Chem. C* **2016**, *120* (14), 7804–7809. <https://doi.org/10.1021/acs.jpcc.5b11968>.
- (16) Vecchioni, S.; Capece, M. C.; Toomey, E.; Nguyen, L.; Ray, A.; Greenberg, A.;

- Fujishima, K.; Urbina, J.; Paulino-Lima, I. G.; Pinheiro, V.; et al. Construction and Characterization of Metal Ion-Containing DNA Nanowires for Synthetic Biology and Nanotechnology. *Sci. Rep.* **2019**, *9* (1), 1–15. <https://doi.org/10.1038/s41598-019-43316-1>.
- (17) Galindo, M. A.; Linares, F.; Orte, A.; Rodríguez-Diéguez, A.; García-Fernández, E.; Domingo-García, M.; López-Garzón, F. J. Multifunctional Behavior of Molecules Comprising Stacked Cytosine–Ag I –Cytosine Base Pairs; towards Conducting and Photoluminescence Silver-DNA Nanowires . *Chem. Sci.* **2018**, *10* (4), 1126–1137. <https://doi.org/10.1039/c8sc04036b>.
- (18) Leon, J. C.; Stegemann, L.; Peterlechner, M.; Litau, S.; Wilde, G.; Strassert, C. A.; Muller, J. Formation of Silver Nanoclusters from a DNA Template Containing Ag(I)-Mediated Base Pairs. *Bioinorg. Chem. Appl.* **2016**, *2016* (I), 1–10. <https://doi.org/10.1155/2016/7485125>.
- (19) Li, Y.; Gong, N.; Jiang, X.; Zheng, X.; Wang, Y.; Huan, S. Poly(Cytosine)-Templated Silver Nanoclusters as Fluorescent Biosensor for Highly Sensitive Detection of Uric Acid. *J. Chinese Chem. Soc.* **2016**, *63* (8), 660–667. <https://doi.org/10.1002/jccs.201600121>.
- (20) Ritchie, C. M.; Johnsen, K. R.; Kiser, J. R.; Antoku, Y.; Dickson, R. M.; Petty, J. T. Ag Nanocluster Formation Using a Cytosine Oligonucleotide Template. *J. Phys. Chem. C* **2007**, *111* (1), 175–181. <https://doi.org/10.1021/jp0648487>.
- (21) Yourston, L. E.; Lushnikov, A. Y.; Shevchenko, O. A.; Afonin, K. A.; Krasnoslobodtsev, A. V. First Step Towards Larger DNA-Based Assemblies of Fluorescent Silver Nanoclusters: Template Design and Detailed Characterization of Optical Properties. *Nanomaterials* **2019**, *9* (4), 613. <https://doi.org/10.3390/nano9040613>.
- (22) Zhang, Y.; Li, M.; Liu, H.; Ge, S.; Yu, J. Label-Free Colorimetric Logic Gates Based on Free Gold Nanoparticles and the Coordination Strategy between Cytosine and Silver Ions. *New J. Chem.* **2016**, *40* (6), 5516–5522. <https://doi.org/10.1039/c5nj03471j>.
- (23) Deng, W.; Xu, H.; Ding, W.; Liang, H. DNA Logic Gate Based on Metallo-Toehold Strand Displacement. *PLoS One* **2014**, *9* (11), 1–8.

<https://doi.org/10.1371/journal.pone.0111650>.

- (24) Lai, Y. H.; Sun, S. C.; Chuang, M. C. Biosensors with Built-in Biomolecular Logic Gates for Practical Applications. *Biosensors* **2014**, *4* (3), 273–300. <https://doi.org/10.3390/bios4030273>.
- (25) Lippert, B.; Sanz Miguel, P. J. The Renaissance of Metal-Pyrimidine Nucleobase Coordination Chemistry. *Acc. Chem. Res.* **2016**, *49* (8), 1537–1545. <https://doi.org/10.1021/acs.accounts.6b00253>.
- (26) Sigel, A.; Sigel, H.; Sigel, R. K. O. *Interplay between Metal Ions and Nucleic Acids*; Sigel, A., Sigel, H., Siegel, R. K. O., Eds.; Springer US, 2012; Vol. 10. <https://doi.org/10.1007/978-94-007-2172-2>.
- (27) Yamane, T.; Davidson, N. On The Complexing of Deoxyribonucleic Acid by Silver(I). *Biochim. Biophys. Acta* **1962**, *55*, 609–621.
- (28) Sinha, I.; Fonsecaguerra, C.; Müller, J. A Highly Stabilizing Silver(I)-Mediated Base Pair in Parallel-Stranded DNA. *Angew. Chemie - Int. Ed.* **2015**, *54* (12), 3603–3606. <https://doi.org/10.1002/anie.201411931>.
- (29) Urata, H.; Yamaguchi, E.; Nakamura, Y.; Wada, S. I. Pyrimidine-Pyrimidine Base Pairs Stabilized by Silver(I) Ions. *Chem. Commun.* **2011**, *47* (3), 941–943. <https://doi.org/10.1039/c0cc04091f>.
- (30) Khlobystov, A. N.; Blake, A. J.; Champness, N. R.; Lemenovskii, D. A.; Majouga, A. G.; Zyk, N. V.; Schröder, M. Supramolecular Design of One-Dimensional Coordination Polymers Based on Silver(I) Complexes of Aromatic Nitrogen-Donor Ligands. *Coord. Chem. Rev.* **2001**, *222* (1), 155–192. [https://doi.org/10.1016/S0010-8545\(01\)00370-8](https://doi.org/10.1016/S0010-8545(01)00370-8).
- (31) Blake, A. J.; Champness, N. R.; Hubberstey, P.; Li, W.-S.; Withersby, M. A.; Schröder, M. Inorganic Crystal Engineering Using Self-Assembly of Tailored Building-Blocks. *Coord. Chem. Rev.* **1999**, *183*, 117–138. https://doi.org/10.1007/0-387-25078-6_6.
- (32) Terrón, A.; Moreno-Vachiano, B.; Bauzá, A.; García-Raso, A.; Fiol, J. J.; Barceló-Oliver, M.; Molins, E.; Frontera, A. X-Ray Crystal Structure of a Metalled Double-

Helix Generated by Infinite and Consecutive C*-Agl-C* (C*:N1-Hexylcytosine) Base Pairs through Argentophilic and Hydrogen Bond Interactions. *Chem. - A Eur. J.* **2017**, 23 (9), 2103–2108. <https://doi.org/10.1002/chem.201604331>.

- (33) Liu, H.; Shen, F.; Haruehanroengra, P.; Yao, Q.; Cheng, Y.; Chen, Y.; Yang, C.; Zhang, J.; Wu, B.; Luo, Q.; et al. A DNA Structure Containing AgI-Mediated G:G and C:C Base Pairs. *Angew. Chemie - Int. Ed.* **2017**, 56 (32), 9430–9434. <https://doi.org/10.1002/anie.201704891>.
- (34) Kondo, J.; Tada, Y.; Dairaku, T.; Saneyoshi, H.; Okamoto, I.; Tanaka, Y.; Ono, A. High-Resolution Crystal Structure of a Silver(I)-RNA Hybrid Duplex Containing Watson-Crick-like C-Silver(I)-C Metallo-Base Pairs. *Angew. Chemie - Int. Ed.* **2015**, 54 (45), 13323–13326. <https://doi.org/10.1002/anie.201507894>.
- (35) Kondo, J.; Tada, Y.; Dairaku, T.; Hattori, Y.; Saneyoshi, H.; Ono, A.; Tanaka, Y. A Metallo-DNA Nanowire with Uninterrupted One-Dimensional Silver Array. *Nat. Chem.* **2017**, 9 (10), 956–960. <https://doi.org/10.1038/nchem.2808>.
- (36) Terrón, A.; Moreno-Vachiano, B.; Bauzá, A.; García-Raso, A.; Fiol, J. J.; Barceló-Oliver, M.; Molins, E.; Frontera, A. X-Ray Crystal Structure of a Metalled Double-Helix Generated by Infinite and Consecutive C*-Agl-C* (C*:N1-Hexylcytosine) Base Pairs through Argentophilic and Hydrogen Bond Interactions. *Chem. - A Eur. J.* **2017**, 23 (9), 2103–2108. <https://doi.org/10.1002/chem.201604331>.
- (37) Mistry, L.; Hofer, W.; Pope, T.; Horrocks, B. R.; El-Zubir, O.; Clegg, W.; Dura, G.; Wright, N.; Waddell, P. G.; Houlton, A. Addressing the Properties of “Metallo-DNA” with a Ag(I)-Mediated Supramolecular Duplex. *Chem. Sci.* **2019**, 10, 3186–3195. <https://doi.org/10.1039/c8sc05103h>.
- (38) Li, Y. M.; Xiao, C. Y.; Xu, Y. H.; Wang, S. B.; Yang, D. G. The Syntheses and Structures of Two Silver Compounds Based on Phdat. *Russ. J. Coord. Chem.* **2013**, 39 (3), 293–296. <https://doi.org/10.1134/s107032841303010x>.
- (39) Abu-Youssef, M. A. M.; Soliman, S. M.; Langer, V.; Gohar, Y. M.; Hasanen, A. A.; Makhyoun, M. A.; Zaky, A. H.; Öhrström, L. R. Synthesis, Crystal Structure, Quantum Chemical Calculations, DNA Interactions, and Antimicrobial Activity of [Ag(2-Amino-3-Methylpyridine) 2]NO₃ and [Ag(Pyridine-2-Carboxaldoxime)NO₃]. *Inorg. Chem.* **2010**, 49 (21), 9788–9797.

<https://doi.org/10.1021/ic100581k>.

- (40) Iwasaki, F.; Hirota, M.; Yamazaki, N.; Yasui, M. Absolute Structures of (+)-(RS,RC)-1-Phenylethyl 2-Quinolyl Sulfoxide and (–)-(RC,RC)-Bis[2-(1-Phenylethyl)Quinolato]Silver Perchlorate. *Acta Crystallogr. Sect. C Cryst. Struct. Commun.* **1991**, *C47* (11), 2406–2410. <https://doi.org/10.1107/S010827019100608X>.
- (41) Lindley, P. F.; Woodward, P. An X-Ray Investigation of Silver Nitrate: A Unique Metal Nitrate Structure. *J. Chem. Soc.* **1966**, 123–126.
- (42) Meyer, P.; Rimsky, A.; Chevalier, R. Structure d'une Phase Du Nitrate d'argent Instable à Température et Pression Ordinaires. *Acta Crystallogr. Sect. B Struct. Crystallogr. Cryst. Chem.* **2002**, *32* (4), 1143–1146. <https://doi.org/10.1107/s0567740876004846>.
- (43) Linares, F.; García-Fernández, E.; López-Garzón, F. J.; Domingo-García, M.; Orte, A.; Rodríguez-Diéguez, A.; Galindo, M. A. Multifunctional Behavior of Molecules Comprising Stacked Cytosine-Ag I -Cytosine Base Pairs; Towards Conducting and Photoluminescence Silver-DNA Nanowires. *Chem. Sci.* **2019**, *10* (4), 1126–1137. <https://doi.org/10.1039/c8sc04036b>.
- (44) Mistry, L.; El-Zubir, O.; Dura, G.; Clegg, W.; Waddell, P. G.; Pope, T.; Hofer, W. A.; Wright, N. G.; Horrocks, B. R.; Houlton, A. Addressing the Properties of “Metallo-DNA” with a Ag(I)-Mediated Supramolecular Duplex. *Chem. Sci.* **2019**, *10* (11), 3186–3195. <https://doi.org/10.1039/c8sc05103h>.
- (45) Arakawa, H.; Neault, J. F.; Tajmir-Riahi, H. A. Silver(I) Complexes with DNA and RNA Studied by Fourier Transform Infrared Spectroscopy and Capillary Electrophoresis. *Biophys. J.* **2001**, *81* (3), 1580–1587. [https://doi.org/10.1016/S0006-3495\(01\)75812-2](https://doi.org/10.1016/S0006-3495(01)75812-2).
- (46) Dirico, D. E.; Keller, P. B.; Hartman, K. A. Volume 13 Number 1 1985 Nucleic Acids Research The Infrared Spectrum and Structure of the Type I Complex of Silver and DNA Nucleic Acids Research. *Nucleic Acids Res.* **1985**, *13* (1), 251–260.
- (47) Palafox, M. A. Computational Chemistry Applied to Vibrational Spectroscopy: A

Tool for Characterization of Nucleic Acid Bases and Some of Their 5-Substituted Derivatives. *Phys. Sci. Rev.* **2017**, 2 (8), 1–21. <https://doi.org/10.1515/psr-2016-0132>.

- (48) Mathlouthi, M.; Koenig, J. L. FTIR and Laser-Raman Spectra of Cytosine and Cytidine. *Carbohydr. Res.* **1986**, 146, 1–13.
- (49) Ten, G. N.; Baranov, V. I. Calculation and Analysis of the IR Spectra of Cytosine in Various Phase States. *J. Appl. Spectrosc.* **2005**, 72 (2), 155–163. <https://doi.org/10.1007/s10812-005-0048-y>.
- (50) Pichierri, F.; Holthenrich, D.; Zangrando, E.; Lippert, B.; Randaccio, L. Metal-Stabilized Rare Tautomers of Nucleobases. *JBIC J. Biol. Inorg. Chem.* **2002**, 1 (5), 439–445. <https://doi.org/10.1007/s007750050076>.
- (51) Bazsó, G.; Tarczay, G.; Fogarasi, G.; Szalay, P. G. Tautomers of Cytosine and Their Excited Electronic States: A Matrix Isolation Spectroscopic and Quantum Chemical Study. *Phys. Chem. Chem. Phys.* **2011**, 13 (15), 6799–6807. <https://doi.org/10.1039/c0cp02354j>.
- (52) Kwiatkowski, J. S.; Leszczyński, J. Molecular Structure and Vibrational IR Spectra of Cytosine and Its Thio and Seleno Analogues by Density Functional Theory and Conventional Ab Initio Calculations. *J. Phys. Chem.* **1996**, 100 (3), 941–953. <https://doi.org/10.1021/jp9514640>.
- (53) Alonso, J. L.; Vaquero, V.; Peña, I.; López, J. C.; Mata, S.; Caminati, W. All Five Forms of Cytosine Revealed in the Gas Phase. *Angew. Chemie - Int. Ed.* **2013**, 52 (8), 2331–2334. <https://doi.org/10.1002/anie.201207744>.
- (54) Gorman, M. The Evidence from Infrared Spectroscopy for Hydrogen Bonding: A Case History of the Correlation and Interpretation of Data. *J. Chem. Educ.* **1957**, 34 (6), 304–306. <https://doi.org/10.1021/ed034p304>.
- (55) Wiseman, T.; Williston, S.; Brandts, J. F.; Lin, L. N. Rapid Measurement of Binding Constants and Heats of Binding Using a New Titration Calorimeter. *Anal. Biochem.* **1989**, 179 (1), 131–137. [https://doi.org/10.1016/0003-2697\(89\)90213-3](https://doi.org/10.1016/0003-2697(89)90213-3).

- (56) Brechignac, C.; Houdy, P.; Lahmani, M. *Nanomaterials and Nanochemistry*; Springer: Berlin, Heidelberg, New York, 2004.
- (57) Prasad Yadav, T.; Manohar Yadav, R.; Pratap Singh, D. Mechanical Milling: A Top Down Approach for the Synthesis of Nanomaterials and Nanocomposites. *Nanosci. Nanotechnol.* **2012**, 2 (3), 22–48. <https://doi.org/10.5923/j.nn.20120203.01>.
- (58) Koch, C. C. The Synthesis and Structure of Nanocrystalline Materials Produced by Mechanical Attrition: A Review. *Nanostructured Mater.* **1993**, 2 (2), 109–129. [https://doi.org/10.1016/0965-9773\(93\)90016-5](https://doi.org/10.1016/0965-9773(93)90016-5).
- (59) Milling, H. B. Mechanosynthesis Learn More about Mechanosynthesis Mechanochemical Synthesis of Metal- Lic – Ceramic Composite Powders. **2013**.
- (60) Cahn, R. W. *Mechanical Milling - Encyclopedia of Materials: Science and Technology*; ScienceDirect, 2001.
- (61) Kubota, K.; Pang, Y.; Miura, A.; Ito, H. Redox Reactions of Small Organic Molecules Using Ball Milling and Piezoelectric Materials. *Science (80-.).* **2019**, 366 (6472), 1500–1504. <https://doi.org/10.1126/science.aay8224>.

Chapter 3.

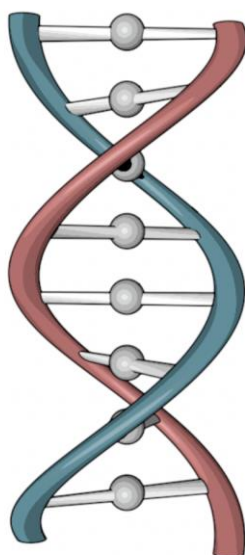
“Metallo-DNA”; Ag^I-Mediated Supramolecular Duplex with Self-Healing Gelatinous Properties.

This chapter is based upon the following publication:

Liam Mistry, Osama El-Zubir, Gema Dura, William Clegg, Paul G. Waddell, Thomas Pope, Werner A. Hofer, Nick G. Wright, Benjamin R. Horrocks and Andrew Houlton, *Chem. Sci.*, 2019, **10**, 3186 – 3195

3.1. Introduction

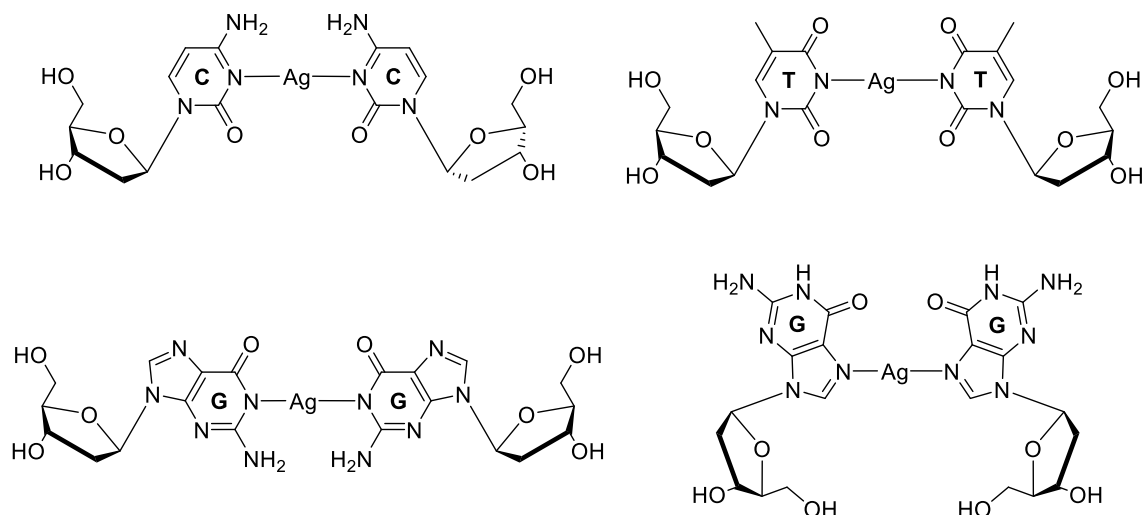
“Metallo-DNA” has become a highly interesting class of nano-material that offers the sequence programmability of DNA coupled with many of the interesting properties of metals.^{1–7} Fundamentally, many of the intermolecular Watson-Crick hydrogen bonds between base-pairs are replaced by coordination bonds across a metal-ion; resulting in a contiguous metal core running through the double stranded helix (**Scheme 3.1**). This bottom-up approach has proven to be a particularly powerful method of controlled assembly of metal-ions into regular linear arrays. Both hetero- and homometallic systems have been previously demonstrated. However, existing examples have often required modifications of nucleosides to accommodate the range of demands of the metal for coordination to occur.^{5,6,8,9}



Scheme 3.1 An illustration of a DNA duplex (B-form) section, metal-mediated across every base-pair instance.

Silver-ions are unusual in this regard as they can metal-mediate base-pairs with natural nucleosides.^{7,10–18} The d^{10} electronic configuration of Ag^I allows for a range of coordination numbers and geometries, however a tendency exists to form low-coordination linear systems.¹⁹ As a result, the use of silver-chemistry with DNA-based structures is particularly promising for the development of nanomaterials, *e.g.* nanowires,^{20–24} quantum confined metal clusters or particles^{25–32} and plasmonic materials^{33,34} as molecular systems. By far the most common occurrence of Ag^+ metal-mediation happens across a C-C mispair, C-Ag-C (C: cytidine), however other purine-pyrimidine combinations are possible (**Scheme 3.2**).^{12,18,23,35} A M-DNA examples have

recently been resolved by single crystal X-ray diffraction^{12,18}; the most interesting of which is a dodecamer ($d(\text{GGACTC}^{\text{Br}}\text{GATCC})$) bearing silver-ion coordination's at every base-pair site; generating an infinite chain of Ag^{I} -ions running down the c -axis (100) of the crystal structure.²³ Analogous arrays of have recently been observed in the solid state featuring a modified nucleobase $[\text{Ag}^{\text{I}}-(N^3\text{-alkyl-cytosine})_2]^+$.^{36,37} Metallo-DNA systems bearing continuous metal-ion arrays have often considered as molecular/nano-wires.^{23,38,39} However, studies into their electrical properties are sparse.^{37,40–43}



Scheme 3.2 Examples of crystallographically characterised silver-mediated base-pair with natural nucleosides identified in M-DNA.^{12,18,23,35}

Herein, we report the metal-mediated natural nucleoside coordination complex $[\text{Ag}^{\text{I}}-(N^3\text{-cytidine})_2]^+$, **1**, that self-assembles into a metallo-DNA analogue in both the solid and gel states. Complex **1** offers a comparable model M-DNA duplex bearing the nucleobase and ribose moieties. This allows for the physico-chemical properties of such systems to be investigated. During this investigation we addressed the “nano-wire” attributes and reductive behaviour for these types of systems. Furthermore, we demonstrate for the first time a self-assembled metallo-array which exhibits a self-healing “thixotropic” property in the gel form. These features can be rationalised by the reversibility of the inter-complex hydrogen- and argentophilic-interactions in the supramolecular structure.

While our work was under-review a study by Galindo *et al.* released with an examination of the electrical properties and cold-H plasma reduction of the modified-

nucleobase complex $[\text{Ag}^{\text{I}}-(N^3\text{-methylcytosine})_2]^+$ appeared.³⁷ The work conducted by both groups are complementary.

3.2. Results & Discussion

Synthesis and Characterisation of a “Metallo-DNA” Model, $[\text{Ag}^{\text{I}}-(N^3\text{-cytidine})_2]\cdot[\text{NO}_3]$, **1**.

An aqueous reaction between silver nitrate and cytidine at a ligand to metal-ion ratio of 2:1 yielded $[\text{Ag}^{\text{I}}-(N^3\text{-cytidine})_2]\cdot[\text{NO}_3]$, **1**, a solid white powder. Upon recrystallisation within a vapour diffusion set-up (using a water/acetonitrile solvent system) allowed for the spontaneous growth of colourless needle-shaped crystals. Single X-ray diffraction analysis revealed the structure to have a chiral $P3_2$ space group encompassing five crystallographically unique C-Ag^I-C species along a linear array accounting for the large unit cell ($a = b = 30.382(7)$ Å; $c = 14.976(3)$ Å) (**Figure 3.1**).

The complex assembles into a right-handed supramolecular double-helix through a combination of argentophilic and complementary intermolecular hydrogen bonding interactions. The contiguous array extends continuously throughout the crystal in-line with identical neighbours. This results in a near linear continuous silver-ion core down the *c*-axis with Ag⁺...Ag⁺...Ag⁺ distance of between 2.982(2) – 3.055(2) Å, close to the metallic radius of 2.88 Å. The deviations from the mean straight-line are 0.162 – 0.273 Å with angles ranging from 162.34(7) – 170.63(6)°. The two cytidine ligands bound across each silver-ion are significantly twisted with an inter-planar dihedral angle ranging from 71.2(5) – 74.9(5)°, adopting a slightly *cisoid* arrangement. It is easy to imagine such a unit cell was achieved through stacking of individual C-Ag^I-C units.

For each unit of the duplex two-pairs of complementary $N^4\text{-H}\cdots\text{O}^2$ intermolecular hydrogen bonding exist with each neighbour, explaining the inter-planar twist. These H-bonding interactions have distances ranging from 2.870(18) to 3.020(17) Å. Similarities in these intermolecular interactions can be observed when compared to the previously discussed M-DNA structure $[\text{Ag}^{\text{I}}_{11}\text{-(dodecamer)}_2]$ by Kondo *et al.* and $[\text{Ag}^{\text{I}}-(N^3\text{-hexycytosine})_2]$ by Terrón & Frontera. However, for **1** the argentophilic interactions appear stronger indicated by shorter Ag⁺...Ag⁺ distances of 2.982(2) – 3.055(2) Å, close to that of the metallic radius (2.88 Å). For a direct comparison the intermetallic distances for $[\text{Ag}^{\text{I}}_{11}\text{-(dodecamer)}_2]$ and $[\text{Ag}^{\text{I}}-(N^3\text{-hexycytosine})_2]$ are 3.2 –

3.4 and 3.2 Å respectively. Interestingly, a recently reported $[\text{Ag}^I\text{-(1-Me-cytosine)}_2]^+$ complex by Galindo *et al.* featured equally short $\text{Ag}^+\cdots\text{Ag}^+$ distances of 2.902 – 3.088(2) Å. This shows that the ribose moiety of **1** does not hinder sterically the inter-complex interactions.

The diameter of the duplex was measured across the 5'-OH sugar groups of individual complex ions, with widths very similar to that of biological DNA at 17.5(1) Å. The ribose sugars favour a 2'exo-**N'**-twist confirmation at each instance in the solid state.

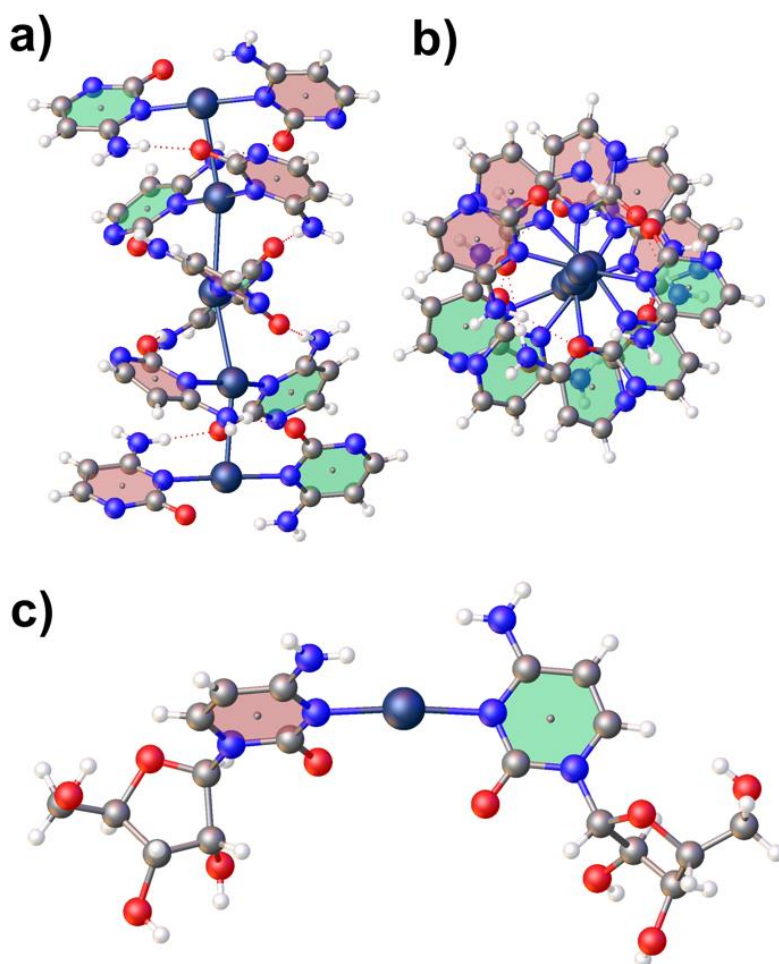


Figure 3.1 X-Ray crystallographically identified the single-crystal as a continuous linear array of silver-ions in a right-handed supramolecular double-helix of $[\text{Ag}^I\text{-(N}^3\text{-cytidine)}_2]$, **1**, a metallo-DNA model. View a) side-on, b) top-down and c) a single C-Ag-C complex showing a slightly favoured *cisoidal* conformation. *Ribose group's omitted for clarity.

3.3. Self-healing metallo-gel formation Study

By replacing solvent from water to methanol in the synthesis of **1**, a sample spanning colourless gel was observed to form overnight yielding **1**_{MeOH}. Analysis *via* Fourier-transform infrared spectroscopy (FTIR) and electrospray-ionisation mass spectrometry (ESI-MS) confirmed the formation of the expected two-coordinate $[\text{Ag}^{\text{I}}\text{-(cytidine)}_2]^+$ complex (**Figures 3.2 – 3.4**).

Peak broadening was observed in the IR for both **1** and **1**_{MeOH} across the spectral range 400 – 4000 cm^{-1} when compared to their parent complex IR's (**Figure 3.2** and **3.3**). Subtle decreases in the wavenumber of the peak observed around 1600 cm^{-1} ; characteristic of changes of the C^2 carbonyl. A shift to lower wavenumbers and peak broadening is indicative of H-bonding interactions. The spectroscopic differences were generally found to be consistent with the newly formed associations seen within the crystal structures for **1**. Additional computational studies would further help assign spectral features.

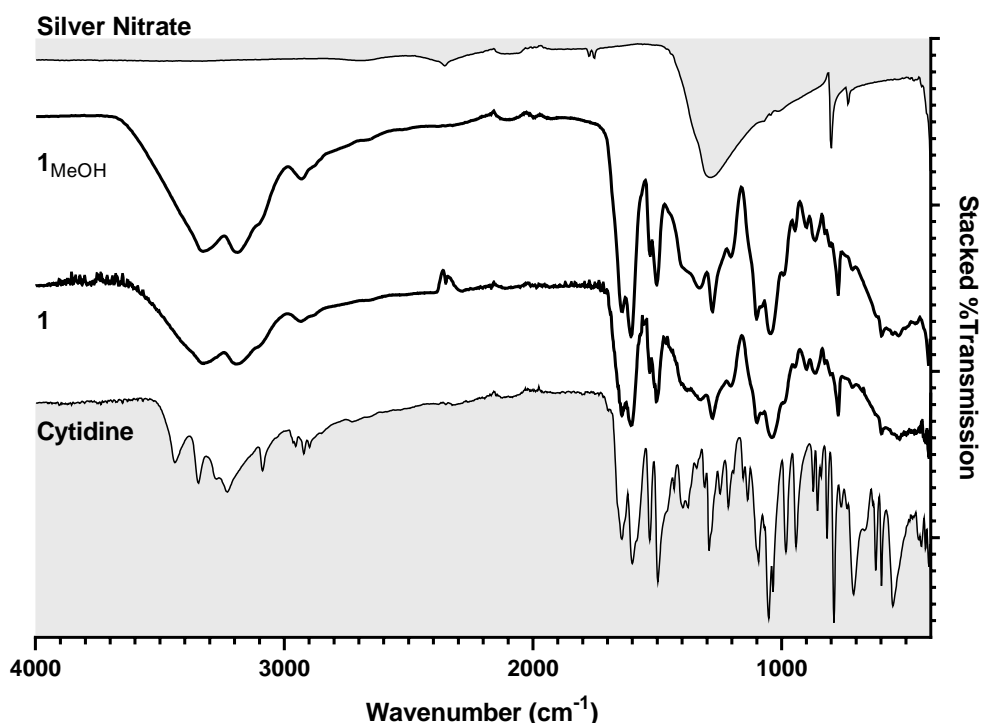


Figure 3.2 FTIR data (range: 400 – 4000 cm^{-1}) stacked for cytidine, AgNO_3 *versus* compounds **1** and **1**_{MeOH}.

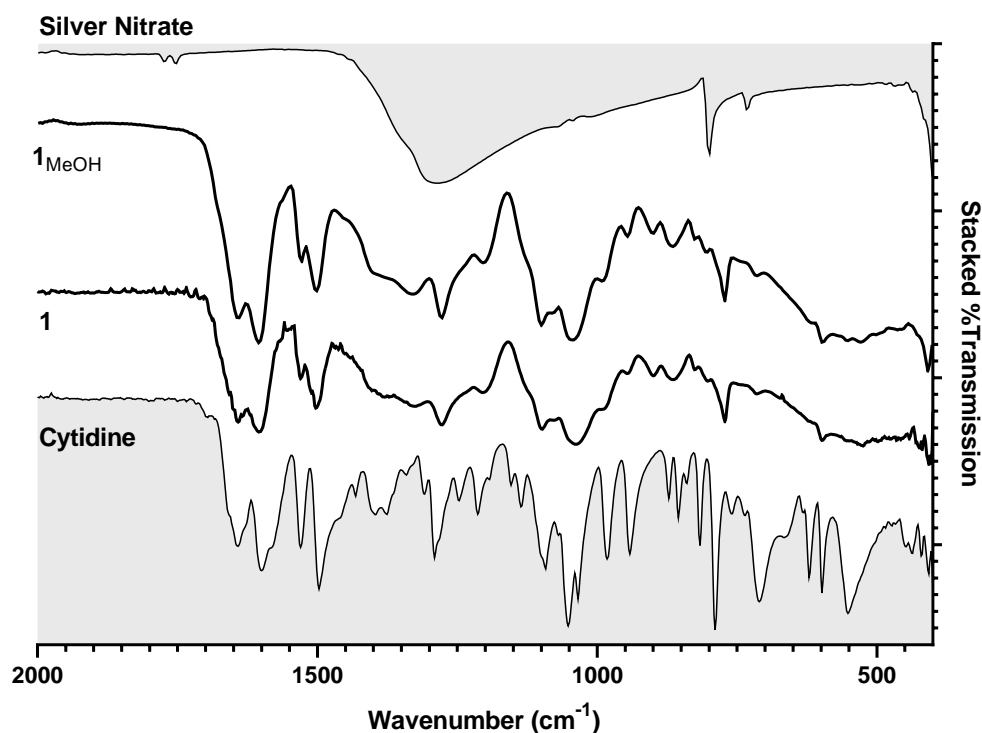


Figure 3.3 FTIR data shown above across the range of 400 – 2000 cm^{-1} for cytidine, AgNO_3 versus compounds **1** and **1**_{MeOH} .

Electrospray-Ionisation-Mass Spectrometry (ESI-MS) was used as a qualitative technique to confirm the presence of the *bis*- $[\text{Ag}^{\text{I}}-(N^3\text{-Cytidine})_2]^+$ complex in aqueous solution. The expected Cyt- Ag^{I} -Cyt complex was observed as a $[\text{M}+2\text{L}]^+$ ion (M: metal, L: ligand) using ESI-MS (direct injection, positive ion mode) at 593.1029 m/z (**Figure 3.4**). Isotope patterns, splitting and masses aligned well with the theoretical values calculated for a 1:2 Ag-Cytidine complex derived from the crystal structures; Calc. $\text{C}_{18}\text{H}_{26}\text{AgN}_6\text{O}_{10}$, $[\text{M}+2\text{L}]^+$, 593.0761 m/z (monoisotopic mass). Peak separation of 1.0 m/z suggests a species bearing a plus one charge, which was achieved by the metal ion without the loss of a proton. Silver possess two unique stable isotopes, ^{107}Ag (328.9986 m/z) and ^{109}Ag (330.9939 m/z) with ^{107}Ag being slightly more abundant (51.839%). The calculated mass and isotope pattern matched those of the experimental spectra in both positive and negative-ion modes.

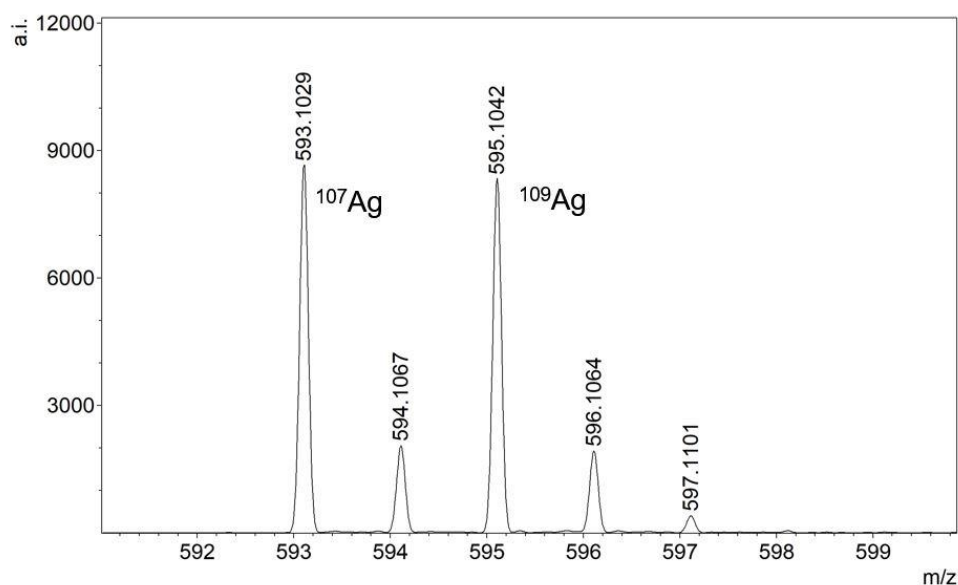


Figure 3.4 Electrospray-ion Mass-Spectrometry (ESI-MS) data measured for **1** collected in high resolution positive-ion mode. Both major isotopes for silver are clearly observed ^{107}Ag & ^{109}Ag at 593.1029 and 595.1042 m/z.

Akin to chapter 2, we further interrogate the structure and binding modes observed in the solid states using Isothermal titration calorimetry (ITC) was used as a method of thermal quantification of bonding interactions. The amount of heat liberated (exothermic (-)) or absorbed (endothermic (+)) as the reaction proceeds can be quantified as coordination events. The number of thermally quantified coordination events can be used to identify a binding mode. This analysis assumes the only interaction between the silver ion and cytidine ligand occur at the expected N^3 . The heat of solvation or dilution effects are easily accounted during prior control experiments.

A concentrated solution of AgNO_3 (5.0 mM) was titrated against cytidine (0.1 mM) held at 25°C gave a clear sigmodal isotherm (**Figure 3.5**). The negative peaks indicate an exothermic reaction, releasing -12790 cal/mol of energy (ΔH). The total number of available sites or molar ratio gave $n = 0.5$, in agreement with a 2:1 reaction ligand-to-metal stoichiometry observed in the single crystal.

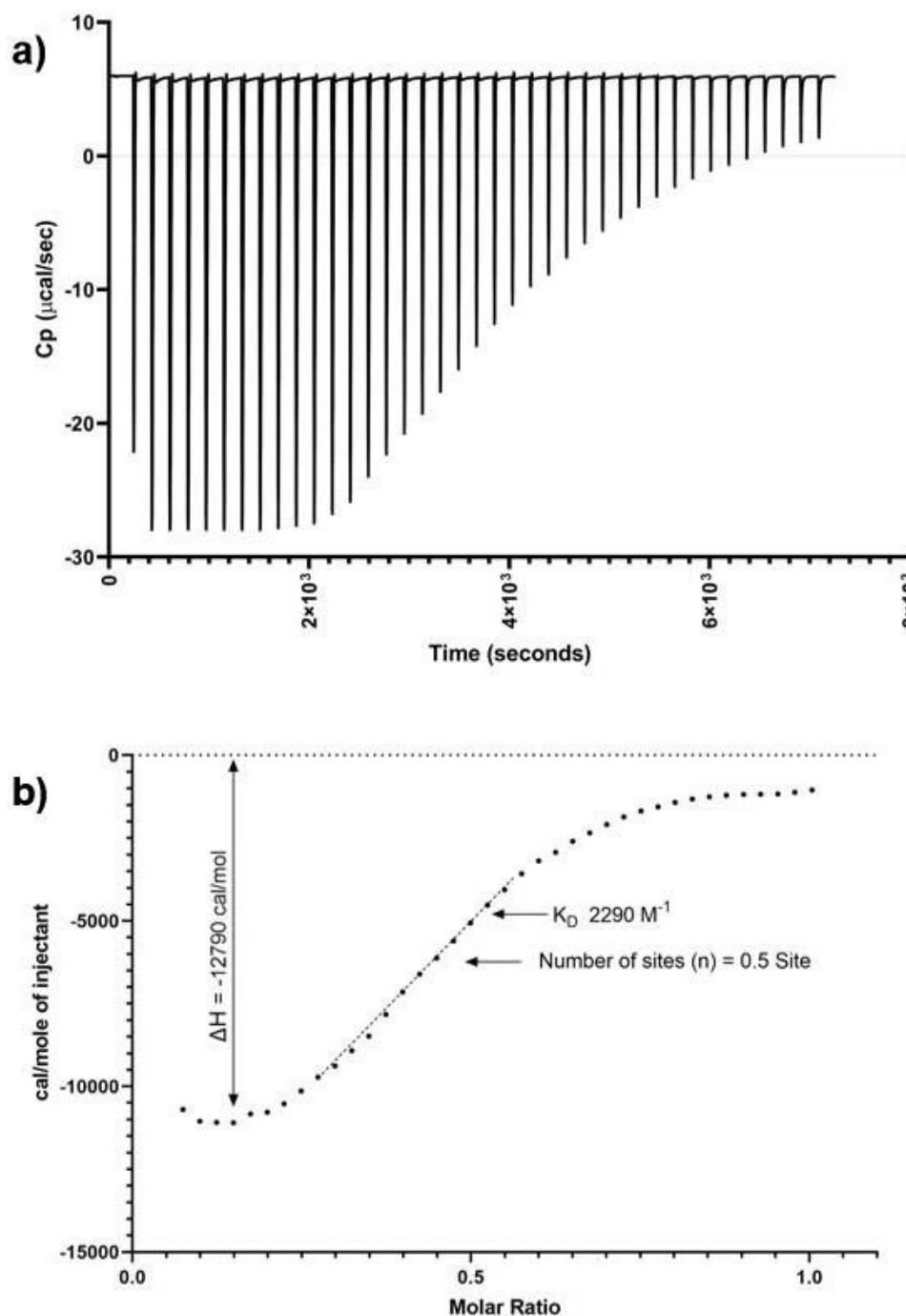


Figure 3.5 a.) Isothermal titration calorimetry (ITC) data recorded by titrating Ag^+ ions against cytidine (40-injections with time intervals of 120 seconds per injection). b.) Integrated peaks as a Wiseman plot presenting binding isotherms vs. molar ratio.

Imaging of **1**_{MeOH} xerogel sample by scanning electron microscopy (SEM) revealed one-dimensional fibres with lengths of many microns; consistent with the extended supramolecular structure of **1** (**Figure 3.6**). The fibres are highly entangled forming a

porous network capable of trapping solvent. Surface images show bundles of fibres much larger in diameter than those in the interior.

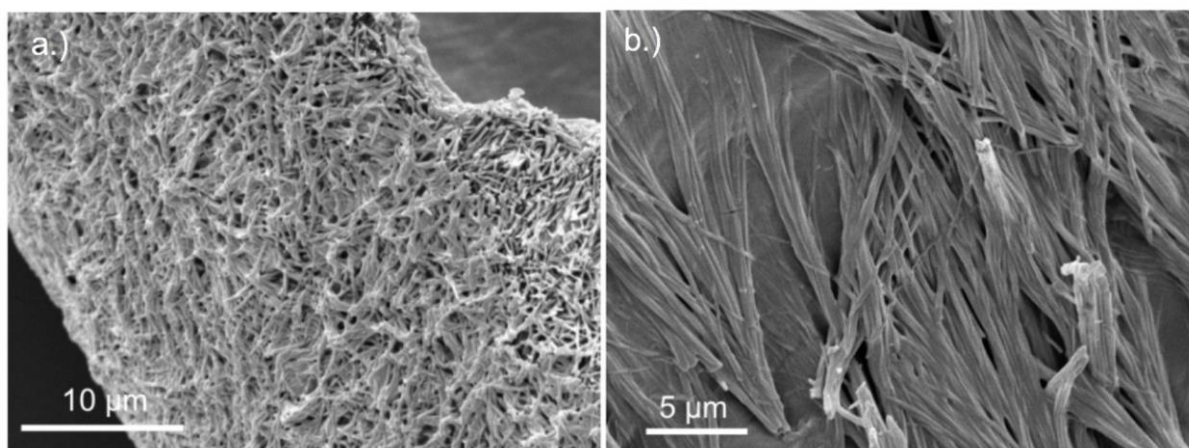


Figure 3.6 SEM images of $[\text{Ag}^{\text{I}}\text{-(cytidine)}_2]$ xerogel; a.) image into the bulk showing a highly entangled polymer matrix; b.) a surface image showing bundling of the fibres on the xerogel surface.

Tapping-mode atomic force microscopy (AFM) shows the regularity in fibre dimensions when drop-cast onto silicon at the prepared concentration of 4.0 mg/ml (**Figure 3.7**). Interestingly, the fibres show no tendency to coil and remain linear across the surface. The regularity of these fibres indicates a hierarchical assembly process. Image analysis showed these fibres to be approximately 6.3 ± 0.45 nm in diameter. With the assumption that the fibres consist of an identical structure to **1**, twelve individual helices would be required to match those dimensions (**Figure 3.7b inset**).

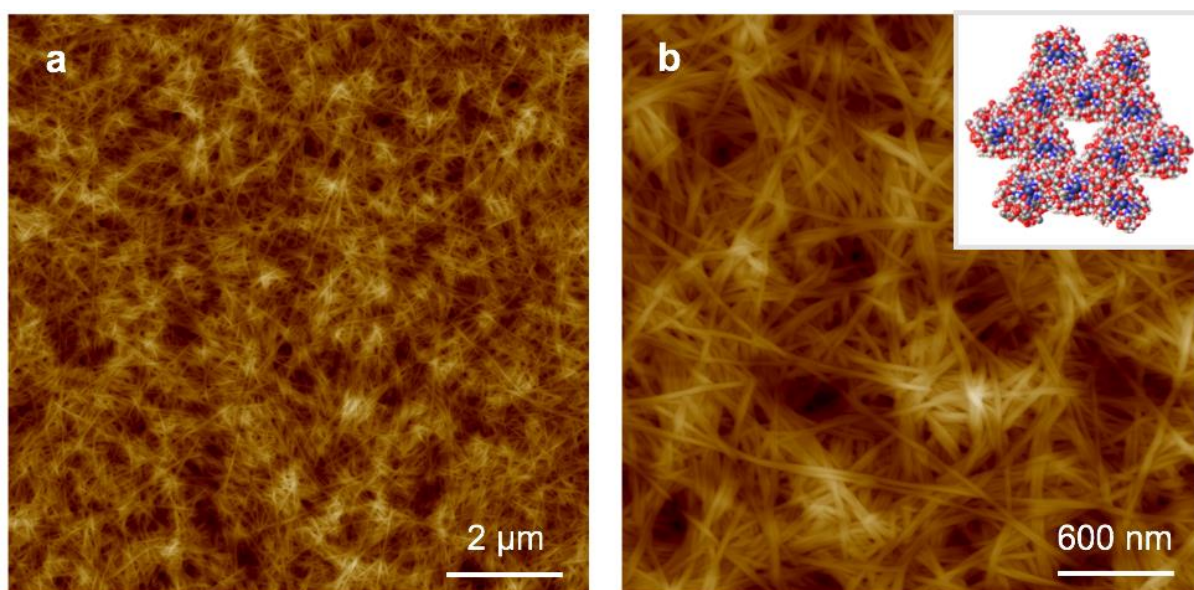


Figure 3.7 AFM images of the xerogel deposited onto a silicon wafer. Wide-scan a.) and zoomed image b.) of AFM height images illustrating the uniform nature of the

fibres. (inset) A space filled molecular model of a bundle composed of twelve 2D fibres with a matching height of 6.3 nm like those in the AFM images.

Circular dichroic (CD) spectroscopy is used to routinely observed the conformational properties of helical structures like DNA. Differences in the absorption of left- and right-handed circularly polarised light by chiral molecules is termed CD. Differences are described as ellipticity, θ and has units of degrees ($^\circ$).⁴⁴ A more common method of using CD for characterisation is the use of molar extinction coefficients, $[M^{-1}cm^{-1}]$ (equation 1 below).⁴⁴

$$\Delta\varepsilon = \varepsilon_L - \varepsilon_R \quad (1)$$

CD offers several advantages over alternative spectroscopic (UV, FTIR) or absolute methods (X-ray, NMR) of characterisation. CD is now considered cheap, quick and can easily distinguish between different conformational isomerisation's at low concentrations.^{44,45} For these reasons and more, CD is absolutely essential for any characterisation of DNA or similar biopolymers.

Consistent with the microscopy, the gel, **1**_{MeOH}, displays remarkably enhanced chiroptic absorption properties compared to the parent nucleoside (**Figure 3.8**). The newly observed negative CD profile is diagnostic of a helical arrangement of the Ag-mediated cytidine base-pair sequence^{18,46–48}, a structural analogue of **1**. Alternatively, the data could display the “cotton effect” which infers a change to the stereostructure.^{49,50}

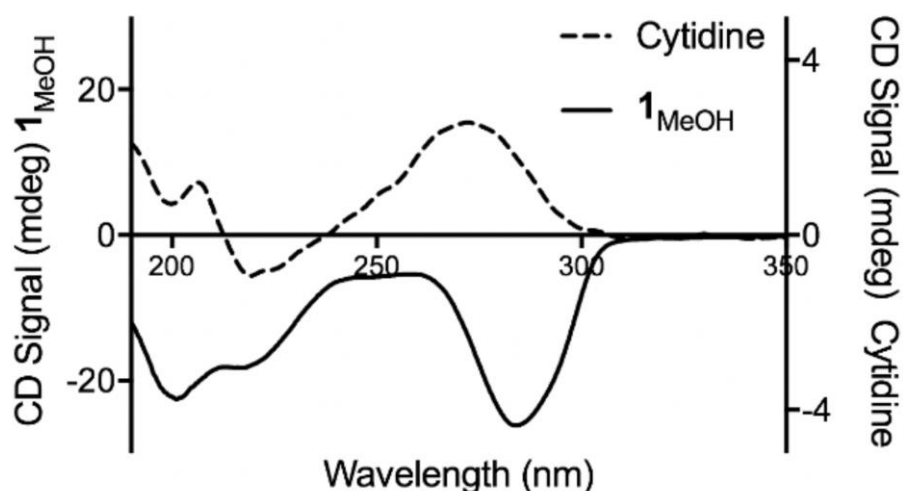


Figure 3.8 Circular dichroism data for cytidine (dotted-line) vs. metallogel (solid-line) at matched concentrations of 4.0 mg/ml.

Further confirmation of the isostructural nature was obtained using XRD techniques and pattern analysis. Upon removal of solvent from gel **1**_{MeOH} *via* freeze-drying or simply allowed to evaporate in air, the XRD pattern for the resulting xerogel displayed significantly sharper features. This is an indication that the xerogel has a greater degree of crystallinity and order (**Figure 3.9**) when compared to the gel-state. The major peak at $2\theta = 6.43^\circ$ corresponds to a distance of 13.7 Å. If a microcrystalline powder of **1** is also freeze-dried a similar reflection is observed. We interpreted this as a slight-shrinkage of the original fibre upon loss of the solvent.

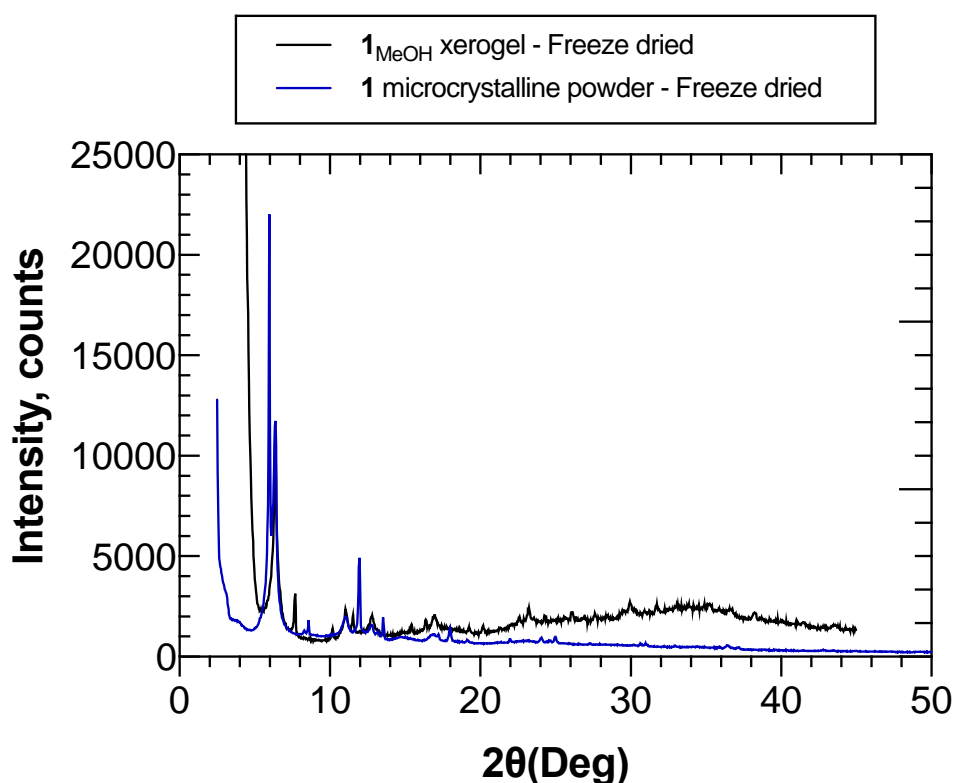


Figure 3.9 PXRD data for the xerogel **1**_{MeOH} (black-line) and **1** powder (blue-line) acquired *via* freeze-drying techniques.

The gel **1**_{MeOH} displayed broad features typical of polymeric materials (**Figure 3.10**). This was expected given the gels fibrous nature of the observed structures *via* AFM and SEM. Nonetheless, the data was analysed by fitting to a sum of Gaussian function in a similar way to the Rietveld method. Analysis *via* this method shows a relatively narrow peak close to $2\theta = 5.94^\circ$ (14.8 Å) which can be interpreted as a broadened [001] reflection, consistent with the *c*-axis of the unit cell of the crystal. This data

suggests that the structures of **1** and **1**_{MeOH} are essentially identical, the crystal structure of **1** with the axis of the fibres lying along the *c*-axis of the crystal lattice.

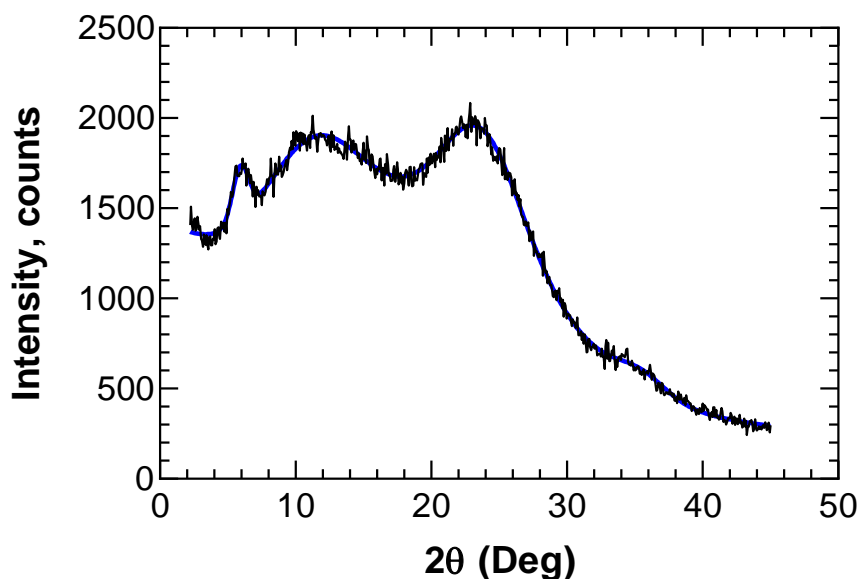


Figure 3.10 XRD data for the gel **1**_{MeOH} with fit shown in blue.

3.4. Thixotropic metallo-DNA Gel Formation

A rheological assessment using oscillatory sweep tests confirmed **1**_{MeOH} to behave as expected for a gel, and not a viscous liquid (**Figure 3.11**). The storage modulus value (G') was larger than the loss modulus (G''); the stiffness of the gel was measure to be 1.3 kPa. Frequency dependent oscillatory measurements demonstrated that the G' was dominant across the range of frequencies tested (0.1 – 100 rad/s) showing the elastic nature of the gel. Additionally, G' was virtually independent of frequency, indicative of a persistent gelatinous network. The linear viscoelastic region (LVE) of the gel, where G' is independent of the applied strain, was evaluated using oscillatory strain testing and was found to be approximately 1% of strain. Within this LVE region, the structure of the network is not disrupted and therefore remains intact throughout the deformation applied. The transition from gel to liquid where $G' = G''$ was observed at 10% strain. This suggests that the structure is easily disrupted consistent with other supramolecular silver gels.⁵¹

The organogel **1**_{MeOH} possess a highly interesting property of being thixotropic, *i.e.* the recovery of its gelatinous form after a period of rest. The gel collapses into a sol state upon the application of slight shear forces (*e.g.* slow vial inversion, minimal vibration),

however, after a period of approximately 20 minutes **1**_{MeOH} reassembles its gel network. This was indicated by a simple vial inversion test (**Figure 3.11a**). The viscosity of the gel was studied as a function of shear rate and showed a shear-thinning behaviour. The viscosity was reduced by three-orders of magnitude as the shear rate increased; characteristic of many supramolecular gels. Furthermore, the forward and reverse scans did not overlap, suggesting that the network is disrupted by the applied shear and cannot recover instantaneously. The gel reduced its stiffness from $G' = 1.3$ kPa to ~ 6 Pa post-deformation. The recovery of the material was approximately 60% of the initial G' values (760 Pa) after standing for 48 hours confirming the self-healing properties and re-assembly of the gel's network.

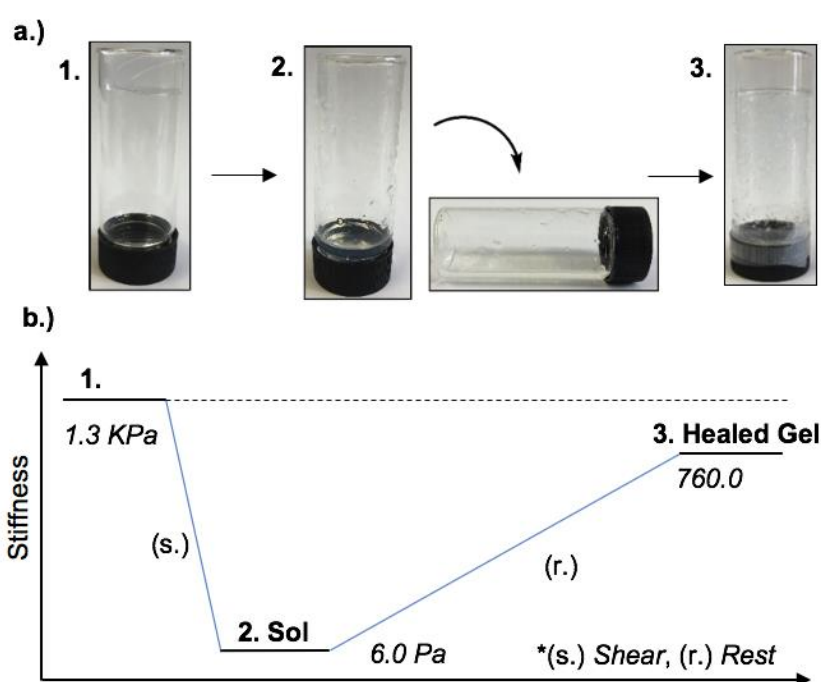


Figure 3.11 a) Optical images of the material through application or removal of shear. Inversion test showing the thixotropic nature of **1**_{MeOH} ((1) gel, (2) sol and (3) healed gel). b) illustrative scheme representing the stiffness of the gel over a thixotropic cycle.

The addition of 1.0 M urea to **1**_{MeOH} led to the rapid collapse of the gel network, resulting in the sample reverting back to a solution state. This and the “self-healing” nature of **1**_{MeOH} can be easily understood based on the reversibility of the intermolecular interactions observed in the supramolecular structure of **1**. This behaviour is entirely consistent with that of the intermolecular hydrogen bonding playing a major role in the construction of the gel super-structure and fibres.

3.5. Electrical conductivity measurements and band structure calculations on a continuous M-DNA model system

The electrical properties of M-DNA systems have been actively pursued following reports by Lee *et al.* ($M = \text{Co}^{2+}$, Ni^{2+} or Zn^{2+}).^{38,39} Despite conflicting evidence for such systems,^{52–55} M-DNA remains an attractive route towards molecular or nano-wire fabrication. These assumptions apply primarily on the linearity of closely held metallic arrays.²³ The tendency for monovalent Ag^+ to participation in metallophilic interactions⁵⁶ makes such systems ever more intriguing. Unfortunately, studies on the electrical properties of Ag^{I} -DNA systems are few.^{40–43} Only the most recent publication by Galindo *et al.* is of materials that have been crystallographically identified.³⁷

Compound **1** is a particularly useful and well-defined M-DNA model structure with many of the traits expected for a molecular wire. These features allowed us to address the electrical properties and molecular wire credentials. Furthermore, our abilities to grow high quality single crystals of **1** allowed for the electrical measurements on orientated samples, *i.e.* end-to-end, in the direction of the metal-array along the crystallographic *c*-axis (**Figure 3.12**). In this orientation any charge passed through the single crystal would allow the flow to pass along the metallic central array. Single crystals of **1** were tested using an electrical-probe-station, with the probe needles in direct contact with the crystal. Due to the brittle nature of the crystals of **1**, the needles were contacting either directly or *via* Ga-In eutectic pads.

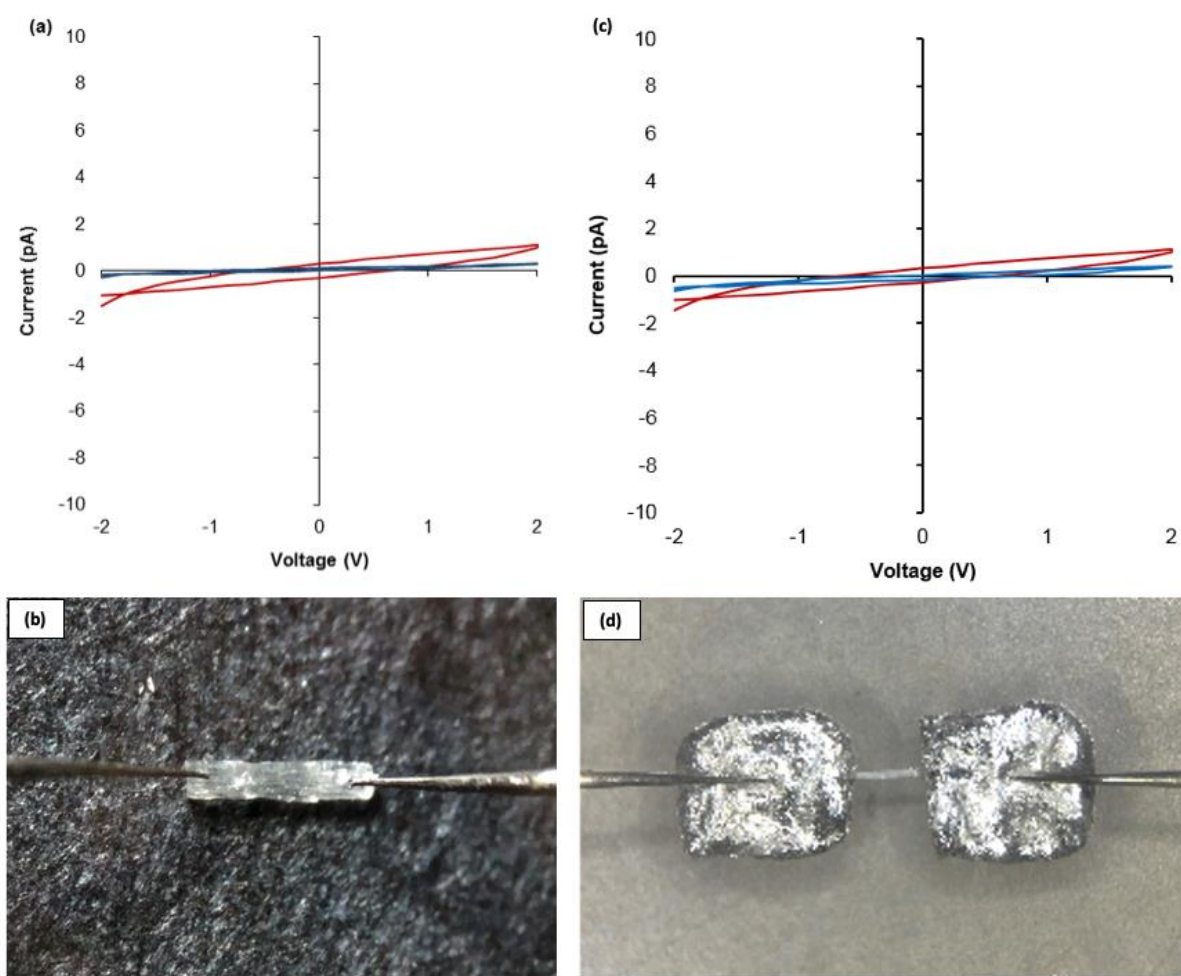


Figure 3.12 (Top) I–V curves of the **1**_{MeOH} xerogel (red) and single crystals of **1** (blue). (bottom) Optical microscope images of a single crystal of **1** connected to probe station tips (b) directly or through (d) Ga–In eutectic along the crystallographic *c*-axis.

I–V sweeps over a ± 2 V range displayed only background levels of current (<1 pA), indicative of a very effective insulator material (measured only at room-temperature, 294 K). Similar results were found to exist for the xerogel of **1**_{MeOH}. The evidence collected herein is in agreement with conductivity measurements and the electrostatic force microscopy (EFM) measurements of Galindo *et al.* on microcrystals of $[\text{Ag}^{\text{I}}(\text{methylcytosine})_2]^+$; with similarly short Ag...Ag distances.³⁷ It is worth re-stating that the Ag...Ag distances in the crystal structure of **1** are within $<5\%$ of the metallic distance; which are shorter than those found in Ag^I-modified oligonucleotides²³ and other similar systems.³⁶

To examine the charge mobility further, Electrostatic force microscopy (EFM) was used. This technique provides a highly sensitive probe to measure the polarisation of individual fibres which can be seen as a height image (**Figure 3.12a**) similar to standard AFM techniques (**Figure 3.13b**). To gain access to individual fibres the standard 4.0 mg/ml solution with methanol by a factor of twenty, then drop-cast onto Si(100)/200 nm SiO₂ wafer, then kept in a methanol-saturated closed system to allow for self-healing. After several hours, the sample was removed and allowed to air-dry to form the xerogel, **1**_{xe}. Control experiments confirmed that the fibres observed under AFM and EFM were not derived from solvent impurities.

AFM height images and the corresponding EFM phase images for single and aggregated fibres can be seen. An obvious effect of the dilution is the shortening and thinning of the fibres indicating that the assembly process is concentration dependent. The single fibres are now typically less than 500 nm in length and around 2 nm in height, similar to the diameter of an individual duplex. Analysis of the phase shift image (**Figure 3.13b**) shows a small positive value of $\sim 0.7^\circ$ across an individual fibre (**Figure 3.13b & 3.13d**, blue-line), indicating a non-conductive region. Further evidence of non-conductance in agreement with the results obtained with the single crystals of **1** and cAFM and EFM experiments by Galindo *et al.*³⁷

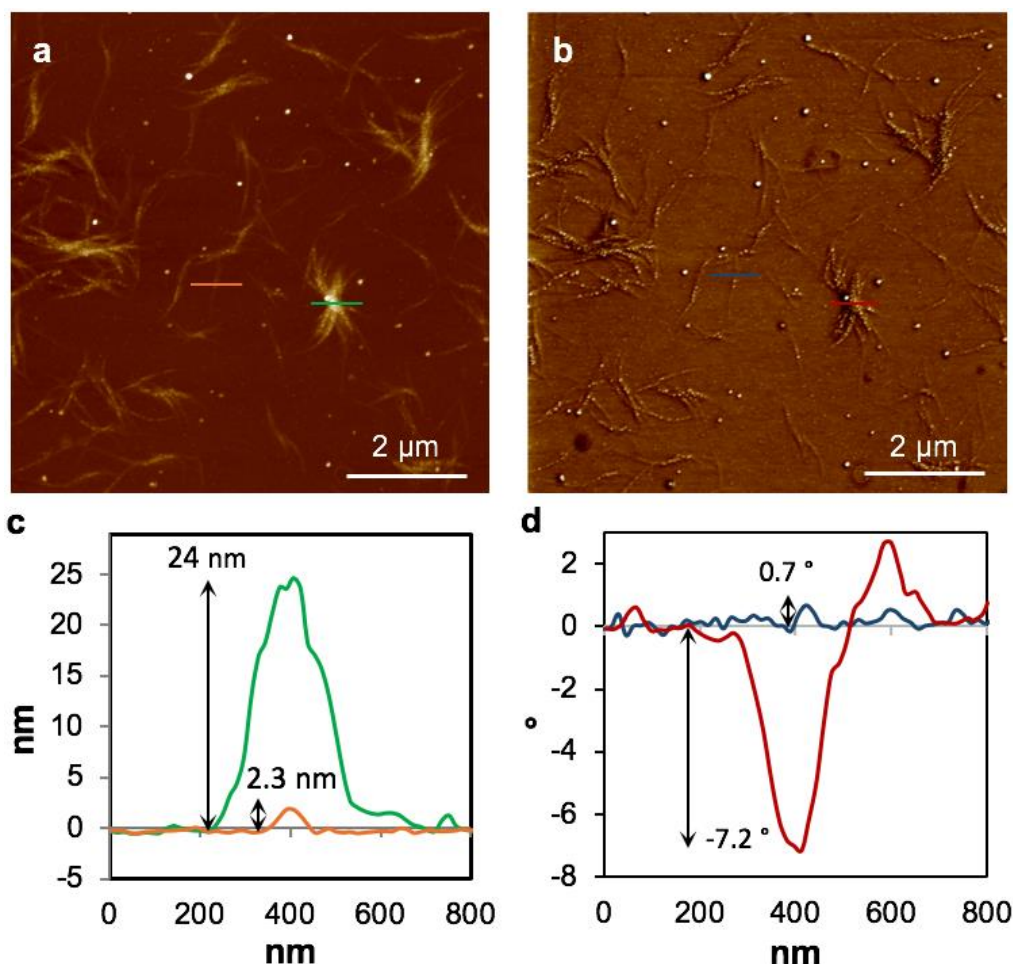


Figure 3.13 AFM height image (tapping mode) of 1_{MeOH} (20 times diluted); (a) EFM phase image, (c) line profiles corresponding to the green and orange lines in the AFM height image. (d) line profiles corresponding to the blue and red lines in the EFM phase image (b). The EFM image has been captured at applied DC bias +10 V and a lift height of 30 nm.

It is worthwhile to state that the STM measurements on a single molecule Ag^{I} -poly-dC structures⁴⁰ showed evidence of tunnelling currents, which are not in contradiction with the absence of conductivity; as seen in **1** and 1_{Xe} . The STM measurements demonstrate tunnelling over nm-scales of distance, however, given the exponential variations of such currents with interelectrode separation, it's expected that at the 100 nm scales probed by SCM the conductivity is negligible and more so for the single crystal *I-V* measurements on the mesoscale. In general, the linear variation of resistance with electrode separation in a conductive material is a distinct phenomenon from the exponential decay of tunnelling rates in STM or break-junction experiments. Clearly insulating materials may show significant tip currents at shorter distances.

The electrical behaviour observed is consistent with the calculated local density of state, for the ground state systems of a single chain of **1*** containing five molecules in the unit cell (**1*** - [Ag^I-(N³-(N¹-methylcytosine))₂]). By plotting the ground-state projected density of state on the central silver ions and the surrounding organic structures the band-gap was measured at the Fermi energy of 2.502 eV (495.54 nm) (**Figure 3.14**). However, it is commonly known that DFT often underestimates depictions of the electron-electron interactions and therefore the band-gap.^{57–59} Therefore, we can view the value calculated as a lower boundary and state with a high level of assurance that the structure would not be expected to conduct in the ground-state. Furthermore, the band-gap value can go some-way in explaining why the solid material is colourless.

If a surplus of electrons was introduced into this system, for example by chemical reduction, the LUMO states of the molecule would become occupied. This would shift the Fermi energy into the LUMO region. A plot of the Local Density of States (LDOS) for the energy window of 1.9 – 2.9 eV relative to the Fermi level, encompassing the first band of LUMO states (**Figure 3.14a**, dark-blue band). The electron density is heavily located on the surrounding organic structure, not the central Ag⁺ array; suggesting that even in the reduced case the structure would not be a metal-based conductor. However, that the material is not stable under those conditions and readily transforms into nanocomposites containing both luminescent silver-clusters and larger aggregate particles

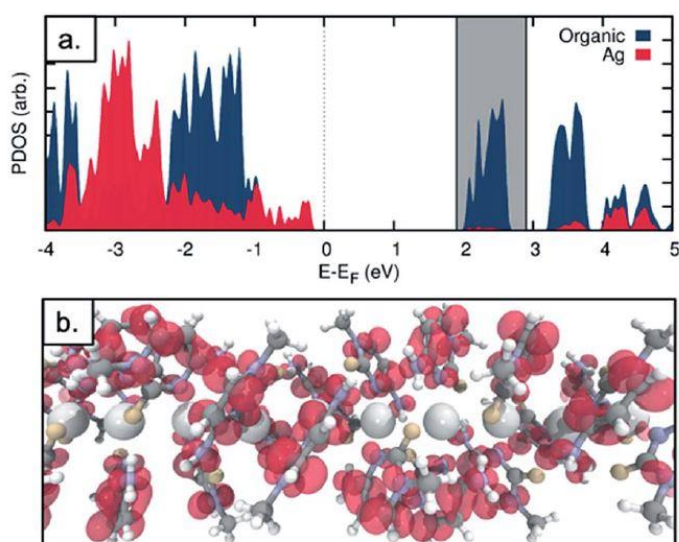


Figure 3.14 (a) Projected density of states (PDOS) for the Ag^+ array structure. The density on the central Ag atoms (red) and on the surrounding organic structure (blue) are plotted. (b) Local density of states (LDOS) for an energy window of 1.9 - 2.9 eV relative to the Fermi energy (shaded grey in figure (a)).

While the xerogel 1_{Xe} is not electrically conductive, the EFM data indicated that certain parts of the sample, where fibres had aggregated together, enhanced charge mobility was observed to occur. This can be seen in the EFM images as darker regions which correspond to negative phase shifts. These areas vary quadratically with the applied voltage between ± 10 V. It should be noted that negative phase shifts cannot be assigned to purely polarisable structures and the parabolic bias voltage dependence also rules out electrostatic or trapped charge effects, which give linear dependences. Such negative phase shifts are evidence of structures that allow charge transfer away from the immediate tip area. The AFM also reveals the presence of small particles, likely arising from photoreduction of the silver-ions (**Figure 3.15**). These particles can be observed to be embedded within the fibres. In parts of the sample, these can be quite monodisperse (ca. 14 nm total height), and somewhat regularly spaced along individual fibres (**Figure 3.15d**). In most cases those particles are sufficiently separated so that they do not contact. They therefore only show positive phase shifts in EFM as they provide a route for the charge to flow away from the tip during the contact with the surface of the material. Regions where the fibres aggregate are seen to aggregate show clustering of nanocomposites, *i.e.* NPs and NCs. This explains the charge-mobility “hot-spots” observed by EFM. These findings are also consistent with those observed using cAFM of $[\text{Ag}^+(\text{methylcytosine})_2]^+$ reduced using cold H-plasma.³⁷

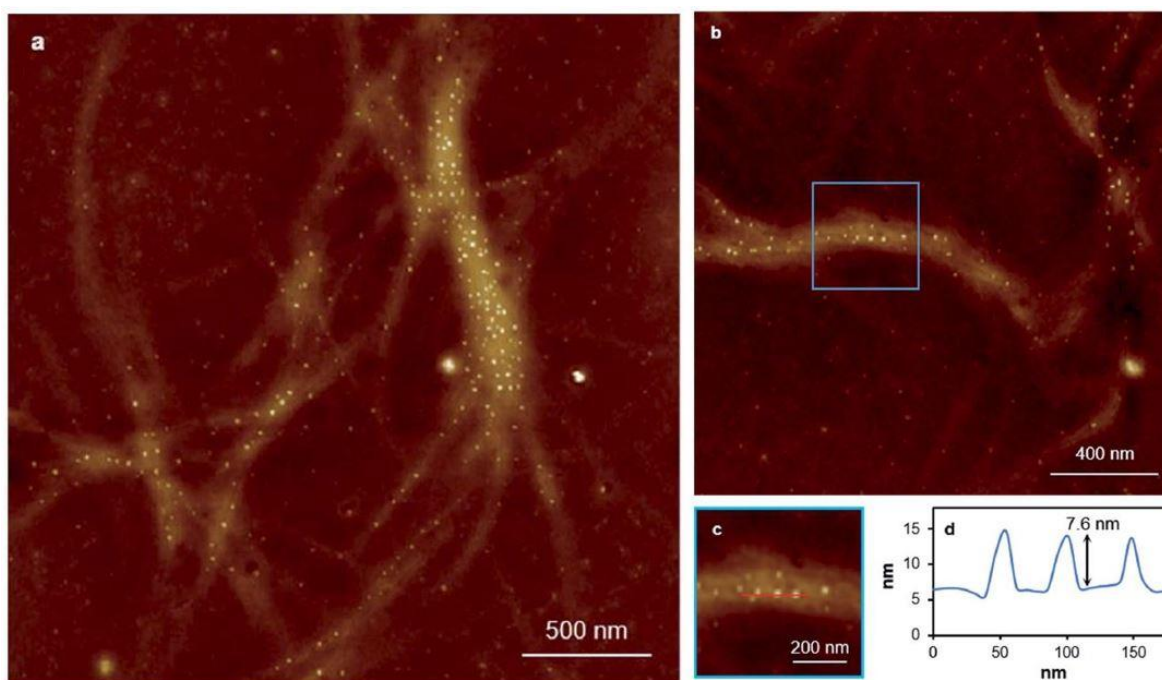


Figure 3.15 AFM height images for a 20x diluted samples of **1**_{MeOH} xerogel. Large imaging area (a), zoomed-in (b) showing Ag-particles embedded in the gel fibres. Zoomed-in area (c) shows the location of the blue-line-profile, and (d) a red-line-profile corresponding to (d). The line profile (d) shows a single fibre shows nanoparticles protruding from along it's back by ~7.6 nm with an estimated overall size of ~14 nm diameter.

3.6. Photoreduction of an Ag^I-Mediated Base-Pair arrays and Subsequent Luminescent Cluster Formation.

The nanocomposites (Ag⁰-particles and clusters) observed led us to investigate the reduction behaviour of the material further, particularly in light of its relevance to the formation of DNA-templated luminescent silver clusters. Reports by Dickson *et al.*^{26,27} have explored and identified similar materials as optical materials^{29,60} in bio-sensing applications.²⁵ The highly-ordered continuous argentophilic arrays such as **1** and similar materials³⁷ offer interesting systems for investigating reactivity and can provide an insight into the nature of the resulting products. The Ag⁺-cytosine interaction is a key feature in the synthesis of luminescent silver-clusters.^{28,31,48,61–64}

It was found early in the investigation that even freshly-prepared **1**_{MeOH} showed emission ($\lambda_{Em} = 395$ nm, $\lambda_{Ex} = 330$ nm), suggesting that the material is relatively photosensitive. Upon UV irradiation ($\lambda_{Ex} = 300$ nm) the gel undergoes a colourless-to-

red change with corresponding increasing in emission intensity with exposure time up to 1 hour (**Figure 3.16**). The results are consistent with silver(I)-ion reduction with the formation of quantum-confined silver-clusters. The emission indicates that those clusters are sufficiently small, in the order of the Fermi wavelength (~ 0.5 nm for Ag, <30 atoms), for a band-gap to form. Exposures past one-hour yielded no further increases in emission intensity and, in fact a slight loss of intensity was observed. This is consistent with the formation of larger, non-emissive plasmonic nanoparticles followed by the appearance of an absorption band at ~ 398 nm. The emission persisted unchanged for >1 month suggesting the clusters are stabilised within their chemical environment.

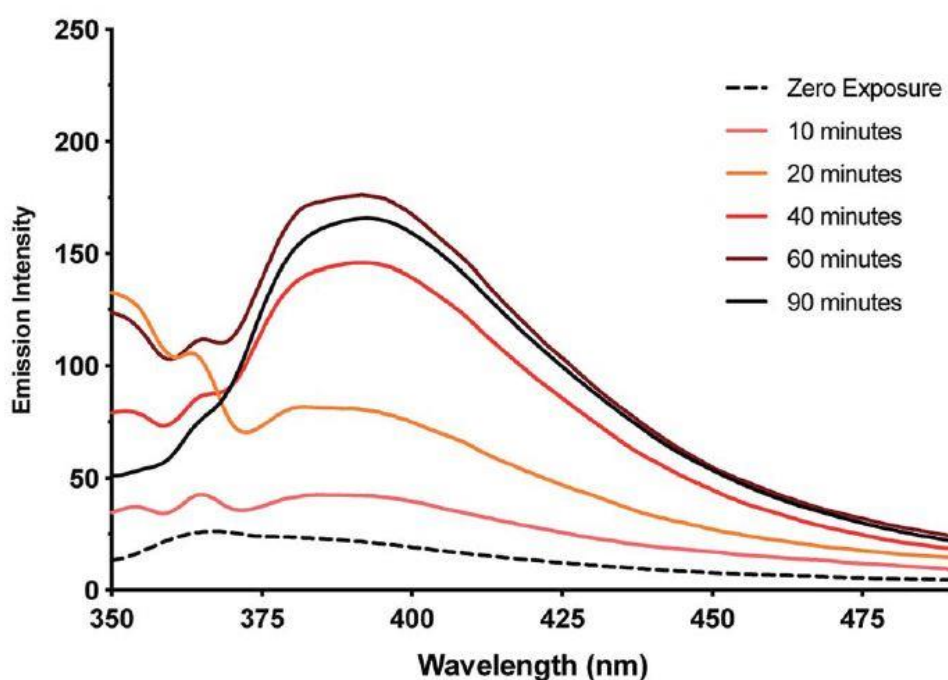


Figure 3.16 Fluorescence data showing the increasing emission intensity of the gel 1_{MeOH} , each sample faced increased exposure times to UV-light (λ_{Em} : 395 nm, λ_{Ex} : 330 nm).

TEM images comparing fresh *versus* exposed 1_{MeOH} illustrates this transformation towards photo-emissive materials (**Figure 3.17**). Within thinner areas of the fresh-gel several features can be observed that can be ascribed to the onset of cluster/particle formation. This is consistent with the AFM studies which show particles embedded within the gel-fibres. Particles size analysis of these images gave a range of between 1 - 4 nm; too large to be emissive, however, much smaller than the particles observed after exposure to UV-light. This effect is observed in **figure 3.17b**, whereby the formation of electron dense particles coincident with the fibre axis giving a

heterogeneous appearance. This compares to the homogeneous nature of the fibres before exposure as expected for the regularly spaced array of silver-ions in **1**.

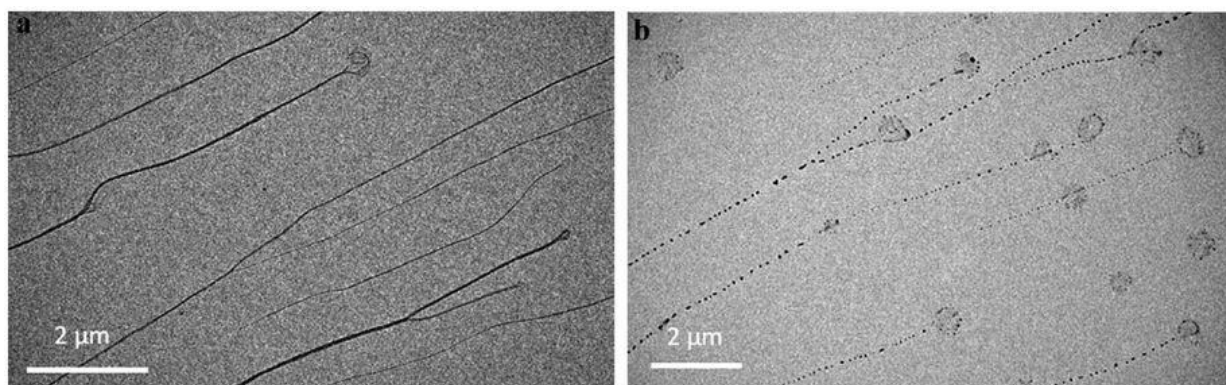


Figure 3.17 TEM bright field (TEM-BF) images of **1**_{MeOH} before and after exposure to UV-light. (a) Uniform fibres in agreement with that observed for the gel showing regular metallo-arrays and (b) after photoreduction showing the formation of electron-dense nano-particles/clusters.

High resolution scanning of an individual particle shows the expected crystal lattice fringes consistent with that of silver metal, with typical spacing of 0.25 ± 0.02 nm (**Figure 3.18**).

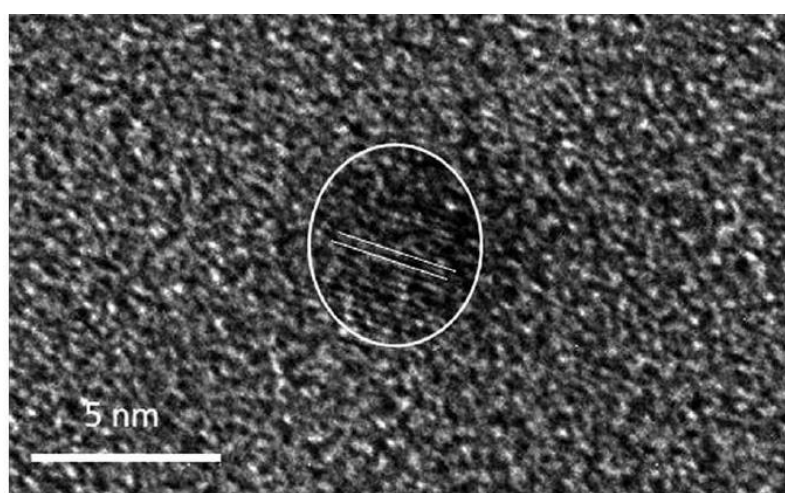


Figure 3.18 High-resolution TEM (HR-TEM) image of a dark spot identified as a silver particle (dia. 4.3 nm). Its lattice fringe spacing was measured at 0.25 ± 0.02 nm corresponding to the interplanar distance of (111) for Ag.

3.7. Conclusions

Throughout this chapter we have demonstrated that a simple metal-mediated base-pair $[\text{Ag}^{\text{I}}-(\text{N}^3\text{-cytidine})_2]$ **1Aq**, formed by the coordination between Ag^{I} and cytidine spontaneously assembles into a supramolecular double-helix. Driven by a plethora of complementary reversible interactions this material showed a remarkable self-healing ability when in the gel form. These results highlight the favourability of these building blocks to adopt structures akin to natural DNA with our example being analogous to that of metallo-DNA. This allows for a comparable insight into this class of material, moreover it's viability as a molecular conducting wire. With some of the shortest reported $\text{Ag}\cdots\text{Ag}$ distances (close to the metallic radii of 2.88 Å) electrical conductivity was measure using a range of highly sensitive techniques. The material demonstrated insulating properties experimentally, explained using computational theory. A filled valence band and sizable band gap goes further to support experimental findings. Reduction of the Ag-ions would in theory enhance the electrical conductivity, however such ventures readily produced Ag^0 particles as expected.

References

- (1) Atwell, S.; Meggers, E.; Spraggon, G.; Schultz, P. G. Structure of a Copper-Mediated Base Pair in DNA. *J. Am. Chem. Soc.* **2001**, *123* (49), 12364–12367. <https://doi.org/10.1021/ja011822e>.
- (2) Shionoya, M.; Takezawa, Y.; Kaul, C.; Clever, G. H.; Yamada, Y.; Tanaka, K.; Carell, T. Programmable Self-Assembly of Metal Ions inside Artificial DNA Duplexes. *Nat. Nanotechnol.* **2006**, *1* (3), 190–194. <https://doi.org/10.1038/nnano.2006.141>.
- (3) Tanaka, K.; Tengeiji, A.; Kato, T.; Toyama, N. Supporting Online Material for A Discrete Self-Assembled Metal Array in Artificial DNA. *Science* (80-.). **2003**, *299*, 1212–1213.
- (4) Clever, G. H.; Kaul, C.; Carell, T. DNA-Metal Base Pairs. *Angew. Chemie - Int. Ed.* **2007**, *46* (33), 6226–6236. <https://doi.org/10.1002/anie.200701185>.
- (5) Takezawa, Y.; Shionoya, M. Metal-Mediated DNA Base Pairing: Alternatives to Hydrogen-Bonded Watson-Crick Base Pairs. *Acc. Chem. Res.* **2012**, *45* (12), 2066–2076. <https://doi.org/10.1021/ar200313h>.

- (6) Clever, G. H.; Shionoya, M. Metal-Base Pairing in DNA. *Coord. Chem. Rev.* **2010**, *254* (19–20), 2391–2402. <https://doi.org/10.1016/j.ccr.2010.04.014>.
- (7) Jash, B.; Müller, J. Application of a Metal-Mediated Base Pair to the Detection of Medicinally Relevant Single Nucleotide Polymorphisms. *Eur. J. Inorg. Chem.* **2017**, *2017* (33), 3856. <https://doi.org/10.1002/ejic.201700881>.
- (8) Scharf, P.; Müller, J. Nucleic Acids with Metal-Mediated Base Pairs and Their Applications. *Chempluschem* **2013**, *78* (1), 20–34. <https://doi.org/10.1002/cplu.201200256>.
- (9) Su, M.; Tomás-Gamasa, M.; Carell, T. DNA Based Multi-Copper Ions Assembly Using Combined Pyrazole and Salen Ligandosides. *Chem. Sci.* **2015**, *6* (1), 632–638. <https://doi.org/10.1039/c4sc01567c>.
- (10) Menzer, S.; Sabat, M.; Lippert, B. Ag(I) Modified Base Pairs Involving Complementary (G, C) and Noncomplementary (A, C) Nucleobases. On the Possible Structural Role of Aqua Ligands in Metal-Modified Nucleobase Pairs. *J. Am. Chem. Soc.* **1992**, *114* (12), 4644–4649. <https://doi.org/10.1021/ja00038a030>.
- (11) Lippert, B.; Sanz Miguel, P. J. The Renaissance of Metal-Pyrimidine Nucleobase Coordination Chemistry. *Acc. Chem. Res.* **2016**, *49* (8), 1537–1545. <https://doi.org/10.1021/acs.accounts.6b00253>.
- (12) Kondo, J.; Tada, Y.; Dairaku, T.; Saneyoshi, H.; Okamoto, I.; Tanaka, Y.; Ono, A. High-Resolution Crystal Structure of a Silver(I)-RNA Hybrid Duplex Containing Watson-Crick-like C-Silver(I)-C Metallo-Base Pairs. *Angew. Chemie - Int. Ed.* **2015**, *54* (45), 13323–13326. <https://doi.org/10.1002/anie.201507894>.
- (13) Ono, A.; Cao, S.; Togashi, H.; Tashiro, M.; Fujimoto, T.; MacHinami, T.; Oda, S.; Miyake, Y.; Okamoto, I.; Tanaka, Y. Specific Interactions between Silver(i) Ions and Cytosine-Cytosine Pairs in DNA Duplexes. *Chem. Commun.* **2008**, No. 39, 4825–4827. <https://doi.org/10.1039/b808686a>.
- (14) Wada, S.; Ono, A.; Nakagawa, O.; Aotani, M.; Funai, T.; Miyazaki, Y.; Urata, H.; Torigoe, H.; Yamaguchi, E. AgI Ion Mediated Formation of a C-A Mispair by DNA Polymerases. *Angew. Chemie Int. Ed.* **2012**, *51* (26), 6464–6466. <https://doi.org/10.1002/anie.201109191>.
- (15) Funai, T.; Nakamura, J.; Miyazaki, Y.; Kiri, R.; Nakagawa, O.; Wada, S. I.; Ono, A.; Urata, H. Regulated Incorporation of Two Different Metal Ions into

- Programmed Sites in a Duplex by DNA Polymerase Catalyzed Primer Extension. *Angew. Chemie - Int. Ed.* **2014**, *53* (26), 6624–6627. <https://doi.org/10.1002/anie.201311235>.
- (16) Sychrovský, V.; Dairaku, T.; Okamoto, I.; Ono, A.; Yamanaka, D.; Šebera, J.; Furuita, K.; Nakashima, K.; Kondo, J.; Sato, H.; et al. Structure Determination of an Ag I -Mediated Cytosine-Cytosine Base Pair within DNA Duplex in Solution with 1 H/ 15 N/ 109 Ag NMR Spectroscopy . *Chem. - A Eur. J.* **2016**, *22* (37), 13028–13031. <https://doi.org/10.1002/chem.201603048>.
- (17) Ono, A.; Torigoe, H.; Tanaka, Y.; Okamoto, I. Binding of Metal Ions by Pyrimidine Base Pairs in DNA Duplexes. *Chem. Soc. Rev.* **2011**, *40* (12), 5855–5866. <https://doi.org/10.1039/c1cs15149e>.
- (18) Liu, H.; Shen, F.; Haruehanroengra, P.; Yao, Q.; Cheng, Y.; Chen, Y.; Yang, C.; Zhang, J.; Wu, B.; Luo, Q.; et al. A DNA Structure Containing AgI-Mediated G:G and C:C Base Pairs. *Angew. Chemie - Int. Ed.* **2017**, *56* (32), 9430–9434. <https://doi.org/10.1002/anie.201704891>.
- (19) Lamming, G.; El-Zubir, O.; Kolokotroni, J.; McGurk, C.; Waddell, P. G.; Probert, M. R.; Houlton, A. Two-Dimensional Frameworks Based on Ag(I)-N Bond Formation: Single Crystal to Single Molecular Sheet Transformation. *Inorg. Chem.* **2016**, *55* (19), 9644–9652. <https://doi.org/10.1021/acs.inorgchem.6b01365>.
- (20) Braun, E.; Eichen, Y.; Sivan, U.; Ben-Yoseph, G. DNA-Templated Assembly and Electrode Attachment of a Conducting Silver Wire. *Nature* **1998**, *391* (6669), 775–778. <https://doi.org/10.1038/35826>.
- (21) Braun *, E.; Keren, K. From DNA to Transistors. *Adv. Phys.* **2004**, *53* (4), 441–496. <https://doi.org/10.1080/00018730412331294688>.
- (22) Müller, J. Chemistry: Metals Line up for DNA. *Nature* **2006**, *444* (7120), 698. <https://doi.org/10.1038/444698a>.
- (23) Kondo, J.; Tada, Y.; Dairaku, T.; Hattori, Y.; Saneyoshi, H.; Ono, A.; Tanaka, Y. A Metallo-DNA Nanowire with Uninterrupted One-Dimensional Silver Array. *Nat. Chem.* **2017**, *9* (10), 956–960. <https://doi.org/10.1038/nchem.2808>.
- (24) Klinov, D.; Fardian-Melamed, N.; Basmanov, D.; Gutkin, V.; Porath, D.; Levi-Kalishman, Y.; Rotem, D.; Kotlyar, A.; Eidelstein, G. Synthesis and Properties of Novel Silver-Containing DNA Molecules. *Adv. Mater.* **2016**, *28* (24), 4839–4844.

<https://doi.org/10.1002/adma.201505049>.

- (25) Choi, S.; Dickson, R. M.; Yu, J. Developing Luminescent Silver Nanodots for Biological Applications. *Chem. Soc. Rev.* **2012**, *41* (5), 1867–1891. <https://doi.org/10.1039/c1cs15226b>.
- (26) Petty, J. T.; Zheng, J.; Hud, N. V.; Dickson, R. M. DNA-Templated Ag Nanocluster Formation. *J. Am. Chem. Soc.* **2004**, *126* (16), 5207–5212. <https://doi.org/10.1021/ja031931o>.
- (27) Vosch, T.; Tzeng, Y.-L.; Bongiorno, A.; Dickson, R. M.; Richards, C. I.; Choi, S.; Antoku, Y.; Hsiang, J.-C. Oligonucleotide-Stabilized Ag Nanocluster Fluorophores. *J. Am. Chem. Soc.* **2008**, *130* (15), 5038–5039. <https://doi.org/10.1021/ja8005644>.
- (28) Ritchie, C. M.; Johnsen, K. R.; Kiser, J. R.; Antoku, Y.; Dickson, R. M.; Petty, J. T. Ag Nanocluster Formation Using a Cytosine Oligonucleotide Template. *J. Phys. Chem. C* **2007**, *111* (1), 175–181. <https://doi.org/10.1021/jp0648487>.
- (29) Copp, S. M.; Schultz, D. E.; Swasey, S.; Gwinn, E. G. Atomically Precise Arrays of Fluorescent Silver Clusters: A Modular Approach for Metal Cluster Photonics on DNA Nanostructures. *ACS Nano* **2015**, *9* (3), 2303–2310. <https://doi.org/10.1021/nn506322q>.
- (30) Markešević, N.; Schultz, D.; Bouwmeester, D.; Copp, S. M.; Gwinn, E.; Gardner, K.; Oemrawsingh, S. S. R. Dual-Color Nanoscale Assemblies of Structurally Stable, Few-Atom Silver Clusters, As Reported by Fluorescence Resonance Energy Transfer. *ACS Nano* **2013**, *7* (11), 9798–9807. <https://doi.org/10.1021/nn4033097>.
- (31) Schultz, D.; Gardner, K.; Oemrawsingh, S. S. R.; Markešević, N.; Olsson, K.; Debord, M.; Bouwmeester, D.; Gwinn, E. Evidence for Rod-Shaped DNA-Stabilized Silver Nanocluster Emitters. *Adv. Mater.* **2013**, *25* (20), 2797–2803. <https://doi.org/10.1002/adma.201204624>.
- (32) Swasey, S. M.; Karimova, N.; Aikens, C. M.; Schultz, D. E.; Simon, A. J.; Gwinn, E. G. Chiral Electronic Transitions in Fluorescent Silver Clusters Stabilized by DNA. *ACS Nano* **2014**, *8* (7), 6883–6892. <https://doi.org/10.1021/nn5016067>.
- (33) Copp, S. M.; Schultz, D.; Swasey, S. M.; Faris, A.; Gwinn, E. G. Cluster Plasmonics: Dielectric and Shape Effects on DNA-Stabilized Silver Clusters. *Nano Lett.* **2016**, *16* (6), 3594–3599.

<https://doi.org/10.1021/acs.nanolett.6b00723>.

- (34) Gwinn, E.; Schultz, D.; Copp, S.; Swasey, S. DNA-Protected Silver Clusters for Nanophotonics. *Nanomaterials* **2015**, *5* (1), 180–207. <https://doi.org/10.3390/nano5010180>.
- (35) Santamaría-Díaz, N.; Méndez-Arriaga, J. M.; Salas, J. M.; Galindo, M. A. Highly Stable Double-Stranded DNA Containing Sequential Silver(I)-Mediated 7-Deazaadenine/Thymine Watson-Crick Base Pairs. *Angew. Chemie - Int. Ed.* **2016**, *55* (21), 6170–6174. <https://doi.org/10.1002/anie.201600924>.
- (36) Terrón, A.; Moreno-Vachiano, B.; Bauzá, A.; García-Raso, A.; Fiol, J. J.; Barceló-Oliver, M.; Molins, E.; Frontera, A. X-Ray Crystal Structure of a Metalled Double-Helix Generated by Infinite and Consecutive C*-Agl-C* (C*:N1-Hexylcytosine) Base Pairs through Argentophilic and Hydrogen Bond Interactions. *Chem. - A Eur. J.* **2017**, *23* (9), 2103–2108. <https://doi.org/10.1002/chem.201604331>.
- (37) Linares, F.; García-Fernández, E.; López-Garzón, F. J.; Domingo-García, M.; Orte, A.; Rodríguez-Diéguez, A.; Galindo, M. A. Multifunctional Behavior of Molecules Comprising Stacked Cytosine-Agl-Cytosine Base Pairs; Towards Conducting and Photoluminescence Silver-DNA Nanowires. *Chem. Sci.* **2019**, *10* (4), 1126–1137. <https://doi.org/10.1039/c8sc04036b>.
- (38) Aich, P.; Labiuk, S. L.; Tari, L. W.; Delbaere, L. J. T.; Roesler, W. J.; Falk, K. J.; Steer, R. P.; Lee, J. S. M-DNA: A Complex between Divalent Metal Ions and DNA Which Behaves as a Molecular Wire. *J. Mol. Biol.* **1999**, *294* (2), 477–485. <https://doi.org/10.1006/jmbi.1999.3234>.
- (39) Vedeneev, A. S.; Aich, P.; Lee, J. S.; Papadopoulos, C.; Xu, J. M.; Rakitin, A.; Kobzar, Y. Metallic Conduction through Engineered DNA: DNA Nanoelectronic Building Blocks. *Phys. Rev. Lett.* **2002**, *86* (16), 3670–3673. <https://doi.org/10.1103/physrevlett.86.3670>.
- (40) Toomey, E.; Xu, J.; Vecchioni, S.; Rothschild, L.; Wind, S.; Fernandes, G. E. Comparison of Canonical versus Silver(I)-Mediated Base-Pairing on Single Molecule Conductance in Polycytosine DsDNA. *J. Phys. Chem. C* **2016**, *120* (14), 7804–7809. <https://doi.org/10.1021/acs.jpcc.5b11968>.
- (41) Léon, J. C.; She, Z.; Kamal, A.; Shamsi, M. H.; Müller, J.; Kraatz, H. B. DNA Films Containing the Artificial Nucleobase Imidazole Mediate Charge Transfer in a Silver(I)-Responsive Way. *Angew. Chemie - Int. Ed.* **2017**, *56* (22), 6098–6102.

<https://doi.org/10.1002/anie.201700248>.

- (42) Jash, B.; Müller, J. Metal-Mediated Base Pairs: From Characterization to Application. *Chem. - A Eur. J.* **2017**, *23* (68), 17166–17178. <https://doi.org/10.1002/chem.201703518>.
- (43) Ban, G.; Dong, R.; Li, K.; Han, H.; Yan, X. Study on the Electric Conductivity of Ag-Doped DNA in Transverse Direction. *Nanoscale Res. Lett.* **2009**, *4* (4), 321–326. <https://doi.org/10.1007/s11671-008-9245-y>.
- (44) Kypr, J.; Kejnovská, I.; Renčuk, D.; Vorlíčková, M. Circular Dichroism and Conformational Polymorphism of DNA. *Nucleic Acids Res.* **2009**, *37* (6), 1713–1725. <https://doi.org/10.1093/nar/gkp026>.
- (45) Baker, E. S.; Bowers, M. T. B-DNA Helix Stability in a Solvent-Free Environment. *J. Am. Soc. Mass Spectrom.* **2007**, *18* (7), 1188–1195. <https://doi.org/10.1016/j.jasms.2007.03.001>.
- (46) Espinosa Leal, L. A.; Karpenko, A.; Swasey, S.; Gwinn, E. G.; Rojas-Cervellera, V.; Rovira, C.; Lopez-Acevedo, O. The Role of Hydrogen Bonds in the Stabilization of Silver-Mediated Cytosine Tetramers. *J. Phys. Chem. Lett.* **2015**, *6* (20), 4061–4066. <https://doi.org/10.1021/acs.jpclett.5b01864>.
- (47) Swasey, S. M.; Leal, L. E.; Lopez-Acevedo, O.; Pavlovich, J.; Gwinn, E. G. Silver (I) as DNA Glue: Ag⁺-Mediated Guanine Pairing Revealed by Removing Watson-Crick Constraints. *Sci. Rep.* **2015**, *5* (April), 1–9. <https://doi.org/10.1038/srep10163>.
- (48) Swasey, S. M.; Gwinn, E. G. Silver-Mediated Base Pairings: Towards Dynamic DNA Nanostructures with Enhanced Chemical and Thermal Stability. *New J. Phys.* **2016**, *18* (4), 1–14. <https://doi.org/10.1088/1367-2630/18/4/045008>.
- (49) Yamada, T.; Kitada, H.; Kajimoto, T.; Numata, A.; Tanaka, R. The Relationship between the CD Cotton Effect and the Absolute Configuration of FD-838 and Its Seven Stereoisomers. *J. Org. Chem.* **2010**, *75* (12), 4146–4153. <https://doi.org/10.1021/jo100496f>.
- (50) Yamada, T.; Ohshima, M.; Yuasa, K.; Kikuchi, T.; Tanaka, R. Assignment of the CD Cotton Effect to the Chiral Center in Pseurotins, and the Stereochemical Revision of Pseurotin A2. *Mar. Drugs* **2016**, *14* (4), 1–8. <https://doi.org/10.3390/md14040074>.
- (51) Dowdall, F. L.; Das, R. N.; Dash, J.; Mann, S.; Patil, A. J. Supramolecular

Hydrogels Derived from Silver Ion-Mediated Self-Assembly of 5'-Guanosine Monophosphate. *Soft Matter* **2011**, *7* (18), 8120. <https://doi.org/10.1039/c1sm05839h>.

- (52) Gomez-Navarro, C.; Bar, A. M.; Moreno, F.; Gomez-Herrero, J.; Moreno-Herrero, F.; Herrero, P.; Colchero, J. Topographic Characterization and Electrostatic Response of M-DNA Studied by Atomic Force Microscopy. *Nanotechnology* **2003**, *14* (2), 128–133. <https://doi.org/10.1088/0957-4484/14/2/305>.
- (53) Liu, B.; Bard, A. J.; Li, C. Z.; Kraatz, H. B. Scanning Electrochemical Microscopy. 51. Studies of Self-Assembled Monolayers of DNA in the Absence and Presence of Metal Ions. *J. Phys. Chem. B* **2005**, *109* (11), 5193–5198. <https://doi.org/10.1021/jp045050v>.
- (54) Mizoguchi, K.; Tanaka, S.; Ogawa, T.; Shiobara, N.; Sakamoto, H. Magnetic Study of the Electronic States of B-DNA and M-DNA Doped with Metal Ions. *Phys. Rev. B - Condens. Matter Mater. Phys.* **2005**, *72* (3), 1–4. <https://doi.org/10.1103/PhysRevB.72.033106>.
- (55) Spring, B. Q.; Clegg, R. M. Fluorescence Measurements of Duplex DNA Oligomers under Conditions Conducive for Forming M-DNA a Metal-DNA Complex. *J. Phys. Chem. B* **2007**, *111* (33), 10040–10052. <https://doi.org/10.1021/jp0725782>.
- (56) Schmidbaur, H.; Schier, A. Argentophilic Interactions. *Angew. Chemie - Int. Ed.* **2015**, *54* (3), 746–784. <https://doi.org/10.1002/anie.201405936>.
- (57) Perdew, J. P.; Zunger, A. Self-Interaction Correction to Density-Functional Approximations for Many-Electron Systems. *Phys. Rev. B* **1981**, *23* (10), 5048–5079. <https://doi.org/10.1103/PhysRevB.23.5048>.
- (58) Perdew, J. P.; Levy, M. Physical Content of the Exact Kohn-Sham Orbital Energies: Band Gaps and Derivative Discontinuities. *Phys. Rev. Lett.* **1983**, *51* (20), 1884–1887. <https://doi.org/10.1103/PhysRevLett.51.1884>.
- (59) Orpen, A. G.; Brammer, L.; Allen, F. H.; Kennard, O.; Watson, D. G.; Taylor, R. Tables of Bond Lengths Determined by X-Ray and Neutron Diffraction. Part 2. Organometallic Compounds and Co-Ordination Complexes of the d- and f-Block Metals. *J. Chem. Soc., Dalt. Trans.* **1989**, 0 (September 1985), S1–S83.
- (60) Petty, J. T.; Story, S. P.; Hsiang, J. C.; Dickson, R. M. DNA-Templated Molecular Silver Fluorophores. *J. Phys. Chem. Lett.* **2013**, *4* (7), 1148–1155.

<https://doi.org/10.1021/jz4000142>.

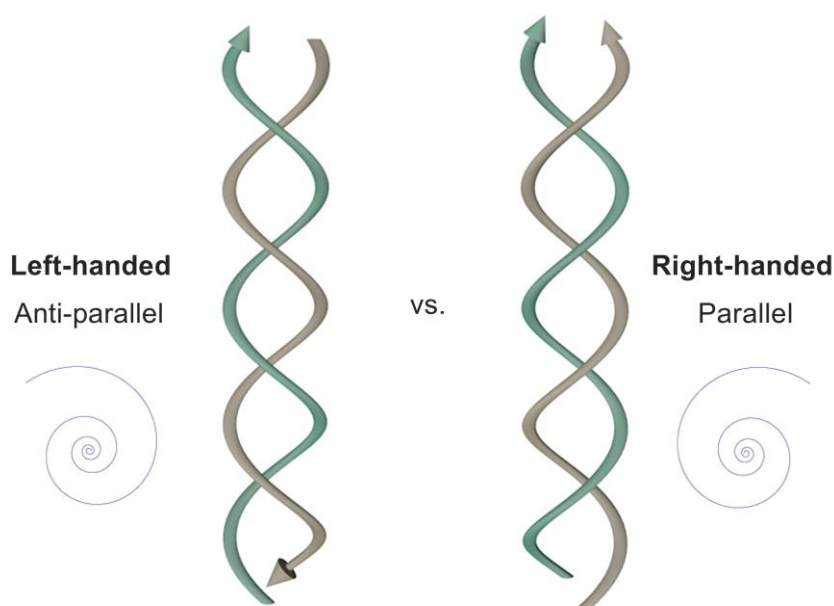
- (61) Copp, S. M.; Bogdanov, P.; Debord, M.; Singh, A.; Gwinn, E. Base Motif Recognition and Design of DNA Templates for Fluorescent Silver Clusters by Machine Learning. *Adv. Mater.* **2014**, *26* (33), 5839–5845. <https://doi.org/10.1002/adma.201401402>.
- (62) Sengupta, B.; Corley, C.; Cobb, K.; Saracino, A.; Jockusch, S. DNA Scaffolded Silver Clusters: A Critical Study. *Molecules* **2016**, *21* (2), 1–15. <https://doi.org/10.3390/molecules21020216>.
- (63) Li, T.; He, N.; Wang, J.; Li, S.; Deng, Y.; Wang, Z. Effects of the I-Motif DNA Loop on the Fluorescence of Silver Nanoclusters. *RSC Adv.* **2016**, *6* (27), 22839–22844. <https://doi.org/10.1039/c5ra22489f>.
- (64) Sengupta, B.; Springer, K.; Buckman, J. G.; Story, S. P.; Abe, O. H.; Hasan, Z. W.; Prudowsky, Z. D.; Rudisill, S. E.; Degtyareva, N. N.; Petty, J. T. DNA Templates for Fluorescent Silver Clusters and I-Motif Folding. *J. Phys. Chem. C* **2009**, *113* (45), 19518–19524. <https://doi.org/10.1021/jp906522u>.

Chapter 4.

Metallo-DNA: Left- vs. Right-Handed Helical Rotation in the Solid-State for Ag^I-Mediated Supramolecular Duplexes.

4.1. Introduction

Left- and right-handed helical structures have long been observed in numerous polymeric repeating structures in both synthetic^{1–3} and biological settings^{4,5}. The screw axis gives rise to detectable optically active complexes when measured using circularly polarised light (CD), due to chirality of the supramolecular structure (**Scheme 4.1**).^{2,3,6} Detectable optical activity implies that one rotation or screw sense prevails. If two helical senses exist or can interconvert then optical activity is not observed.



Scheme 4.1 Helical sense diagram; left (anti-clockwise) vs. right-hand (clockwise) and anti-parallel vs. parallel strand direction.

DNA in particular has been well characterised in both clockwise (right-handed, A- and B-DNA) and anticlockwise (left-handed, Z-DNA) conformations.^{7–12} The covalent structure of DNA polynucleotide sequences is persistent between all DNA-types; however, the base sequence is variable and therefore dictates the helical handedness produced. The transition observed between B- and Z-DNA is based on electrostatic interactions and has subsequently become one of the best characterised conformational changes in double stranded DNA. The transition of B-form to Z-form DNA is termed “denaturation”. This involves the breaking of two sets of interactions integral to duplex stability; base-pair hydrogen-bonding and base stacking interactions.

The reverse process is called renaturation or annealing. These processes are essential for many biological processes.

A-, B- and Z-forms of DNA are now well understood spectroscopically (**Figure 4.1**). Their component nucleotide units have limited chirality and are only weakly observed using CD with low signal intensity.¹³ Chirality within these nucleic units originates at a single site, the C1' of the sugar. Formation of a double helix generates significant spectra changes owed to supramolecular chirality of the structure. All variations of B-type DNA (with canonical base-pairs) have common global spectroscopic CD features. These are characterised by a positive long wavelength peak or band at 260 - 280 nm and a negative band around 245 nm.^{13,14} The positions and amplitudes of these peaks can differ tremendously due to the sequence specific conformational properties intrinsic to DNA. A-type DNA is similar to RNA spectroscopically, and is common for G, C rich DNA. The spectra are commonly characterised by a dominant positive band at 260 nm and a negative band at 210 nm.^{13,14} Both of these DNA types represent right-handed double helices. Z-type DNA represents a left-handed helix which can be seen as a near inversion of the CD spectra common for right-handed B-DNA.¹³ A negative band at 290 nm followed by a positive band at 260 nm and a strong negative band at approximately 205 nm are characteristic.^{13,14}

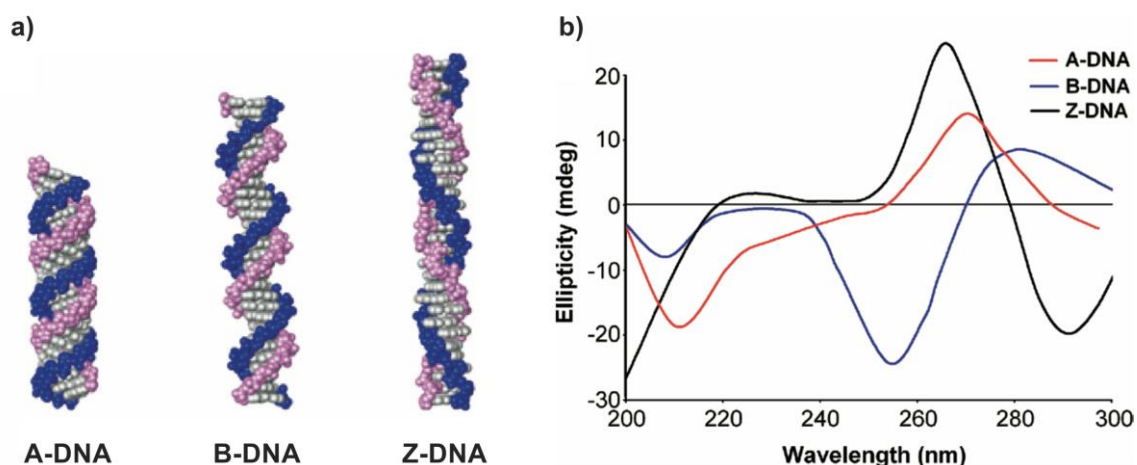


Figure 4.1 a) Illustrations of A-, B- and Z-DNA types. b) Typical CD spectrum for A- (red), B- (blue) and Z-DNA (black).¹⁴

Kondo *et al.* have been at the forefront of metallo-DNA (M-DNA) structural characterisation, publishing several examples of metal-mediated duplexes across a

range of traditional and newly observed base-pair partners. A right-handed (clockwise, antiparallel) DNA double helix was structurally characterised from a single crystal following insertion of Hg^{II} across T:T and T:G base-pairs of d(TTTGC) (NDB: 6IUE) (**Figure 4.2a**).¹⁵ A second example used a dodecamer d(GGACT(^{Br}C)GACTCC) (^{Br}C = 5-bromo-2'-deoxycytosine), to produce an uninterrupted one-dimensional Ag^I array across C:C, G:G, CG and T:T base-pairs (NDB: 5IX7) (**Figure 4.2b**); again, the helical rotation was right-handed.¹⁶ A single example exists of m-RNA, involving the metalation of r(GGACU[^{Br}C]GACUCC) by Ag^I to produce an A-form duplex with a right-handed double-helix (NDB: 5AY2) (**Figure 4.2c**).¹⁷ The M-DNA examples described offer alternative base-pair interactions and would produce unique spectroscopic characteristics. At the time of writing, all crystallographically characterised examples of M-DNA described have a right-handed (clockwise) anti-parallel double helix. Insertion of Ag^I or Hg^{II} ions have little effect on the base-pairing distances over the canonical Watson-Crick interactions. The reduced size of pyrimidines when compared to purines allows for a gap between bases of 4.4 Å; large enough for a single Ag^I and Hg^{II} ion to coordinate within the core of helix.^{18–20}

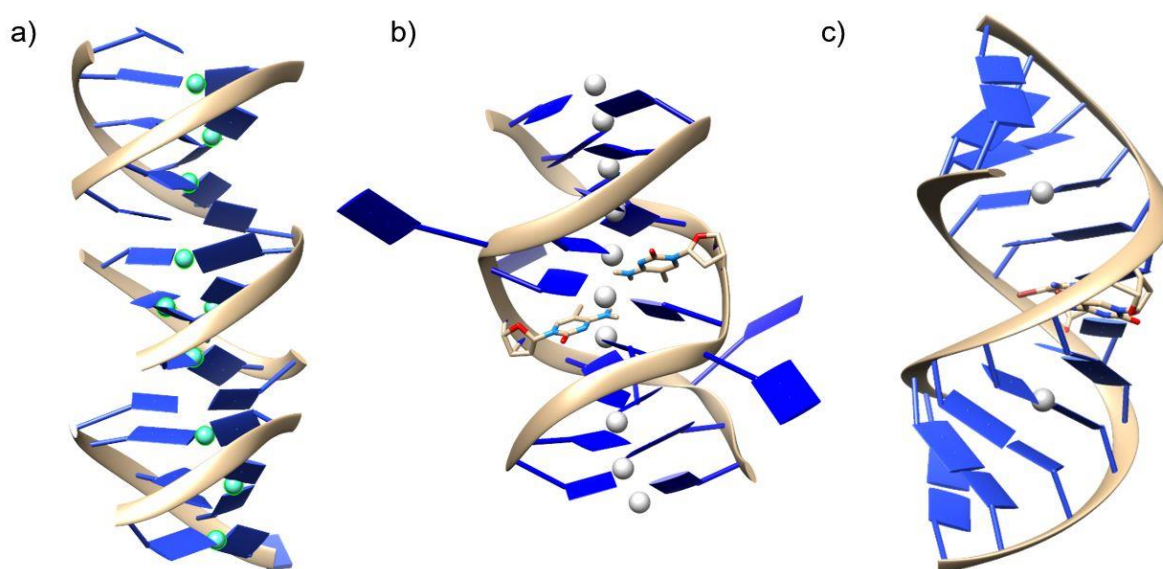


Figure 4.2 Crystal structures of a) Hg^{II}-DNA helical wire, b) Ag^I-DNA dodecamer (d(GGACT(^{Br}C)GACTCC)) with an uninterrupted silver array and c) Ag^I-RNA duplex (r(GGACU[^{Br}C]GACUCC)), each demonstrating metal-mediated right-handed (clockwise) antiparallel double-helices.

Terrón and Frontera recently published a crystallographically characterised structure of a pseudo M-DNA system analogous to that of the DNA systems previously discussed.²¹ They describe a metal-mediated double helix generated from the assembly of the complex formed by Ag^{I} ions and N^1 -hexylcytosine as ligands, $\text{C}^{\ast}\text{-Ag}^{\text{I}}\text{-C}^{\ast}$, $[\text{Ag}^{\text{I}}\text{-(}N^3\text{-(}N^1\text{)-hexylcytosine)}_2]\cdot[\text{SbF}_6]\cdot[\text{MeOH}]$ (CCDC code: YASGIL) (**Figure 4.3**). The *bis*-complex ions assemble in-line to form a 1D polymeric double helix stabilised through intermolecular base-base hydrogen bonding ($N^4\text{-H}\cdots\text{O}^2$), hydrophobic and argentophilic interactions. Interestingly, both left- and right-handed senses are observed as a racemic mixture in the solid-state. Unfortunately, no spectroscopic data was published alongside the crystal structure.

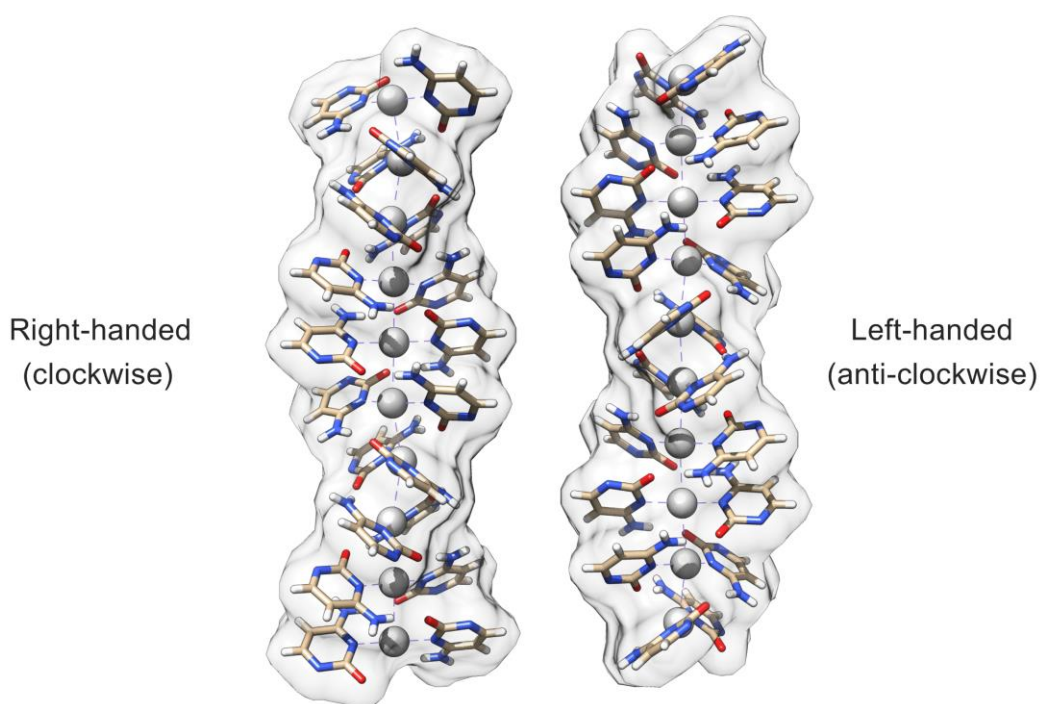
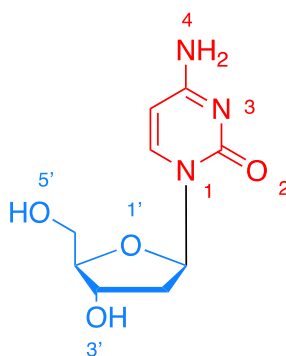


Figure 4.3 Single crystal X-ray structures of $[\text{Ag}^{\text{I}}\text{-(}N^3\text{-(}N^1\text{)-hexylcytosine)}_2]$ from the Frontera group displaying both helical senses; left and right-handed duplexes. N^1 -Hexyl chains, methanol and SbF_6 counter anions removed for clarity.²¹

Herein, we describe the preparation, characterisation (Part I) and crystallisation phenomena observed *via* AFM (Part II) for $[\text{Ag}^{\text{I}}(\text{N}^3\text{-2'deoxyctidine)}_2][\text{NO}_3]$. The structure is analogous to that of $[\text{Ag}^{\text{I}}(\text{N}^3\text{-cytidine)}_2][\text{NO}_3]$ discussed previously in chapter 3, yet a subtle change in the sugar, the loss of an -OH group at the O^2 position (**Scheme 4.2**), gives the opposing left-handed (anticlockwise) helix.



Scheme 4.2 2'-Deoxycytidine (alpha) with atomic numbering. The base is represented in red and deoxyribose in blue.

4.2. Results & Discussion

Synthesis and characterisation of $[\text{Ag}^{\text{I}}-(N^3\text{-}2'\text{deoxycytidine})_2][\text{NO}_3]$, **1** – An aqueous reaction between 2'-deoxycytidine (DCyt., **Scheme 4.2**) and AgNO_3 in a 2:1 stoichiometric ratio yielded $[\text{Ag}^{\text{I}}-(N^3\text{-}2'\text{deoxycytidine})_2][\text{NO}_3]$, **1**, as a white powder in a quantitative yield. Recrystallisation from water/acetonitrile gave colourless needle-shaped crystals with acicular habit. Initial analysis of the crystalline material was performed using FTIR and MS.

FTIR was measured for **1** and its parent ligand, 2'deoxycytidine (**Figure 4.4**), in the solid-state. The two spectra share many common features, with changes occurring within regions associated with amino ($3000 - 3600 \text{ cm}^{-1}$ and $\sim 1500 \text{ cm}^{-1}$) and carbonyl ($\sim 1600 \text{ cm}^{-1}$) groups. Furthermore, **1** demonstrated peak broadening generally associated with hydrogen bonding. These spectroscopic differences between the parent nucleoside and complex ion are consistent with those observed in chapter 3 for $[\text{Ag}^{\text{I}}-(N^3\text{-cytidine})_2]$. It is therefore likely that **1** is analogous $[\text{Ag}^{\text{I}}-(N^3\text{-cytidine})_2]$, forming a duplex structure in the solid-state.

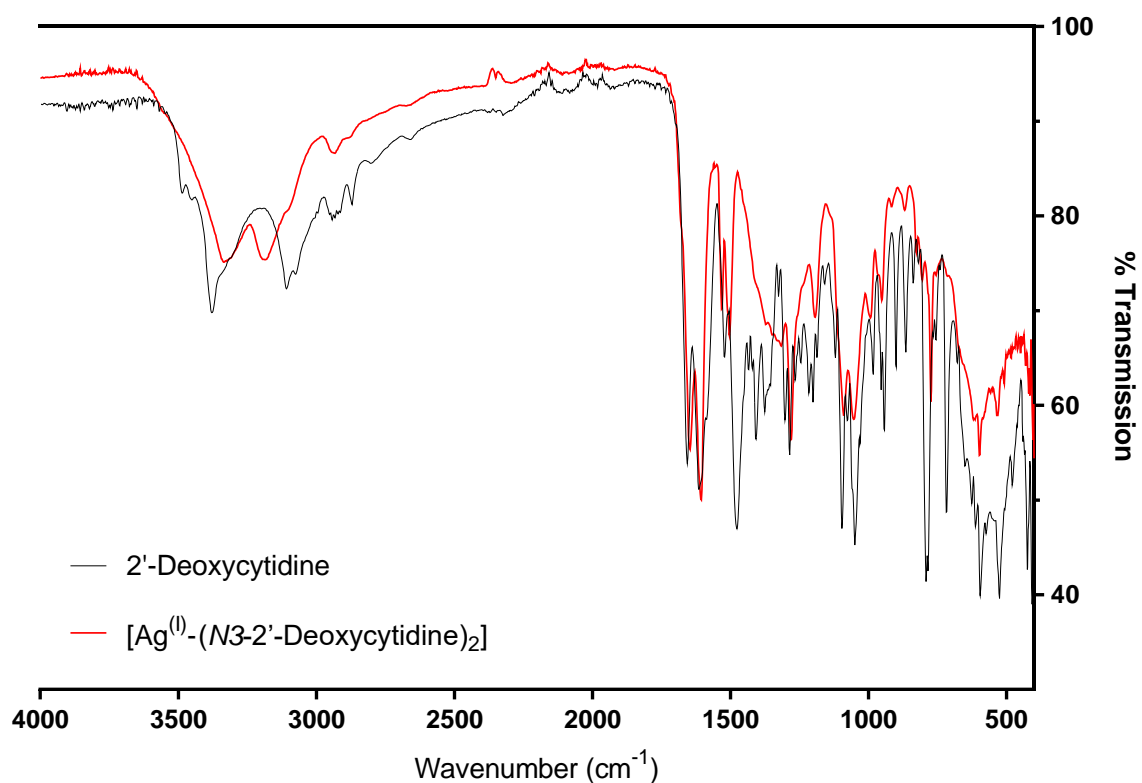


Figure 4.4 FTIR data collected for 2'-deoxycytidine (black-line) and [Ag^I-(N³-2'-deoxycytidine)₂], **1** (red-line)

The intermolecular hydrogen bonding between neighbouring N^4 and O^2 exocyclic heteroatoms necessary for duplex formation were further analysed (**Figure 4.5**). At longer wavelengths significant shifts were observed for $\nu_{as}(\text{NH}_2)$ $3381 \rightarrow 3329 \text{ cm}^{-1}$ and $\nu_s(\text{NH}_2)$ $3109 \rightarrow 3192 \text{ cm}^{-1}$ vibrations and at lower wavelengths $\nu(\text{CO})$ is decreased, $1657 \rightarrow 1647 \text{ cm}^{-1}$. Additionally, the $\beta_{sc}(\text{NH}_2)$ at 1476 cm^{-1} broadens and shifts to a lower wavenumber.^{28,29} All changes observed (*i.e.* shifts to lower frequencies and peak broadening) in the FTIR were consistent with the observed H-bonding interactions found for [Ag^I-(N³-cytidine)₂] suggesting a similar structure.^{30,31}

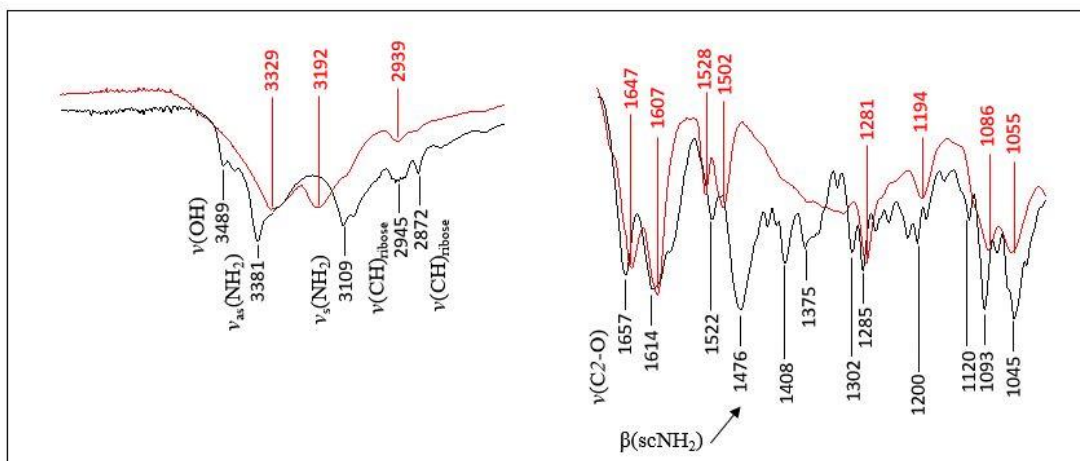


Figure 4.5 Analysis of FTIR spectra for 2'-deoxycytidine (black-line) and $[\text{Ag}^{\text{I}}-(N^3\text{-}2'\text{-deoxycytidine})_2]$, **1** (red-line)

The expected *bis*-complex, $[\text{Ag}^{\text{I}}-(\text{DCyt})_2]^+$, was observed using ESI-MS (direct injection, positive ion mode) at 561.4462 m/z (**Figure 4.6**). Isotope patterns, splitting and masses aligned well with the theoretical values calculated for the expected *bis*-complex ($\text{C}^*-\text{Ag}^+-\text{C}^*$) derived from the crystal structure ($\text{C}^* - \text{DCyt}$); Calc. $\text{C}_{18}\text{H}_{26}\text{AgN}_6\text{O}_8$, $[\text{M}]^+$, 561.0900 m/z. Peak separation of 1.0 m/z suggests species bearing a plus one charge state. The +1 charge of the silver ion was sufficient for detection in positive ion mode demonstrating no proton loss needed to occur during ionisation. The isotope pattern was characteristic of a species bearing a single silver ion (^{107}Ag 51.839%, ^{109}Ag 48.161%) per mass detected.

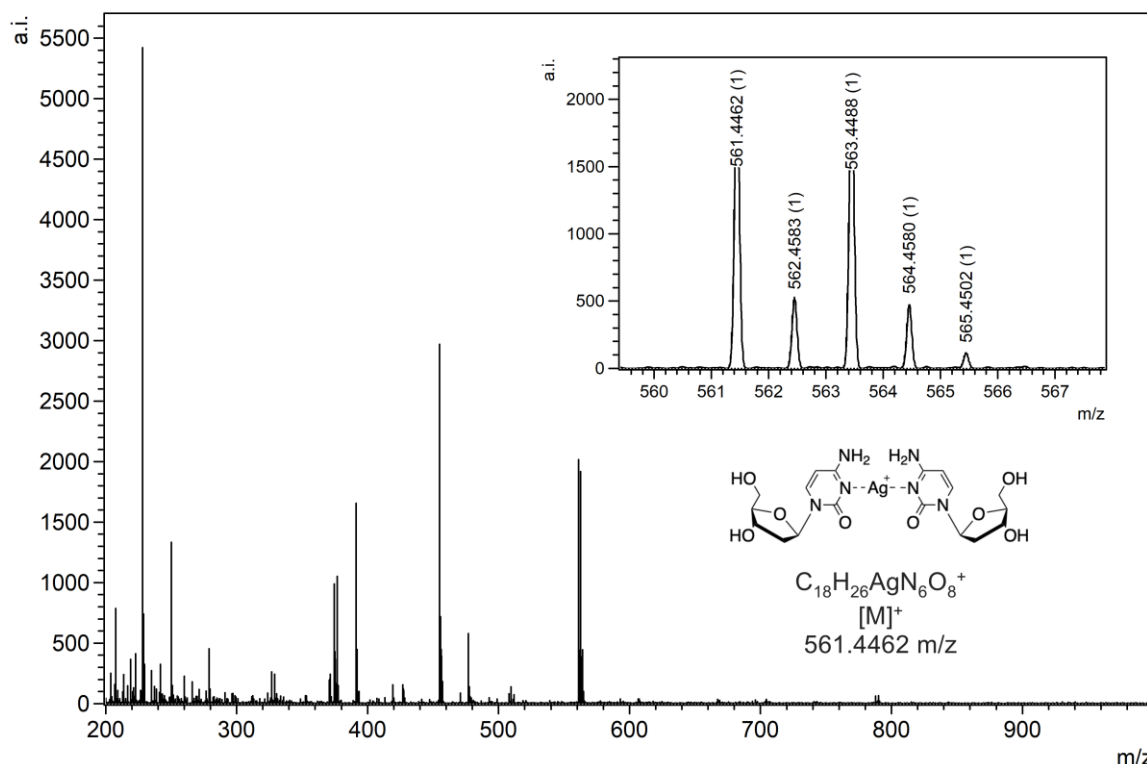


Figure 4.6 ESI-MS (positive ion mode) for an aqueous solution of 2'-deoxycytidine and silver nitrate at a 2:1 ratio within the range of 0 – 1000 m/z (inset, 560 – 568 m/z).

Curiously, a peak was detected at 788.10 m/z. The detected mass had low intensity, representing approximately 3% of the total metal-mediated mass by way of peak intensity (**Figure 4.7**). The isotope pattern, again, was indicative of a species bearing a single silver ion with a plus-one charge represented by a splitting of 1.0 m/z. The peaks detected aligned well with the theoretical values calculated for a complex bearing three DCyt ligands around a single Ag^+ ; $[\text{Ag}^+(\text{DCyt})_3]^+$, Calc. ($\text{C}_{27}\text{H}_{39}\text{AgN}_9\text{O}_{12}$, $[\text{M}]^+$) 788.1764 m/z. Searching the Cambridge Crystallographic Database Centre (CCDC) using ConQuest® (Version 2.0.5) for examples of *tris*-($\text{Ag}^+(\text{N})_3$) crystal structures returned 1706 hits, confirming the feasibility of a 3:1, *tris*- $[\text{Ag}^+(\text{N}^3\text{-DCyt})_3]^+$, binding motif as observed in MS.

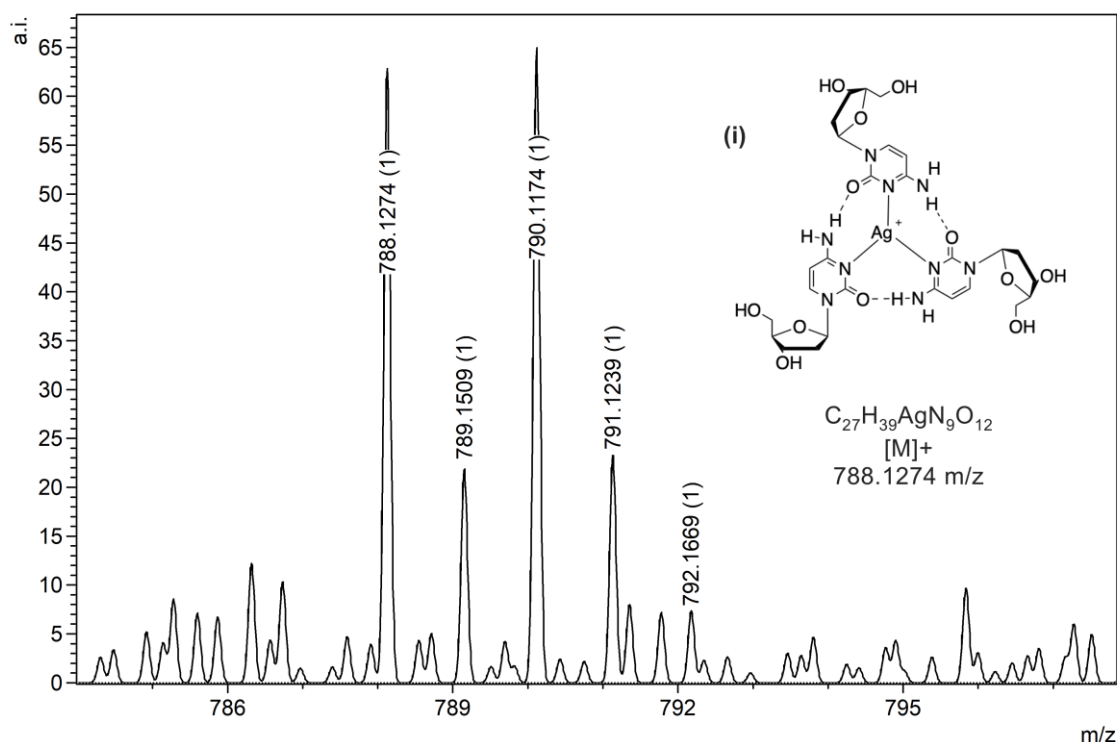


Figure 4.7 ESI-MS (positive ion mode) for an aqueous solution of 2'-deoxycytidine and silver nitrate at a 2:1 ratio within the range of 783 – 797 m/z . Inset (i) a 3:1 ligand-to-metal coordination complex.

X-ray diffraction of a single crystal revealed a N^3 metal-mediated *bis*-complexes $C^*-Ag^I-C^*$ (C^* : 2'-deoxycytidine) reflecting the 2:1 stoichiometry of the reagents (**Figure 4.8**). $Ag-N^3$ bond lengths have a narrow range between 2.15 and 2.17 Å. The $N-Ag-N$ angle is $\sim 165^\circ$, similar to analogous silver-pyrimidine complexes that have been previously discussed in Chapters 2 and 3. The DCyt pyrimidine rings of each metal complex are twisted significantly from co-planarity with a mean planar twist angle between bases of 67.5° . An angle of $<90^\circ$ shows a preference towards a *cisoidal* conformation. Despite a slight preference towards a *cisoid* orientation the bases are near perpendicular allowing for intermolecular hydrogen bonding interactions across the exocyclic N^4 -donor and O^2 -acceptor sites between adjacent neighbouring ligands in the linear chain-like assembly (heteroatom distances 2.9 Å; N^4-O^{2A} (2.922(11) Å), O^2-N^{4B} (2.826(12) Å) and $O^{2B}-N^{4A}$ (2.937(12) Å). These intermolecular bonding interactions lead to a 1D left-handed (anti-clockwise) double-helix composed of stacked N^3 metal-mediated $C^*-Ag^I-C^*$ (C^* : 2'-deoxycytidine) complexes (**Figure 4.8**). The assembly is held in-line by a combination of ligand-to-ligand intermolecular

exocyclic $N^4\cdots O^2$ hydrogen bonding and argentophilic interactions leading to a continuous array of silver ions through the core of a left-handed double-helix. The unit cell ($a = b = 16.931(5)$ Å, $c = 53.194(13)$ Å) is defined by a $P6_122$ hexagonal space group with a remarkably linear contiguous argentophilic ($Ag^+\cdots Ag^+$) down the helical c -axis (100). The repeating unit cell consists of two silver ions and three cytosine ligands. The helical pitch is approximately 36.5° between the silver mediated DCyt complexes, with a complete rotation every ten units; akin to natural DNA. The chain of Ag^+ ions is almost linear, with deviations of approximately 7.5° over ten complex ions, from the mean straight line which is parallel to the trigonal c -axis, and with $Ag\cdots Ag\cdots Ag$ angles of $135.61(9)^\circ$. The $Ag^+\cdots Ag^+$ distances are short at $2.955(2)$ and $3.0553(11)$ Å. The diameter of the duplex is approximately 16.7 Å, as measured across $5'$ -OH groups on individual complex ions, which is similar to that of natural DNA. For each "strand" of the duplex, there is a polar arrangement of nucleosides which directs the formation of these complementary $N^4\cdots O^2$ interactions between neighbouring complexes. Individual complexes form two pairs of $N^4\cdots H\cdots O^2$ hydrogen bonding interactions. Essentially an identical pattern of intercomplex base-pair interactions is seen for $[Ag^I\cdots (N^3\text{-cytidine})_2][NO_3]$ in chapter 3.

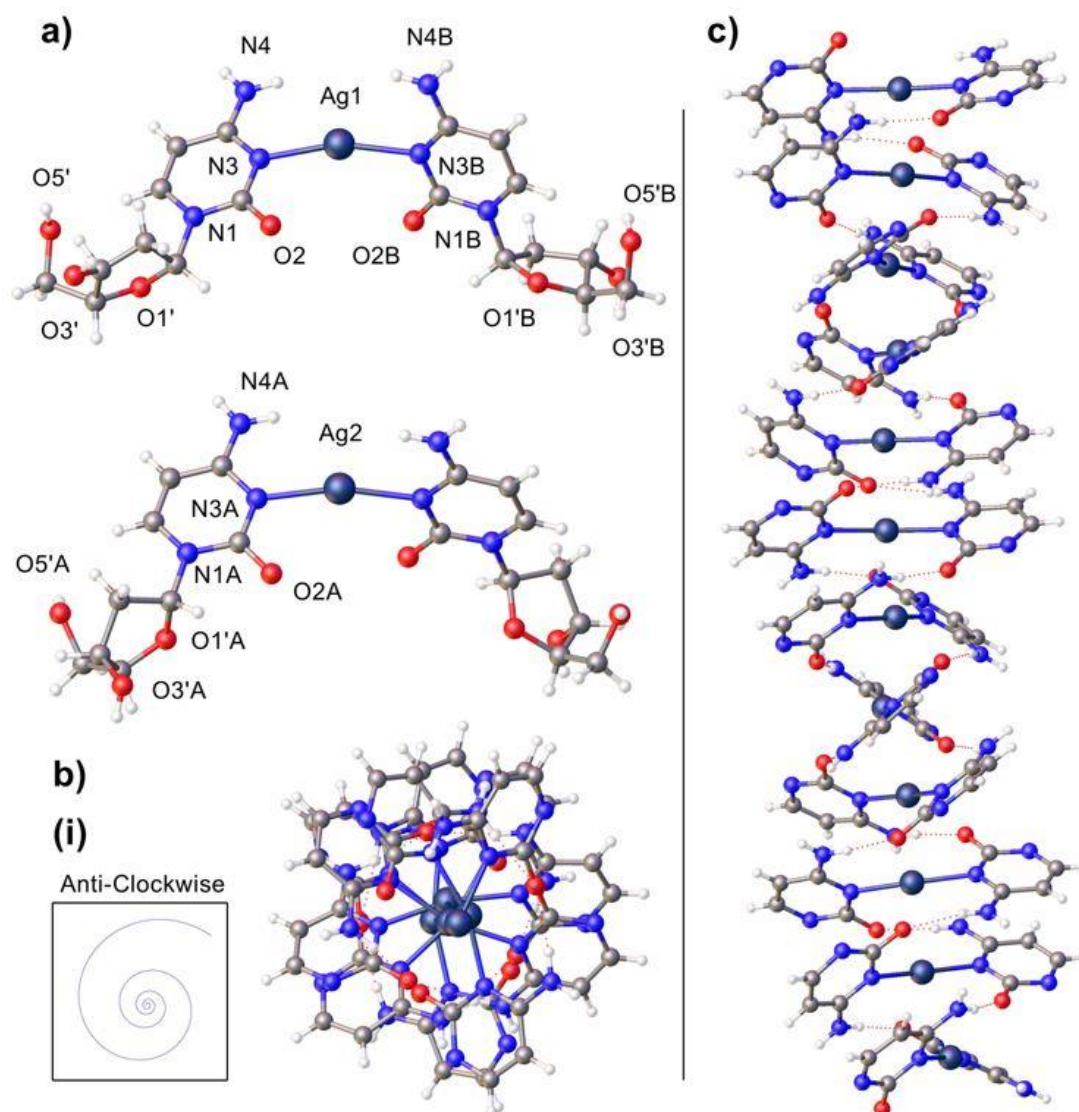


Figure 4.8 Single crystal X-ray structure of $[\text{Ag}^{\text{I}}-(\text{N}^3\text{-2'}\text{Deoxyctidine})_2]$; (a) Details and labelling of the two unique repeating silver ions, (b) Top-down (100) view of the 1D chain showing an anti-clockwise (left-handed) helical rotation; (i) An illustration of an anti-clockwise logarithmic spiral, (c) Side-on view showing the contiguous 1D argentophilic array within the helix. Sugar groups omitted in (b) and (c) for clarity

A view along the *c*-axis or [100] direction of the packed lattice reveals channels or voids, as shown in **Figure 4.9**. These voids are approximately 5.0 Å in diameter and likely occupied by solvent and nitrate counter ions. Accurate modelling of these molecules within the voids was not possible due to disorder. The duplex core structure occupied by silver ions was notably absent of any solvent or counter ions. Such porous materials have been previously identified to have useful applications as host lattice materials.²² Compounds or materials small enough can be embedded or stored within

the voids until changes in the surrounding lattice grant their release. Such materials have also been investigated as methods of filtration as ultra-thin porous membranes.^{23–27}

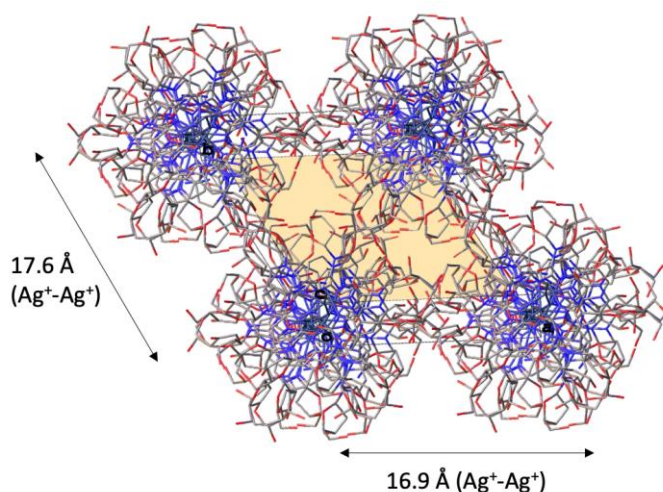


Figure 4.9 Top-down view (*c*-axis, [100]) into a packed crystal lattice showing voids or channels (filled yellow) between four 1D chains.

Akin to naturally occurring *A*- and *B*-form DNA, 10 silver-mediated cytosine base-pairs give one complete rotation of the helix with increments of $\sim 36.5^\circ$ between each complex-ion base-pair. As mentioned, the duplex rotation of **1** is left-handed (anticlockwise). However, the most common forms of DNA and its ribose counterpart $[\text{Ag}^{\text{I}}-(\text{cytidine})_2]$ the helical rotation observed is right-handed (clockwise). Directly comparing the crystal structures of $[\text{Ag}^{\text{I}}-(N^3\text{-cytidine})_2]$ (clockwise, right-hand) and $[\text{Ag}^{\text{I}}-(N^3\text{-2'-deoxycytidine})_2]$ (anticlockwise, left-hand), **1**, show nearly identical compositions in terms of metal-ligand geometries and bonding distances. Ag-N average distances are 2.161 and 2.102 Å, N-Ag-N average angles are 163° and 171° , average base-to-base plane twist angles are 71.7° and 73.0° , rotation per complex ion is 36.5° and 35.1° respectively for $[\text{Ag}^{\text{I}}-(\text{DCyt})_2]$ and $[\text{Ag}^{\text{I}}-(\text{Cyt})_2]$. However, a notable difference can be seen in the pucker-type conformations of the sugar groups.

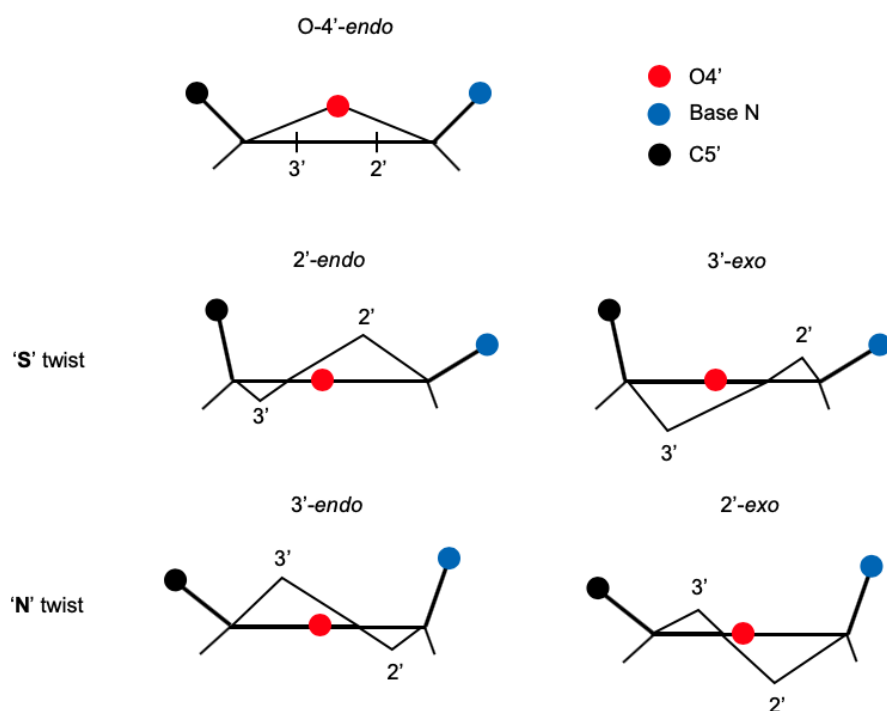


Figure 4.10 An illustration of the five sugar pucker types found in DNA.

There are five main ribose pucker types found in DNA (**Figure 4.10**).^{5,9,32,33} The sugar group's pucker is known to have a significant influence on overall structure and helicity of the double helix.^{5,9,32-34} A-, B and Z- form DNA are identical in terms of their component nucleotide units, however these all differ in their ribose conformations. For example, the S-twist type pucker is common to A- and B-form of DNA (right-handed), extend their nucleobase pairs towards the centre of the helix equally.³³ This allows for a centred interaction between the double strands of the helix. Z-DNA (left-handed) possess *N*-twist puckered sugars in addition to S-twist, leading to an imbalanced or non-centred base-pair interaction as demonstrated in **Figure 4.11**.³³ This leads to a zigzag structure to which Z-DNA gets its name.

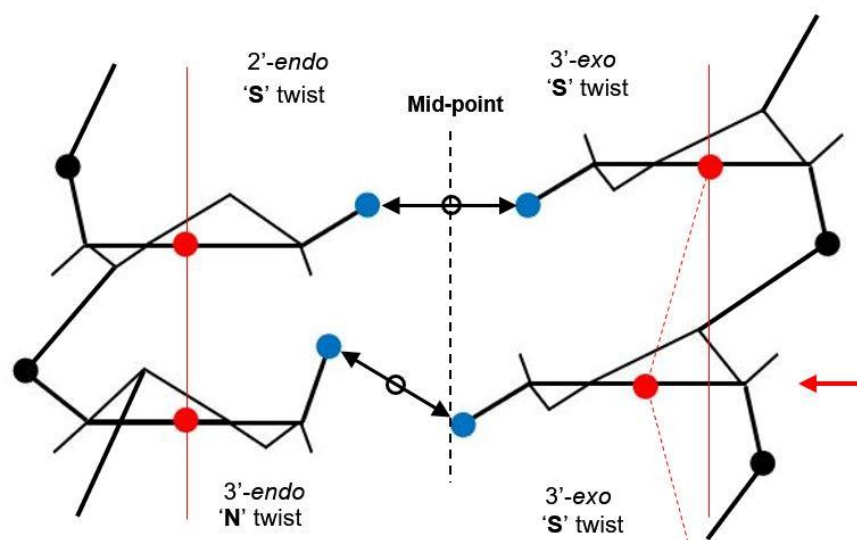


Figure 4.11 An illustration to show the effects on duplex structure of N-twist sugar pucker type conformations *versus* S-twist.

Analysis of $[\text{Ag}^I-(N^3\text{-}2'\text{deoxycytidine})_2]^+$ shows sugar pucker conformations with two instances of S-twist-3'exo and one N-Twist-3'-endo pucker-type. In comparison to its ribose counterpart $[\text{Ag}^I-(N^3\text{-cytidine})_2]$, which displayed predominantly the N-twist-2'exo; although Instances of the S-Twist-2'endo and S-Twist-3'exo also exist. Unfortunately, no clear trend in the preference of pucker type could be directly associated with the left- or right-handed helical rotation for $[\text{Ag}^I-(N^3\text{-}2'\text{deoxycytidine})_2]$ or $[\text{Ag}^I-(N^3\text{-cytidine})_2]$ respectfully. Without the phosphate backbone any changes in the pucker type has no clear effects on the helix structure. It is more likely that the pucker types adopted and observed within the solid state for $[\text{Ag}^I\text{-(Cyt)}_2]$ and $[\text{Ag}^I\text{-(DCyt)}_2]$ are configured for electrostatic and solvent interactions in the solid-state.

Analysis of any further interactions from the deoxyribose sugar groups for **1** revealed hydrogen bonding between adjacent O5' hydroxyl functional groups (**Figure 4.12**). The sugars orientate themselves in pairs to have the smallest O^{5'}...O^{5'} distances (2.725(9) Å). No additional interactions could be observed due to disorder of the solvent within these voids.

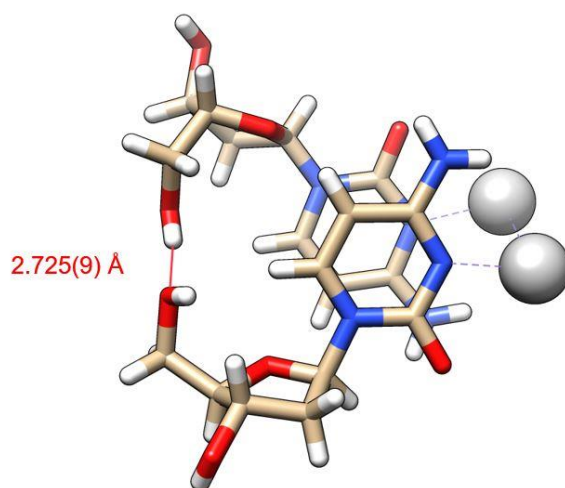


Figure 4.12 Analysis of the deoxyribose intermolecular interactions.

Ultra-violet (UV) light is commonly used as a method of analysis for nucleic acids. Concentration and purity can be determined by absorption and optical density (OD) at 260 and 280 nm. Changes in the nucleobase conjugation or helix can also be investigated by UV-vis or melting-point studies. However, the UV absorption (λ_{max}) for 2'-deoxycytidine was measured at 271 nm and remained unchanged following the addition of silver ions (AgNO_3) at the expected 2:1 stoichiometry (**Figure 4.13**). A lack of change in the UV was consistent with silver- N^3 -cytosine complexation as fundamentally the conjugation in the nucleobases was not altered following coordination to the metal ion at the N^3 position.

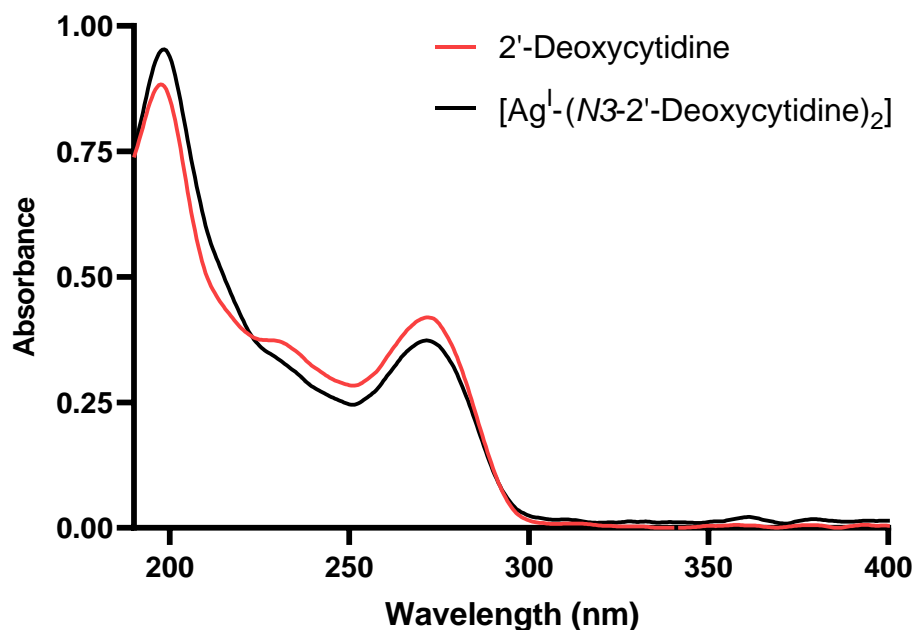


Figure 4.13 UV-Vis absorption data for aqueous solutions of 2'-deoxycytidine (dotted-line) and $[\text{Ag}^{\text{I}}-(\text{DCyt})_2]$, **1** (solid-line).

To assess whether the self-assembly of the helical structure could be observed in solution circular dichroism (CD) was used to identify spectroscopic differences in the optical activities between $[\text{Ag}^{\text{I}}-(\text{Cyt})_2]$ and $[\text{Ag}^{\text{I}}-(\text{DCyt})_2]$, **1**, respectively.

The CD for both species were spectroscopically similar; both having two dominant negative bands which is consistent with the formation of a metal-mediated helical assembly in solution.^{35,36} The aqueous solution of $[\text{Ag}^{\text{I}}-(\text{Cyt})_2]$ possessed three negative peaks at 200, 217 and 283 nm. The deoxy analogue, **1**, has two major negative peaks at 245 and 287 nm. Both helical assemblies showed significant transformations when compared to their parent ligands. The large negative bands at higher wavelengths (283 and 287 nm) for both $[\text{Ag}^{\text{I}}-(\text{N}^3\text{-Cyt})_2]$ and $[\text{Ag}^{\text{I}}-(\text{N}^3\text{-DCyt})_2]$ are remarkably similar in magnitude and position to each other. Furthermore, they are similar to the negative peak at 290 nm characteristic of Z-DNA. At lower wavelengths $[\text{Ag}^{\text{I}}-(\text{N}^3\text{-Cyt})_2]$ appears to share similar characteristics with the CD profile of A-DNA (peak at 210 nm), and $[\text{Ag}^{\text{I}}-(\text{N}^3\text{-DCyt})_2]$ with B-DNA (peak at 245 nm).

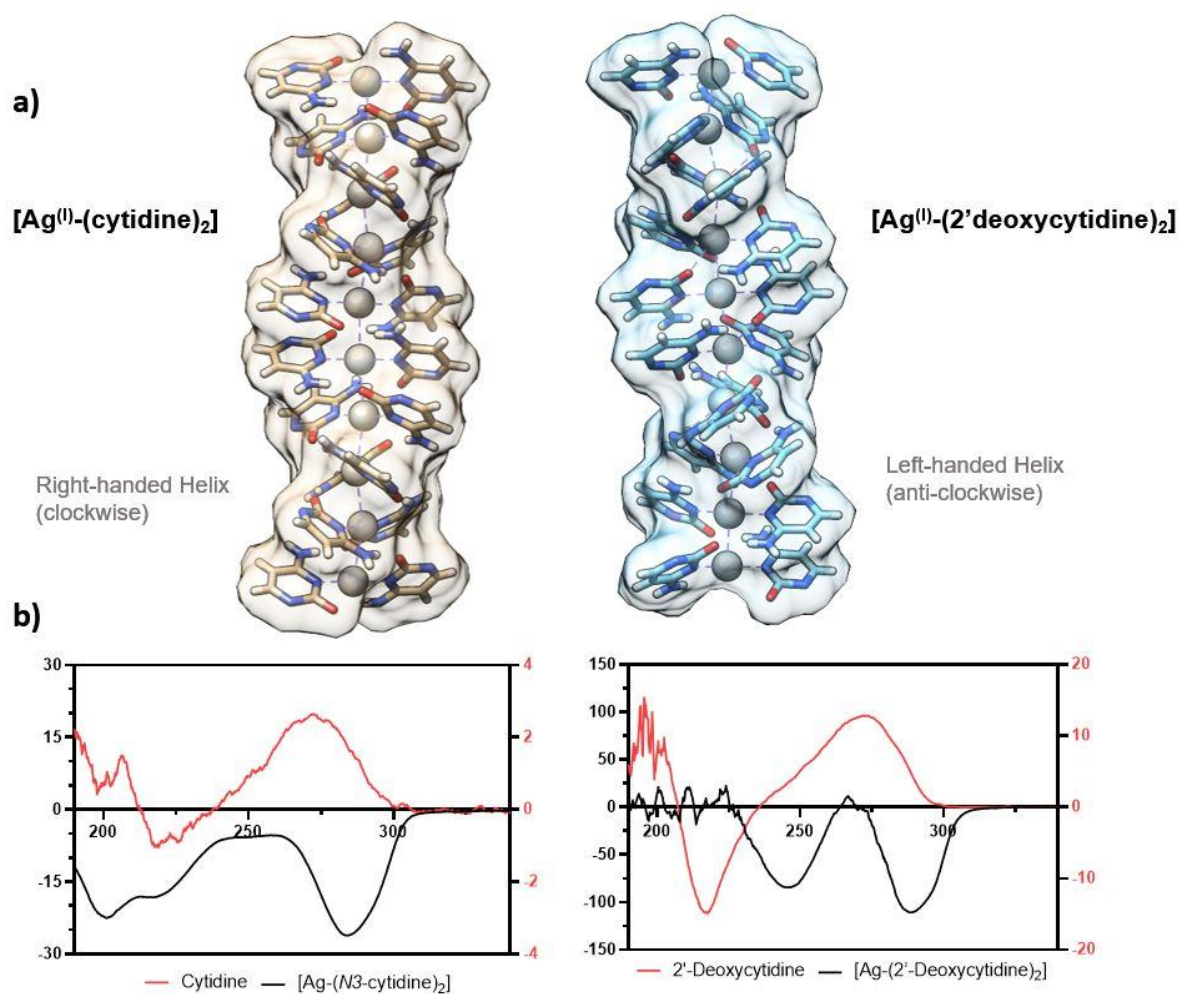


Figure 4.14 [Ag^I-(*N*³-cytidine)₂] versus [Ag^I-(*N*³-2'deoxyctidine)₂] (Sugar groups removed for clarity), a) Molecular structures highlighting the right and left-handed nature of each 1D polymer and b) CD spectra of the silver complexes (black) vs. ligands (red) in aqueous solutions.

4.3. Part II: Crystal Growth of Ag^I-Mediated Supramolecular Duplexes, as Observed using Atomic Force Microscopy.

Crystallisation is essential to many natural and synthetic processes on this planet. The spontaneous assembly and isolation of a single species from a supersaturated solution can yield unique materials with tailored physical properties. However, observing the formation of crystals as they nucleate is no easy task. It is common to only observe crystals once they have assembled to macroscopic dimensions.³⁷ It is clear from the literature that the fundamentals to crystal growth and nucleation are poorly understood with no widely supported consensus or description. The methods involved in successful crystallisation is often considered more of an art than science.

At the earliest stages of crystallisation, referred to as nucleation, a metastable phase whereby the rate, size and purity of crystals produced is determined.³⁸ The nuclei is defined as the minimum amount of a new phase which is able to exist independently.³⁸ Since the 1930s, researchers have been developing more advanced theories and models of how nucleation occurs. A common approach to investigating nucleation involves observing small “crystallites” or cluster, typically <100 nm (often referred to as an “embryo”). There exists a “critical nucleus”, a point where a crystallite reaches a delicate tipping point, this is due to their extremely high surface area to volume ratio. This equilibrium point is often thought as a stage bearing between 20 - 50 molecules³⁷ or 100 – 1000 atoms³⁸, which is unstable enough to readily re-dissolving back into solution. If, however, the crystallite persists, nucleation and therefore crystal growth can occurs.³⁷ The organisation of molecules prior to nucleation is considered the rate-determining step.³⁸ The growth stages thereafter is diffusion limited as particles are assimilated at the surface of the nuclei onto the crystal lattice.

Classical nucleation theory (CNT) of a crystallite and nucleation assumes a spherical model, however more recent studies using apoferritin (a protein with slow crystallisation characteristics) describe a sheet like theory with planar layers.³⁹ A third theory describes the possibility that the critical nucleus is not crystalline at all, more a pseudo-liquid aggregation of molecules with a high degree of disorder, with crystallinity only appearing in later stages of growth.³⁷

The CNT were described over 90 years ago and is widely used today for its analytical simplicity for ionic supersaturated solutions. Several alternative theories exist including Lothe & Pound (LPT) theory and Reiss nucleation theory (RNT), which impose fewer or changed assumptions to CNT.⁴⁰

The thermodynamic explanation for crystal formation was developed by Josiah Willard Gibbs at the end of the 19th century.³⁸ The free energy change required for nucleation (ΔG) is the total free energy for the phase transformation (ΔG_v) and the free energy change for the formation of a surface (ΔG_s).³⁸ The first term therefore describes the spontaneous deposition from a supersaturated solution, as the solid state has a greater stability than the liquid, ΔG_v becomes negative, lowering the Gibbs free energy of the system. In opposition, the introduction of a new interface increases the free energy proportionally to the surface area of the crystal surface.³⁸ Therefore, the ability for crystal growth depends on the competition between ΔG_v (growth) and ΔG_s (dissolution).³⁸ There exists a critical point (r_c) at which the size of the nuclei causes the total free energy to decrease resulting in an overall negative free energy, therefore growth of the entity becomes energetically favourable.^{38,41}

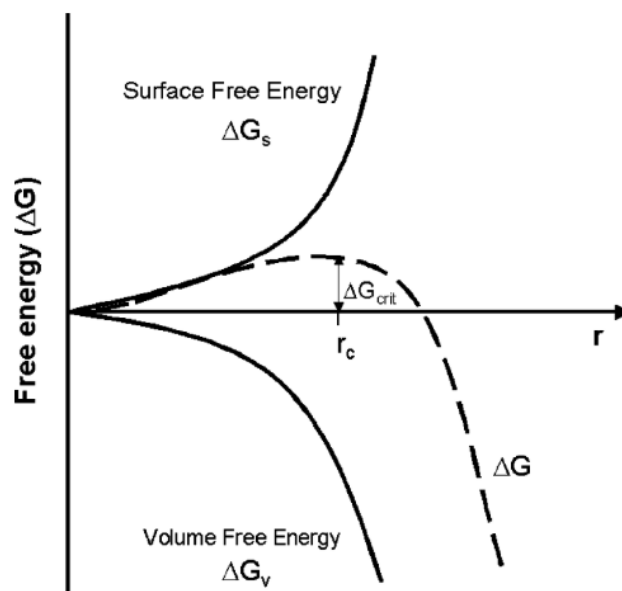


Figure 4.15 A free energy diagram of nucleation.³⁸

A kinetic theory involves a steady-state rate of nucleation (J), which is proportional to the number and rate of nuclei formed in a given volume. More specifically the kinetic

factor describes the incorporation of molecules to the critical nucleus, therefore depends on molecular mobility; hence, temperature plays a significant role.

$$J = A \exp\left(-\frac{\Delta G_{crit}}{kT}\right)$$

The theory can be expressed as an Arrhenius rate equation, where k is the Boltzmann constant and A is the pre-exponential factor ($10^{30} \text{ cm}^{-1} \text{ s}^{-1}$; however, is difficult to measure). There are significant assumptions imposed to simplify the description, these are: The nuclei are spherical droplets, stable surface tension values critical for existence in both phases, growth of nuclei occurs one monomer/molecule at a time ignoring any destructive collision between nuclei, the nucleation rate is time independent and the nuclei are incompressible. The rigidity of these assumptions has the potential to oversimplify models, therefore cannot account for binary nucleation occurrences. Nor can it account for nuclei collisions which have been shown to play a significant role using computational studies.

One of the most common approaches to observing crystallites is by atomic force microscopy (AFM) due to the soft means of acquiring surface detail at nanometre resolution.³⁹ Proteins are often used in these studies due to their relatively slow assembly processes when compared to ionic solids. However, observing these processes remains difficult as crystallites are extremely small, freely move throughout the available solution, existing only for short periods.³⁸

4.4. Results and Discussion (Part-II)

Due to the structural similarities between $[\text{Ag}^{\text{I}}-(\text{DCyt})_2]$ and $[\text{Ag}^{\text{I}}-(\text{Cyt})_2]$, AFM imaging techniques were used to search for individual fibres or strands akin to those analysed in chapter 3. A concentrated aqueous solution of $[\text{Ag}^{\text{I}}-(N^3-2'-\text{deoxycytidine})_2]$ was prepared and drop-cast onto a silicon wafer. However, nothing was immediately identified as being fibrous. Methanol was added to the dry sample area and allowed to slowly evaporate in a sealed environment for 16 hours. The subsequent images showed the formation of large nm sized crystals uniformly distributed across the sample area. Imagining within the voids between crystals revealed individual coiled fibres many μm in length with a height of 10 nm.

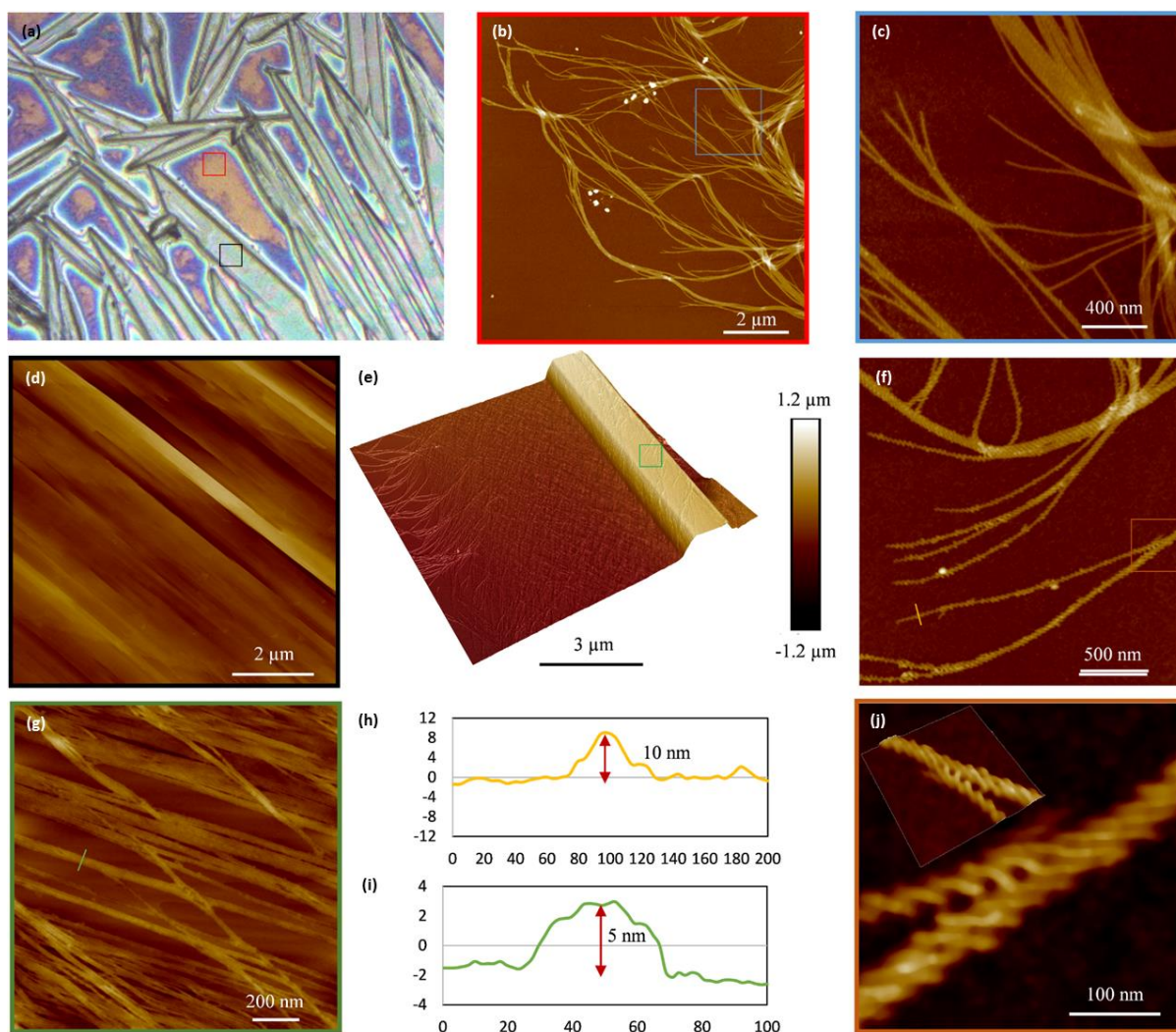


Figure 4.16 Optical microscope and AFM images of $[\text{Ag}^{\text{I}}-(N^3\text{-}2'\text{deoxyctidine})_2]$. (a) An optical microscope image of $[\text{Ag}^{\text{I}}-(N^3\text{-}2'\text{deoxyctidine})_2]$ drop-cast onto a silicon wafer. Large-scan (b) and a zoom area (c) of AFM height images of *bis*-($\text{Ag}^{\text{I}}\text{-}2'\text{deoxyctidine}$) fibres, showing the fibres packing together to create a flat structure on a silicon surface. (d) An AFM height images of the face of a crystal (black box in image (a)). (e) 3D AFM height image of a small crystal and fibres on and around the edge of the crystal. (f) AFM image of helical fibres that anneal together close to crystal structure in the image (e) and (h) a corresponding line section showing the height of a single fibre. (g) A zoom in area of AFM image on the top of the face of the crystal in the image (e), and (i) a corresponding line section showing the height of the fibres on the top of the crystal face. (j) 2D and 3D AFM height images showing the annealing helical structures of molecular chains.

The coils show a right-handed (clockwise) screw twist. Interestingly, the meeting of two individual coils resulted in a merger with no observable change in height as seen in

Figure 4.16 (j). Imaging closer to a crystal showed a much higher coil/fibre density. Furthermore, the coils had closely arranged themselves in a common direction neatly in line with a uniform height of 10 nm. Regions that overlapped gave a step height difference of 10 nm. Images taken from the topside of the nearest crystal showed again aligned fibres in a common direction of the long axis of the crystal. Step height on top of the crystal was 5 nm.

Figure 4.17 best illustrates how the structures observed by AFM could fit to a crystal lattice with linear 1D arrays. Using the dimensions of a single 1D silver array in the crystalline state a series of steps were conceptualised to explain the transformations and structures observed in **Figure 4.16**. A single 1D duplex or strand has a diameter of 1.7 nm (16.7 Å) from solid-state and a single coiled fibre has a height of 10 nm. Assuming the coil is not flattened against the surface and holds a 3D screw conformation along a rigid axis the true diameter of the fibre would be approximately 5 nm. A coil bearing seven 1D duplexes distributed to fit a cylindrical spacing would have a height of 4.7 nm.

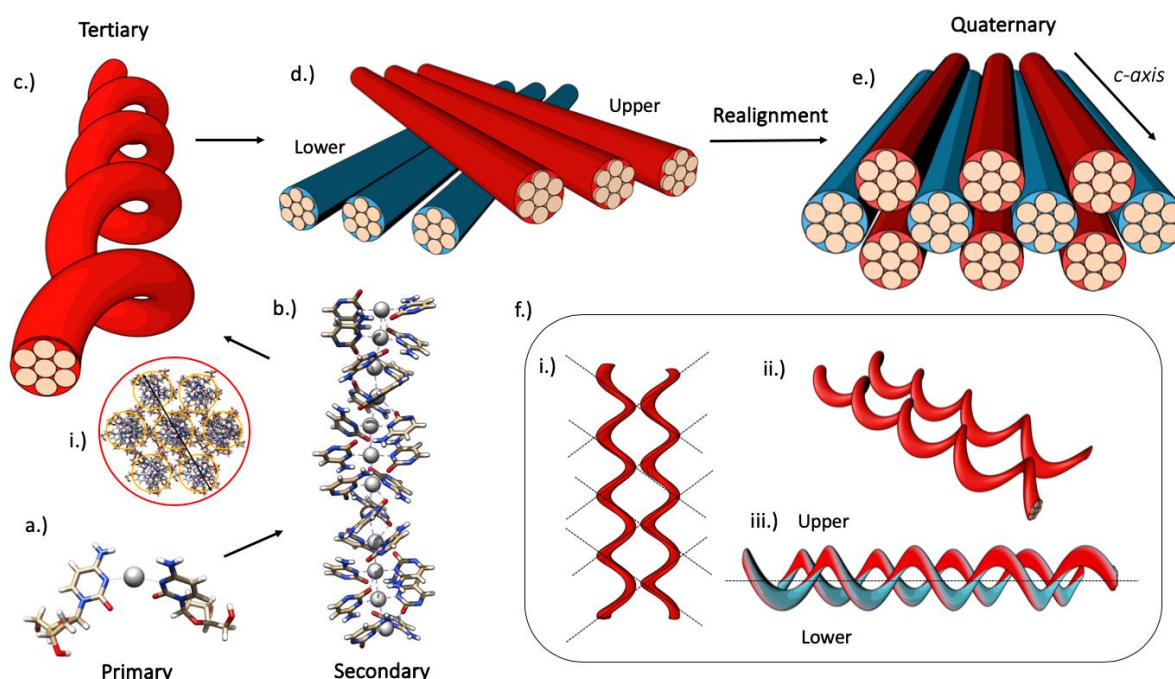


Figure 4.17 An illustration of the proposed mechanism of crystal formation inferred from AFM height images: a.) The primary C-Ag^I-C molecular structure, b.) the secondary helical array, c.) A coiled tertiary structure observed under AFM and i.) shows a bundle of seven helices with a calculated diameter of 4.7 nm; d.) Strand cross-over with a linear direction with a step difference between the two directions of

approximately 5 nm, e.) Strand realignment towards in the *c*-axis as observed in the single crystal. Inset f.) shows i.) a top-down view of two neighbouring tertiary coils showing alignment of upper and lower surfaces (dotted lines), ii.) diagonal view and iii.) side-on view showing the aligned upper (red) and lower (blue) sections (separated by a dotted line).

Stage-one, upon addition of metal-ions to DCyt a *bis*-complex ion, $[\text{Ag}^{\text{I}}-(\text{N}^3\text{-DCyt})_2]$, is spontaneously formed which stacks inline to produce the duplex as observed in CD. This stage represents the transition from a primary (discrete complex ion) to secondary structure (single duplex). Stage two, 1D duplexed strands assemble in groups or bundles of approximately seven strands to produce a thicker fibre or tertiary structure with a height of 4.7 nm which coils. The coiling could be a result of gained torsion during the drying process or strands braiding along the fibre. The coils are observed to have uniform heights of around 10 nm. The third stage involves the transition from a tertiary or coiled structure, to linear structures representative of the crystal. This required a significant transformation. The simplest way this could be achieved involves a rearrangement of the intermolecular interactions (*i.e.* hydrogen-bonds, argentophilic, and hydrophobic interactions). The upper and lower turns of a coil merge in-line with its neighbours to generate linear strands. The fourth and final stage, involves the realignment of the now perpendicular upper and lower arrays assemblies or layers. This is likely occurred as strands embed into the highly organised bulk crystal.

4.5. Conclusions

It has been demonstrated that $[\text{Ag}^{\text{I}}-(\text{N}^3\text{-DCyt})_2]$ spontaneously forms upon coordination between Ag^+ ions and 2'-deoxycytidine. A remarkable self-assembly process occurs to form a supramolecular double helix in solution. The results highlight the tendency of these *bis*-complex ion building blocks to stack into structures similar to their corresponding biopolymers (*i.e.* DNA) with assemblies closely matching those of M-DNA. The left-handed helix sense found within the solid-state was compared against its right-handed (clockwise) ribose counterpart, $[\text{Ag}^{\text{I}}-(\text{N}^3\text{-Cyt})_2]$. Analysis of the binding interactions and geometries found in the solid-state for both structures were highly similar. Furthermore, the sugar pucker conformations were investigated, but not found to directly influence the helical sense of the helix. It is more likely that packing or

hydrophilic interactions in the solid-state play a more important role in the outcome of the helix rotation.

We have identified several solid-state structures using AFM of $[\text{Ag}^{\text{I}}-(\text{N}^3\text{-DCyt})_2]$ at various stages of crystallisation. The transformation from a 1D coil (height of 10 nm) to bulk crystalline material with a regular lattice of linear 1D supramolecular double helices was observed. It is proposed that a significant rearrangement occurs to align upper and lower sections of neighbouring coils. This involves a denaturation process where the intermolecular hydrogen, argentophilic and hydrophobic interactions are broken. Realignment yields a packing of linear 1D strands representative of the crystal structure. These images have captured a remarkable insight into the mechanism involved for polymeric crystal growth.

4.6. References

- (1) Meurer, K. P.; Vögtle, F. Helical Molecules in Organic Chemistry. *Org. Chem.* **2006**, 1–76. <https://doi.org/10.1007/bfb0049438>.
- (2) Polymer Characterization - Helical Structures. **1989**.
- (3) McLachlan, A. D. Optical Rotation in Helical Polymers. *R. Soc.* **1967**, 297 (1448), 141–149.
- (4) Cohen, C.; Szent-Gyorgyi, A. G. Optical Rotation and Helical Polypeptide Chain Configurations in A-Proteins. *Commun. to Ed.* **1956**, 79, 248.
- (5) Sundaralingam, M.; Westhof, E. Structural Motifs of the Nucleotidyl Unit and the Handedness of Polynucleotide Helices. *Int. J. Quantum Chem.* **1981**, 20 (8 S), 287–306. <https://doi.org/10.1002/qua.560200727>.
- (6) Loxsom, F. M. Optical Rotation of Helical Polymers: End Effects. *Int. J. Quantum Chem.* **1969**, 3 (S3A), 147–152. <https://doi.org/10.1002/qua.560030719>.
- (7) Crick, F.; Watson, J. © 1953 Nature Publishing Group. **1953**.
- (8) Ussery, D. W. DNA Structure: A-, B- and Z-DNA Helix Families. *Encycl. Life Sci.* **2002**, No. 1998. <https://doi.org/10.1038/npg.els.0003122>.
- (9) Rich, A. The Double Helix: A Tale of Two Puckers. *Nat. Struct. Biol.* **2003**, 10 (4), 247–249. <https://doi.org/10.1038/nsb0403-247>.

- (10) Wing, R.; Drew, H.; Takano, T.; Broka, C.; Tanaka, S.; Itakura, K.; Dickerson, R. E. Crystal Structure Analysis of a Complete Turn of B-DNA. *Nature* **1980**, 287 (5784), 755–758. <https://doi.org/10.1038/287755a0>.
- (11) Sinden, R. R. DNA Structure and Function. *DNA Struct. Funct.* **2012**, 282, 1–398. <https://doi.org/10.1016/C2009-0-02451-9>.
- (12) J. D. Watson, F. H. C. C. A Structure for Deoxyribose Nucleic Acid. *Mol. Struct. Nucleic Acids* **1953**, 171 (4356), 737–738.
- (13) Kypr, J.; Kejnovská, I.; Renčíuk, D.; Vorlíčková, M. Circular Dichroism and Conformational Polymorphism of DNA. *Nucleic Acids Res.* **2009**, 37 (6), 1713–1725. <https://doi.org/10.1093/nar/gkp026>.
- (14) Baker, E. S.; Bowers, M. T. B-DNA Helix Stability in a Solvent-Free Environment. *J. Am. Soc. Mass Spectrom.* **2007**, 18 (7), 1188–1195. <https://doi.org/10.1016/j.jasms.2007.03.001>.
- (15) Ono, A.; Kanazawa, H.; Ito, H.; Goto, M.; Nakamura, K.; Saneyoshi, H.; Kondo, J. Novel DNA Helical Wire Containing Hg(II) Mediated T:T and T:G Pairs. *Angew. Chemie Int. Ed.* **2019**. <https://doi.org/10.1002/anie.201910029>.
- (16) Kondo, J.; Tada, Y.; Dairaku, T.; Hattori, Y.; Saneyoshi, H.; Ono, A.; Tanaka, Y. A Metallo-DNA Nanowire with Uninterrupted One-Dimensional Silver Array. *Nat. Chem.* **2017**, 9 (10), 956–960. <https://doi.org/10.1038/nchem.2808>.
- (17) Kondo, J.; Tada, Y.; Dairaku, T.; Saneyoshi, H.; Okamoto, I.; Tanaka, Y.; Ono, A. High-Resolution Crystal Structure of a Silver(I)-RNA Hybrid Duplex Containing Watson-Crick-like C-Silver(I)-C Metallo-Base Pairs. *Angew. Chemie - Int. Ed.* **2015**, 54 (45), 13323–13326. <https://doi.org/10.1002/anie.201507894>.
- (18) Vecchioni, S.; Capece, M. C.; Toomey, E.; Nguyen, L.; Ray, A.; Greenberg, A.; Fujishima, K.; Urbina, J.; Paulino-Lima, I. G.; Pinheiro, V.; et al. Construction and Characterization of Metal Ion-Containing DNA Nanowires for Synthetic Biology and Nanotechnology. *Sci. Rep.* **2019**, 9 (1), 1–15. <https://doi.org/10.1038/s41598-019-43316-1>.
- (19) Liu, X.; Guo, G. C.; Fu, M. L.; Liu, X. H.; Wang, M. S.; Huang, J. S. Three Novel Silver Complexes with Ligand-Unsupported Argentophilic Interactions and Their Luminescent Properties. *Inorg. Chem.* **2006**, 45 (9), 3679–3685. <https://doi.org/10.1021/ic0601539>.
- (20) Yamaguchi, H.; Šebera, J.; Kondo, J.; Oda, S.; Komuro, T.; Kawamura, T.

- Dairaku, T.; Kondo, Y.; Okamoto, I.; Ono, A.; et al. The Structure of Metallo-DNA with Consecutive Thymine-Hg II -Thymine Base Pairs Explains Positive Entropy for the Metallo Base Pair Formation. *Nucleic Acids Res.* **2014**, *42* (6), 4094–4099. <https://doi.org/10.1093/nar/gkt1344>.
- (21) Terrón, A.; Moreno-Vachiano, B.; Bauzá, A.; García-Raso, A.; Fiol, J. J.; Barceló-Oliver, M.; Molins, E.; Frontera, A. X-Ray Crystal Structure of a Metalled Double-Helix Generated by Infinite and Consecutive C*-AgI-C* (C*:N1-Hexylcytosine) Base Pairs through Argentophilic and Hydrogen Bond Interactions. *Chem. - A Eur. J.* **2017**, *23* (9), 2103–2108. <https://doi.org/10.1002/chem.201604331>.
- (22) Bonifacio, L. D.; Lotsch, B. V.; Ozin, G. A. *Comprehensive Nanoscience and Technology*; 2011. <https://doi.org/10.1016/B978-0-12-374396-1.00049-0>.
- (23) Wang, R.; Wei, M.; Wang, Y. Secondary Growth of Covalent Organic Frameworks (COFs) on Porous Substrates for Fast Desalination. *J. Memb. Sci.* **2020**, *604*, 118090. <https://doi.org/10.1016/j.memsci.2020.118090>.
- (24) Wang, Z.; Zhang, S.; Chen, Y.; Zhang, Z.; Ma, S. Covalent Organic Frameworks for Separation Applications. *Chem. Soc. Rev.* **2020**, *49* (3), 708–735. <https://doi.org/10.1039/c9cs00827f>.
- (25) Corcos, A. R.; Levato, G. A.; Jiang, Z.; Evans, A. M.; Livingston, A. G.; Mariñas, B. J.; Dichtel, W. R. Reducing the Pore Size of Covalent Organic Frameworks in Thin-Film Composite Membranes Enhances Solute Rejection. *ACS Mater. Lett.* **2019**, *1* (4), 440–446. <https://doi.org/10.1021/acsmaterialslett.9b00272>.
- (26) Shinde, D. B.; Sheng, G.; Li, X.; Ostwal, M.; Emwas, A. H.; Huang, K. W.; Lai, Z. Crystalline 2D Covalent Organic Framework Membranes for High-Flux Organic Solvent Nanofiltration. *J. Am. Chem. Soc.* **2018**, *140* (43), 14342–14349. <https://doi.org/10.1021/jacs.8b08788>.
- (27) Ying, Y.; Tong, M.; Ning, S.; Ravi, S. K.; Peh, S. B.; Tan, S. C.; Pennycook, S. J.; Zhao, D. Ultrathin Two-Dimensional Membranes Assembled by Ionic Covalent Organic Nanosheets with Reduced Apertures for Gas Separation. *J. Am. Chem. Soc.* **2020**. <https://doi.org/10.1021/jacs.9b13825>.
- (28) Mathlouthi, M.; Koenig, J. L. FTIR and Laser-Raman Spectra of Cytosine and Cytidine. *Carbohydr. Res.* **1986**, *146*, 1–13.
- (29) Rozenberg, M.; Jung, C.; Shoham, G. Low Temperature FTIR Spectra and Hydrogen Bonds in Polycrystalline Cytidine. *Spectrochim. Acta - Part A Mol.*

Biomol. Spectrosc. **2004**, *60* (10), 2369–2375.
<https://doi.org/10.1016/j.saa.2003.12.013>.

- (30) Gorman, M. The Evidence from Infrared Spectroscopy for Hydrogen Bonding: A Case History of the Correlation and Interpretation of Data. *J. Chem. Educ.* **1957**, *34* (6), 304–306. <https://doi.org/10.1021/ed034p304>.
- (31) Dirico, D. E.; Keller, P. B.; Hartman, K. A. Volume 13 Number 1 1985 Nucleic Acids Research The Infrared Spectrum and Structure of the Type I Complex of Silver and DNA Nucleic Acids Research. *Nucleic Acids Res.* **1985**, *13* (1), 251–260.
- (32) Sundaralingam, M.; Yathindra, N. Glycosyl and Backbone Torsional Variation On. **1977**, 303.
- (33) Lescrinier, E.; Froeyen, M.; Herdewijn, P. Difference in Conformational Diversity between Nucleic Acids with a Six-Membered “sugar” Unit and Natural “Furanose” Nucleic Acids. *Nucleic Acids Res.* **2003**, *31* (12), 2975–2989. <https://doi.org/10.1093/nar/gkg407>.
- (34) Rao, S. N.; Sasisekharan, V. Handedness of Duplex DNA: Role of the Glycosydic Torsion. *Int. J. Biol. Macromol.* **1983**, *5* (2), 83–88. [https://doi.org/10.1016/0141-8130\(83\)90016-8](https://doi.org/10.1016/0141-8130(83)90016-8).
- (35) Espinosa Leal, L. A.; Karpenko, A.; Swasey, S.; Gwinn, E. G.; Rojas-Cervellera, V.; Rovira, C.; Lopez-Acevedo, O. The Role of Hydrogen Bonds in the Stabilization of Silver-Mediated Cytosine Tetramers. *J. Phys. Chem. Lett.* **2015**, *6* (20), 4061–4066. <https://doi.org/10.1021/acs.jpcllett.5b01864>.
- (36) Mistry, L.; Hofer, W.; Pope, T.; Horrocks, B. R.; El-Zubir, O.; Clegg, W.; Dura, G.; Wright, N.; Waddell, P. G.; Houlton, A. Addressing the Properties of “Metallo-DNA” with a Ag(I)-Mediated Supramolecular Duplex. *Chem. Sci.* **2019**. <https://doi.org/10.1039/c8sc05103h>.
- (37) Resources, N. Catching Crystals at Birth. *Nature* **2000**, *406*, 464–465.
- (38) Erdemir, D.; Lee, A. Y.; Myerson, A. S. Nucleation of Crystals from Solution: Classical and Two-Step Models. *Acc. Chem. Res.* **2009**, *42* (5), 621–629. <https://doi.org/10.1021/ar800217x>.
- (39) Yau, S.-T.; Vekilov, P. G. Direct Observation of Nucleus Structure and Nucleation Pathways in Apoferritin Crystallization. *J. Am. Chem. Soc.* **2001**, *123* (6), 1080–1089. <https://doi.org/10.1021/ja003039c>.

- (40) Sharaf, M. A.; Dobbins, R. A. A Comparison of Measured Nucleation Rates with the Predictions of Several Theories of Homogeneous Nucleation. *J. Chem. Phys.* **1982**, 77 (3), 1517–1526. <https://doi.org/10.1063/1.443932>.
- (41) Vekilov, P. G. Dense Liquid Precursor for the Nucleation of Ordered Solid Phases from Solution. *Cryst. Growth Des.* **2004**, 4 (4), 671–685. <https://doi.org/10.1021/cg049977w>.

Chapter 5.

Accessing One-Dimensional Argentophilic Arrays base on N-Ag^I-O
bond formation: Single Crystal to Molecular-Sheet Transformation.

5.1. Introduction

As demonstrated in previous chapters, Ag^I-N bond formation is well recognised as a basis for metal mediation with DNA and many one-dimensional (1D) coordination polymers. The d¹⁰ electronic configuration of Ag^I allows for a range of coordination numbers and geometries, however a tendency exists to form low-coordination linear systems. Many studies exist towards the production of 1D materials with closely held contiguous Ag^I arrays. Layered or 2D materials in particular have seen enormous interest as they have potential applications in electronics, displays, sensors and thin-film membrane technologies.^{1–7} However, the nature of typical M-DNA, with low coordination arrangements tend to limit their conformations to 1D systems. It has been shown that 2- or 3D metal-organic frameworks with layered lattice constructions can undergo solvent based exfoliation yielding single molecular sheets. Research into this area have demonstrated both “bottom-up”^{8–12} and “top-down”^{13–18} exfoliation techniques. While these materials have shown catalytic,¹⁹ reversible anion binding¹⁹ and luminescent²⁰ properties, reports demonstrating their credentials towards single molecular sheets are few.²¹

Recently, the discovery of a unique 3D coordination polymer composed of Ag⁺ ions and cytidine-5'-monophosphate (CMP)²² possess a framework capable of providing access of 1- or 2D materials through top-down exfoliation techniques.* The structure was identified as one of only two known examples where the metal ion coordinates at both *N*- and *O*- sites (**Figure 5.1**).^{22,23} The structure retains the remarkably close Ag⁺··Ag⁺ interactions of ~3.0 Å characteristic of traditional Ag-DNA systems. The 3D coordination network is held together by a third O⁷ interstrand coordination from neighbouring phosphodiester groups, linking each 1D chain in the crystal lattice. At the time of writing the structure had been discovered independently by our group prior to publication.

* At the time of publication, we had independently characterised identical compounds; {[Ag^I-N³,O²-CMP]·H₂O} and {[Ag^I-N³,O²-CMP]·MeOH}.

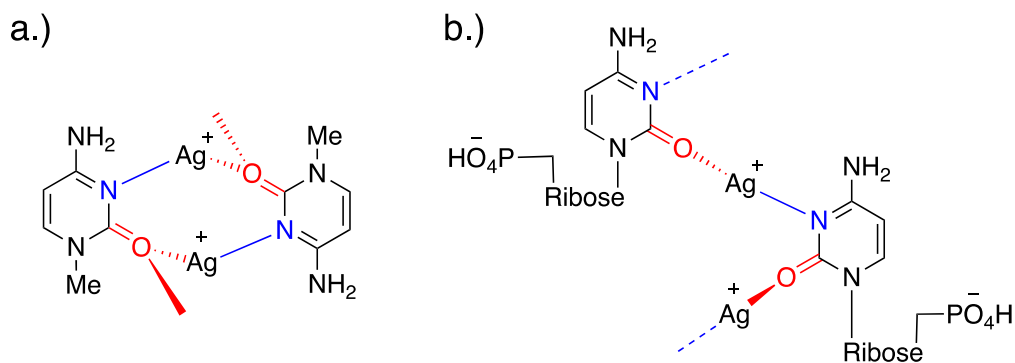


Figure 5.1 Examples of known *N,O*-coordinately bound Ag^{I} -Cyt. systems, (a.) Ag^{I} -1-methylcytosine and (b.) Ag^{I} -Cytidine-5'-monophosphate.^{22,23}

Herein, we report the synthesis and structural characterisation of two analogous 3D coordination polymer bearing different solvent motifs, **1**, $\{[\text{Ag}^{\text{I}}\text{-}N^3, O^2\text{-CMP}]\cdot\text{H}_2\text{O}\}$ and **2**, $\{[\text{Ag}^{\text{I}}\text{-}N^3, O^2\text{-CMP}]\cdot\text{MeOH}\}$. These illustrate a unique N, O binding mode and network topology. In addition, we demonstrate for **1**, that the material is susceptible to liquid-phase exfoliation affording 2D molecular sheets.

5.2. Results & Discussion

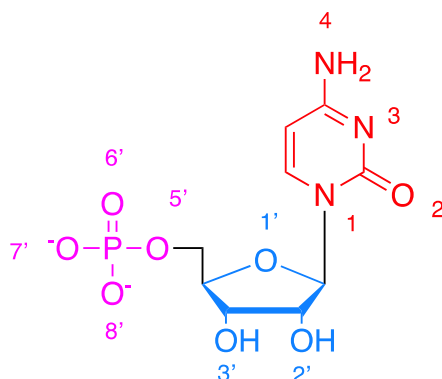


Figure 5.2 Cytidine-5'-monophosphate (CMP) with atomic numbering. The base is represented in red, ribose in blue and phosphodiester in purple.

Synthesis and Characterisation of **1**, {[Ag^I-N³,O²,O^{7'}-Cytidine-5'-monophosphate]·H₂O}

- The aqueous reaction between AgNO₃ and cytidine-5'-monophosphate (CMP) (**Figure 5.2**) in a 1:1 stoichiometric ratio yielded [Ag-O^{7'},O²,N³-CMP]·H₂O, **1**, as a white powder in a quantitative yield. Recrystallization from water gave colourless needle-shaped crystals with acicular habit. X-ray diffraction analysis revealed **1** to be a 3D coordination network with a chiral orthorhombic space group of P2₁2₁2₁ with continuous argentophilic (Ag⁺-Ag⁺) interactions down the [100] direction. The Ag⁺...Ag⁺ distance is 2.9590(5) Å with an angle of 108.33(3)°; resulting in an oscillating “zig-zag” arrangement down the axis (**Figure 5.3**). Each Ag⁺ ion is coordinately bound to three heteroatom donors; O² and N³ of flanking cytosine bases and an adjacent O^{7'}-phosphodiester, with bond lengths of 2.233(4), 2.221(5) and 2.509(5) Å respectively. The O²-Ag⁺-N³ is remarkably linear with an angle of 176.09(17)°. Looking down the [001] axis the bases are arranged coplanar to each other down the RHS and LHS of the chain, with centroid distance of 4.79775(12) Å and plane shift of 3.298(12) Å. There exists a plane twist angle of 89.5(4)° between the RHS and LHS nucleobase planes. The Ag⁺-O^{7'} interaction links four additional 1D neighbouring arrays forming a 3D coordination network. The ribose sugar group exists in a ‘N’-twist 3'-*endo* configuration. Additional hydrogen bonding interactions are observed between N⁴-O^{7'} (2.851(7) Å) and O^{3'}-H₂O (2.773(7) Å). Solvent occupy voids between adjacent 1D chains bridging through the O^{3'} of the ribose (2.773(7) and 2.902(7) Å). The width of the 1D structure

extends from O7' RHS to O7' LHS is 20.403(8) Å, similar to the diameter of natural double-stranded DNA (~20 Å).

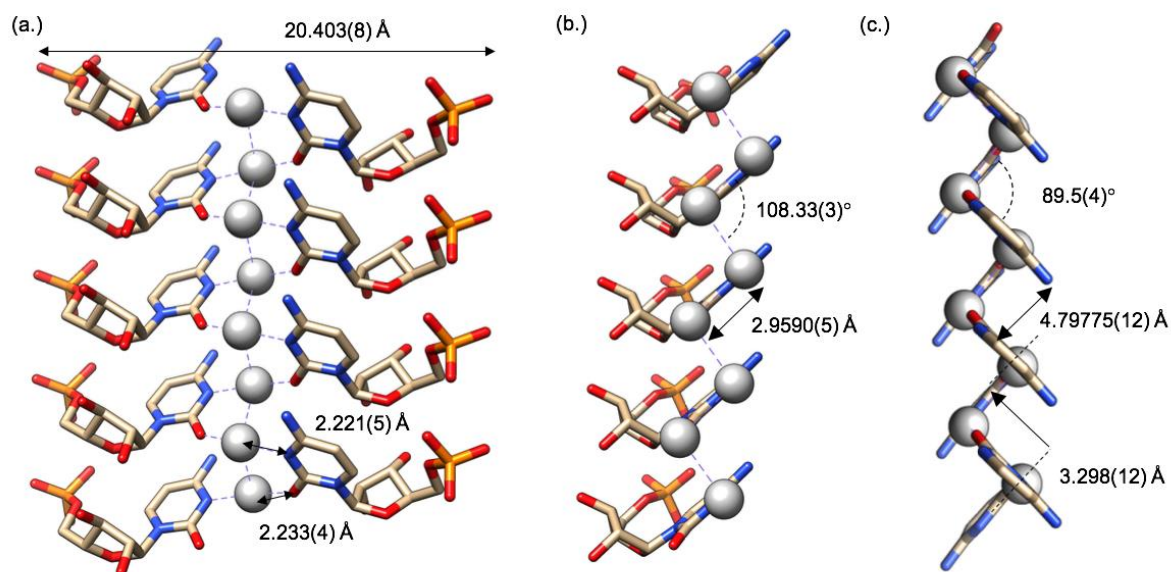


Figure 5.3 Single crystal X-ray structure of complex **1**; (a.) Details of the 1D chain running down the [100] direction with a 1:1 stoichiometry, (b.) Side-on sectional view showing the 1D “zig-zag” contiguous chain and (c.) Side-on view showing the right-angle base twist RHS to LHS of the silver core.

Synthesis and Characterisation of **2**, {[Ag^I-N³, O², O7'-Cytidine-5'-monophosphate]·MeOH}. Single crystals were isolated in methanol from a reaction of CMP and AgNO₃ at 2:1 metal:ligand stoichiometry. CMP does not readily dissolve in methanol, therefore an excess was used under reflux conditions to achieve a 1:1 complexation. **2** slowly dropped out of solution as colourless needle-shaped crystals with acicular habit. Analysed by single crystal X-ray diffraction found **2** to be a solvomorph of **1**, adopting a 3D network structure based on N³, O², O7' coordination (2.204(3), 2.197(3) and 2.527(4) Å respectively) with a chiral orthorhombic space group of P2₁2₁2₁. The Ag⁺...Ag⁺ distances are slightly longer at 3.1398(5) Å with a tighter angle of 95.631(19)°. Further subtle differences in the unit cell can be explained by the accommodation of the larger solvent MeOH motif; larger voids exist as a result (Figure 5.4).

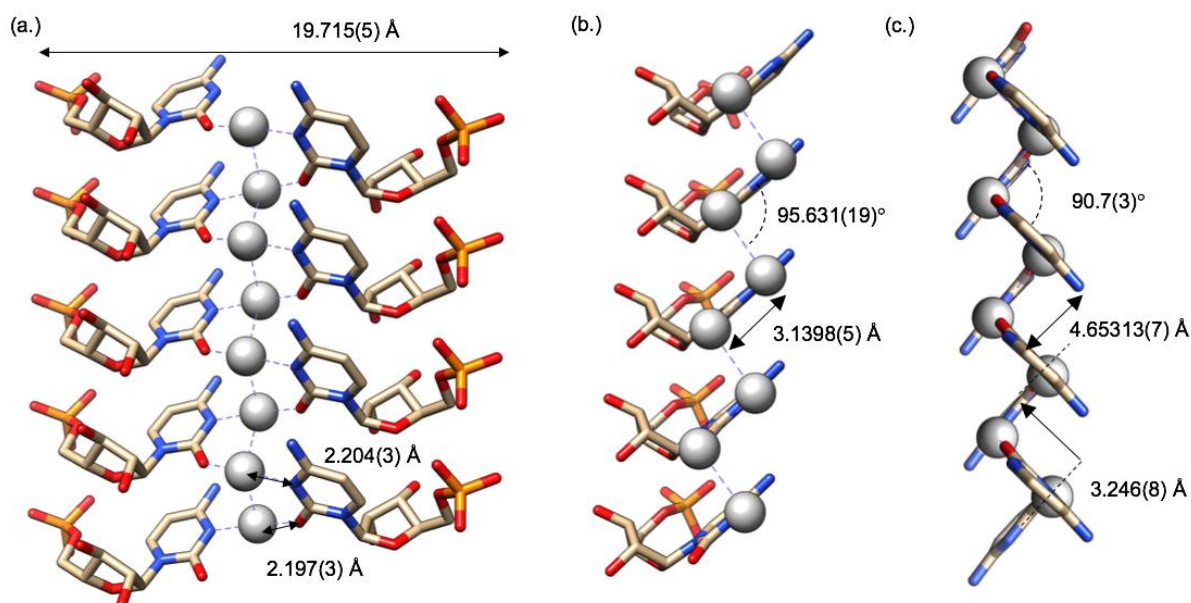


Figure 5.4 Single crystal X-ray structure of complex **2**; (a.) Details of the 1D chain running down the [100] direction with a 1:1 stoichiometry, (b.) Side-on sectional view showing the 1D “zig-zag” contiguous chain and (c.) Side-on view showing the right-angle base twist RHS to LHS of the silver core.

The void spaces that exist between four interconnected silver arrays differ between complexes **1** & **2**. Measurements across C⁵-C⁵ and C^{3'}-C^{3'} give cross-sectional areas of 64.09 Å² and 81.12 Å² for **1** and **2** respectively (**Figure 5.5**). The larger channels in the lattice of **2** are to accommodate the larger methanol solvent molecules *versus* H₂O in **1**.

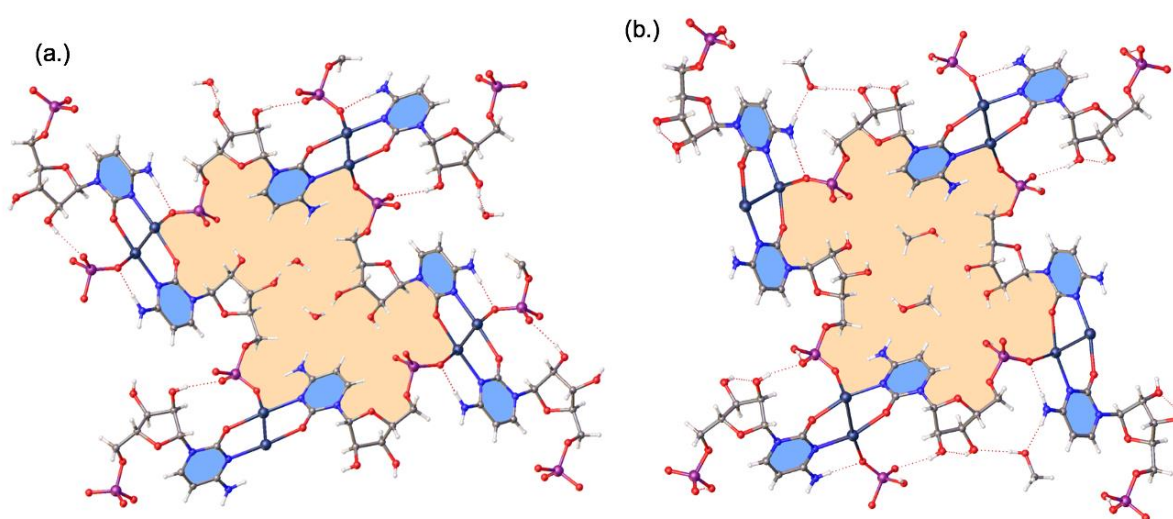


Figure 5.5 Top down packed view of complexes (a.) **1** & (b.) **2** showing the solvent occupied channels that exist in the 3D lattice.

Crystalline material of complexes **1** and **2** were studied spectroscopically using FTIR. Complexes **1** & **2** both showed shifts in their IR character (**Figure 5.6**). The shift of a strong signal at 1650 to 1600-1630 cm^{-1} show changes at the correct wavelength to be associated with the C^2 carbonyl. This vibrational shift corresponds to the formation of the $\text{C}=\text{O}\cdots\text{Ag}^{\text{I}}$ interaction observed in the crystal. The formation of a peak in both spectra at 1485 cm^{-1} is indicative of a CH_2 bending vibration. A shift to lower wavenumbers and peak broadening is indicative of H-bonding interactions. The $\text{N}^4\text{-O}^7$ interaction could be associated with these changes. The spectroscopic differences were generally found to be consistent with the newly formed associations seen within the crystal structures for **1** and **2**.

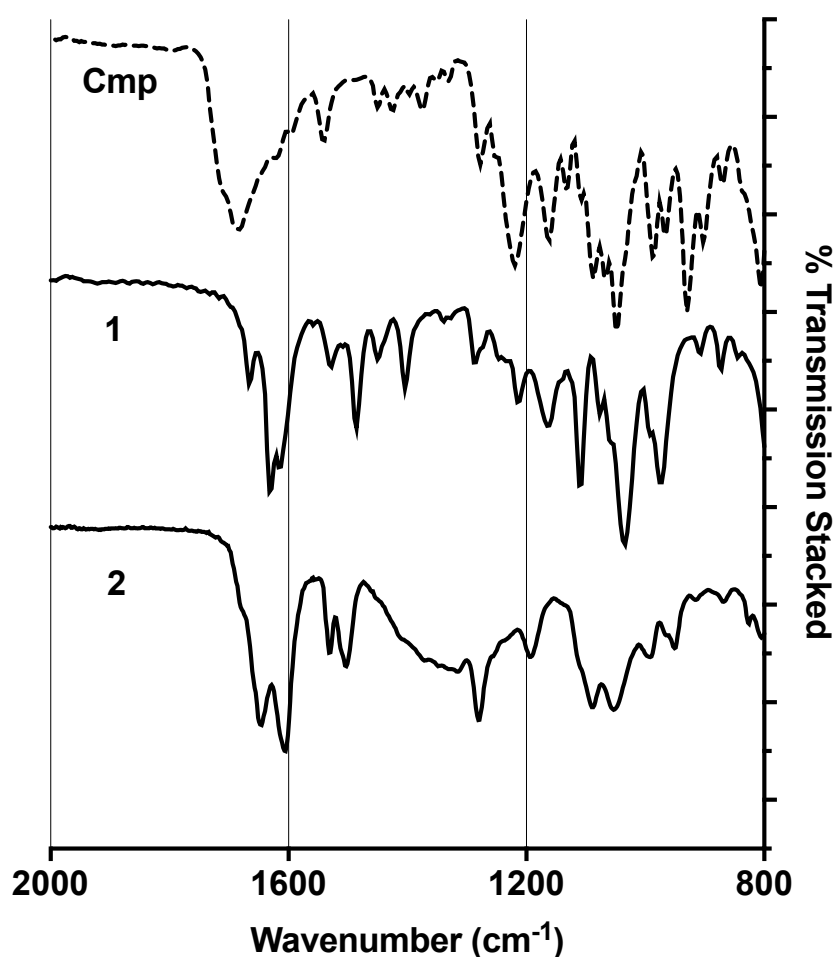


Figure 5.6 FTIR spectra (%transmission mode) of complexes **1** and **2** *versus* CMP over the range of 2000 -800 cm^{-1} .

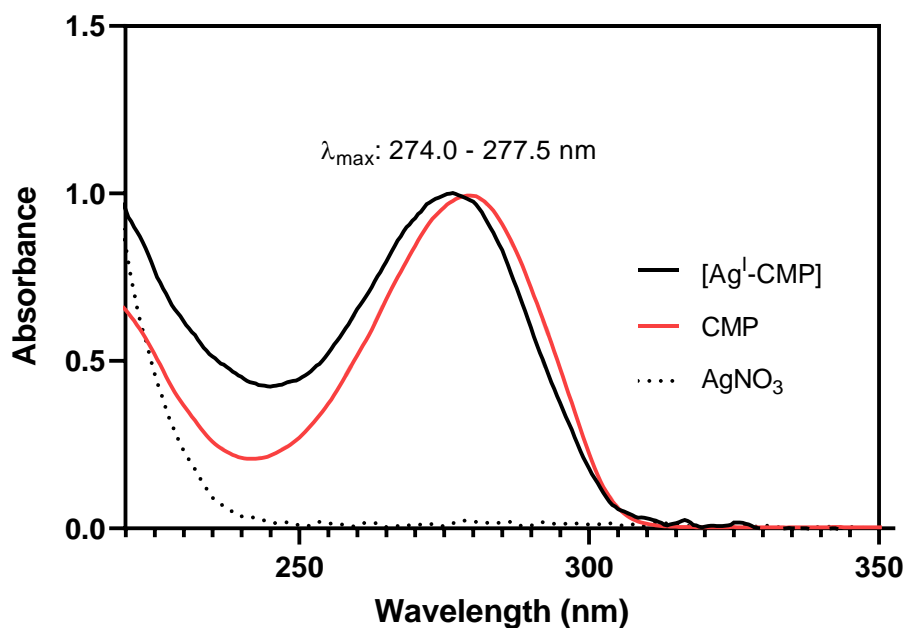


Figure 5.7 UV-vis of complex **1** (Blue line) vs. starting reagents.

Ultra-violet (UV) light is commonly used as a method of analysis for nucleic acids and is used as a method of monitoring structural changes in solution. Previously discussed silver mediated complexes within this thesis showed little or no changes following metal mediation due to their preference towards N^3 coordination. Complexes **1** and **2** have demonstrated a unique coordination now involving the carbonyl at the C^2 position in the solid state. The UV-vis of an aqueous solution of **1** showed a blue-shifted λ_{max} absorption by 3.5 nm when compared to the starting ligand CMP (**Figure 5.7**, λ_{max} : 280 nm). The UV-vis data collected for **2** was found to be identical to that found for **1**. Such spectroscopic change would be expected if the electron density of the ligand was altered following coordination with the metal ion. The lone pair of the oxygen interacts with the silver-ion; being part of a conjugated aromatic system, the chromophore is subsequently altered. A change in the UV absorption to a shorter wavelength corresponds to a greater change in energy from the HOMO to LUMO states. This implies a greater energy π to π^* transition indicating a less conjugated chromophore. Changes are therefore consistent with the coordination observed in the crystal structure indicating that the N^3, O^2 binding motif exists in solution.

$$E = h\nu = \frac{hc}{\lambda}$$

Equitation 5.1 Planck's equation; λ - wavelength (nm), ν – frequency, E – energy, h – universal constant (6.63×10^{-34} J), c – speed of light (3×10^8 m/s).

Qualitative ESI-MS was collected for **1**_(Aq) to further interrogating the unique *N,O* coordination bonding modes observed in the crystal structure. The expected Ag-CMP complex, [Ag-CMP]⁺, was observed using ESI-MS (direct injection, positive ion mode) at 430.0007 m/z (**Figure 5.8**). Isotope patterns, splitting and masses aligned well with the theoretical values calculated for a 1:1 Ag-CMP complex derived from the crystal structure; Calc. C₉H₁₄AgN₃O₈P, [M]⁺, 429.9569 m/z (monoisotopic mass). Peak separation of 1.0 m/z suggests a species bearing a plus one charge, which was achieved by the metal ion without the loss of a proton. The isotope pattern was characteristic of a species bearing a single silver ion (¹⁰⁷Ag 51.839%, ¹⁰⁹Ag 48.161%) per mass detected.

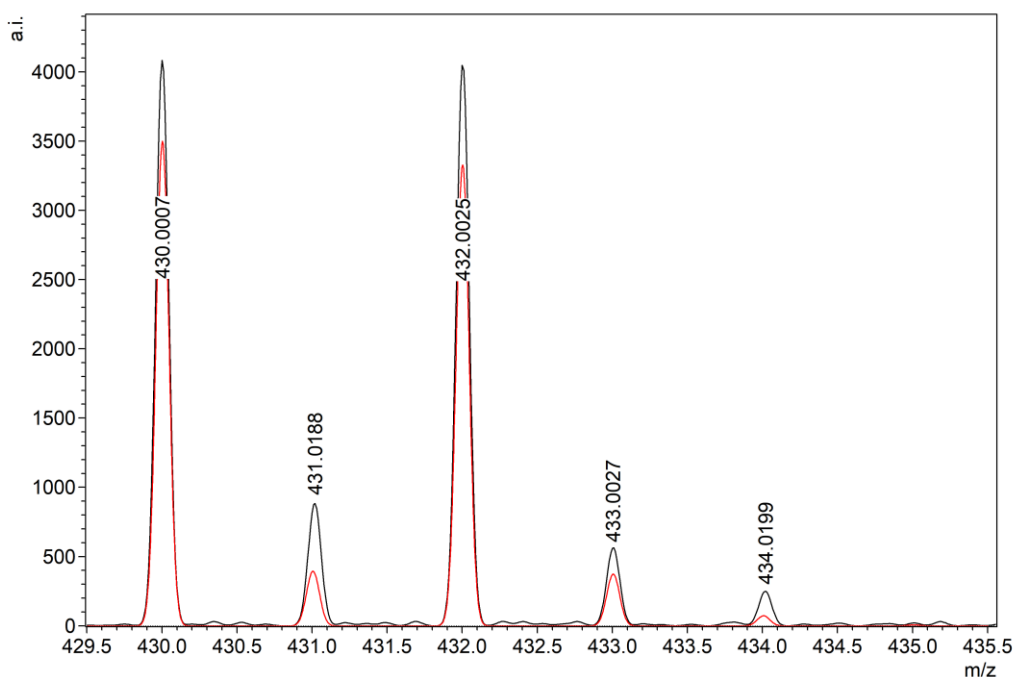


Figure 5.8 ESI-MS (positive ion mode) of **1** (black line) and calculated (red line) for [Ag-CMP]⁺ ([M]⁺, C₉H₁₄AgN₃O₈P).

Additional structural data was collected using powder X-ray diffraction (PXRD). Patterns were obtained from crystalline material for complexes **1** & **2** (**Figure 5.9**). Patterns for **1** & **2** were found to be nearly identical, showing major Bragg peaks that match closely at low angles (7.3, 9.7, 11.1, 14.8, 15.6 and 22.3°). Calculated patterns

predicted from their corresponding X-ray structures match closely to the experimental datasets for both complexes. A preferred orientation was necessary to allow for a close calculated pattern match ($h:0, k:0, l:1$, March-Dollase: 0.45).

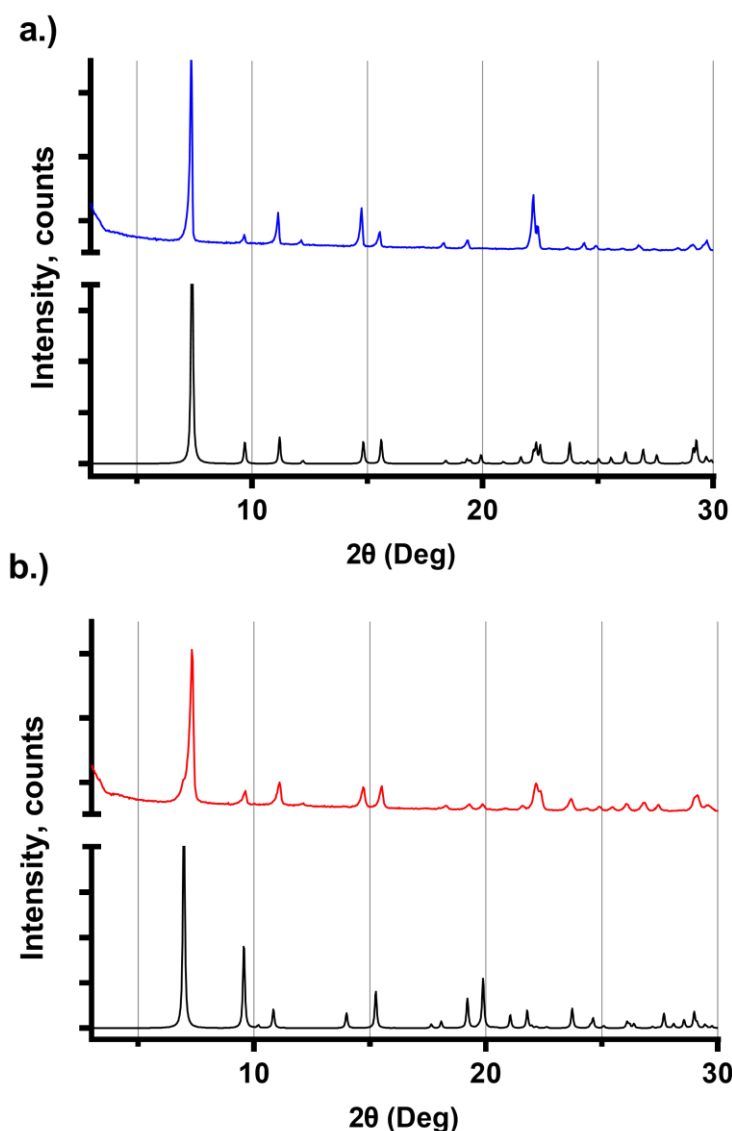


Figure 5.9 PXRD patterns for material corresponding to complexes a) **1** (blue-line) and b) **2** (red-line) showing experimental data over calculated (black-line) patterns from crystal data ($h:0, k:0, l:1$, March-Dollase: 0.45).

Compound **1** is another useful example of a structurally well-defined model of an argentophilic M-DNA array, allowing the electrical properties and molecular-wire credentials to be assessed. A single crystal of **1** was mounted onto an electrical probe station (**Figure 5.10**). The probe needles contacted the crystal through Ga-In eutectic pads at either end of the crystal along the crystallographic long c -axis. This orientation

allows the flow of electrons to pass down the argentophilic “zig-zag” Ag^I-chains. I-V sweeps over a ± 2.0 V range gave only background levels of current (<1.0 pA). This indicates the material is not electrically conducting, but rather a highly effective insulator. It is worth stating that the Ag...Ag distances of **1** are $<5\%$ of the metallic distance. A very similar outcome was concluded on for [Ag^I-(Cytidine)₂] in Chapter 3. It would be a fair to state that such systems are not well-suited as nanowires despite the ongoing efforts of some in the scientific community who use such nomenclature without due cause.

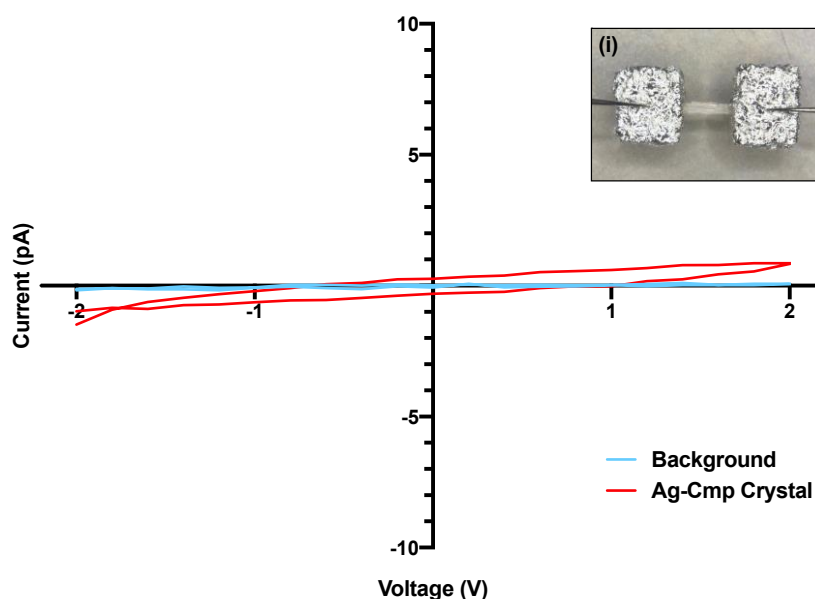


Figure 5.10 I-V curves of the crystal Ag-CMP, **1** (red-line). Inset (i), an optical microscope image of the probe station tips connected across a crystal of **1** through two pads of Ga-In eutectic.

5.3. Mechanical Exfoliation of [Ag^I-N³,O²-CMP][NO₃]-H₂O, **1**.

Solvent based exfoliation methods have become enormously successful as a method achieving top-down access to molecular scale materials. This process involves the sonication of crystalline material in suspended in solvent to allow cleavage between weak molecular bonds or interactions through sheering and vibrational forces.

Crystals of **1** were prepared and dried using acetone. The crystalline material was suspended in approximately 1.5 mL of toluene and sonicated at 40 kHz at room temperature. Samples were removed every 10 minutes (stopping after one-hour) by

glass-pipette (1.0 μL) and drop-cast onto prepared (cleaned by O_2 -plasma) Si- or mica wafers drying and subsequent analysis by AFM (tapping mode) (**Figure 5.11**).

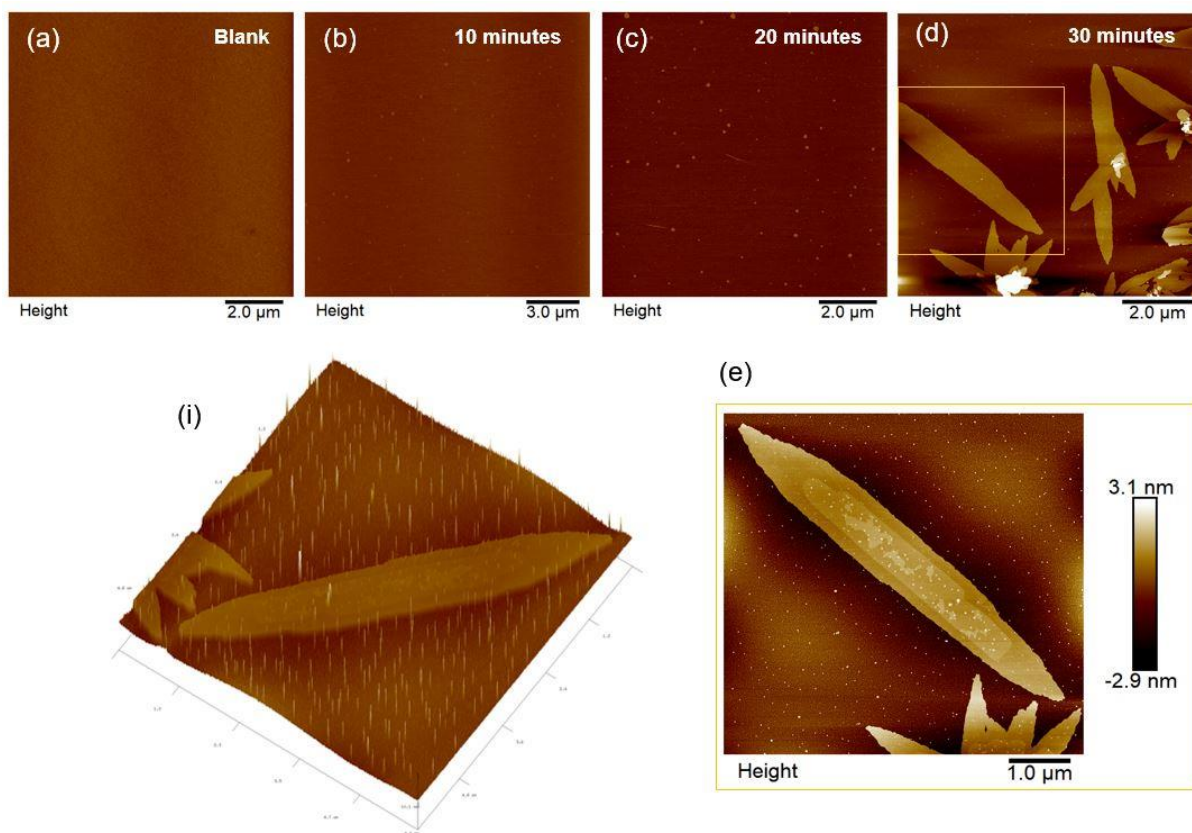


Figure 5.11 AFM images (tapping mode) captured following mechanical exfoliation of a single crystal of **1** in toluene; a) clean-surface, b) 10-, c) 20- and d) 30-minutes of sonication at 40 kHz at room temperature. (e) A single 2D flake with an even height of 3.0 nm can be found (inset (i) 3D view of the single flake).

Following sonication for up to 60 minutes (10-minute sample intervals) the crystal remained visible at the base of the vessel. Images were taken of drop-cast samples every ten minutes until flakes became visible at 30 minutes. 2D flakes with μm^2 ($<4 \mu\text{m}^2$) dimensions were readily seen evenly deposited across the surface. Sonication past 30 minutes showed 2D flakes of diminished dimensions. Up to one-hour of sonication the solution remained clear with no indication of the Tyndall effect (also known as Willis-Tyndall scattering); no large particulates could be seen as a suspension. The suspended solution remained free of sediment for approximately five-days.

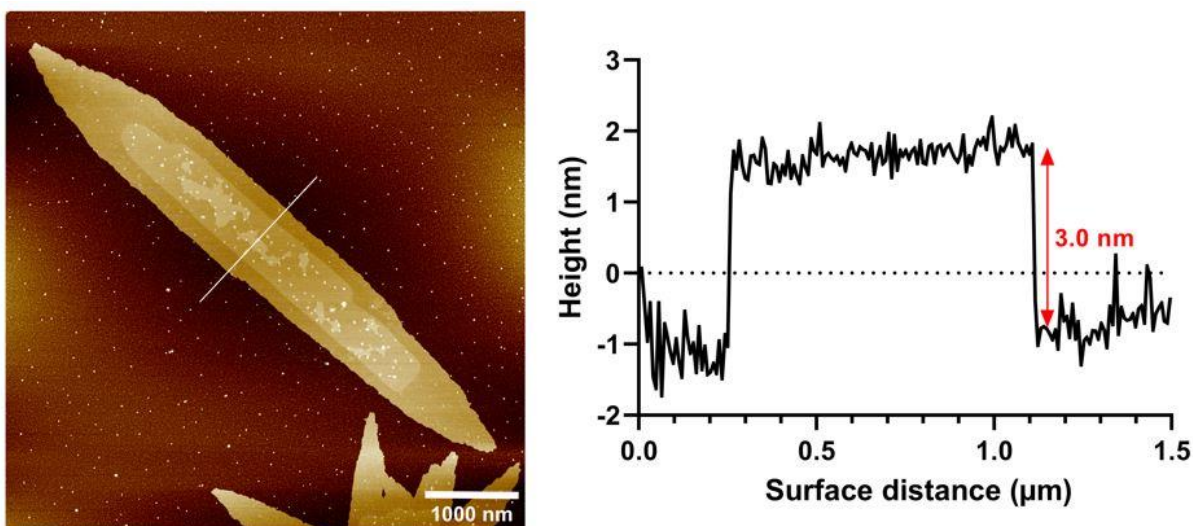


Figure 5.12 AFM height analysis of **1** following mechanical exfoliation using sonication for 30 minutes in toluene, yielding regular 2D flakes with the cross-section analysis showing a height of 3.0 nm.

Using the crystal structure of **1**, we attempted to correlate the AFM heights observed in **Figure 5.12**. The 2D flakes observed by AFM had uniform heights of 3.0 nm, which were backed up by numerous exfoliation repeats. The flake height correlates well with that of two connected CMP-(Ag)₂-CMP units that terminate at the weaker phosphodiester (*O*⁷) coordination as shown in **Figure 5.14**. A double stacked molecular sheet or bilayer, as showing in **Figure 5.14** and **Figure 5.15**, would therefore be a fitting composition and orientation capable of achieving the uniform heights observed. Interestingly, the bilayer molecular sheets retain their continuous silver arrays in this orientation, running parallel to the surface or lengthways along the long flake axis.

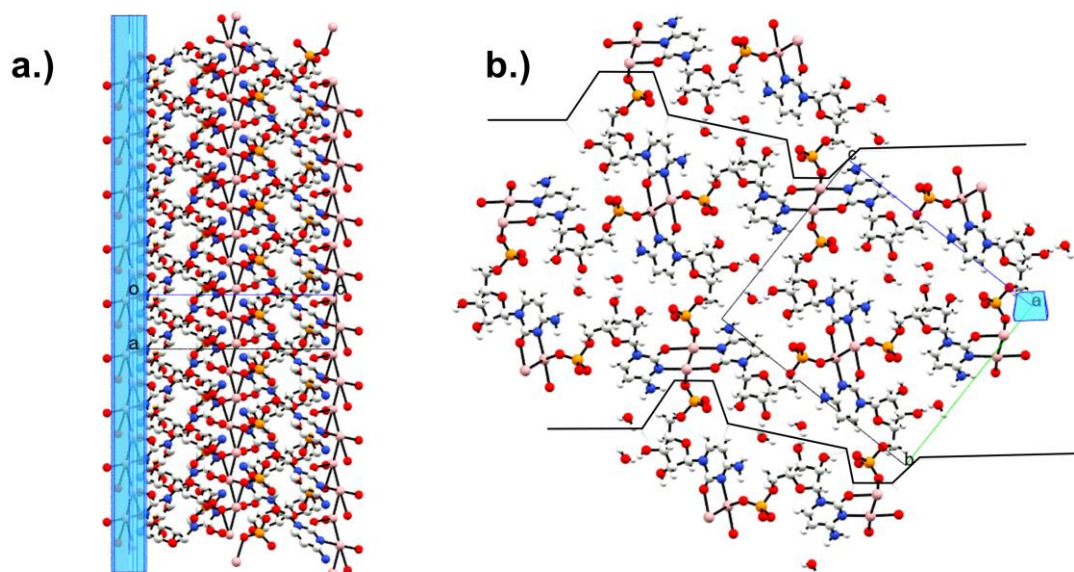


Figure 5.13 Packing of **1** *versus* the crystal habit, represented in blue. **a.)** Side-on view into the b-axis showing the unbroken silver-ion “zig-zag” chain running adjacent to the long crystal axis and **b.)** top-down view into the crystal lattice showing the bisects (black-lines) between Ag-O^{7'}; yielding layers with heights consistent with the observed 2D sheets after 30 minutes of mechanical exfoliation.

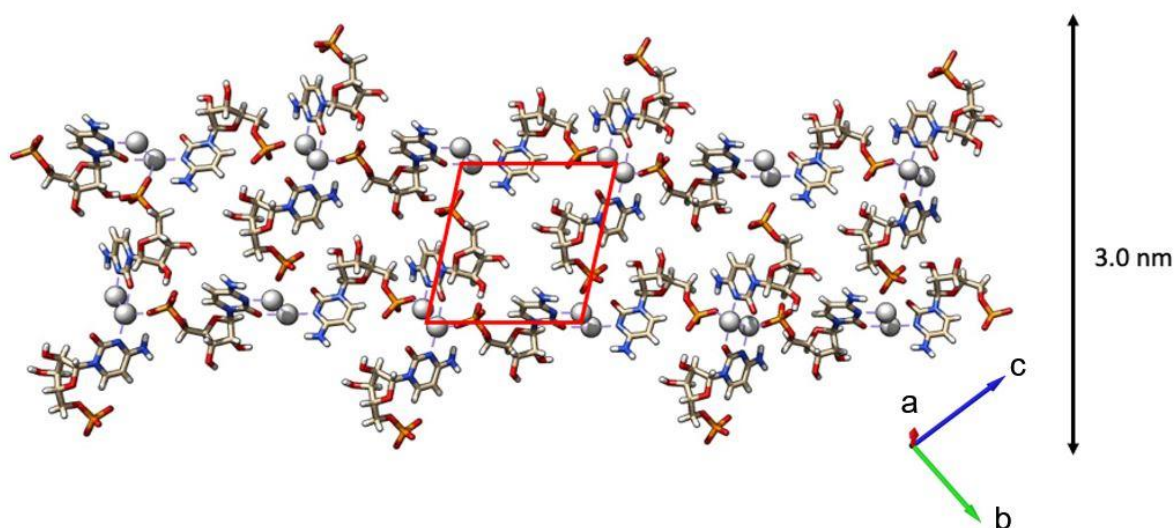


Figure 5.14 A side-on view into the packed crystal structure of complex **1** identified as being the correct height and orientation of a 2D molecular sheet following 30 minutes exfoliation.

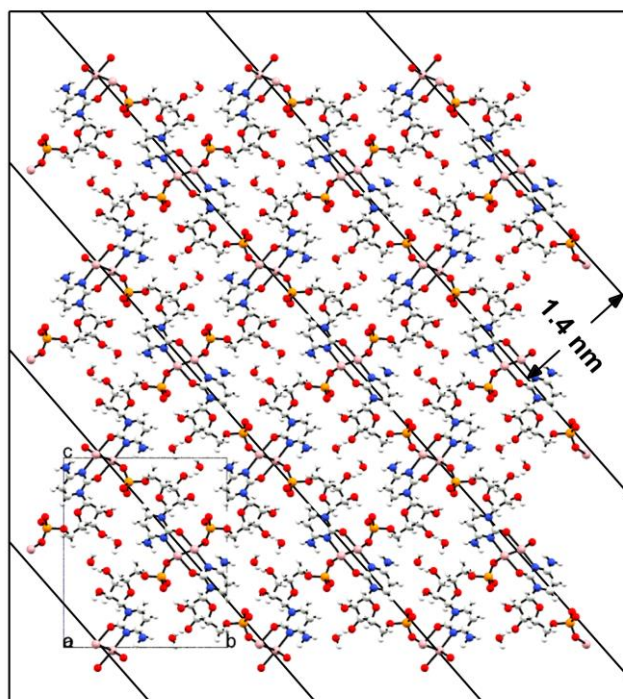


Figure 5.15 A packed crystal view down the *a*-axis of **1**, with diagonal lines illustrating the distances between layer-centres.

PXRD was used to ascertain the orientation of the molecular bilayer 2D sheets when drop-cast or deposited onto a flat surface. Five successive drop-cast layers were needed to achieve sufficient layers for detectable X-ray reflections (**Figure 5.16**). Three intense peaks were identified at 7.4, 14.8 and 22.3° corresponding to the (011), (022) and (033) *h,k,l* planes. Analysis of the peaks *versus* calculated patterns simulated using the single crystal data suggests that exfoliation occurs with a highly preferred orientation (March-Dollase parameter: 0.10), corresponding to the (011) plane in the crystal structure of **1** (**Figure 5.17**). Superimposing a (011) plane through the crystal structure confirmed that the integrity of the arrays of silver ions are therefore preserved following exfoliation. By confirming the orientation through PXRD and height by AFM, it is therefore reasonable to state that sheering forces generated by sonication was able to exfoliate molecular sheet from a single crystal by breaking the predicated O⁷-Ag bonds.

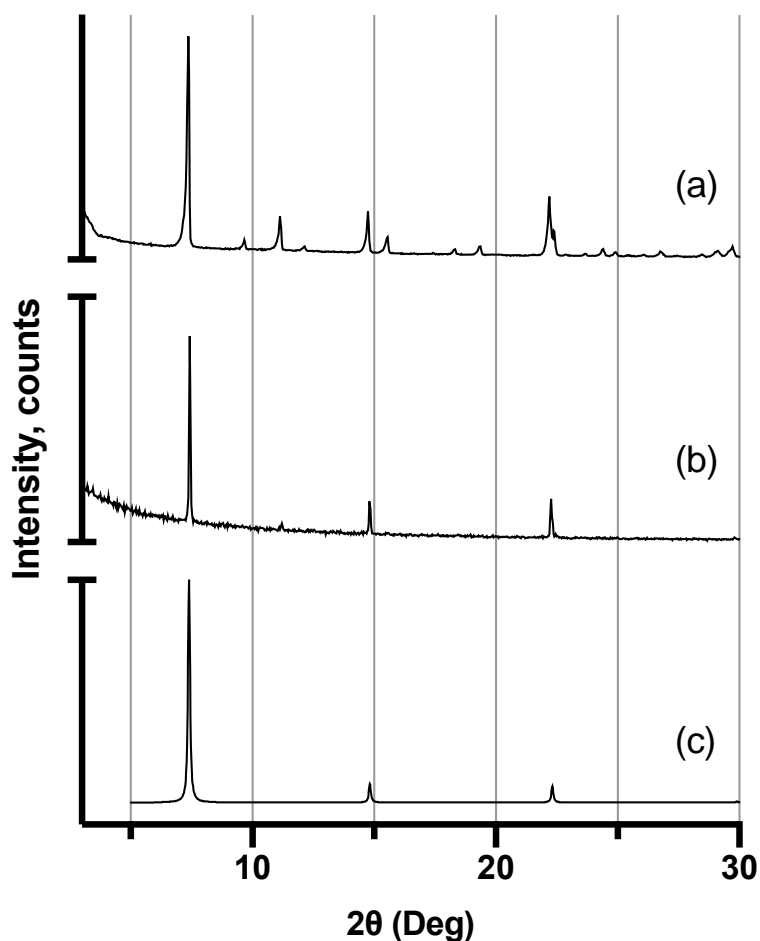


Figure 5.16 Powder X-ray diffraction data for **1**: (a) experimental bulk; (b) Drop-cast 2D sheets (exfoliated for 30 minutes); c) calculated pattern for a preferred [011] orientation with a March-Dollase parameter of 0.10.

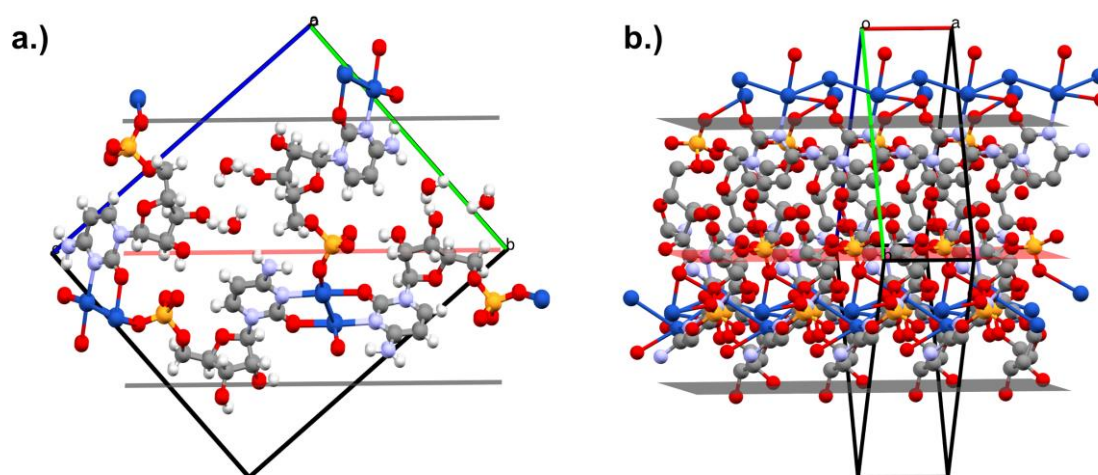


Figure 5.17 Looking a.) down and b.) along the a-axis of **1**, showing the [011] plane superimposed as a red 2D sheet through the centre.

5.4. Conclusions

In summary, we have prepared new examples of 2D coordination framework materials based on N-Ag-O bond formation with cytidine-5'-monophosphate. We have demonstrated the ability to prepare and crystallographically characterise two solvomorphs of $[\text{Ag}^{\text{I}}\text{-N}^3, \text{O}^2\text{-CMP}]$ as 3D coordination polymers. We have demonstrated that large 2D flakes of molecular sheets can be obtained using solvent-exfoliation techniques despite the relatively labile Ag-N,O coordination bonds. The heights measure by AFM correspond to a double layer or bilayer. PXRD demonstrated that the flakes held a [011] preferred orientation, confirming cleavage likely occurred at the Ag-O⁷ position, retaining their contiguous silver arrays which run parallel to the surface along the long axis of the flakes. Deposition occurring as neutral layers onto an oxide substrate. These results demonstrate the suitability of Ag-based coordination polymers compounds as precursors for molecular layer material applications.

5.5. References

- (1) Shekhah, O.; Liu, J.; Fischer, R. A.; Wöll, C. MOF Thin Films: Existing and Future Applications. *Chem. Soc. Rev.* **2011**, *40* (2), 1081–1106. <https://doi.org/10.1039/c0cs00147c>.
- (2) Mas-Ballesté, R.; Gómez-Navarro, C.; Gómez-Herrero, J.; Zamora, F. 2D Materials: To Graphene and Beyond. *Nanoscale* **2011**, *3* (1), 20–30. <https://doi.org/10.1039/c0nr00323a>.
- (3) Furukawa, H.; Cordova, K. E.; O’Keeffe, M.; Yaghi, O. M. The Chemistry and Applications of Metal-Organic Frameworks. *Science (80-.)*. **2013**, *341* (6149). <https://doi.org/10.1126/science.1230444>.
- (4) Rao, C. N. R.; Ramakrishna Matte, H. S. S.; Maitra, U. Graphene Analogues of Inorganic Layered Materials. *Angew. Chemie - Int. Ed.* **2013**, *52* (50), 13162–13185. <https://doi.org/10.1002/anie.201301548>.
- (5) Colson, J. W.; Dichtel, W. R. Rationally Synthesized Two-Dimensional Polymers. *Nat. Chem.* **2013**, *5* (6), 453–465. <https://doi.org/10.1038/nchem.1628>.
- (6) Zacher, D.; Shekhah, O.; Wöll, C.; Fischer, R. A. Thin Films of Metal-Organic Frameworks. *Chem. Soc. Rev.* **2009**, *38* (5), 1418–1429. <https://doi.org/10.1039/b805038b>.

- (7) Gascon, J.; Kapteijn, F. Metal-Organic Framework Membranes-High Potential, Bright Future? *Angew. Chemie - Int. Ed.* **2010**, *49* (9), 1530–1532. <https://doi.org/10.1002/anie.200906491>.
- (8) Stepanow, S.; Lingenfelder, M.; Dmitriev, A.; Spillmann, H.; Delvigne, E.; Lin, N.; Deng, X.; Cai, C.; Barth, J. V.; Kern, K. Steering Molecular Organization and Host-Guest Interactions Using Two-Dimensional Nanoporous Coordination Systems. *Nat. Mater.* **2004**, *3* (4), 229–233. <https://doi.org/10.1038/nmat1088>.
- (9) Bauer, T.; Zheng, Z.; Renn, A.; Enning, R.; Stemmer, A.; Sakamoto, J.; Schlüter, A. D. Synthesis of Free-Standing, Monolayered Organometallic Sheets at the Air/Water Interface. *Angew. Chemie - Int. Ed.* **2011**, *50* (34), 7879–7884. <https://doi.org/10.1002/anie.201100669>.
- (10) Yamada, T.; Otsubo, K.; Makiura, R.; Kitagawa, H. Designer Coordination Polymers: Dimensional Crossover Architectures and Proton Conduction. *Chem. Soc. Rev.* **2013**, *42* (16), 6655–6669. <https://doi.org/10.1039/c3cs60028a>.
- (11) Zheng, Z.; Opilik, L.; Schiffmann, F.; Liu, W.; Bergamini, G.; Ceroni, P.; Lee, L. T.; Schütz, A.; Sakamoto, J.; Zenobi, R.; et al. Synthesis of Two-Dimensional Analogues of Copolymers by Site-to-Site Transmetalation of Organometallic Monolayer Sheets. *J. Am. Chem. Soc.* **2014**, *136* (16), 6103–6110. <https://doi.org/10.1021/ja501849y>.
- (12) Junggeburth, S. C.; Diehl, L.; Werner, S.; Duppel, V.; Sigle, W.; Lotsch, B. V. Ultrathin 2D Coordination Polymer Nanosheets by Surfactant-Mediated Synthesis. *J. Am. Chem. Soc.* **2013**, *135* (16), 6157–6164. <https://doi.org/10.1021/ja312567v>.
- (13) Amo-Ochoa, P.; Welte, L.; González-Prieto, R.; Sanz Miguel, P. J.; Gómez-García, C. J.; Mateo-Martí, E.; Delgado, S.; Gómez-Herrero, J.; Zamora, F. Single Layers of a Multifunctional Lamina Cu(i,li) Coordination Polymer. *Chem. Commun.* **2010**, *46* (19), 3262–3264. <https://doi.org/10.1039/b919647a>.
- (14) Li, P. Z.; Maeda, Y.; Xu, Q. Top-down Fabrication of Crystalline Metal-Organic Framework Nanosheets. *Chem. Commun.* **2011**, *47* (29), 8436–8438. <https://doi.org/10.1039/c1cc12510a>.
- (15) Tan, J. C.; Saines, P. J.; Bithell, E. G.; Cheetham, A. K. Hybrid Nanosheets of an Inorganic-Organic Framework Material: Facile Synthesis, Structure, and Elastic Properties. *ACS Nano* **2012**, *6* (1), 615–621. <https://doi.org/10.1021/nn204054k>.
- (16) Gallego, A.; Hermosa, C.; Castillo, O.; Berlanga, I.; Gómez-García, C. J.; Mateo-

- Martí, E.; Martínez, J. I.; Flores, F.; Gómez-Navarro, C.; Gómez-Herrero, J.; et al. Solvent-Induced Delamination of a Multifunctional Two Dimensional Coordination Polymer. *Adv. Mater.* **2013**, *25* (15), 2141–2146. <https://doi.org/10.1002/adma.201204676>.
- (17) Beldon, P. J.; Tominaka, S.; Singh, P.; Saha Dasgupta, T.; Bithell, E. G.; Cheetham, A. K. Layered Structures and Nanosheets of Pyrimidinethiolate Coordination Polymers. *Chem. Commun.* **2014**, *50* (31), 3955–3957. <https://doi.org/10.1039/c4cc00771a>.
- (18) Hermosa, C.; Horrocks, B. R.; Martínez, J. I.; Liscio, F.; Gómez-Herrero, J.; Zamora, F. Mechanical and Optical Properties of Ultralarge Flakes of a Metal-Organic Framework with Molecular Thickness. *Chem. Sci.* **2015**, *6* (4), 2553–2558. <https://doi.org/10.1039/c4sc03115f>.
- (19) Fei, H.; Rogow, D. L.; Oliver, S. R. J. Reversible Anion Exchange and Catalytic Properties of Two Cationic Metal-Organic Frameworks Based on Cu(I) and Ag(I). *J. Am. Chem. Soc.* **2010**, *132* (20), 7202–7209. <https://doi.org/10.1021/ja102134c>.
- (20) Shen, S. S.; Wang, X.; Hu, H. M.; Yuan, F.; Dong, F. X.; Xue, G. Synthesis, Crystal Structure and Luminescence of Ag(I) Coordination Polymers Based on a New Sulfonate Functionalized Terpyridine Derivative Ligand. *Polyhedron* **2015**, *91*, 52–58. <https://doi.org/10.1016/j.poly.2015.02.021>.
- (21) Lamming, G.; El-Zubir, O.; Kolokotroni, J.; McGurk, C.; Waddell, P. G.; Probert, M. R.; Houlton, A. Two-Dimensional Frameworks Based on Ag(I)-N Bond Formation: Single Crystal to Single Molecular Sheet Transformation. *Inorg. Chem.* **2016**, *55* (19), 9644–9652. <https://doi.org/10.1021/acs.inorgchem.6b01365>.
- (22) Terrón, A.; Tomàs, L.; Bauzá, A.; García-Raso, A.; Fiol, J. J.; Molins, E.; Frontera, A. The First X-Ray Structure of a Silver-Nucleotide Complex: Interaction of Ion Ag(i) with Cytidine-5'-Monophosphate. *CrystEngComm* **2017**, *19* (39), 5830–5834. <https://doi.org/10.1039/c7ce01400g>.
- (23) Kistenmacher, T. J.; Rossi, M.; Marzilli, L. G. Crystal and Molecular Structure of (Nitrate)(l-Methylcytosine)Silver(I): An Unusual Cross-Linked Polymer Containing a Heavy Metal and a Modified Nucleic Acid Constituent. *Inorg. Chem.* **1979**, *18* (2), 240–244. <https://doi.org/10.1021/ic50192a007>.

Chapter 6.

Ag^{I} -Oligonucleotide systems: Controlled Metal-ion Capture within a Hairpin.

6.1. Introduction

DNA based bottom-up techniques have been demonstrated to be a versatile and highly effective methods of accessing stabilised metallic clusters or particles. AgNCs stabilised within R/DNA have been described previously in the literature; with sizes ranging from 10 - 24 atoms.¹ By tuning the design and sequence of the DNA-scaffold, the cluster sizes and shape can be tailored to produce fluorescent colours ranging from blue to near infrared (380 - 780 nm).¹ DNA stabilised AgNCs, exhibit excellent brightness and photostability and are considered promising types of emitters for various applications, including, nanophotonic elements for electronics¹, chemical or biological sensors/probes²⁻⁵ with additional antimicrobial properties⁶ (with low toxicity to humans).

The use of more complex secondary structures of DNA, *i.e.* Hairpins, have the potential for a greater degree of control and uniformity to particle size. Hairpin structures can be formed by sequences with inverted repeats (IRs) or palindromes and can exist in both ss- and ds-DNA forms.⁷ Their function within a cell are plentiful, covering a range of roles including, transcription, repair, rolling-circle replication (RCR), bacterial conjugation, natural transformation, protein recognition and infection by some viruses.⁷ Their structure is composed of a stem and loop region, the latter typically employing the conical Watson-Crick method of base-pairing, while the loop does not (**Figure 6.1**). The non-binding loop region facilitates the folding into a hairpin structure, allowing for the stem to form a duplex.

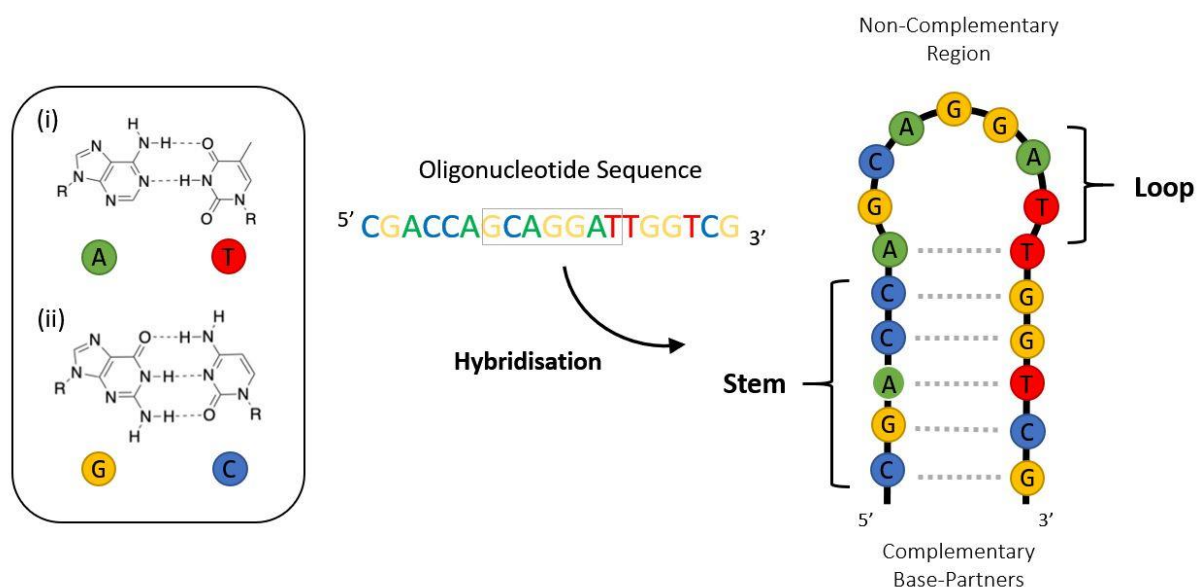


Figure 6.1 A generalised representation of a Hairpin Structure; comprising of both “loop” and “stem” regions. The stem allows for Watson-Crick type complementary base-pairing while the loop does not and therefore act as a natural hinge which allows for the folding into a loop. Inset shows the H-bonding between (i) Adenine-Thymine (A-T) and (ii) Guanine-Cytosine (G-C) that is observed in the stem.

The use of DNA hairpin systems as a bottom up technique towards assembly of silver nanoclusters (Ag-NCs) and site specific C-Ag^I-C binding motif has been explored previously by a number of groups.^{8–12} A general approach involves the use of C-rich looped regions capable of capturing multiple silver ions prior to reduction of Ag^I down to an elemental state (**Figure 6.2**). Upon reduction, zero valent silver atoms spontaneously cluster together to form a particle to reduce their high surface energy. The metallic clusters are stabilised by their confinement and isolation within the hairpin loop. The stem regions often possess standard Watson-Crick type binding allowing for hybridisation and loop closure. Some examples include additional functionality into the duplexing stem regions.^{13,14}

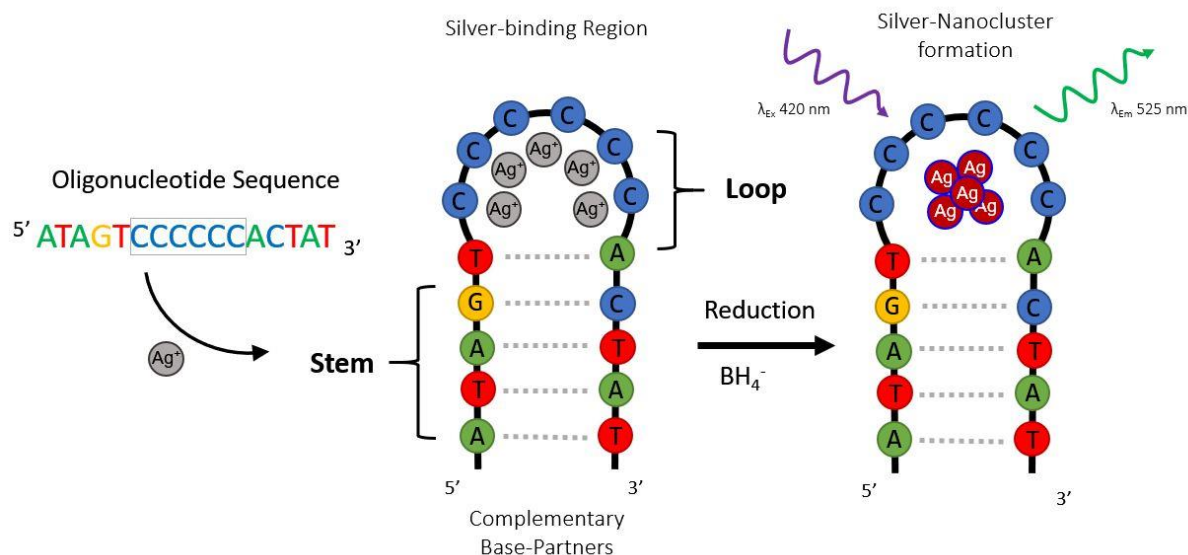


Figure 6.2 An illustration of a looped based route involving Ag^I-DNA hairpin-type systems bearing C-rich loops, towards the formation of emissive silver-nanocluster.⁸

An alternative approach towards hairpin formation was explored by Ono *et al.*, who used a hairpin design concept composing C-rich stem regions (Ag^I binding region) and T-rich loop (Linker) (**Figure 6.3**).¹⁵ Oligonucleotide folding into a Hairpin conformation was confirmed by the quenching of a terminal 3'-(6-Fluorescein) unit as it approaches the terminal 5'-Dabcyl upon addition of silver(I) ions. Fluorescence intensity decreased as a function of silver(I) concentration, acting as an effective metal ion sensor. Interestingly, the loop region (made up of four thymine units) functioned as intended with no evidence given of any competing interactions away from the intended C^{N3}-Ag^I-C^{N3} coordination.

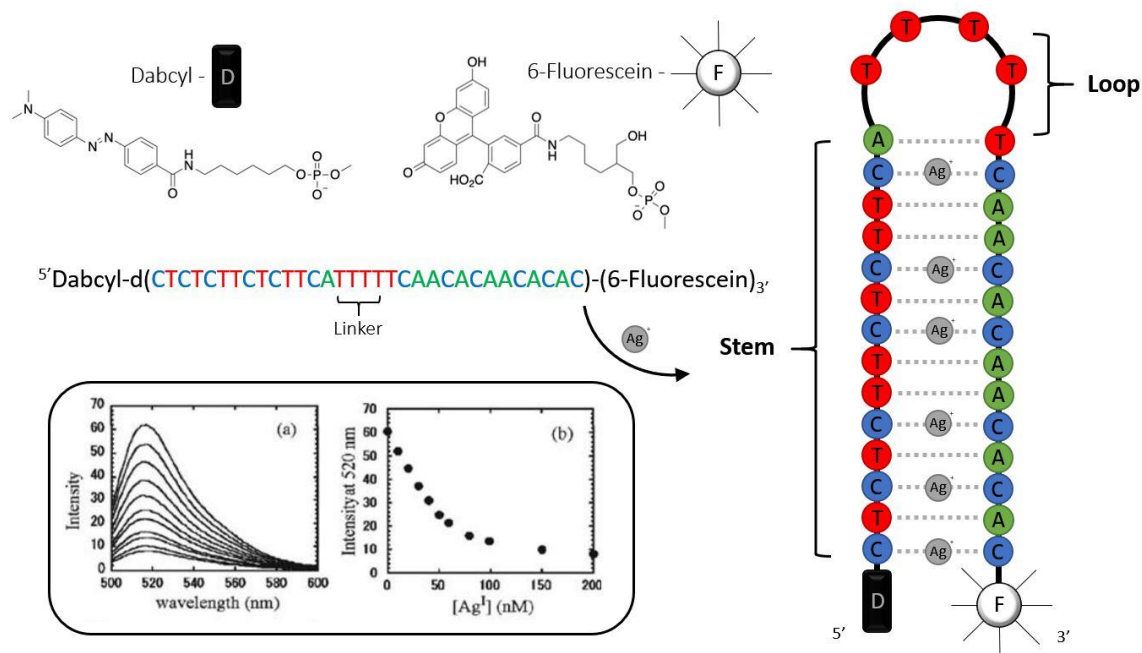


Figure 6.3 Emission based evidence of hairpin formation upon stem C-Ag^I-C metal-mediation by Ono *et al.*¹⁵ Inset, quenching of the fluorescein emission following the addition of silver(I) ions implying hairpin formation.

6.2. Aims and Objectives

This chapter explores the concept and design of hairpin type structures capable of capturing precise numbers of silver(I) ions based on the well-established C^{N3}-Ag^I-C^{N3} (C: Cytosine) coordination (**Figure 6.4**), analogues to the previously discussed M-DNA systems. The development of an M-DNA hairpin-based route towards the bottom-up formation of nanoclusters with extremely precise particle size distributions with atomic resolution. Designer oligonucleotides (bearing C-rich stem regions) will be assessed for their silver(I) ion capture credentials.[†] Optimisations of both the loop and stem regions are explored as part of the development process during this study.

[†] A range of analytical techniques were used to determine the success of metal-binding instances and conformation, these include; electrospray-ionisation mass-spectroscopy (ESI-MS) (including ion mobility separation (IMS)), circular dichroism (CD) and Isothermal titration calorimetry (ITC).

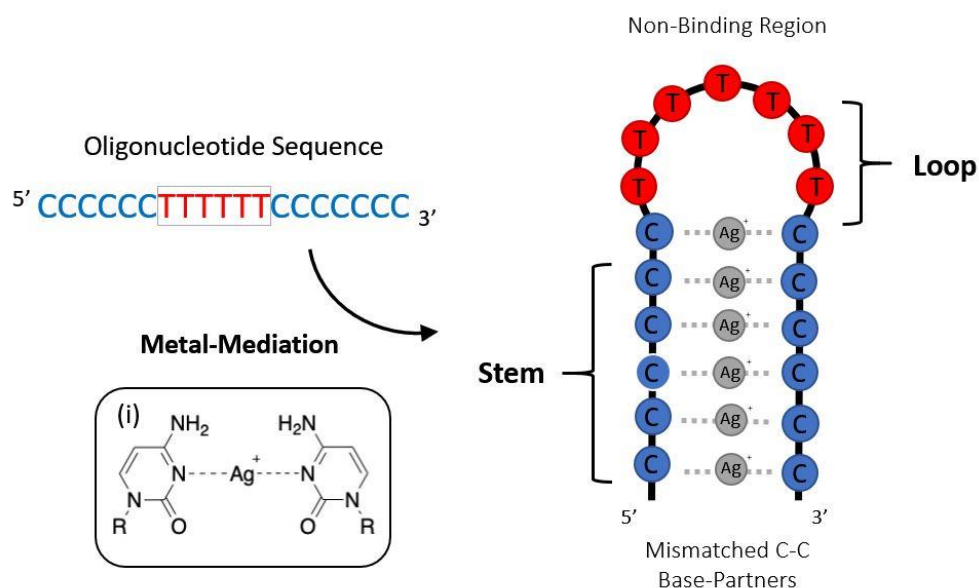


Figure 6.4 A generalised representation of our metallised Hairpin concept, with mismatched C·C stems allowing for metal-mediation with silver(I) in exchange of natural Watson-Crick type duplexing. Inset (i) $C^{N3}\text{-Ag}^{\text{I}}\text{-C}^{N3}$ coordination.

6.3. Results and Discussion

The first stage of investigation was focused towards loop optimisation; how many units are required to give an acceptable hinge with sufficient flexibility to form a loop? Previous studies by Marzilli *et al.* used the well-established mercury-thymine coordination ($\text{T-Hg}^{\text{II}}\text{-T}$) demonstrated that hairpin formation was possible with a minimum loop length of two thymine units under the right conditions (**Figure 6.5**).¹⁶ The study involved the use of a central homo-T region that either duplexed or formed a hairpin structure across the Hg^{II} ions. The resulting conformation was found to heavily depend on stoichiometry (metal:ligand) or sequence composition (T2, T3 or T4).

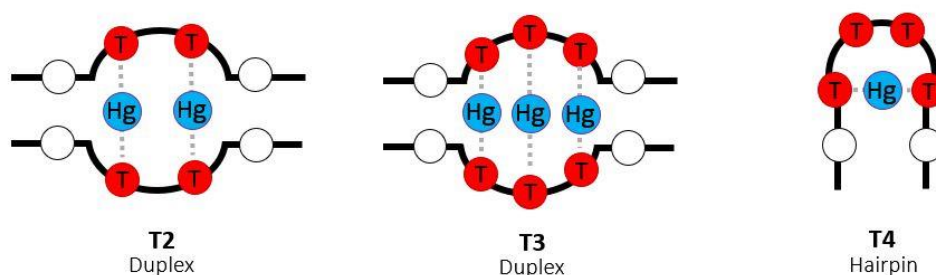


Figure 6.5 Illustrations of Marzilli's Mercury (Hg^{II}) mediated T-rich oligonucleotides following metal coordination, allowing for either duplexed species (T2 and T3) or Hairpin formation (T4).

Over the last couple of years, the range of silver(I) ion coordination partners within M-DNA systems has rapidly expanded beyond the mismatched C-C pair; which has become synonymous with silver-DNA interactions.^{17–20} In addition to this, metal-mediation across $N7\text{G}\cdot\text{G}^{N7}$, $N7\text{G}\cdot\text{C}^{N3}$ and $N3\text{T}\cdot\text{T}^{N3}$ pairs have now been crystallographically observed.^{21,22} For this reason, we initially chose to forgo the use of routinely used natural oligonucleosides units (A, T, C and G) within the loop region, exchanging them for a non-coordinating abasic (a) linker (**Figure 6.6**). The lack of a base subunit has potential to offer greater loop flexibility when compared to existing hairpin examples. Such systems, therefore, are subtly different in construction and application to those existing in the literature.^{8,10,23,24}

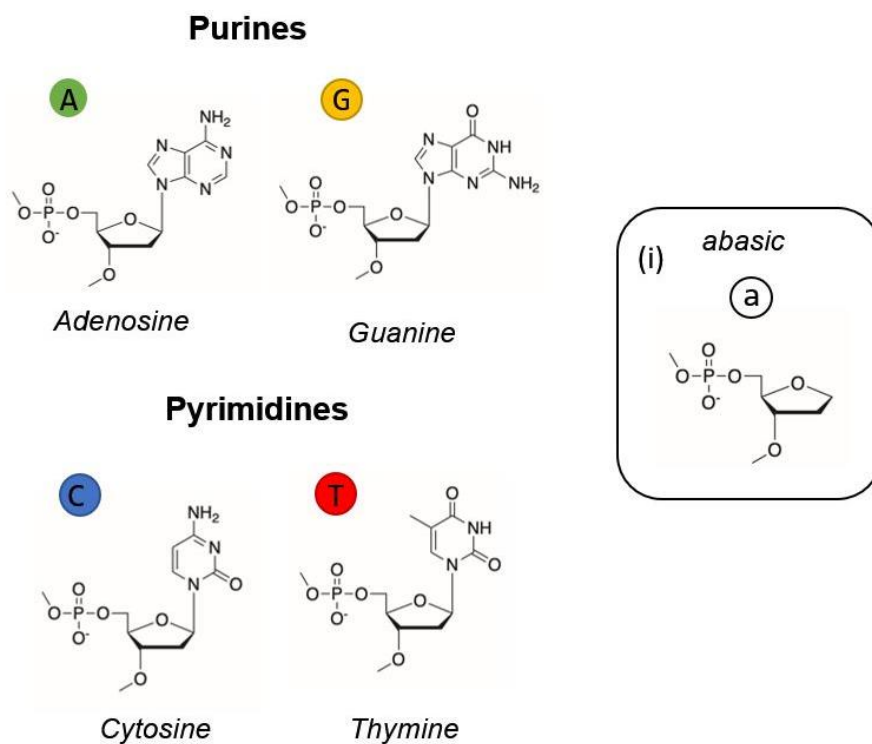


Figure 6.6 Natural deoxyribose nucleotide purines (A & G) and pyrimidines (C & T).
Inset (i) abasic (a) deoxyribose nucleotide.

The following stage of investigation explores higher Ag⁺ capacity systems. This is achieved by increasing the length of the homo-C stem regions (**Figure 6.7**). The increase in C·C mispairings offers additional ^{N3}C-Ag⁺-C^{N3} coordination sites per oligonucleotide.

The third and final stage of investigation revisits the loop in attempts to standardise the design towards an all-natural construction. Exchange of the abasic loop units for routinely available base units (A, T, C and G) which offer similar non-competing properties; at a much lower cost.

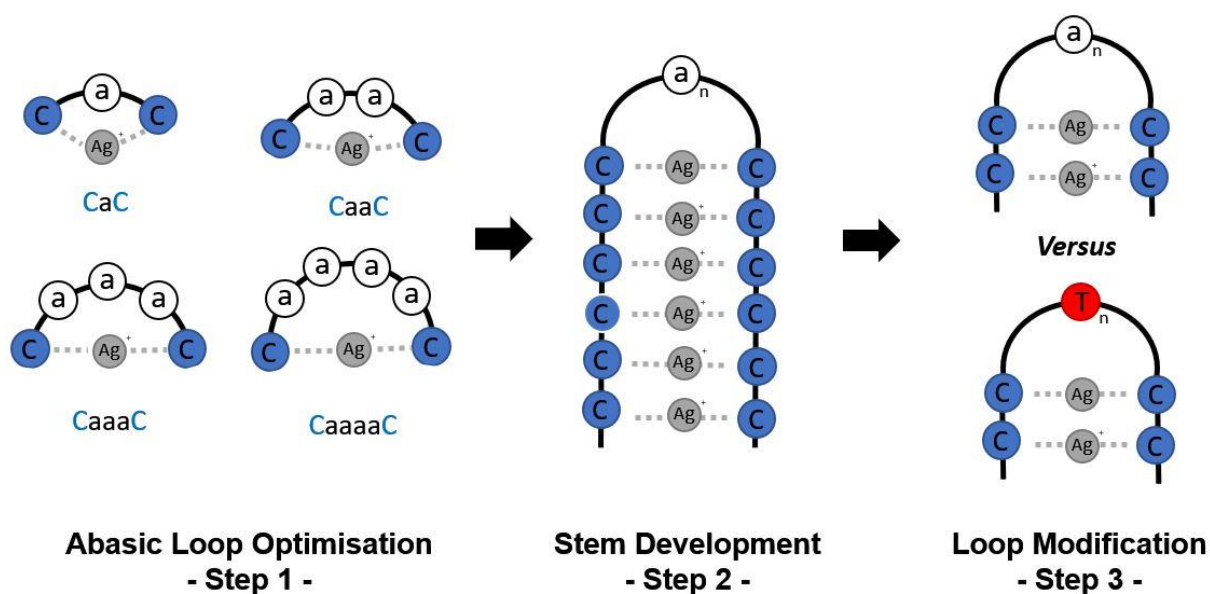


Figure 6.7 Hairpin development steps with a focus on loop (step-1) and stem (step-2) optimisation upon silver(I) coordination across the mismatched C-C pairing (C-Ag^I-C). The third and final step-3 investigates the exchange and subsequent simplification of the loop; replacing the modified abasic units with thymine.

6.4. Step-1, A-basic Loop Optimisation towards Ag-Hairpin Formation.

Four short oligonucleotide species were designed and purchased as a commercially available product from *ATD-Bio*; CaC (^{a1}C₁), CaaC (^{a2}C₁), CaaaC (^{a3}C₁) and CaaaaC (^{a4}C₁), (a: abasic). The phosphoramidite technique was used for the synthesis all oligonucleotides acquired. The exclusion of the nucleobase, “abasic”, from the loop decreases the number of variables or competition from alternative metal-binding sites whilst also increasing loop-flexibility. The backbone therefore consists of only a phosphodiester linker and deoxyribose sugar (See **Figure 6.8** below). All four systems possess identical 3' and 5' terminal cytosine base units, giving each system two *N*³ donors, ideal for the capture or coordination of a single silver(I) ion (C-Ag^I-C).[‡]

[‡] The method of naming follows ^{Loop-type}C_{Ag-capacity} from here on (Type: a_n: abasic, T_n: Thymine (n: number of units in the loop)).

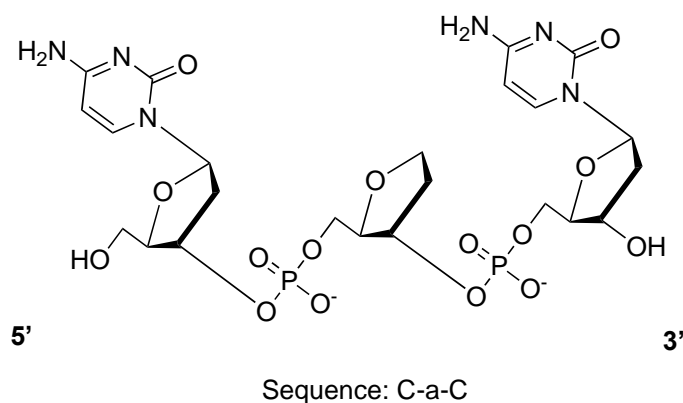


Figure 6.8 A molecular diagram representing a^1C_1 (CaC), the shortest oligonucleotide designed for loop optimisation.

It was critical at this early stage of investigation to recognise the conformational limitations of hairpin-type-structures; *i.e.* a loop too short would encounter significant steric restraints. Such constraints towards hairpin formation could lead to the formation of alternative, undesirable, binding modes; single-site coordination, dimers and polymers (**Figure 6.9**). A loop too long and flexible would be costly and therefore inefficient. Furthermore, such dynamic systems could face folding issues. Therefore, an optimised structure is desirable towards the development of a viable bottom up protocol.

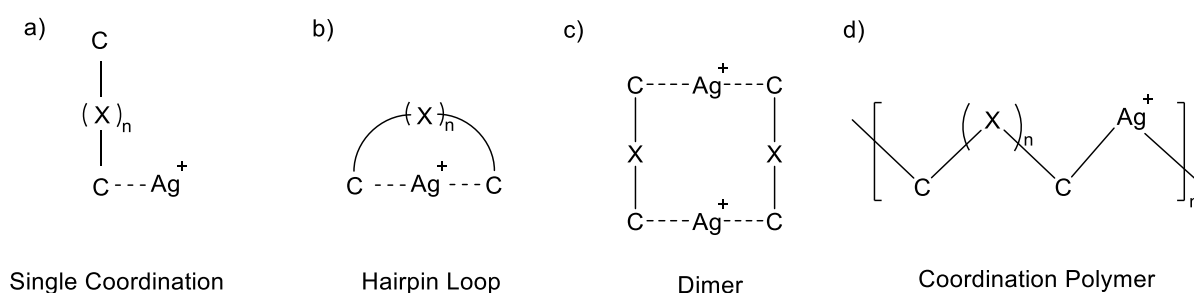


Figure 6.9 Four possible assembly types for Ag^I -oligonucleotide systems utilising the $N^3-Ag^I-N^3$ coordination motif: a) single coordination b) hairpin loop, c) dimer and d) coordination polymer.

Prior to any experimental work a computational study was made possible by looking at the behaviour of these short abasic systems. Computational modelling (classical

molecular minimisation techniques) described herein were performed by the Bronowska group (Joao Victor De Souza Cunha) at Newcastle university. All four of the designed sequences ($a^1\mathbf{C}_1$, $a^2\mathbf{C}_1$, $a^3\mathbf{C}_1$ and $a^4\mathbf{C}_1$) were modelled as macrocyclic systems bound across a single Ag^{I} ion by the N^3 -donors of each terminal cytosine (3' and 5') (Figure 6.10).

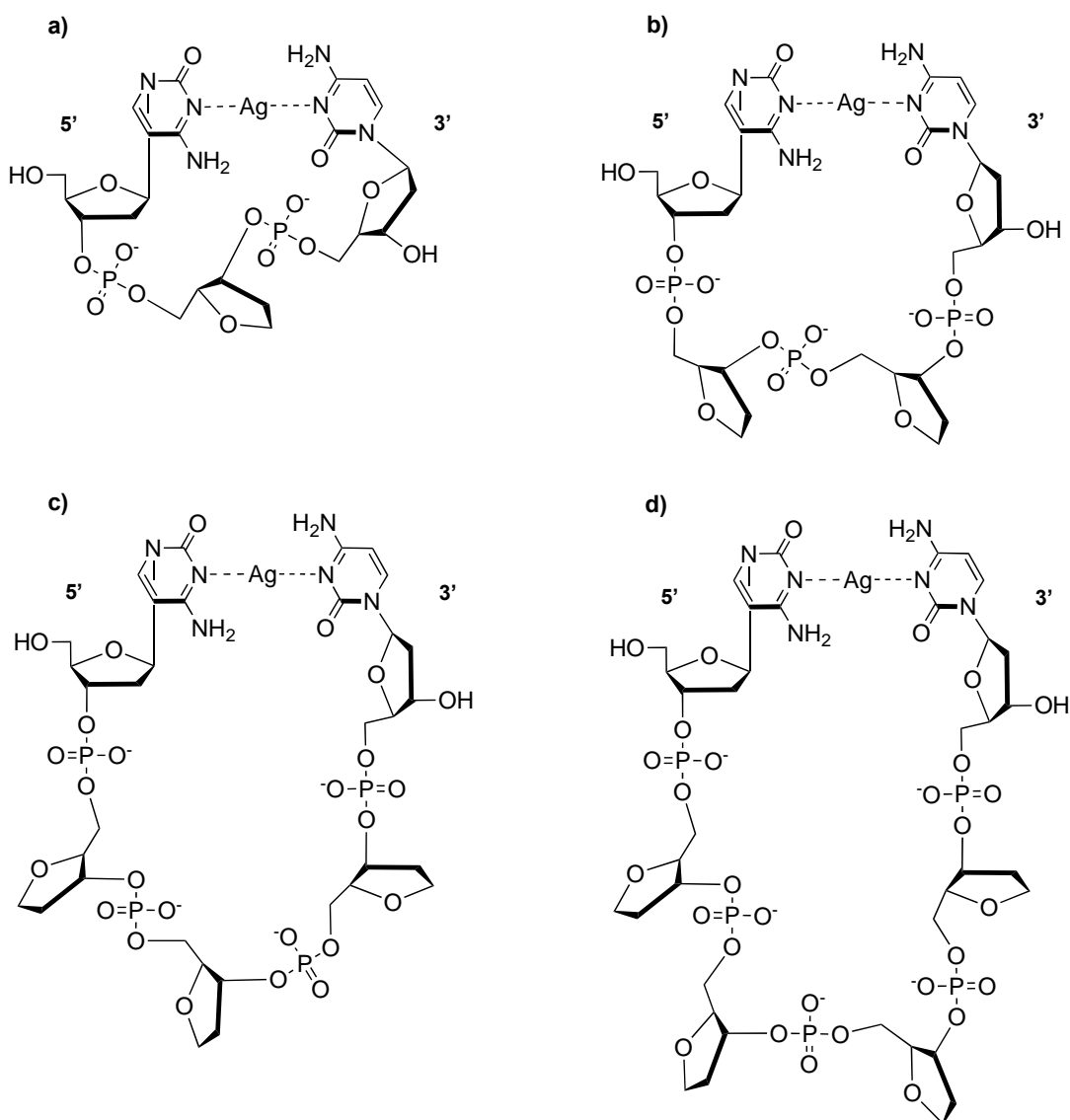


Figure 6.10 Four modelled macrocyclic systems coordinated by silver(I) across the N^3 -donor sites of the 3' and 5' terminal cytosine ligands of the modified abasic oligonucleotides; a) $a^1\mathbf{C}_1$ b) $a^2\mathbf{C}_1$ c) $a^3\mathbf{C}_1$ and d) $a^4\mathbf{C}_1$, analogous to the loop regions of a hairpin system.

The computational models were based on closed loop systems with linear (180°) $\text{Ag}-N^3$ bonds with distances of 2.2 \AA . The geometries for all calculations are proportioned

on a solved crystal structures of a *Trans*-[Ag^I-*N*³-cytosine)₂].[PF₆] explored in Chapter 2. The models represented an approximation for a single C-Ag^I-C complex within a hairpin without further crystallographic information available. Using ConQuest to search The Cambridge Crystallographic Database Centre (CCDC) for Ag-N bonding distances returned 6469 hits with an average distance of 2.263 Å (search range: 1.8 – 2.8 Å). The database search results validated the Ag-*N*³ lengths chosen for these calculations.

Using the parameters outlined, values for an energy minimum was calculated for each silver(I) mediated oligo macrocycle ([Ag^I-^{a1}C₁], [Ag^I-^{a2}C₁], [Ag^I-^{a3}C₁] and [Ag^I-^{a4}C₁]) (**Figure 6.11**). Of the four systems, ^{a2}C₁ and ^{a3}C₁ displayed significantly (~21%) lower minimisation energy compared to ^{a1}C₁ and ^{a4}C₁. Based on these results, an optimal loop design for a hairpin system would require two or three abasic units (^{a2}C₁ > ^{a3}C₁ >> ^{a4}C₁ > ^{a1}C₁).

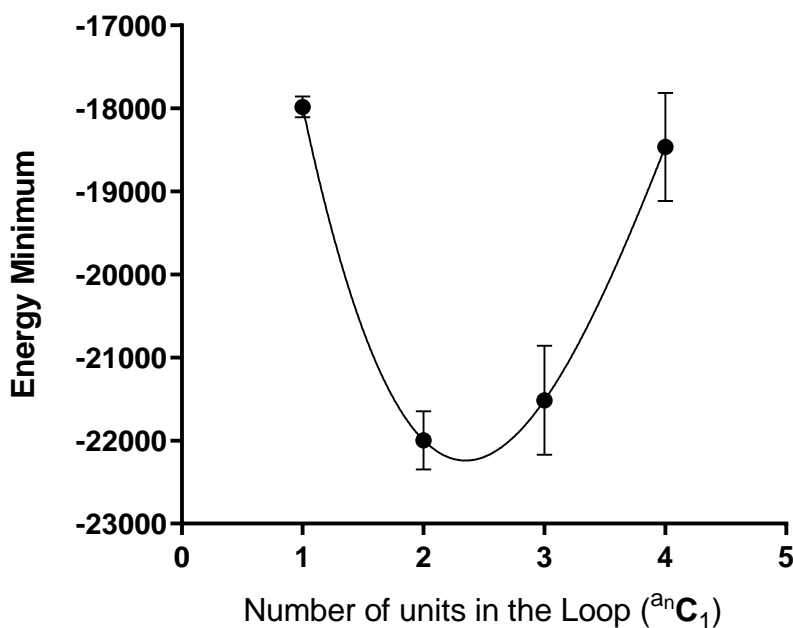


Figure 6.11 Classical molecular minimisation calculations for a series of closed silver(I)-mediated Hairpin systems as loop length varies from one-to-four abasic units (1 - [Ag^I-^{a1}C₁], 2 - [Ag^I-^{a2}C₁], 3 - [Ag^I-^{a3}C₁] and 4 - [Ag^I-^{a4}C₁]).

6.5. Computational Methods

In order to study the dynamics effects of differing loop lengths of $^{an}C_1$ and $^{Tn}C_1$, a series of complexes were simulated. Loops containing one-to-six thymine basis and one-to-six abasic units were constructed in UCSF Chimera.²⁵ Structural hydrogens were added. To avoid the local energy trapping for the models, a series of sequential minimization procedures were made for the starting models: First, 5000 cycles of steepest decent minimization procedures with a 0.02 nm step size were made, followed by 1000 conjugated gradient minimization procedures with a 0.01 nm step size. The following protein parametrisation was performed using the Gromacs 2016.03²⁶ suite with AMBERFF99SB-ILDN²⁷ force field for standard residues and GAFF for non-standard residues using AM1BCC charges. The systems were relaxed with a short equilibrium MD production run. A 1.00 nm cubic box was centred on the structure and the system is solvated with TIP3P waters. Sodium and chloride ions were added to a concentration of 0.1 M resulting in systems with more than seven hundred thousand atoms. Bonds were constrained using the LINCS algorithm.²⁸ The electrostatic interactions were calculated using particle-mesh Ewald method, with a non-bonded cut-off set at 0.10 nm. All structures were minimised via the steepest descent algorithm for 20,000 steps of 0.02 nm, and minimisations were stopped when the maximum force fell below 1000 kJ/mol/nm using the Verlet cut-off scheme.²⁹ After minimisation, temperature equilibration was performed for 100 ps with a time step of 2fs with position restraints applied to the backbone using an NVT. The temperature coupling was set between the protein and the non-protein entities by using a Berendsen thermostat,³⁰ with a time constant of 0.10 psec, and the temperature set to reach 300K with the pressure coupling off. Sequentially, a pressure NPT equilibration was performed followed by 100ps of an NVT equilibration, the following 100 ps of NPT equilibration, and a production run of 100 ns. Temperature was set constant at 300K by using a modified Berendsen thermostat ($\tau = 0.1$ ps).³⁰ Pressure was kept constant at 1.00 bar by Parinello-Rahman isotropic coupling ($\tau = 2.00$ ps) to a pressure bath.³¹ All analysis was made using Gromacs toolset.

6.6. Experimental Data

Experimental measurements and validation against the computational studies were initially performed using electrospray-ionisation mass-spectrometry (ESI-MS). This

technique was chosen for the observation of metal-binding instances for its well-known soft ionisation qualities for thermally labile large molecules achieving minimum fragmentation. Control experiments of the stock oligonucleotides were conducted, checking each species for purity and expected mass prior to the addition of silver ions. All four oligonucleotides showed highly intense species corresponding to their intended structures. Additional lower intensity peaks were identified to include Na⁺ ions, typically found in buffers used during oligonucleotide synthesis. The four modified oligonucleotide species ^{a1}C₁, ^{a2}C₁, ^{a3}C₁ and ^{a4}C₁ (0.1 mmol, 10 µL) were individually added to 10 µL of silver nitrate (AgNO₃, 0.1 mmol) achieving a 1:1 (oligo:metal) or 2:1 (cytosine:metal) ratio. Following the addition of metal ions, the formation of new peaks was readily observed (**Figure 6.12 and Table 6.**). Isotope patterns, splitting and masses aligned well with the theoretical values calculated for each sequence bound to a single silver(I) ion (**Figure 6.13, and Appendices**). Peak separation of 1.0 and 0.5 m/z suggests species bearing a -1 and -2 charge states, indicating the loss of two and three protons respectively, countering the +1 charge of the silver ion.

Charge (z) :		m/-1	m/-2
#	Sample	Exp (calc.) m/z	Exp (calc.) m/z
1	^{a1} C ₁	695.1480 (695.1485)	347.0703 (347.0706)
2	Ag-^{a1}C₁	801.0516 (801.0457)	401.6883 (400.0192)
3	^{a2} C ₁	875.1661 (875.1672)	437.0795 (437.0800)
4	Ag-^{a2}C₁	981.0619 (981.0645)	489.9308 (490.0286)
5	^{a3} C ₁	1055.1833 (1055.1860)	527.0893 (527.0894)
6	Ag-^{a3}C₁	1161.0782 (1161.0832)	580.0104 (580.0380)
7	^{a4} C ₁	1235.1468 (1235.2047)	617.0968 (617.0987)
8	Ag-^{a4}C₁	1341.0357 (1342.1098)	670.0448 (670.5513)

Table 6.1 ESI-MS monoisotopic mass peak data for oligonucleotides: a^1C_1 , a^2C_1 , a^3C_1 and a^4C_1 , following the addition of silver(I) ions *versus* theoretical values for -1 and -2 charge (z) states.

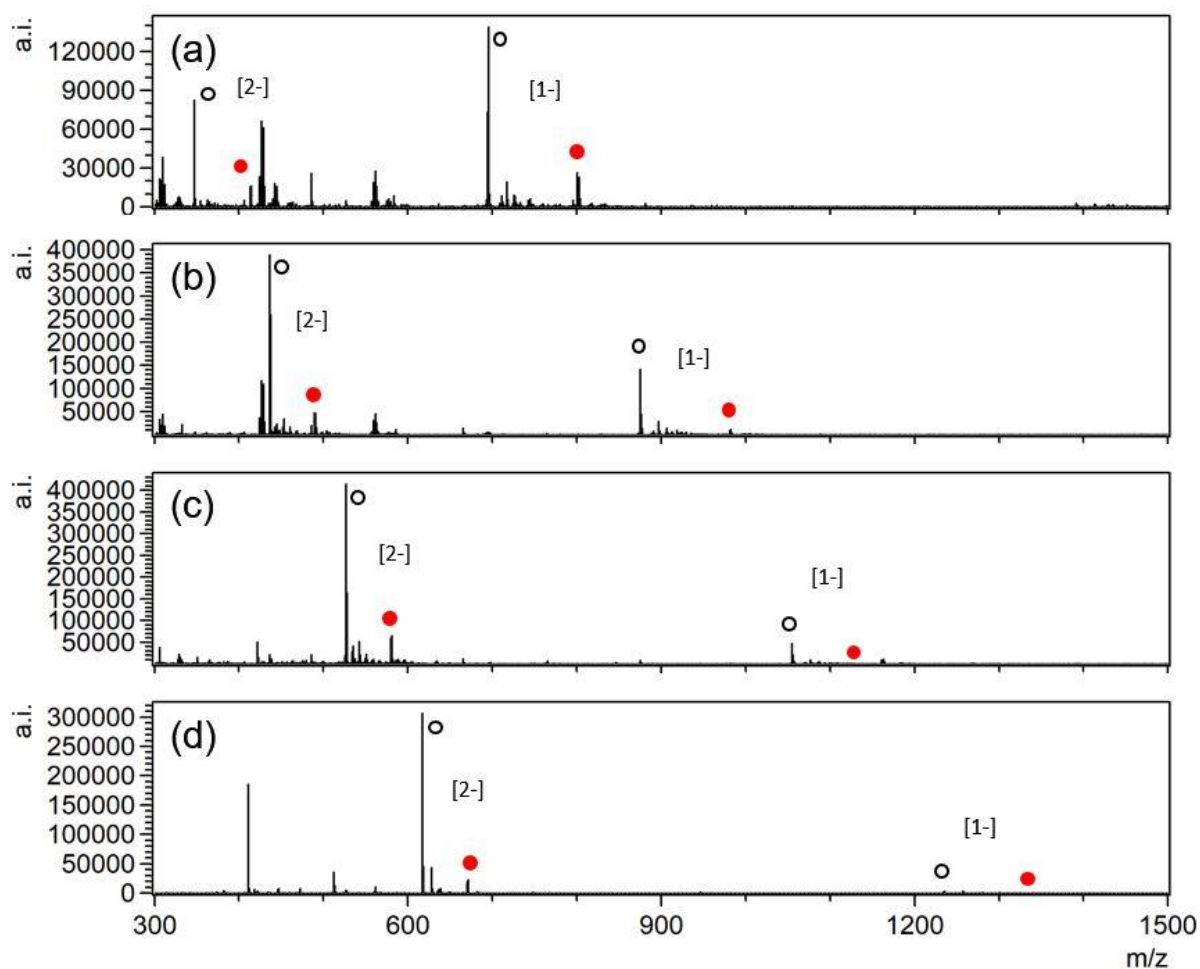


Figure 6.12 ESI-MS spectra (range: 300 – 1500 m/z) for oligonucleotides following the addition of silver(I) ions at a 1:1 ratio: (a) a^1C_1 , (b) a^2C_1 , (c) a^3C_1 and (d) a^4C_1 . Species identified as silver-bound (red-circle) and unbound oligomers (clear-circle) at 1- and 2- charge states (z).

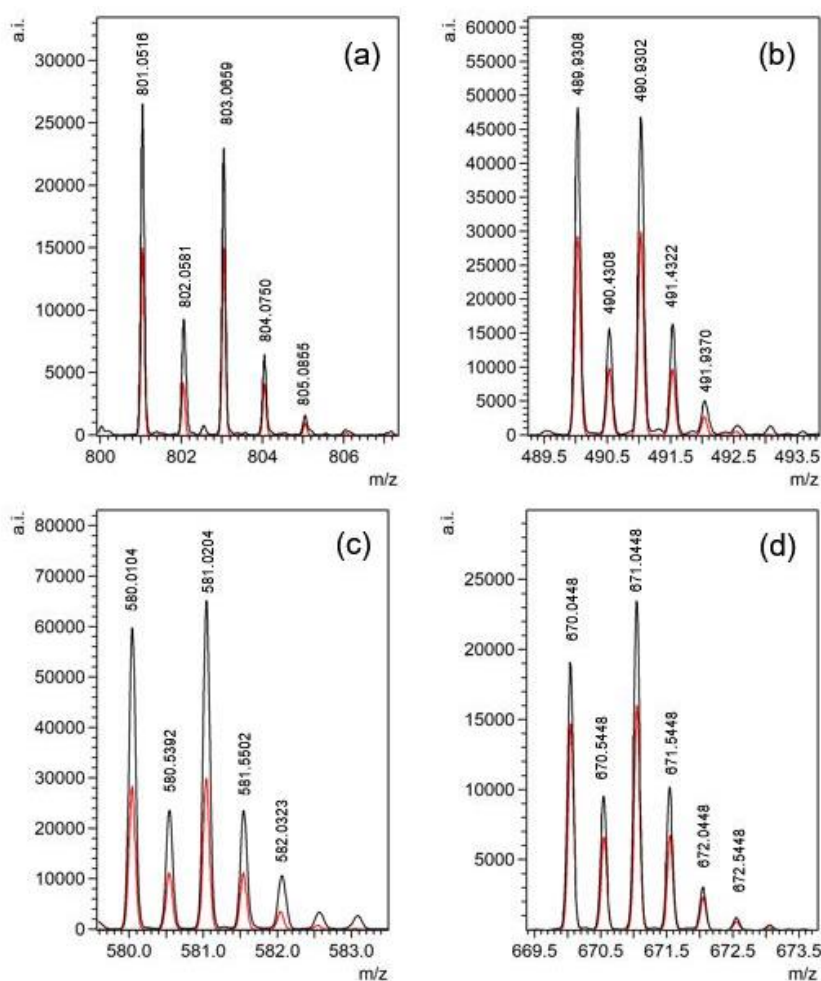


Figure 6.13 ESI-MS (negative ion mode) peak analysis for oligonucleotides (black) (a) $^1\text{C}_1$, (b) $^2\text{C}_1$, (c) $^3\text{C}_1$ and (d) $^4\text{C}_1$ following the addition of silver ions at a 1:1 ratio (Oligo: Ag^+). Overlaid theoretical isotope patterns (red) represent a $[\text{Ag}^+\text{-Oligo}]$ species at matching charge states (z) of -1 (a) or -2 (b - c).

The MS data thus far confirms interactions between a silver(I) ion and oligonucleotides in a 1:1 stoichiometry, however it cannot identify the method of interaction *i.e.* single coordination, hairpin, dimer or coordination polymer (see **Figure 6.9**). Each of these systems possess a one-to-one stoichiometry. No new peaks were observed following the addition of excess of silver, at a 2:1 ratio, however intensities of peaks identified as the metallated species increased relative to the parent oligonucleotide. To this end we incorporated the use of ion-mobility spectrometry (IMS) coupled to MS as a method of identifying larger species such as dimers or coordination polymers, which might have otherwise been concealed. IMS is a method used to separate and characterise ionised molecules in the gas phase based on their ability to move through a carrier

buffer gas. Larger molecules, e.g. dimers can be effectively separated from hairpins or single site coordination species based on their size from monomeric species.³² This additional separation stage allows for the isolation and detection of species that would normally overlap. For example, a doubly charged dimer (mass 200 a.u.) would have peaks appear overlapped with those of a smaller monomer (mass 100 a.u.) with a single charge due to their mass(*m*)-to-charge(*z*) ratios being equivalent. IMS data collected for ^{a1}C₁, ^{a2}C₁, ^{a3}C₁ and ^{a4}C₁ following the addition of silver(I) ions revealed that the dominant population were not of the dimer. Less than 1% of the global species were observed to be dimers and there was no evidence of polymerisation (*i.e.* greater than 1:1).

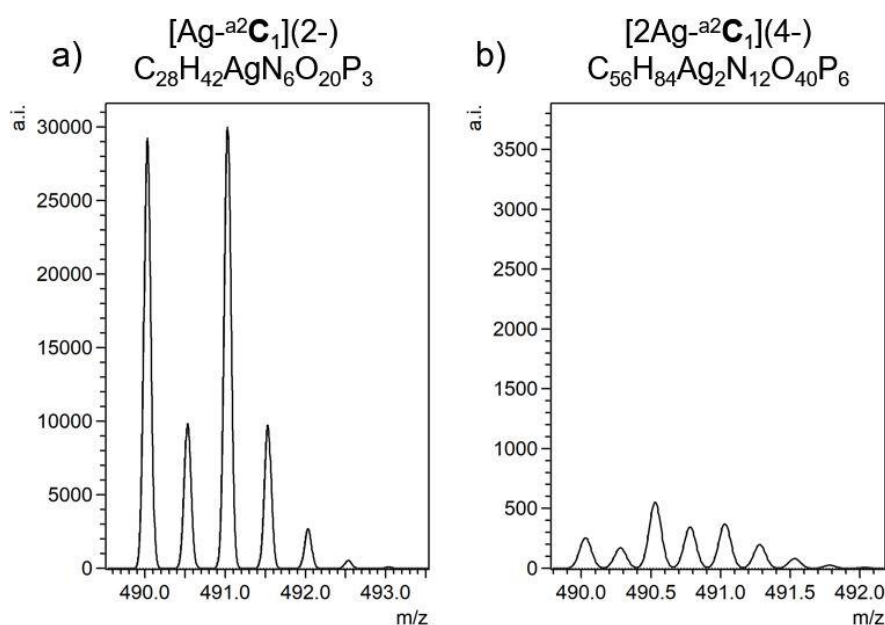


Figure 6.14 IMS-MS data for ^{a2}C₁ following the addition of silver(I) ions at a ratio of 1:1; Observed species a) a single silver(I) coupled with a single oligomer (>99%) and b) trace amounts of a macrocyclic dimer (<1%).

While these results indicate the 1:1 nature of the complex, they do not provide an insight into the structure or metal binding sites. However, circular dichroism (CD) spectroscopy is widely employed as a key method of studying the various structures of DNA (A-, B- and Z-DNA) in solution.³³ The experimental ultraviolet (UV) spectra are often similar between DNA types due to their intramolecular electronic excitations within the nucleic acid bases.³³ Yet, their CD spectra can differ significantly, even when

composed of identical nucleotides. The profile of the CD spectrum is therefore characteristic of helical types or structural differences which directly affect overall chirality.

Unfortunately, circular dichroism (CD) measurements of the short oligonucleotides (a^1C_1 , a^2C_1 , a^3C_1 and a^4C_1) showed little change following the addition of silver(I) ions; peaks observed at 220(-) and 270(+) nm remain largely unchanged when compared to oligomers (**Figure 6.15**). This is likely due to relatively short oligo sequence; which lack the continuous stacking of orientated bases required for observable changes in CD.

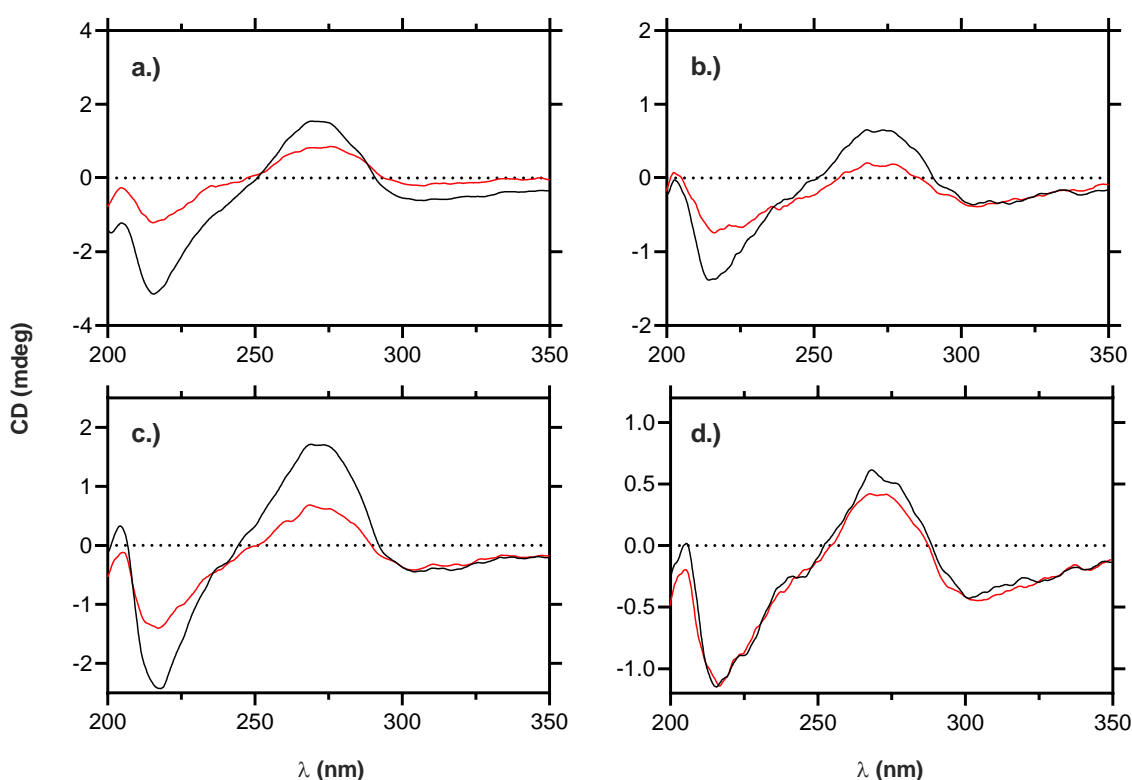


Figure 6.15 CD data for oligonucleotides (a) a^1C_1 , (b) a^2C_1 , (c) a^3C_1 and (d) a^4C_1 with (red-line) and without (black-line) silver(I) ions.

Gwinn and Swasey conducted comparable CD experiments on a series of homo-C oligonucleotides (C_2 , C_3 , C_6 and C_{20}) following the addition of silver ions.³⁴ They observed a marked change in CD character, with newly formed peaks at 290(+), 270(-), 246(+) and 220-225(-) nm (**Figure 6.16**). These changes have been associated with duplex formation achieved through metal-mediation across (N^3)C·C(N^3) sites of two

independent oligomer strands. Lopez-Acevedo *et al.*, again, achieved similar results both computationally and experimentally when investigating Ag^+ -(N^3)-bridged cytosine (C_2) sequenced oligonucleotides.³⁵ Both studies present CD data which is remarkably different in profile to that of DNA (B, Z or A).^{34,35}

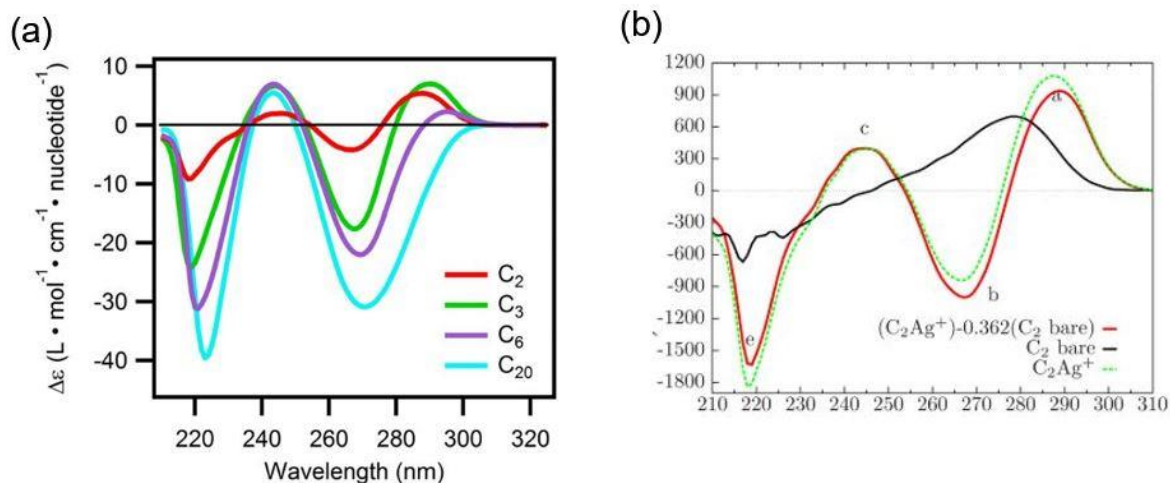


Figure 6.16 Reproduced CD spectra of homo-C short oligonucleotides conducted by (a) Gwinn and Swasey³⁴ and (b) Lopez-Acevedo³⁵ following the addition of silver ions into oligonucleotide sequences.

It is thought that the changes observed in the literature upon metalation occur only for oligonucleotide sequences possessing a minimum of two consecutive nucleobase subunits (2mer). When the bases are bonded an additional source of chirality emerges from a helical stacking of bases, mainly observed in duplexes.³⁶ The abasic loop characteristics of our systems clearly lack the consecutive base units required for such an effect. Therefore, the lack of change observed in CD profile is not evidence to the contrary.

Some conclusions can be drawn at this stage, we can state with confidence that silver-oligonucleotide interactions occur in solution spontaneously in the expected 1:1 ratio regardless of loop length. Each oligonucleotide ($^{\text{a}1}\text{C}_1$, $^{\text{a}2}\text{C}_1$, $^{\text{a}3}\text{C}_1$ and $^{\text{a}4}\text{C}_1$) examined showed masses and isotope patterns consistent with metal-coordination, $[\text{Ag}^{\text{I}}\text{-}^{\text{a}n}\text{C}_1]$ using ESI-MS. Furthermore, IMS showed little evidence for dimers or oligomer products, leaving two plausible conformations of the global species observed; single site coordination or hairpin. No further structural details could be achieved at this stage from CD.

Both $^{a2}\text{C}_n$ and $^{a3}\text{C}_n$ loop designs were judged to offer viable frameworks for stem extension. Based on the both the experimental and theoretical data obtained it was decided that hairpins bearing a $^{a2}\text{C}_n$ loop design would be explored further into stage-2.

6.7. Stage 2 – Stem Expansion

The following stage of investigation involves stem extension, increasing the capacity for metal ion loading and therefore numbers of C-Ag^I-C coordination sites. This was achieved by lengthening the stem regions by increasing the number of cytosine units either side of the central, non-binding, loop. Three oligonucleotides were designed based on the $^{a2}\text{C}_n$ model previously analysed; $^{a2}\text{C}_2$ (CCaaCC), $^{a2}\text{C}_4$ (CCCCaaCCCC) and $^{a2}\text{C}_6$ (CCCCCaaCCCCC). Each species was titrated against silver(I) ions, in attempts to sequentially fill coordination sites up to their intended capacity and analysed by ESI-MS and CD. Excess conditions were further tested against each oligonucleotide (10:1).

The shortest system, $^{a2}\text{C}_2$, initially displayed a very low binding affinity by mass spectroscopy following the titration of up to two equivalents of Ag⁺. The existence of a very low intensity signals (<10%, [Ag_n- $^{a2}\text{C}_2$]) were observed for Ag⁺-Oligo when compared to the bare oligonucleotide parent. Upon addition of an excess of Ag⁺ ions (10 equiv.) peaks correlating to oligonucleotides with both one and two bound Ag⁺ ions were clearly observed at 779 m/z, [Ag- $^{a2}\text{C}_2$]²⁻ and 832 m/z, [Ag₂- $^{a2}\text{C}_2$]²⁻ (**Figure 6.17**). The ratio of oligo, Ag-oligo and Ag₂-oligo (1.0:0.4:0.5) showed that just <50% of the oligonucleotide bound to the silver(I) ions. As mentioned earlier, a quantitative analysis post ionisation may not represent the true solution state of these systems. It is possible that the electrospray ionisation process could be stripping or reducing the captured silver(I) ions prior to detection.

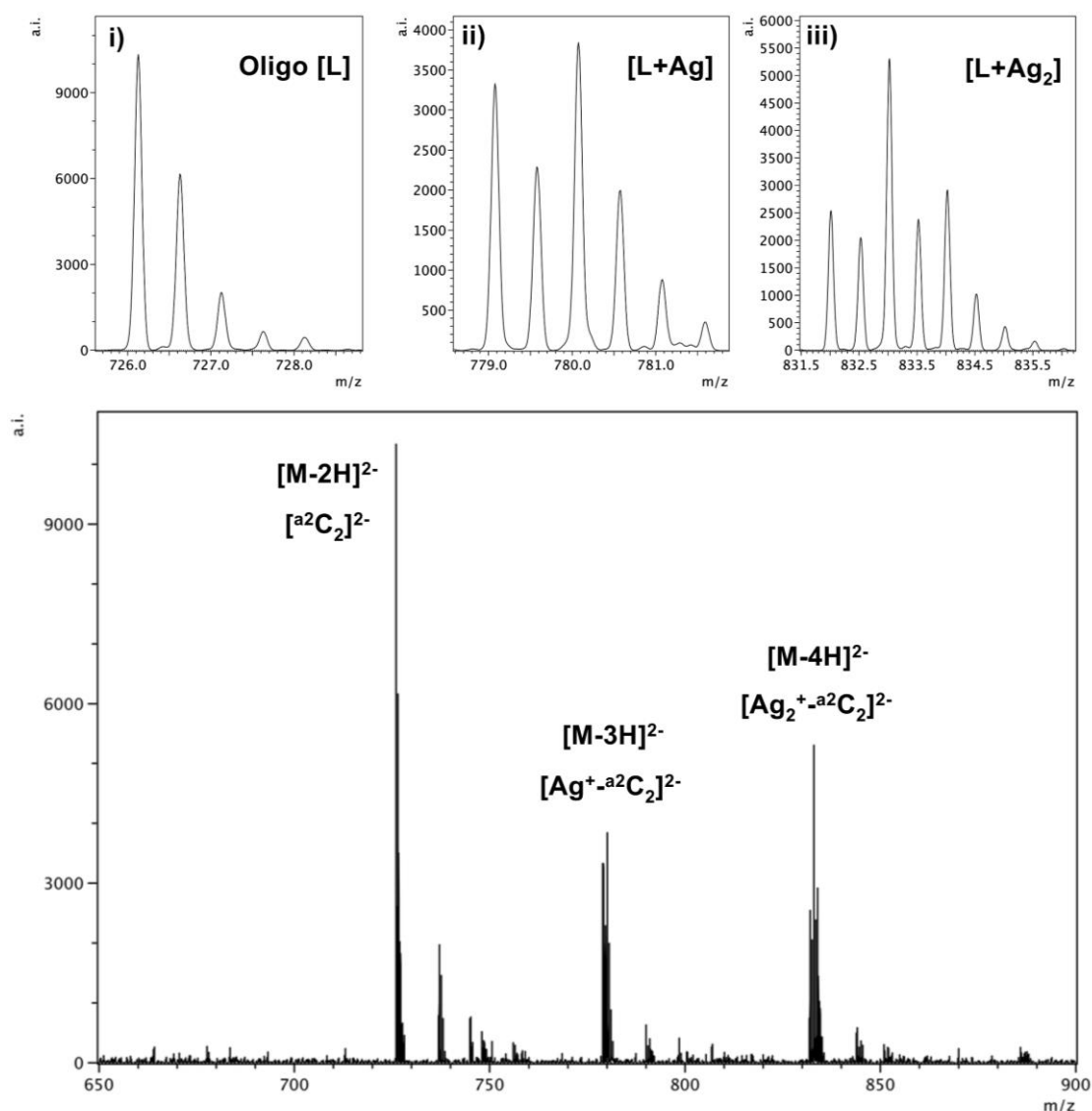


Figure 6.17 Negative ion mode ESI-MS (range 650 – 900 m/z) following the addition of excess Ag^+ (10 equiv.) to the extended hairpin a^2C_2 (a: abasic site). Identified peaks; i) a^2C_2 (726.1270 m/z, $[\text{M}-2\text{H}]^{2-}$), ii) $\text{Ag}-\text{a}^2\text{C}_2$ (779.0803 m/z, $[\text{M}-3\text{H}]^{2-}$) and iii) $\text{Ag}_2-\text{a}^2\text{C}_2$ (832.0180 m/z, $[\text{M}-4\text{H}]^{2-}$). Calculated values: 726.1263 m/z (2-) ($\text{C}_{46}\text{H}_{65}\text{N}_{12}\text{O}_{32}\text{P}_5$), 779.0750 m/z (2-) ($\text{C}_{46}\text{H}_{64}\text{AgN}_{12}\text{O}_{32}\text{P}_5$) and 832.0180 m/z (2-) ($\text{C}_{46}\text{H}_{63}\text{Ag}_2\text{N}_{12}\text{O}_{32}\text{P}_5$).

CD measurements of a^2C_2 change significantly upon addition of silver(I) ions at a 2:1 ratio of metal to oligo. Peaks common to oligonucleotides (277(+), 220(-) and 204(+) nm) saw significantly change following metal ion addition (**Figure 6.18**). Peaks newly formed at 288(+), 266(-), 213(-) and 197(+) nm are observed. The newly formed bands

change CD profile to match those of the literature for similar Ag-DNA metal-mediated systems, suggesting the N^3 -Ag^I- N^3 binding mode is present.^{34,35}

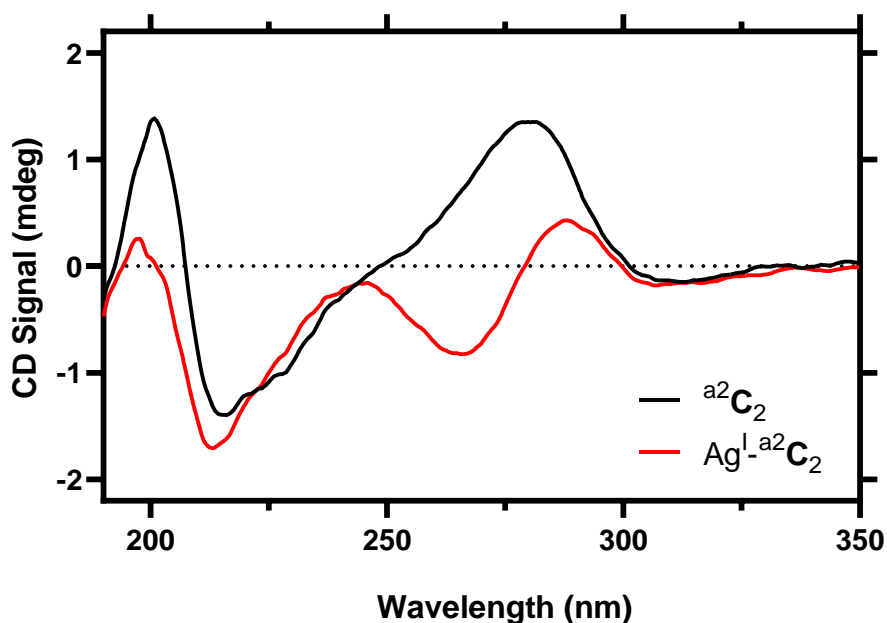


Figure 6.18 CD data for a^2C_2 before (black-line) and after (red-line) the addition of silver(I) ions at a 1:2 ratio (Oligo:Ag^I), meeting the designed metal-ion capture capacity.

MS and CD analysis of the higher capacity systems, a^2C_4 and a^2C_6 were similarly titrated against silver(I) ions. Metal ion binding was apparent in MS as the expected peaks were clearly visible relating to $[Ag_n-a^2C_x]$ (**Figure 6.19**). Again, low Ag^I-binding affinities were observed at sub-saturation stoichiometries of the C·C stem sites (ratios- 2:1, 4:1 and 6:1 (metal:oligomer)). Upon addition of an excess Ag⁺ ions (10 equiv.) the filled Ag-bound oligonucleotides are readily observed for all three cases (a^2C_2 , a^2C_4 and a^2C_6).

CD profiles for a^2C_2 , a^2C_4 and a^2C_6 all showed changes associated with metal-mediation akin to those in the literature for similar Ag-DNA systems.^{34,35,37,38} Peaks at 288(+), 266(-), 213(-) and 197(+) nm are observed upon addition of silver(I) at the 2:1, 4:1 and 6:1 ratio's for a^2C_2 , a^2C_4 and a^2C_6 respectively (**Figure 6.19**).

MS data showed a distribution of peaks within a given charge state (z), which were identified containing one-to-four bound silver for a^2C_4 , and one, three, four and five for a^2C_6 . The inability for a^2C_6 to achieve a filled state bearing six silver ions was puzzling.

Perhaps higher capacity systems encounter a previously unseen energetic barrier, reducing their abilities to fill to their designed maximum capacity, even under excess metal ion conditions.

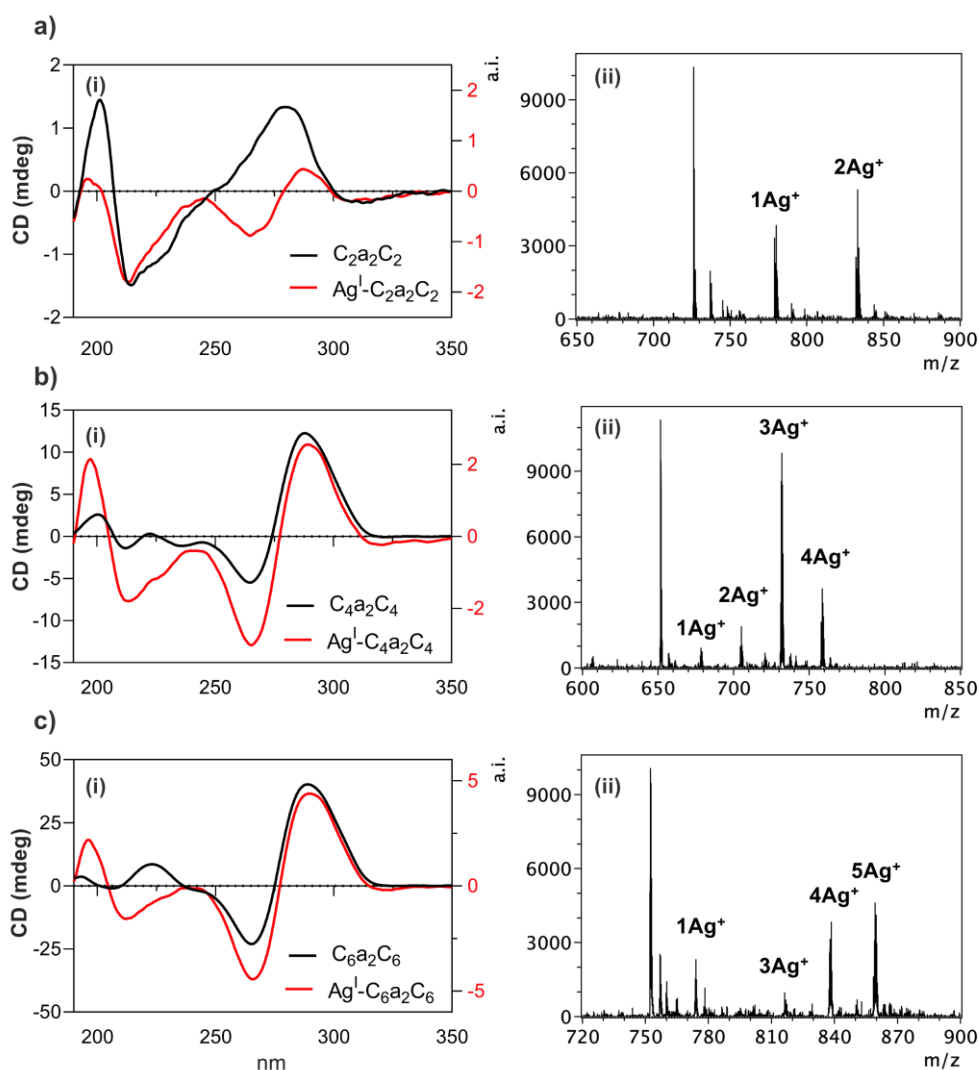


Figure 6.19 (i) Circular Dichroism (at 25°C, γ = MDeg) at a) 2:1, b) 4:1 and c) 6:1 metal to oligomer ratios (2:1 base-to-metal ratio). (ii) ESI-MS (negative ion mode) data for all three-oligonucleotide designed for stem optimisation; a) a^2C_2 , b) a^2C_4 and c) a^2C_6 following the addition of excess Ag^I ions (10 equiv.).

It was interesting to observe that upon elongation of the oligomer stem regions (**C₂**, **C₄** and **C₆**) the CD profile changed significantly (**Figure 6.20**). The CD transformations observed were remarkably similar to those achieved in the literature following coordination with silver, although the amplitude is much greater. Peaks at 290(+), 270(-) and 225(+) grow-in with an increased signal intensity as the oligonucleotide

systems increases in length. A significant change in the amplitude around the split CD curve. This has the effect of shifting the exciton splitting value from 250 nm (a^2C_2) to 275 nm (a^2C_4 and a^2C_6). Such a dramatic shift in the profile of the CD is thought to be indicative of metal-mediation and is consistent with the changes observed for similar systems in the literature.

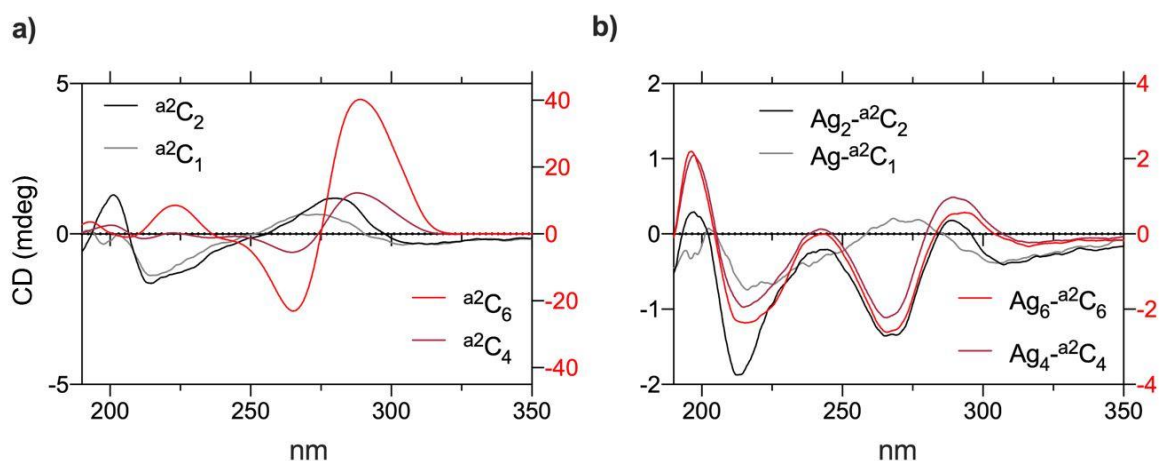


Figure 6.20 Circular dichroism data for a^2C_n hairpin oligonucleotide series (n : 1, 2, 4 and 6); a) before and b) after the addition of excess silver(I) ions (10 equiv.).

It is interesting to note here that natural DNA strands which are cytosine rich tend to spontaneously generate duplexes or dimers (also known as an *i*-motif). The mismatched C-C pair connect through a hemi-protonated C^+ (**Figure 6.21**).³⁹ These cytosine dimers have a characteristic CD spectrum with a dominant positive band at 290 nm. However, such systems are known to have intrinsically slow kinetics and require slightly acidic conditions ($pH < 6.5$).⁴⁰ This effect could explain the phenomena seen in **Figure 6.20**. All experimental measurements conducted in this study were carried out in nanopure-deionised-water; however, the pH was not monitored.

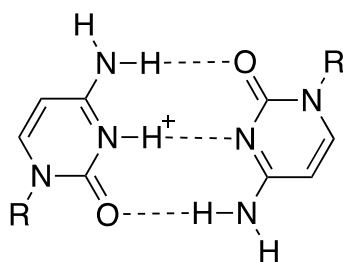
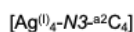
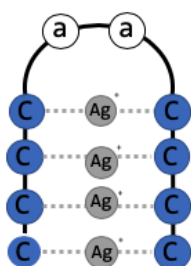


Figure 6.21 Hemiprotonated C-C⁺ pair promoted by slightly acidic pH (pK_a ~4.5⁴¹).^{39,40}

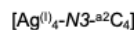
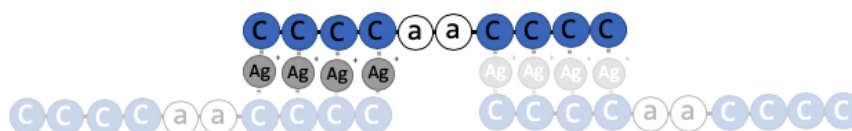
To further interrogate the structure and binding modes observed in both MS and CD, Isothermal titration calorimetry (ITC) was used as a method of thermal quantification of bonding interactions between the oligonucleotides and introduced metal ions. The amount of heat liberated (exothermic (-)) or absorbed (endothermic (+)) as the reaction proceeds can be quantified as coordination events. The number of thermally quantified coordination events can be used to identify a binding mode (**Figure 6.22**). This analysis assumes the only interaction between the silver ion and oligo occur at the expected N³ position along the C-rich stem.

8 coordination events per oligo



Hairpin Structure

4 coordination events per oligo



Single Site Coordination

Figure 6.22 An illustration of the two theoretically possible binding modes, hairpin (LHS) vs. single site interaction (RHS), highlighting the number of possible coordination events per oligonucleotide sequence.

A concentrated solution of AgNO_3 (5.0 mM) was titrated against ${}^{\text{a}2}\text{C}_4$ (0.1 mM) held at 25°C gave a clear sigmodal isotherm (**Figure 6.23**). The negative peaks indicate an exothermic reaction, releasing -14.3 kcal/mol of energy.⁴² Using ITC data from chapter 2 as a reference; a simple silver-cytosine (nucleobase) interaction ($\text{C-Ag}^+-\text{C}$) released -5.1 Kcal/mol of energy. We observed approximately a threefold difference in energy (ΔH) for the metalation of ${}^{\text{a}2}\text{C}_4$. The molar ratio (n) was calculated at 1.45 and binding constant (K_{a}) was 7006 M^{-1} .

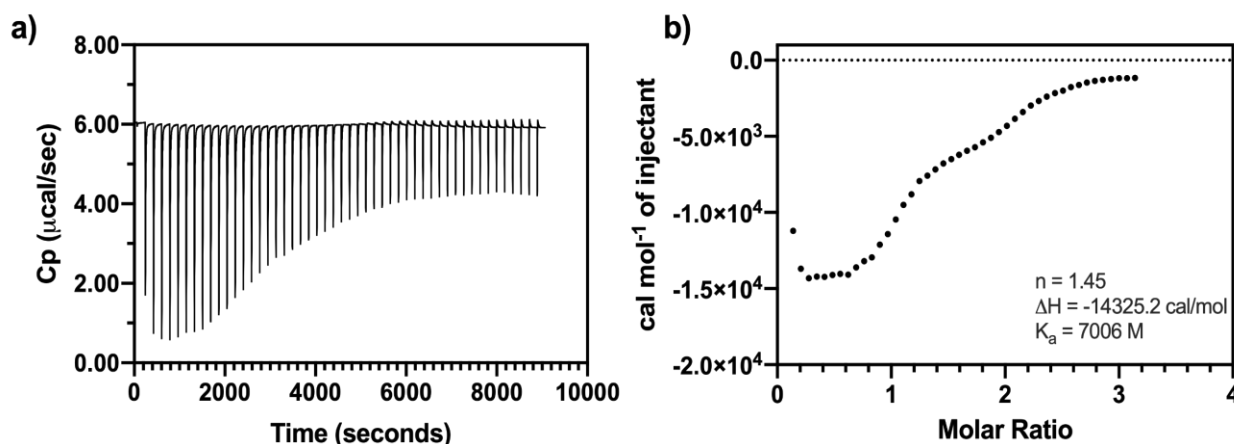


Figure 6.23 Isothermal titration calorimetry (ITC) (a) raw isotherm data and (b) A integrated Wiseman plot for the hairpin sequence ${}^{\text{a}2}\text{C}_4$ (0.1 mM) following the injection of silver(I) ions (AgNO_3 , 5.0 mM, 25°C).

The ${}^{\text{a}2}\text{C}_4$ system has shown characteristics which make it a suitable model at this stage of investigation to help identify the most likely binding mode; Hairpin vs. single site. By collaborating the results from MS and ITC we can make such a deduction.

ESI-MS for ${}^{\text{a}2}\text{C}_4$ displayed strong interactions with silver(I) ions with up to four bound per oligo as intended. The most abundant M-oligo species was $[\text{Ag}^{\text{I}}_3\text{-}{}^{\text{a}2}\text{C}_4]$ with 35% (59% metal ion loading). Species identifiable as coordination-polymers (single site, **Figure 6.22**) were not observed in MS and IMS studies previously only showed only trace amounts of dimerization. However, individual single site and hairpin conformations are both still possible from the available MS data.

To further evaluate the method of binding ITC was used. ITC was able to thermally quantify binding events. If the molar ratio value deduced by ITC was eight or less, it would indicate hairpin formation; two coordination sites per silver ion, with a maximum

of four silver ions per oligo. If this value was greater, it would likely indicate single site coordination. Using the simplest system, $[\text{Ag}^{\text{I}}\text{-(cytosine)}_2]$ (-5.1 kcal/mol) as a reference the addition of silver ions to $^{\text{a}2}\text{C}_4$ released -14.3 kcal/mol (**Figure 6.23**), approximately three times greater. This is consistent with the MS data which demonstrated a $\frac{3}{4}$ filled species as most abundant. If a single site binding mode had occurred, the species detected in MS would have six bound silver ions per oligo, which would be clearly characterized in the isotope splitting patterns. This was not observed; therefore, a hairpin-type structure is the most likely outcome for $[\text{Ag}^{\text{I}}_n\text{-}^{\text{a}2}\text{C}_4]$ species.

The weaknesses in this method of analysis lie in a single site interaction model used. For instances of cooperativity or multiple binding sites, means a single-site models are not particularly accurate. Therefore, molar ratio (n) and binding constants (K_{a}) are not considered. However, the overall energy released from the system (ΔH) remains accurate regardless of the mathematical model used.

In conclusion to this second stage of investigation exploring the extension of homo-C stem regions and therefore increasing the number of C-Ag-C sites, we have demonstrated the ability of silver(I) ions to coordinate to a series oligonucleotide ($^{\text{a}2}\text{C}_2$, $^{\text{a}2}\text{C}_4$ and $^{\text{a}2}\text{C}_6$) by spectroscopic (CD) and physical techniques (ESI-MS, ITC). We were able to determine the binding characteristics within higher silver ion capacity oligonucleotide systems. Furthermore, we are finally able to infer a preference towards hairpin type conformations over a single site coordination motif. This was achieved by ITC, a thermal quantification technique. Thus far, we have established a suitable loop length (two or greater) and have proven that metal-mediation can occur with homo-C stem regions likely forming the desired hairpin type structures.

At present these designer oligomer sequences are not cost efficient due to the modified abasic loop units, therefore, more common nucleotide alternative units will be considered hereafter.

6.8. Stage 3 – Exchanging abasic for thymine loop units

The third stage of the investigation focuses on replacement of the modified abasic units within in loop for a standardised DNA base. This is achieved by exchanging the abasic (a) units for thymine (T) (**Figure 6.24**). At the time of investigation, thymine was known to have limited interactions with silver(I) ions.^{43,44} By making this exchange we aim to

retain a flexible non-binding loop region using more economic building blocks. Furthermore, we hope to address concerns found during the second stage of our investigation, whereby loops of just two-units were potentially hindering the saturation of metal ions. This was observed by the incomplete filling of the mismatched stem C·C sites in the MS. The characteristics and properties of two- and three T-looped (T^2C_n and T^3C_n) systems were evaluated and compared against their abasic counterparts.

To begin, we re-evaluated loop performance akin to stage-1, exchanging abasic units with thymine (**Figure 6.24**). Oligonucleotides C-(T) $_n$ -C (T: Thymine, $n = 1 - 4$) (T^1C_1 (CTC), T^2C_1 (CTTC), T^3C_1 (CTTTC) and T^4C_1 (CTTTTC)) were designed.

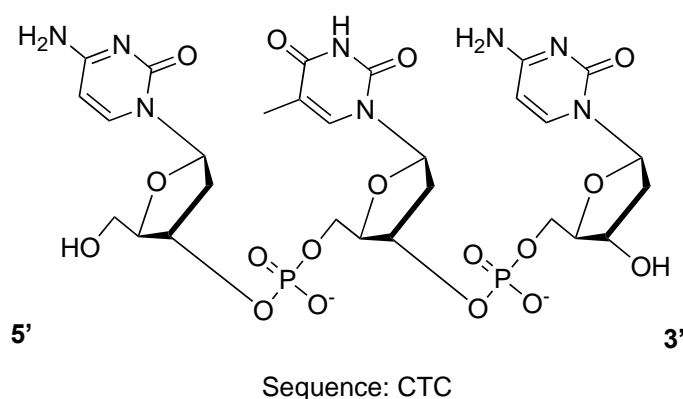


Figure 6.24 A diagram representing the shortest T-loop oligonucleotide, T^1C_1 (CTC).

Analogous to the short abasic oligonucleotides explored in stage 1, a series of computational calculations were conducted, again, using classical molecular minimisation techniques performed by the Bronowska group (Joao Victor De Souza Cunha) at Newcastle university. The inclusion of the T nucleoside units into the loop region introduces additional bulk and is therefore likely, to be a less flexible or have encumbered system towards the folding into a hairpin complex. The computational studies described below, investigate such effects.

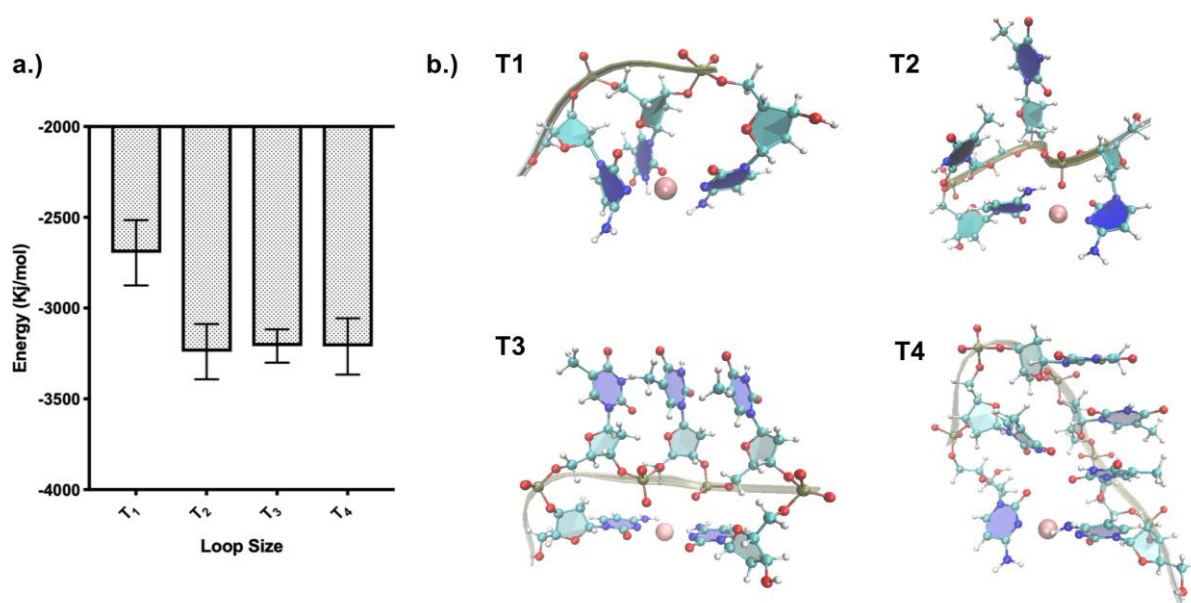


Figure 6.25 a) Energy minimisation results for a series of silver(I) coordinated short T-loop hairpin-systems (T^1C_1 , T^2C_1 , T^3C_1 and T^4C_1) using classical molecular minimisation techniques. b) Illustrations of the lowest energy confirmations possible for each silver-mediated T-looped system.

The T-loop hairpin models represent four macrocyclic systems bound across a single silver ion at the terminal 3' and 5' N^3 -cytosine bases. The designed loops have one-to-four thymine units. These structures were classically minimised in water in an identical fashion to those in stage 1 (180° angles of restraint across the N^3 -Ag^I- N^{3*} and distances of 2.2 Å between the N^3 -donors and the central coordinating Ag^I-ion). The data received and displayed in **Figure 6.25**, represent the energy profiles for Ag⁺-mediated T-loop hairpins, which clearly favours loops dimensions of greater than one base unit ($T^2C_1 > T^3C_1 > T^4C_1 > T^1C_1$). T^2C_1 , T^3C_1 and T^4C_1 loops are all remarkably similar and have the highest average energetic gain (-450 kJ/mol) compared to T^1C_1 following coordination of the Ag^I-ion.

The shortest model, T^1C_1 clearly displays non-coplanar coordinating cytosine bases due to the accommodation of a linear (180°) N^3 -Ag⁺- N^3 geometry. Interestingly, the T^1C_1 loop demonstrated a third coordination through the O^2 acceptor of the thymine (distance: 2.3 Å). Thymine has the potential to establish metal binding at O^2 , N^3 and O^4 sites, but generally the exocyclic O donors are favoured. However, these produce

compounds with relatively low thermodynamic stability.⁴⁴ Nevertheless, an interesting phenomenon that is unseen in any of the longer oligo macrocycles.

It is positive to note that the hairpins formed by longer loop regions have greater preference towards a chelate configuration, likely due to their reduced internal strain. This was also observed within abasic loop calculation. Interestingly, the two longest T-loops (T^3C_1 and T^4C_1) allow for the formation of stabilizing π - π stacking interactions between both T...T and C...T ring systems. This effect is somewhat offset by the increased flexibility of longer systems; therefore, the stabilizing effect does not lead to any significant gains energetically over a T^2C_2 hairpin. From these simulations, it was concluded that the use of T^2C_n and T^3C_n were both good candidates for further experimental study. Energetically they both have similar characteristics, however, concerns from stage 2 lead us to lean towards longer looped systems. Due to the lower costs associated with T-looped short oligonucleotides, we opted to experimentally characterise all four oligonucleotides: T^1C_1 , T^2C_1 , T^3C_1 and T^4C_1 .

Experimental MS and CD were conducted following the computational simulations of short T-loop oligonucleotides (T^1C_1 , T^2C_1 , T^3C_1 and T^4C_1), with a designed capacity of a single silver(I) ion across the terminal C-C base units (3' and 5') forming a metal-mediated macrocycle akin to stage 1.

ESI-MS data collected confirmed the presence and isotope patterns predicted for oligonucleotides T^1C_1 , T^2C_1 , T^3C_1 and T^4C_1 solutions with charge states (z) of -1, -2 and -3 being most abundant. Following the addition of silver(I) ions at a 1:1 (metal:oligomer) ratio, new peaks were observed with m/z values and isotope patterns expected for the addition of a single silver(I) ion per oligonucleotide ($Ag-T^1C_1$, $Ag-T^2C_1$, $Ag-T^3C_1$ and $Ag-T^4C_1$) (**Table 6.2** and **Figure 6.26**).

#	Sample	Exp (calc.) m/z		
		m/-1	m/-2	m/-3
1	^{T1} C ₁	819.1757 (818.5784)	409.0821 (408.7855)	-
2	Ag- ^{T1} C ₁	925.0674 (925.0730)	462.0374 (462.0329)	-
3	^{T2} C ₁	1123.2208 (1123.2218)	561.1089 (561.1072)	-
4	Ag- ^{T2} C ₁	1230.0981 (1230.1269)	614.0522 (614.5598)	-
5	^{T3} C ₁	-	713.1301 (713.1303)	475.0981 (475.0844)
6	Ag- ^{T3} C ₁	-	766.5810 (766.5828)	510.7200 (510.7195)
7	^{T4} C ₁	-	865.2001 (863.6415)	576.4510 (575.4253)
8	Ag- ^{T4} C ₁	-	-	612.0689 (611.0603)

Table 6.2 ESI-MS monoisotopic mass peak data for oligonucleotides: ^{T1}C₁, ^{T2}C₁, ^{T3}C₁ and ^{T4}C₁, following the addition of silver(I) ions *versus* theoretical values for -1, -2 and -3 charge (z) states (See Appendix for full spectra).

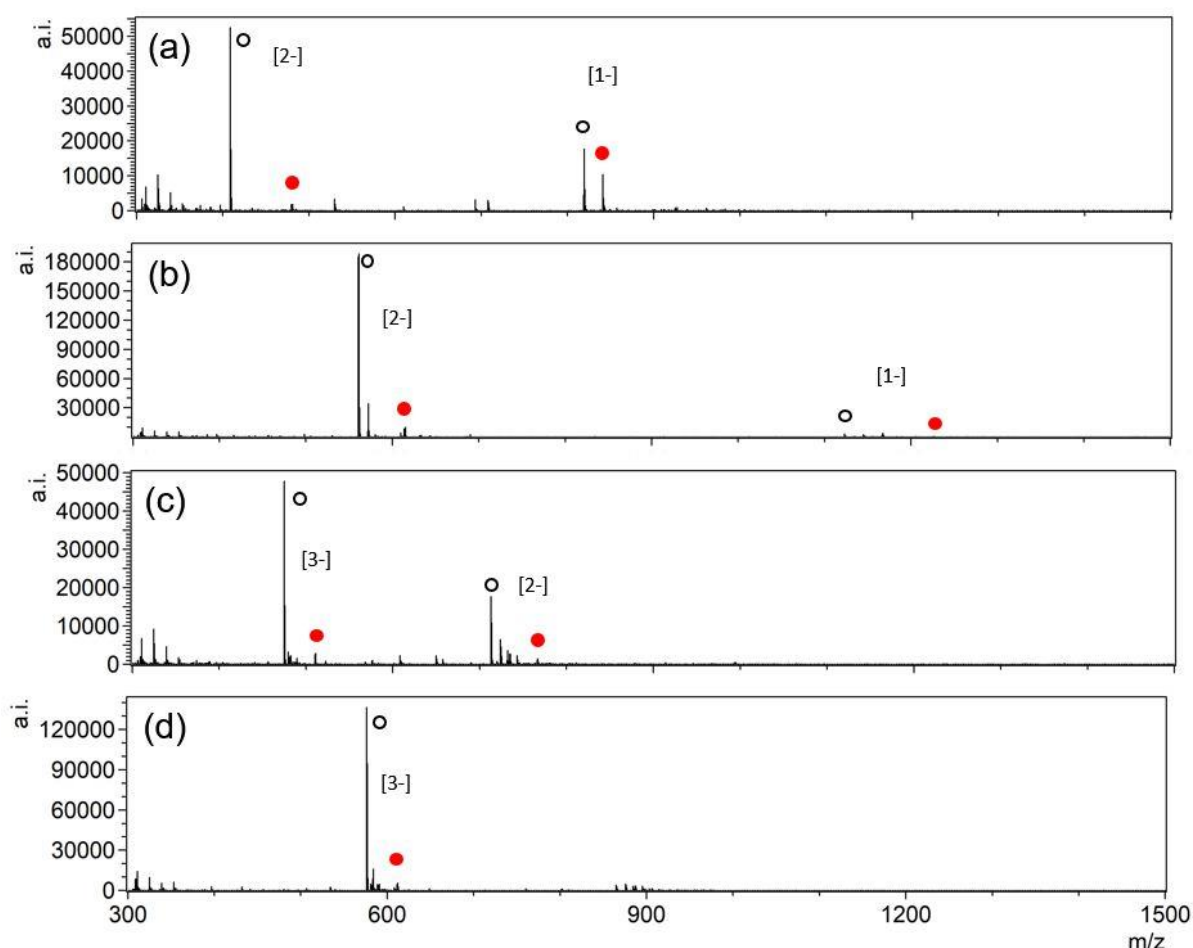


Figure 6.26 ESI-MS spectra (range: 300 – 1500 m/z) for oligonucleotides: (a) T^1C_1 , (b) T^2C_1 , (c) T^3C_1 and (d) T^4C_1 , following the addition of silver(I) ions at a 1:1 ratio. Species identified as silver-bound (red-circle) and unbound oligomers (clear-circle) at 1-, 2- and 3- charge states (z).

CD spectra for T^1C_1 , T^2C_1 , T^3C_1 and T^4C_1 showed the expected peaks common to ss-DNA at 278(+), 237(-), 213(-) and 193(+) nm (**Figure 6.27**). Following the addition of silver(I) (1:1 ratio) several changes occur in the CD profiles for all oligonucleotides. A red shift can be seen as the exciton splitting point appears at a longer wavelength. This effect differs between each silver-bound oligomer; 255 → 276 (T^1C_1), 260 → 272 (T^2C_1) and 263 → 266 nm (T^3C_1 and T^4C_1). These shifts become lesser as oligomer length increases. The shortest two oligomer T^1C_1 and T^2C_1 displayed several new peaks that can be seen at : 265(-), 282(+) and 214(+), 252(-), 281(+) nm respectfully. It is unclear why T^3C_1 and T^4C_1 did not experience similar changes. Speculation as to why this is the case could lead one to assume the existence of alternative binding modes

exclusive to extremely short oligomers, *i.e.* dimers, coordination polymers or T-Ag-T interactions.

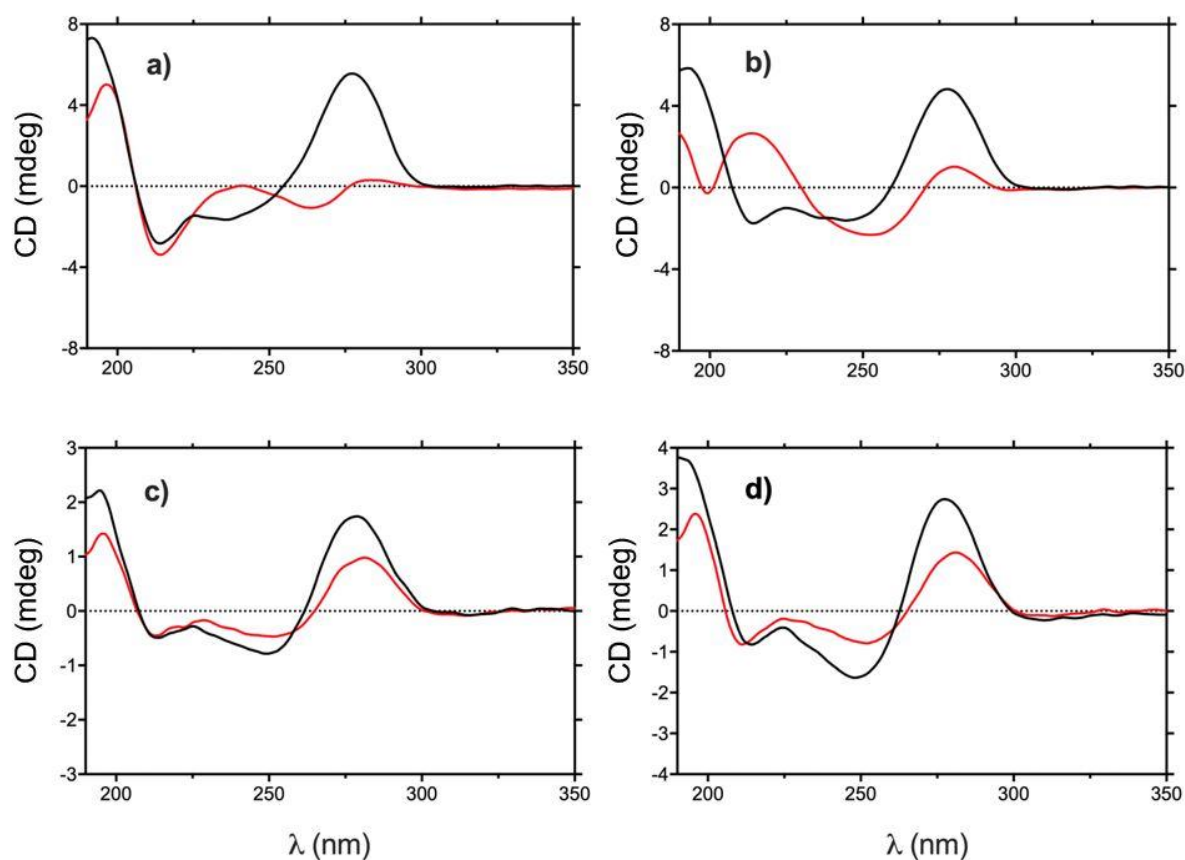


Figure 6.27 CD data for short T-looped oligonucleotides a) T^1C_1 , b) T^2C_1 , c) T^3C_1 and d) T^4C_1 before (black) and after (red) the addition of silver(I) ions at a 1:1 (metal:oligomer) ratio.

Having evaluated a series of viable thymine-loop oligonucleotide designs, the investigation moved onto extending the C-rich stem region of T^2C_n and T^3C_n systems (where $n = 2, 4$ or 6). Increasing the length of the C-rich stem regions will increase the capacity for silver ion capture, akin to stage 2. Two sets of oligonucleotides were acquired, T^2C_2 , T^2C_4 , T^2C_6 and T^3C_2 , T^3C_4 , T^3C_6 .

CD spectra for T^2C_2 , T^2C_4 and T^2C_6 were as expected for ss-DNA, showing peaks at 198(+), 212(-), 249(-) and 281(+) nm (**Figure 6.28**). Following the addition of silver(I) ions (at 2:1, 4:1 and 6:1 (metal:oligomer) ratios respectively) their CD profiles changed

significantly, peaks appeared at 196(+), 214(-), 242(+), 266(-) and 290(+) nm, matching those in literature for similar duplexed M-DNA type system.

Confirmation of Ag^+ binding to $^{\text{T}2}\text{C}_2$, $^{\text{T}2}\text{C}_4$ and $^{\text{T}2}\text{C}_6$ was observed in the MS data. Upon titration of silver nitrate (up to an excess of 10 equiv.), the formation of peaks associated with metal-oligonucleotide complexation could clearly be seen. Isotope patterns revealed the binding of metal ions up to each oligomer's designed Ag^+ capacity. $^{\text{T}2}\text{C}_2$ was observed to bind one (602 m/z, 7%) and two (637 m/z, 91%) silver(I) ions with a -3 charge (z). $^{\text{T}2}\text{C}_4$ was observed to bind one (740 m/z, 3%), two (767 m/z, 10%), three (793 m/z, 46%) and four (820 m/z, 39%) silver(I) ions identified with a -4 charge (z). $^{\text{T}2}\text{C}_6$ was observed to bind three (865 m/z, 3%), four (887 m/z, 24%), five (908 m/z, 57%) and six (929 m/z, 16%) silver(I) ions identified with a -5 charge (z). Encouragingly, very little of the bare oligonucleotides remained visible in the MS spectra following the addition of metal ions; a notable improvement over analogous abasic systems explored in stage 2.

For the longest two oligomer systems, $^{\text{T}2}\text{C}_4$ and $^{\text{T}2}\text{C}_6$, a distribution of populated states can be seen. The most populous species are three and five bound Ag^+ for $^{\text{T}2}\text{C}_4$ and $^{\text{T}2}\text{C}_6$ respectively. This behaviour is indicative of cooperativity and will further be discussed later in this chapter.

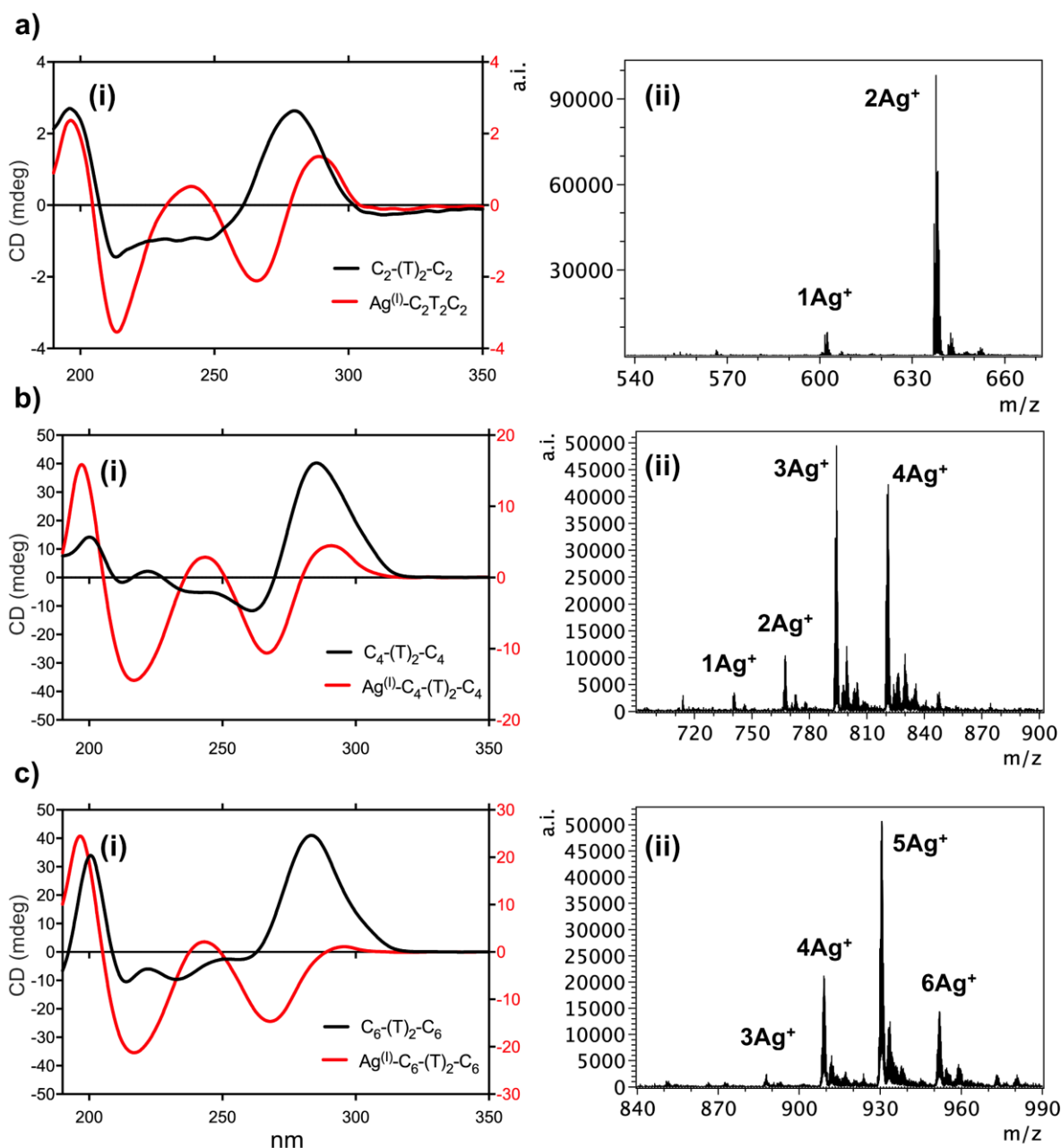


Figure 6.28 (i) CD (at 25°C, $y = M$ Deg) at a) 2:1, b) 4:1 and c) 6:1 metal to oligomer ratios. (ii) ESI-MS (negative ion mode) data for three T^2C_n oligonucleotides (n : 2, 4 and 6); a) T^2C_2 , b) T^2C_4 and c) T^2C_6 following the addition of excess Ag^+ ions (10:1 metal to oligomer ratio).

CD spectra for T^3C_2 , T^3C_4 and T^3C_6 were again as expected for ss-DNA, showing bands at 223(+), 261(-) and 277(+) nm (**Figure 6.29**). Following the addition of silver(I) ions (at 2:1, 4:1 and 6:1 (metal:oligo) ratios respectively) the CD profiles changed significantly for $[Ag_n-T^3C_2]$, $[Ag_n-T^3C_4]$ and $[Ag_n-T^3C_6]$; matching those in the literature

for duplexed M-DNA system. Peaks appear at 197(+), 216(-), 242(+), 262(-) and 286(+) nm with a red shift of between 6 - 18 nm in the exciton splitting.

Confirmation of Ag^+ binding to $^{\text{T}3}\text{C}_2$, $^{\text{T}3}\text{C}_4$ and $^{\text{T}3}\text{C}_6$ was again observed in the MS data (**Figure 6.29**). Upon titration of silver nitrate (up to an excess of 10 equiv.), the formation of peaks associated with metal-oligonucleotide complexation could clearly be seen. Isotope patterns revealed the binding of metal ions up to each oligomer's designed Ag^+ capacity. $^{\text{T}3}\text{C}_2$ was observed to bind one (703 m/z, 21%) and two (738 m/z, 29%) silver(I) ions identified with a -3 charge (z). $^{\text{T}3}\text{C}_4$ was observed to bind one (653 m/z, 2%), two (674 m/z, 18%), three (695 m/z, 69%) and four (716 m/z, 9%) silver(I) ions identified with a -5 charge (z). $^{\text{T}3}\text{C}_6$ was observed to bind three (772 m/z, 2%), four (790 m/z, 9%), five (807 m/z, 52%) and six (825 m/z, 37%) silver(I) ions identified with a -6 charge (z). Akin to the $^{\text{T}2}\text{C}_n$ systems, very little could be observed of the stock oligonucleotides in the MS data following the addition of metal ions.

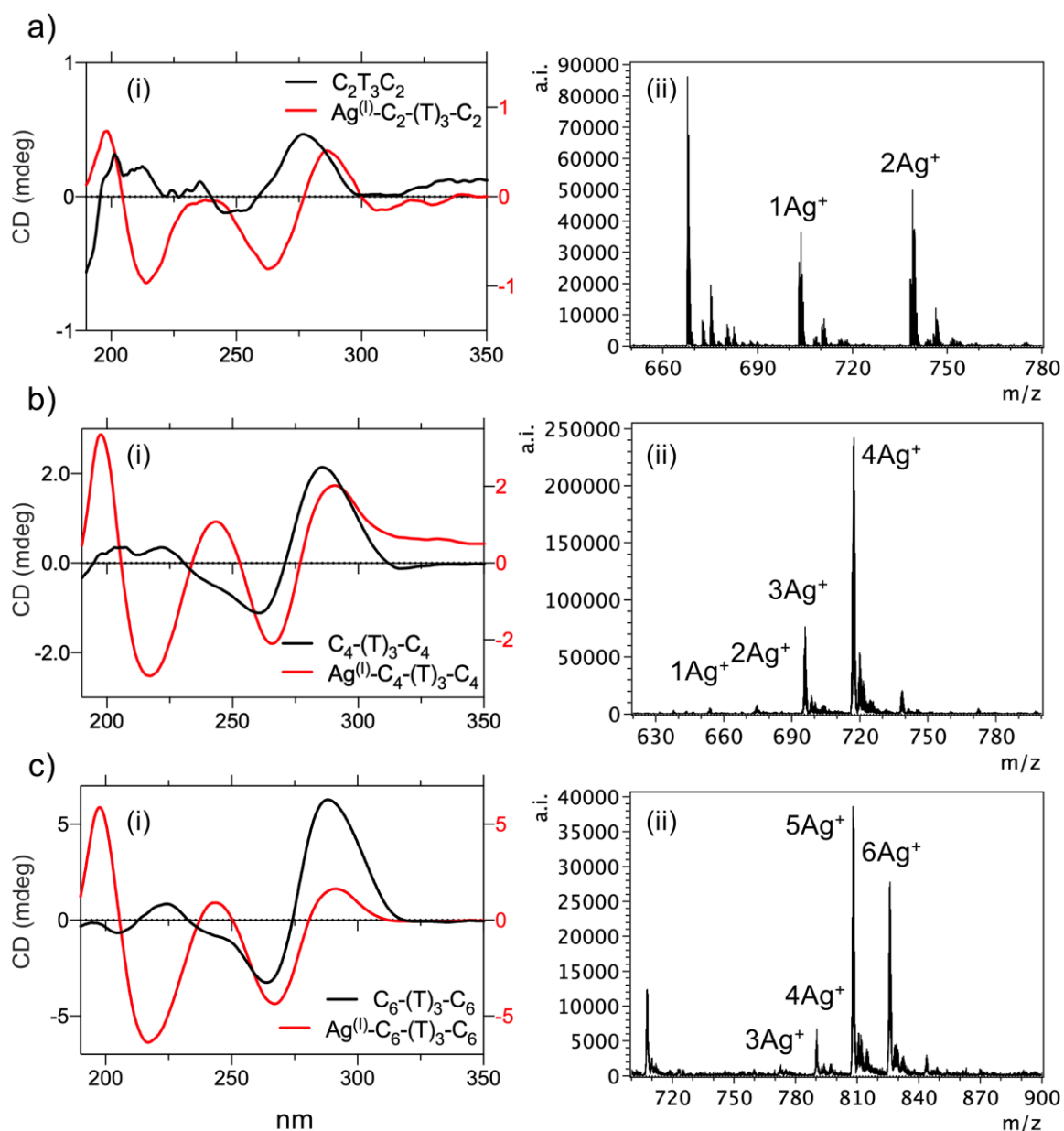


Figure 6.29 (i) CD (at 25°C, $y = M\text{Deg}$) at a) 2:1, b) 4:1 and c) 6:1 metal to oligomer ratios. (ii) ESI-MS (negative ion mode) data for three T^3C_n oligonucleotides (n : 2, 4 and 6); a) T^3C_2 , b) T^3C_4 and c) T^3C_6 following the addition of excess Ag^I ions (10:1 metal to oligomer ratio).

Figure 6.30 below directly compares MS peak intensities of the oligonucleotides a^2C_n , T^2C_n and T^3C_n ($n = 2, 4$ and 6) following metal ion addition (excess-only) in an attempt to review the characteristics of each oligo type (a^2C_n , T^2C_n and T^3C_n) side-by-side. All oligonucleotide systems behave similarly, binding with Ag^+ ions up to but not exceeding their designed capacity. Both T^2C_n and T^3C_n have demonstrated a general ability to bind

better with silver ions than the $^{a2}\text{C}_n$ type oligonucleotides. At each stem length tested ($n = 2, 4$ or 6), a significant population of oligonucleotide remained unbound to any Ag^+ for abasic ($^{a2}\text{C}_n$) loop species. However, both $^{T2}\text{C}_n$ and $^{T3}\text{C}_n$ type oligonucleotides typically achieved $>97\%$ metalation with silver(I), with the exception being $^{T3}\text{C}_2$. Generally, $^{T2}\text{C}_n > ^{T3}\text{C}_n$ at lower capacities ($n = 2$ and 4), but reversed, $^{T3}\text{C}_n > ^{T2}\text{C}_n$, at higher capacities ($n = 6$). It is thought that higher capacity hairpin systems require greater flexibility in the loop, however, this is speculation based on the limited data presented here.

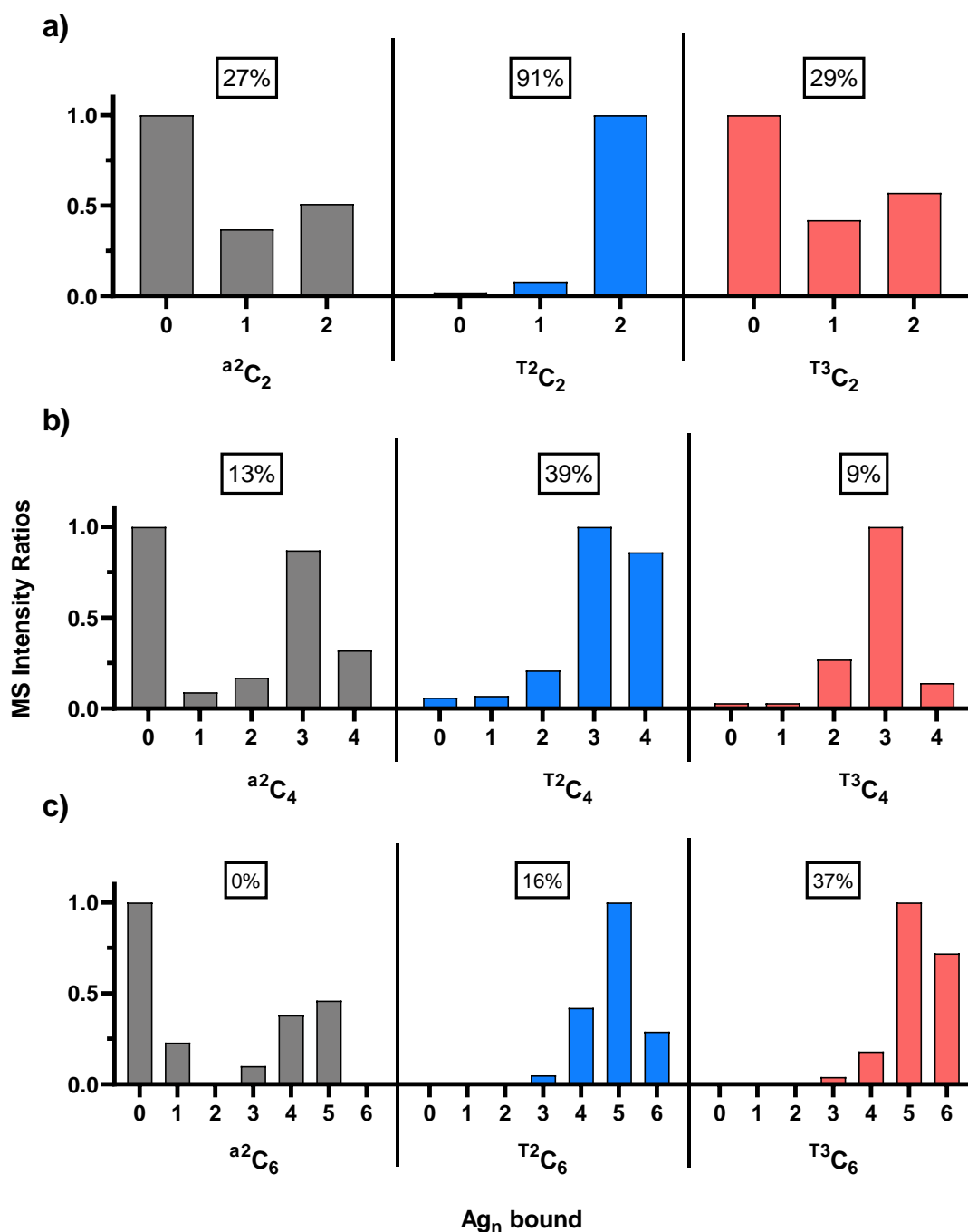


Figure 6.30 ESI-MS peak intensity analysis between a^2C_n (grey), T^2C_n (blue) and T^3C_n (red) oligonucleotides ratios following the addition of excess silver(I)-ions (10:1 metal to oligomer). Homo-C stem length or Ag^+ capacity: a) two, b) four and c) six. Inset; percentages of filled Ag_n -bound species *versus* the total sum of partially bound and unbound oligonucleotide species.

Isothermal titration calorimetry of T^2C_4 and T^3C_4 (0.1 mM) titrated against $AgNO_3$ (5.0 mM) held at 25°C gave ideal sigmodal isotherms that were converted into Wiseman plots for analysis (**Figure 6.31** below). Due to the limitations of the single site model used in the calorimetric analysis, only enthalpy values were considered. Binding constants (K_a or K_d) cannot be accurately calculated using single site models for systems, such as these, with multiple binding events. The overall energies (ΔH) for both systems were expectedly close at 11.2 kcal/mol for a T^2C_4 and 10.3 Kcal/mol for T^3C_4 . When compared against the simplest system ($[Ag(cytosine)_2]^+$, -5.1 kcal/mol) the exothermic values were 2.2 and 2.0 times greater for T^2C_4 and T^3C_4 respectively. The quantified energy released following silver ions titration is lower than expected or observed in MS. The cause is unclear, however consistent between both T^2C_4 and T^3C_4 , suggesting loop type (T2 vs. T3) is negligible.

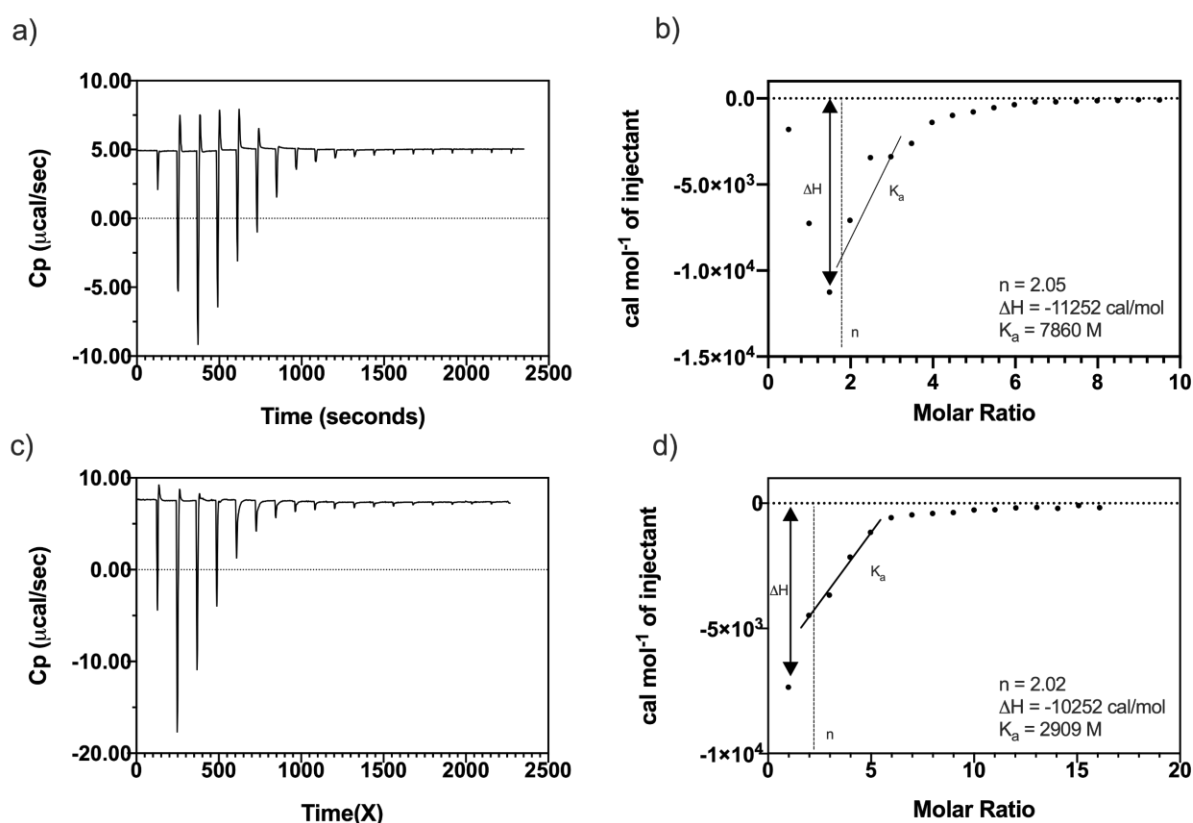


Figure 6.31 Isothermal titration calorimetry (ITC) isotherms (a & c) and integrated Wiseman plots (b & d) for oligonucleotides T^2C_4 (a - b) and T^3C_4 (c - d) (0.1 mM) following the addition of silver(I) ions (5.0 mM, $AgNO_3$).

Further extending the homo-C stem, and therefore capacity of the T-loop oligonucleotides to capture twelve silver(I) ions seemed a logical next step. This was achieved by designing two additional oligonucleotides; T^2C_{12} and T^3C_{12} . These were compared against a homo-C-oligonucleotide, dC_{12} , with literature precedent when titrated against silver(I).⁴⁵

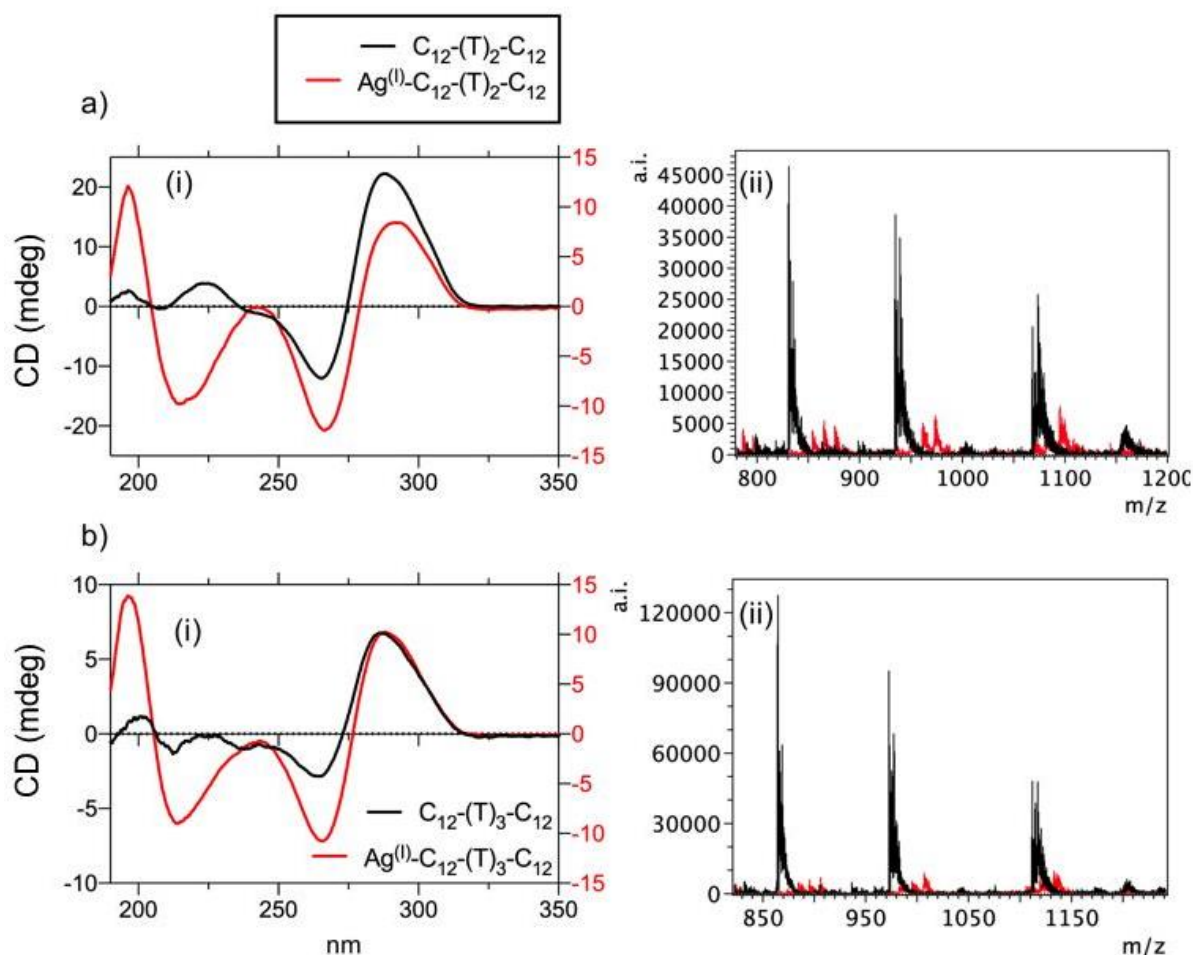


Figure 6.32 (i) Circular Dichroism (at 25°C) at a 12:1 metal to oligomer ratio. (ii) ESI-MS (negative ion mode) data for a) T^2C_{12} and b) T^3C_{12} before (black) and after (red) the addition of excess Ag^I ions (20 equiv.).

CD and MS (**Figure 6.32**) were collected for both T^2C_{12} and T^3C_{12} oligonucleotides, which were as expected for ss-DNA, showing peaks at 201(+), 264(-) and 286(+) nm. Following the addition of silver(I) ions (at 12:1 (metal:oligomer) ratio) the CD profiles changed to match those of dC_{12} found in the literature and of those explored previously in this chapter. Characteristic evidence supporting duplex formation brought about by

metal-mediation.⁴⁵ Peaks appear at 197(+), 214(-), 242(+), 265(-) and 290(+) nm with a red shift of 5 nm in the exciton splitting for both oligomers.

The MS interpretation and analysis of $^{T2}C_{12}$ and $^{T3}C_{12}$ proved challenging. The longer oligonucleotide systems possessed many higher charge states ($[M]^{14-}$ - $[M]^{7-}$), therefore little peak separation observed, coupled with multiple isotope patterns common to complex systems with higher numbers of silver(I) ions. For these reasons, identifying specific Ag_n -oligo peaks accurately was not feasible for either $^{T2}C_{12}$ or $^{T3}C_{12}$. However, taking a broader perspective, certain features are informative when compared against their respective parent oligonucleotides. The formation of new populations with slightly greater masses than those identified as ss-DNA at a given charge state are seen and the peaks only grow-in following the addition of silver(I) ions. Using their nearest parent oligo peak, the newly formed species can be rationalised as the addition of one, two, three and four bound silver(I) atoms. The lower observed affinity for metal binding was confirmed at earlier stages of the titration with no observable changes at additions less than six equivalents of Ag^+ . It has been proposed that the differences between the bound metal ion concentration may be due to weaker adducts that can form at higher silver concentrations, which can be susceptible to dissociation during desolvation or ionisation.⁴⁶

Isothermal titration calorimetry (ITC) was used to thermally quantify bonding interactions of the $^{T2}C_{12}$ and $^{T3}C_{12}$ hairpin oligonucleotides (0.1 mM) following the addition of $AgNO_3$ (5 mM and 0.5 mM) (**Figure 6.33**). As seen previously, both isotherms demonstrate negative peaks indicative of an exothermic reaction.⁴² Molar ratios (n) were calculated to be 2.1 for $^{T2}C_{12}$ and 2.6 for $^{T3}C_{12}$. Enthalpy changes (ΔH) calculated from the peak maximum were -11.3 and -14.7 Kcal/mol, approximately 2.2 and 2.9 times greater than that measured for a single C- Ag^+ -C (C: cytosine, -5.1 Kcal/mol) formation. Both ITC and MS displayed far lower values than expected for such systems. However, again for long systems the T3-hairpin systems seems to possess a slightly greater binding abilities than the T2-hairpin.

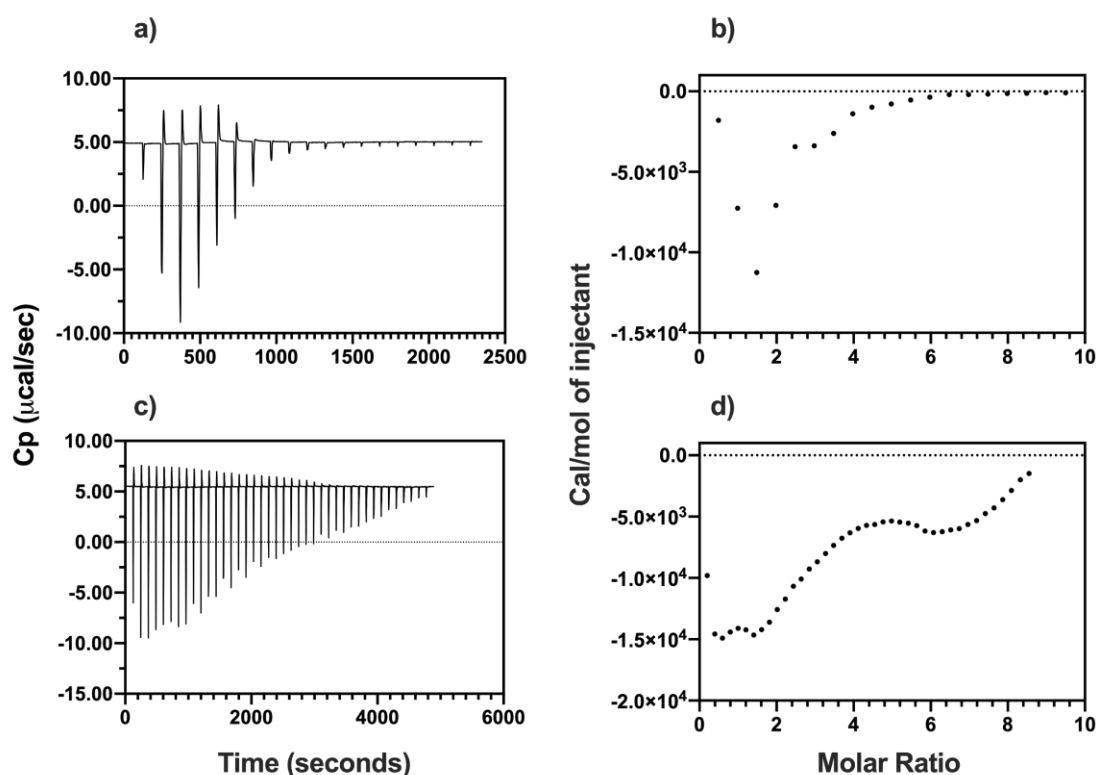


Figure 6.33 Isothermal titration calorimetry (ITC) Raw data isotherm (LHS) and integrated Wiseman plot (RHS) for the hairpin sequence T^2C_{12} (a & b) and T^3C_{12} (c & d) (0.1 mM) following the injection of silver(I) ions ($AgNO_3$, 5 mM and 0.5 mM respectively) held at 25°C (see appendix for reference data).

As a means of comparison, a dC_{12} oligonucleotide sequences was acquired and its silver(I)-binding credentials tested. Dickson & Petty demonstrated the ability to bind six silver ions per dC_{12} stands and up to 12 within a double-stranded duplex using MS.⁴⁷ Successful replication of these results was achieved following the addition of silver nitrate to dC_{12} at both equal equivalence to the number of C sites, and at an excess (20 equiv.). In both instances the formation of newly formed peaks was observed in MS (**Figure 6.34**). Peaks relating to the oligonucleotide dC_{12} bound with one-to-seven silver(I) ions was observed with a -4 charge (z). Species with greater than seven bound silver-ions exist, however these carried a substantial mass increase. These species also had isotope patterns and peak separation values expected for that of a duplexed M-DNA complex ($z = -6$), successfully replicating the results in the literature.⁴⁷

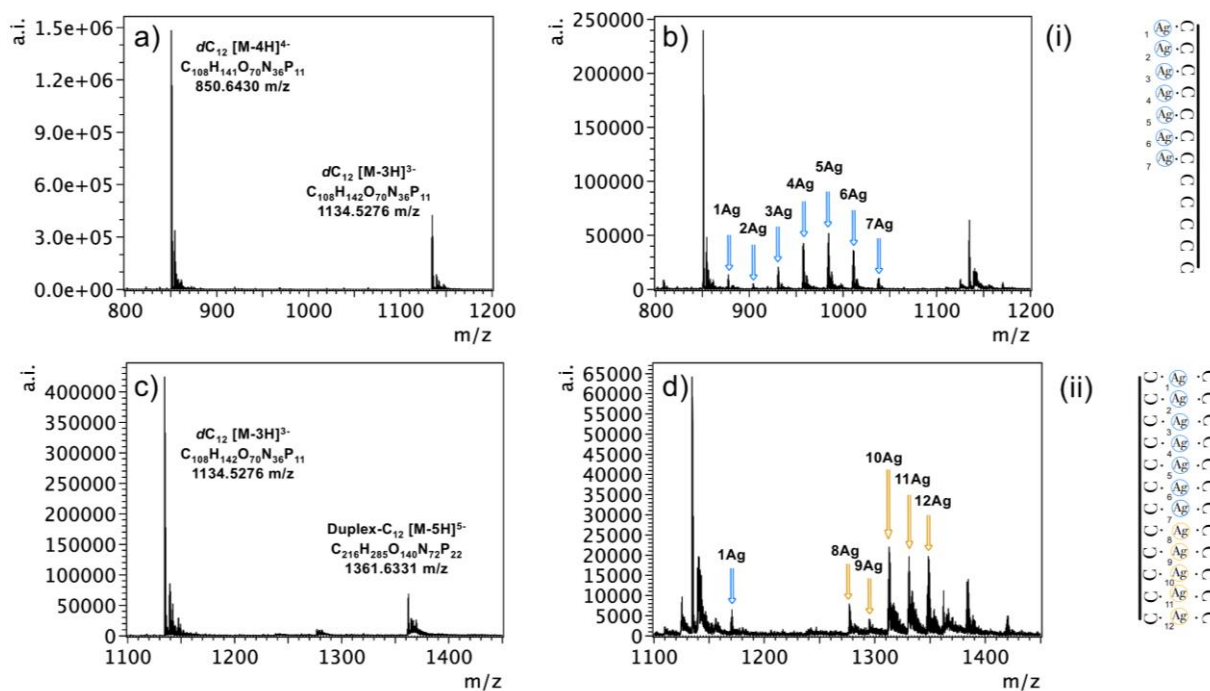


Figure 6.34 a - d) ESI-MS (negative-ion mode) of $d\text{C}_{12}$ following the addition of silver(I) ions (AgNO_3). Blue arrows silver bound to ss-DNA and yellow arrows signifying a duplexed ds-DNA complex. Illustrations (i) and (ii) demonstrate both metal-mediated ss- and ds-DNA species observed in MS.

ITC of $d\text{C}_{12}$ (0.1 mM) following the titration of silver nitrate (5.0 mM) gave the expected negative isotherm profile (exothermic) with a molar ratio of 7.1 Kcal/mol and enthalpy change (ΔH) of -5.6 Kcal/mol (**Figure 6.35**). The molar ratio is in agreement with the MS data for ss-DNA with a 7:1 metal:ligand ratio observed. The enthalpy change value is not consistent with the formation of seven C-Ag-C coordinations, neither is it consistent with the observed MS data.

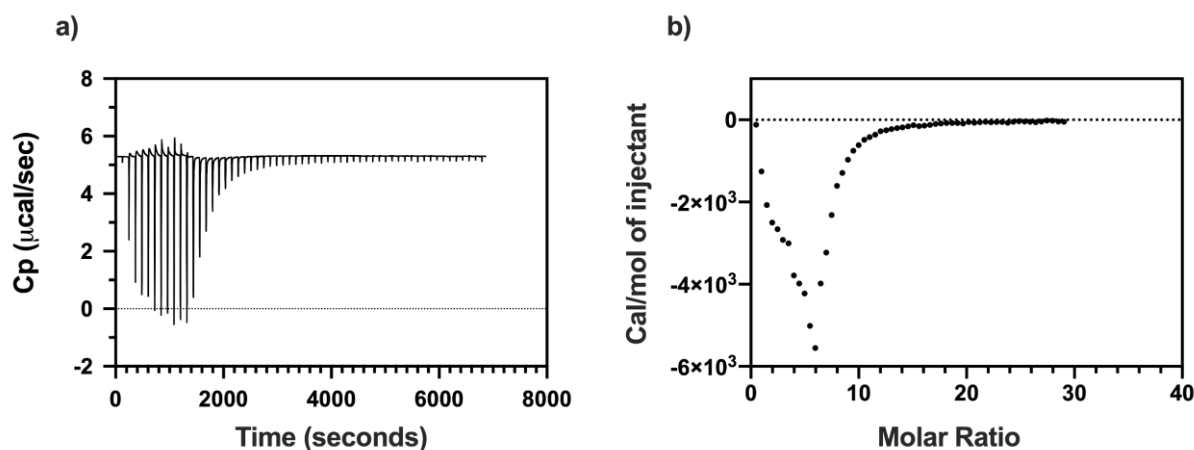


Figure 6.35 Isothermal titration calorimetry (ITC) Raw data isotherm (a) and integrated Wiseman plot (b) for the C-rich oligonucleotide sequence dC_{12} (0.1 mM) following the injection of silver(I) ions ($AgNO_3$, 5.0 mM) held at 25°C.

The phenomenon observed is possibly accounted for by cooperativity effects. Systems possessing identical or near-identical elements which act dependently on each other. The abilities for silver ions to fill identical C-C sites appears dependent on the occupancy of the oligo. To further investigate this, the MS poisson peak intensity distribution is analysed.

6.9. Cooperativity (ΔG) of Ag^I -Oligomers

Gibbs energy (G) reflects the balance behind the driving forces of a reaction; ΔH versus ΔS . Some reactions are spontaneous due to the energy they release ($\Delta H < 0$, which causes an increase in the entropy of the surroundings) and others are spontaneous due to the increased disorder of the chemical system ($\Delta S > 0$). This balance is reflected in the equation (1) for Gibbs energy changes.

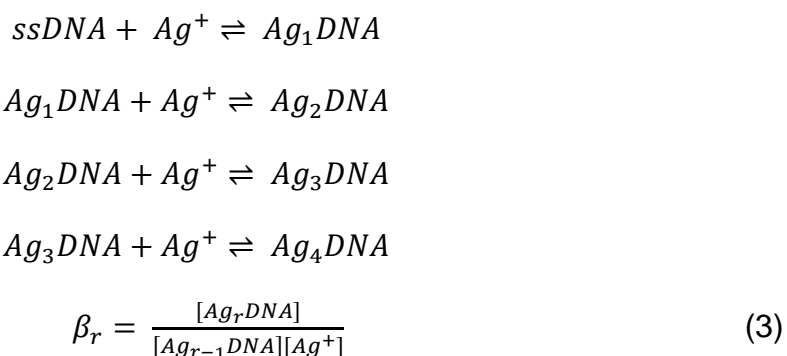
$$\Delta G^o = \Delta H^o - T\Delta S^o \quad (1)$$

If $\Delta G < 0$ (exergonic), the reaction is favourable or spontaneous and if $\Delta G > 0$ (endergonic) it is unfavourable or not spontaneous. The Gibbs energy change under standard conditions (1 bar pressure, ideal behaviour and solutes at 1 mol kg⁻¹) is simply related to the equilibrium constant for the process.

$$\Delta G^o = -RT\ln K \quad (2)$$

Where ΔG^o in equation (2) denotes the standard Gibbs energy change. In this chapter equation (2) is used to estimate Gibbs energies from the mass spectrometry data by relating the observed peak intensities to the mole fractions of individual species and computing the stepwise binding constants from that data.

Calculating a stepwise binding constant (β_r) for interactions between the designer hairpin oligos and silver ions. The following equilibrium reaction equations were considered for a hairpin with a capacity of four; for metal-mediation with silver ions (**xC₄**):



Using equation (2) ΔG^o_r was calculated for each hairpin loop types investigated (**a²C_n**, **T²C_n** and **T³C_n**), specifically those designed to capture four and six Ag^I ions. The equilibrium constant β_r for the binding of the r^{th} Ag^I ion was calculated using the MS peak intensity ratios for r and $r-1$ bound Ag^I ions and the remaining free Ag⁺ was estimated using the total amount of Ag⁺ and subtracting the concentrations of all observed species from $r=0$ to $r=4$ or 6, each appropriately weighted by the number of bound Ag⁺.

$$\Delta G^o_r = -RT \ln \beta_r \quad (4)$$

Since r Ag^I may occupy several different binding sites on a hairpin with up to $n=4$ or 6 sites, the binding constants also contain a hidden statistical factor of nC_r corresponding to the number of ways of choosing r binding sites from a total of n (**Figure 6.36**). The stepwise binding constants were therefore also corrected for this factor by dividing by the ratio of the statistical factor for r and $r-1$:

$$\frac{{}^nC_r}{{}^nC_{r-1}} = \frac{n-r+1}{r} \quad (5)$$

ΔG^o_r values for all species were found to be exergonic and most favourable at the mid-point of titration (**Figure 6.36**); when the hairpins are partially filled, showing that the

spontaneity increases after capture of the first metal ion, indicative of cooperativity. ΔG^o_r then expectedly decreases as further free sites are filled and the systems reaches saturation. Interestingly, both data sets show comparable profiles with $-\Delta G^o_r$ maximums of ~ 2.5 and ~ 3.5 for ${}^x\text{C}_4$ and ${}^x\text{C}_6$ respectively. This analysis of the mass spectrometry data assumes that the peak intensities are governed by the relative populations of each binding state *at equilibrium* and not by kinetic factors or the efficiency of detection or stability of the ions during electrospray. Support for our interpretation is given by the observation that the derived Gibbs energies are essentially independent of the mole ratio of $\text{Ag}^+:\text{DNA}$.

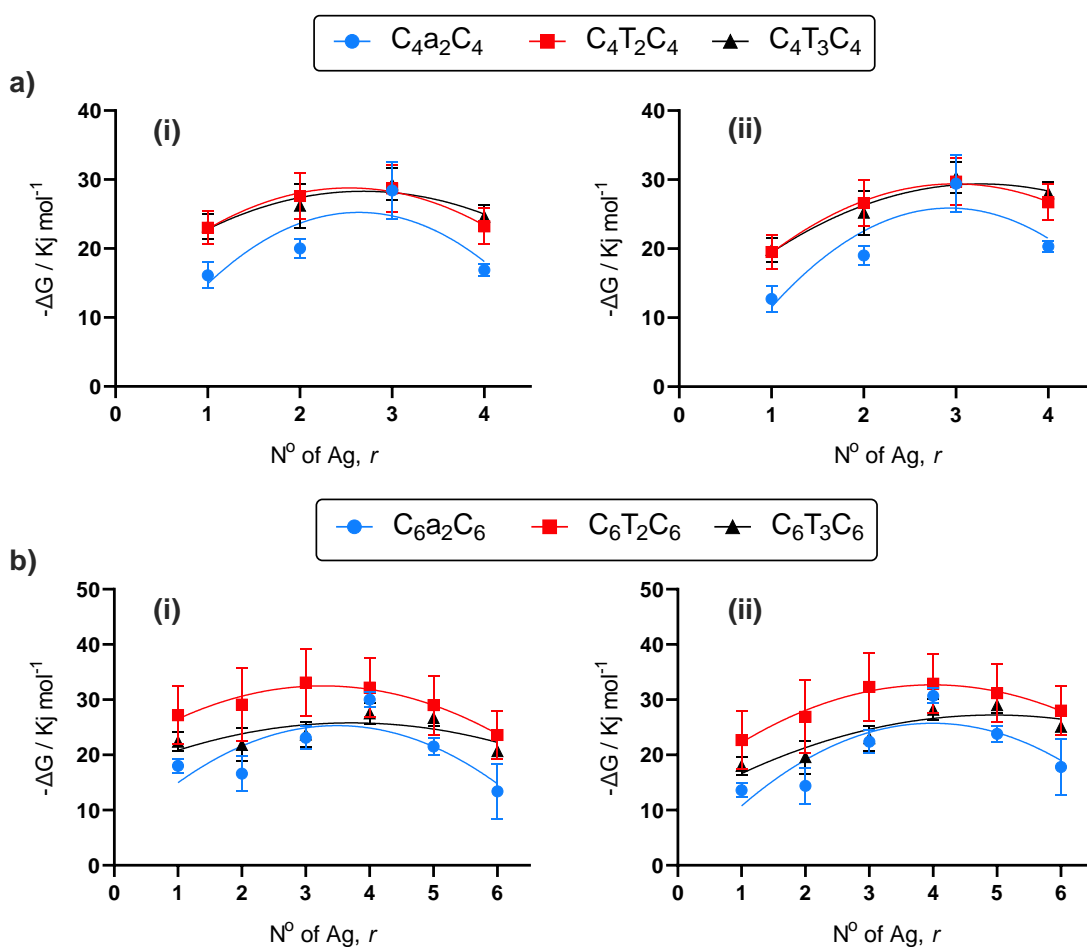


Figure 6.36 Non-corrected (i) and corrected (ii) Gibbs energy (ΔG^o_r) profiles calculated from MS-titration data of Ag^+ into a) ${}^x\text{C}_4$ or b) ${}^x\text{C}_6$ for “a-basic”, “T2” and “T3” loop types at 298 K. All species demonstrate cooperativity as spontaneity increases following the first Ag^+ -oligo interaction. Spontaneity decreases as oligos reach their designed saturation.

In summary, the use of thymine in place of abasic loop units yielded no negative effects on the silver binding characteristics of the oligonucleotides. The CD for all thymine-looped oligonucleotides behaved as expected upon metalation, shifting towards that of duplexed or M-DNA profile. Analysis of the MS data showed $T^2C_n > T^3C_n > a^2C_n$ at capturing metal-ions towards a saturated state. Cooperativity was found to play a role in the mechanisms of coordination by silver(I) across the mismatched C·C stem sites.

6.10. Conclusions

Within this chapter, we have demonstrated the abilities of C-rich ss-DNA oligonucleotides to capture silver(I) ions. The insertion of a central non-binding region was designed to allow for the folding into a hairpin. The use of both spectroscopic (CD) and physical techniques (ESI-MS, IMS and ITC) allowed for characterisation of several loop and stem compositions. Loop optimisations experiments demonstrated $T^2C_n > T^3C_n > a^2C_n$. Exchange of abasic (a^2C_n) units for thymine (T^2C_n and T^3C_n) was not found to adversely affect the outcome of metalation. Stem development explored a range of Ag^+ capacities ($n = 1, 2, 4, 6$ and 12) by extending the homo-C regions flanking the central loop. In each instance, the coordination of silver(I) across C·C sites was observed. Establishing the formation of a hairpin structure was achieved using multiple techniques. IMS ruled out dimer formation, MS and ITC eliminated single site coordination and CD confirmed the formation of a M-DNA duplex. Metalation of higher capacity oligonucleotide ($n > 6$) were found to exhibit cooperativity as C·C sites filled. This was found to have a negative effect on our abilities to fully occupy all possible coordination sites within the hairpins structure. Extending the capacity of such systems further could prove to be problematic, as cooperativity would play an ever-increasing role in the uptake of silver(I) ions. It could be interesting to further investigate the processes by which hairpins fill or capture metal ions. Could it be that they “zip-up/down” or are sites occupied randomly? It seems equally likely that they either fill in sequence, analogous to a zip or randomly with a rearrangement of metal ions necessary.

6.11. References

- (1) Schultz, D.; Brinson, R. G.; Sari, N.; Fagan, J. A.; Bergonzo, C.; Lin, N. J.; Dunkers, J. P. Structural Insights into DNA-Stabilized Silver Clusters. *Soft Matter* **2019**, *15* (21), 4284–4293. <https://doi.org/10.1039/c9sm00198k>.
- (2) Obliosca, J. M.; Liu, C.; Yeh, H. C. Fluorescent Silver Nanoclusters as DNA Probes. *Nanoscale* **2013**, *5* (18), 8443–8461. <https://doi.org/10.1039/c3nr01601c>.
- (3) Petty, J. T.; Nicholson, D. A.; Sergeev, O. O.; Graham, S. K. Near-Infrared Silver Cluster Optically Signaling Oligonucleotide Hybridization and Assembling Two DNA Hosts. *Anal. Chem.* **2014**, *86* (18), 9220–9228. <https://doi.org/10.1021/ac502192w>.
- (4) Vdovichev, A. A.; Sych, T. S.; Reveguk, Z. V.; Smirnova, A. A.; Maksimov, D. A.; Ramazanov, R. R.; Kononov, A. I. Structure of Fluorescent Metal Clusters on a DNA Template. *J. Phys. Conf. Ser.* **2016**, *741* (1). <https://doi.org/10.1088/1742-6596/741/1/012069>.
- (5) Copp, S. M.; Schultz, D.; Swasey, S.; Pavlovich, J.; Debord, M.; Chiu, A.; Olsson, K.; Gwinn, E. Magic Numbers in DNA-Stabilized Fluorescent Silver Clusters Lead to Magic Colors. *J. Phys. Chem. Lett.* **2014**, *5* (6), 959–963. <https://doi.org/10.1021/jz500146q>.
- (6) Javani, S.; Lorca, R.; Latorre, A.; Flors, C.; Cortajarena, A. L.; Somoza, Á. Antibacterial Activity of DNA-Stabilized Silver Nanoclusters Tuned by Oligonucleotide Sequence. *ACS Appl. Mater. Interfaces* **2016**, *8* (16), 10147–10154. <https://doi.org/10.1021/acsami.6b00670>.
- (7) Bikard, D.; Loot, C.; Baharoglu, Z.; Mazel, D. Folded DNA in Action: Hairpin Formation and Biological Functions in Prokaryotes. *Microbiol. Mol. Biol. Rev.* **2010**, *74* (4), 570–588. <https://doi.org/10.1128/mmbr.00026-10>.
- (8) Lin, X.; Xiao, F.; Li, X.; Li, F.; Liu, C.; Xiao, X.; Hu, N.; Yang, S. A Cytosine-Rich Hairpin DNA Loaded with Silver Nanoclusters as a Fluorescent Probe for Uranium(IV) and Mercury(II) Ions. *Microchim. Acta* **2019**, *186* (8). <https://doi.org/10.1007/s00604-019-3625-0>.

- (9) Shen, F.; Qian, H.; Cheng, Y.; Xie, Y.; Yu, H.; Yao, W.; Pei, R.; Guo, Y.; Li, H.-W. Three-Way Junction-Promoted Recycling Amplification for Sensitive DNA Detection Using Highly Bright DNA-Silver Nanocluster as Label-Free Output. *Talanta* **2020**, *206* (August 2019), 120216. <https://doi.org/10.1016/j.talanta.2019.120216>.
- (10) Xiao, Y.; Wu, Z.; Wong, K. Y.; Liu, Z. Hairpin DNA Probes Based on Target-Induced in Situ Generation of Luminescent Silver Nanoclusters. *Chem. Commun.* **2014**, *50* (37), 4849–4852. <https://doi.org/10.1039/c4cc01154f>.
- (11) Leng, X.; Wang, Y.; Li, R.; Liu, S.; Yao, J.; Pei, Q.; Cui, X.; Tu, Y.; Tang, D.; Huang, J. Circular Exponential Amplification of Photoinduced Electron Transfer Using Hairpin Probes, G-Quadruplex DNAzyme and Silver Nanocluster-Labeled DNA for Ultrasensitive Fluorometric Determination of Pathogenic Bacteria. *Mikrochim. Acta* **2018**, *185* (3), 168. <https://doi.org/10.1007/s00604-018-2698-5>.
- (12) Del Bonis-O'Donnell, J. T.; Pennathur, S.; Fygenson, D. K. Changes in Spectra and Conformation of Hairpin DNA-Stabilized Silver Nanoclusters Induced by Stem Sequence Perturbations. *Langmuir* **2016**, *32* (2), 569–576. <https://doi.org/10.1021/acs.langmuir.5b03934>.
- (13) Shen, F.; Qian, H.; Cheng, Y.; Xie, Y.; Yu, H.; Yao, W.; Pei, R.; Guo, Y.; Li, H.-W. Three-Way Junction-Promoted Recycling Amplification for Sensitive DNA Detection Using Highly Bright DNA-Silver Nanocluster as Label-Free Output. *Talanta* **2020**, *206* (August 2019), 120216. <https://doi.org/10.1016/j.talanta.2019.120216>.
- (14) Xiao, Y.; Wu, Z.; Wong, K. Y.; Liu, Z. Hairpin DNA Probes Based on Target-Induced in Situ Generation of Luminescent Silver Nanoclusters. *Chem. Commun.* **2014**, *50* (37), 4849–4852. <https://doi.org/10.1039/c4cc01154f>.
- (15) Ono, A.; Cao, S.; Togashi, H.; Tashiro, M.; Fujimoto, T.; MacHinami, T.; Oda, S.; Miyake, Y.; Okamoto, I.; Tanaka, Y. Specific Interactions between Silver(i) Ions and Cytosine-Cytosine Pairs in DNA Duplexes. *Chem. Commun.* **2008**, *39*, 4825–4827. <https://doi.org/10.1039/b808686a>.
- (16) Kuklenyik, Z.; Marzilli, L. G. Mercury(II) Site-Selective Binding to a DNA Hairpin. Relationship of Sequence-Dependent Intra- and Interstrand Cross-Linking to the Hairpin-Duplex Conformational Transition. *Inorg. Chem.* **1996**, *35* (19), 5654–

5662. <https://doi.org/10.1021/ic960260a>.

- (17) Ono, A.; Torigoe, H.; Tanaka, Y.; Okamoto, I. Binding of Metal Ions by Pyrimidine Base Pairs in DNA Duplexes. *Chem. Soc. Rev.* **2011**, *40* (12), 5855–5866. <https://doi.org/10.1039/c1cs15149e>.
- (18) Clever, G. H.; Kaul, C.; Carell, T. DNA-Metal Base Pairs. *Angew. Chemie - Int. Ed.* **2007**, *46* (33), 6226–6236. <https://doi.org/10.1002/anie.200701185>.
- (19) Houlton, A. New Aspects of Metal - Nucleobase Chemistry. *Adv. Inorg. Chem.* **2002**, *53*, 87–158.
- (20) Lippert, B.; Sanz Miguel, P. J. The Renaissance of Metal-Pyrimidine Nucleobase Coordination Chemistry. *Acc. Chem. Res.* **2016**, *49* (8), 1537–1545. <https://doi.org/10.1021/acs.accounts.6b00253>.
- (21) Liu, H.; Shen, F.; Haruehanroengra, P.; Yao, Q.; Cheng, Y.; Chen, Y.; Yang, C.; Zhang, J.; Wu, B.; Luo, Q.; et al. A DNA Structure Containing AgI-Mediated G:G and C:C Base Pairs. *Angew. Chemie - Int. Ed.* **2017**, *56* (32), 9430–9434. <https://doi.org/10.1002/anie.201704891>.
- (22) Kondo, J.; Tada, Y.; Dairaku, T.; Hattori, Y.; Saneyoshi, H.; Ono, A.; Tanaka, Y. A Metallo-DNA Nanowire with Uninterrupted One-Dimensional Silver Array. *Nat. Chem.* **2017**, *9* (10), 956–960. <https://doi.org/10.1038/nchem.2808>.
- (23) Kim, S.; Gang, J. The Detection of a Mismatched DNA by Using Hairpin DNA-Templated Silver Nanoclusters. *Anal. Biochem.* **2018**, *549*, 171–173. <https://doi.org/10.1016/j.ab.2018.03.026>.
- (24) Del Bonis-O'Donnell, J. T.; Pennathur, S.; Fygenson, D. K. Changes in Spectra and Conformation of Hairpin DNA-Stabilized Silver Nanoclusters Induced by Stem Sequence Perturbations. *Langmuir* **2016**, *32* (2), 569–576. <https://doi.org/10.1021/acs.langmuir.5b03934>.
- (25) Pettersen, E. F.; Goddard, T. D.; Huang, C. C.; Couch, G. S.; Greenblatt, D. M.; Meng, E. C.; Ferrin, T. E. UCSF Chimera--a Visualization System for Exploratory Research and Analysis. *J. Comput. Chem.* **2004**, *25* (13), 1605–1612. <https://doi.org/10.1002/jcc.20084>.
- (26) Abraham, M. J.; Murtola, T.; Schulz, R.; Páll, S.; Smith, J. C.; Hess, B.; Lindah, E. Gromacs: High Performance Molecular Simulations through Multi-Level

Parallelism from Laptops to Supercomputers. *SoftwareX* **2015**, 1–2, 19–25. <https://doi.org/10.1016/j.softx.2015.06.001>.

- (27) Lindorff-Larsen, K.; Piana, S.; Palmo, K.; Maragakis, P.; Klepeis, J. L.; Dror, R. O.; Shaw, D. E. Improved Side-Chain Torsion Potentials for the Amber Ff99SB Protein Force Field. *Proteins Struct. Funct. Bioinforma.* **2010**, 78 (8), 1950–1958. <https://doi.org/10.1002/prot.22711>.
- (28) Hess, B. P-LINCS: A Parallel Linear Constraint Solver for Molecular Simulation. *J. Chem. Theory Comput.* **2008**, 4 (1), 116–122. <https://doi.org/10.1021/ct700200b>.
- (29) Verlet, L. Computer “Experiments” on Classical Fluids. I. Thermodynamical Properties of Lennard-Jones Molecules. *Phys. Rev.* **1967**, 159 (1), 98–103.
- (30) Bussi, G.; Donadio, D.; Parrinello, M. Canonical Sampling through Velocity Rescaling. *J. Chem. Phys.* **2007**, 126 (1). <https://doi.org/10.1063/1.2408420>.
- (31) Parrinello, M.; Rahman, A. Polymorphic Transitions in Single Crystals: A New Molecular Dynamics Method. *J. Appl. Phys.* **1981**, 52 (12), 7182–7190. <https://doi.org/10.1063/1.328693>.
- (32) Lanucara, F.; Holman, S. W.; Gray, C. J.; Evers, C. E. The Power of Ion Mobility-Mass Spectrometry for Structural Characterization and the Study of Conformational Dynamics. *Nat. Chem.* **2014**, 6 (4), 281–294. <https://doi.org/10.1038/nchem.1889>.
- (33) Miyahara, T.; Nakatsuji, H.; Sugiyama, H. Helical Structure and Circular Dichroism Spectra of DNA: A Theoretical Study. *J. Phys. Chem. A* **2013**, 117 (1), 42–55. <https://doi.org/10.1021/jp3085556>.
- (34) Swasey, S. M.; Gwinn, E. G. Silver-Mediated Base Pairings: Towards Dynamic DNA Nanostructures with Enhanced Chemical and Thermal Stability. *New J. Phys.* **2016**, 18 (4). <https://doi.org/10.1088/1367-2630/18/4/045008>.
- (35) Espinosa Leal, L. A.; Karpenko, A.; Swasey, S.; Gwinn, E. G.; Rojas-Cervellera, V.; Rovira, C.; Lopez-Acevedo, O. The Role of Hydrogen Bonds in the Stabilization of Silver-Mediated Cytosine Tetramers. *J. Phys. Chem. Lett.* **2015**, 6 (20), 4061–4066. <https://doi.org/10.1021/acs.jpcllett.5b01864>.
- (36) Norden, B.; Rodger, A.; Dafforn, T. *Linear Dichroism and Circular Dichroism*;

2010.

- (37) Swasey, S. M.; Karimova, N.; Aikens, C. M.; Schultz, D. E.; Simon, A. J.; Gwinn, E. G. Chiral Electronic Transitions in Fluorescent Silver Clusters Stabilized by DNA. *ACS Nano* **2014**, *8* (7), 6883–6892. <https://doi.org/10.1021/nn5016067>.
- (38) Swasey, S. M.; Leal, L. E.; Lopez-Acevedo, O.; Pavlovich, J.; Gwinn, E. G. Silver (I) as DNA Glue: Ag⁺-Mediated Guanine Pairing Revealed by Removing Watson-Crick Constraints. *Sci. Rep.* **2015**, *5* (April), 1–9. <https://doi.org/10.1038/srep10163>.
- (39) Moehlig, A. R.; Djernes, K. E.; Krishnan, V. M.; Hooley, R. J. Cytosine Derivatives Form Hemiprotonated Dimers in Solution and the Gas Phase. *Org. Lett.* **2012**, *14* (10), 2560–2563. <https://doi.org/10.1021/ol300861r>.
- (40) Kypr, J.; Kejnovská, I.; Renčiuk, D.; Vorlíčková, M. Circular Dichroism and Conformational Polymorphism of DNA. *Nucleic Acids Res.* **2009**, *37* (6), 1713–1725. <https://doi.org/10.1093/nar/gkp026>.
- (41) Reilly, S. M.; Morgan, R. K.; Brooks, T. A.; Wadkins, R. M. Effect of Interior Loop Length on the Thermal Stability and PKa of I-Motif DNA. *Biochemistry* **2015**, *54* (6), 1364–1370. <https://doi.org/10.1021/bi5014722>.
- (42) Shukla, S.; Sastry, M. Probing Differential Ag + -Nucleobase Interactions with Isothermal Titration Calorimetry (ITC): Towards Patterned DNA Metallization. *Nanoscale* **2009**, *1* (1), 122–127. <https://doi.org/10.1039/b9nr00004f>.
- (43) Santamaría-Díaz, N.; Méndez-Arriaga, J. M.; Salas, J. M.; Galindo, M. A. Highly Stable Double-Stranded DNA Containing Sequential Silver(I)-Mediated 7-Deazaadenine/Thymine Watson-Crick Base Pairs. *Angew. Chemie - Int. Ed.* **2016**, *55* (21), 6170–6174. <https://doi.org/10.1002/anie.201600924>.
- (44) Lippert, B.; Sanz Miguel, P. J. The Renaissance of Metal-Pyrimidine Nucleobase Coordination Chemistry. *Acc. Chem. Res.* **2016**, *49* (8), 1537–1545. <https://doi.org/10.1021/acs.accounts.6b00253>.
- (45) Ritchie, C. M.; Johnsen, K. R.; Kiser, J. R.; Antoku, Y.; Dickson, R. M.; Petty, J. T. Ag Nanocluster Formation Using a Cytosine Oligonucleotide Template. *J. Phys. Chem. C* **2007**, *111* (1), 175–181. <https://doi.org/10.1021/jp0648487>.
- (46) Petty, J. T.; Zheng, J.; Hud, N. V.; Dickson, R. M. DNA-Templated Ag

Nanocluster Formation. *J. Am. Chem. Soc.* **2004**, *126* (16), 5207–5212. <https://doi.org/10.1021/ja031931o>.

- (47) Ritchie, C. M.; Johnsen, K. R.; Kiser, J. R.; Antoku, Y.; Dickson, R. M.; Petty, J. T. Ag Nanocluster Formation Using a Cytosine Oligonucleotide Template. *J. Phys. Chem. C* **2007**, *111* (1), 175–181. <https://doi.org/10.1021/jp0648487>.

Chapter 7.

Conclusions and Outlook

This thesis has served to demonstrate several examples of the silver-pyrimidine interaction found within M-DNA systems. Furthermore, their credentials as nanoscale functional materials, or routes towards such endeavours were tested. Excellent progress has been made over the course of this investigation in understanding the fundamental interactions that occur between Ag^+ and the “C”-pyrimidine nucleic acid. The addition of Ag^+ to each natural cytosine analogue or oligonucleotide system explored established coordination at the N^3 -donor site with few exceptions.

The well-established N^3 *bis*-coordination motif between silver(I) and cytosine was observed for the first time crystallographically in **chapter 2**. The structural details of which were intriguing with three solvomorphs discovered suitable for x-ray diffraction generated. Conformations of both *cisoidal/transoidal* and bent/linear were observed. A bent *Cisoidal* orientations of the bases was preferred due to the long H-bonding distances involved between the complementary exocyclic O^2 -acceptor and N^4 -donor groups required for the *trans*-motif. The importance of solvent bridges capable of mitigating those distance was remarked. This finding was further demonstrated by DFT studies which showed stability as $\mathbf{T_{bent}} > \mathbf{T_{linear}} > \mathbf{C_{linear}} > \mathbf{C_{bent}}$.

Chapter 3 demonstrated the same N^3 -binding motif (*cisoidal*) existed for cytidine, the C-nucleoside (ribose), however a stacking behaviour lead to a unique polymeric material which self-assembled into a relatively soft gel in an alcoholic solvent ($\text{MeOH} > \text{EtOH} > \text{IPA}$). The structure was characterised by single X-ray diffraction revealing an infinite array of closely held silver ions down the central axis of a remarkable right-handed (clockwise) double helix. The secondary helical structure was the result of intermolecular H-bonding interactions across the exocyclic O^2 -acceptor and N^4 -donor groups above and below each complex ion. The material generated presented molecular wire-like features which made it an ideal candidate for conductivity experiments. Despite having $\text{Ag}\cdots\text{Ag}$ distances within <5% of the metallic radii, the material was experimentally shown to be electrically insulating. These finding were backed up by DFT studies.

The deoxy counterpart was structurally characterised in **chapter 4** to be an almost identical double helix, however for reasons that remain unclear, the left-handed (anticlockwise) sense prevailed. Details surrounding its crystallisation and nucleation processes were investigated by AFM. Astonishingly, AFM images showed how 1D

fibres (3 nm dia.) assembly into larger bundle before organising into a regular lattice in the solid state. A multi-step crystal growth mechanism was purposed to explain the phenomena observed.

Two solvates (H₂O and MeOH) of the metallated nucleotide complex (Ag-Cmp) were prepared and structurally characterised by X-ray diffraction methods in **chapter 5**. They demonstrated the unique O²-Ag^I-N³ binding motif reported by Terrón & Frontera. Despite close silver-silver distances, the material was again found to be electrically insulating, further validating the existence of a large band gap for such systems. A weak Ag-O^{7'} coordination was identified as a possible route or opportunity for top-down mechanical exfoliation of a crystal down to single molecular layer or sheet. Attempts to access and isolate single Ag-chains from the crystalline material by mechanical exfoliation (sonication) proved successful, with regular flakes observed by AFM. PXRD suggested that the cleavage likely occurred at the Ag-O^{7'} position resulting in flakes consisting of a bilayer with Ag^I-chains running perpendicular to the substrate in the [101] direction.

Chapter 6 concluded this investigation by establishing the Ag⁺ binding properties of short C-rich oligonucleotides. The designed oligo sequences were specifically designed to capture set quantities of silver ions across the well-established C-Ag-C binding motif. All sequences were designed with a central non-binding region intended for the folding into a hairpin-type structure. The use of both spectroscopic (CD) and physical techniques (ESI-MS, IMS and ITC) for characterisation confirmed Ag⁺_n capture and hairpin formation. Metalation of higher capacity oligonucleotide (n > 6) were found to encounter significant cooperativity effects as C-C sites became occupied with Ag⁺. Extending the capacity of such systems beyond six sites proved to be problematic, as cooperativity would play an ever-increasing role in the uptake of Ag⁺. Certainly, such systems have shown potential as a route towards controlled ion capture towards nanocluster formation or heavy metal sensors. The limitations of which have presented a new challenge for further investigation.

In closing, we have made a number of steps towards using DNA with transition metals towards the formation of nanoscale functional materials based on the silver-pyrimidine interactions described herein. Further increasing our understanding of the highly specific silver(I)-cytosine relationship, we have explored these structures as a “top-

down” route to metal-cluster formation. Several articles have been successfully published on simple nucleobase (**Chapter 2**) and nucleoside silver mediated (**Chapter 3**) systems. It is our hopes that **Chapters 4 - 6** will also be readily found in the literature in the near future.

Chapter 8. Experimental Detail

8.1. General Methodology

Reagents were used as obtained from Sigma-Aldrich unless otherwise stated.

NANOpure® deionised water (18 MΩ cm resistivity) was obtained from a NANOpure® Diamond™ Life Science ultrapure water system equipped with a Diamond™ RO Reverse Osmosis System (Barnstead International).

NMR spectra were recorded using Bruker either a 400 or 700 MHz spectrometer at rt. ¹H-NMR shifts were referenced to D₂O [¹H-NMR, δ (D₂O) = 4.80 ppm].

Experimental IR spectra in the solid state were measured with a Shimadzu IRAffinity-1S spectrometer using LabSolutions RF software. Spectra were recorded over the 400 – 4000 cm⁻¹ range with 50 scans.

UV-Vis measurements (in the range of 190 - 850 nm) were conducted using a Thermo Scientific™ NanoDrop™ One^C Microvolume spectrophotometer. A 1.5 µl sample droplet was prepared with an auto-ranging pathlength 0.03 – 1.00 mm (wavelength accuracy ± 1 nm).

Microanalyses were carried out by the Elemental Analysis Service in the School of Human Sciences, London Metropolitan University. Solutions were freeze dried to remove solvent prior to analysis. The individual C, H, N values did not differ by more than ±0.3 %. The mean C, H, N values are reported.

Emission spectroscopy (in the range of 300 – 800 nm) in a gel or liquid state were measured using a Shimadzu RF-6000 Spectro Fluorophotometer using a quartz cuvette (50 µl) with a path length of 1.5 mm. Scan intervals were acquired every 0.5 nm at a scan speed of 600 nm/min, within an emission and excitation bandwidth of 5.0 nm. The system was controlled using LabSolutions RF software.

Circular dichroism spectra were measured in a high precision quartz SUPRASIL (Hellma Analytics®) cell with a light path of 0.1 mm. Data was acquired using a JASCO J-810 spectropolarimeter under nitrogen (5 - 10 ml/min) connected to a PTC-423S temperature controller maintaining 25°C using a Julabo water bath.

Isothermal Titration Calorimetry was performed using an iTC200 MicroCal™ instrument connected to a MicroCal™ Incorporated ThermoVac (set at 24.6°C) running through Malvern instruments MicroCal™ ITC200 software (Version 1.26.4). Data analysis was performed using Origin 7 SR4 software (version 7.0552(B552)). Samples were held at 25°C (reference power: 6) within the iTC200 sample chamber with injection volumes of 0.1 µL.

High-resolution electrospray ionization mass spectrometry (ESI-MS) studies, samples were analyzed in ultrapure (type 1) water at concentrations in the order of 100 ng ml⁻¹ or over a range of 0.100 - 0.001 mM. Measurements were either made on a Waters Micromass LCT Premier TOF Mass Spectrometer or a Waters Synapt G2s Mass Spectrometer and data was processed using the Mmass software (version 5.5.0).

Rheological measurements were performed with a HR-2 Discovery Hybrid Rheometer (TA Instruments) with a standard steel parallel-plate geometry of 20 mm diameter with a gap of 1 mm. The strain and the frequency were set to 1% and 1 Hz, respectively.

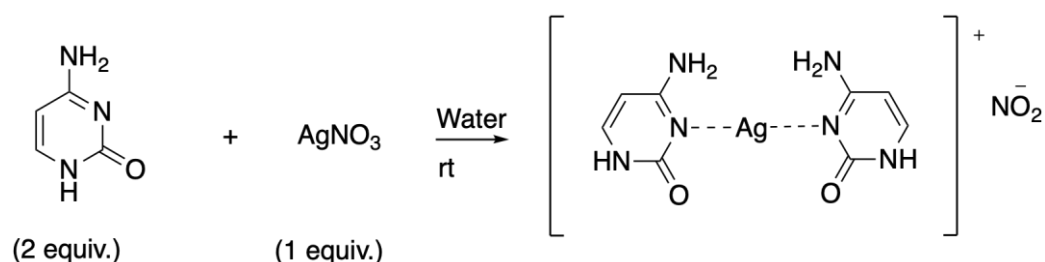
SEM samples were mounted on an aluminium stub with Achesons Silver Dag and then dried overnight. Examined using a TESCAN VEGA LMU Scanning Electron Microscope, housed within EM Research Services, Newcastle University. Digital images collected with TESCAN supplied software.

Diffraction patterns were generated using a PANalytical X'Pert Pro Multipurpose Diffractometer (MPD) using a PW1730 Cu K α radiation source (λ = 1.540 Å). Solutions were freeze dried to remove solvent prior to analysis.

Atomic force microscopy (AFM) used a Multimode 8 atomic force microscope with Nanoscope V controller and a “E” scanner (Bruker, Germany) was used for acquiring AFM height images. Nanoscope software version 9.1 was used to control the microscope. The system was operated in a peak force tapping mode in air (ScanAsyst)

at ultra-low forces minimize damage to the material. An isolation table/acoustic enclosure (Veeco Inc., Metrology Group) was used to decrease vibrational noise. Silicon tips on V-shaped silicon nitride cantilevers (ScanAsyst-Air, Bruker) were used for imaging. The nominal tip radius was approximately 2 nm, resonant frequency 70 kHz, and spring constant $k \sim 0.4$ N/m. The AFM height images were analysed with NanoScope Analysis 1.5 software (Bruker).

8.2. Chapter 2 – Experimental Detail



Synthesis of *Cisoid*-[Ag(*N*³-Cytosine)₂][NO₃]

Cytosine (100 mg, 0.90 mmol, 2.0 equiv.) was dissolved in water (11.0 ml). To this solution another solution of AgNO₃ (76.45 mg, 0.45 mmol, 1.0 equiv.) in water (0.5 ml) was added slowly in the dark. The mixture was maintained in a close system at room temperature. After a period of 7 days, colourless crystals appeared. The yield of the crystals was 81%. ¹H NMR (700 MHz, Deuterium Oxide) δ 7.51 (d, $J = 7.2$ Hz, ¹H, H⁴), 5.99 (d, $J = 7.0$ Hz, ¹H, H⁵); IR: $\tilde{\nu} = 3318, 3163, 3102, 2947, 2882, 1612, 1523, 1504, 1462, 1323, 1278, 1231, 1150, 1103, 980, 787, 772, 598, 571$ and 532 cm^{-1} ; MS (ESI – Negative Ion): m/z calculated for [C₈H₁₂AgN₆O₂]⁻: 331.01; found: 331.00, MS (ESI – Positive Ion): m/z calculated for [C₈H₁₀AgN₆O₂]⁺: 328.9916; found: 328.9986. Elemental analysis found(calc): C 19.56(19.49); H 2.37(2.45); N 17.03(17.05).

Synthesis of *Transoid*-[Ag(*N*³-Cytosine)₂][NO₃].H₂O

Cytosine (100 mg, 0.90 mmol, 2.0 equiv.) was dissolved in water (12.5 ml). To this solution another aqueous (0.5 ml) solution of AgNO₃ (76.45 mg, 0.45 mmol, 1.0 equiv.) was added slowly in the dark. The mixture was layered with acetonitrile to generate solvent diffusion phase boundary within a closed system at room temperature. After a period of 14 days, colourless crystals appeared. ¹H-NMR (700 MHz, Deuterium Oxide) δ 7.49 (d, $J = 7.2$ Hz, ¹H, H⁴), 5.97 (d, $J = 7.2$ Hz, ¹H, H⁵); IR: $\tilde{\nu} = 3292, 3196, 2951, 2881, 2382, 1589, 1508, 1504, 1448, 1346, 1263, 1211, 1134, 1107, 1005, 964, 837,$

822, 789, 770, 733, 601, 530, 509 cm^{-1} ; MS (ESI – Negative Ion): m/z calculated for $[\text{C}_8\text{H}_{12}\text{AgN}_6\text{O}_2]^-$: 331.01; found: 331.00. Elemental analysis found(calc): C 23.35(23.43); H 2.85(2.95); N 23.29(23.91).

Synthesis of *Transoid*-[Ag(*N*³-Cytosine)₂][PF₆] \cdot 2H₂O

Cytosine (100 mg, 0.90 mmol, 2.0 equiv.) was dissolved in water (12.5 ml). To this solution another solution of AgPF₆ (113.78 mg, 0.45 mmol, 1.0 equiv.) in water (0.5 ml) was added slowly in the dark. Crystals were grown over a period of 21-days at room temperature using a thermal vapour diffusion chamber using acetonitrile as an anti-solvent. ¹H-NMR (700 MHz, Deuterium Oxide) δ 7.51 (d, J = 7.2 Hz, ¹H, H⁴), 7.71 (d, J = 7.2 Hz, ¹H, H⁴), 7.70 (d, J = 7.2 Hz, ¹H, H⁴), 6.00 (d, J = 7.1 Hz, ¹H, H⁵), 5.99 (d, J = 7.1 Hz, ¹H, H⁵), 5.98 (d, J = 7.1 Hz, ¹H, H⁵); IR: $\tilde{\nu}$ = 3275, 2978, 1612, 1516, 1462, 1377, 1292, 1234, 1080, 995, 775, 768, 602, 579 and 513 cm^{-1} ; MS (ESI – Negative Ion): m/z calculated for $[\text{C}_8\text{H}_{12}\text{AgN}_6\text{O}_2]^-$: 331.01; found: 331.02. Elemental analysis found(calc): C 19.56(19.49); H 2.37(2.45); N 17.03(17.05).

Synthesis of 1-Methylcytosine

Step 1 - A mixture of dry cytosine (1.00 g, 9 mmol), N,N-dimethylformamide dialkyl (diaralkyl) acetal (5.4 – 9.5 g, 45 - 80 mmol) and dry N,N-dimethylformamide (3 - 20 mL, 0.948 g/mL) was heated at 90 °C to reflux under a nitrogen atmosphere for 24 hr. The reaction mixture was cooled and evaporated to dryness on a rotary evaporator at 60 °C in vacuo, and an orange solid was obtained and recrystallized from benzene-Chloroform (Mp: 203 - 204°C). ¹H NMR (300 MHz, Deuterium Oxide) δ 8.50 (d, J = 4.9 Hz, ¹H), 7.69 (dd, J = 22.3, 7.0 Hz, ¹H), 6.16 (d, J = 7.0 Hz, ¹H), 3.42 (s, ²H), 3.23 (s, ³H), 3.08 (s, ³H).

Step 2 – The solid obtained was added to concentrated ammonium hydroxide solution (10 mL) was stirred at room temperature for 17 hr and then heated on a steam bath for 30 min to drive off excess ammonia. The solution was evaporated to dryness on a rotary evaporator. The solid residue obtained was recrystallized from MeOH-Petroleum ether yielding single crystals analysed by X-ray diffraction (Mp: 301 - 302°C). IR: $\tilde{\nu}$ = 3445, 3345, 3171, 2932, 2901, 2812, 1628, 1624, 1524, 1497, 1493, 1443, 1373, 1342, 1335, 1292, 1261, 1238, 1211, 1157, 1130, 1053, 987, 964, 883, 810, 783, 663, 621, 598, 575, 563, 478, 420 cm^{-1} ;

Isothermal titration Calorimetry

Isothermal Titration Calorimetry was performed using an iTC200 MicroCal™ instrument connected to a MicroCal™ Incorporated ThermoVac (set at 24.6°C) running through Malvern instruments MicroCal™ ITC200 software (Version 1.26.4). Data analysis was performed using Origin 7 SR4 software (version 7.0552(B552)).

200 µL of a 54.0 mM cytosine solution was held at 25°C (reference power: 6) within the iTC200 sample chamber. forty 0.1 µL injections of a 5004.0 mM solution of AgNO₃ were titrated over a period of 70 minutes.

Ligand Transformation prep.

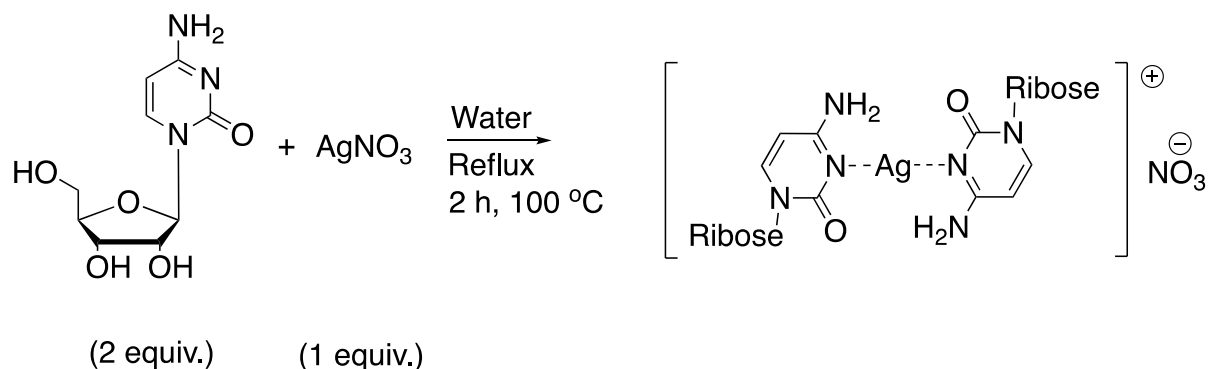
An aqueous solution of cytosine (100.0 mg, 0.90 mmol, 2 equiv.) and AgNO₃ (76.5 mg, 0.45 mmol, 1 equiv.) was prepared in 11.5 mL H₂O at rt. A second solution of either sodium chloride (52.6 mg, 0.90 mmol) or potassium chloride (67.1 mg, 0.90 mmol) dissolved in 1.15 mL H₂O was added dropwise yielding a white precipitate.

Mechanical Synthesis Prep.

Mechanical synthesis was achieved using a Retsch MM 400 high-energy ball-mill using a frequency of 14 Hz using a solid stainless-steel ball-bearing (13.6 g, 15 mm dia.) within a hardened steel screw-top cell (25 mL). Samples were subsequently analysed using FTIR and PXRD.

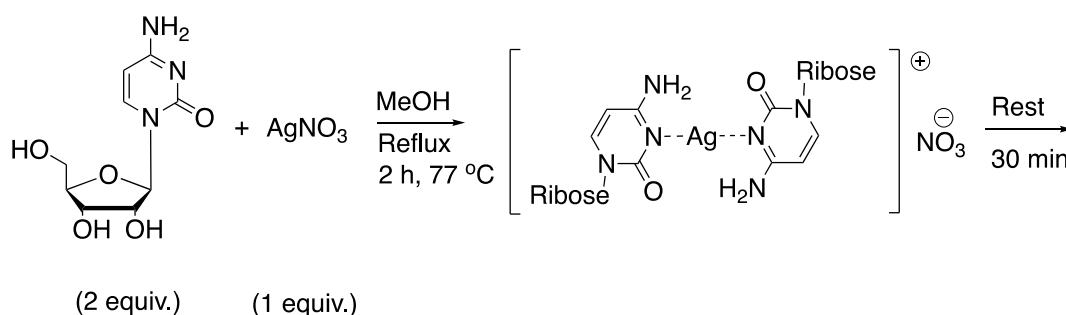
Cytosine (1.00 g, 9.0 mmol, 2 equiv.) was mixed with AgNO₃ (0.77g, 4.5 mmol, 1 equiv.) and was milled for a total of 5 hours with (ca. 50 mg) samples taken at one-hour intervals.

8.3. Chapter 3 – Experimental Detail



Synthesis of [Ag-(*N*³-cytidine)₂][NO₃], (1)

Cytidine (200.0 mg, 0.88 mmol, 2.0 equiv.) was dissolved in water (4.5 ml). To this solution, another aqueous solution (0.5 ml) of AgNO₃ (74.7 mg, 0.44 mmol, 1.0 equiv.) was added slowly. The mixture was heated under reflux (100 °C) for 2 h in the dark. The solution was filtered while still warm; Long needle-like crystals were grown over a period of 14-days at room temperature using a thermal vapor diffusion chamber with acetonitrile as anti-solvent. The yield of crystals was 67%. ¹H NMR (400 MHz, Deuterium Oxide) δ 7.91 (d, *J* = 7.6 Hz, 1H), 6.09 (d, *J* = 7.5 Hz, 1H), 5.89 (d, *J* = 3.8 Hz, 1H), 4.33 – 4.25 (m, 1H), 4.19 (t, *J* = 5.7 Hz, 1H), 4.16 – 4.10 (m, 1H), 3.95 (dd, *J* = 12.7 Hz, 1H), 3.81 (dd, *J* = 12.8, 4.2 Hz, 1H); IR: $\tilde{\nu}$ = 3337, 3208, 2945, 1643, 1606, 1529, 1504, 1330, 1280, 1209, 1101, 1043, 950, 903, 870, 772, 717, 600 and 407 cm⁻¹; ESI-MS (C₁₈H₂₆AgN₆O₁₀) calculated: 593.0800, Experimental: 593.0957 (m/z); Elemental analysis ([Ag^I-(*N*³-cytidine)₂].NO₃.2H₂O) Calculated: C - 31.23%, H - 4.37%, N - 14.16%, Experimental: C - 31.79%, H - 4.25%, N - 13.91%.



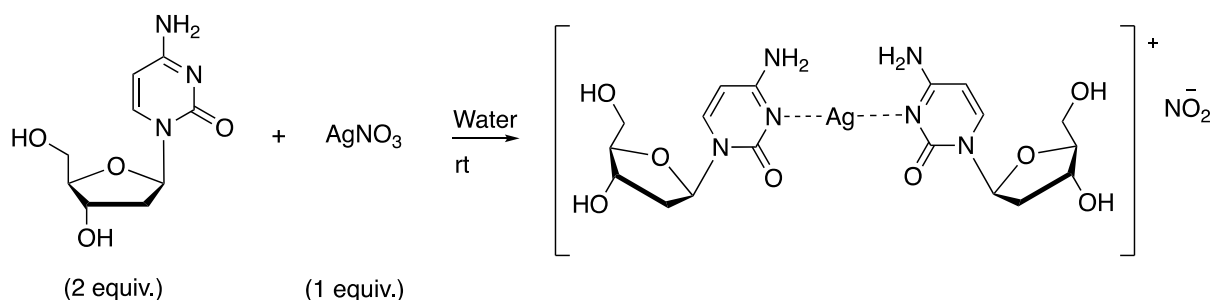
Synthesis of [Ag-(*N*³-cytidine)₂][NO₃], (1_{MeOH}) gel.

Cytidine (200.0 mg, 0.88 mmol, 2.0 equiv.) was dissolved in methanol (25 ml). To this solution, another solution of AgNO₃ (74.7 mg, 0.44 mmol, 1.0 equiv.) in methanol (25 ml) was added slowly. The mixture was heated under reflux (77 °C) for 2 h in the dark. The solution was filtered while still warm, then left to stand at room-temperature where a sample spanning colourless gel formed over 30 minutes. The corresponding xerogel was obtained by freeze-drying the gel. IR: $\tilde{\nu}$ = 3340, 3201, 2943, 1643, 1604, 1528, 1504, 1338, 1280, 1207, 1099, 1049, 995, 948, 902, 867, 771, 717, 597 and 409 cm⁻¹; ESI-MS (C₁₈H₂₆AgN₆O₁₀) calculated: 593.0800, Experimental: 593.0712 (m/z);

Elemental analysis ($[\text{Ag}-(N^3\text{-cytidine})_2]\cdot\text{NO}_3\cdot 2\text{H}_2\text{O}$) Calculated: C - 31.23%, H - 4.37%, N - 14.16%, Experimental: C - 31.78%, H - 4.33%, N - 13.84%.

8.4. Chapter 4 – Experimental Detail

Preparation & Characterisation of $[\text{Ag}^I-(N^3\text{-}2'\text{-Deoxycytidine})_2][\text{NO}_3]$.



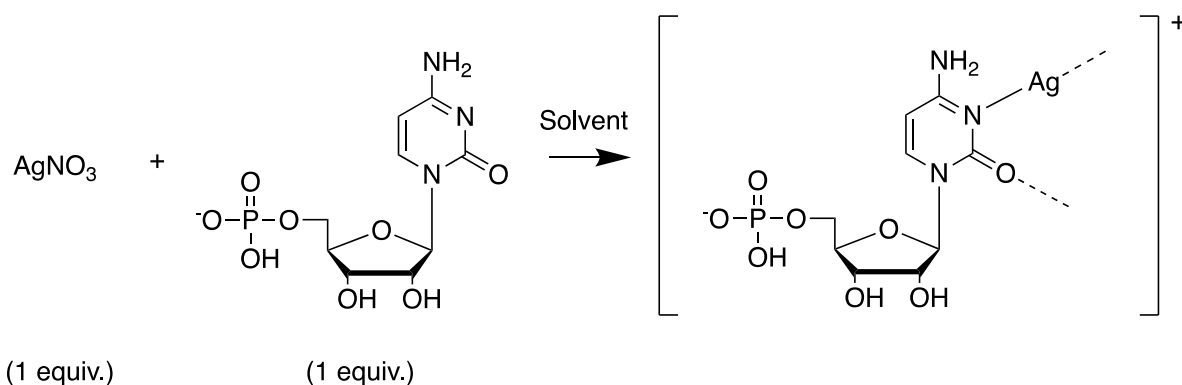
Preparation of $[\text{Ag}^I-(N^3\text{-}2'\text{-Deoxycytidine})_2][\text{NO}_3]$

2'-Deoxycytidine (100.0 mg, 0.44 mmol, 2.0 equiv.) was dissolved in water (13.0 ml). To this solution AgNO_3 (37.4 mg, 0.22 mmol, 1.0 equiv.) in water (0.5 ml) was added slowly in the dark. The mixture was placed into a thermal vapour diffusion chamber with acetonitrile as the counter solvent. After a period of 21 days at room temperature colourless crystals emerged. Abs λ_{max} (H_2O): 271 nm; ^1H -NMR (700 MHz, Deuterium Oxide (D_2O)) δ 7.74 (dd, $J = 7.5, 2.8$ Hz, 1H; H^4), 6.17 (td, $J = 6.7, 2.0$ Hz, 1H; H^3), 5.96 (dd, $J = 7.6, 3.0$ Hz, 1H; H^5), 4.33 (ddt, $J = 8.3, 6.3, 2.9$ Hz, 1H; H^{10}), 4.01 – 3.91 (m, 1H; H^8), 3.74 (ddd, $J = 12.5, 3.6, 2.2$ Hz, 1H; H^8), 3.65 (ddd, $J = 12.5, 5.2, 2.1$ Hz, 1H; $\text{H}^{11,12}$), 2.33 (ddd, $J = 13.3, 6.5, 2.9$ Hz, 1H; H^6), 2.25 – 2.18 (m, 1H; H^7); IR: $\tilde{\nu} = 3339, 3198, 3117, 2943, 2679, 1647, 1607, 1531, 1504, 1373, 1350, 1335, 1319, 1281, 1194, 1090, 1055, 995, 966, 951, 918, 870, 827, 806, 773, 758, 716, 673, 621, 598, 534$ and 509 cm^{-1} . ESI-MS ($\text{C}_{18}\text{H}_{26}\text{AgN}_6\text{O}_8$, $[\text{M}]^{1+}$) calculated: 561.09, Experimental: 561.1015 (m/z). Elemental analysis ($[\text{Ag}^I-(N^3\text{-}2'\text{-Deoxycytidine})_2]\cdot\text{NO}_3\cdot\text{H}_2\text{O}$) Calculated: C - 33.66%, H - 4.39%, N - 15.26%; Experimental: C - 33.39%, H - 4.33%, N - 15.54%.

8.5. Chapter 5 – Experimental Detail

Electrical measurements (I-V). Current/voltage curves were recorded on the probe station (Cascade Microtech with a B1500A parameter analyser, Agilent). All of the

electrical measurements were carried out under dry nitrogen without light illumination. For measurements on a single crystal, a crystal of **1** was electrically insulated on glass slide and the ends of the crystal were connected both directly and to tow pads of Ga-In eutectic.



Preparation of **1**, [Ag^I-(O²,N³,O⁷'-Cytidine-5'-monophosphate)]·H₂O –

Cytidine-5'-monophosphate (200.0 mg, 0.62 mmol, 1.0 equiv.) was dissolved in water (15 mL, 16.3 g/L). To this another solution of AgNO₃ (105.4 mg, 0.62 mmol, 1.0 equiv.) in water (1 mL) was added slowly in the dark. The mixture was then heated at reflux (110 °C) for 2 h and the final solution was filtered out while still warm and left to stand to crystalize in the dark. 21 days later at rt colourless crystalline material emerged. Abs. λ_{max} (H₂O): 274 nm; IR: $\tilde{\nu}$ = 3553, 3388, 3278, 3140, 2970, 2893, 1666, 1631, 1616, 1526, 1485, 1450, 1404, 1285, 1215, 1165, 1110, 1076, 1033, 975, 910, 871, 795, 760, 708, 597, 524, 480 cm⁻¹; ESI-MS (C₉H₁₃AgN₃O₈P) calculated [M]⁺¹: 429.9569, Experimental: 430.0007 (m/z). Elemental analysis [Ag-N³,O²-Cmp] Calculated: C – 25.14%, H – 3.05%, N – 9.77%, Experimental: C – 24.22%, H – 3.01%, N – 9.53%.

Preparation of **2**, [Ag^I-(O²,N³,O⁷'-Cytidine-5'-monophosphate)]·MeOH –

Cytidine-5'-monophosphate (400.0 mg, 0.62 mmol, 2.0 equiv.) was dissolved in methanol (100 mL) at 60°C. To this solution AgNO₃ (105.4 mg, 0.62 mmol, 1.0 equiv.) was added slowly in the dark. The mixture was then heated at reflux (77 °C) for 2 h and the final solution was filtered while still warm and left to stand to crystalize. 10 days later colourless crystals emerged while stored in the dark at room temperature. Abs. λ_{max} (H₂O): 275 nm; IR: $\tilde{\nu}$ = 3331, 3196, 2945, 1647, 1606, 1531, 1504, 1321, 1280, 1195, 1089, 1057, 995, 951, 773, 597 cm⁻¹; ESI-MS (C₉H₁₃AgN₃O₈P) calculated [M+H]⁺¹: 429.9564, Experimental: (m/z) 429.9233; Elemental analysis [Ag-N³,O²-Cmp]

Calculated: C – 25.14%, H – 3.05%, N – 9.77%, Experimental: C – 24.99%, H – 2.90%, N – 9.63%.

Preparation of 2D Molecular Sheets by Solvent-Based Mechanical Exfoliation –

A crystalline sample of **1** (ca. 10 mg) was transferred to filter paper. This was washed with acetone (3 x 10 mL) and allowed to dry in air for 5 minutes. The sample was added to toluene (1.5 mL) and the mixture was sonicated at 40 kHz using a Langford Sonomatic 475H for 30 minutes. The solution was pipetted (1-2 μ L) onto either mica or silicon wafer, allowed to dry, then analysed by AFM.

Single-Crystal X-ray Diffraction - Crystal structure data for **1** and **2** were collected at 150.0(2) K on an Xcalibur, Atlas, Gemini ultra-diffractometer equipped with a sealed X-ray tube ($\lambda_{\text{Cu K}\alpha} = 1.54184 \text{ \AA}$) and an Oxford Cryosystems CryostreamPlus open-flow N_2 cooling device. Cell refinement, data collection, and data reduction were undertaken via the software CrysAlisPro.^[1] Intensities were corrected for absorption analytically using a multifaceted crystal model created by indexing the faces of the crystal for which data were collected.^[2]

All structures were solved using XT^[3] and refined by XL^[4] using the Olex^{2[5]} interface. Hydrogen atoms were positioned with idealized geometry, with the exception of those bound to heteroatoms which were located from peaks in the Fourier difference map. The thermal parameters of the hydrogen atoms were constrained using the riding model with $U_{(\text{H})}$ set at $1.2U_{\text{eq}}$ for the parent atom.

8.6. Chapter 6 – Experimental Details

Silver nitrate (99.9+%) was used as received from Sigma-Aldrich unless otherwise stated. Oligonucleotides (ss-DNA) were prepared as instructed by the vendor (ATDBio or Eurofins Genomics), typically 1.0 mL of H_2O was added to the dehydrated powder yielding a 0.1 mM (100 pmol/ μ L) solution (H_2O volumes may have varied based on the synthesis scale). Manufacture for all oligos was achieved using salt-free methods and HPLC purification. Oligo concentrations were checked by absorbance using molar absorptivity and masses via ESI-MS (negative ion mode).

Sample preparation

A 10.0 mM stock solution of silver nitrate (AgNO_3 , 169.87 g/mol, 170 mg) was prepared in 100 mL of nanopure H_2O at the start of any experiment. This protocol ensures the lasting potency of silver(I) ions due to the risk of photoreduction *via* ambient light sources. The silver(I) solution was typically diluted by a factor of x10 or 100 achieving a 1.0 or 0.1 mM stock equivalent to the concentration of the prepared oligonucleotide (0.1 mM or 100 pmol/ μL). The two solutions were combined in ratios predetermined to suite the experiment. Samples were tested immediately after mixing, typically within 5 minutes.

References:

1. CrysAlisPro, 1.171.35; Agilent Technologies: 2010.
2. Clark, R. C.; Reid, J. S. OLEX2. Acta Crystallogr., Sect. A: Found. Crystallogr. 1995, A51, 887–897.
3. Sheldrick, G. M. A short history of SHELX. Acta Crystallogr., Sect. A: Found. Crystallogr. 2008, A64, 112–122.
4. Sheldrick, G. M. SHELXT - Integrated space-group and crystal- structure determination. Acta Crystallogr., Sect. A: Found. Adv. 2015, A71, 3–8.
5. Dolomanov, O. V.; Bourhis, L. J.; Gildea, R. J.; Howard, J. A. K.; Puschmann, H. J. Appl. Crystallogr. 2009, 42, 339–341.

Appendix

Exploring Silver-Pyrimidine Chemistry and the Controlled Assembly of M-DNA Systems

Liam Mistry

Table of Contents

S.1. Chapter 2. <i>Transoid</i> and <i>Cisoid</i> Conformations in Silver-Mediated Cytosine Base Pairs. Hydrogen-Bonding Dictates Argentophilic Interactions in the Solid-State.	246
S.1.1. General Methodology.....	246
S.1.2. Crystallographic Data.....	248
S.1.3. Spectroscopic Data.....	254
S.1.4. Mechanical Synthesis – Additional Data	258
S.1.5. 1-Methylcytosine Synthesis & Characterisation.....	259
S.2. Chapter 3, “Metallo-DNA”; Ag ^I -Mediated Supramolecular Duplex with Self-healing gelatinous properties.	261
S.2.1. Synthesis and Crystallographic Data.	261
S.2.2. X-Ray Crystal Structure Determination for complex 1.	263
S.2.3. Rheology	270
S.2.4. Microscopy, including SEM and AFM images.	271
S.2.5. Conductivity Measurements, IV and EFM.	275
S.2.6. Reduction Behaviour.....	278
S.2.7. Band Structure Calculations.....	282
S.3. Chapter 6. Ag ^I -Oligonucleotide Hairpin formation towards controlled cluster assembly	283
S.3.1. General Methodology.....	283
S.3.2. Electrospray Ionisation Mass Spectrometry	285
S.3.3. ΔG ; Gibbs Energy Calculations using MS peak intensity data.....	333

S.1. Chapter 2. *Transoid* and *Cisoid* Conformations in Silver-Mediated Cytosine Base Pairs. Hydrogen-Bonding Dictates Argentophilic Interactions in the Solid-State.

S.1.1. General Methodology

Computational calculations were performed using Gaussian 09 with the B3LYP functional and LanL2DZ basis set processed using Newcastle University's Rocket HPC services (high performance computing).

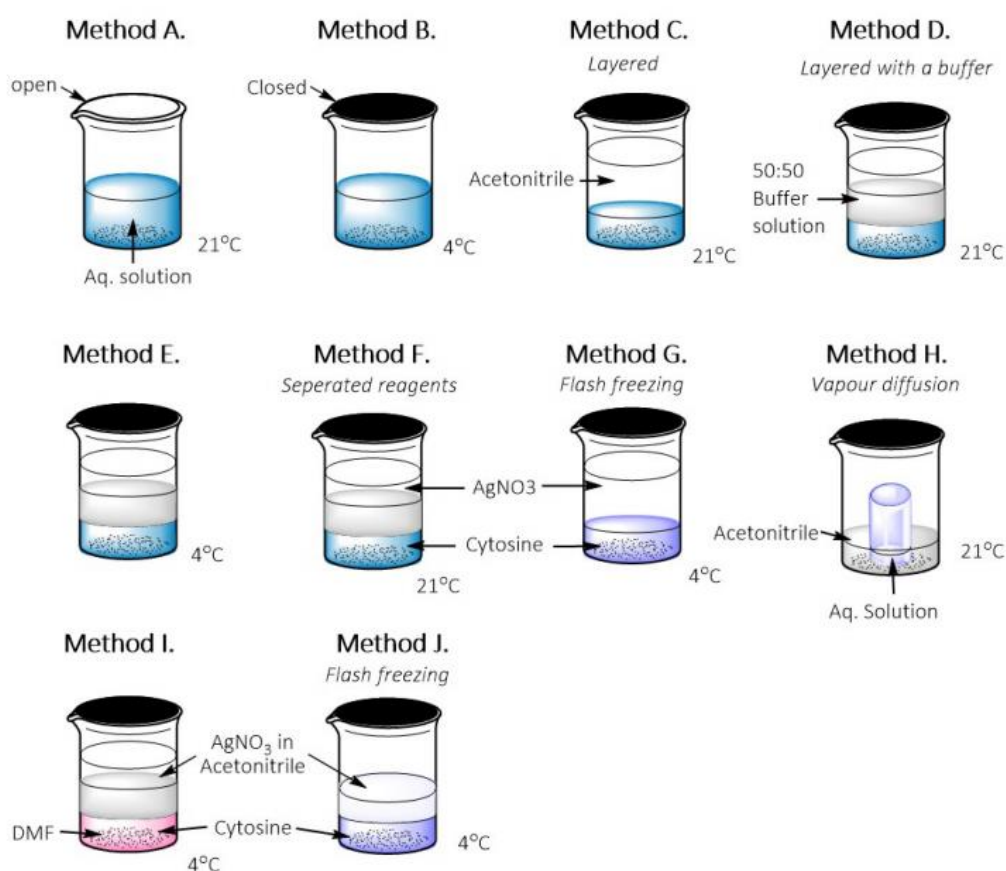


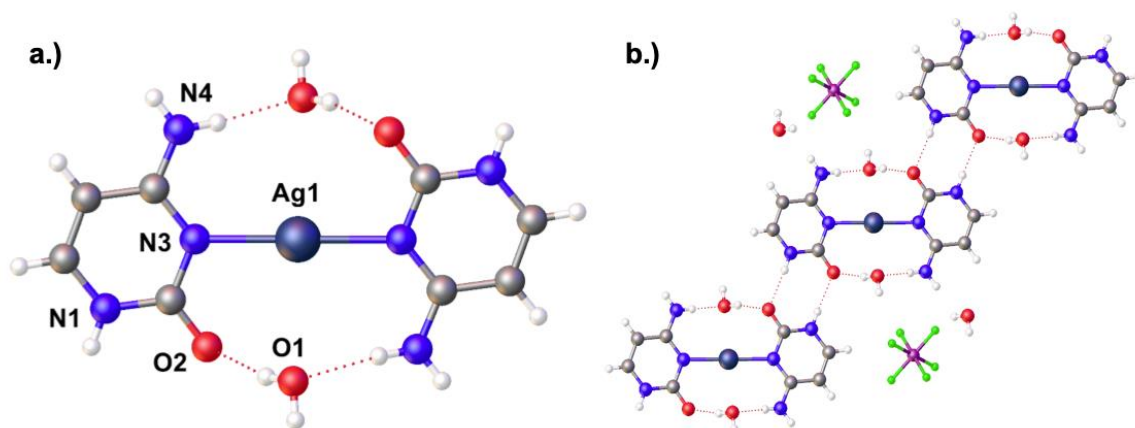
Figure 1. Crystallization methods attempted: (A) evaporation at room temperature (21°C), (B) storage at low temperatures (4°C), diffusion by means of a layered approach with (D – F, I) and without (C and G) a buffer, (H) Vapour diffusion and (J) flash freezing and subsequent slow warming of the reactant solution. The antisolvent of choice was acetonitrile (MeCN) at a 1:1 ratio.

Table 1. Crystallization outcome, Method (Figure 1) *versus* Silver(I) salt.

Methods	AgNO ₃	AgBF ₄	AgPF ₆
A	O	X	X
B	X	X	X
C	O	X	X
D	X	X	X
E	X	X	X
F	X	X	X
G	X	X	X
H	X	X	O
I	X	X	X
J	X	X	X

O – Single Crystals gained, X - Failed

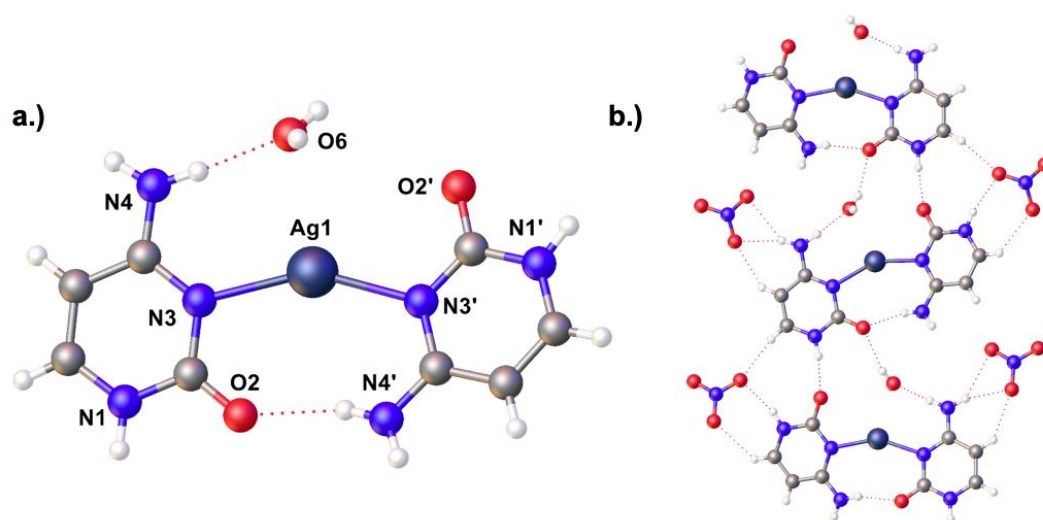
S.1.2. Crystallographic Data



<i>Trans</i> -[Ag(I)(N3-cytosine) ₂][PF ₆]·2H ₂ O, 1	
Empirical formula	C ₈ H ₁₄ AgF ₆ N ₆ O ₄ P
Formula weight	511.09
Temperature/K	150.0(2)
Crystal system	triclinic
Space group	P-1
<i>a</i> /Å	5.73550(10)
<i>b</i> /Å	8.2571(2)
<i>c</i> /Å	8.64840(10)
α /°	88.005(2)
β /°	79.213(2)
γ /°	75.358(2)
Volume/Å ³	389.239(13)
<i>Z</i>	1
ρ_{calc} /cm ³	2.180
μ /mm ⁻¹	1.497
<i>F</i> (000)	252.0
Crystal size/mm ³	0.33 × 0.2 × 0.08
Radiation	MoK α (λ = 0.71073)
2 θ range for data collection/° 6.956 to 58.5	

Index ranges	$-7 \leq h \leq 7, -11 \leq k \leq 11, -11 \leq l \leq 11$
Reflections collected	31082
Independent reflections	1852 [$R_{\text{int}} = 0.0208, R_{\text{sigma}} = 0.0083$]
Data/restraints/parameters	1852/0/136
Goodness-of-fit on F^2	1.097
Final R indexes [$I \geq 2\sigma(I)$]	$R_1 = 0.0153, wR_2 = 0.0411$
Final R indexes [all data]	$R_1 = 0.0156, wR_2 = 0.0412$
Largest diff. peak/hole / $e \text{ \AA}^{-3}$	0.54/-0.29
Empirical formula	$\text{C}_8\text{H}_{14}\text{AgF}_6\text{N}_6\text{O}_4\text{P}$

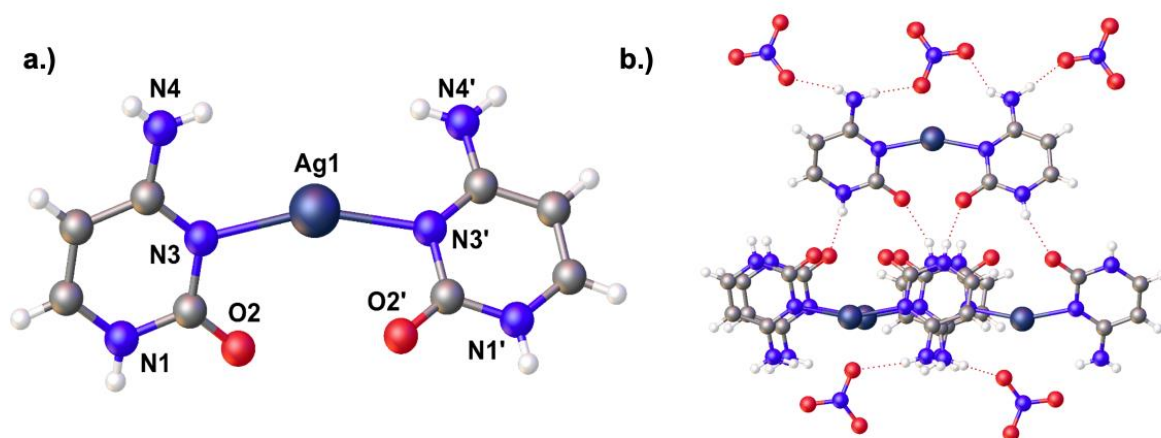
Table 2. Crystal data and structural refinement for *Trans*-[Ag(I)-(N³-cytosine)₂][PF₆] \cdot 2H₂O; **1**.



<i>Trans</i> -[Ag(I)(<i>N</i> 3-cytosine) ₂][NO ₃]·H ₂ O, 2	
Empirical formula	C ₈ H ₁₂ AgN ₇ O ₆
Formula weight	410.12
Temperature/K	150.0(2)
Crystal system	monoclinic
Space group	P2 ₁
<i>a</i> /Å	3.56438(8)
<i>b</i> /Å	15.5555(3)
<i>c</i> /Å	11.9263(3)
α /°	90
β /°	93.143(2)
γ /°	90
Volume/Å ³	660.27(2)
<i>Z</i>	2
ρ_{calc} /cm ³	2.063
μ /mm ⁻¹	12.711
<i>F</i> (000)	408.0
Crystal size/mm ³	0.18 × 0.07 × 0.012
Radiation	CuK α (λ = 1.54184)
2 θ range for data collection/°	7.424 to 133.688
Index ranges	-3 ≤ <i>h</i> ≤ 4, -18 ≤ <i>k</i> ≤ 18, -14 ≤ <i>l</i> ≤ 14

Reflections collected	9380
Independent reflections	2331 [$R_{\text{int}} = 0.0466$, $R_{\text{sigma}} = 0.0391$]
Data/restraints/parameters	2331/16/223
Goodness-of-fit on F^2	1.028
Final R indexes [$I \geq 2\sigma(I)$]	$R_1 = 0.0231$, $wR_2 = 0.0478$
Final R indexes [all data]	$R_1 = 0.0277$, $wR_2 = 0.0501$
Largest diff. peak/hole / $e \text{ \AA}^{-3}$	0.44/-0.43
Flack parameter	-0.043(6)

Table 3. Crystal data and structural refinement for *Trans*-[Ag(I)-(N³-cytosine)₂][NO₃]·H₂O; **2**.



Cis-[Ag(I)(*N*3-cytosine)₂][NO₃], **3**

Empirical formula	C ₈ H ₁₀ AgN ₇ O ₅
Formula weight	392.10
Temperature/K	295.0(2)
Crystal system	Monoclinic
Space group	P2 ₁ /c
<i>a</i> /Å	13.6114(5)
<i>b</i> /Å	7.1848(2)
<i>c</i> /Å	12.7288(4)
α /°	90
β /°	101.922(3)
γ /°	90
Volume/Å ³	1217.97(7)
<i>Z</i>	4
ρ_{calc} /g/cm ³	2.138
μ /mm ⁻¹	13.681
<i>F</i> (000)	776.0
Crystal size/mm ³	0.17 × 0.02 × 0.01
Radiation	CuK α (λ = 1.54184)
2 θ range for data collection/°	13.296 to 133.5

Index ranges	-16 ≤ h ≤ 16, -8 ≤ k ≤ 6, -15 ≤ l ≤ 15
Reflections collected	8982
Independent reflections	2167 [R _{int} = 0.0410, R _{sigma} = 0.0345]
Data/restraints/parameters	2167/294/316
Goodness-of-fit on F ²	1.004
Final R indexes [I ≥ 2σ (I)]	R ₁ = 0.0248, wR ₂ = 0.0522
Final R indexes [all data]	R ₁ = 0.0398, wR ₂ = 0.0591
Largest diff. peak/hole / e Å ⁻³	0.24/-0.36

Table 4. Crystal data and structural refinement for *cis*-[Ag(I)-(N³-cytosine)₂][NO₃]; **3**.

All crystal structure data were collected on an Xcalibur, Atlas, Gemini ultra-diffractometer equipped with an Oxford Cryosystems CryostreamPlus open-flow N₂ cooling device. Data for **3** and **2** were collected using copper radiation ($\lambda_{\text{CuK}\alpha} = 1.54184 \text{ \AA}$) and the intensities corrected for absorption using a multifaceted crystal model created by indexing the faces of the crystal for which data were collected.¹ Data for **1** were collected using molybdenum radiation ($\lambda_{\text{MoK}\alpha} = 0.71073 \text{ \AA}$) and the intensities corrected for absorption empirically using spherical harmonics. Data were collected at 150 K except in the case of **3** for which data were collected at 295 K as crystals of this compound underwent a phase transition at lower temperatures. Cell refinement, data collection and data reduction were undertaken via the software CrysAlisPro.²

All structures were solved using XT³ and refined by XL⁴ using the Olex2 interface⁵. All non-hydrogen atoms were refined anisotropically and hydrogen atoms were positioned with idealised geometry, with the exception of those bound to heteroatoms, the positions of which were located using peaks in the Fourier difference map. The displacement parameters of the hydrogen atoms were constrained using a riding model with U_(H) set to be an appropriate multiple of the U_{eq} value of the parent atom.

1. Clark, R. C.; Reid, J. S. The Analytical Calculation of Absorption in Multifaceted Crystals. *Acta Cryst.* **1995**, A51, 887-897.
2. CrysAlisPro. *Rigaku Oxford Diffraction*. Tokyo, Japan.
3. Sheldrick, G. M. SHELXT - integrated space-group and crystal-structure determination. *Acta Crystallogr. A: Found Adv.* **2015**, 71, 3-8 DOI: 10.1107/S2053273314026370.
4. Sheldrick, G. M. A short history of SHELX. *Acta Crystallogr. A: Found Adv.* **2008**, 64, 112-22 DOI: 10.1107/S0108767307043930.
5. Dolomanov, O. V.; Bourhis, L. J.; Gildea, R. J.; Howard, J. A. K.; Puschmann, H. OLEX2: a complete structure solution, refinement and analysis program. *J. Appl. Cryst.* **2009**, 42 (2), 339-341 DOI: 10.1107/s0021889808042726.

S.1.3. Spectroscopic Data

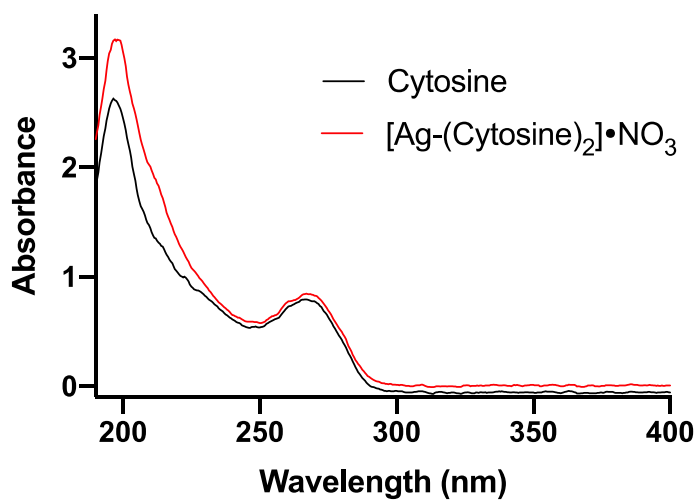


Figure 2. UV-vis data for aqueous solutions of cytosine (black-line) and [Ag-(Cytosine)₂] (red-line).

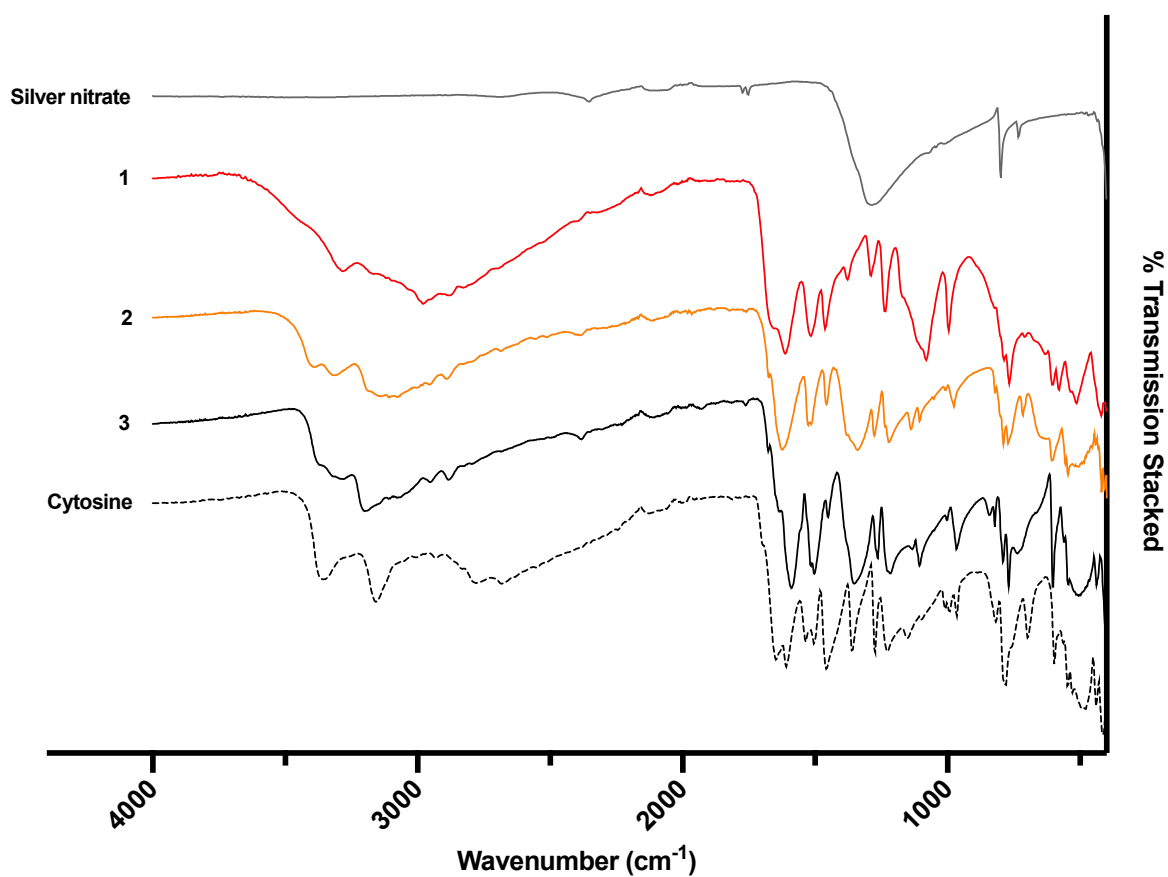


Figure 3. FTIR data for complexes 1 - 3 (red-, yellow- and black-lines), cytosine (dotted-line) and silver nitrate (grey-line).

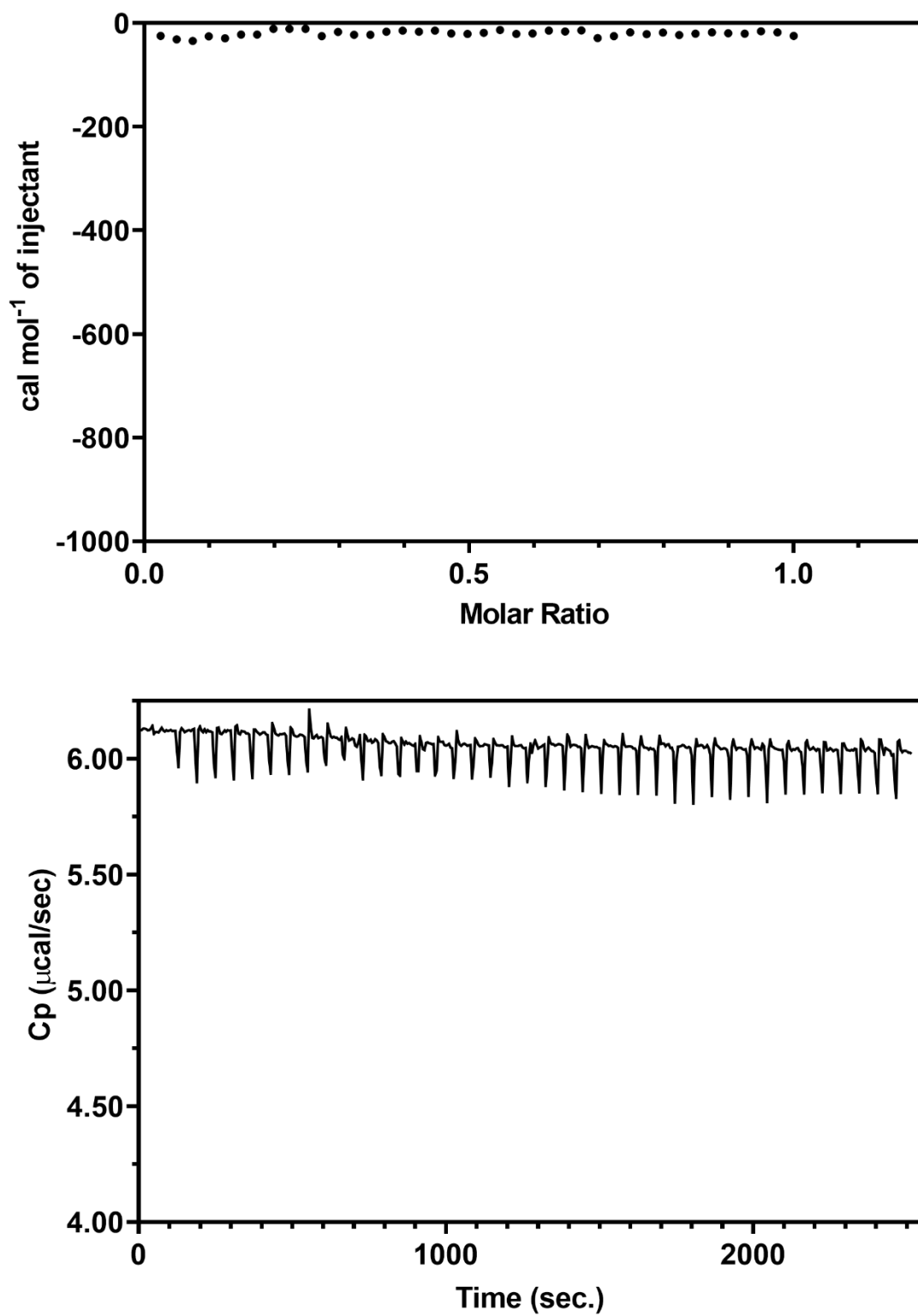


Figure 4. ITC water-into-water blank to account for dilution affects.

Table 5. FTIR peak assignment for bis-(cytosine)-Ag⁺ complexes **1-3** (Range: 700-4000 cm⁻¹)

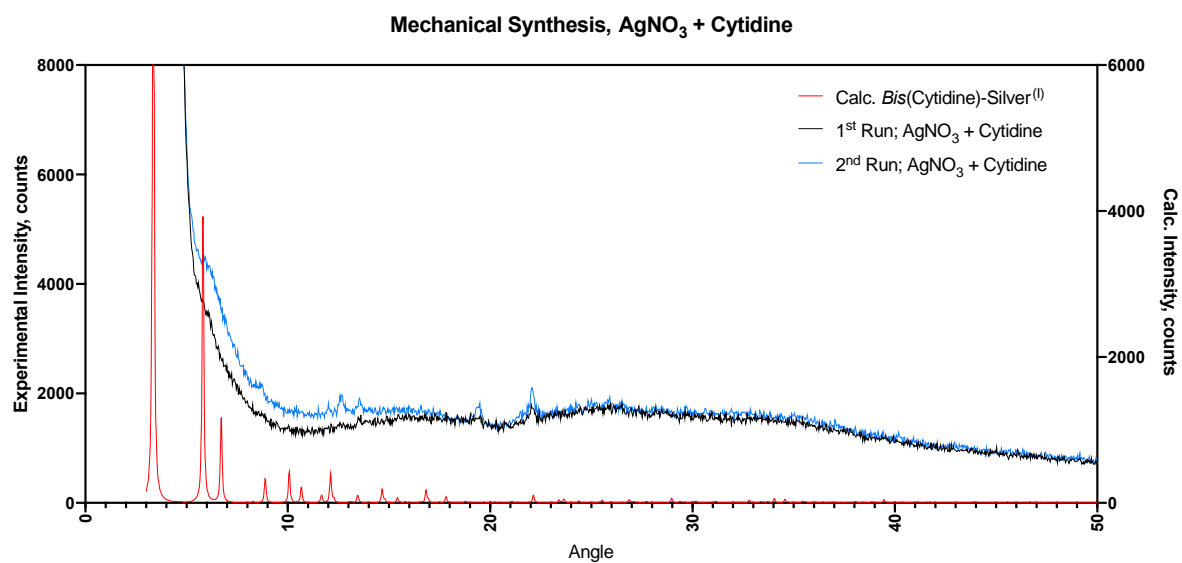
Cytosine	<i>Cis</i> -[Ag-(cytosine) ₂], 1	<i>Trans</i> -[Ag-(cytosine) ₂]-[H ₂ O], 2	<i>Trans</i> -[Ag-(cytosine) ₂]-[2H ₂ O], 3	Assignment
3364	3374	3399	-	$\nu_{as}(\text{NH}_2)$
-	3298	3325	-	
3159	3203	3190	3187	$\nu_s(\text{NH}_2)$
-	-	3148	3179	
-	-	3113	-	
-	3084	3084	-	
-	2960	2964	2982	
2789	2889	2897	2893	$\nu(\text{C-H})$
2689	-	-	2835	$\nu(\text{C-H})$
-	-	2694	2708	
-	-	2567	-	
-	-	2529	-	
-	2390	2396	2407	
-	-	-	2129	
1697	1678	1676	1658	$\delta(\text{NH}_2)$
1647	1637	1628	1612	$\nu(\text{C}=\text{O})$
1608	1591	-	-	$\nu(\text{C}5=\text{C}6)$
-	1557	-	-	
1535	-	1528	-	$\delta(\text{N-H})$ in plane
-	1518	1516	1519	

1).

Table 6. FTIR peak assignment continued (Range: 400-700 cm⁻¹).

1504	1504	-	-	$\nu(\text{C4}=\text{N3})$ and $\nu(\text{C4}-\text{N4})$
1458	1452	1458	1462	$\nu(\text{C4}-\text{N3})$ and $\nu(\text{C2}-\text{N3})$
-	-	1381	1377	
1362	1356	1365	-	$\delta(\text{C}=\text{C}-\text{H})$
-	-	1344	-	
1273	1265	1277	1292	$\nu(\text{C2}-\text{N1})$ & $\nu(\text{C6}-\text{N1})$
1231	1219	1236	1238	$\nu(\text{C4}-\text{N4})$
-	-	1223	-	
1153	1134	1140	1169	$\nu(\text{C}-\text{O})$
1099	1107	1107	1111	$r(\text{NH}_2)$
-	-	-	1080	
-	-	1053	-	
1011	1003	1009	-	$\delta(\text{N1}-\text{C6}-\text{H})$ in plane
995	-	-	995	$\delta(\text{C4}-\text{C5}-\text{H})$ in plane
964	966	978	-	$\nu(\text{C4}-\text{C5})$
-	845	822	825	
818	821	802	802	$\delta(\text{N}-\text{H})$ out of-plane
783	791	789	787	$\nu(\text{ring})$
-	770	771	768	
-	740	-	-	
-	-	718	710	

S.1.4. Mechanical Synthesis – Additional Data



S.1.5. 1-Methylcytosine Synthesis & Characterisation

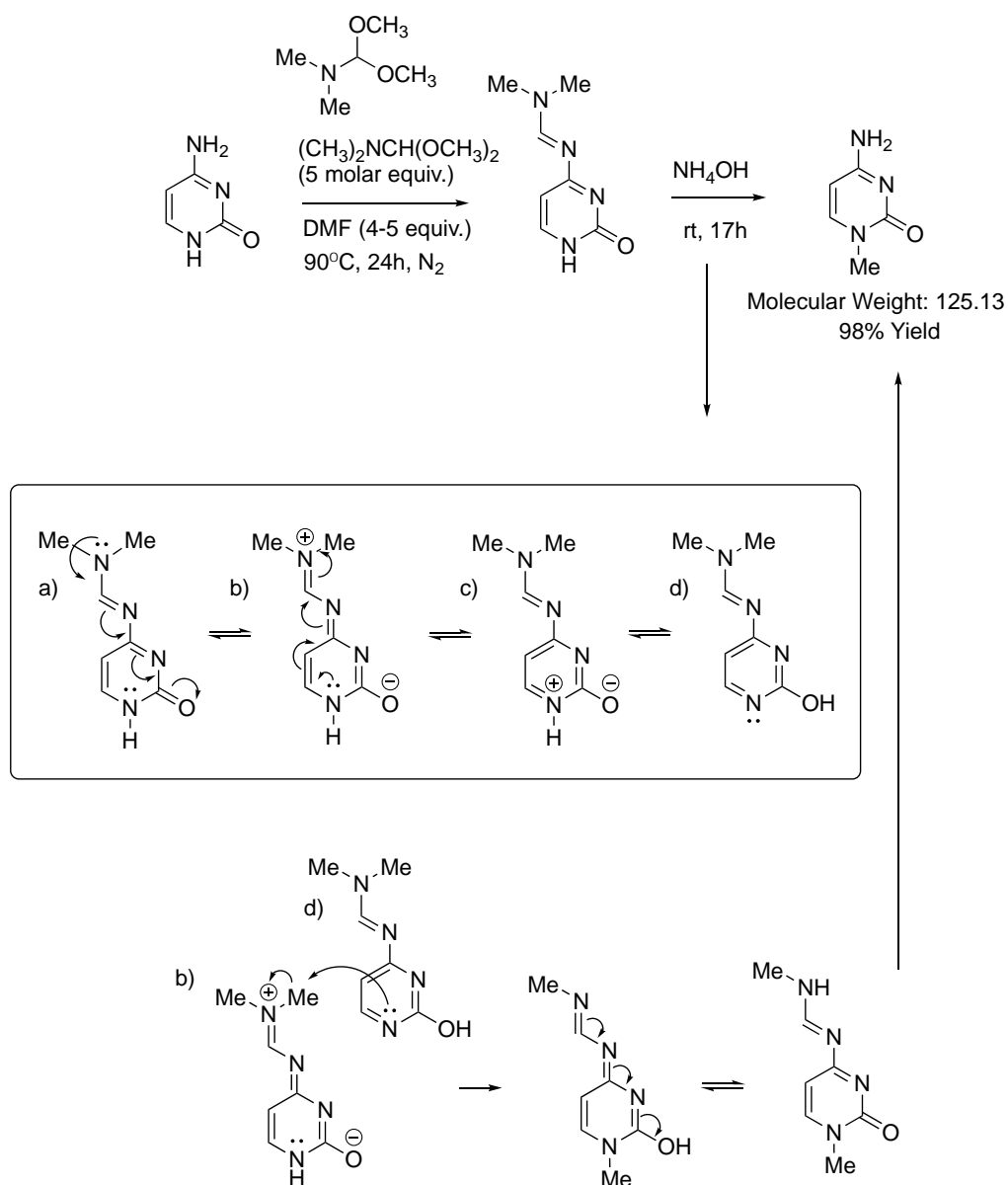


Figure 5. Reaction scheme for the synthesis of 1-methylcytosine including detailed reaction pathway proposal.

Step 1 - A mixture of dry cytosine (1 g, 9 mmol), *N,N*-dimethylformamide dialkyl (diaralkyl) acetal (Mw: 119.16; 5.4 – 9.5 g, 45 - 80 mmol), and dry *N,N*-dimethylformamide (3 - 20 mL (0.948 g/mL)) was heated at 90°C to reflux under a nitrogen atmosphere for 24h. The reaction mixture was cooled and evaporated to dryness on a rotary evaporator at 60°C in vacuo, and the white solid obtained was recrystallized from benzene-Chloroform (Mp: $203\text{-}204^\circ\text{C}$). Toluene was added to the solution to encourage evaporation. ^1H NMR (300 MHz, Deuterium Oxide) δ 8.50 (d, J = 4.9 Hz, 1H), 7.69 (dd, J = 22.3, 7.0 Hz, 1H), 6.16 (d, J = 7.0 Hz, 1H), 3.42 (s, 2H), 3.23 (s, 3H), 3.08 (s, 3H).

Step 2 - Concentrated ammonium hydroxide solution (10 mL) was added to the product (0.5 mmol) obtained from step 1 and stirred at room temperature for 17h. The solution was then heated in a steam bath for 30 min to drive off excess ammonia evaporating to dryness, and the solid residue obtained was recrystallized from MeOH-Petroleum ether (Mp: 301-302°C). A yellow solid was collected yielding a low 1.8% (180.6 mg). The single X-ray diffraction techniques of the crystals confirmed the

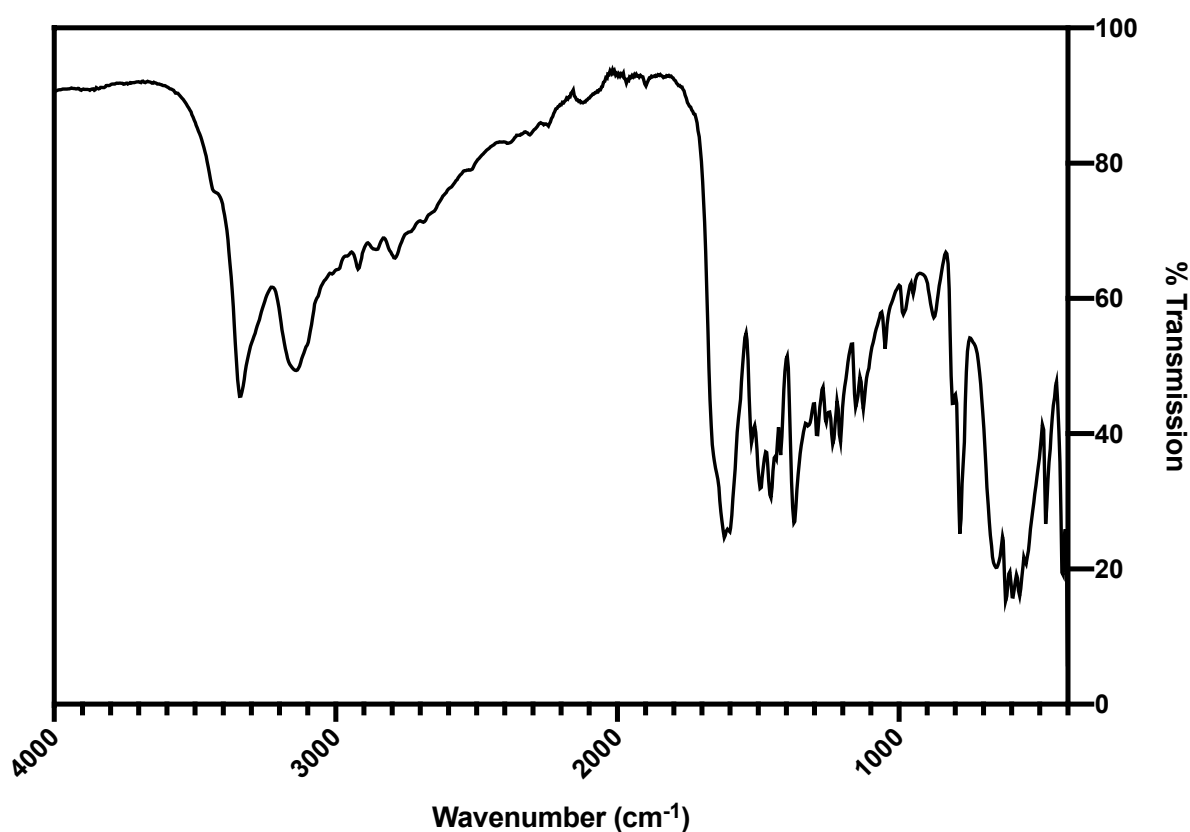
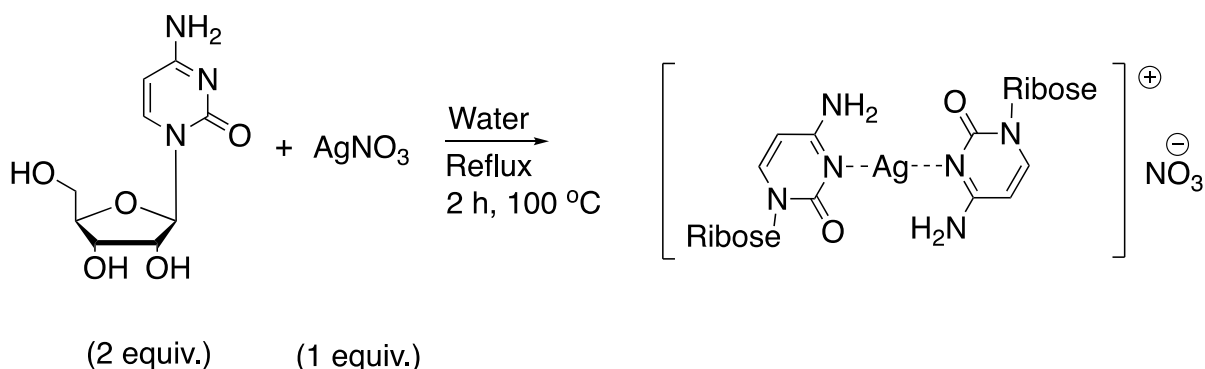


Figure 6. FTIR of 1-methylcytosine

S.2. Chapter 3, “Metallo-DNA”; Ag^I-Mediated Supramolecular Duplex with Self-healing gelatinous properties.

S.2.1. Synthesis and Crystallographic Data.



Synthesis of [Ag(*N*³-cytidine)₂][NO₃], (1)

Cytidine (200.0 mg, 0.88 mmol, 2.0 equiv.) was dissolved in water (4.5 ml). To this solution, another aqueous solution (0.5 ml) of AgNO₃ (74.7 mg, 0.44 mmol, 1.0 equiv.) was added slowly. The mixture was heated under reflux (100 °C) for 2 h in the dark. The solution was filtered while still warm; Long needle-like crystals were grown over a period of 14-days at room temperature using a thermal vapor diffusion chamber with acetonitrile as anti-solvent. The yield of crystals was 67%. ¹H NMR (400 MHz, Deuterium Oxide) δ 7.91 (d, *J* = 7.6 Hz, 1H), 6.09 (d, *J* = 7.5 Hz, 1H), 5.89 (d, *J* = 3.8 Hz, 1H), 4.33 – 4.25 (m, 1H), 4.19 (t, *J* = 5.7 Hz, 1H), 4.16 – 4.10 (m, 1H), 3.95 (dd, *J* = 12.7 Hz, 1H), 3.81 (dd, *J* = 12.8, 4.2 Hz, 1H); IR: $\tilde{\nu}$ = 3337, 3208, 2945, 1643, 1606, 1529, 1504, 1330, 1280, 1209, 1101, 1043, 950, 903, 870, 772, 717, 600 and 407 cm⁻¹; ESI-MS (C₁₈H₂₆AgN₆O₁₀) calculated: 593.0800, Experimental: 593.0957 (*m/z*); Elemental analysis ([Ag(*N*³-cytidine)₂] \cdot NO₃ \cdot 2H₂O) Calculated: C - 31.23%, H - 4.37%, N - 14.16%, Experimental: C - 31.79%, H - 4.25%, N - 13.91%.

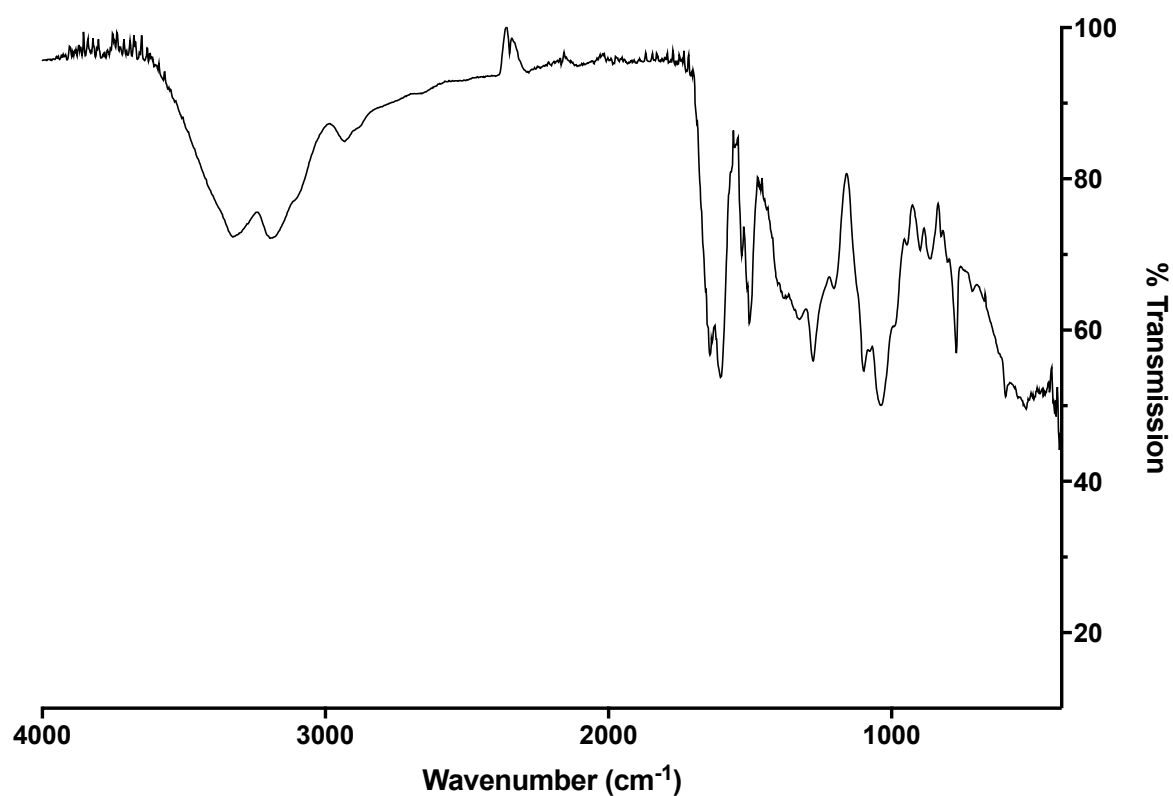


Figure S7. FTIR data of complex **1**, over the 400 – 4000 cm^{-1} range.

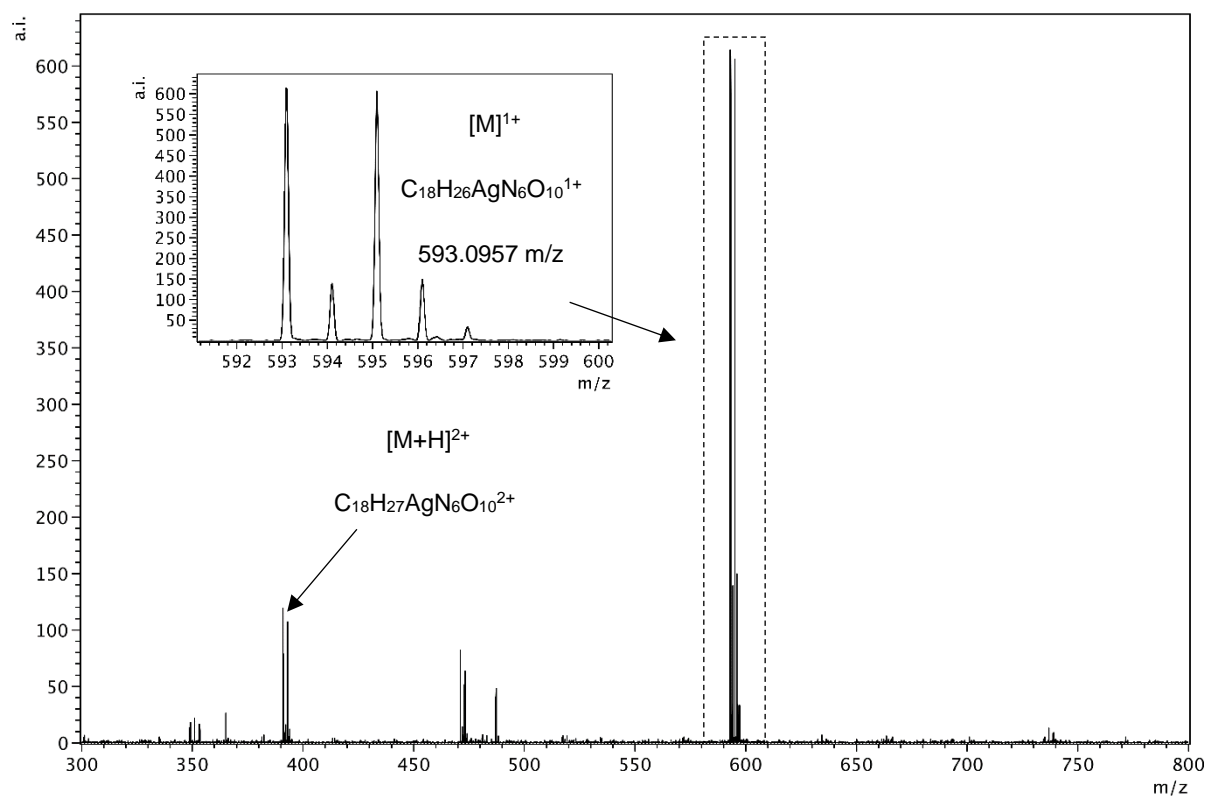


Figure S8. ESI-MS data measured for **1** collected in high resolution positive-ion mode.

S.2.2. X-Ray Crystal Structure Determination for complex 1.

The crystallographic study of **1** was hampered by a number of factors. Available crystals were too small and weakly diffracting for investigation using standard in-house facilities, even with enhanced microsource X-ray intensities. The weakness of the diffraction was subsequently found to be exacerbated by extensive structural disorder and pseudo-symmetry. After repeated attempts an adequate set of single-crystal diffraction data was obtained at beamline I19 of Diamond Light Source,¹ providing a reliable unit cell geometry and a clear indication of the space group (one of an enantiomeric pair), which had been uncertain from earlier attempts, possibly because of some merohedral twinning.

Standard multiscan corrections were applied for absorption and for incident beam intensity variations.² The positions of Ag atoms were readily found by a variety of routine direct and heavy-atom methods. These, however, are arranged in a regular and almost linear chain along the crystallographic *c* axis, with 5 Ag atoms in the asymmetric unit. This leads to a dominance of the diffraction pattern by strong reflections with $l = 5n$. Use of all available routine methods for structure solution failed due to the pseudo-symmetry of the helical structure of the polymeric cation chain, which was subsequently found to display approximate non-crystallographic fivefold screw axis symmetry; the threefold crystallographic screw axis relate cation chains to each other. The structure was eventually solved with successive manual selection of possible ligand atom positions from the multiple images in electron density maps insufficiently phased by the silver atoms, relying on the recognition of fragments of cytidine rings.

To aid refinement, geometrical similarity restraints were applied to the bond lengths and angles of the 10 ligands in the asymmetric unit, together with similarity and rigid-bond restraints on their anisotropic displacement parameters.³ H atoms were included in geometrically calculated positions and refined with a riding model; those on OH groups were allocated to give a reasonably self-consistent set of positions appropriate for hydrogen bonds where these could be identified. Reliable positions could not be found for the nitrate counter-anions or solvent molecules, which occupy large apparent voids between cation polymer chains; these were treated by the SQUEEZE procedure of PLATON.⁴ Nitrate anions, but not solvent molecules, are included in the chemical formula and calculated physical properties.

Resonant ('anomalous') scattering effects of the silver atoms are significant and provide confirmation of the absolute configuration of the overall structure, consistent with that known for the ligand sugar component,⁵ giving a refined value of 0.08(4) for the absolute structure parameter.

$\text{C}_{18}\text{H}_{26}\text{AgN}_6\text{O}_{10}^+ \text{NO}_3^-$, $M = 656.3$, trigonal, space group $P3_2$, $a = b = 30.382(7)$, $c = 14.976(3)$ Å, $V = 11972(6)$ Å³, $Z = 15$ ($Z' = 5$), crystal size $0.194 \times 0.016 \times 0.014$ mm³, $T = 100$ K,

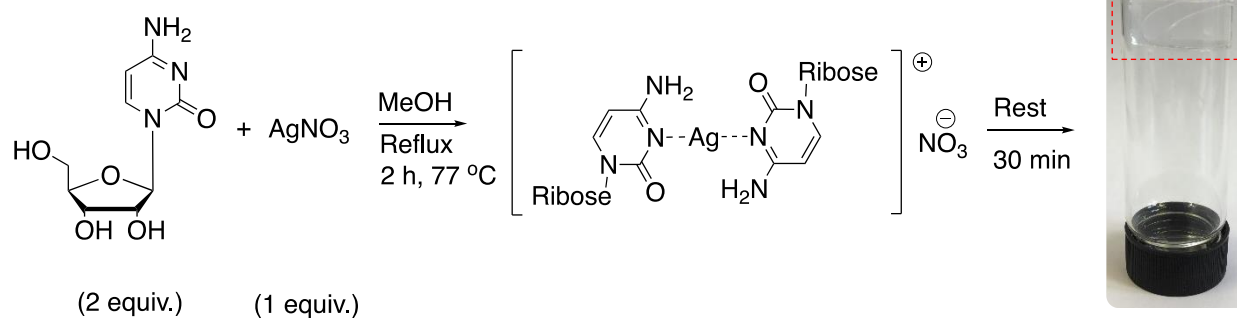
$\lambda(\text{synchrotron}) = 0.6889 \text{ \AA}$, 93293 reflections measured, 26785 unique ($R_{\text{int}} = 0.0718$), transmission 0.86–0.99; $R(F, F^2 > 2\sigma) = 0.0904$, $R_w(F^2, \text{all data}) = 0.2777$, goodness-of-fit on $F^2 = 0.955$, for 1576 refined parameters and 4509 restraints, final difference map peaks and holes between 1.53 and -0.66 e \AA^{-3} .

Table S1. Crystal data and structure refinement parameters for [Ag^(I)-N3-(Cytidine)₂]-MeCN·H₂O

Identification code	aho170073	
Chemical formula (moiety)	C ₁₈ H ₂₆ AgN ₆ O ₁₀ ⁺ ·NO ₃	
Chemical formula (total)	C ₁₈ H ₂₆ AgN ₇ O ₁₃	
Formula weight	656.33	
Temperature	100(2) K	
Radiation, wavelength	synchrotron, 0.6889 Å	
Crystal system, space group	trigonal, P3 ₂	
Unit cell parameters	a = 30.382(7) Å	α = 90°
	b = 30.382(7) Å	β = 90°
	c = 14.976(3) Å	γ = 120°
Cell volume	11972(6) Å ³	
Z	15	
Calculated density	1.366 g/cm ³	
Absorption coefficient μ	0.644 mm ⁻¹	
F(000)	5010	
Crystal color and size	colorless, 0.194, 0.016, 0.014 mm ³	
Reflections for cell refinement	9382 (θ range 2.2 to 23.4°)	
Data collection method	fixed-χ diffractometer with Pilatus 2M detector	
	narrow-frame ω and φ scans	
θ range for data collection	0.8 to 24.1°	
Index ranges	h 35 to 34, k 35 to 35, l 17 to 17	
Completeness to θ = 24.1°	98.7 %	
Reflections collected	93293	
Independent reflections	26785 (R _{int} = 0.0718)	
Reflections with F ² > 2σ	14630	
Absorption correction	multi-scan	
Min. and max. transmission	0.860 and 0.990	
Structure solution	Dual-space iterative method	
Refinement method	Full-matrix least-squares on F ²	
Weighting parameters a, b	0.1772, 0	
Data / restraints / parameters	26785 / 4509 / 1576	
Final R indices [F ² > 2σ]	R1 = 0.0904, wR2 = 0.2500	
R indices (all data)	R1 = 0.1248, wR2 = 0.2777	
Goodness-of-fit on F ²	0.955	
Absolute structure parameter	0.08(4)	
Largest and mean shift/su	0.017 and 0.000	
Largest diff. peak and hole	+1.53 and -0.66 e Å ⁻³	

References

1. (a) Allan, D. R.; Nowell, H.; Barnett, S. A.; Warren, M. R.; Wilcox, A.; Christensen, J.; Saunders, L. K.; Peach, A.; Hooper, M. T.; Zaja, L.; Patel, S.; Cahill, L.; Marshall, R.; Trimnell, S.; Foster, A. J.; Bates, T.; Lay, S.; Williams, M. A.; Hathaway, P. V.; Winter, G.; Gerstel, M.; Wooley, R. W. *Crystals* 2017, **7**, 336. (b) Johnson, N. T.; Waddell, P. G.; Clegg, W.; Probert, M. R. *Crystals* 2017, **7**, 360.
2. Krause, L.; Herbst-Irmer, R.; Sheldrick, G. M.; Stalke, D. *J. Appl. Crystallogr.* 2015, **48**, 3.
3. Sheldrick, G. M. *Acta Crystallogr., Sect. C* 2015, **71**, 3.
4. Spek, A. L. *Acta Crystallogr., Sect. C* 2015, **71**, 9.
5. Flack, H. D. *Acta Crystallogr., Sect. A* 1983, **39**, 876. (b) Parsons, S.; Flack, H. D.; Wagner, T. *Acta Crystallogr., Sect. B* 2013, **69**, 249.



Synthesis of $[Ag(N^3\text{-cytidine})_2][NO_3]$, (1_{MeOH}) gel.

Cytidine (200.0 mg, 0.88 mmol, 2.0 equiv.) was dissolved in methanol (25 ml). To this solution, another solution of $AgNO_3$ (74.7 mg, 0.44 mmol, 1.0 equiv.) in methanol (25 ml) was added slowly. The mixture was heated under reflux (77 °C) for 2 h in the dark. The solution was filtered while still warm, then left to stand at room-temperature where a sample spanning colourless gel formed over 30 minutes. The corresponding xerogel was obtained by freeze-drying the gel. IR: $\tilde{\nu} = 3340, 3201, 2943, 1643, 1604, 1528, 1504, 1338, 1280, 1207, 1099, 1049, 995, 948, 902, 867, 771, 717, 597$ and 409 cm^{-1} ; ESI-MS ($C_{18}H_{26}AgN_6O_{10}$) calculated: 593.0800, Experimental: 593.0712 (m/z); Elemental analysis ($[Ag(N^3\text{-cytidine})_2] \cdot NO_3 \cdot 2H_2O$) Calculated: C - 31.23%, H - 4.37%, N - 14.16%, Experimental: C - 31.78%, H - 4.33%, N - 13.84%.

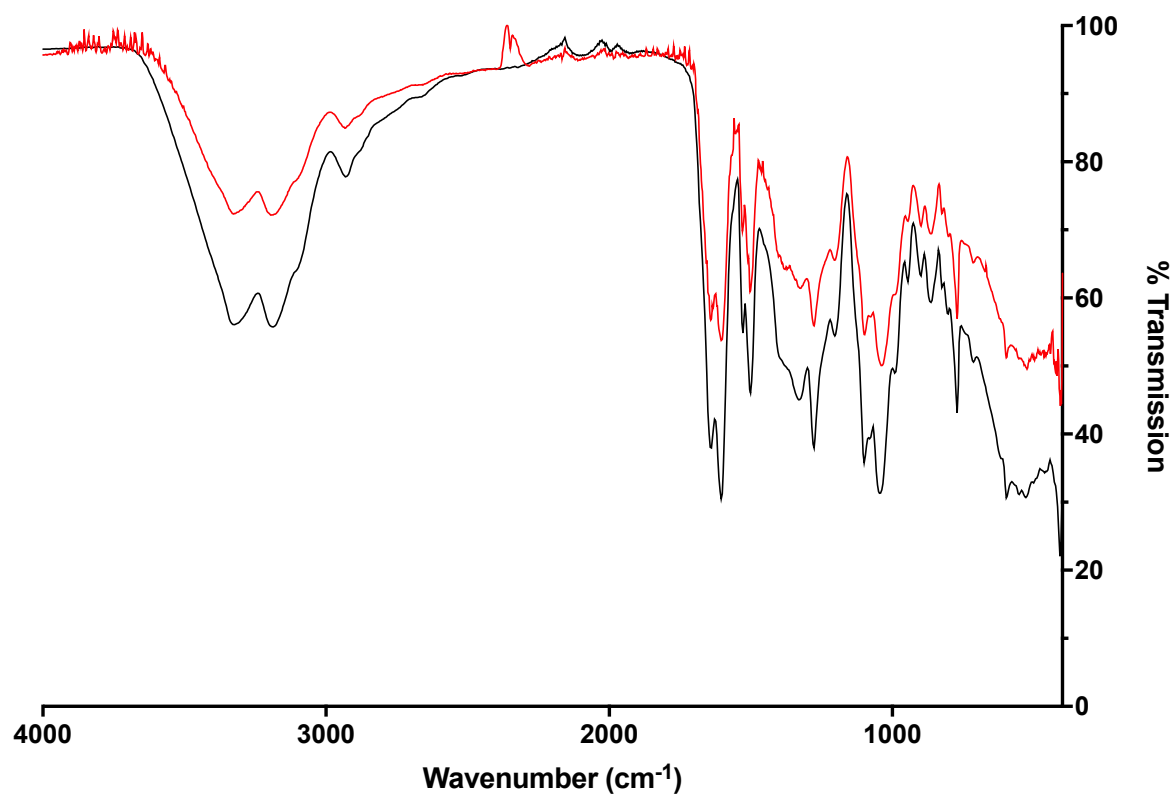


Figure S9. FTIR data of the solid **1** (red line) vs. xerogel of **1**_{MeOH} (black line)

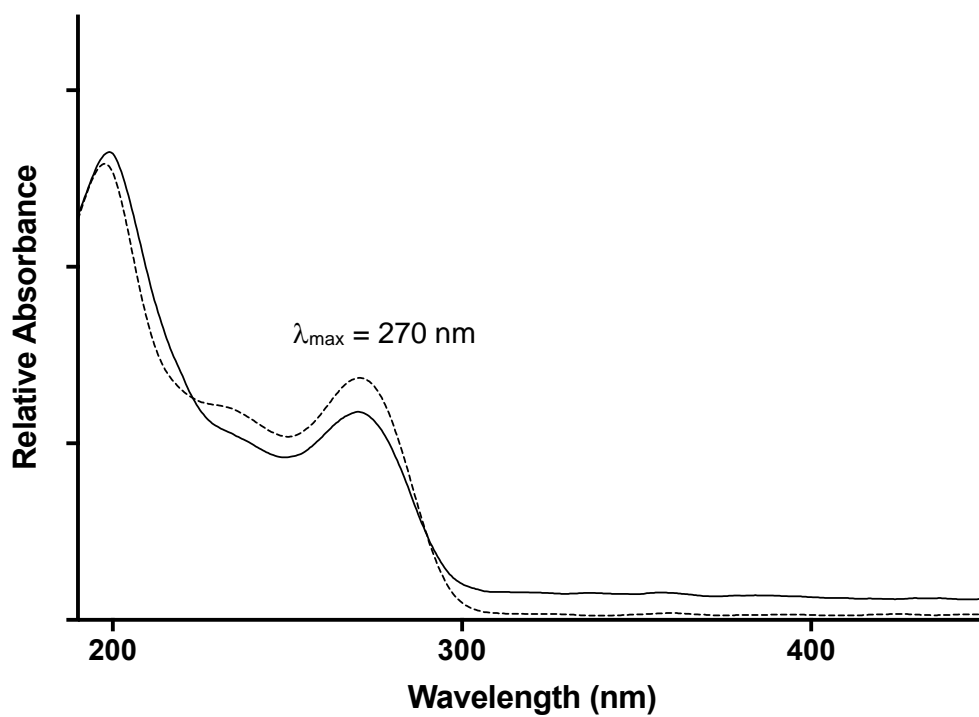


Figure S10. UV-vis spectra of **1**_{MeOH} (solid line) vs. cytidine (dotted line).

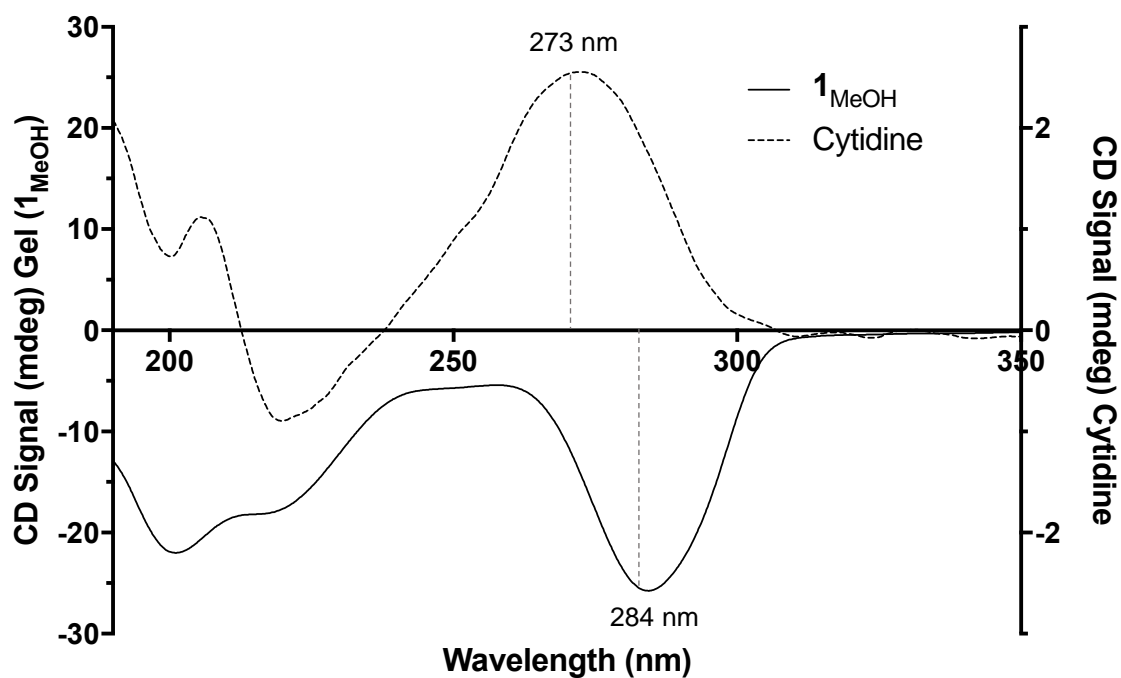


Figure S11. Circular Dichroism spectra for cytidine (dotted line) and 1_{MeOH} (solid line) at concentrations of 4 mg/ml.

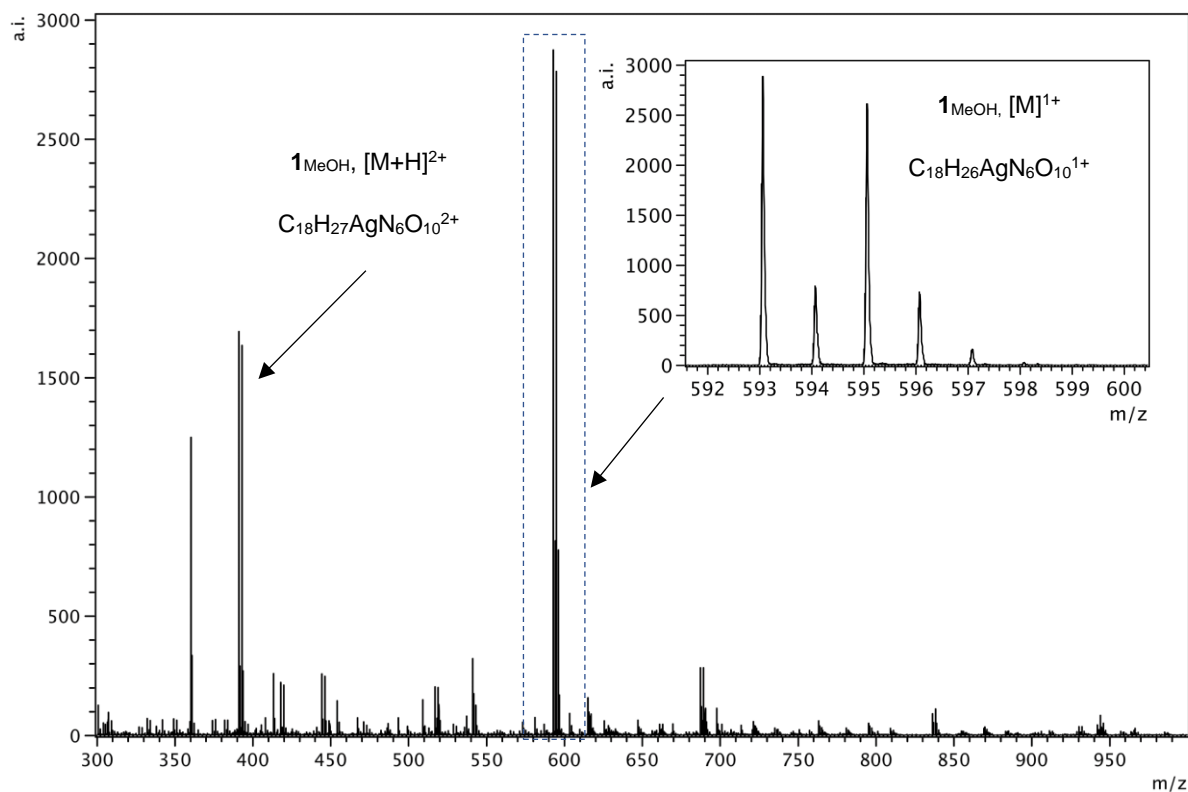


Figure S12. ESI-MS data measured for 1_{MeOH} , collected in high resolution positive-ion mode.

S.2.3. Rheology

Rheological measurements were performed with a HR-2 Discovery Hybrid Rheometer (TA Instruments) with a standard steel parallel-plate geometry of 20 mm diameter with a gap of 1 mm. The strain and the frequency were set to 1% and 1 Hz, respectively.

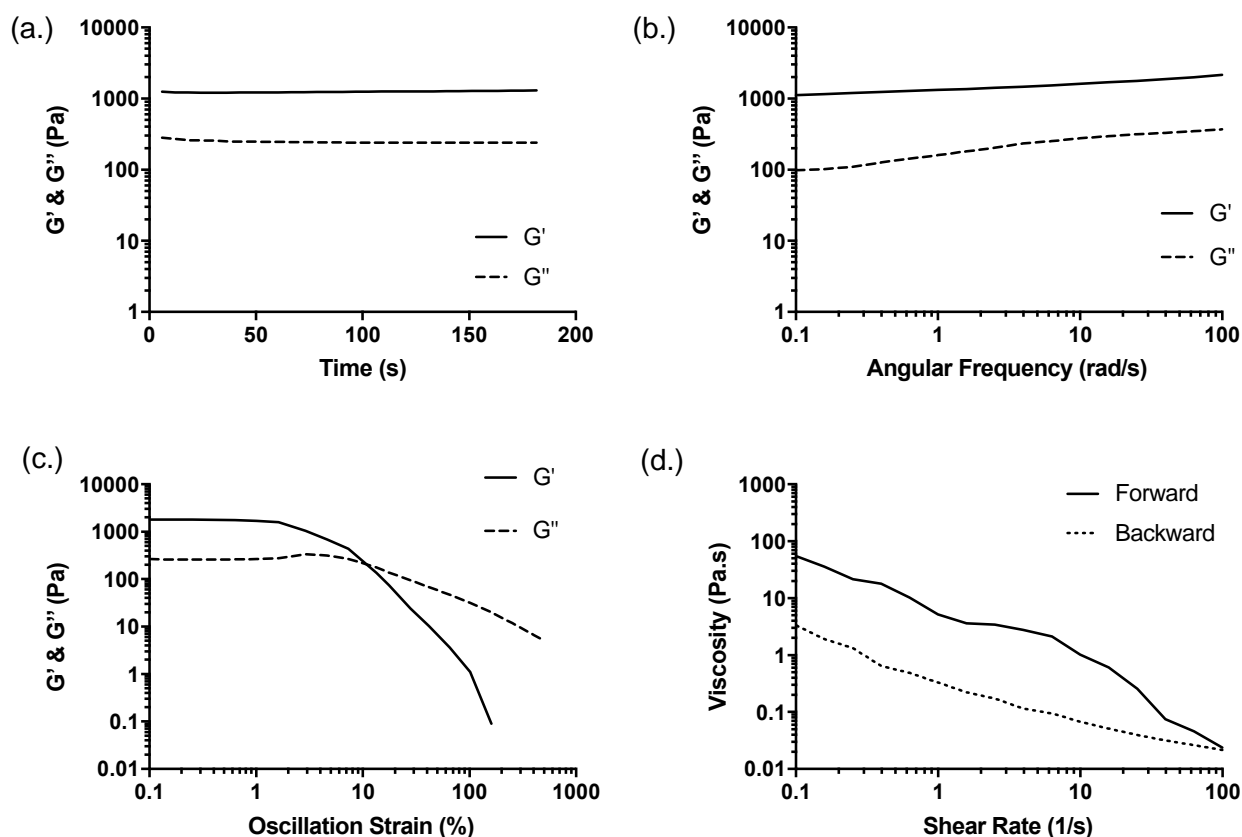


Figure S13. (a.) Rheology time sweep of 1_{MeOH} gel at 4.0 mg mL^{-1} performed at 1% strain, 1 Hz; (b.) Frequency sweep of 4.0 mg mL^{-1} metallogel (1_{MeOH}) conducted at 1% strain from 0.1 to 100 rad/s; (c.) Strain sweep of metallogel (1_{MeOH}) at 4.0 mg mL^{-1} conducted at 1 Hz, from 0.1 to 500 % of strain. $G' = G''$ point, transition sol-gel; (d.) Viscosity versus shear rate profile between 0.1 and 100 s^{-1}

S.2.4. Microscopy, including SEM and AFM images.

SEM samples of 1_{MeOH} xerogel were mounted on an aluminium stub with Achesons Silver Dag and then dried overnight. Examined using a TESCAN VEGA LMU Scanning Electron Microscope, housed within EM Research Services, Newcastle University. Digital images collected with TESCAN supplied software.

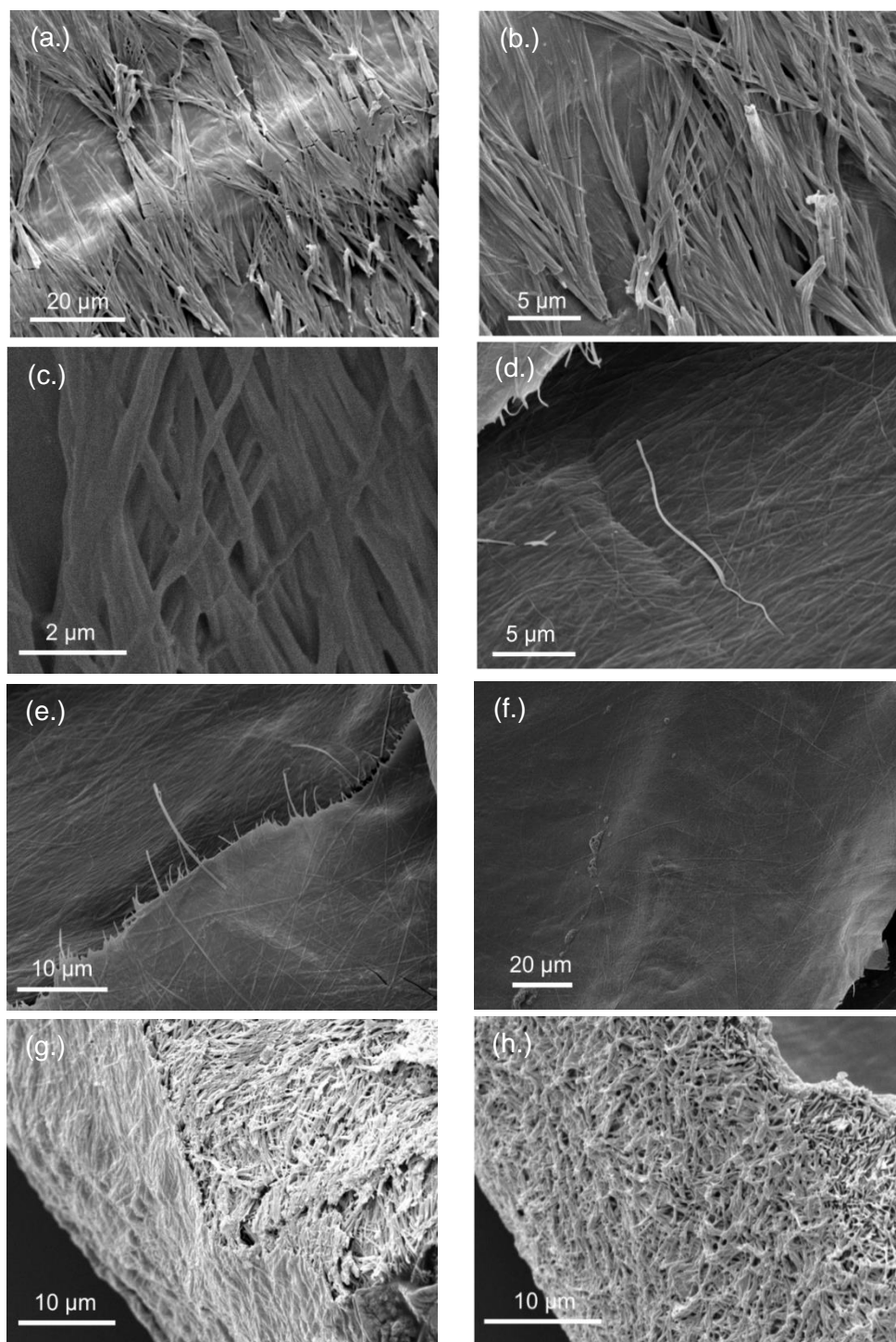


Figure S14. SEM images of 1_{MeOH} xerogel showing long fibres $> 6 \mu\text{m}$ in length; (a. - f.) top-down view of the surface of the xerogel; (g. – h.) Side-on view showing the voids within the network.

Atomic force microscopy (AFM). A Multimode 8 atomic force microscope with Nanoscope V controller and a “E” scanner (Bruker, Germany) was used for acquiring AFM height images. Nanoscope software version 9.1 was used to control the microscope. The system was operated in a peak force tapping mode in air (ScanAsyst) at ultra-low forces minimise damage to the gel fibres. An isolation table/acoustic enclosure (Veeco Inc., Metrology Group) was used to decrease vibrational noise. Silicon tips on V-shaped silicon nitride cantilevers (ScanAsyst-Air, Bruker) were used for imaging. The nominal tip radius was approximately 2 nm, resonant frequency 70 kHz, and spring constant $k \sim 0.4$ N/m. The AFM height images were analysed with NanoScope Analysis 1.5 software (Bruker). The cytidine-Ag xerogel sample was prepared by drop-casting 1 μ l of $\mathbf{1}_{\text{MeOH}}$ gel onto a clean silicon wafer. The sample was kept in 9 ml closed glass vial for 3 days. The gel has been transferred to the silicon surface by micropipette that led to dismantling the fibres structure. If the $\mathbf{1}_{\text{MeOH}}$ complex dried fast on silicon surface after it was transferred immediately, it will look like a film of dried material in the AFM images. Thus, it was kept for a while to self-assemble to reform the fibres again. After that the gel was dried in air.

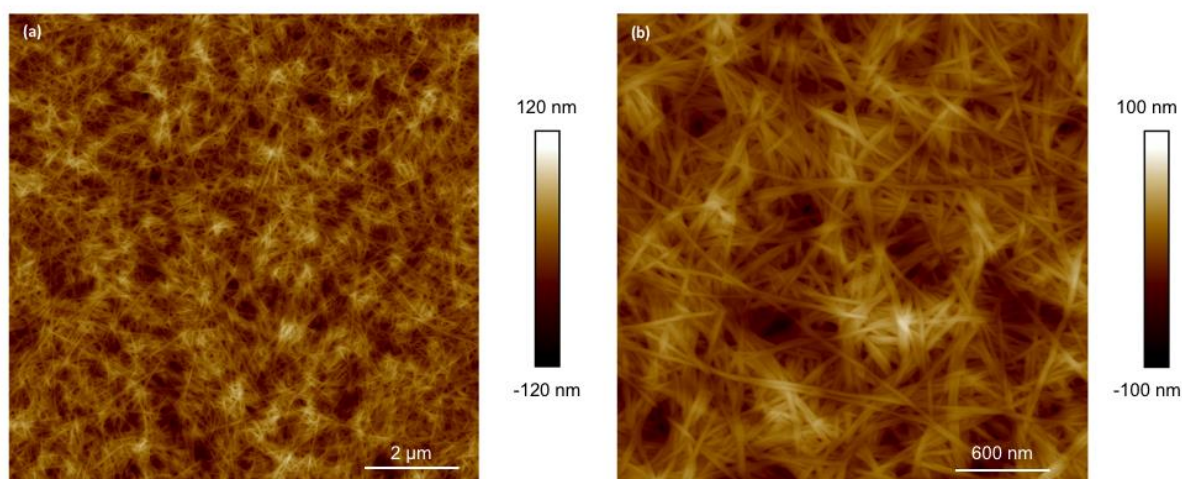


Figure S15. AFM images of $\mathbf{1}_{\text{MeOH}}$ xerogel drop-cast onto a silicon wafer. Large-scan (a) and a zoom area (b) of AFM height images of $\mathbf{1}_{\text{MeOH}}$ xerogel.

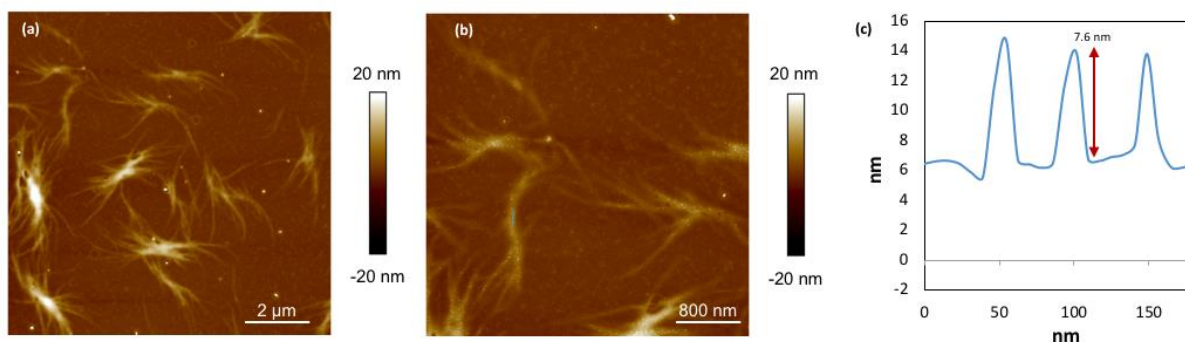


Figure S16. A zoom out height image (a) and zoom in image (b) of the 20 times diluted 1_{MeOH} gel solution, and a line profile corresponding to the blue line in the image (c). The sample has been prepared by deposit 1 μL of 1_{MeOH} solution has been diluted 20 time in methanol upon a Si slide. The slide was kept surrounded by 10 μL of methanol in a close 9 ml glass vial for 30 min, and then it was opened to dry for 10 min.

AFM Height Analysis – The mean diameter of the fibres was estimated using AFM images of the xerogel. First, the distribution of heights in the image was determined using Gwyddion¹ with a bin width of 0.188 nm; it is important the bin width is much smaller than the typical feature size. This distribution is shown in Figure 12(a). Next, a pseudo-Voigt function was fitted to the measured distribution by a standard least-square method and the residual was plotted in Figure 12(b). Clear peaks (labelled 1-6) are seen in the residual which are a result of unresolved components in Figure 12(a) originating from the stacking of fibres in the AFM image. The mean fibre diameter can then be obtained by linear regression of the heights at the peaks of Figure 12(b) against an integer index. This is shown in Figure 12(c) and the fibre diameter was estimated to be 6.3 ± 0.45 nm.

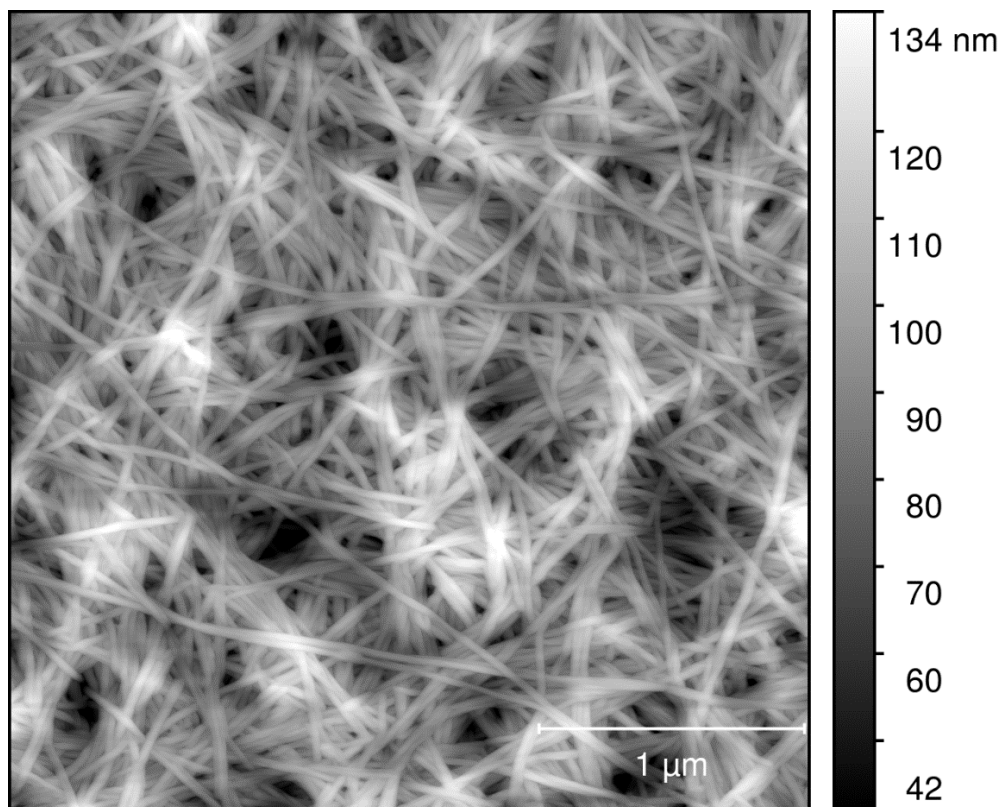


Figure S11. AFM images of 1_{MeOH} xerogel drop-cast onto a silicon wafer adjusted to greyscale for analysis.

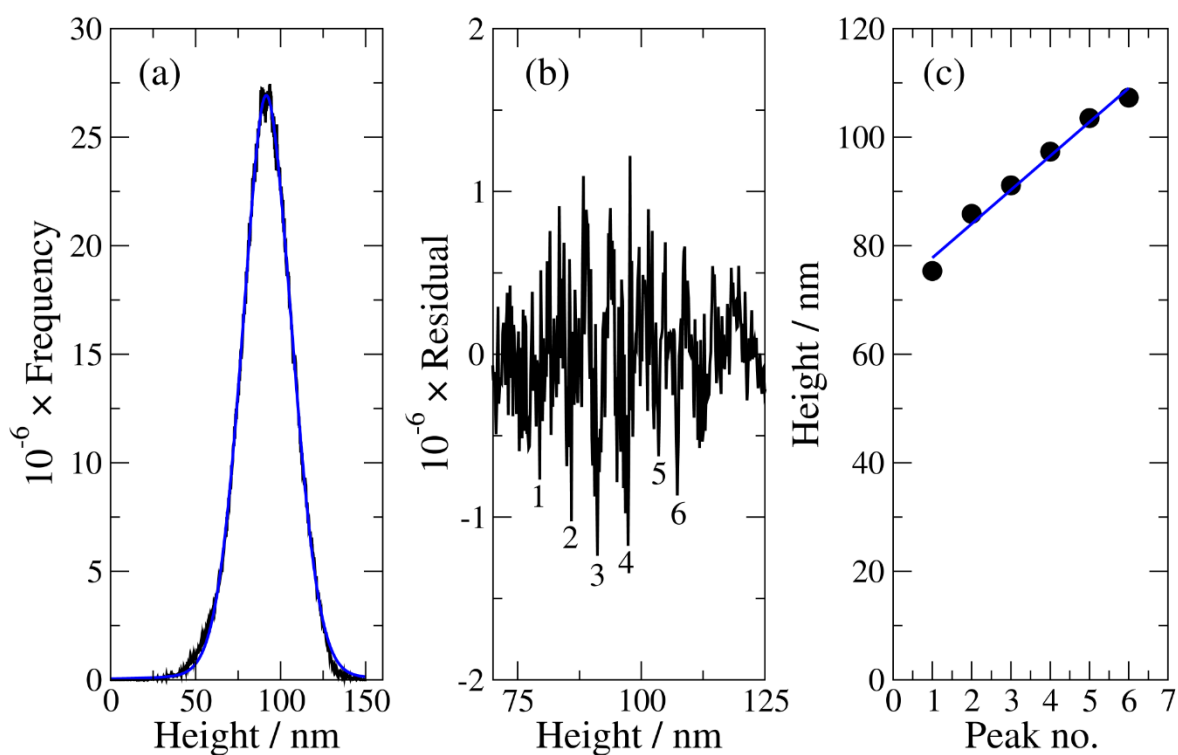


Figure S12. (a) Distribution of height, (b) A fitted pseudo-Voigt function of the measured distribution by a standard least-square method and the residual and (c) Estimated fibre diameter (6.3 ± 0.45 nm).

References

1. David Nečas and Petr Klapetek, *Central European Journal of Physics*, 2012, **10**, 181–188

S.2.5. Conductivity Measurements, IV and EFM.

Electrical measurements (I-V). Current/voltage curves were recorded on the probe station (Cascade Microtech with a B1500A parameter analyser, Agilent). All of the electrical measurements were carried out under dry nitrogen without light illumination. Platinum MBEs (Smart Microsystems Pt MB-4000, Windsor Scientific Ltd., Slough, UK) were used to fabricate electronic devices for electrical characterisation of **1**_{MeOH} xerogel. The MBEs were made on Si/SiO₂ substrates. Four independent platinum electrodes were patterned on the top of the SiO₂ layer. The height of the electrodes is 200 nm and their width is 10 µm with 10 µm spaces between them. The surfaces of the MBEs were electrically insulated except for a 2 × 2 mm² area for depositing the gel. The platinum MBEs were washed with ethanol and dried with nitrogen gas. The clean platinum electrodes were analysed on a probe station and reference current/voltage curves were recorded, which showed the background currents to be less than 100 fA at 2 V. A drop (0.5 µl) of **1**_{MeOH} was cast onto the platinum MBEs and was left to dry. The gel droplet dried to produce a film of the **1**_{MeOH} fibres across the Pt-electrodes. The electrodes were connected to the probe station and current/voltage curves were collected. For measurements on a single crystal, a crystal of **1** was electrically insulated on glass slide and the ends of the crystal were connected both directly and to tow pads of Ga-In eutectic. The crystal was connected to the probe station needles through the Ga-In pads.

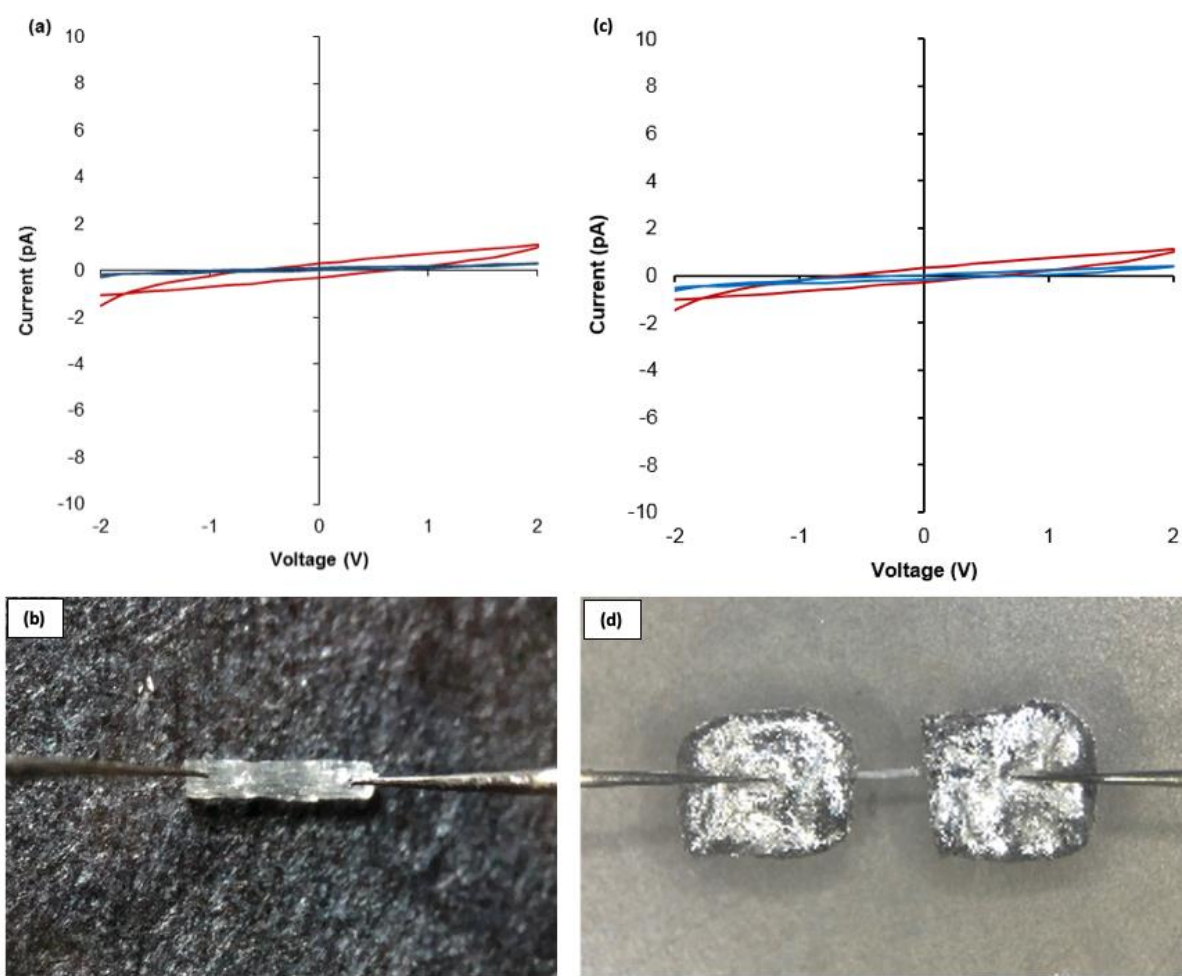


Figure S13. (a & c) I-V curves of the 1_{MeOH} xerogel (red) and crystal of **1** (blue). Optical microscope images of probe station tips making direct contact (b) or that have been connected to a crystal of cytidine-Ag through Ga-In eutectic (d).

Electrostatic Force Microscopy (EFM). Electric force microscopy (EFM) operated in the dynamic non-contact mode to provide a useful contactless tool for qualitative testing of the conductivity of a single nanowire prior to any quantitative measurement of its conductivity.^{1,2} The method is based on the storage of energy in the tip/nanowire/substrate capacitor and the nanowire conductance influences the measurement via the RC time constant for polarisation of the nanowire. For EFM studies, the nanowires are aligned on Si/SiO₂ chips with an oxide thickness ~200 nm and the phase shift between the driving force and the tip motion is recorded as a function of applied dc bias (V) as the tip crosses above the fibre at a constant lift height. As shown by Staii and co-workers,³ a negative phase shift with a V^2 applied bias dependence is an indication of a conductive nanowire. Objects which are merely polarisable and do not have charges which can move away from the vicinity of the tip produce a positive phase shift.

Both EFM phase images and the corresponding topographic images were acquired using the Multimode 8 atomic force microscope (Bruker, Germany). Data were analysed using

NanoScope Analysis 1.5 software. EFM was performed in air using AFM tips on n-doped Si cantilevers (MESP-LM-V2, Bruker), both of the probe sides were coated with Cobalt/Chromium layer. The nominal tip radius was approximately 25 nm, resonant frequency 75 kHz, and spring constant $k \sim 3$ N/m. The EFM phase images has been captured at applied DC bias between +10 and -10 volts with a scan lift height of 30 nm. The cytidine-Ag(I) gel was prepared in methanol and diluted 20 times. A sample was prepared by drop-casting 1 μ L of the diluted cytidine-Ag(I) solution onto a Si<100>/200 nm SiO₂ slide. The slide with the drop- cast solution was kept surrounded by 10 μ L of methanol in a closed glass vial (with a volume ~ 9 ml) for 30 min. Then, it was left to dry in air for 10 min.

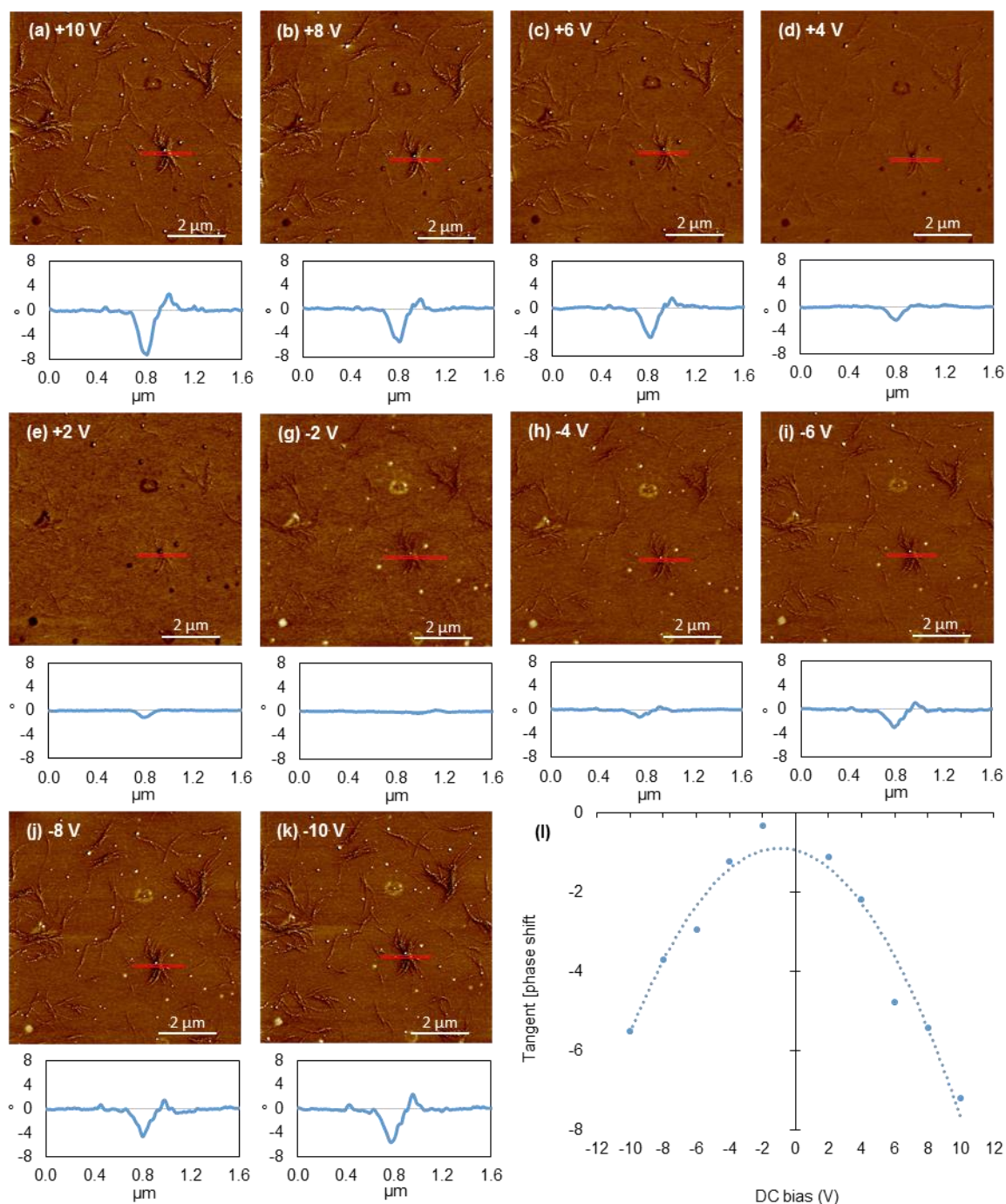


Figure S14. EFM phase image of the 1_{MeOH} xerogel and the line profiles corresponding to the boxes in the EFM phase images (a-k). The EFM phase images were captured at applied DC bias between +10 V and -10 V, and a lift height of 30 nm. (i) A plot of the tangent of the measured phase angle arising from the aggregation of fibres as a function of applying different DC biases.

- (1) S. M. D. Watson, A. R. Pike, J. Pate, A. Houlton and B. R. Horrocks, *Nanoscale*, 2014, **6**, 4027 – 4037.
- (2) M. Bockrath, N. Markovic, A. Shepard, M. Tinkham, L. Gurevich, L. P. Kouwenhoven, M. W. Wu and L. L. Sohn, *Nano Lett.*, 2002, **2**, 187 - 190.
- (3) C. Staii, A. T. Johnson and N. J. Pinto, *Nano Lett.*, 2004, **4**, 859 - 862.

S.2.6. Reduction Behaviour

Photoreduction was achieved by suspending vials of 1_{MeOH} (2 ml) within a Southern New England Ultraviolet Company Photochemical reactor, using eight RMR-3000 (50/60 Hz, 120

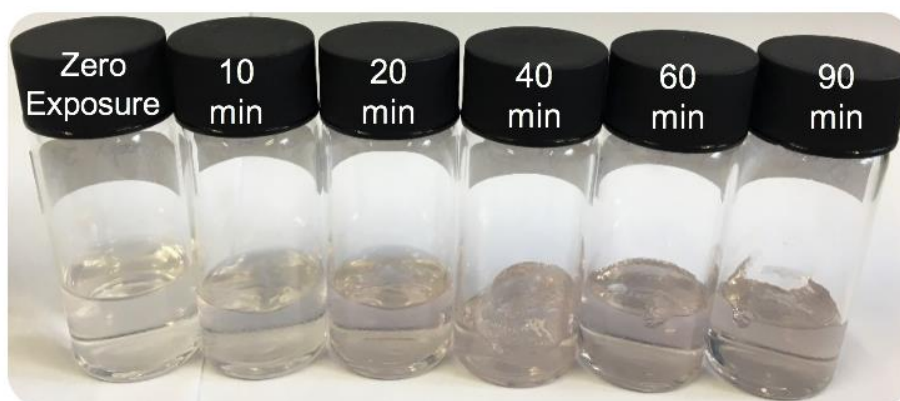


Figure S15. An image showing a series of 1_{MeOH} samples exposed to UV-light (300 nm) for up to 90 minutes.

Volts, 300 nm) UV bulbs. Exposure times ranged from 1 - 90 minutes.

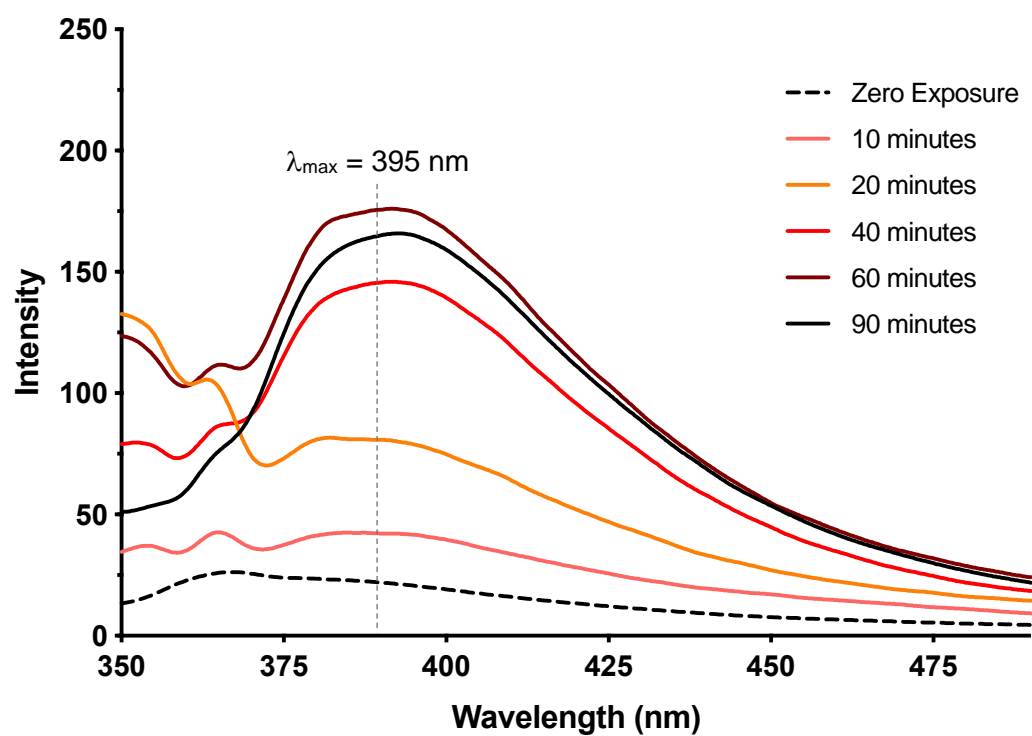


Figure S16. Emission data of 1_{MeOH} from λ_{ex} of 330 nm.

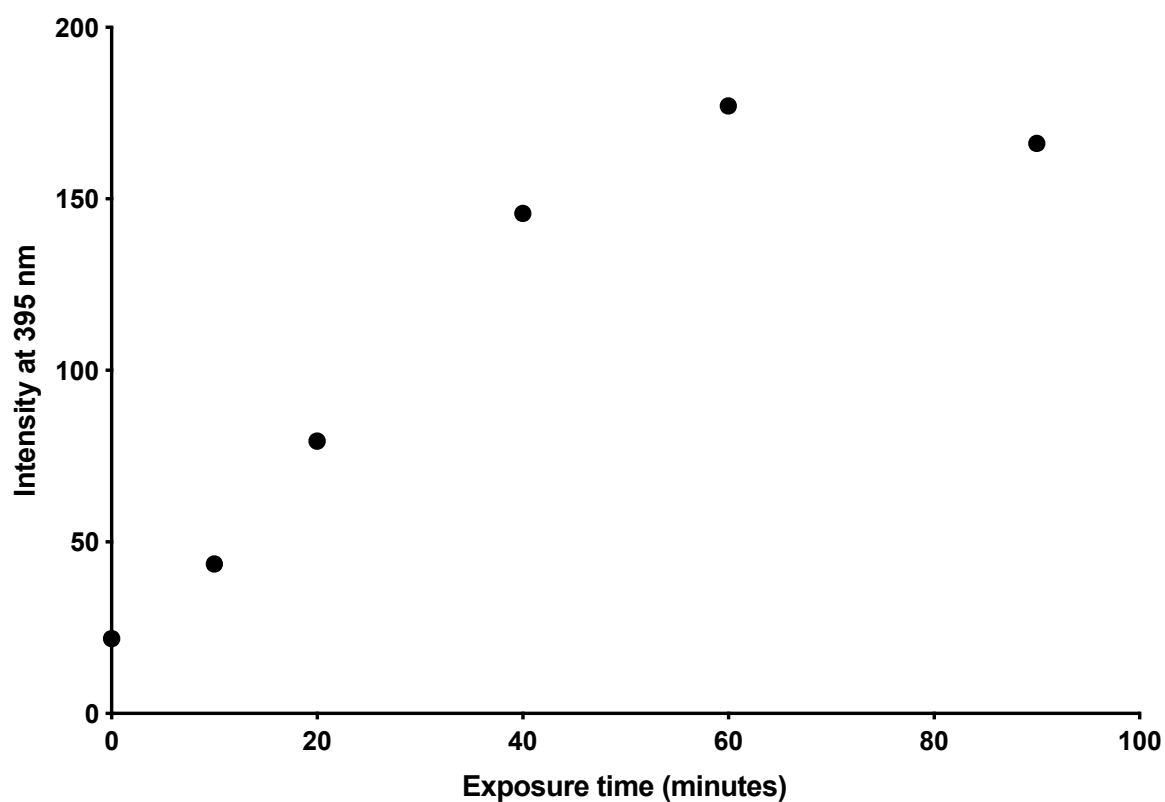


Figure S17. Emission intensity (λ_{em} : 395 nm, λ_{ex} : 330 nm) of photoreduced 1_{MeOH} vs. exposure time to UV-light.

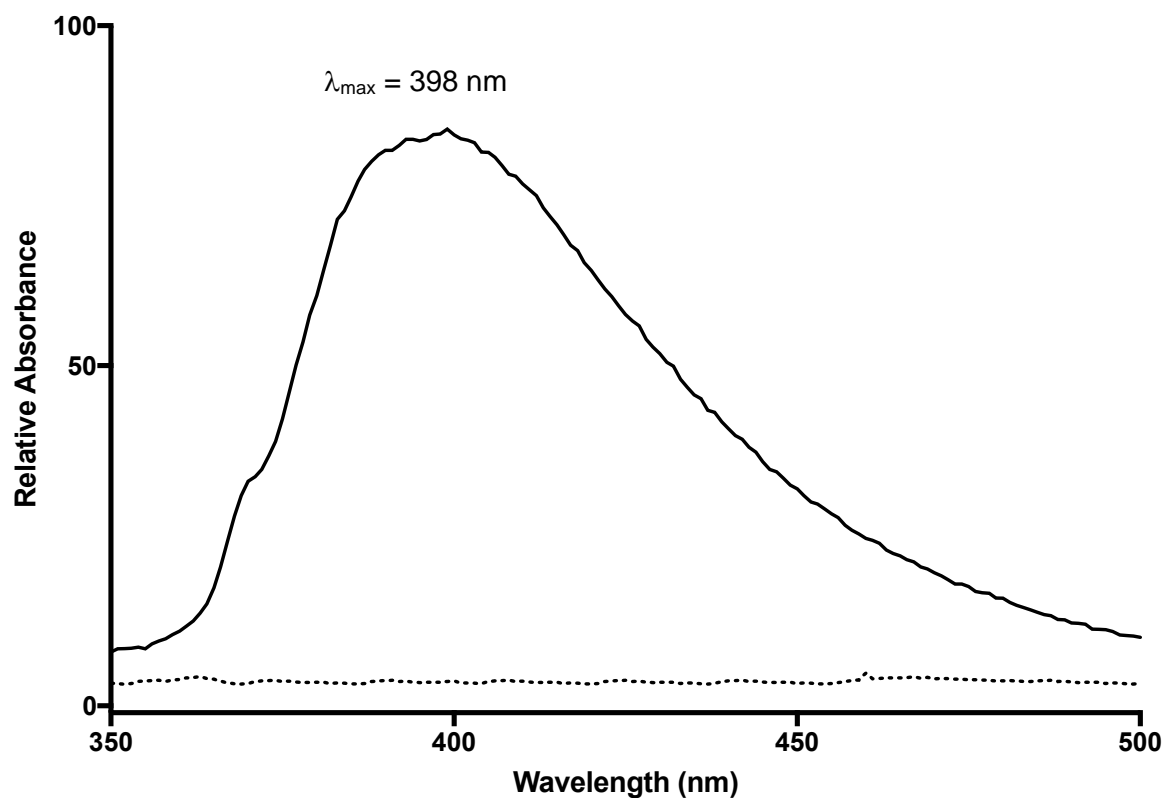


Figure S18. Absorption spectrum for 1_{MeOH} gel after photoreduction (90 minutes) (Solid line) vs. zero exposure (dotted line) showing the appearance of the plasmon band for Ag nanoparticles.

Samples of 1_{MeOH} gel were drop cast on to a silicon (SiMPore, SN100-A50Q10) grid and then air dried over 15 minutes. The grids are examined using a JEOL 2100F (FEG) Transmission Electron Microscope and digital images are collected using a Gatan Orius CCD camera housed within the School of Physics, Durham University – Dr B. Mendis.

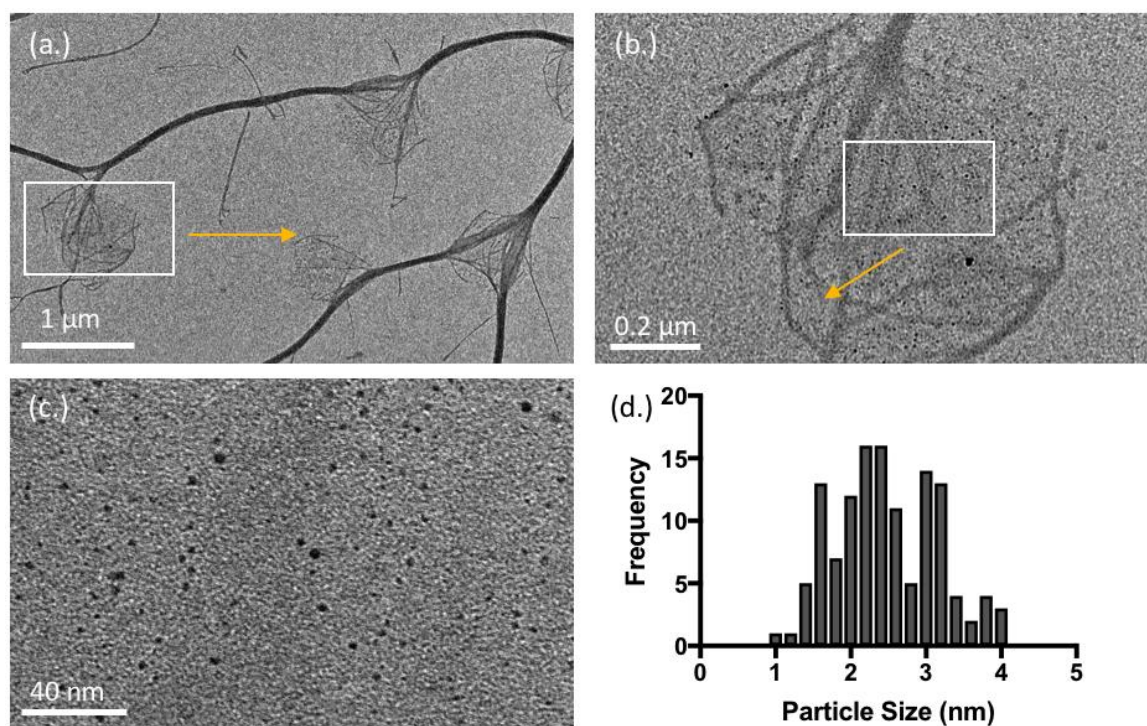


Figure S19. TEM Images of 1_{MeOH} in a xerogel state deposited on a SiN grid; (a. & b.) Bright field images of the xerogel showing long fibres $> 5 \mu\text{m}$ in length (14 – 82 nm width), (c. & d.) Electron dense particles within a fray with particle size distribution analysis (1.0 – 4.0 nm dia., 2.4 nm average dia.)

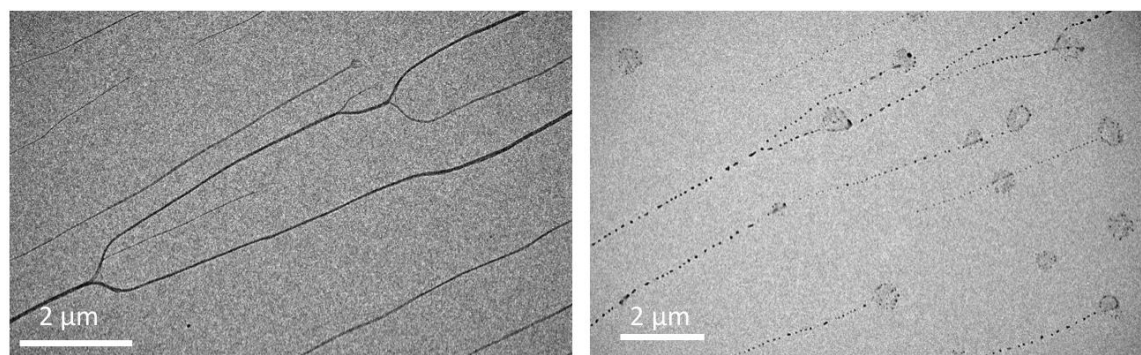


Figure S20. TEM bright field images of 1_{MeOH} fibres in a xerogel state deposited on a SiN grid; (a) freshly deposited ($>10 \mu\text{m}$ length, 14 - 82 nm width) and (b.) exposed to ambient light showing the presence of electron-dense particle (14 - 50 nm dia.).

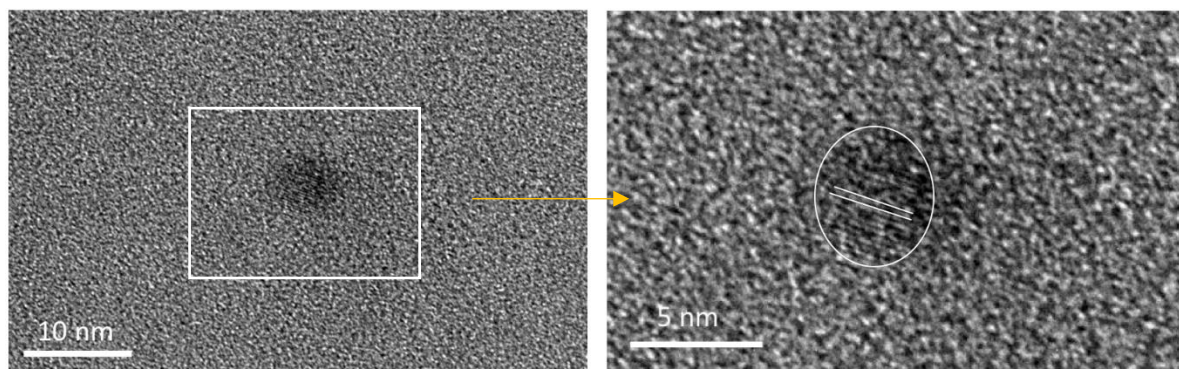


Figure S21. HR-TEM image of a silver particle (4.6 nm dia.) with lattice fringe spacing of 0.25 nm \pm 0.02 corresponds to the interplanar distances of (111)

S.2.7. Band Structure Calculations

All spin-polarized density functional theory (DFT) calculations were performed with the Vienna ab-initio Simulation Package (VASP)¹ and the projector augmented wave (PAW) method.^{2,3} The exchange-correlation potential was described by the Perdew-Burke-Ernzerhof (PBE) functional⁴ extended to incorporate a Van der Waals correction.⁵ We use a k-point grid of 1 \times 1 \times 5, so that 5 *k*-points in the transport direction.

1. G. Kresse and J. Hafner, *Phys. Rev. B*, 1993, **47**, 558; 1994, **49**, 14251; G. Kresse and J. Furthmüller, *Phys. Rev. B*, 1996, **54**, 11169; *Comput. Mat. Sci.*, 1996, **6**, 15 (1996).
2. P. E. Blöchl, *Phys. Rev. B*, 1994, **50**, 17953.
3. G. Kresse and D. Joubert, *Phys. Rev. B*, 1999, **59**, 1758.
4. J. P. Perdew, K. Burke, and M. Ernzerhof, *Phys. Rev. Lett.*, 1996, **77**, 3865.
5. S. Grimme, *J. Comput. Chem.*, 2006, **27**, 1787.

S.3. Chapter 6. Ag^I-Oligonucleotide Hairpin formation towards controlled cluster assembly

S.3.1. General Methodology

Oligonucleotides (ss-DNA) were prepared as instructed by the vendor (ATDBio or Eurofins Genomics), typically 1.0 mL of H₂O was added to the lyophilised powder yielding a 0.1 mM (100 pmol/μL) solution (H₂O volumes may have varied based on the synthesis scale). Manufacture for all oligos was achieved using salt-free methods and HPLC purification. Oligo concentrations were checked by absorbance using molar absorptivity and masses *via* ESI-MS (negative ion mode).

Isothermal Titration Calorimetry was performed using an iTC200 MicroCal™ instrument connected to a MicroCal™ Incorporated ThermoVac (set at 24.6°C) running through Malvern instruments MicroCal™ ITC200 software (Version 1.26.4). Data analysis was performed using Origin 7 SR4 software (version 7.0552(B552)). Samples were held at 25°C (reference power: 6) within the iTC200 sample chamber with injection volumes of 0.1 μL.

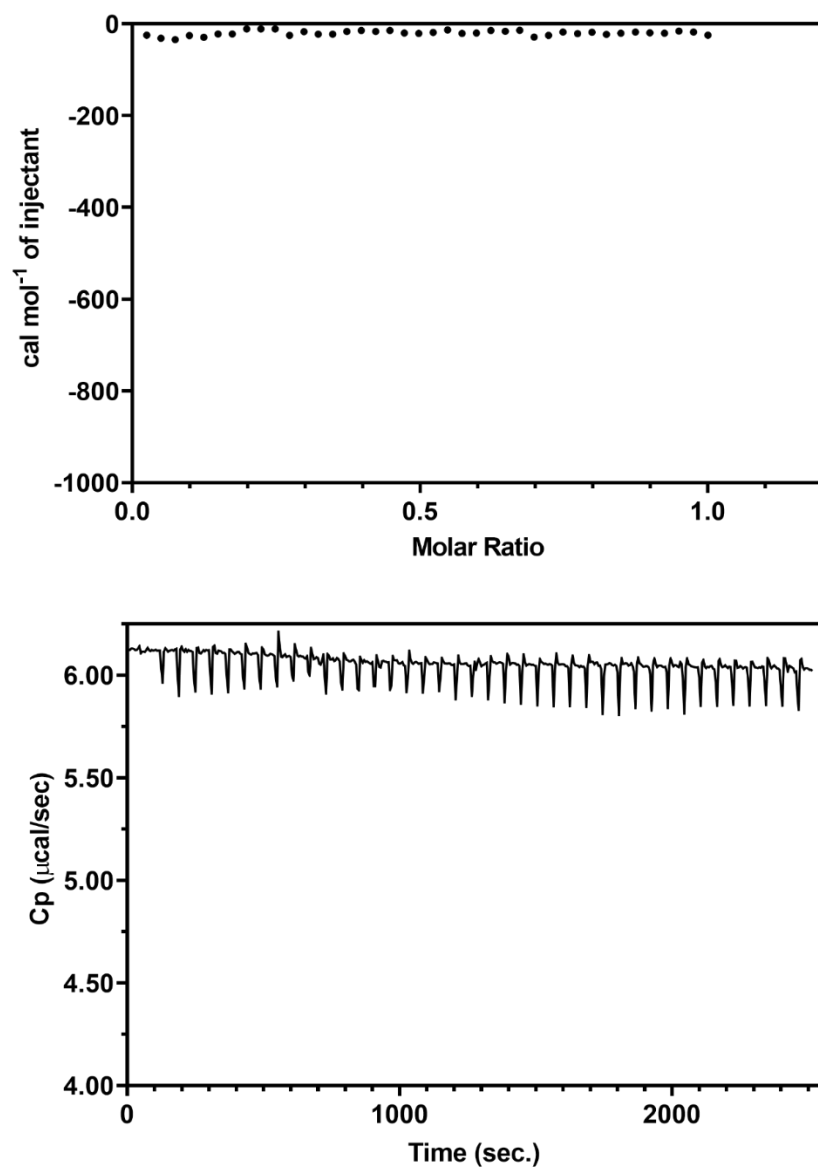


Figure S17. ITC water-into-water blank to account for dilution affects.

S.3.2. Electrospray Ionisation Mass Spectrometry

High-resolution electrospray ionisation mass spectrometry (ESI-MS) studies in ultrapure (type 1) water at 0.001 mM concentrations. Measurements were made on a Waters Synapt G2s Mass Spectrometer and data was processed using the Mmass software (version 5.5.0).

The isotopes within a single metallated short oligonucleotide system include: Hydrogen (^1H 99.9885%, ^2H 0.0115%), Carbon (^{12}C 98.632%, ^{13}C 1.07%), Nitrogen (^{14}N 99.632%, ^{15}N 0.368%), Oxygen (^{16}O 99.757%, ^{17}O 0.038%, ^{18}O 0.205%), Phosphorus (^{31}P 100%) and Silver (^{107}Ag 51.839%, ^{109}Ag 48.161%). Calculations using a minimum abundance value of 0.1% were used when evaluating the experimental Ag^+ -oligonucleotide data.

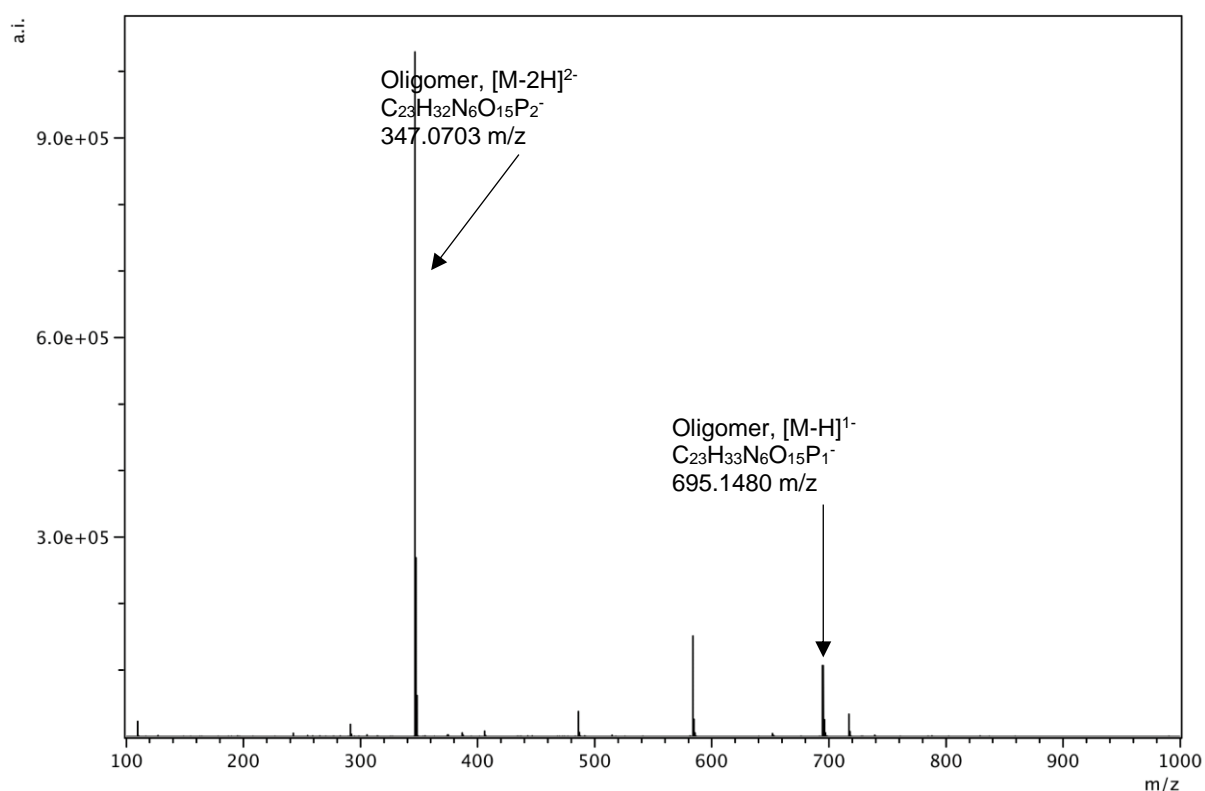


Figure S18. Negative ion mode ESI-MS of the oligonucleotide C-(a)₁-C, ^{a1}C₁ (a: abasic site).

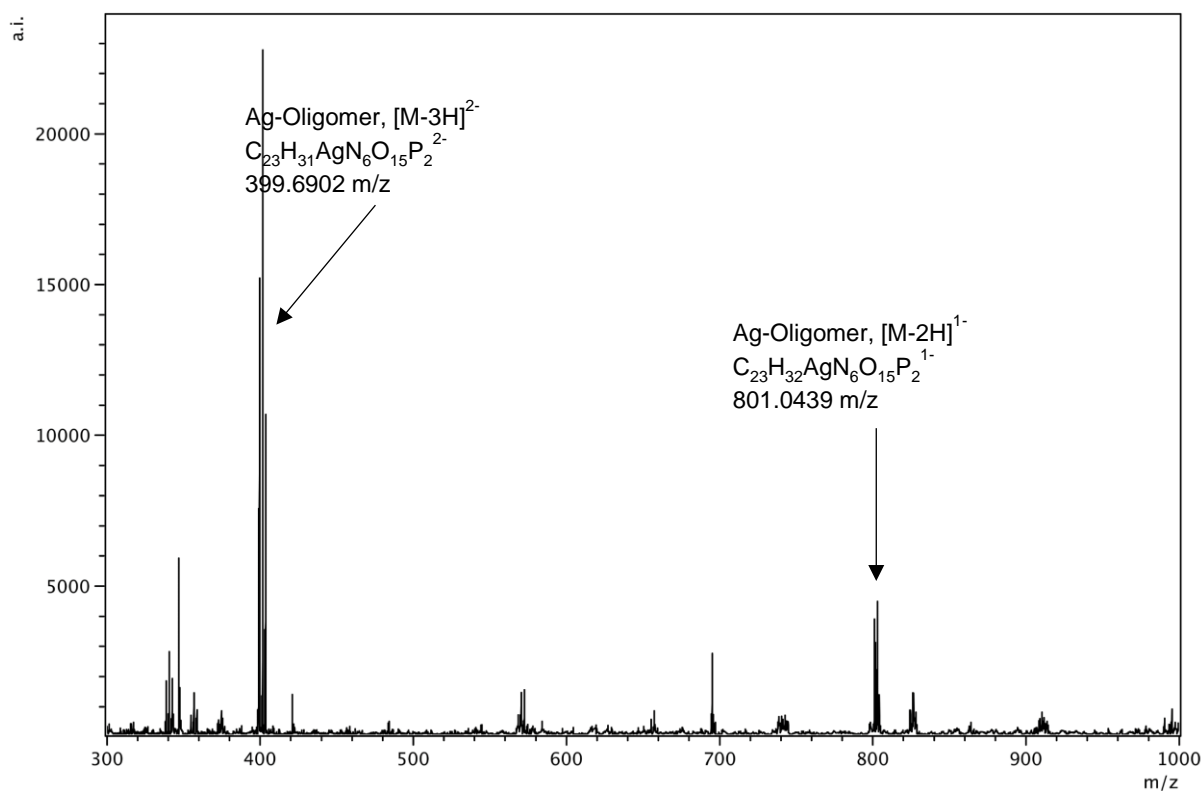


Figure S19. Negative ion mode ESI-MS following the 1:1 addition of Ag^+ to the oligonucleotide C-(a)₁-C, ^{a1}C₁ (a: abasic site).

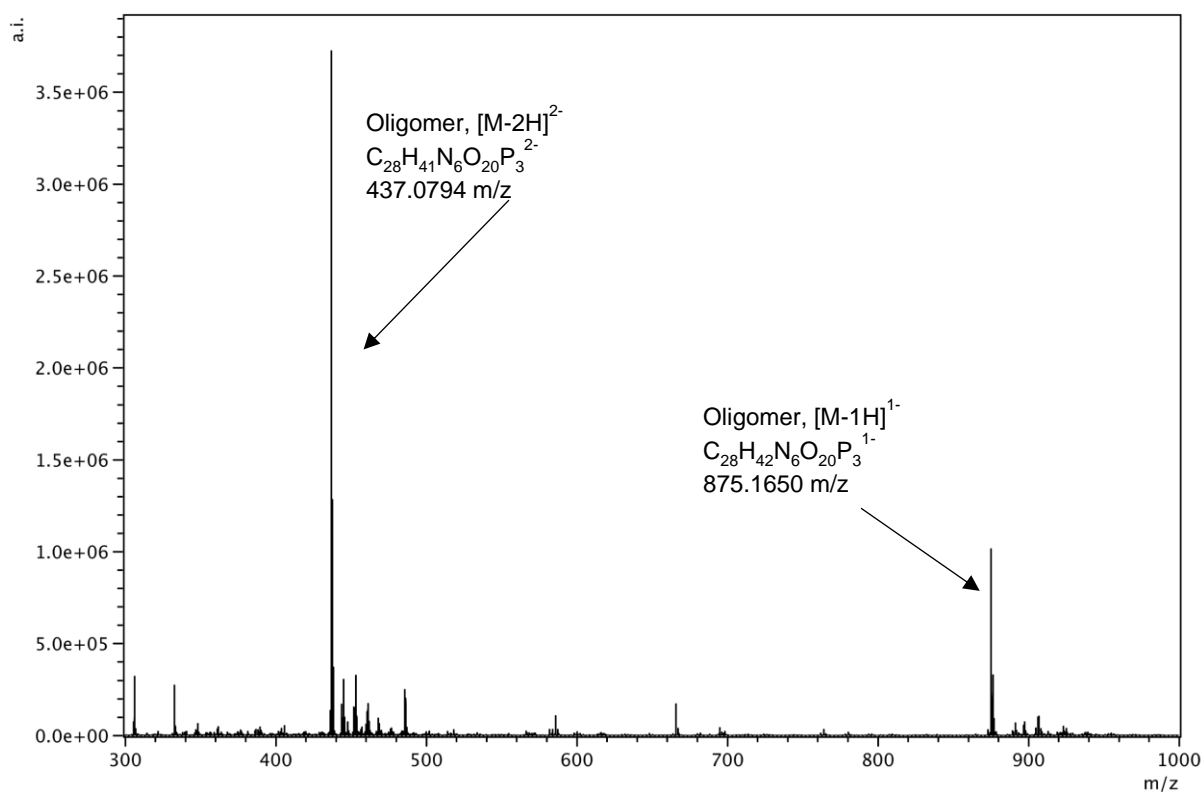


Figure S20. Negative ion mode ESI-MS of the oligonucleotide C-(a)₂-C, ^{a2}C₁ (a: abasic site).

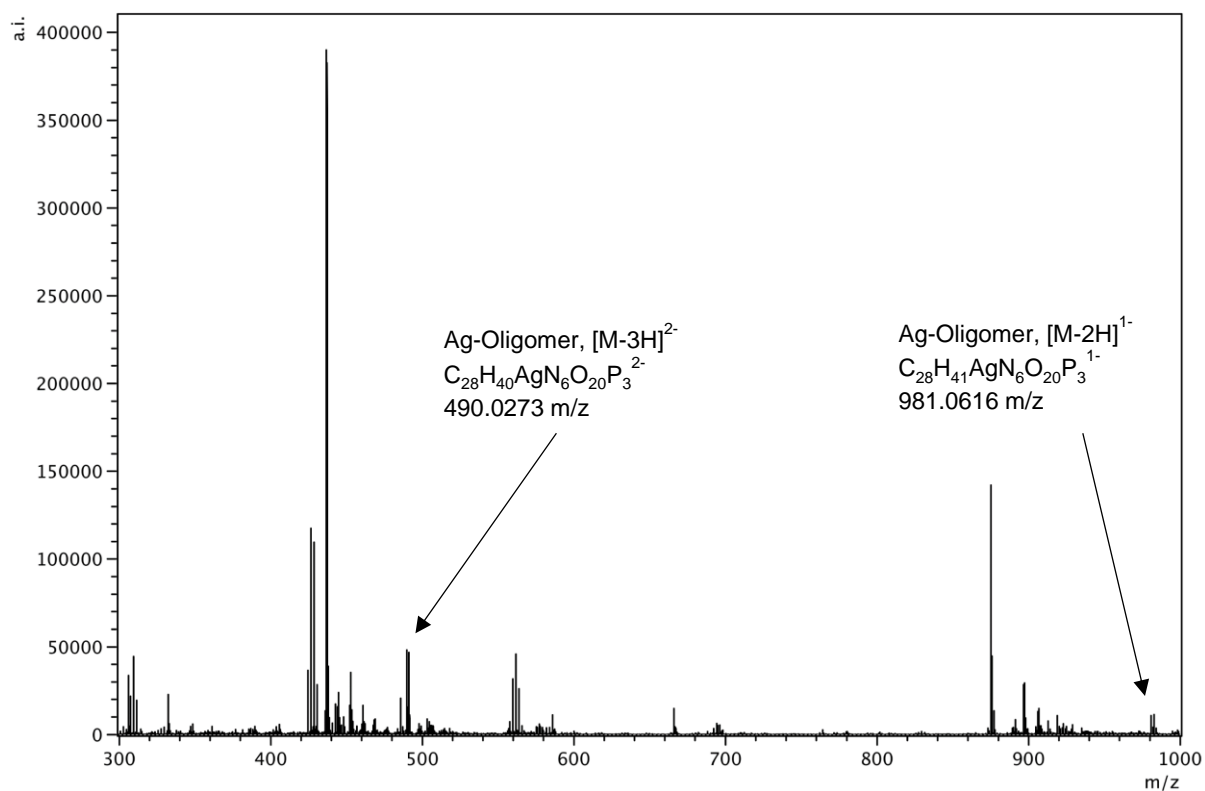


Figure S21. Negative ion mode ESI-MS following the 1:1 addition of Ag^+ to the oligonucleotide C-(a)₂-C, ^{a2}C₁ (a: abasic site).

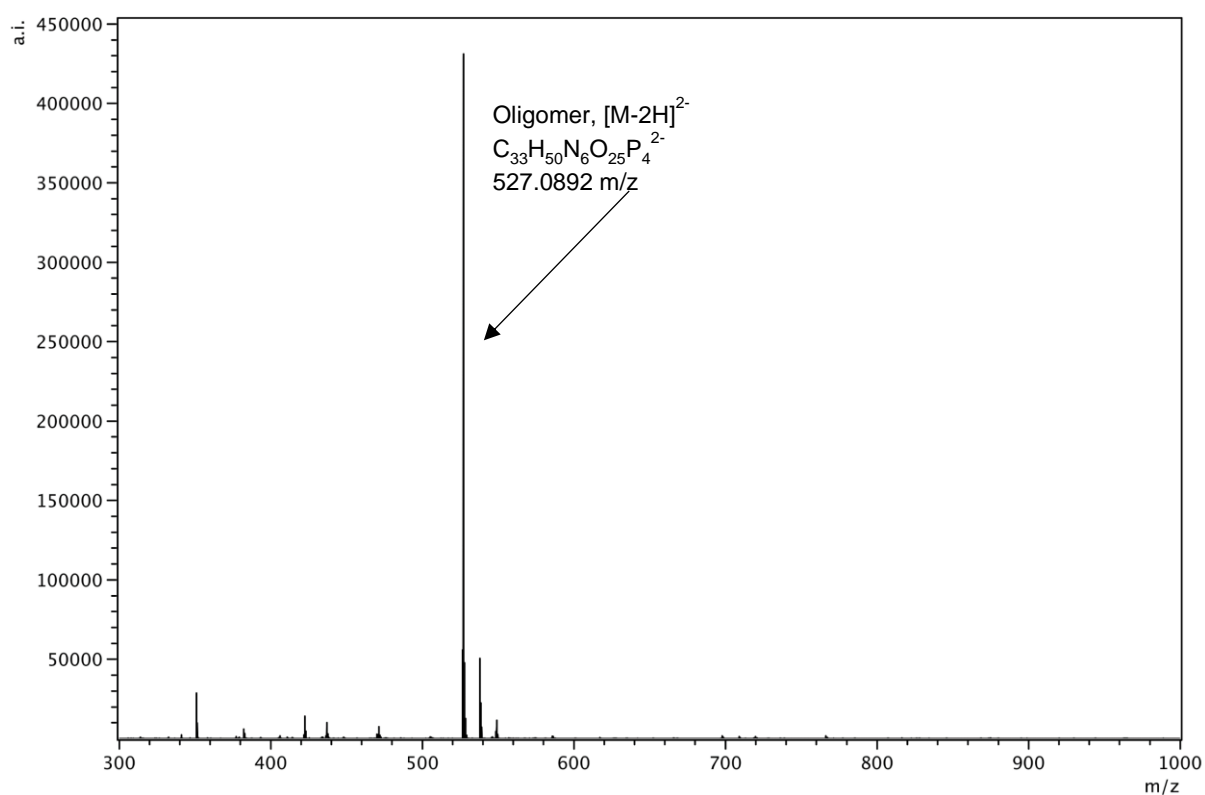


Figure S22. Negative ion mode ESI-MS of the oligonucleotide C-(a)₃-C, ^{a3}C₁ (a: abasic site).

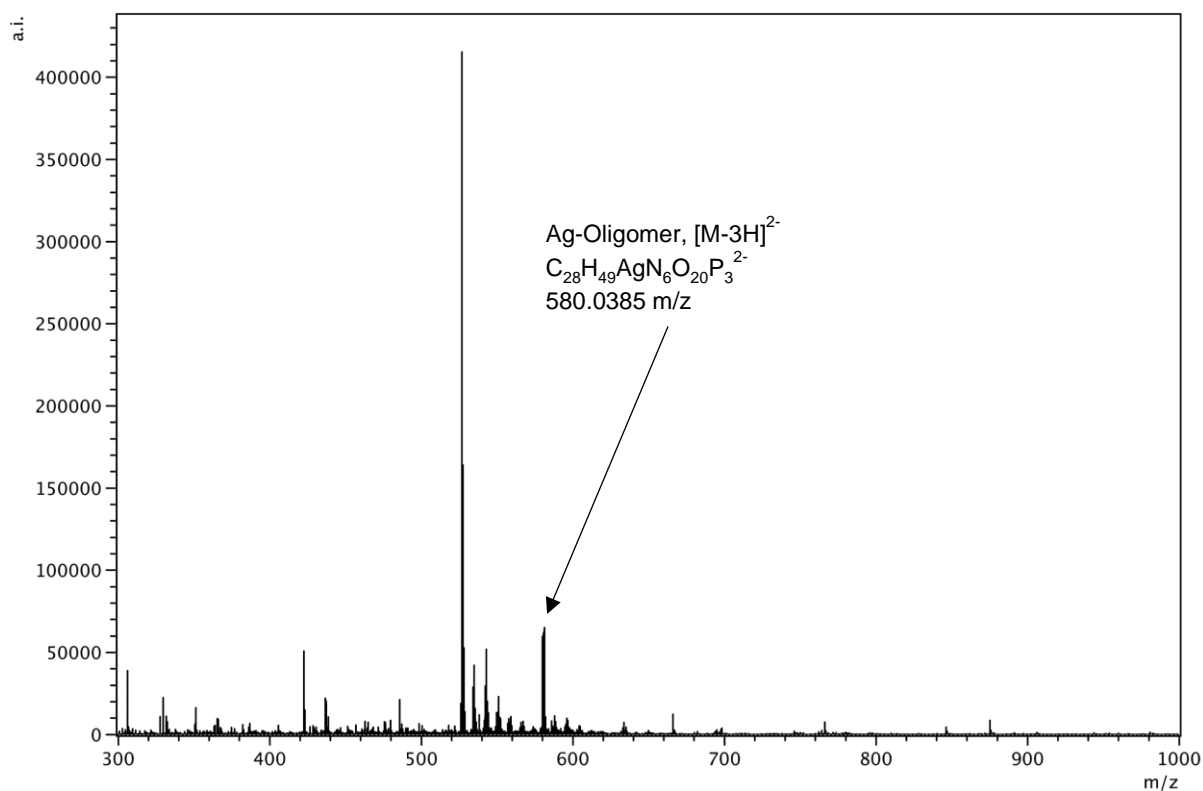


Figure S23. Negative ion mode ESI-MS following the 1:1 addition of Ag^+ to the oligonucleotide C-(a)₃-C, $^{a3}C_1$ (a: abasic site).

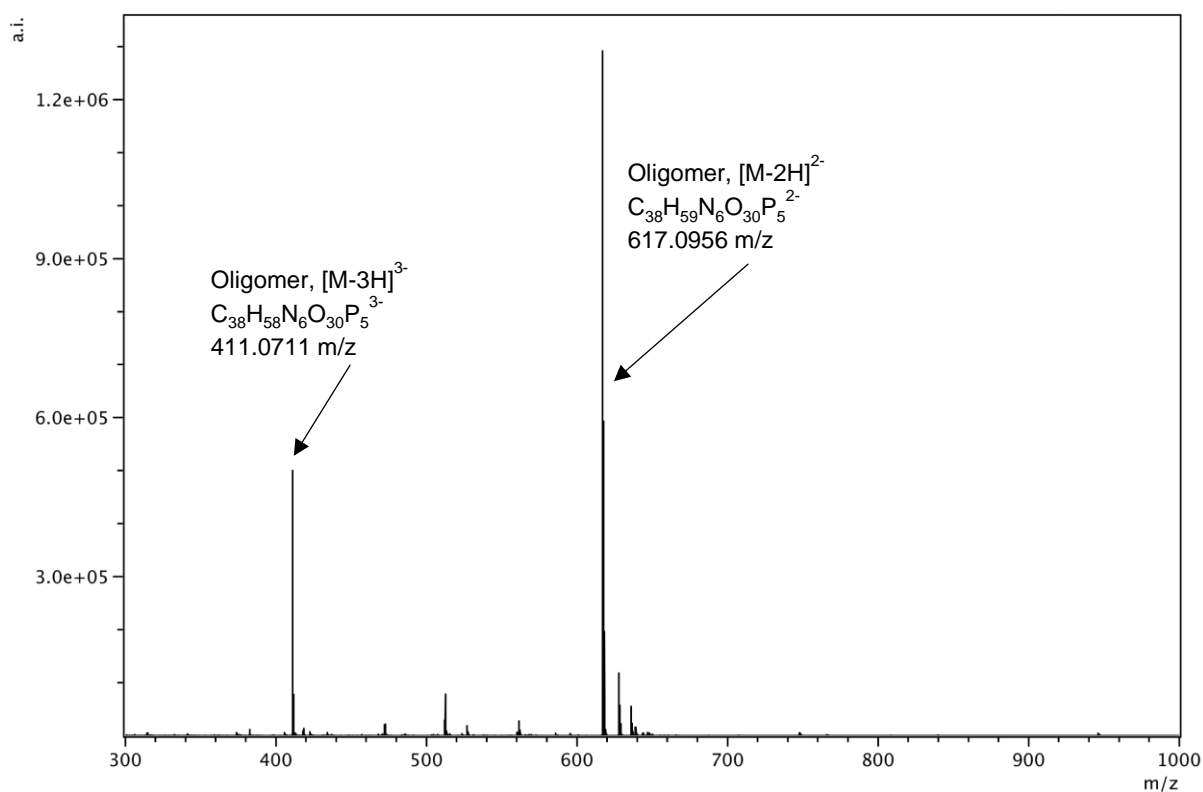


Figure S24. Negative ion mode ESI-MS of the oligonucleotide C-(a)₄-C, $^{a4}C_1$ (a: abasic site).

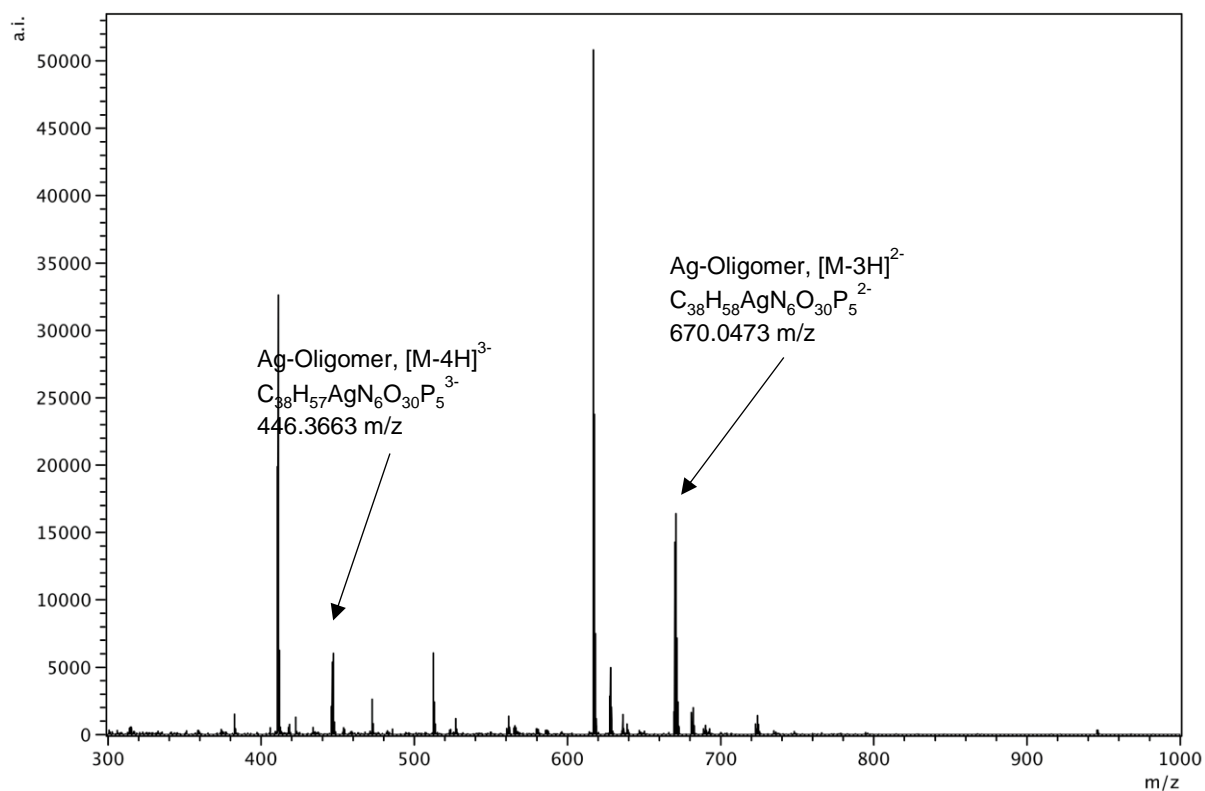


Figure S25. Negative ion mode ESI-MS following the 1:1 addition of Ag^+ to the oligonucleotide C-(a)₄-C, ^{a4}C₁ (a: abasic site).

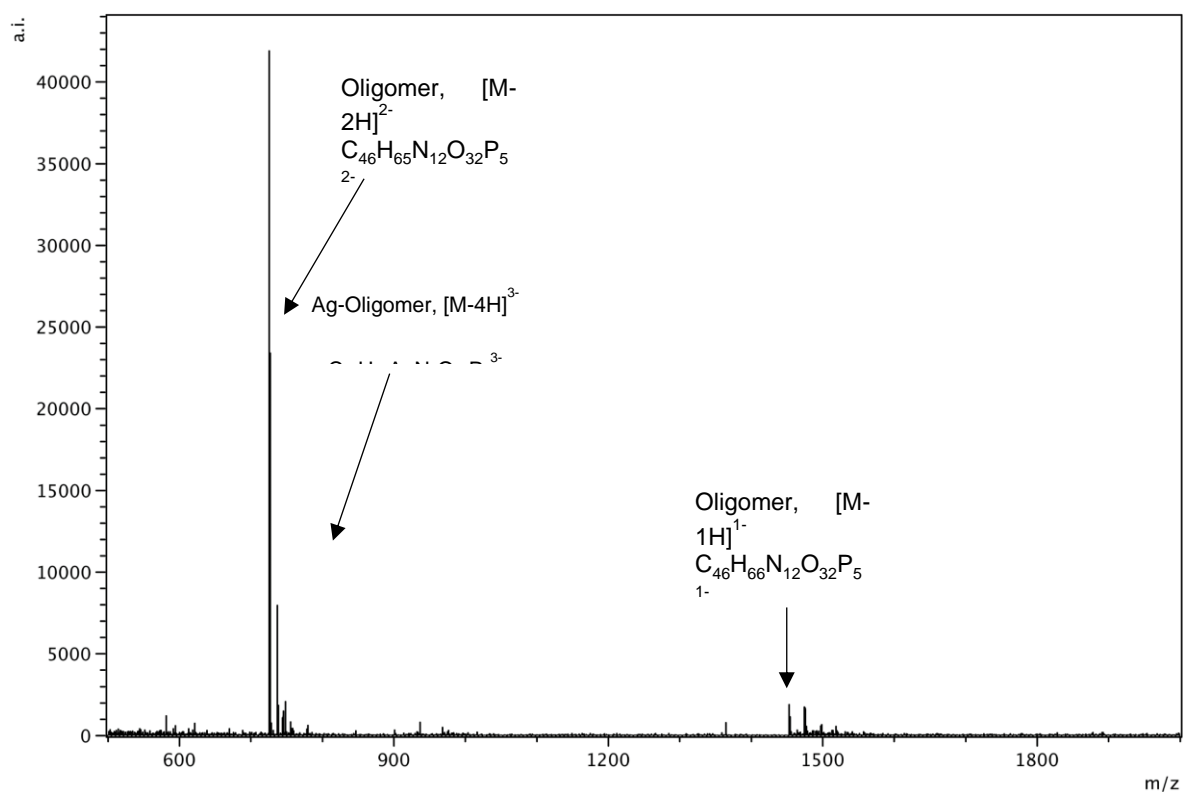


Figure S26. Negative ion mode ESI-MS of the oligonucleotide C₂-(a)₂-C₂, ^{a2}C₂ (a: abasic site).

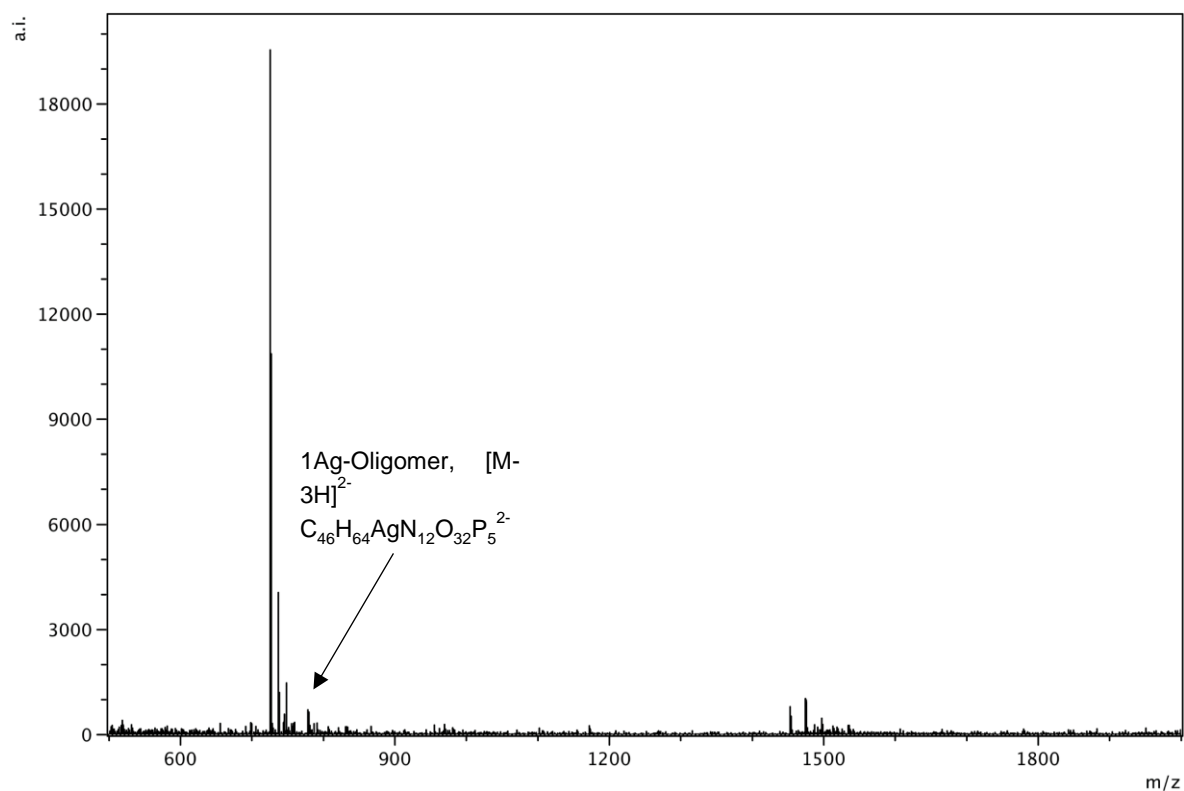


Figure S27. Negative ion mode ESI-MS following the addition of Ag^+ (1 equiv.) to the oligonucleotide $C_2-(a)_2-C_2, {}^{a2}C_2$ (a: abasic site).

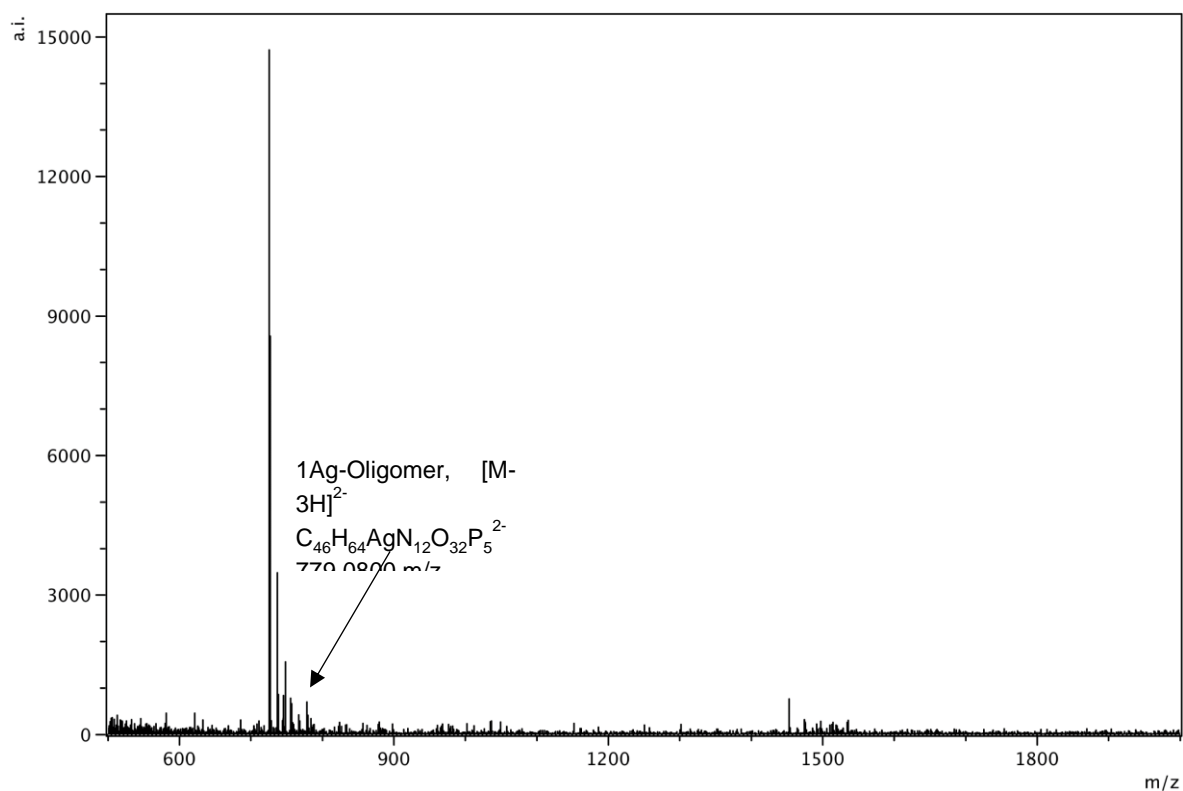


Figure S28. Negative ion mode ESI-MS following the addition of Ag⁺ (2 equiv.) to the oligonucleotide C₂-(a)₂-C₂, ^{a2}C₂ (a: abasic site).

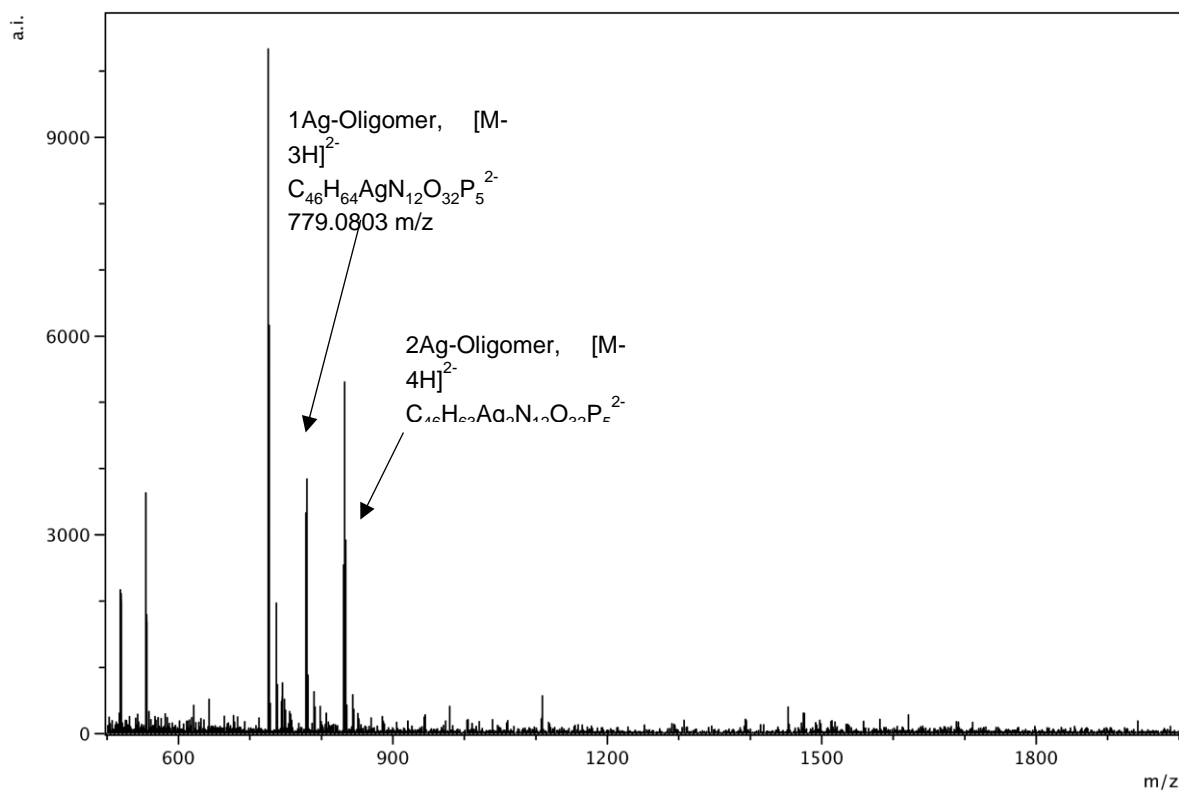


Figure S29. Negative ion mode ESI-MS following the addition of excess Ag⁺ (10 equiv.) to the oligonucleotide C₂-(a)₂-C₂, ^{a2}C₂ (a: abasic site).

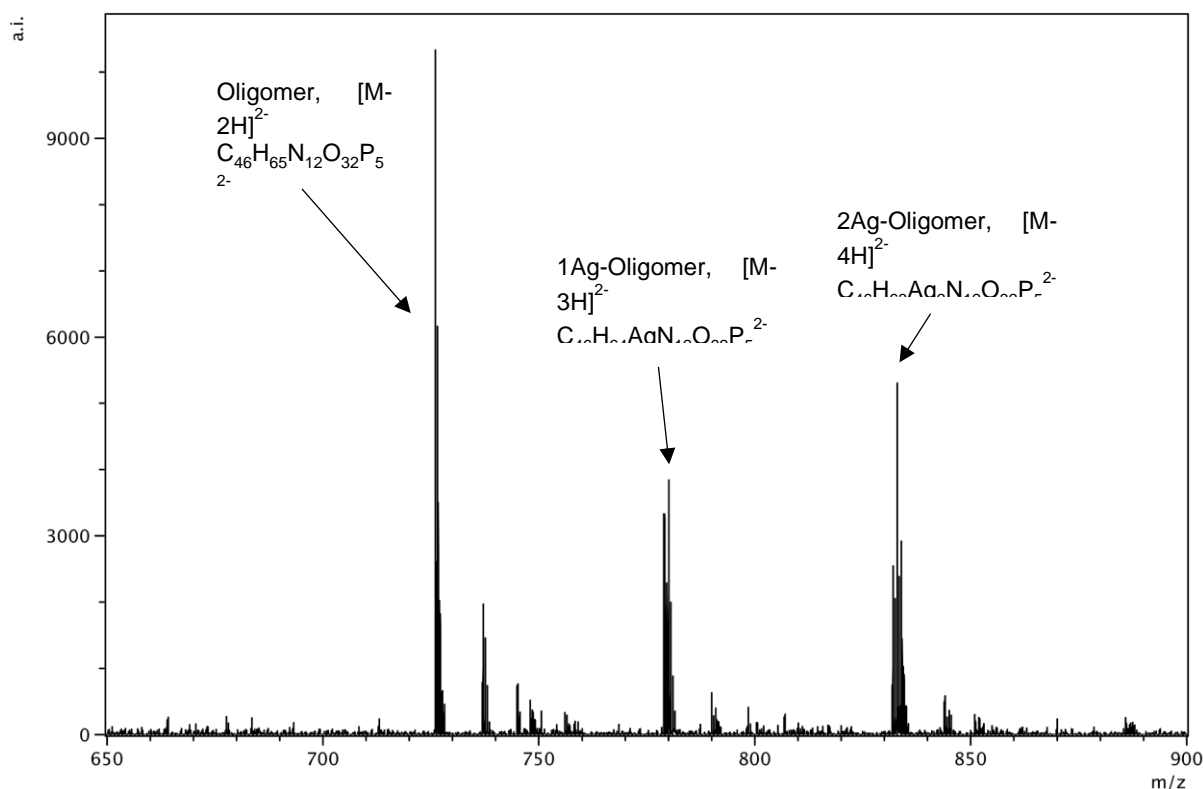


Figure S30. Negative ion mode ESI-MS (range 650 – 900 m/z) following the addition of excess Ag^+ (10 equiv.) to the oligonucleotide $C_2-(a)_2-C_2$, $^{a2}C_2$ (a: abasic site). Ratio: 1.00 : 0.36 : 0.51.

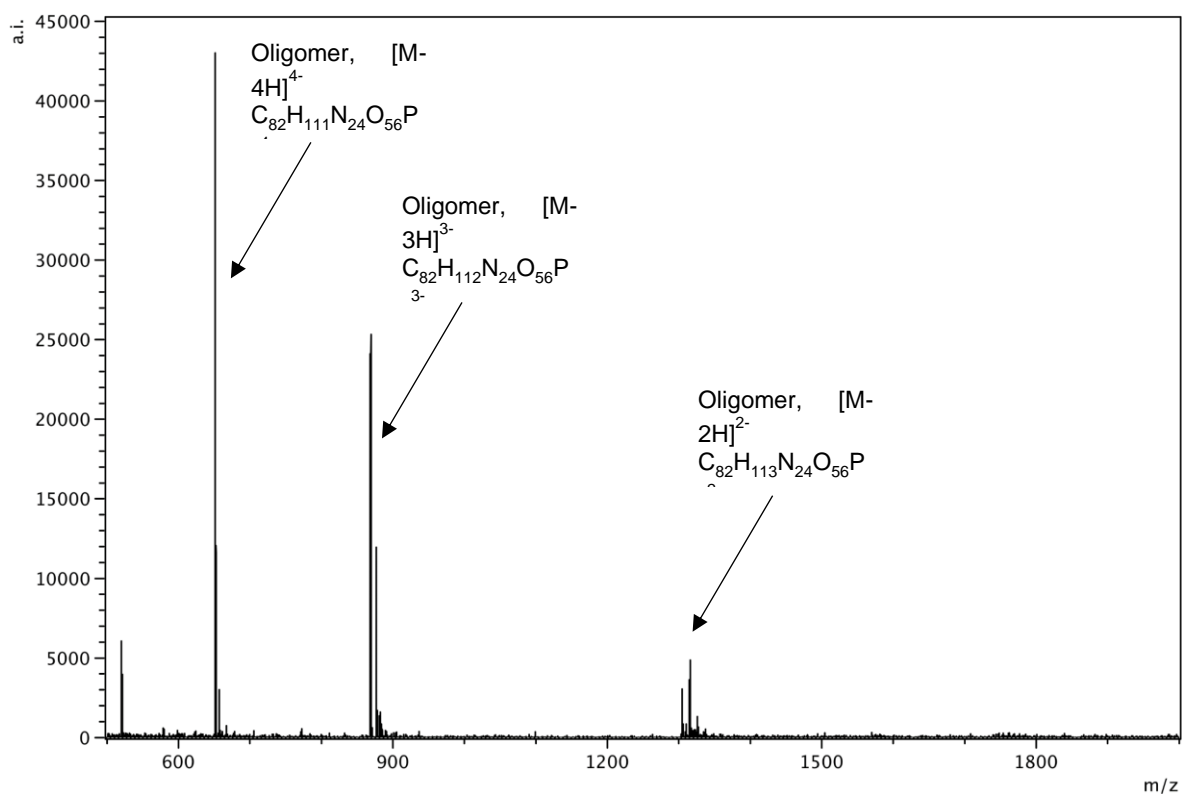


Figure S31. Negative ion mode ESI-MS of the oligonucleotide $C_4-(a)_2-C_4$, $^{a2}C_4$ (a: abasic site).

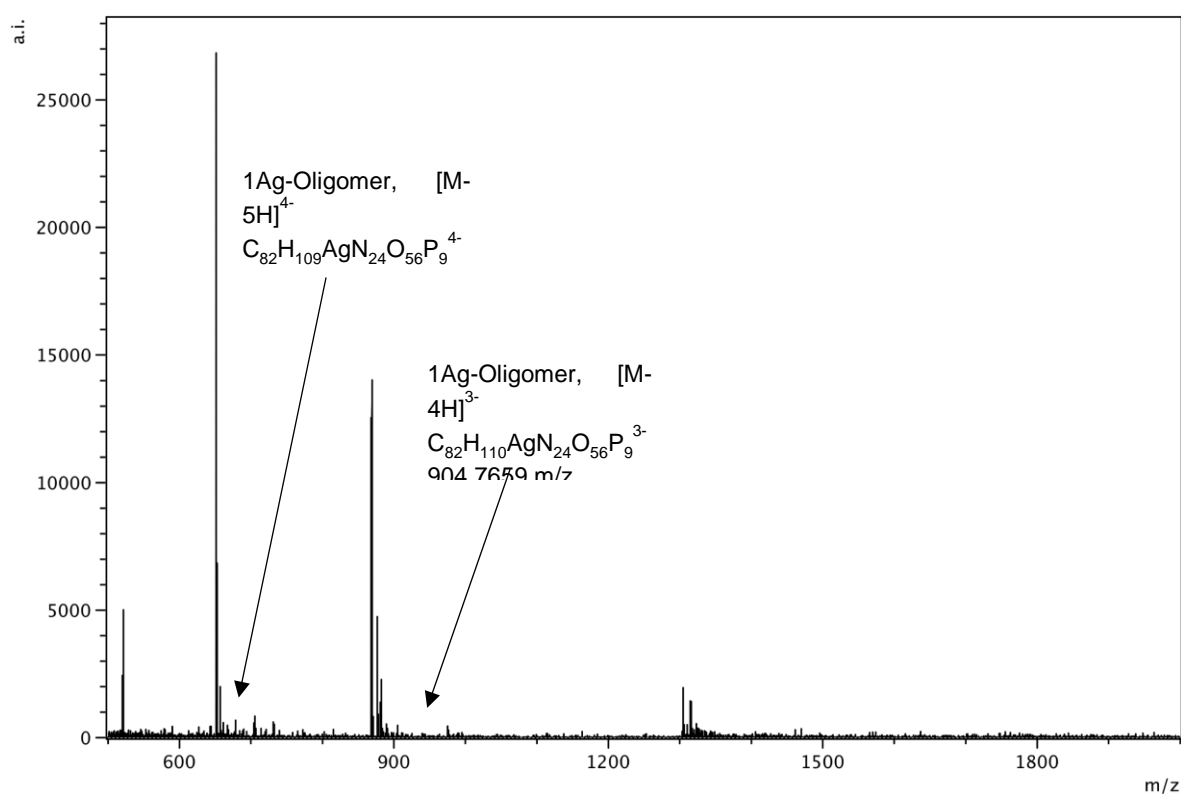


Figure S32. Negative ion mode ESI-MS following the addition of Ag⁺ (1 equiv.) to the oligonucleotide C₄-(a)₂-C₄, ^{a2}C₄ (a: abasic site).

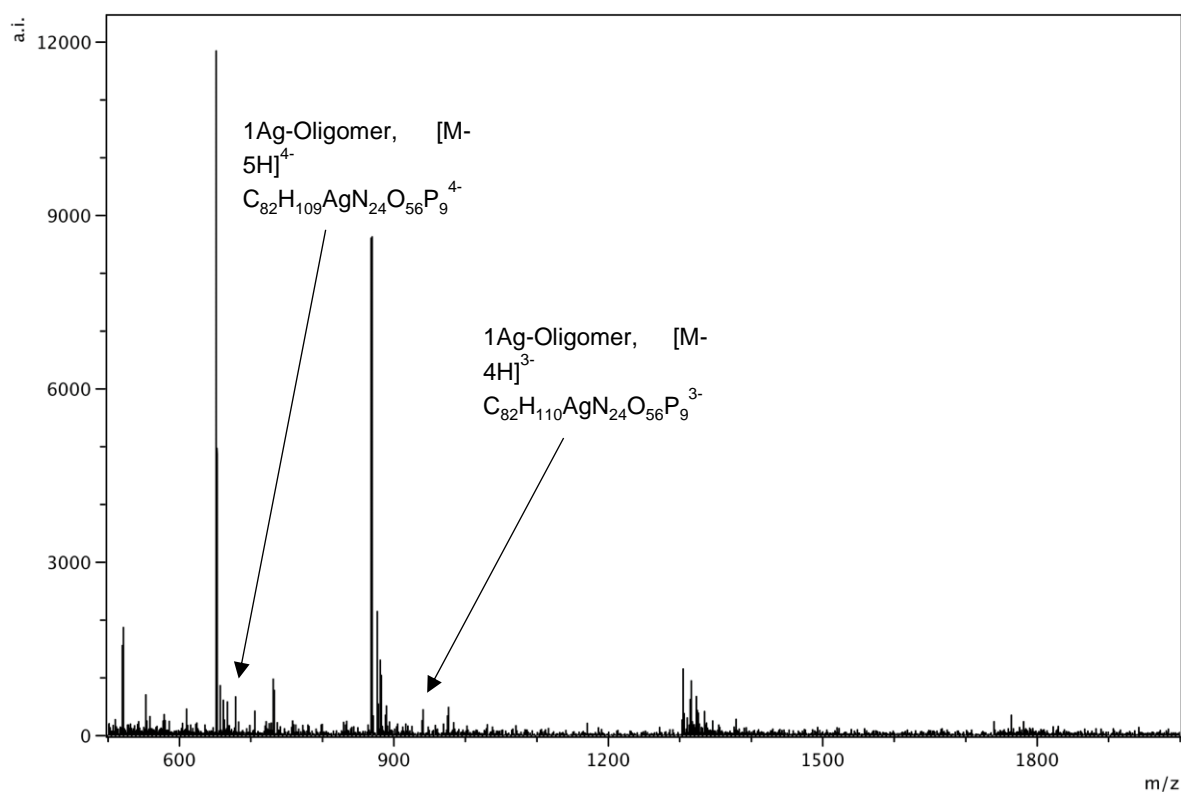


Figure S33. Negative ion mode ESI-MS following the addition of Ag⁺ (2 equiv.) to the oligonucleotide C₄-(a)₂-C₄, ^{a2}C₄ (a: abasic site).

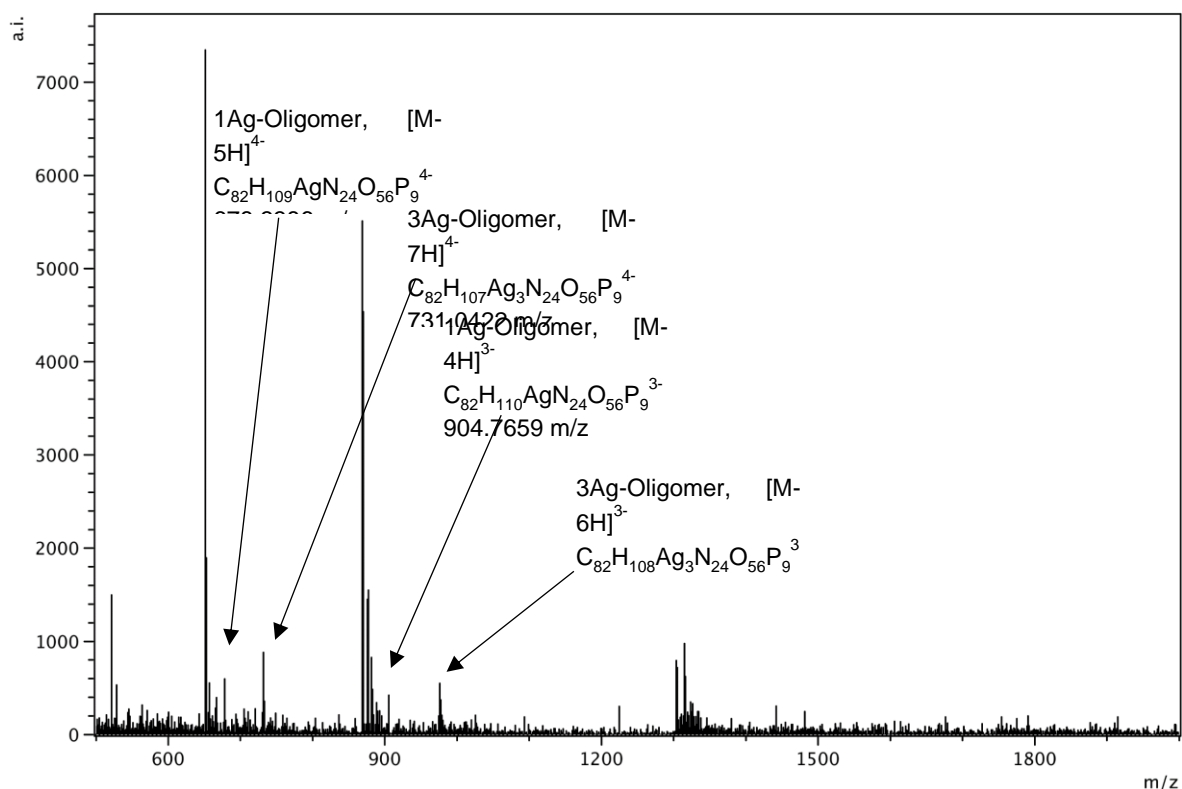


Figure S34. Negative ion mode ESI-MS following the addition of Ag^+ (3 equiv.) to the oligonucleotide $\text{C}_4\text{-(a)}_2\text{-C}_4$, a^2C_4 (a: abasic site).

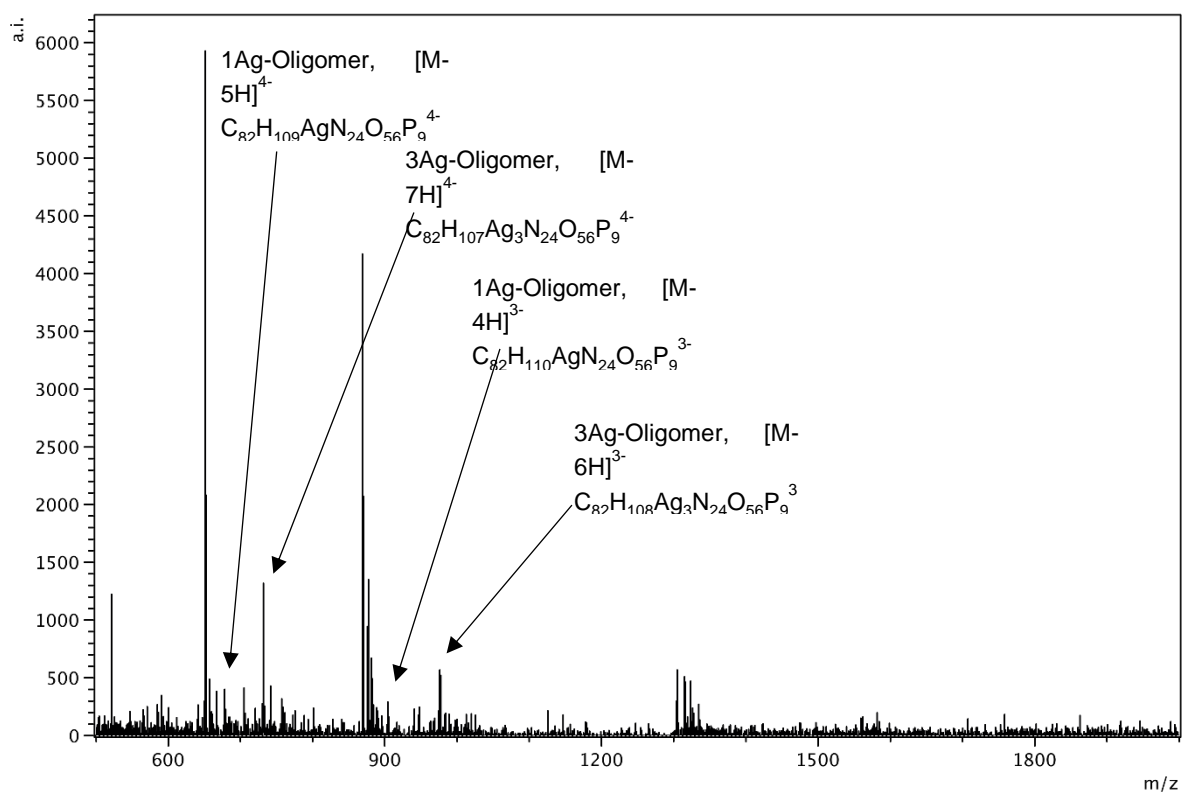


Figure S35. Negative ion mode ESI-MS following the addition of Ag^+ (4 equiv.) to the oligonucleotide $\text{C}_4\text{-(a)}_2\text{-C}_4$, a^2C_4 (a: abasic site).

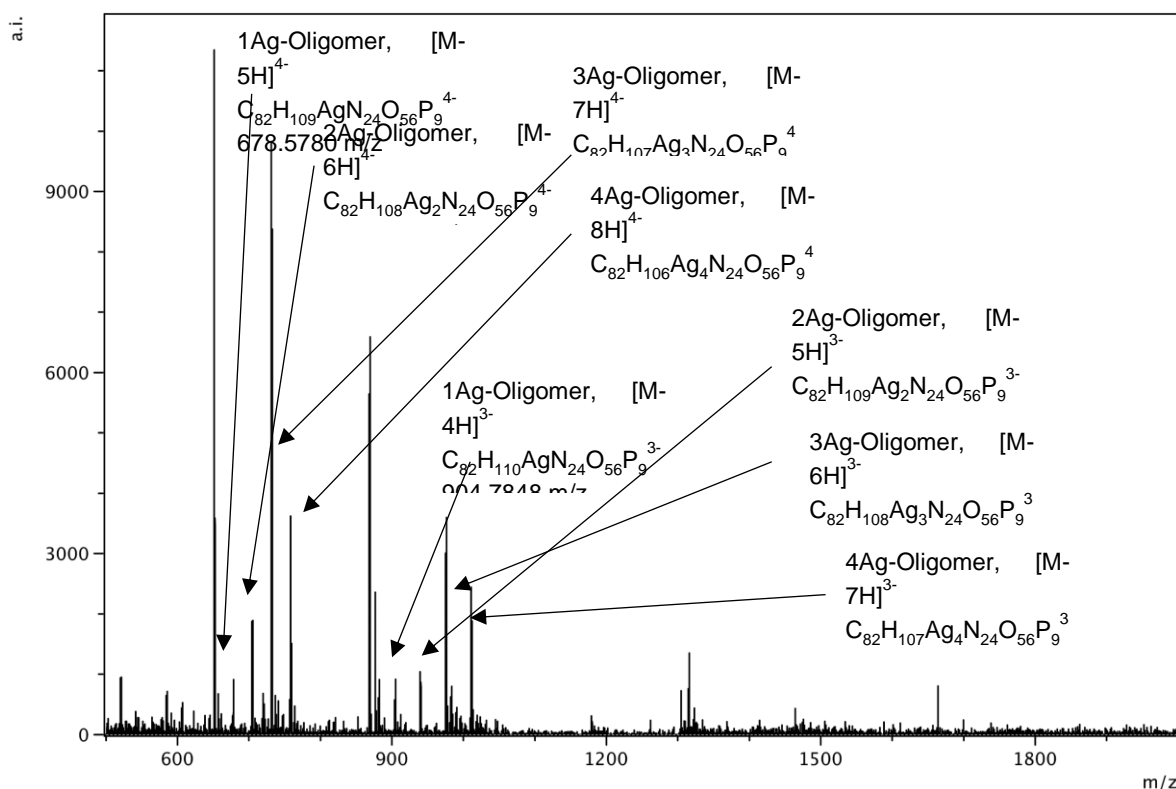


Figure S36. Negative ion mode ESI-MS following the addition of excess Ag^+ (10 equiv.) to the oligonucleotide $\text{C}_4\text{-(a)}_2\text{-C}_4$, $^{a2}\text{C}_4$ (a: abasic site).

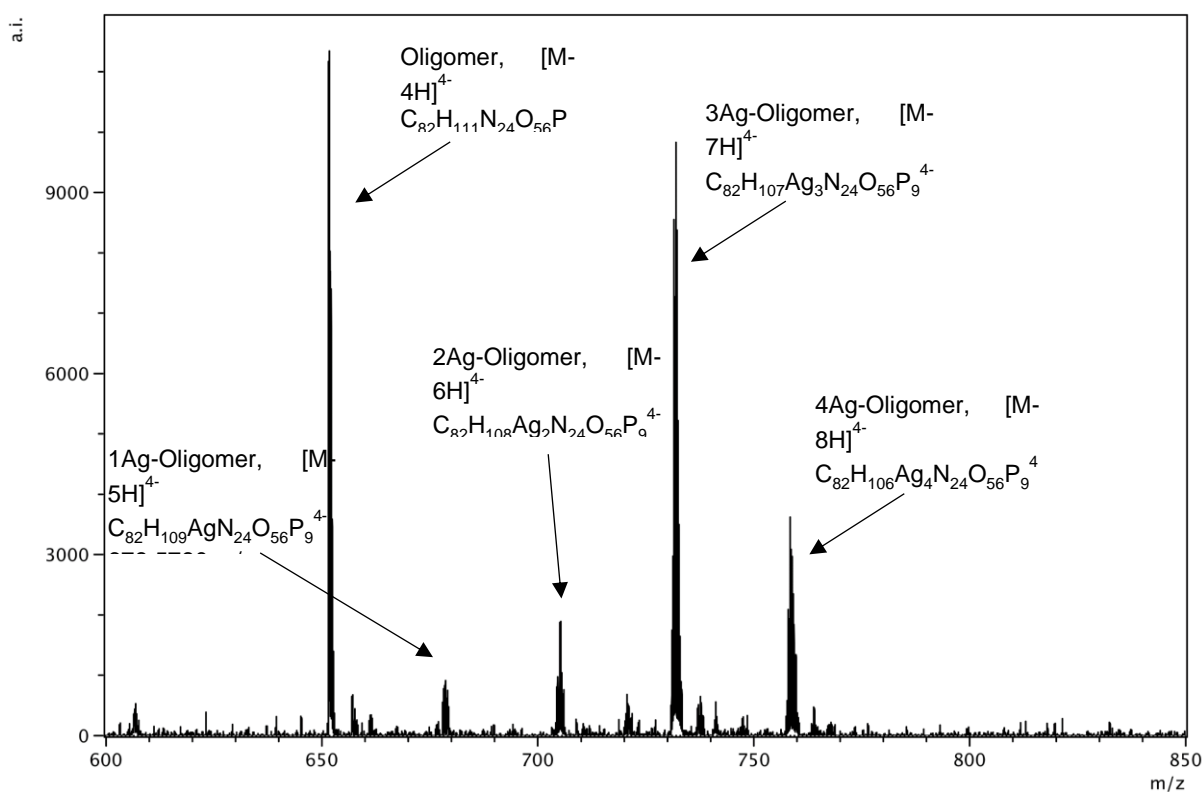


Figure S37. Negative ion mode ESI-MS (range 650–850 m/z) following the addition of excess Ag^+ (10 equiv.) to the oligonucleotide $\text{C}_4\text{-(a)}_2\text{-C}_4$, $^{a2}\text{C}_4$ (a: abasic site). Ratio: 1.00 : 0.08 : 0.15 : 0.87 : 0.31.

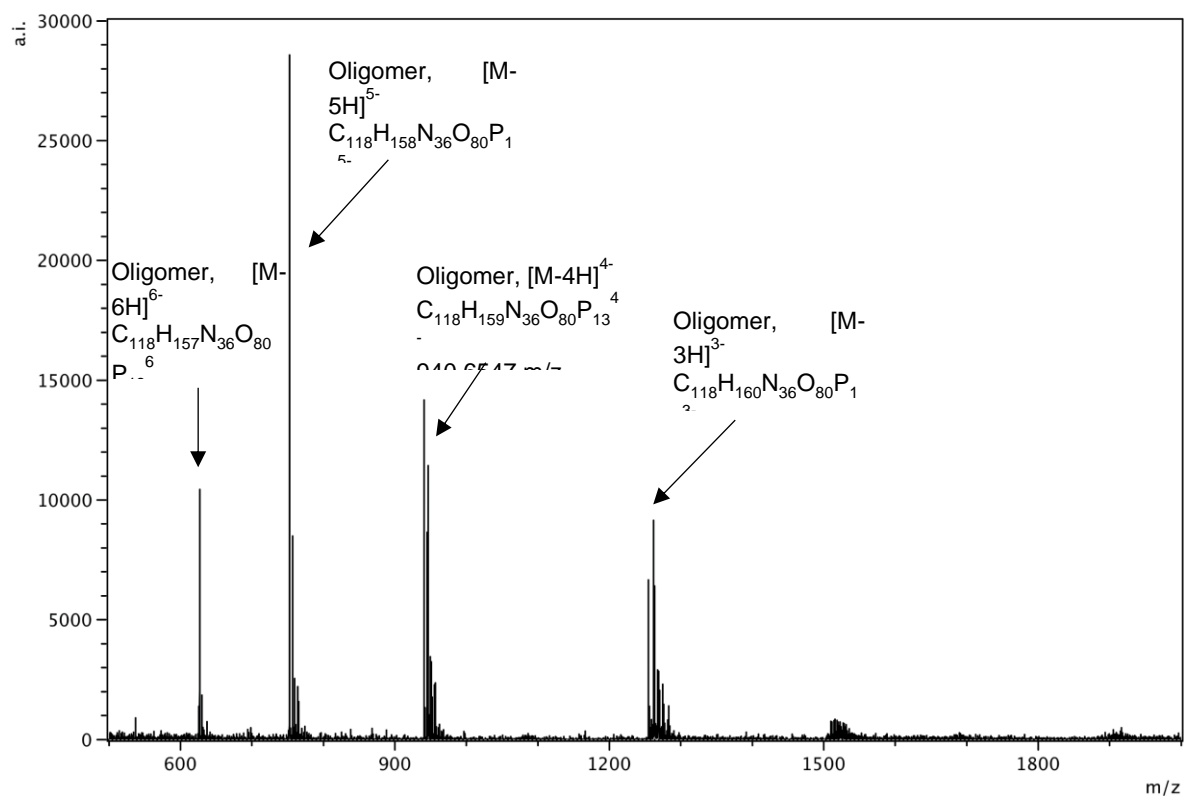


Figure S38. Negative ion mode ESI-MS of the oligonucleotide $C_6-(a)_2-C_6, {}^{a2}C_6$ (a: abasic site).

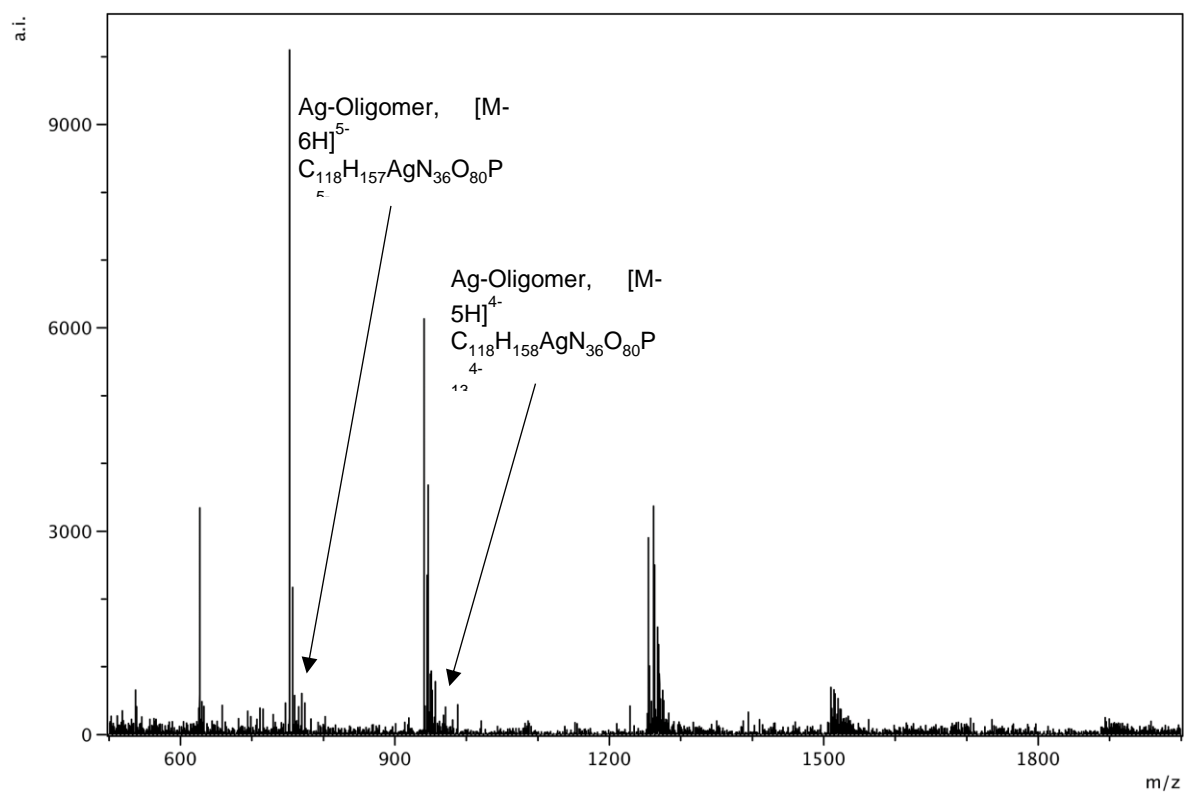


Figure S39. Negative ion mode ESI-MS following the addition of Ag^+ (1 equiv.) to the oligonucleotide $C_6-(a)_2-C_6, {}^{a2}C_6$ (a: abasic site).

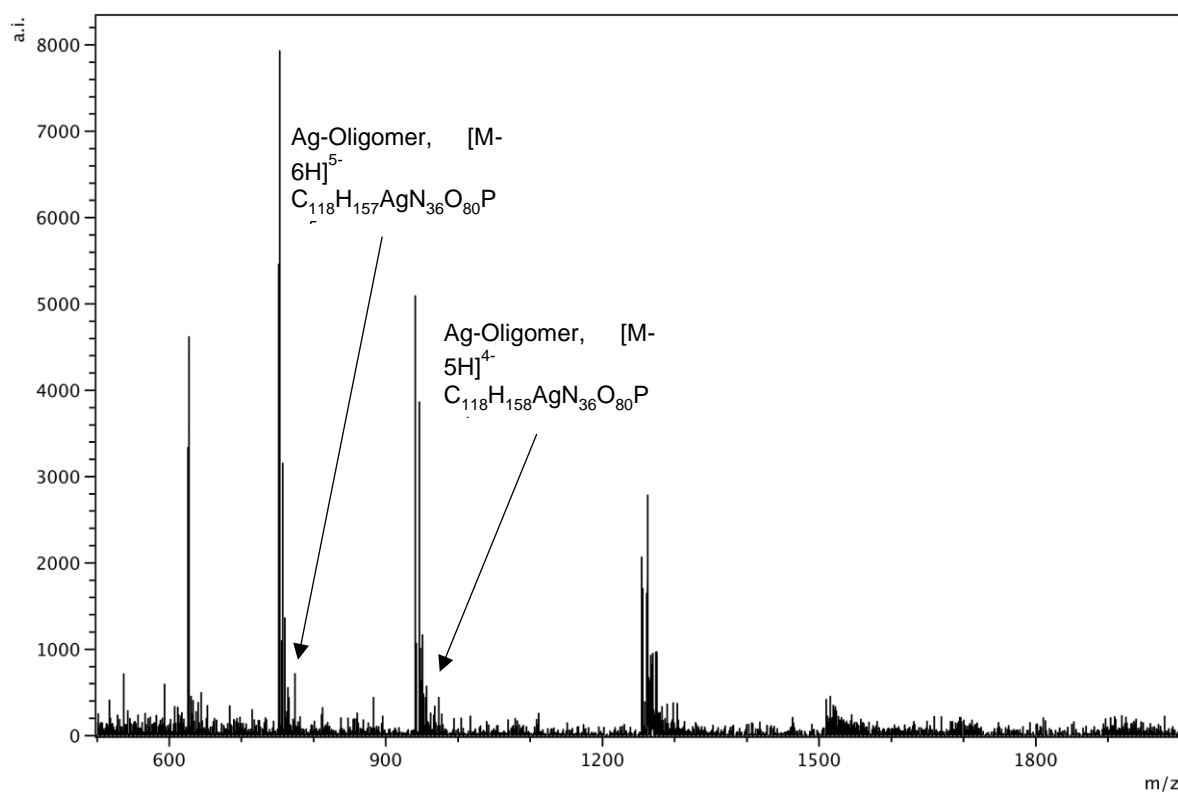


Figure S40. Negative ion mode ESI-MS following the addition of Ag^+ (2 equiv.) to the oligonucleotide $\text{C}_6\text{-(a)}_2\text{-C}_6, {}^{\text{a}2}\text{C}_6$ (a: abasic site).

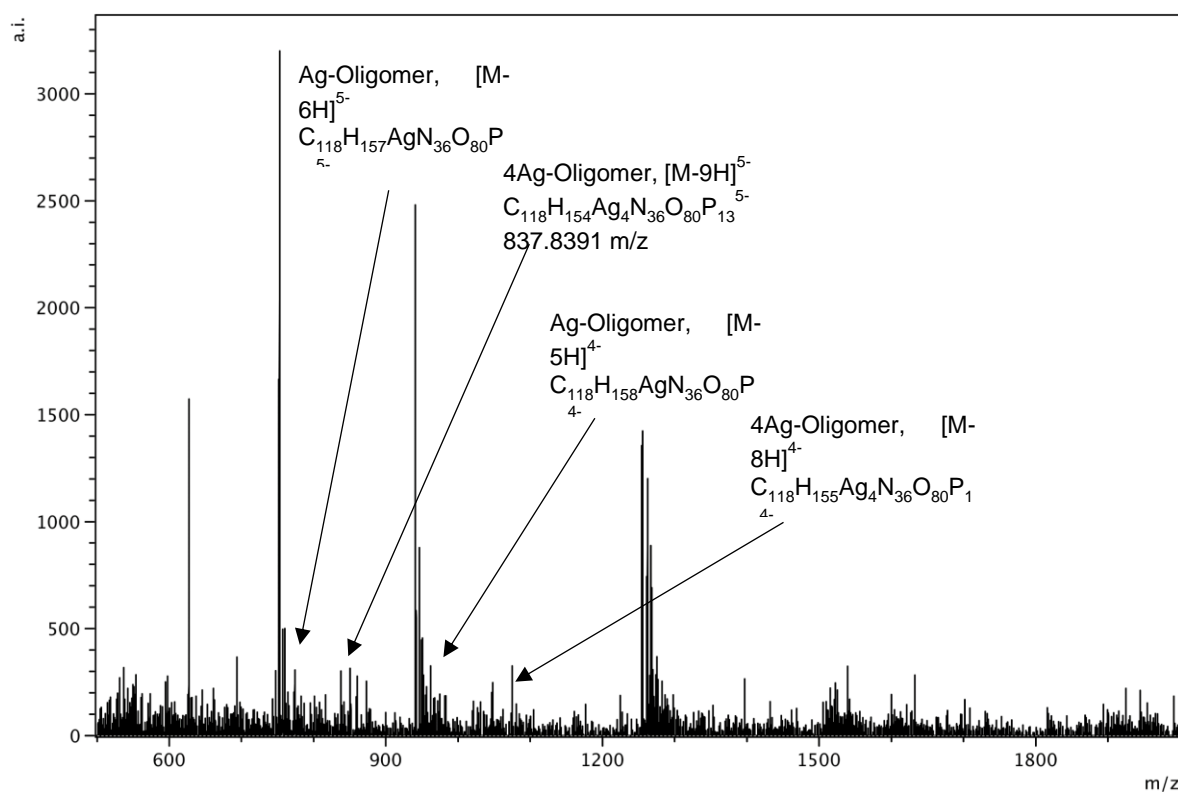


Figure S41. Negative ion mode ESI-MS following the addition of Ag^+ (4 equiv.) to the oligonucleotide $\text{C}_6\text{-(a)}_2\text{-C}_6, {}^{\text{a}2}\text{C}_6$ (a: abasic site).

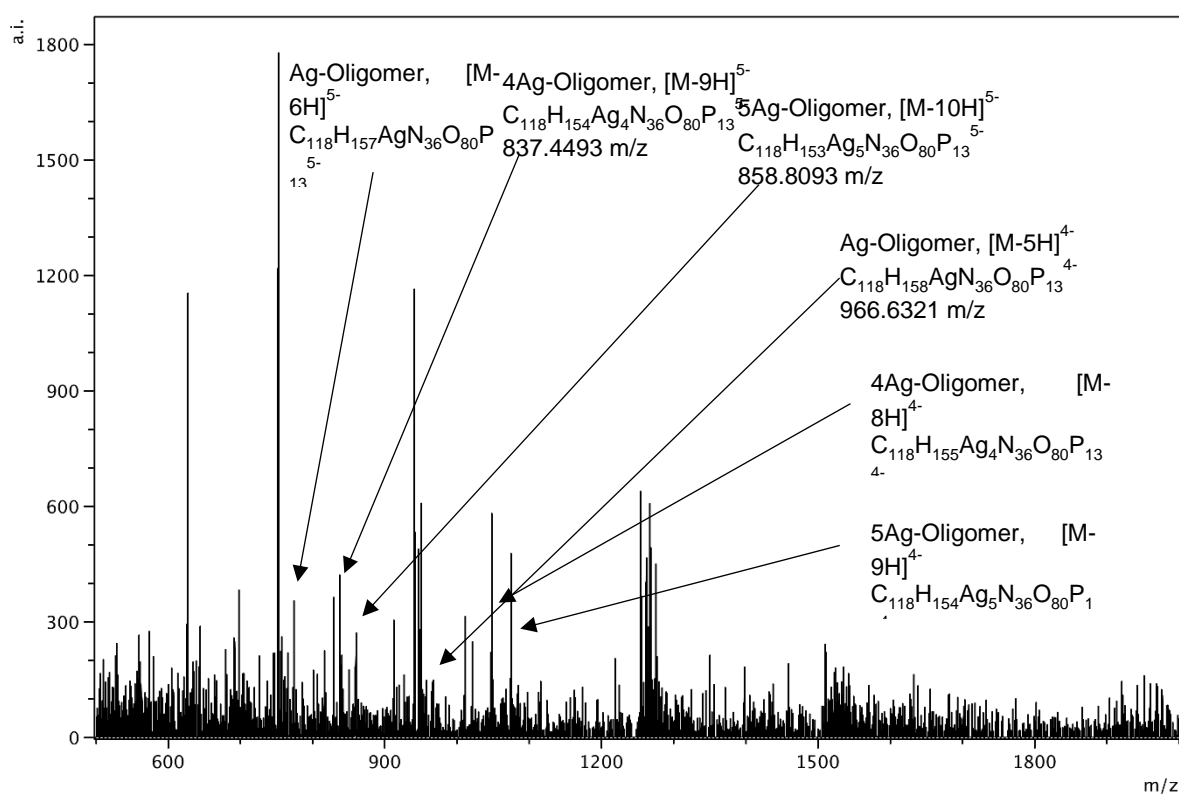


Figure S42. Negative ion mode ESI-MS following the addition of Ag^+ (6 equiv.) to the oligonucleotide $\text{C}_6\text{-(a)}_2\text{-C}_6$, $^{a2}\text{C}_6$ (a: abasic site).

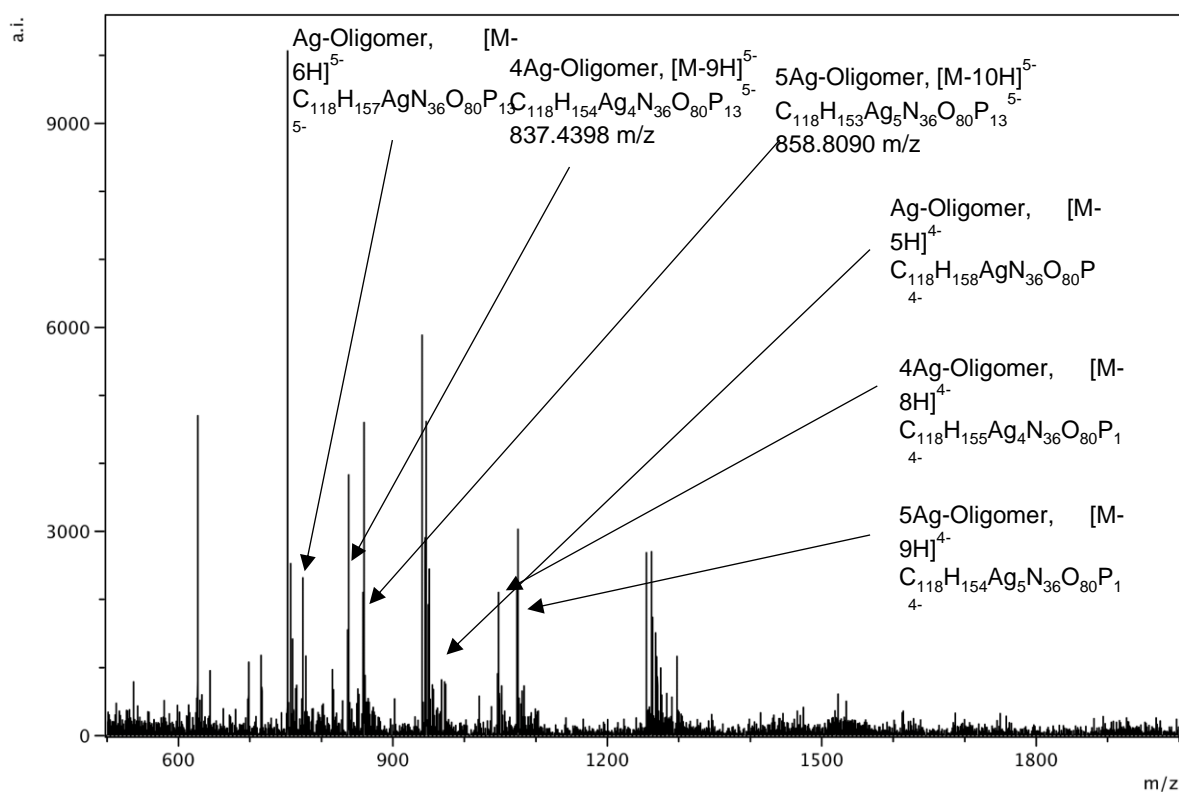


Figure S43. Negative ion mode ESI-MS following the addition of excess Ag^+ (10 equiv.) to the oligonucleotide $\text{C}_6\text{-(a)}_2\text{-C}_6$, $^{a2}\text{C}_6$ (a: abasic site).

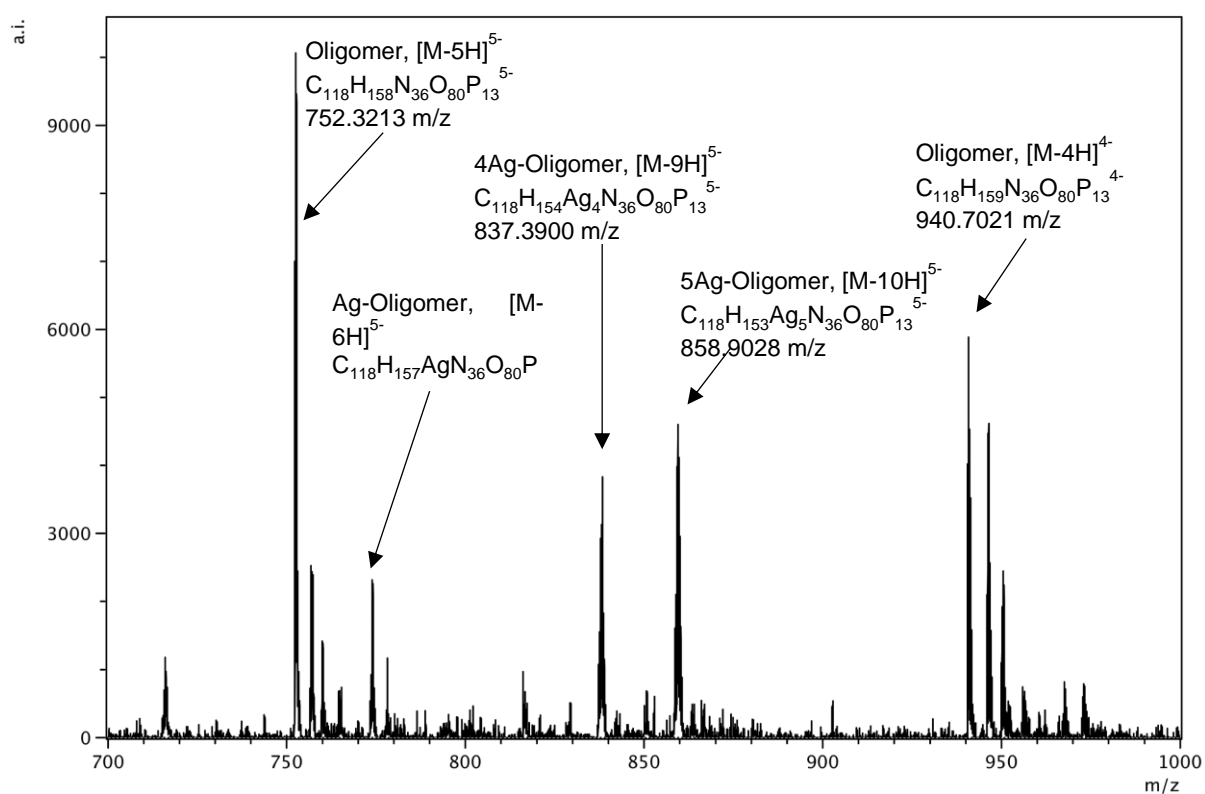


Figure S44. Negative ion mode ESI-MS (range 700 –1000 m/z) following the addition of excess Ag^+ (10 equiv.) to the oligonucleotide $\text{C}_6\text{-(a)}_2\text{-C}_6$, $^{a2}\text{C}_6$ (a: abasic site). Ratio: 1.00 : 0.22 : 0.39 : 0.47.

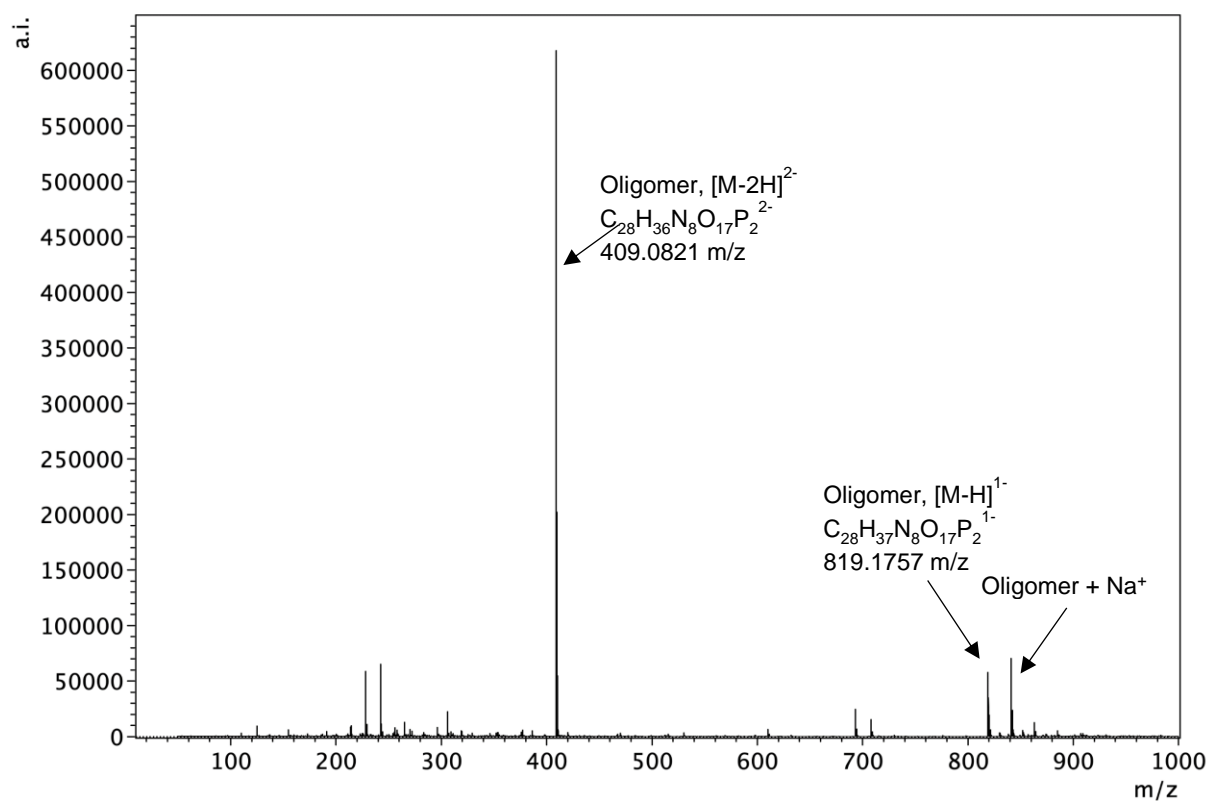


Figure S45. Negative ion mode ESI-MS the oligonucleotide $\text{C}_1\text{-(T)}_1\text{-T}_1$, $^{T1}\text{C}_1$.

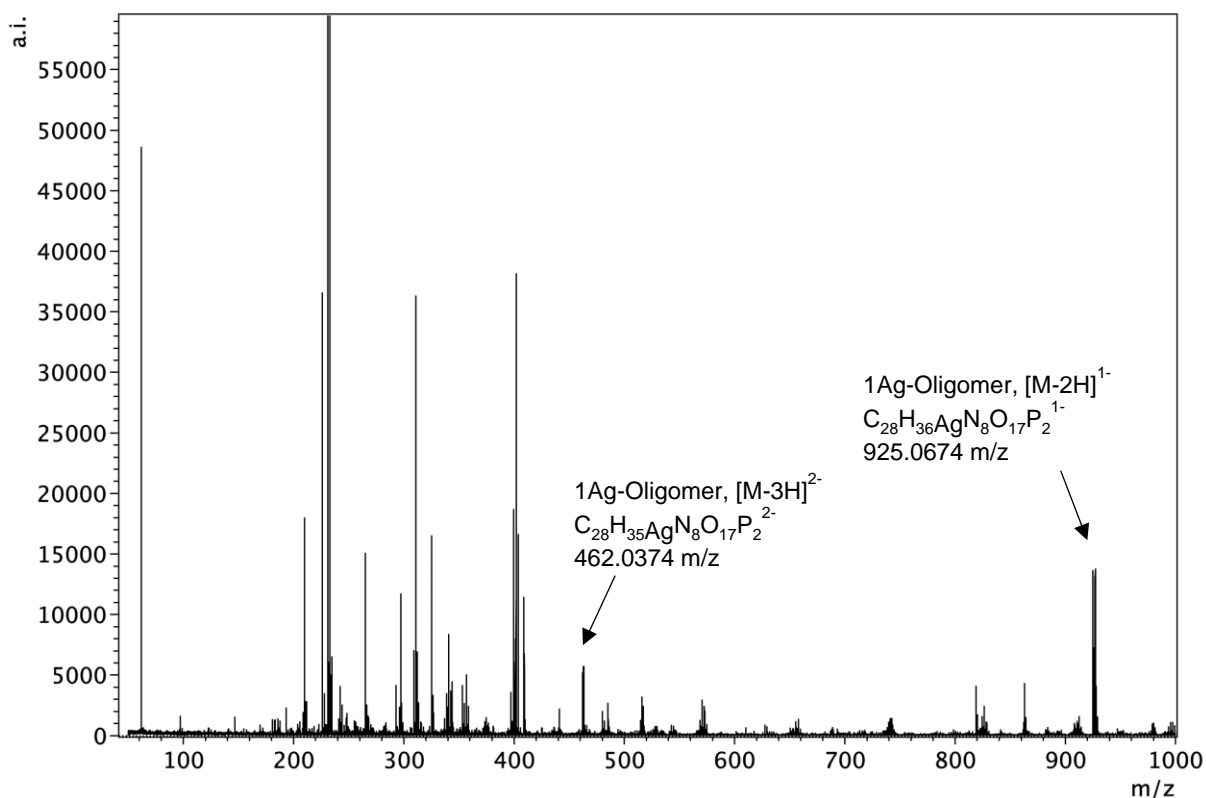


Figure S46. Negative ion mode ESI-MS following the addition of Ag^+ (1 equiv.) to the oligonucleotide $C_1-(T)_1-C_1$, $^{11}C_1$.

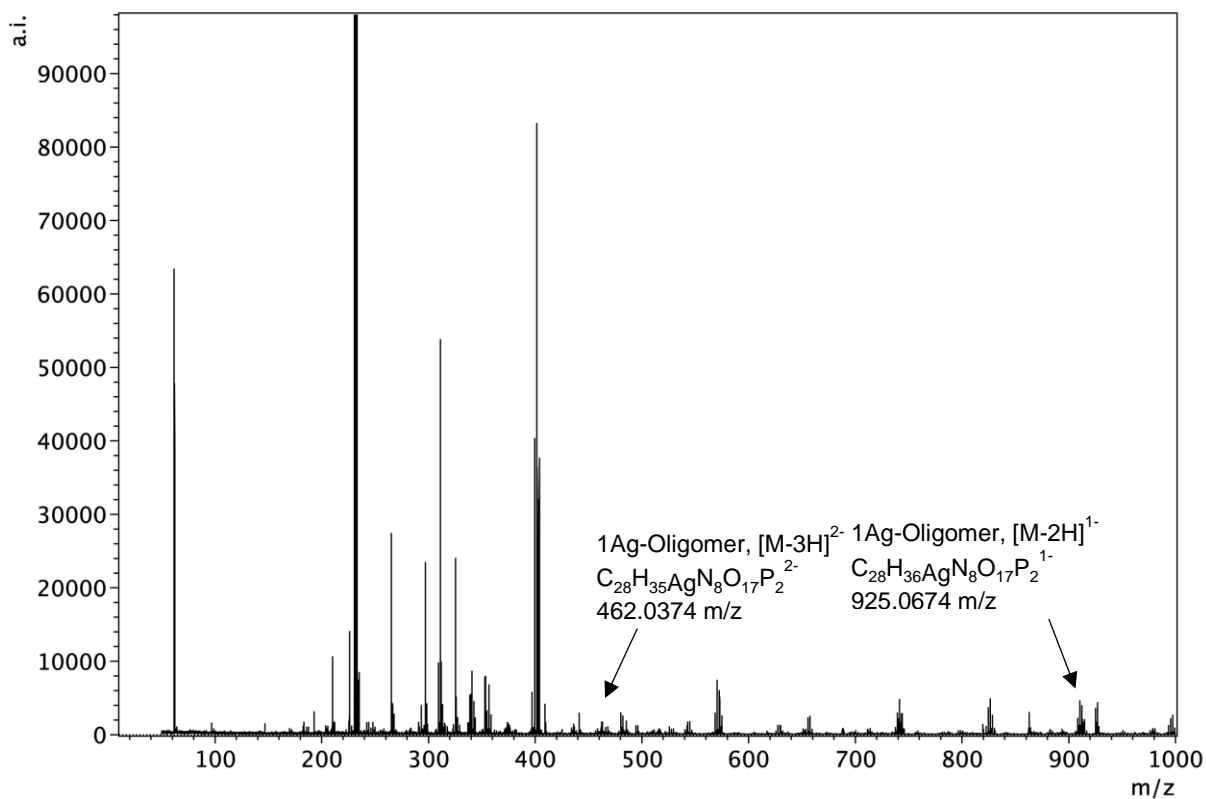


Figure S47. Negative ion mode ESI-MS following the addition of excess Ag^+ (3 equiv.) to the oligonucleotide $C_1-(T)_1-C_1$, $^{11}C_1$.

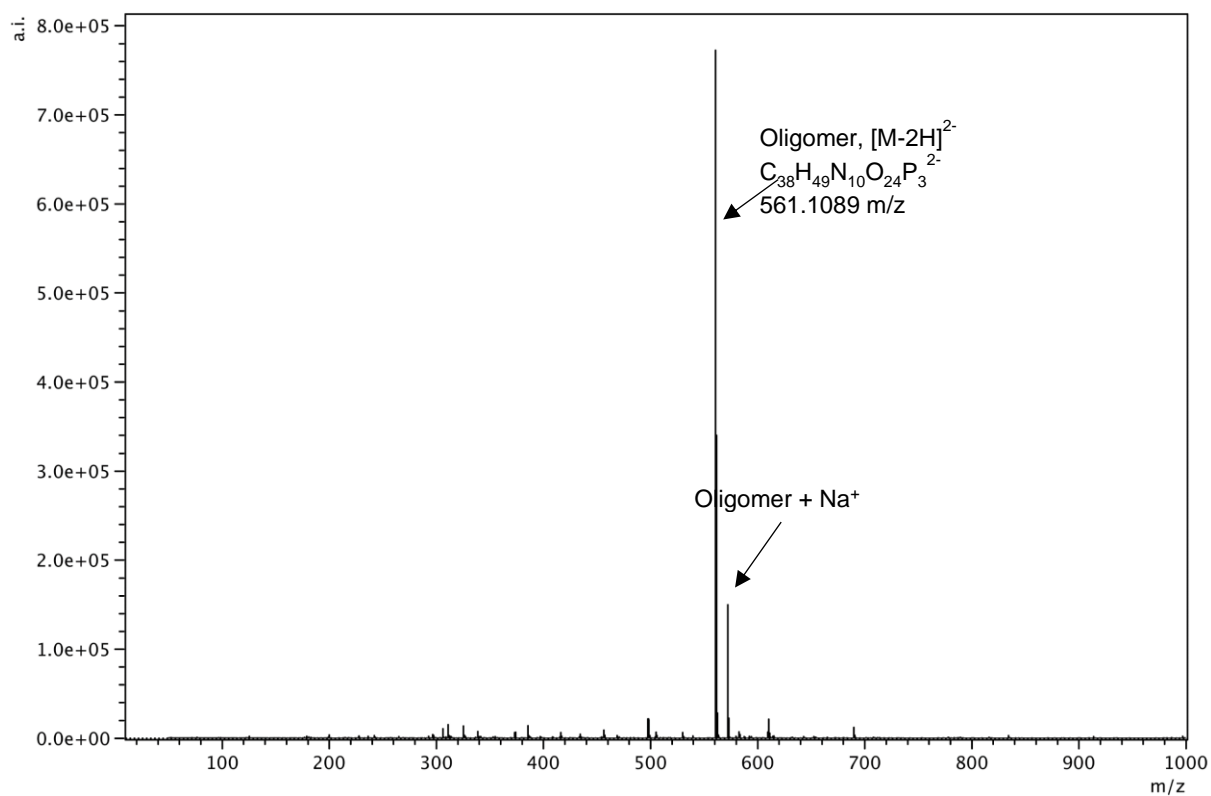


Figure S48. Negative ion mode ESI-MS the oligonucleotide $C_1-(T)_2-T_1, T_2C_1$.

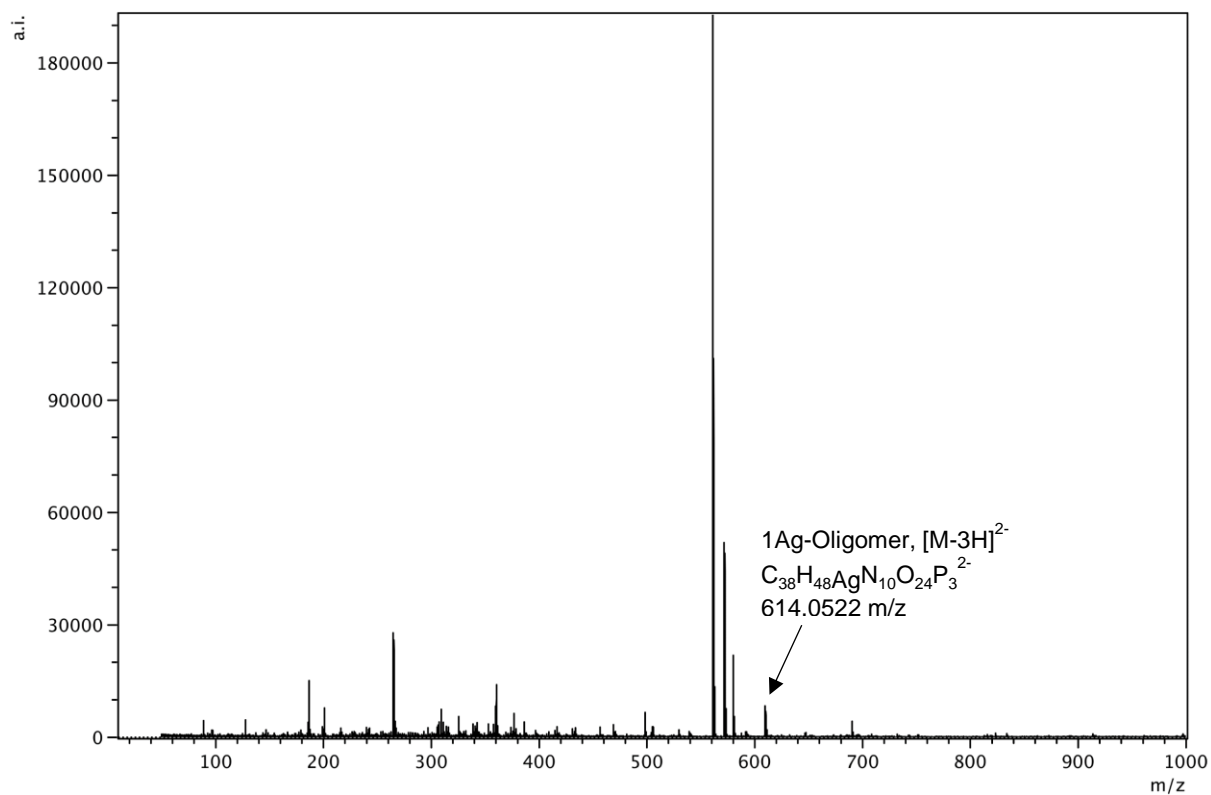


Figure S49. Negative ion mode ESI-MS following the addition of Ag^+ (1 equiv.) to the oligonucleotide $C_1-(T)_2-C_1, T_2C_1$.

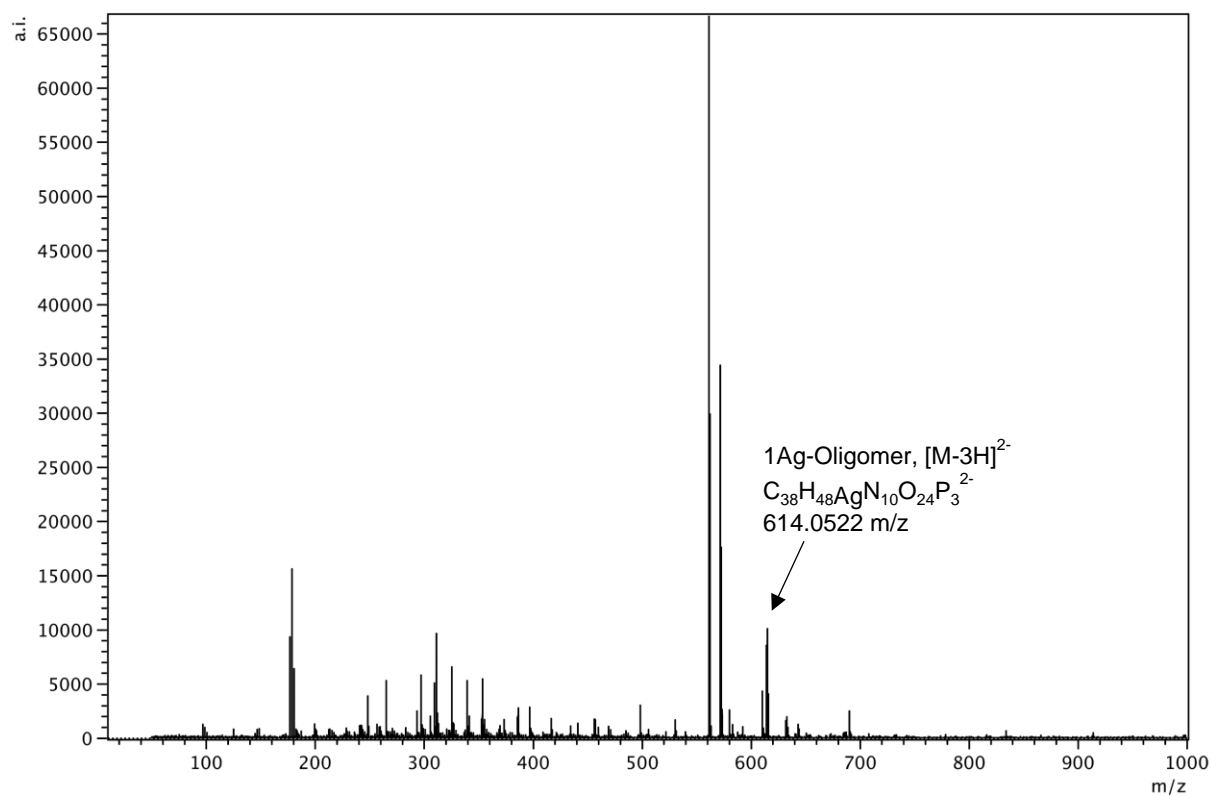


Figure S50. Negative ion mode ESI-MS following the addition of excess Ag⁺ (3 equiv.) to the oligonucleotide C₁-(T)₂-C₁, ^{T2}C₁.

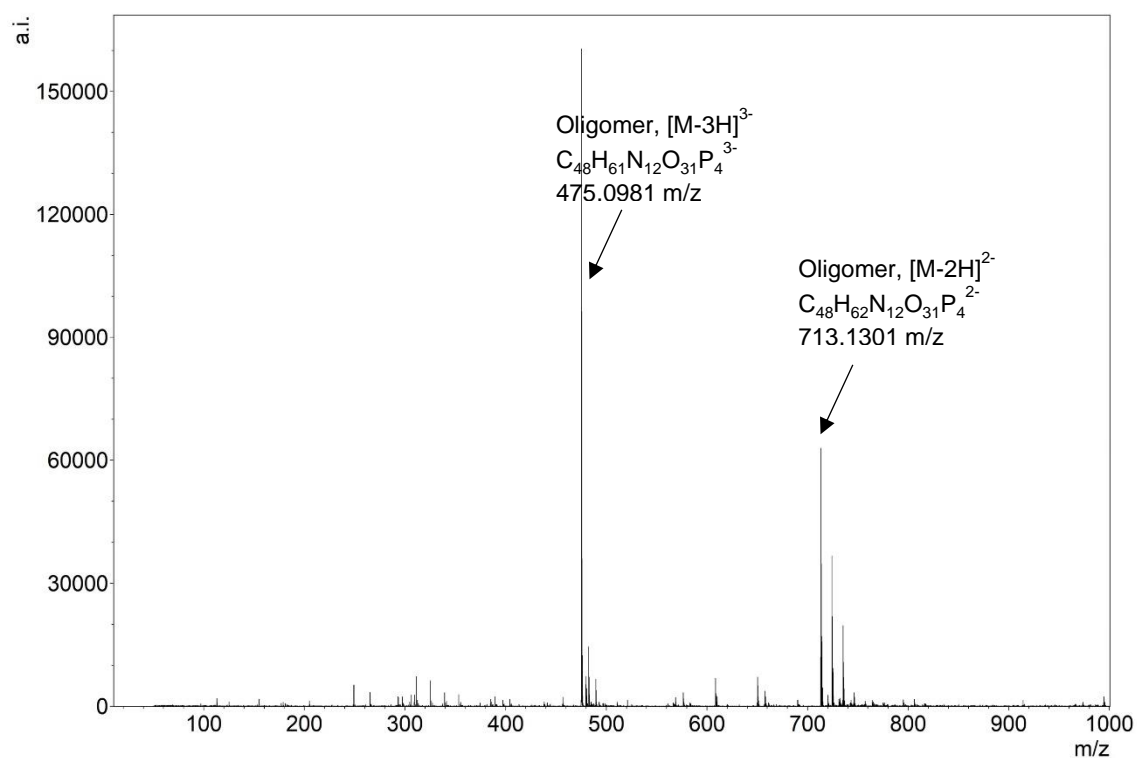


Figure S51. Negative ion mode ESI-MS the oligonucleotide C₁-(T)₃-T₁, ^{T3}C₁.

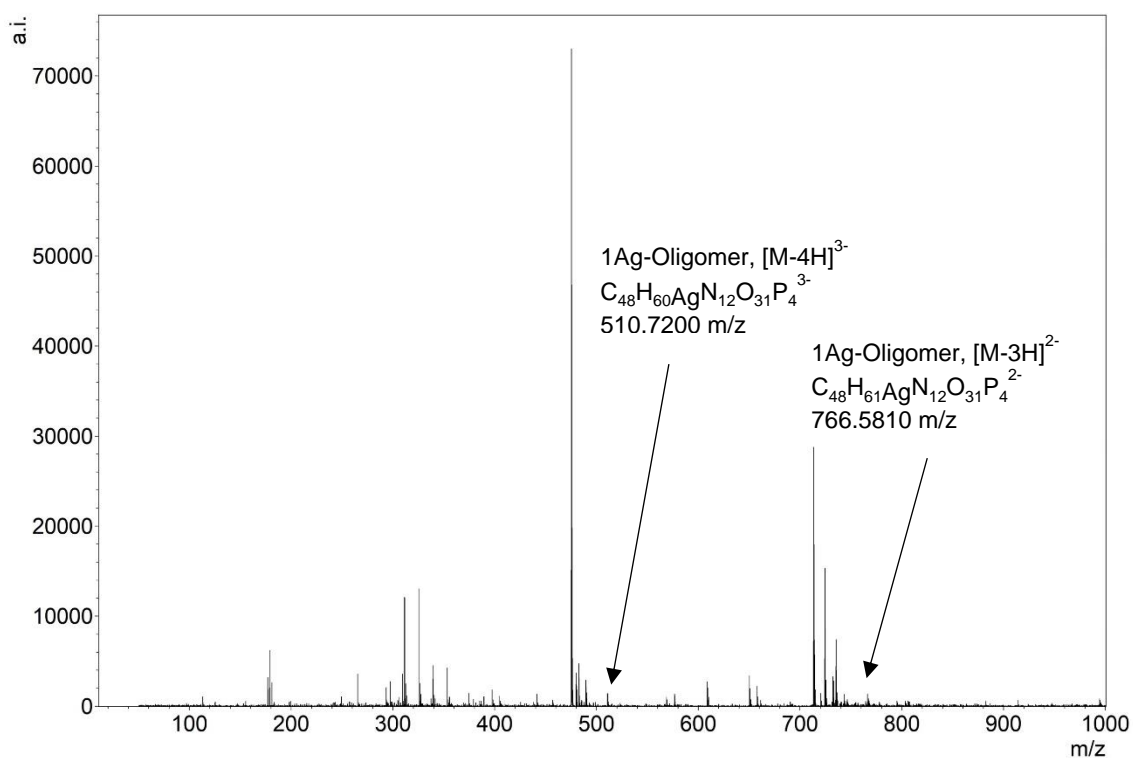


Figure S52. Negative ion mode ESI-MS following the addition of Ag⁺ (1 equiv.) to the oligonucleotide C₁-(T)₃-C₁, ¹³C₁.

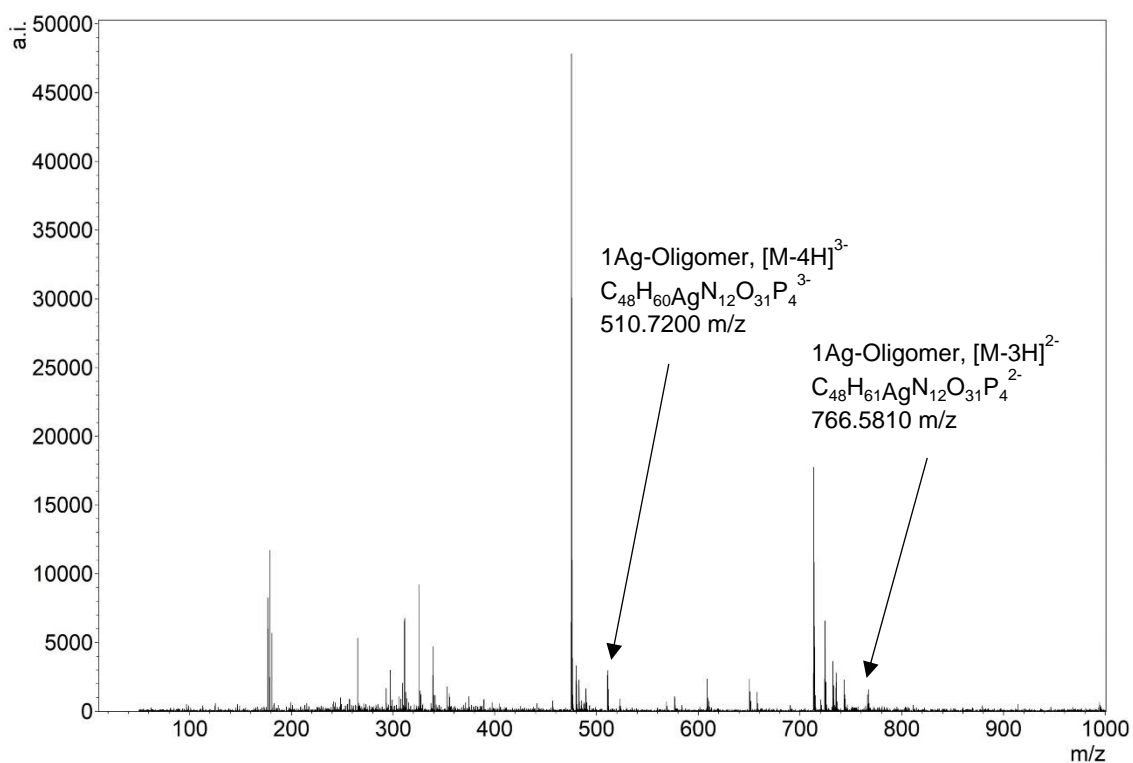


Figure S53. Negative ion mode ESI-MS following the addition of excess Ag⁺ (3 equiv.) to the oligonucleotide C₁-(T)₃-C₁, ¹³C₁.

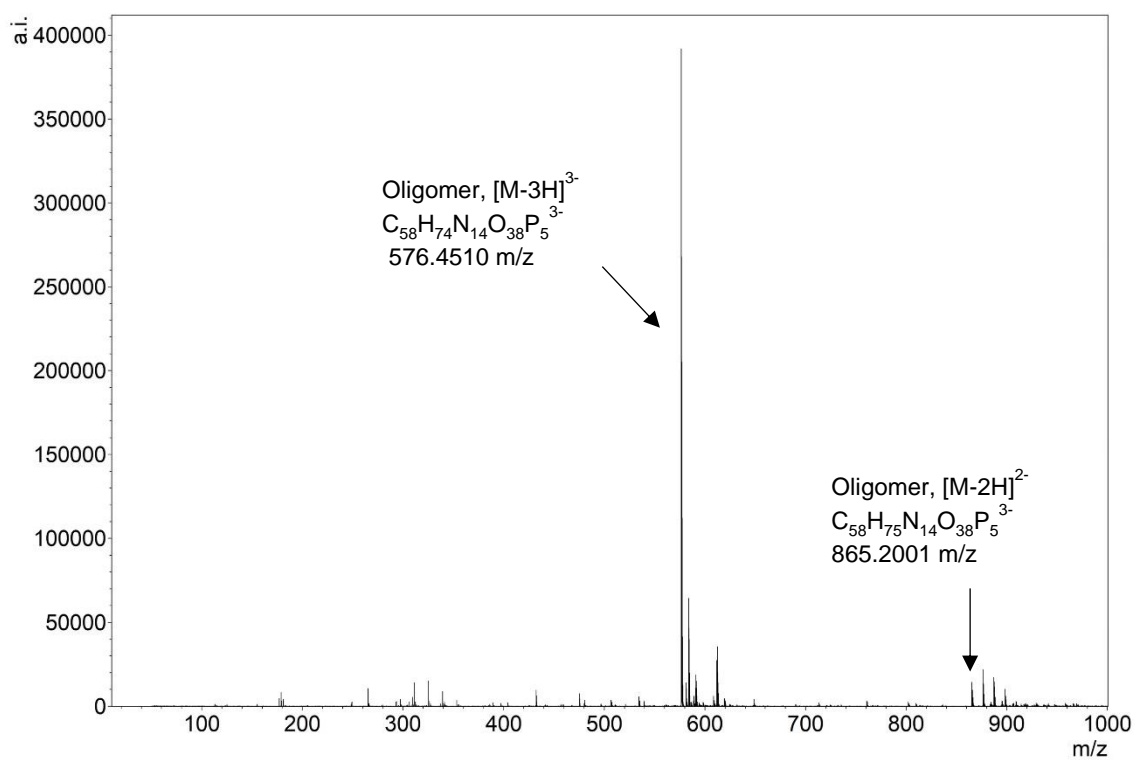


Figure S54. Negative ion mode ESI-MS the oligonucleotide $C_1-(T)_4-T_1$, T^4C_1 .

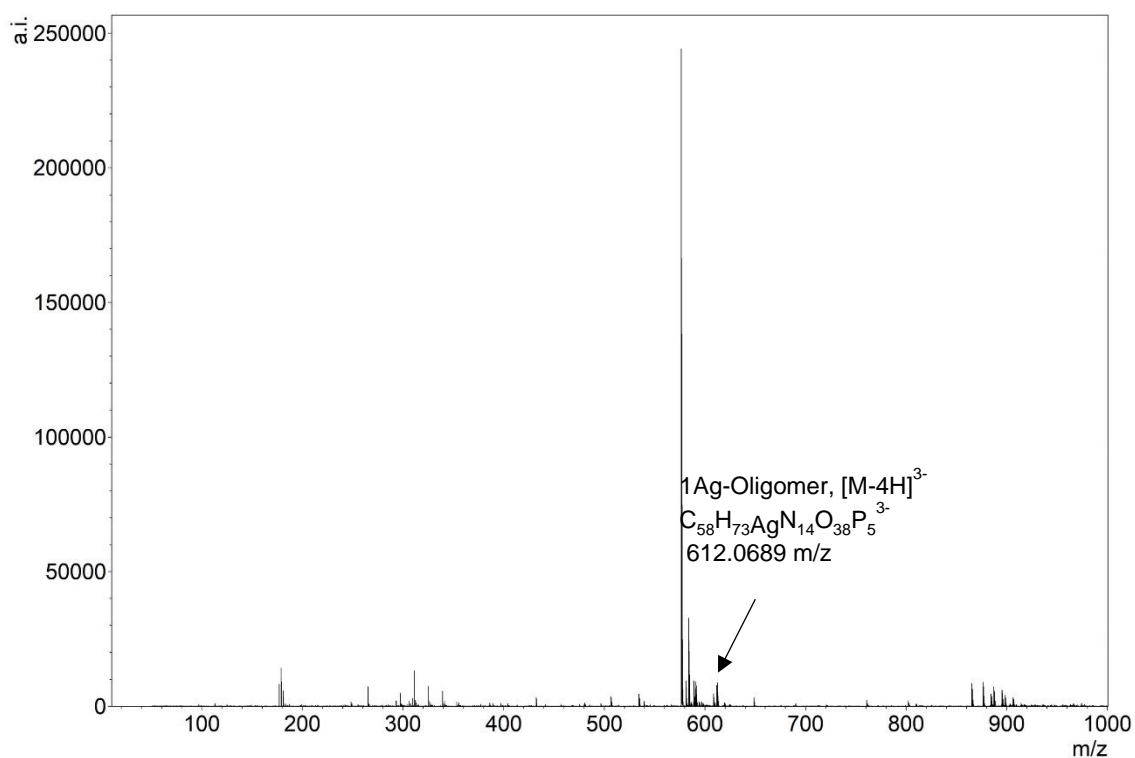


Figure S55. Negative ion mode ESI-MS following the addition of Ag^+ (1 equiv.) to the oligonucleotide $C_1-(T)_4-C_1$, T^4C_1 .

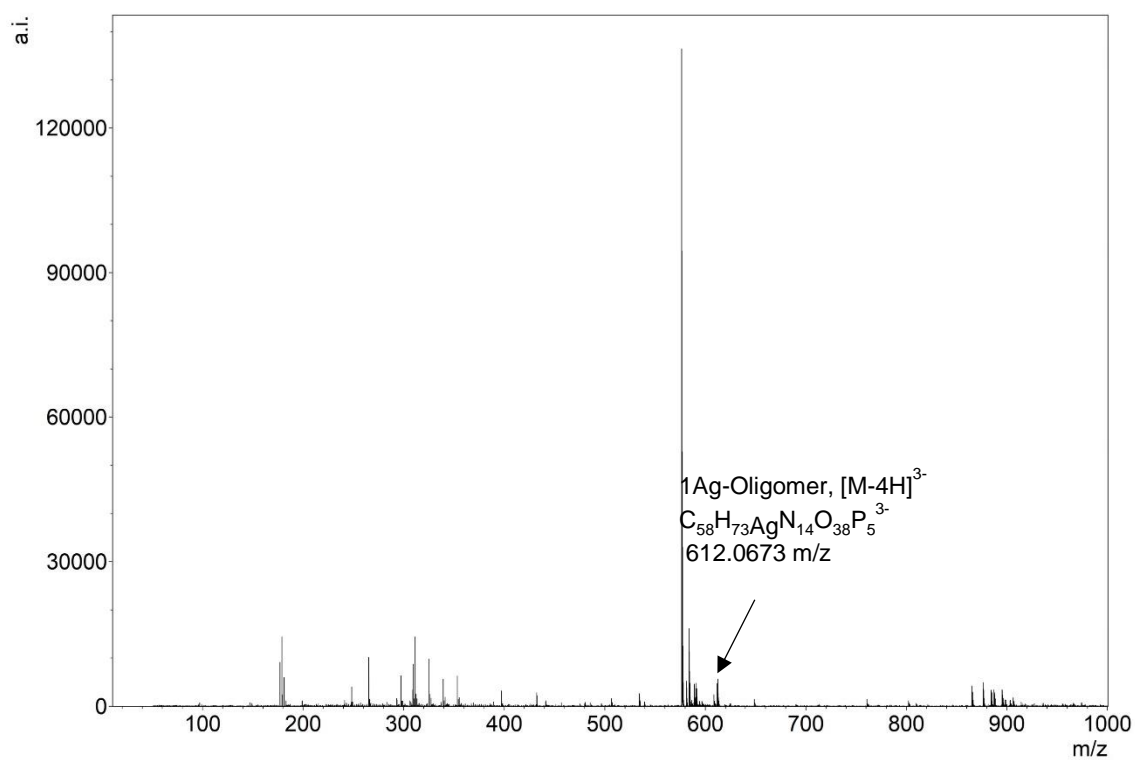


Figure 56. Negative ion mode ESI-MS following the addition of excess Ag^+ (3 equiv.) to the oligonucleotide $C_1-(T)_4-C_1$, T^4C_1 .

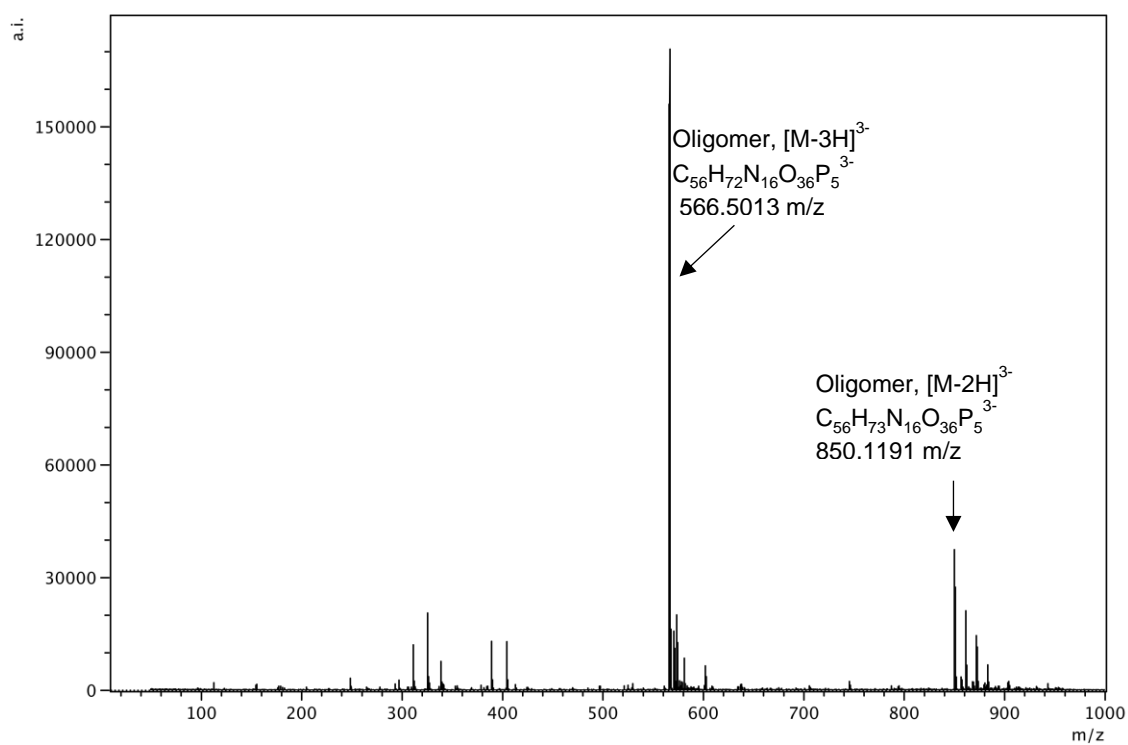


Figure S57. Negative ion mode ESI-MS the oligonucleotide $C_2-(T)_2-T_2$, T^2C_2 .

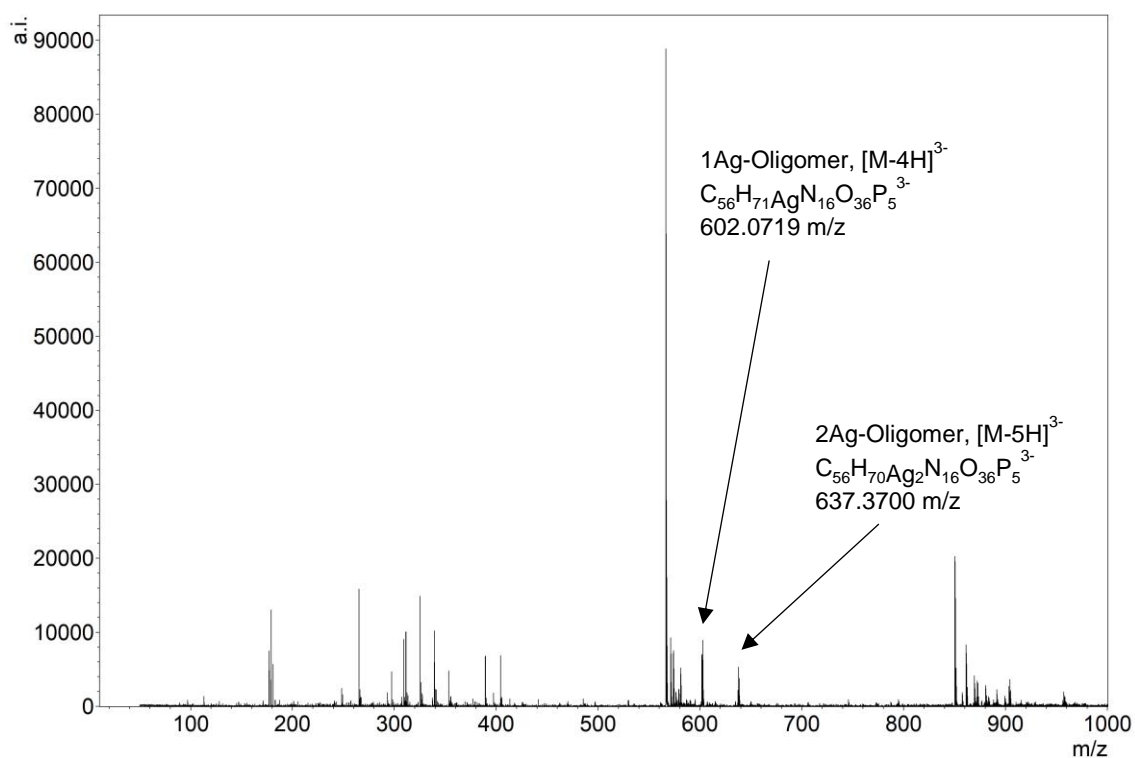


Figure S58. Negative ion mode ESI-MS following the addition of Ag⁺ (1 equiv.) to the oligonucleotide C₂-(T)₂-C₂, ¹²C₂.

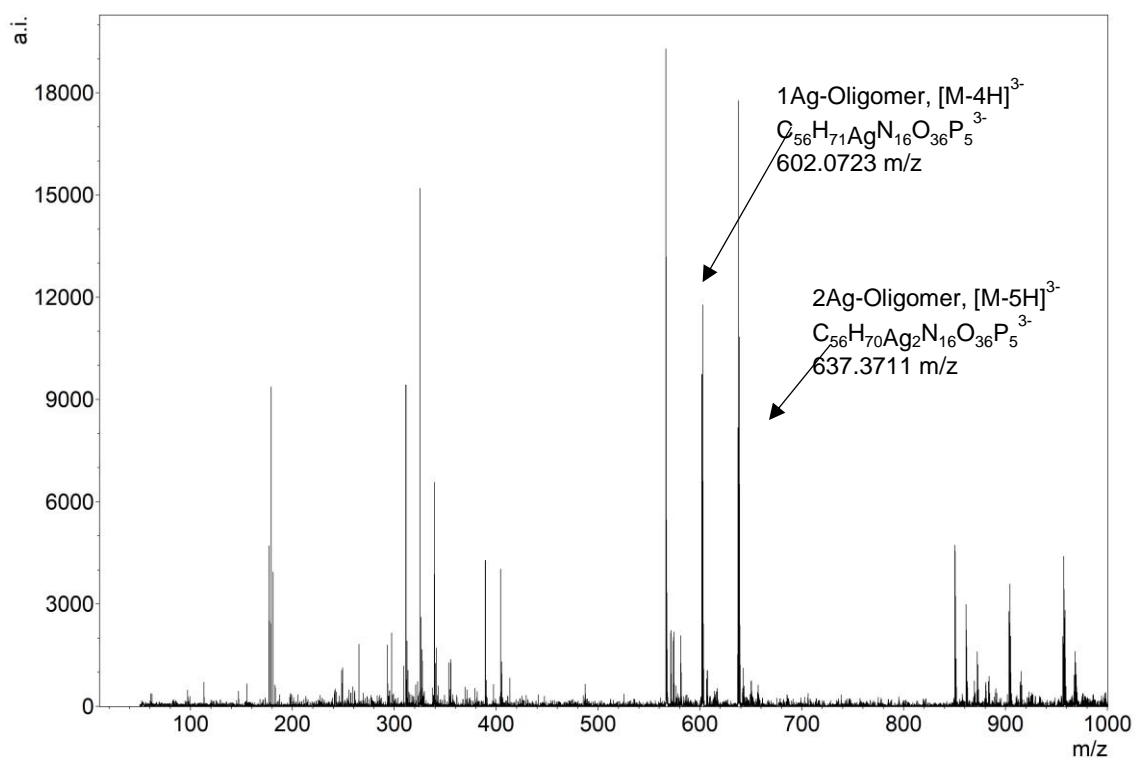


Figure S59. Negative ion mode ESI-MS following the addition of Ag⁺ (2 equiv.) to the oligonucleotide C₂-(T)₂-C₂, ¹²C₂.

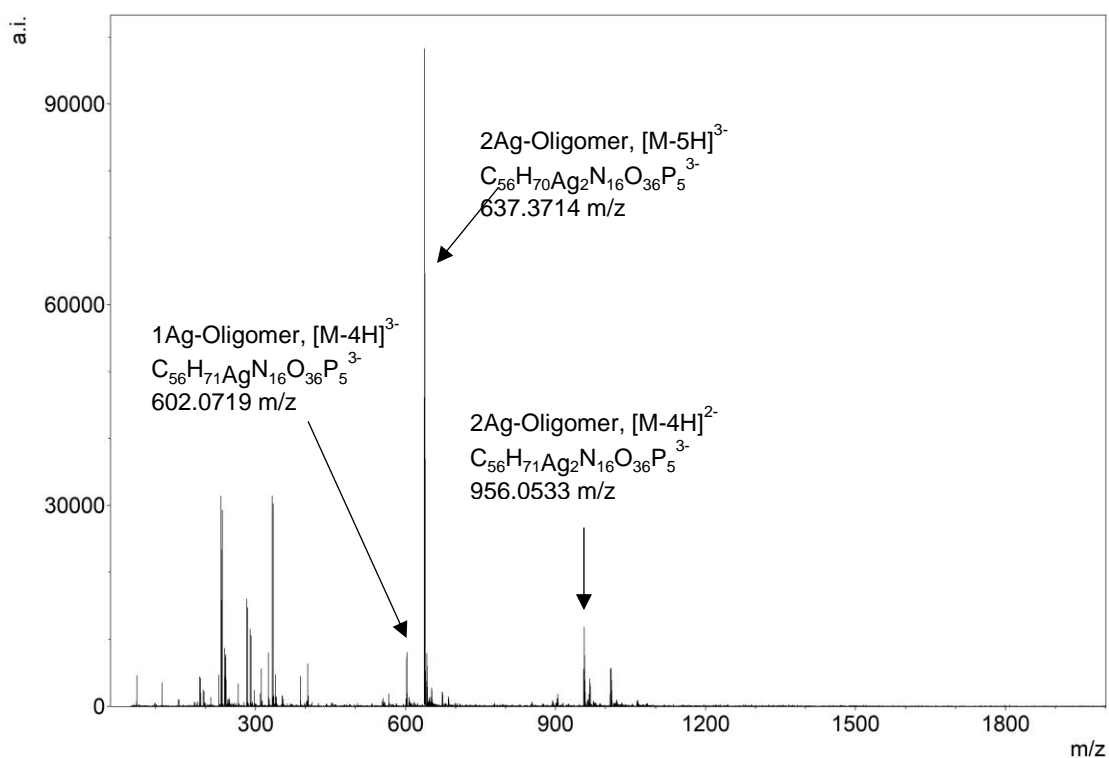


Figure S60. Negative ion mode ESI-MS following the addition of excess Ag^+ (10 equiv.) to the oligonucleotide $C_2-(T)_2-C_2$, $^{12}C_2$.

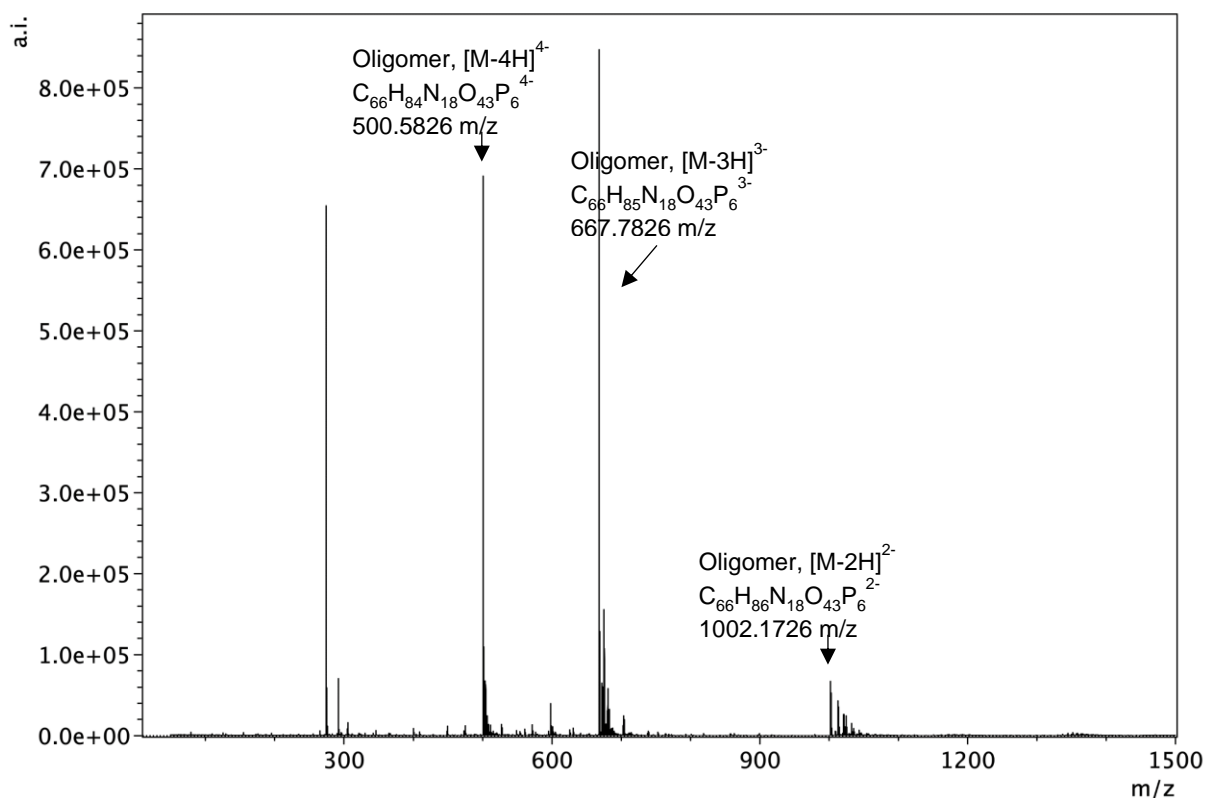


Figure S61. Negative ion mode ESI-MS the oligonucleotide $C_2-(T)_3-T_2$, $^{13}C_2$.

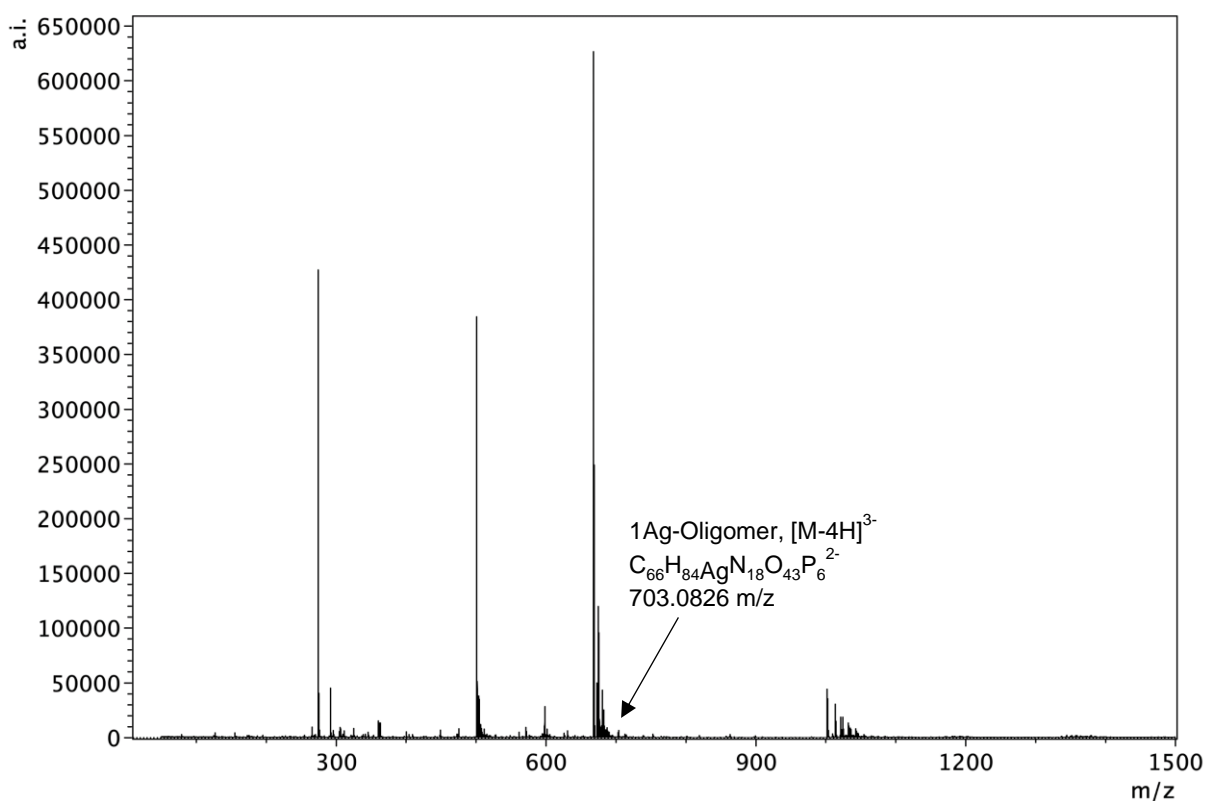


Figure S62. Negative ion mode ESI-MS following the addition of Ag^+ (1 equiv.) to the oligonucleotide $C_2-(T)_3-C_2$, $^{13}C_2$.

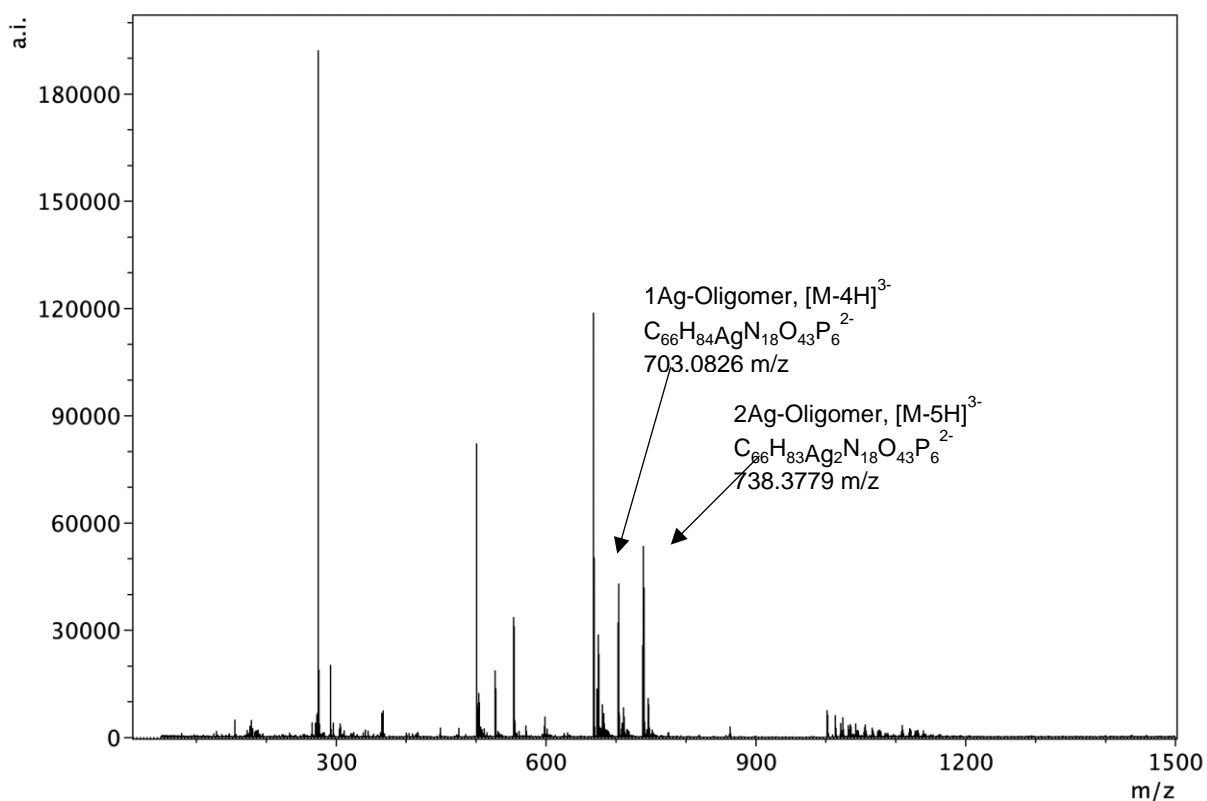


Figure S63. Negative ion mode ESI-MS following the addition of Ag^+ (2 equiv.) to the oligonucleotide $C_2-(T)_3-C_2$, $^{13}C_2$.

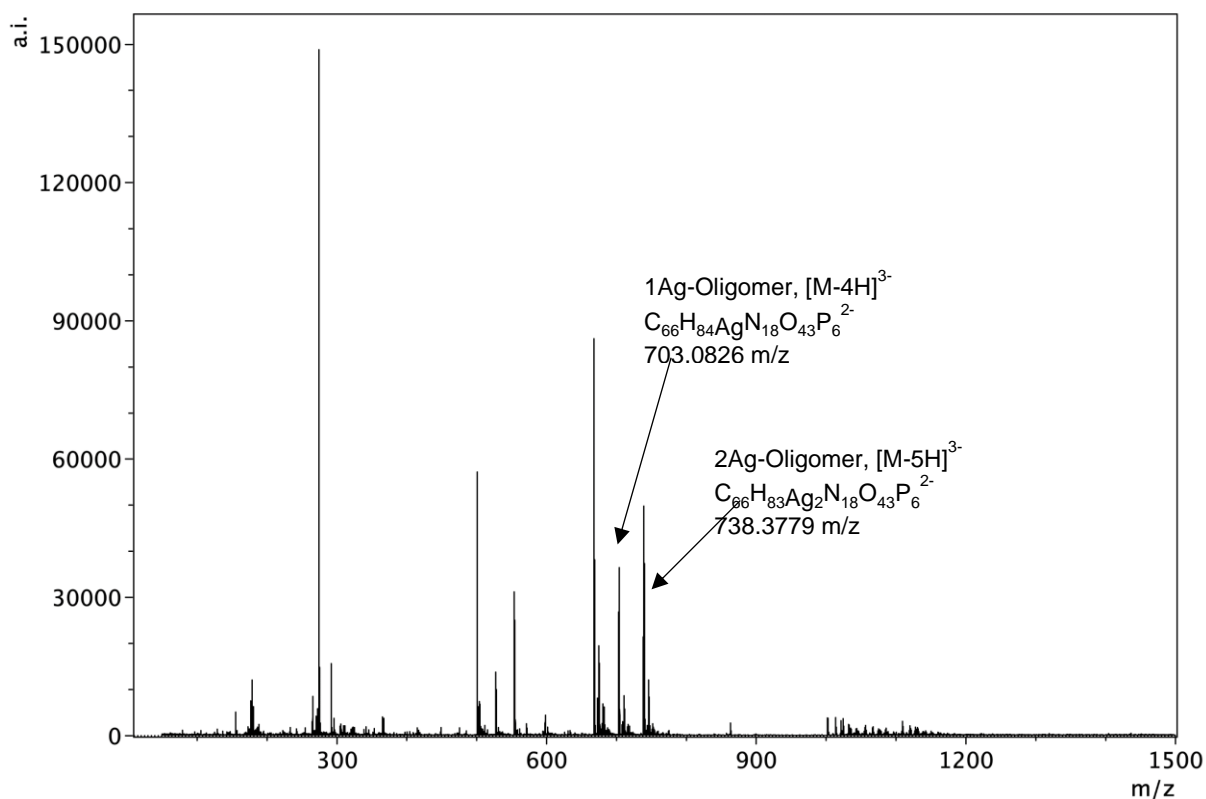


Figure S64. Negative ion mode ESI-MS following the addition of excess Ag^+ (10 equiv.) to the oligonucleotide $\text{C}_2\text{-(T)}_3\text{-C}_2, \text{T}^3\text{C}_2$.

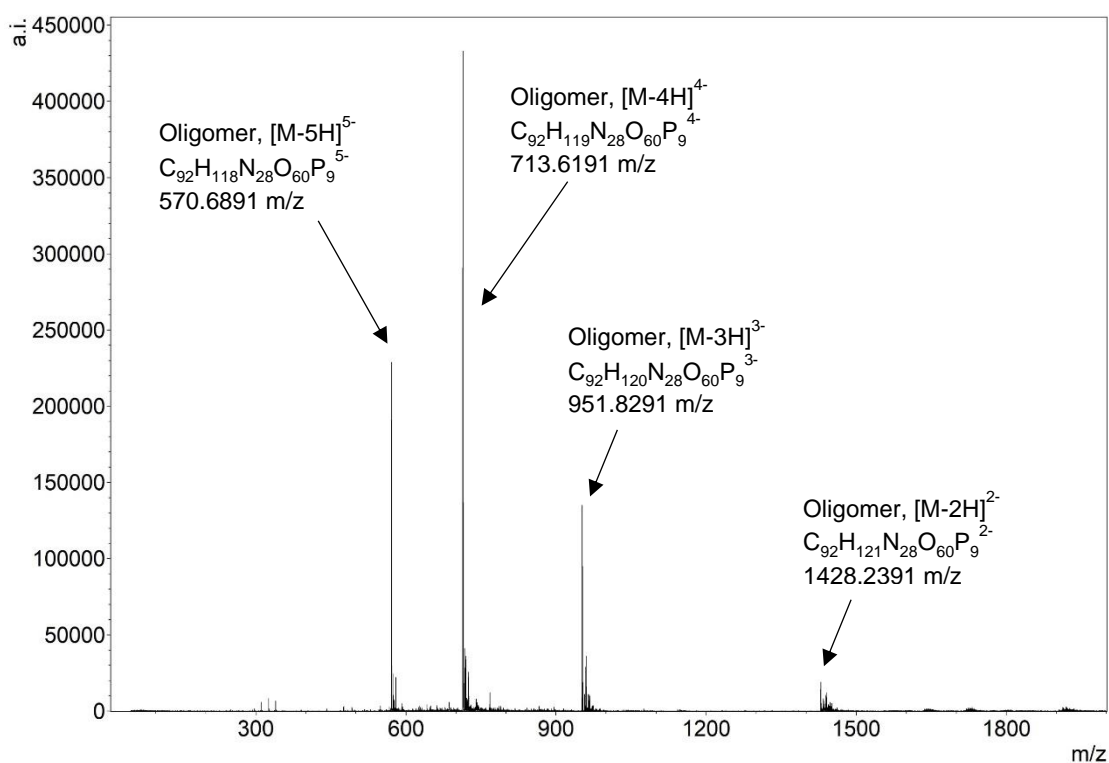


Figure S65. Negative ion mode ESI-MS the oligonucleotide $\text{C}_4\text{-(T)}_2\text{-T}_4, \text{T}^2\text{C}_4$.

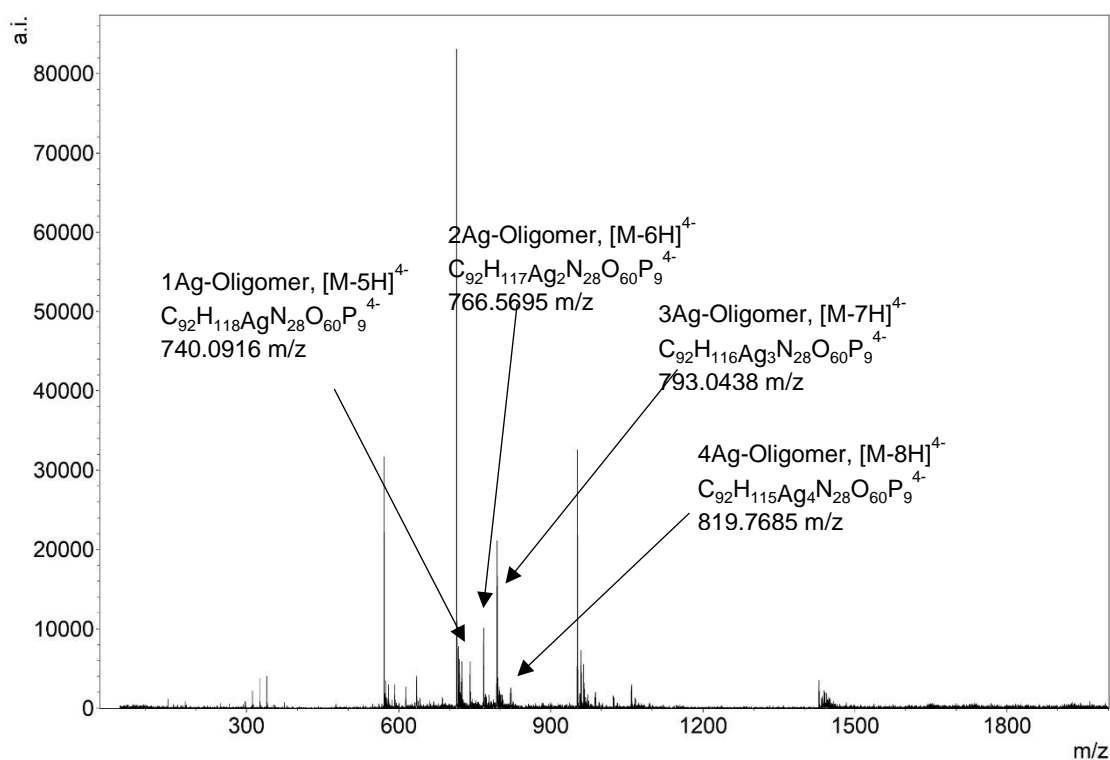


Figure S66. Negative ion mode ESI-MS following the addition of Ag⁺ (1 equiv.) to the oligonucleotide C₄-(T)₂-C₄, ¹²C₄.

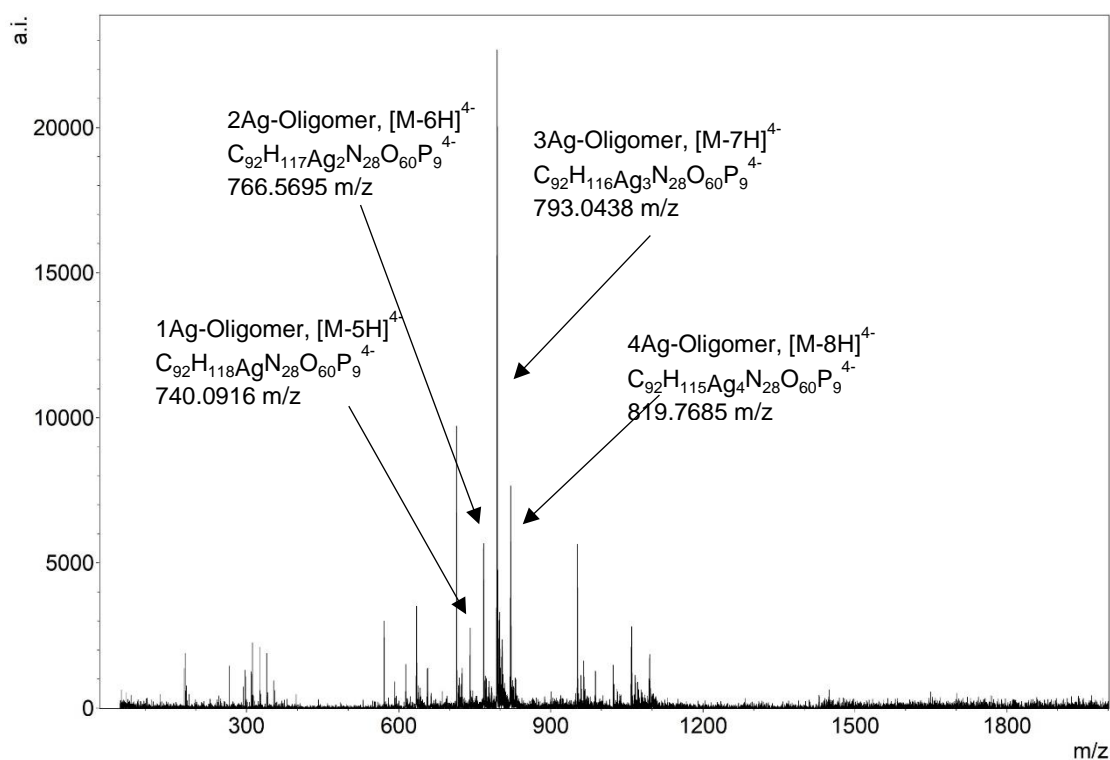


Figure S67. Negative ion mode ESI-MS following the addition of Ag⁺ (2 equiv.) to the oligonucleotide C₄-(T)₂-C₄, ¹²C₄.

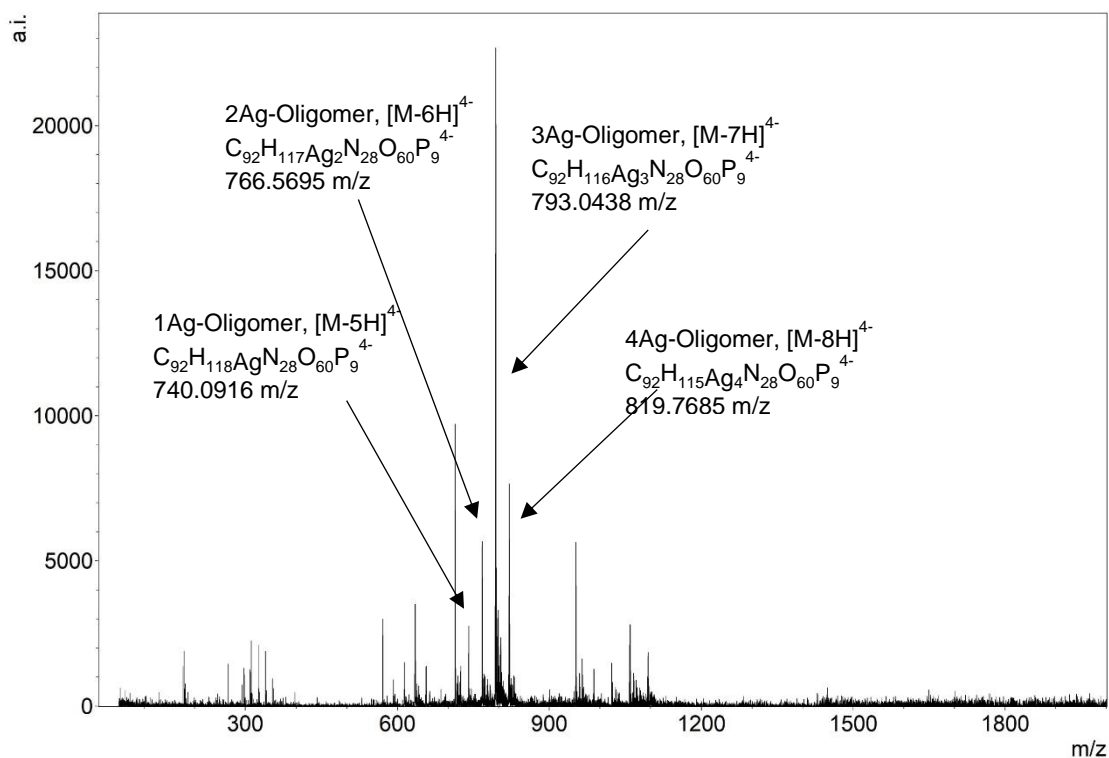


Figure S68. Negative ion mode ESI-MS following the addition of Ag⁺ (3 equiv.) to the oligonucleotide C₄-(T)₂-C₄, T²C₄.

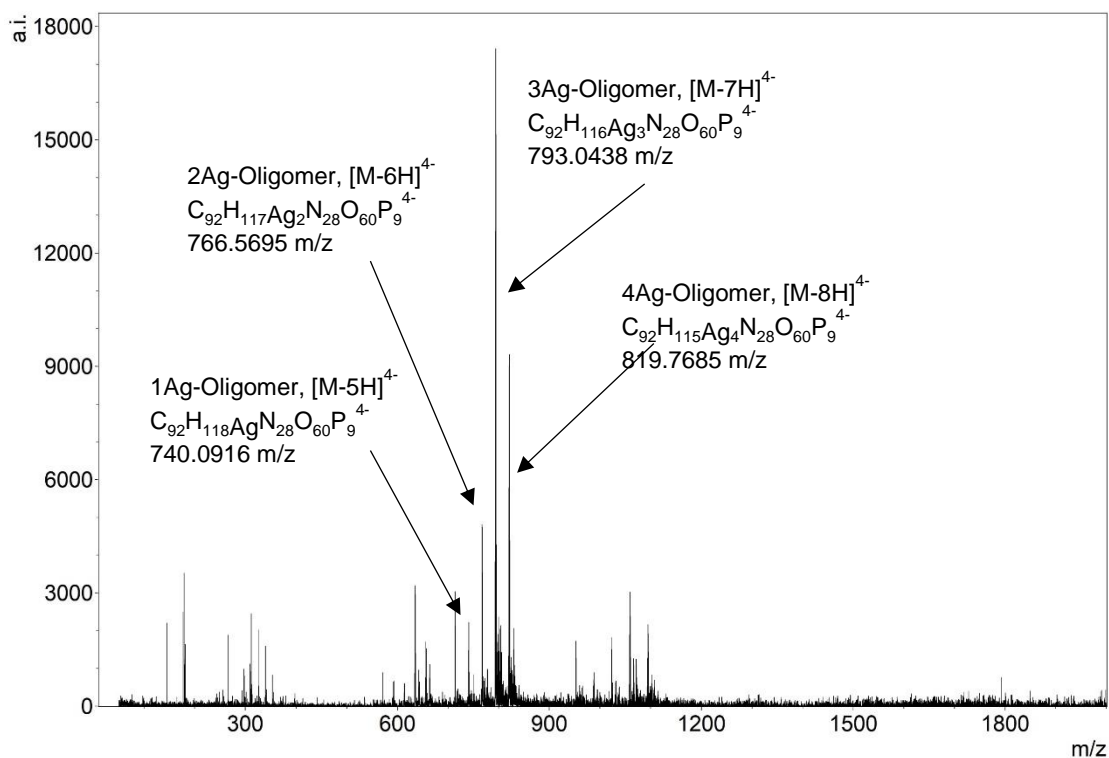


Figure S69. Negative ion mode ESI-MS following the addition of Ag⁺ (4 equiv.) to the oligonucleotide C₄-(T)₂-C₄, T²C₄.

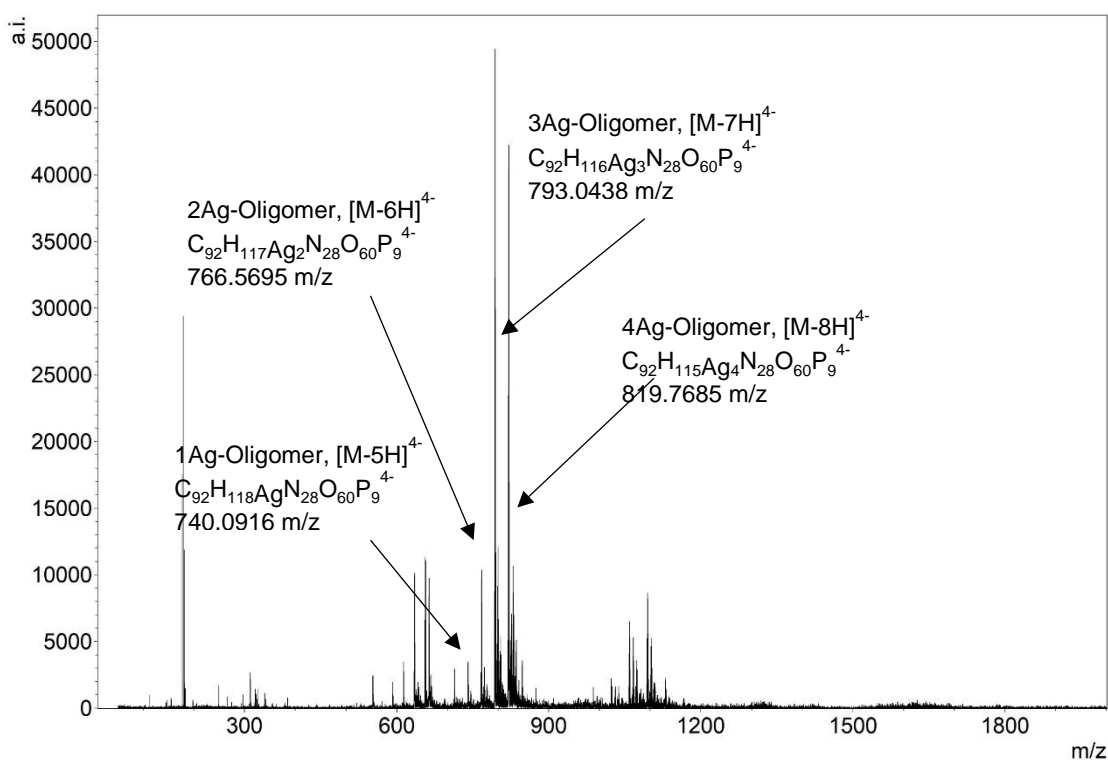


Figure S70. Negative ion mode ESI-MS following the addition of excess Ag^+ (10 equiv.) to the oligonucleotide $\text{C}_4\text{-(T)}_2\text{-C}_4$, T^2C_4 .

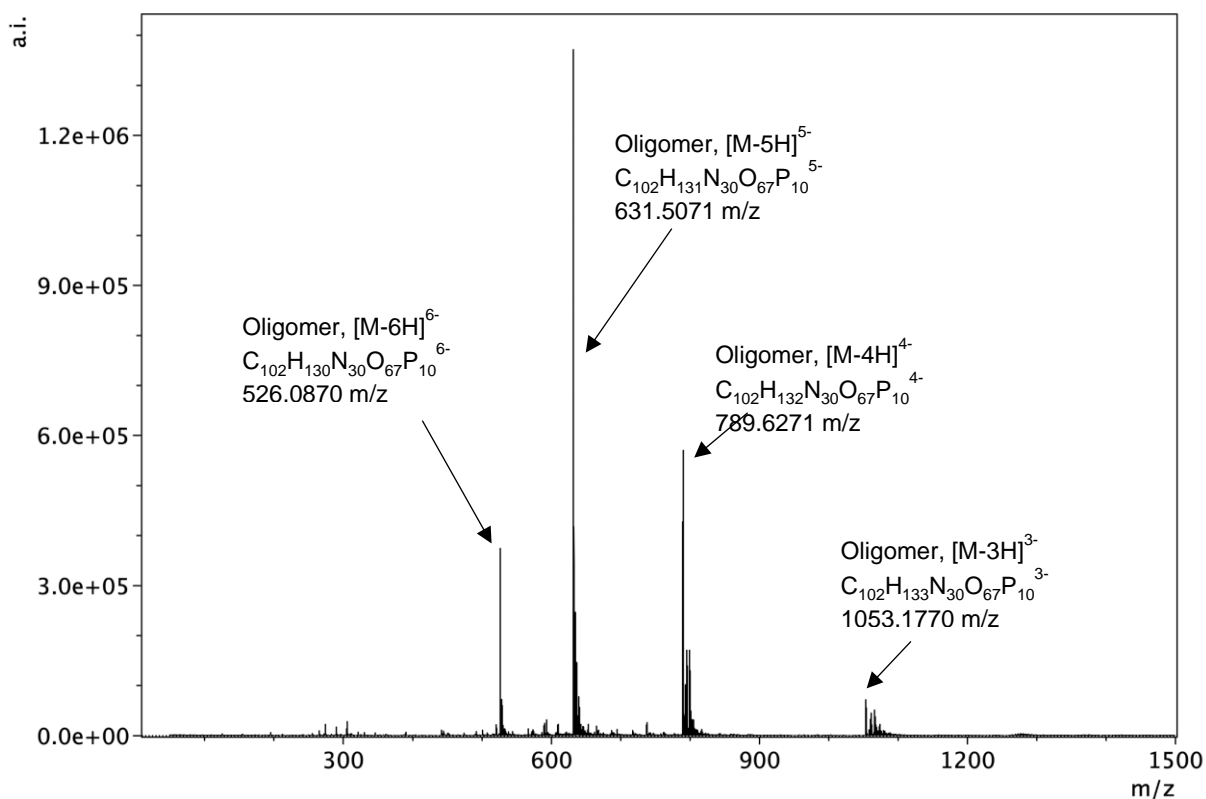


Figure S71. Negative ion mode ESI-MS the oligonucleotide $\text{C}_4\text{-(T)}_3\text{-T}_4$, T^3C_4 .

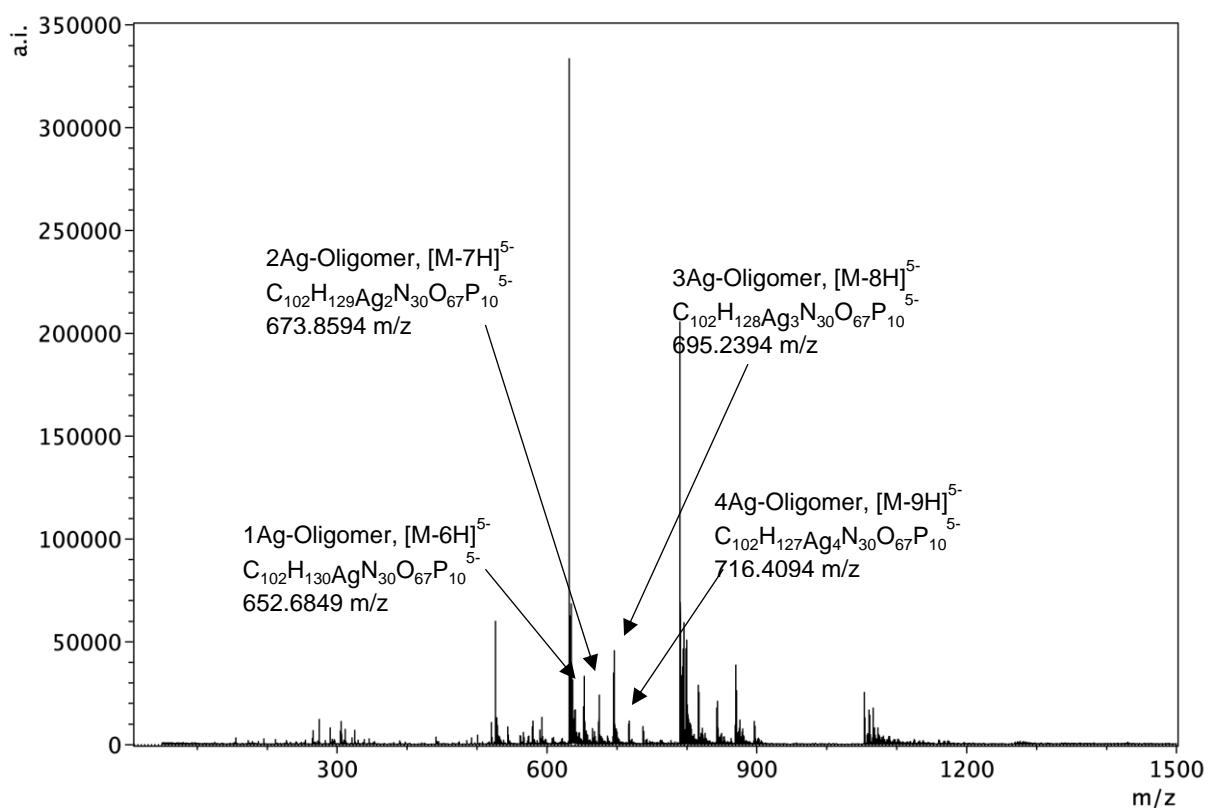


Figure S72. Negative ion mode ESI-MS following the addition of Ag^+ (1 equiv.) to the oligonucleotide $C_4^-(T)_3-C_4$, T^3C_4 .

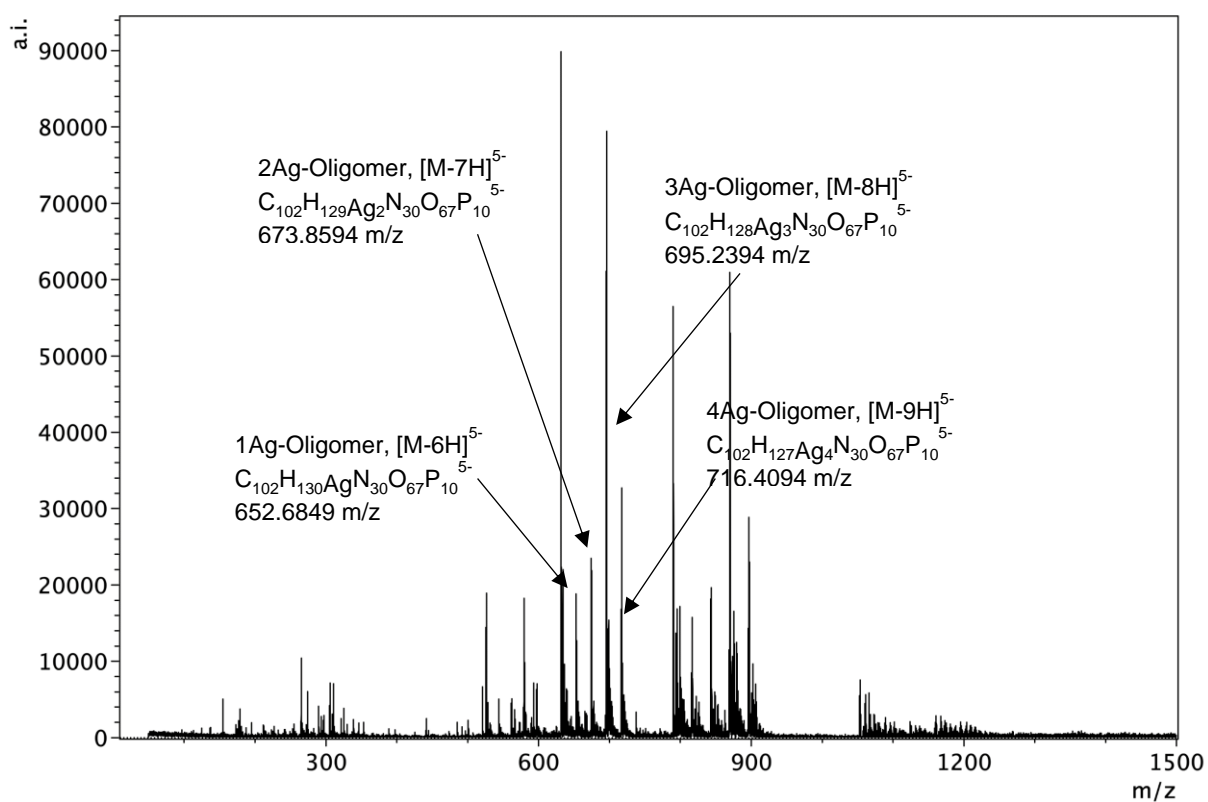


Figure S73. Negative ion mode ESI-MS following the addition of Ag^+ (2 equiv.) to the oligonucleotide $C_4^-(T)_3-C_4$, T^3C_4 .

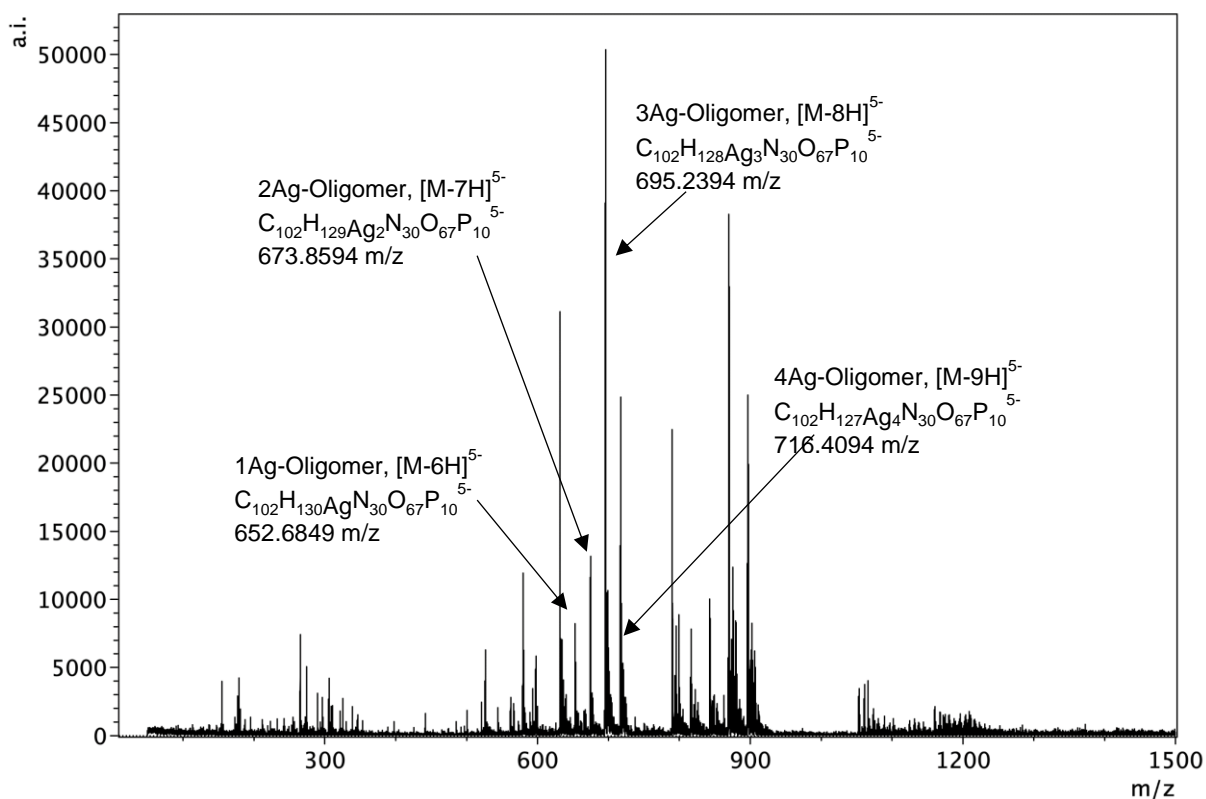


Figure S74. Negative ion mode ESI-MS following the addition of Ag⁺ (3 equiv.) to the oligonucleotide C₄-(T)₃-C₄, ¹³C₄.

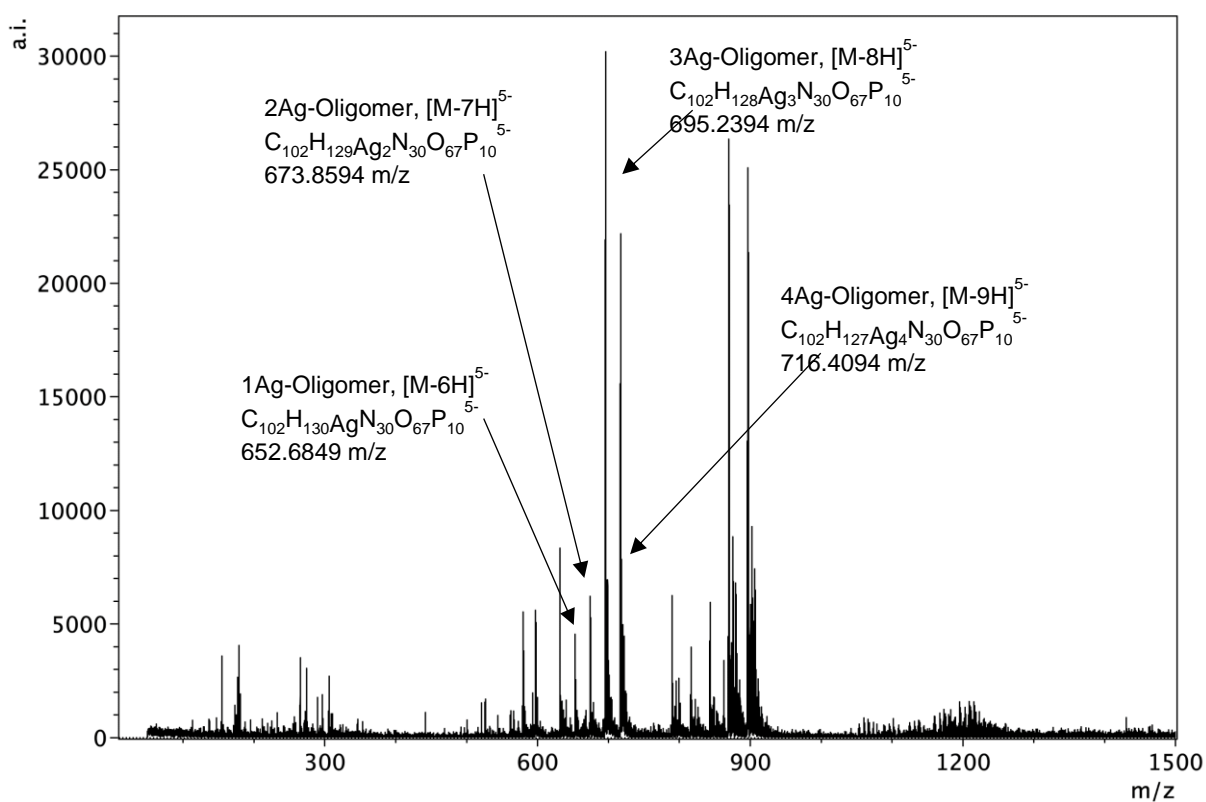


Figure S75. Negative ion mode ESI-MS following the addition of Ag⁺ (4 equiv.) to the oligonucleotide C₄-(T)₃-C₄, ¹³C₄.

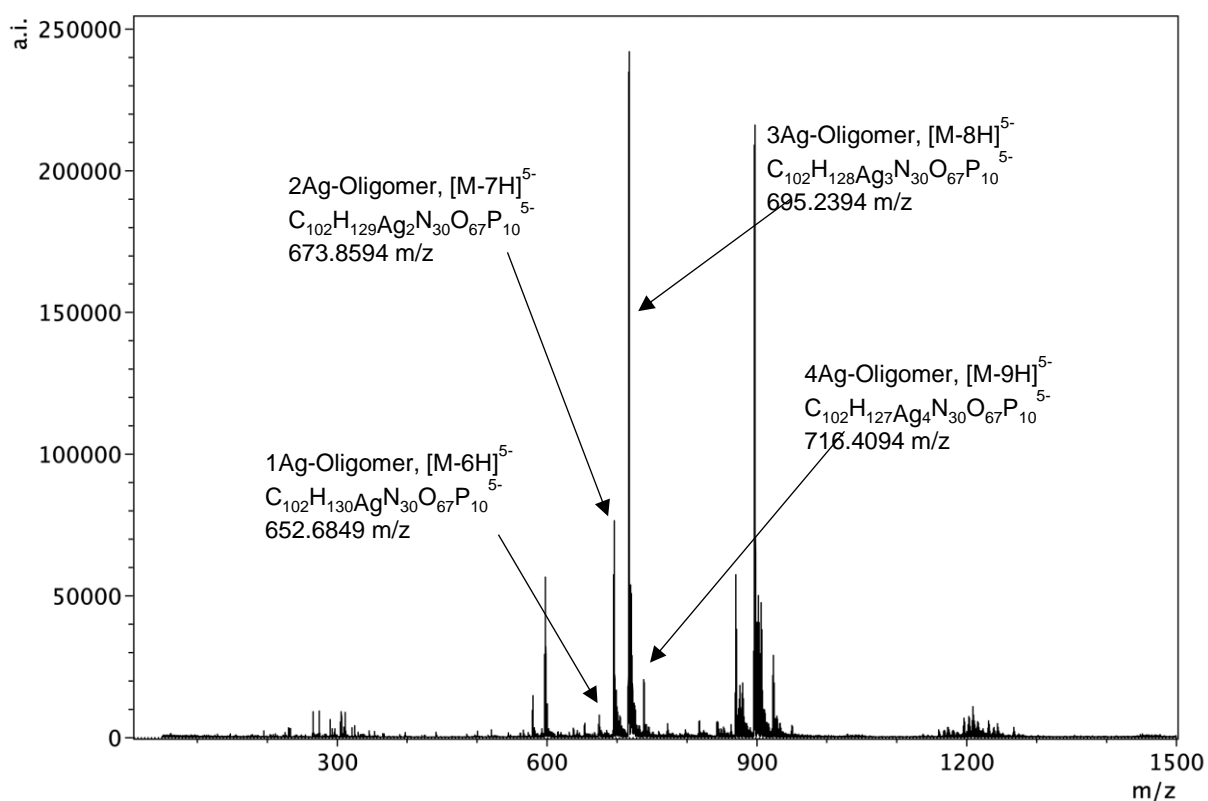


Figure S76. Negative ion mode ESI-MS following the addition of excess Ag⁺ (10 equiv.) to the oligonucleotide C₄-(T)₃-C₄, ^{T3}C₄.

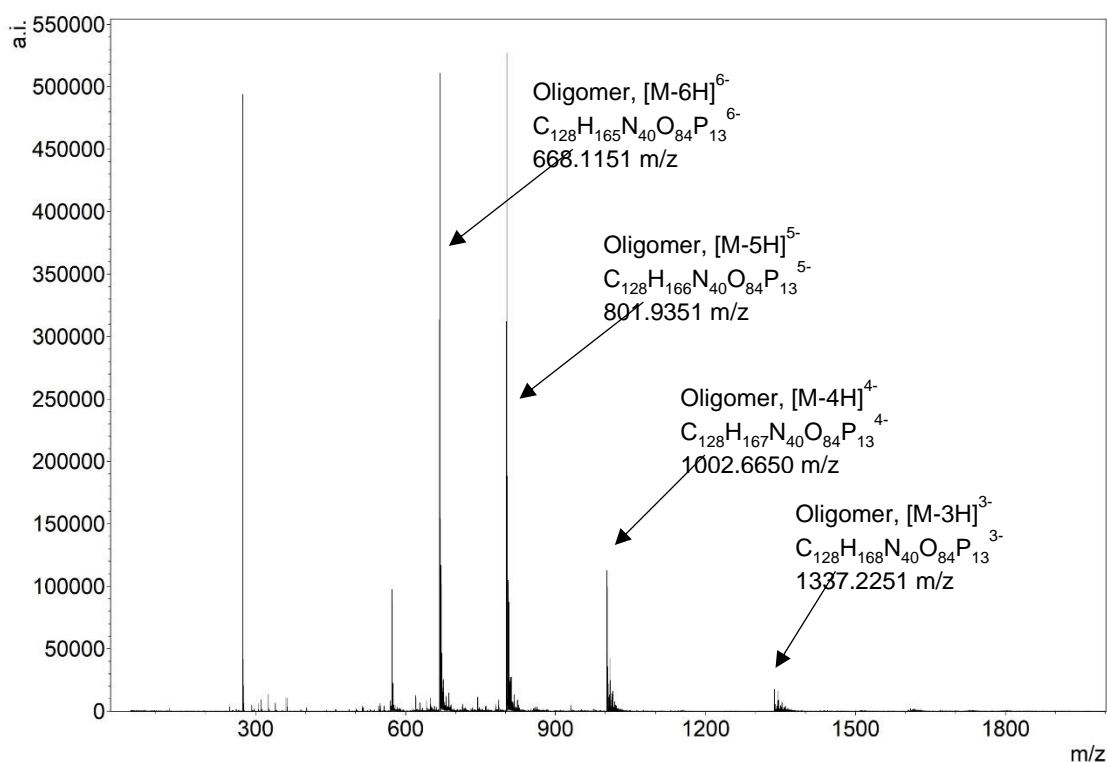


Figure S77. Negative ion mode ESI-MS the oligonucleotide C₆-(T)₂-T₆, ^{T2}C₆.

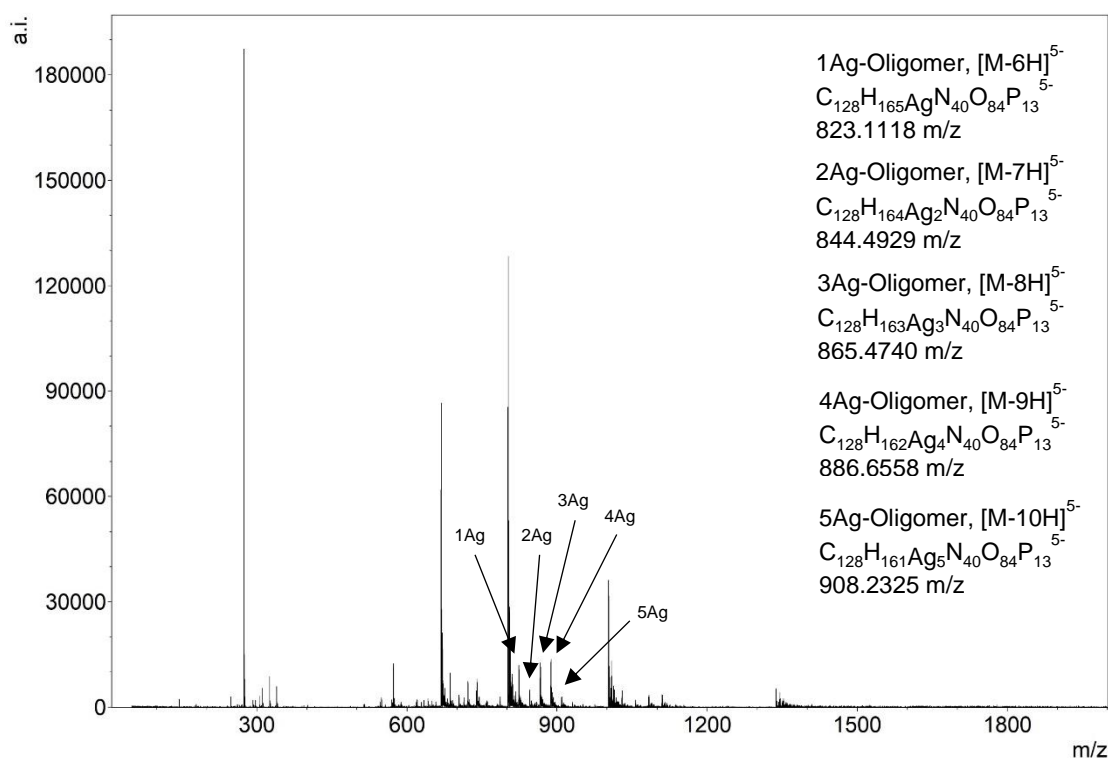


Figure S78. Negative ion mode ESI-MS following the addition of Ag^+ (1 equiv.) to the oligonucleotide $C_6-(T)_2-C_6$, $^{12}C_6$.

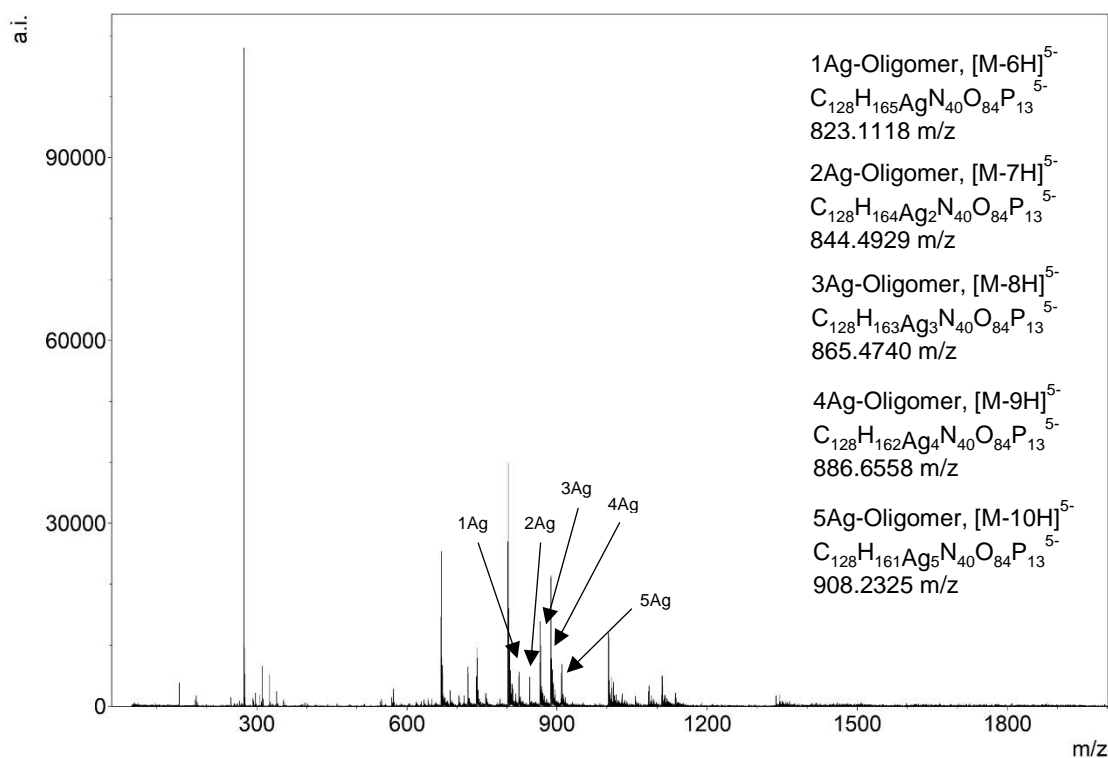


Figure S79. Negative ion mode ESI-MS following the addition of Ag^+ (2 equiv.) to the oligonucleotide $C_6-(T)_2-C_6$, $^{12}C_6$.

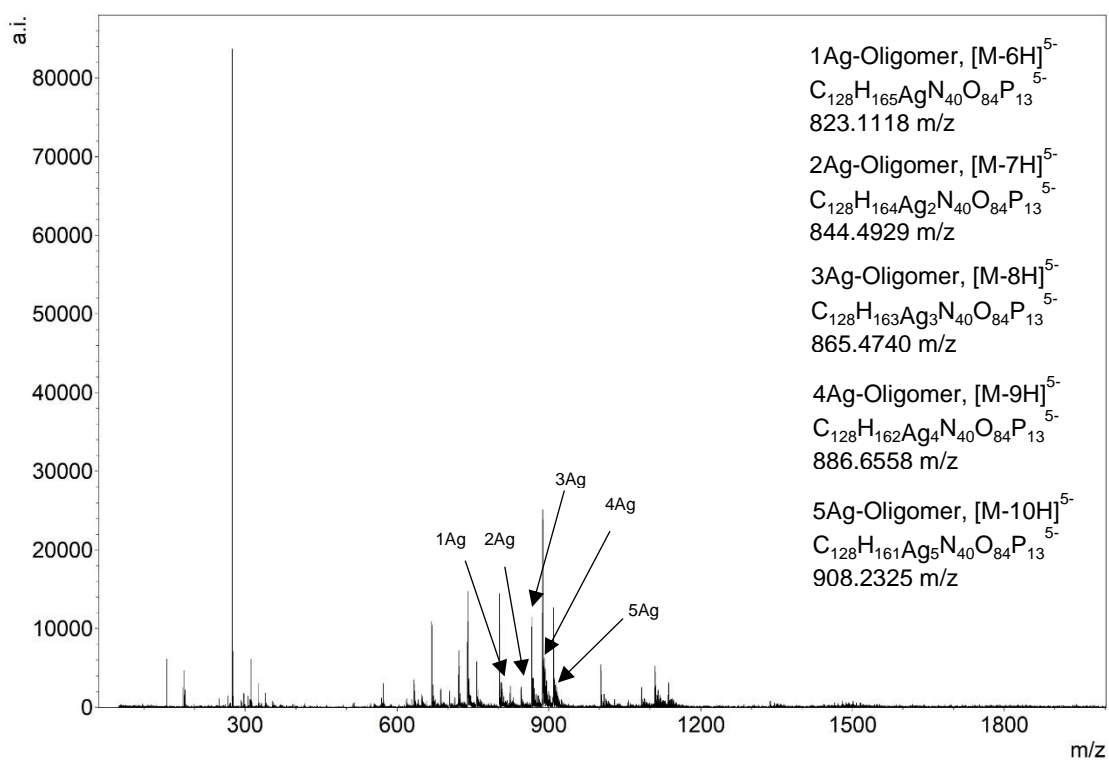


Figure S80. Negative ion mode ESI-MS following the addition of Ag⁺ (3 equiv.) to the oligonucleotide C₆-(T)₂-C₆, ^{T2}C₆.

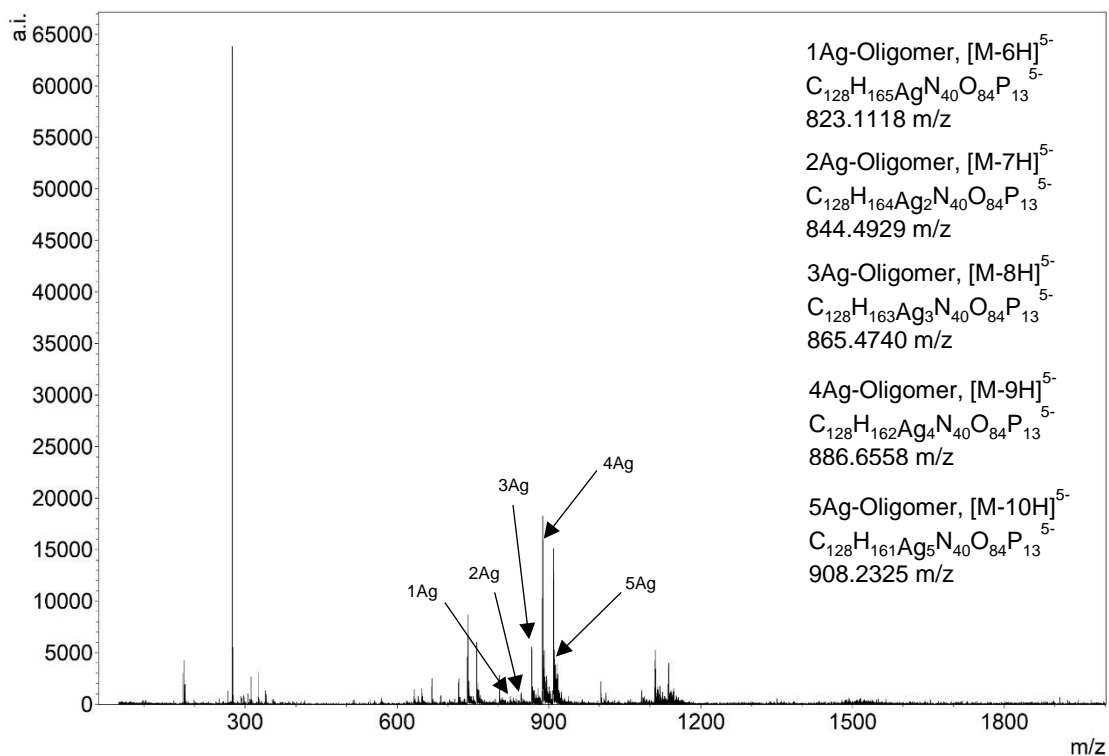


Figure S81. Negative ion mode ESI-MS following the addition of Ag⁺ (4 equiv.) to the oligonucleotide C₆-(T)₂-C₆, ^{T2}C₆.

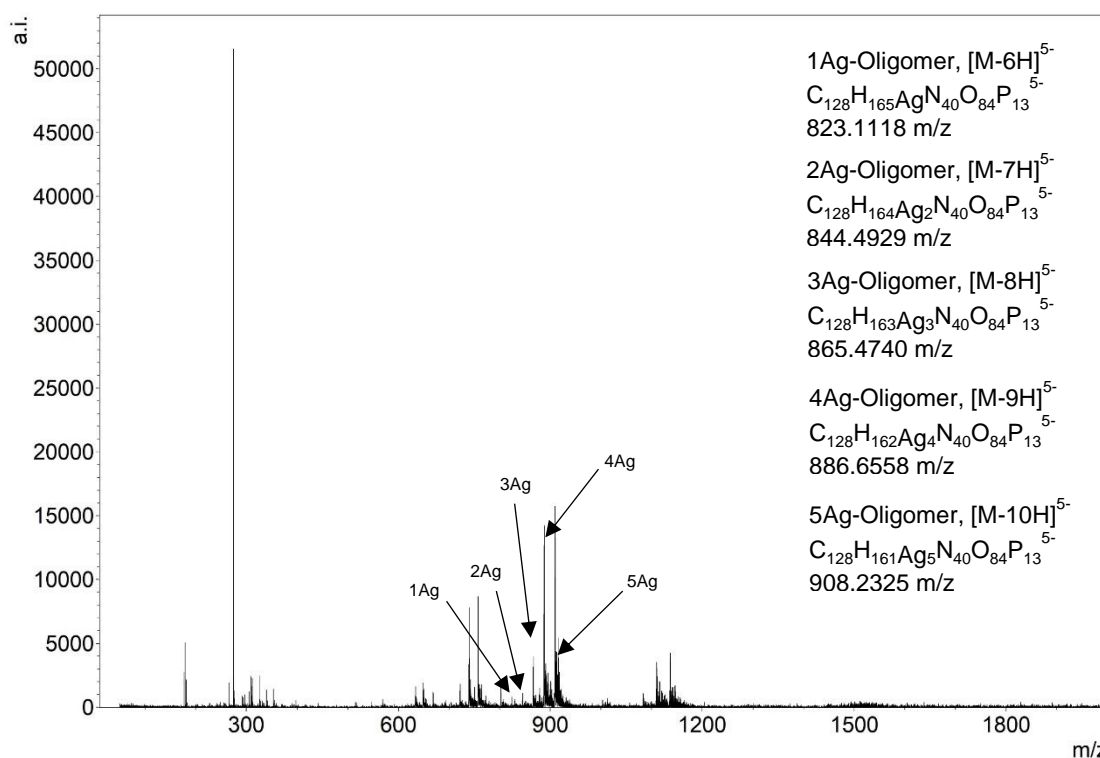


Figure S82. Negative ion mode ESI-MS following the addition of Ag⁺ (5 equiv.) to the oligonucleotide C₆-(T)₂-C₆, ¹²C₆.

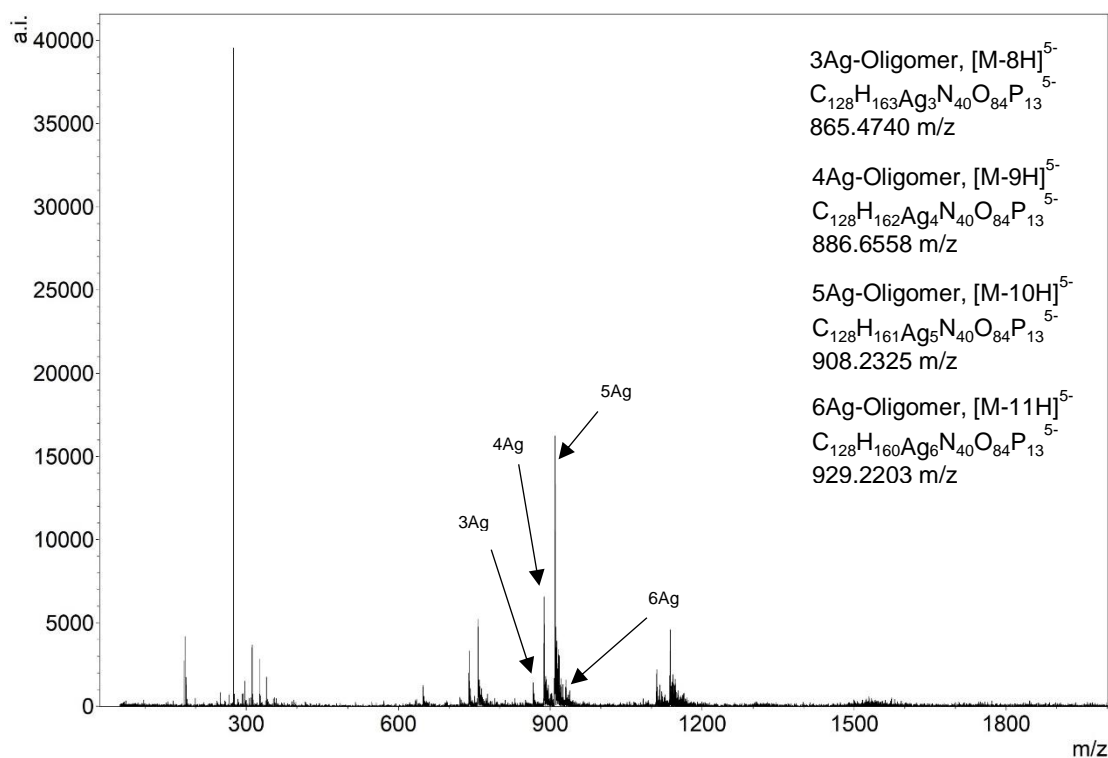


Figure S83. Negative ion mode ESI-MS following the addition of Ag⁺ (6 equiv.) to the oligonucleotide C₆-(T)₂-C₆, ¹²C₆.

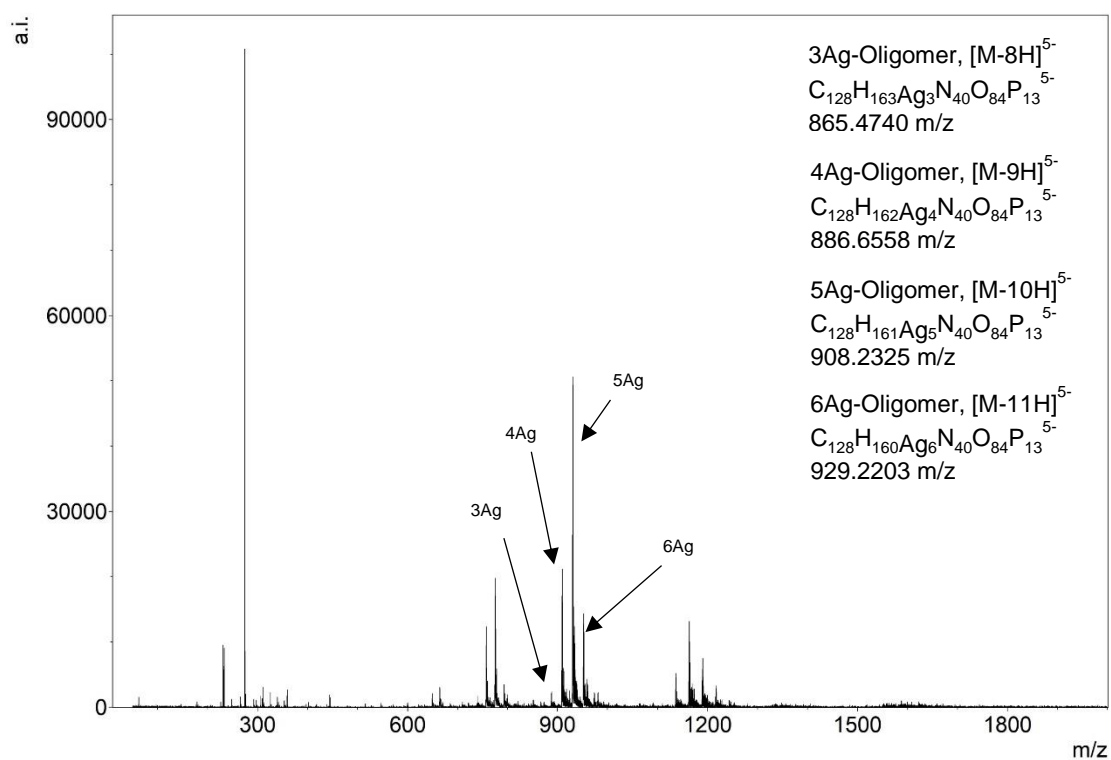


Figure S84. Negative ion mode ESI-MS following the addition of excess Ag^+ (10 equiv.) to the oligonucleotide $\text{C}_6\text{-(T)}_2\text{-C}_6$, T_2C_6 .

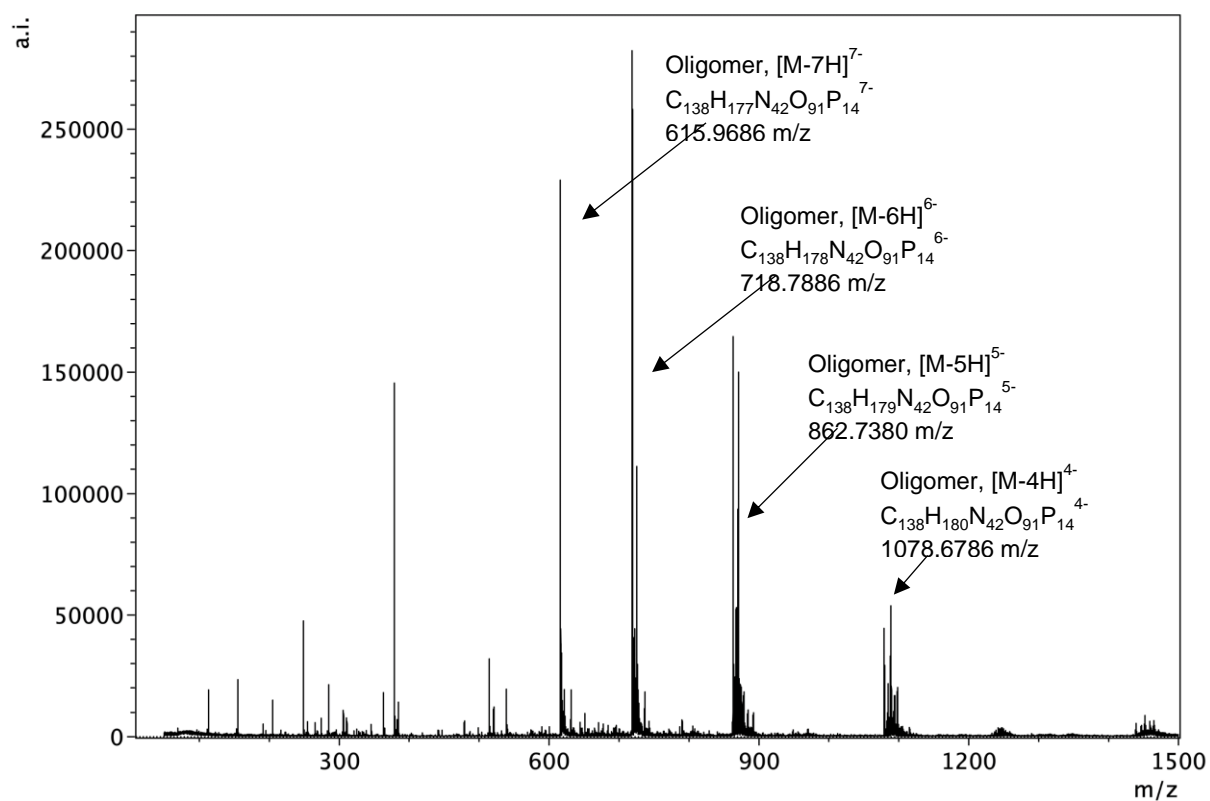


Figure S85. Negative ion mode ESI-MS the oligonucleotide $\text{C}_6\text{-(T)}_3\text{-T}_6$, T_3C_6 .

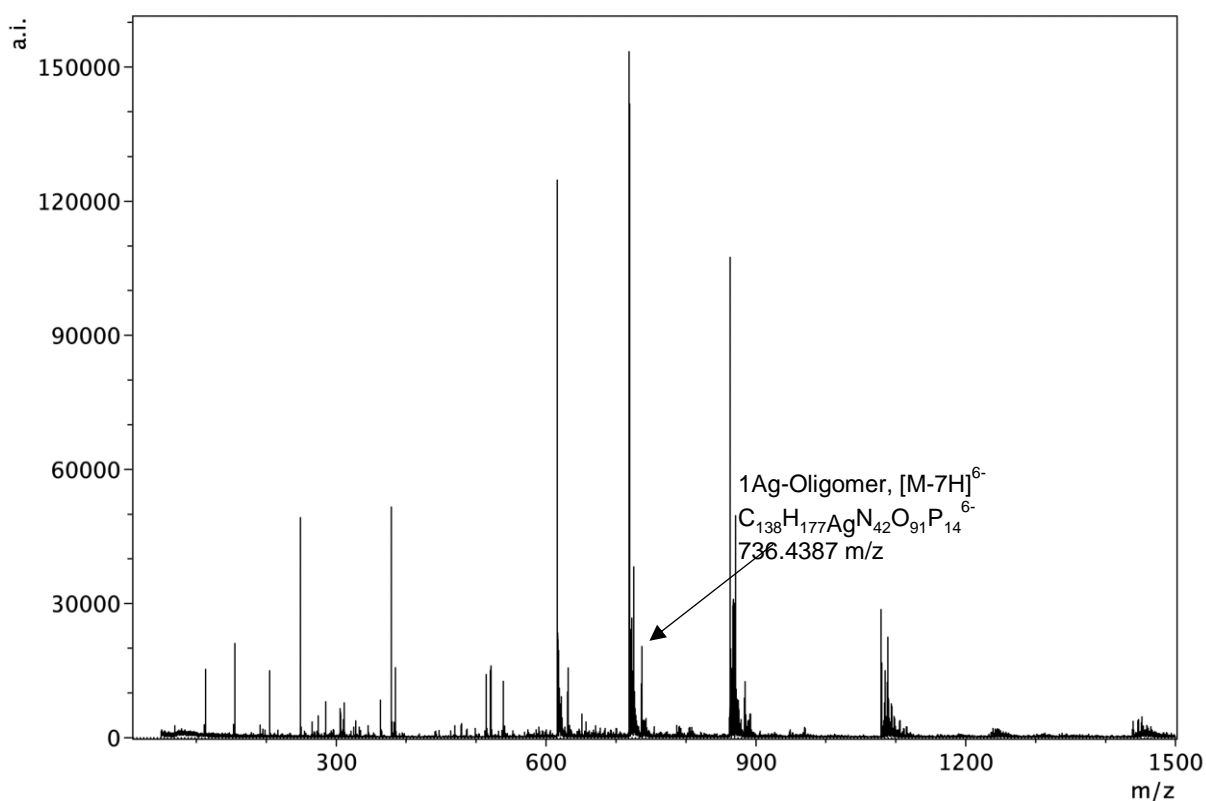


Figure S86. Negative ion mode ESI-MS following the addition of Ag⁺ (1 equiv.) to the oligonucleotide C₆-(T)₃-C₆, ¹³C₆.

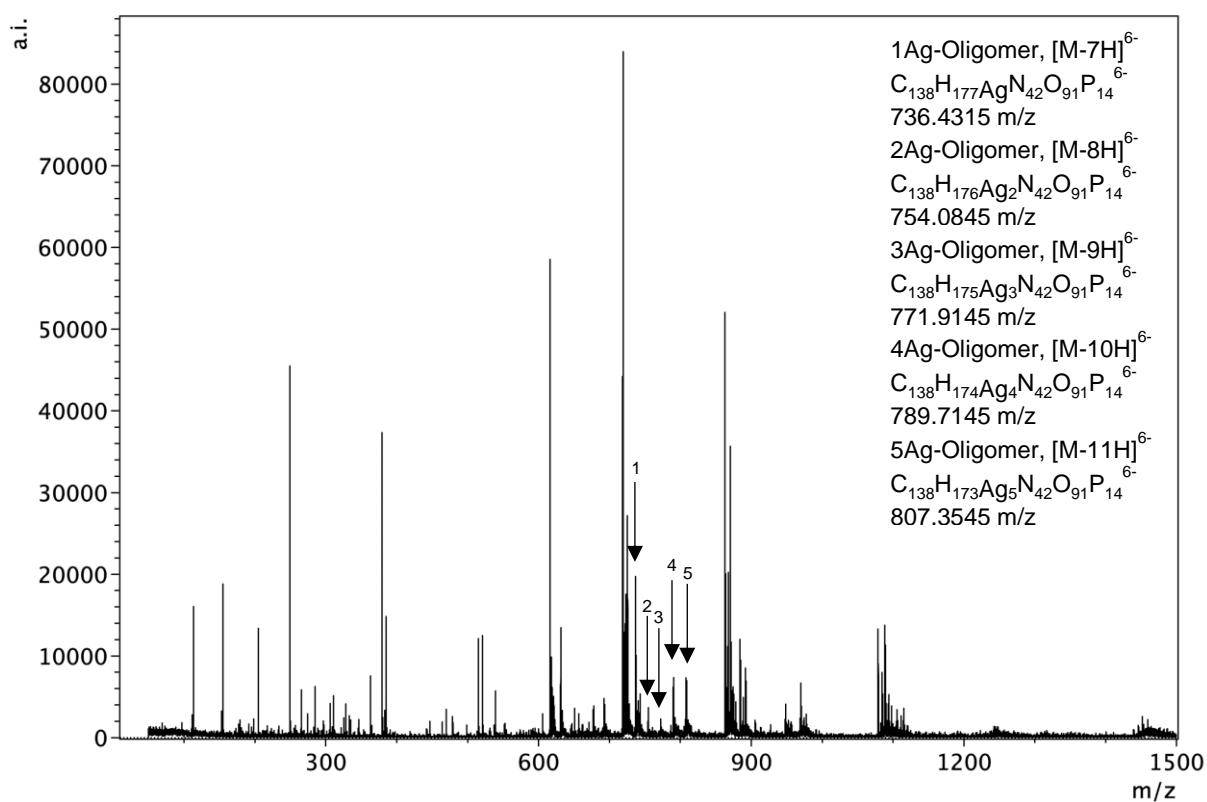


Figure S87. Negative ion mode ESI-MS following the addition of Ag⁺ (2 equiv.) to the oligonucleotide C₆-(T)₃-C₆, ¹³C₆.

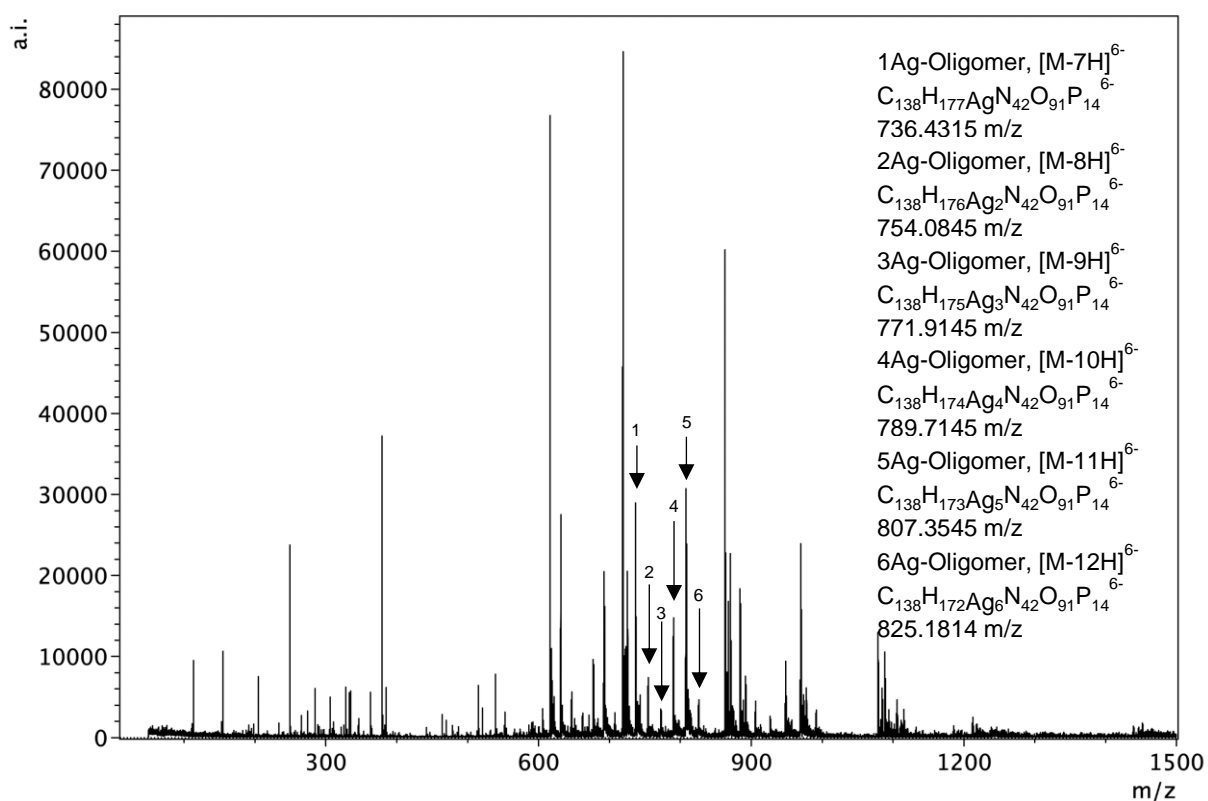


Figure S88. Negative ion mode ESI-MS following the addition of Ag⁺ (3 equiv.) to the oligonucleotide C₆-(T)₃-C₆, T³C₆.

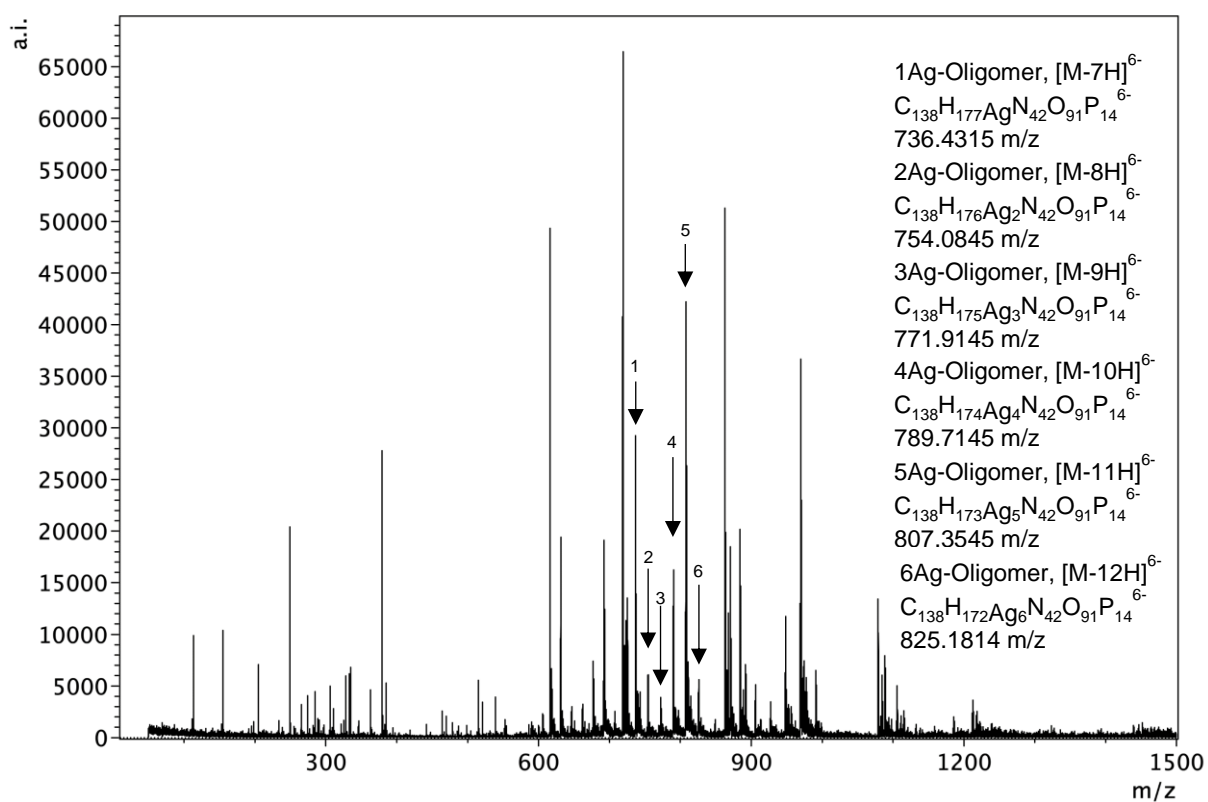


Figure S89. Negative ion mode ESI-MS following the addition of Ag⁺ (4 equiv.) to the oligonucleotide C₆-(T)₃-C₆, T³C₆.

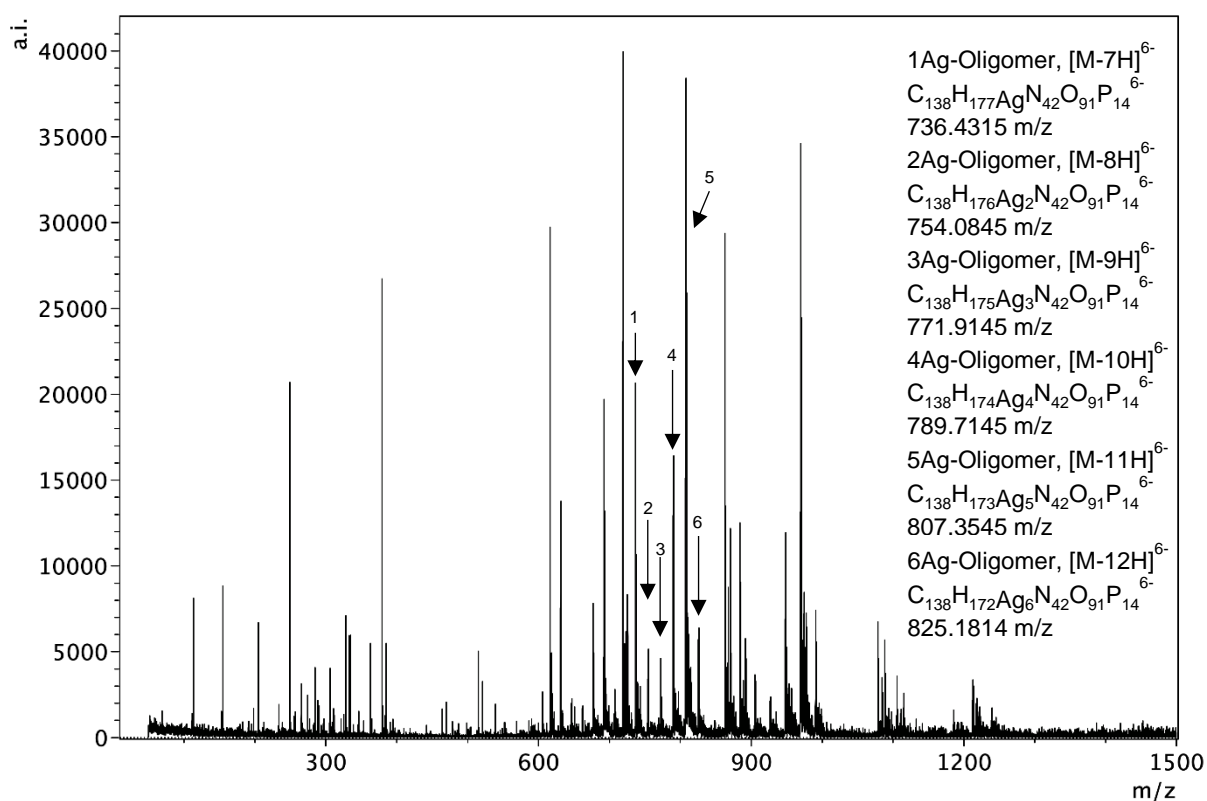


Figure S90. Negative ion mode ESI-MS following the addition of Ag⁺ (5 equiv.) to the oligonucleotide C₆-(T)₃-C₆, ^{T3}C₆.

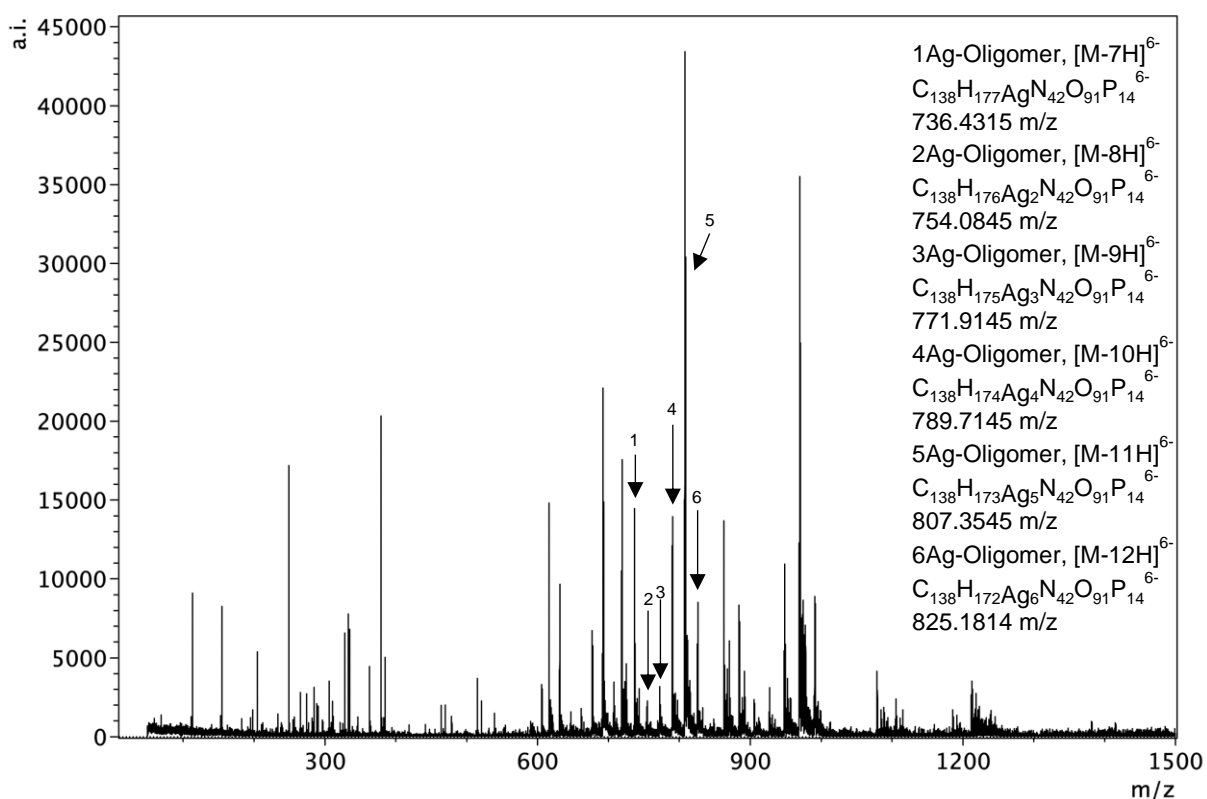


Figure S91. Negative ion mode ESI-MS following the addition of Ag⁺ (6 equiv.) to the oligonucleotide C₆-(T)₃-C₆, ^{T3}C₆.

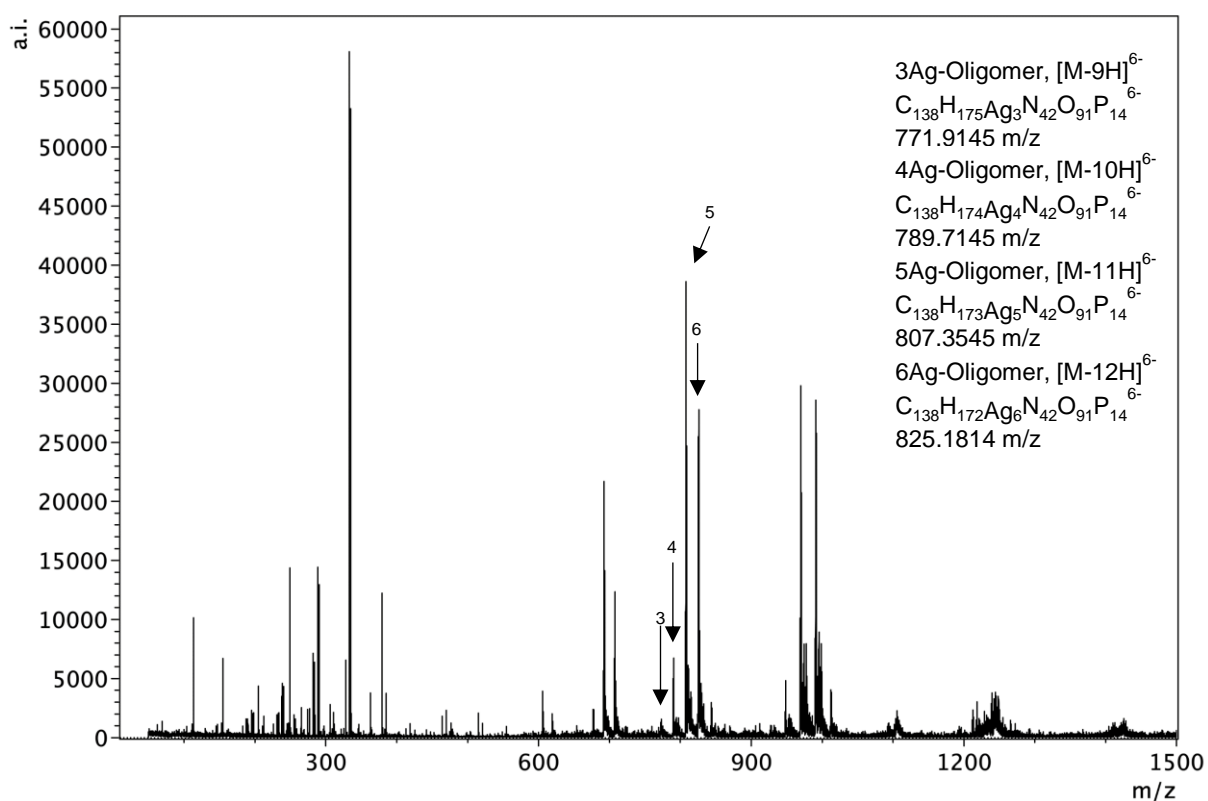


Figure S92. Negative ion mode ESI-MS following the addition of excess Ag^+ (10 equiv.) to the oligonucleotide $\text{C}_6\text{-(T)}_3\text{-C}_6$, $^{13}\text{C}_6$.

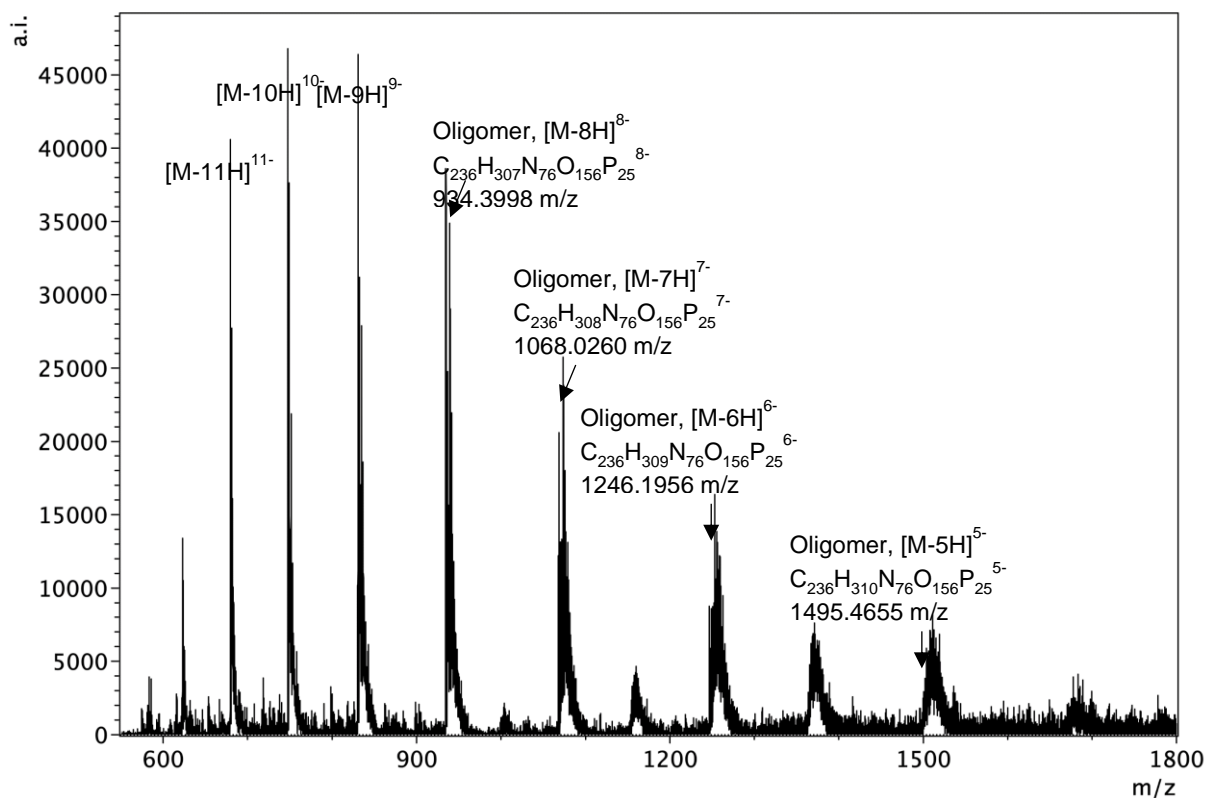


Figure S93. Negative ion mode ESI-MS of the oligonucleotide $\text{C}_{12}\text{-(T)}_2\text{-C}_{12}$, $^{12}\text{C}_{12}$.

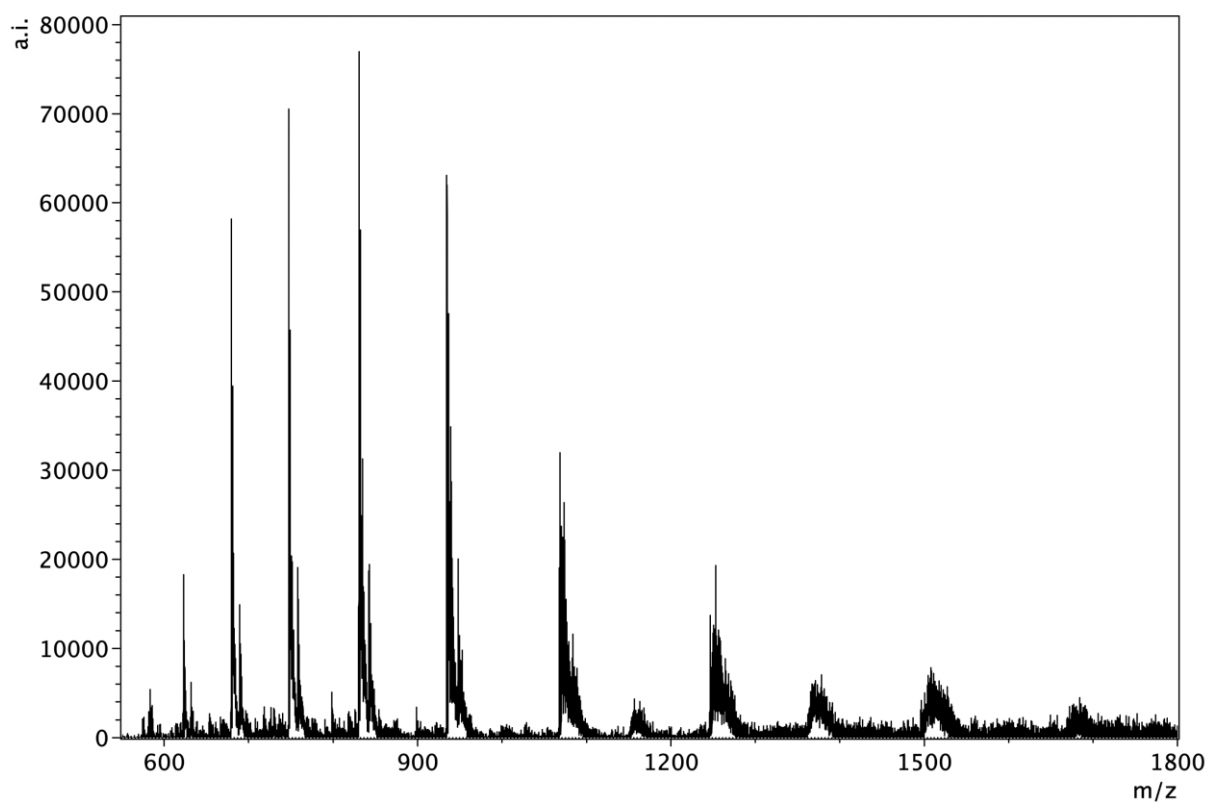


Figure S94. Negative ion mode ESI-MS following the addition of Ag^+ (1 equiv.) to the oligonucleotide $\text{C}_{12}\text{-(T)}_2\text{-C}_{12}$, T^2C_{12} .

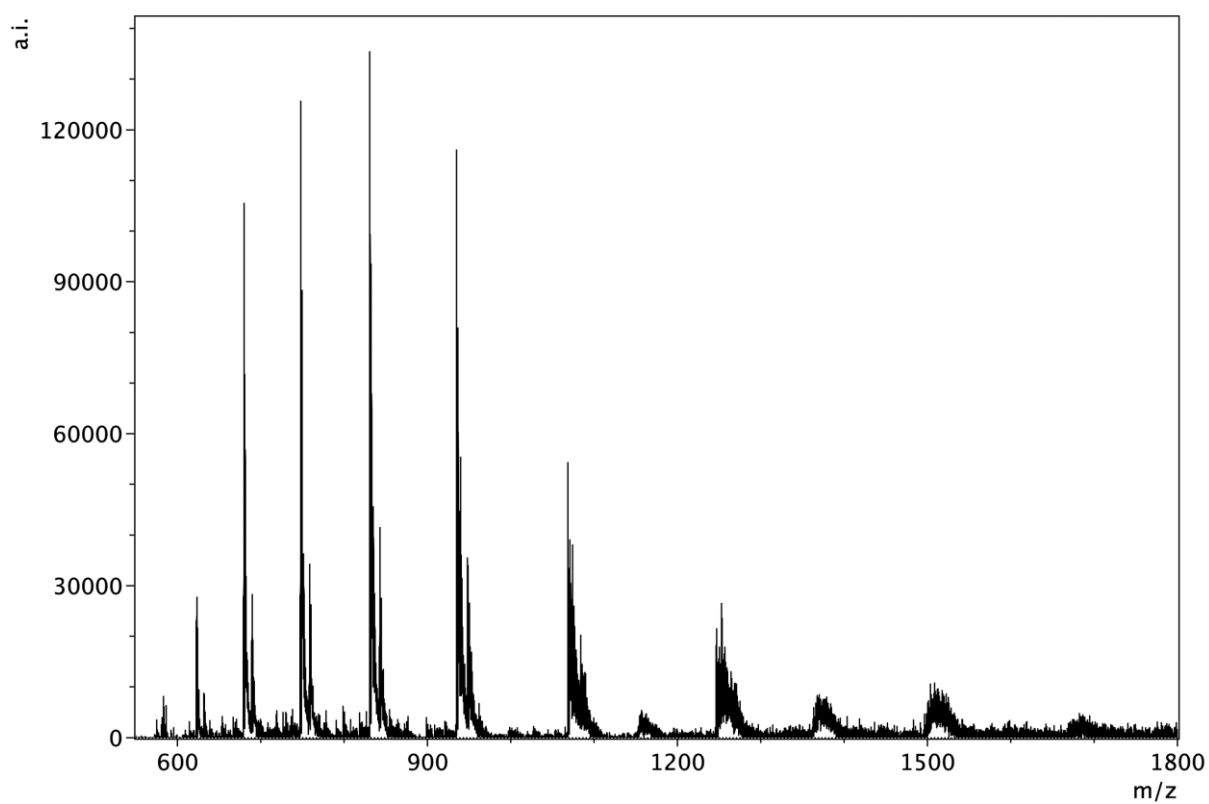


Figure S95. Negative ion mode ESI-MS following the addition of Ag^+ (2 equiv.) to the oligonucleotide $\text{C}_{12}\text{-(T)}_2\text{-C}_{12}$, T^2C_{12} .

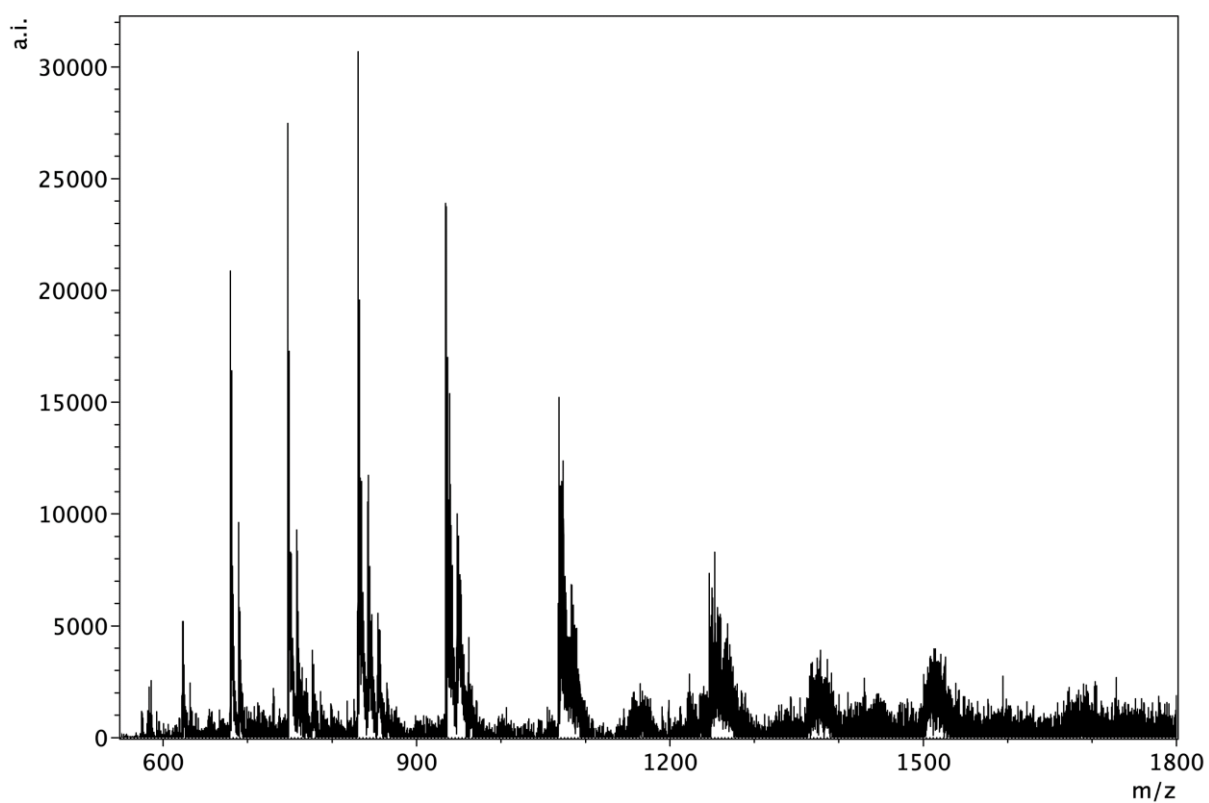


Figure S96. Negative ion mode ESI-MS following the addition of Ag^+ (4 equiv.) to the oligonucleotide $\text{C}_{12}\text{-(T)}_2\text{-C}_{12}$, $^{12}\text{C}_{12}$.

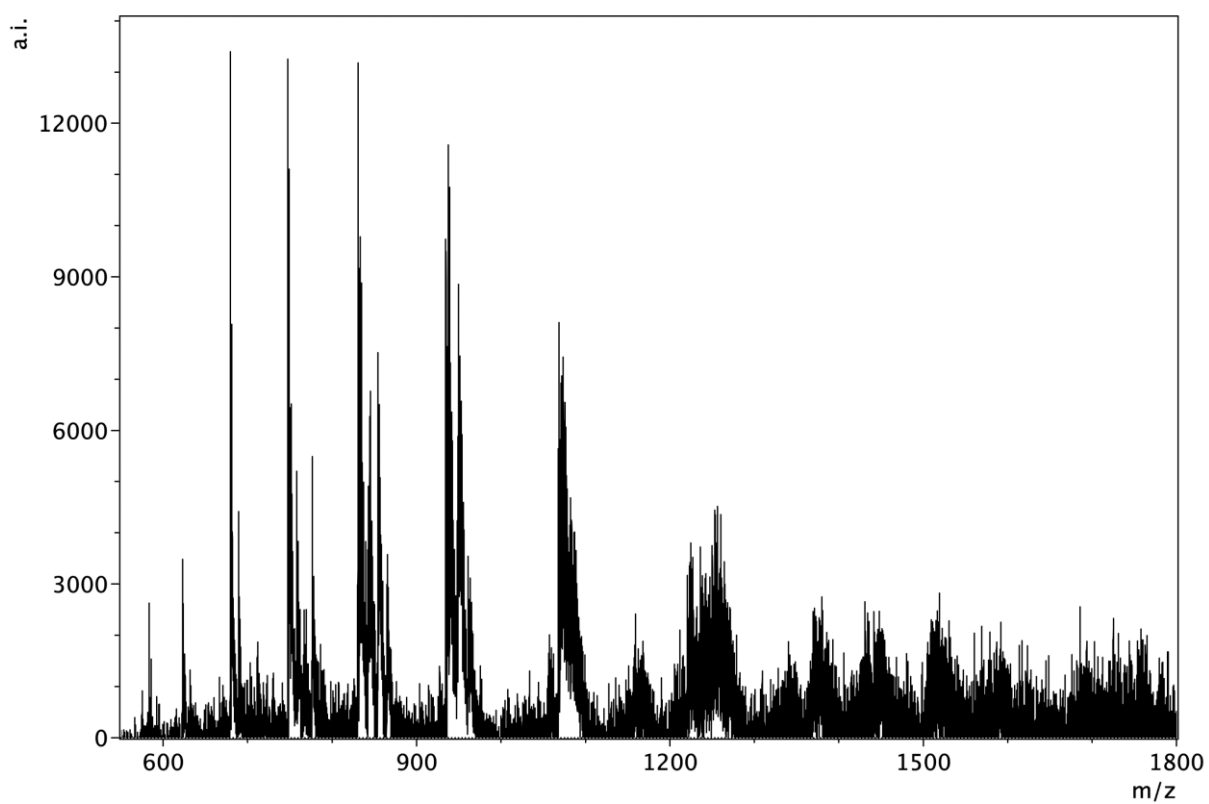


Figure S97. Negative ion mode ESI-MS following the addition of Ag^+ (6 equiv.) to the oligonucleotide $\text{C}_{12}\text{-(T)}_2\text{-C}_{12}$, $^{12}\text{C}_{12}$.

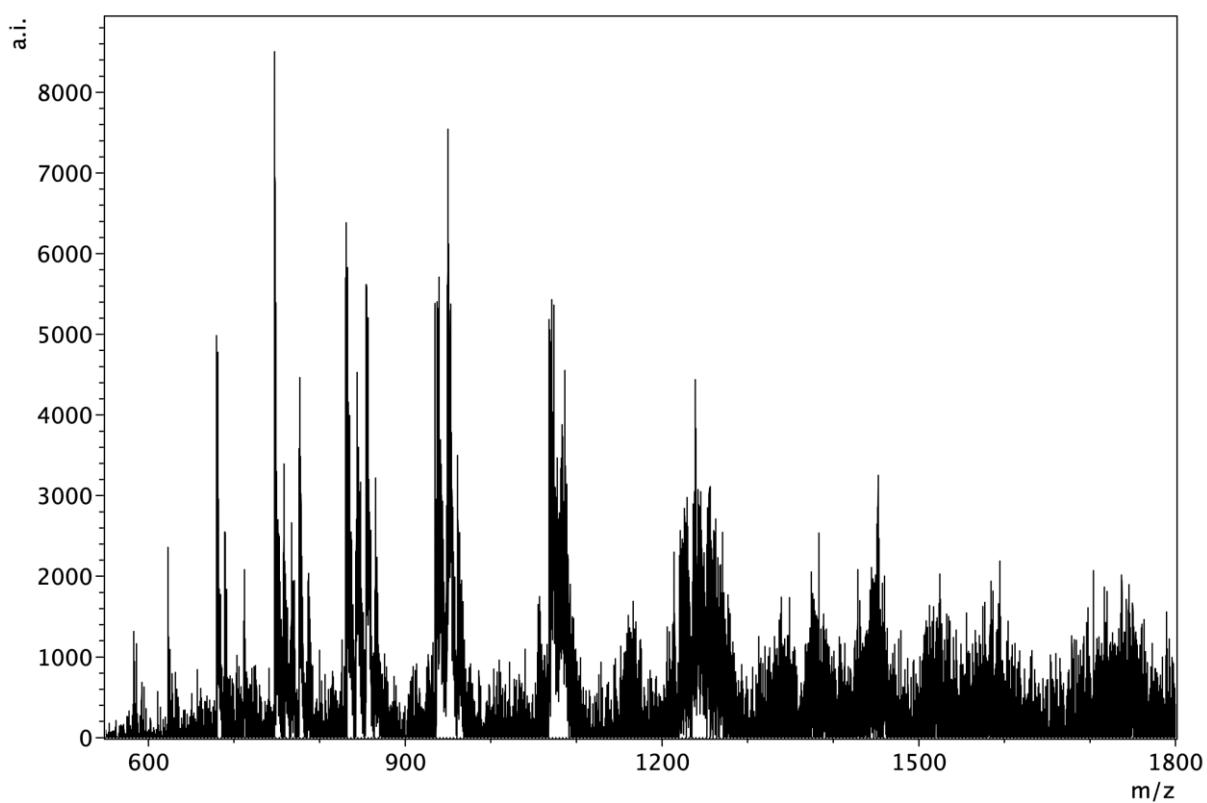


Figure S98. Negative ion mode ESI-MS following the addition of Ag^+ (8 equiv.) to the oligonucleotide $\text{C}_{12}\text{-(T)}_2\text{-C}_{12}$, T^2C_{12} .

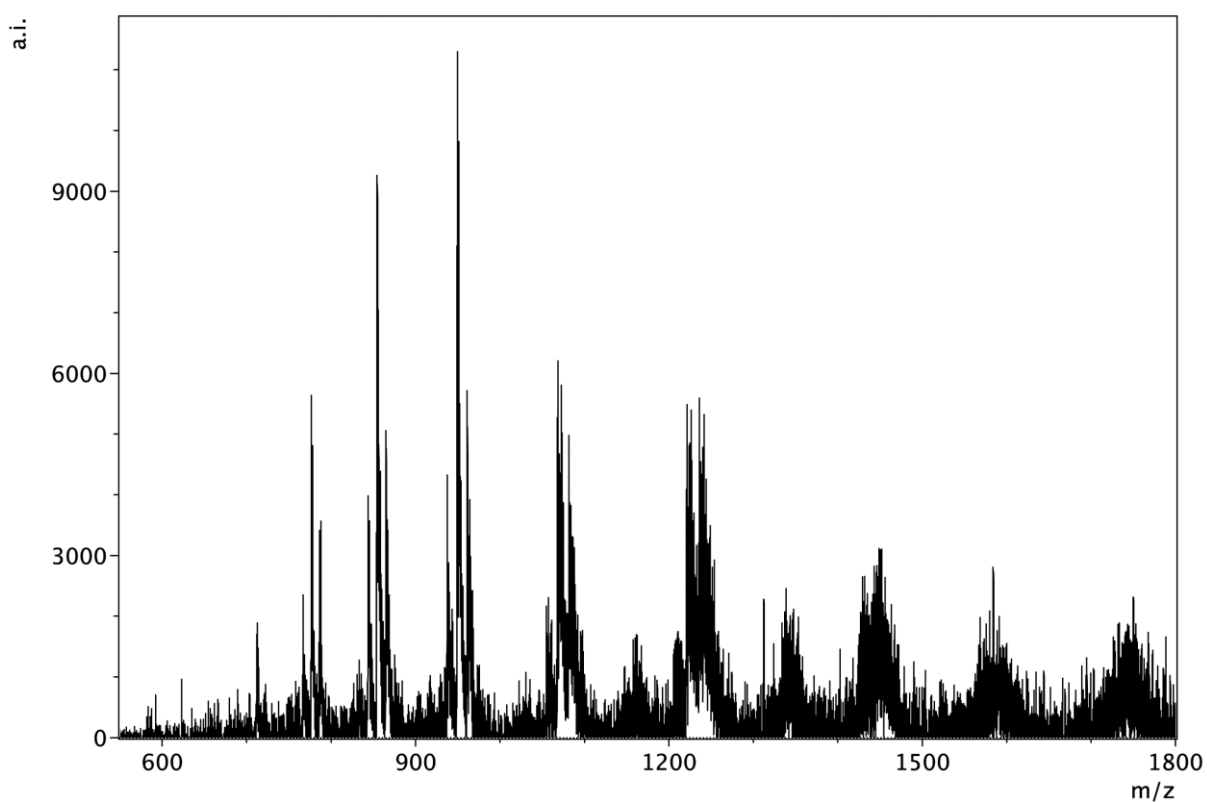


Figure S99. Negative ion mode ESI-MS following the addition of Ag^+ (12 equiv.) to the oligonucleotide $\text{C}_{12}\text{-(T)}_2\text{-C}_{12}$, T^2C_{12} .

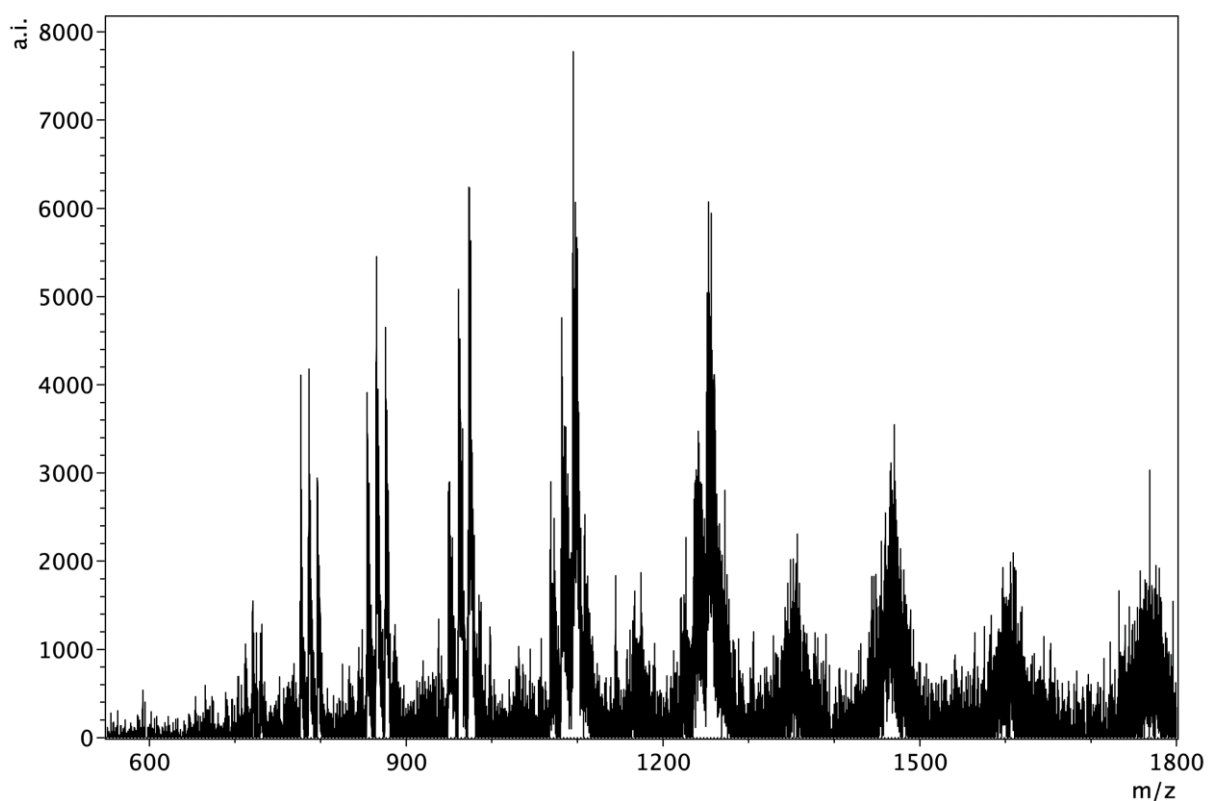


Figure S100. Negative ion mode ESI-MS following the addition of excess Ag^+ (20 equiv.) to the oligonucleotide $\text{C}_{12}\text{-(T)}_2\text{-C}_{12}$, T_2C_{12} .

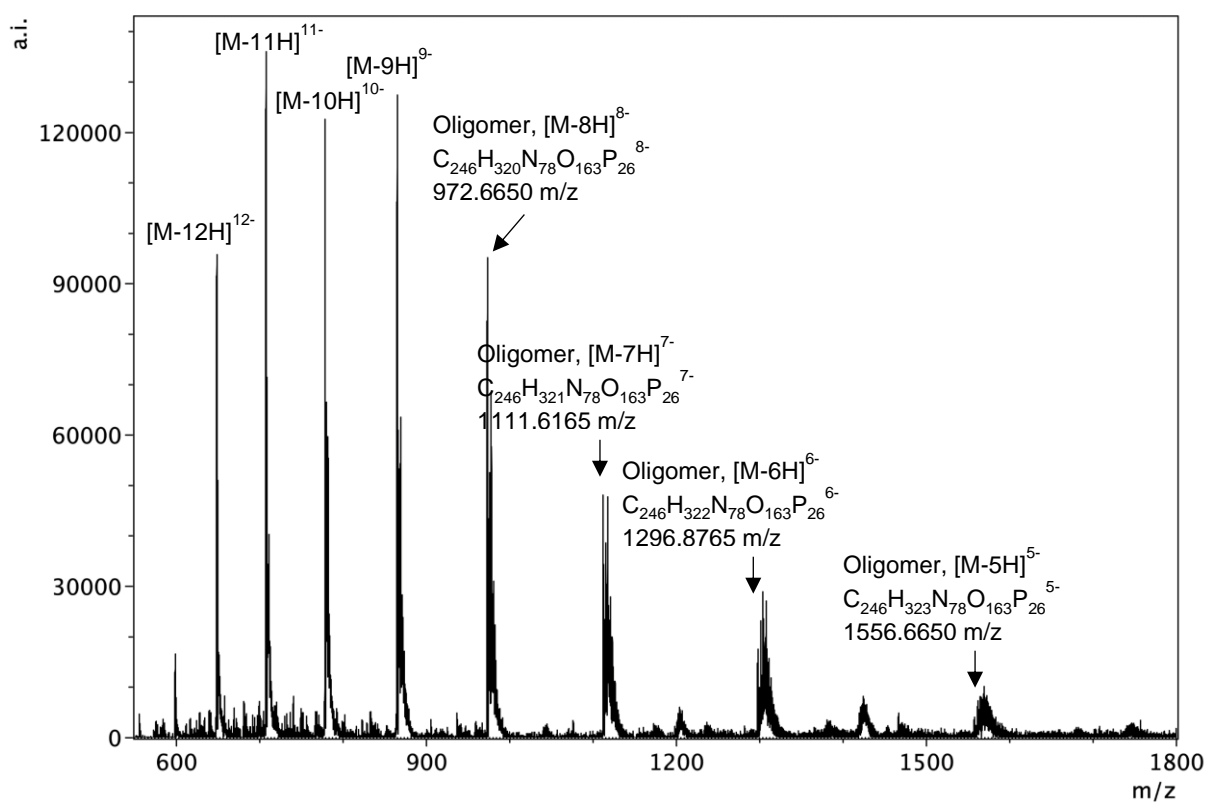


Figure S101. Negative ion mode ESI-MS of the oligonucleotide $\text{C}_{12}\text{-(T)}_3\text{-C}_{12}$, T_3C_{12} .

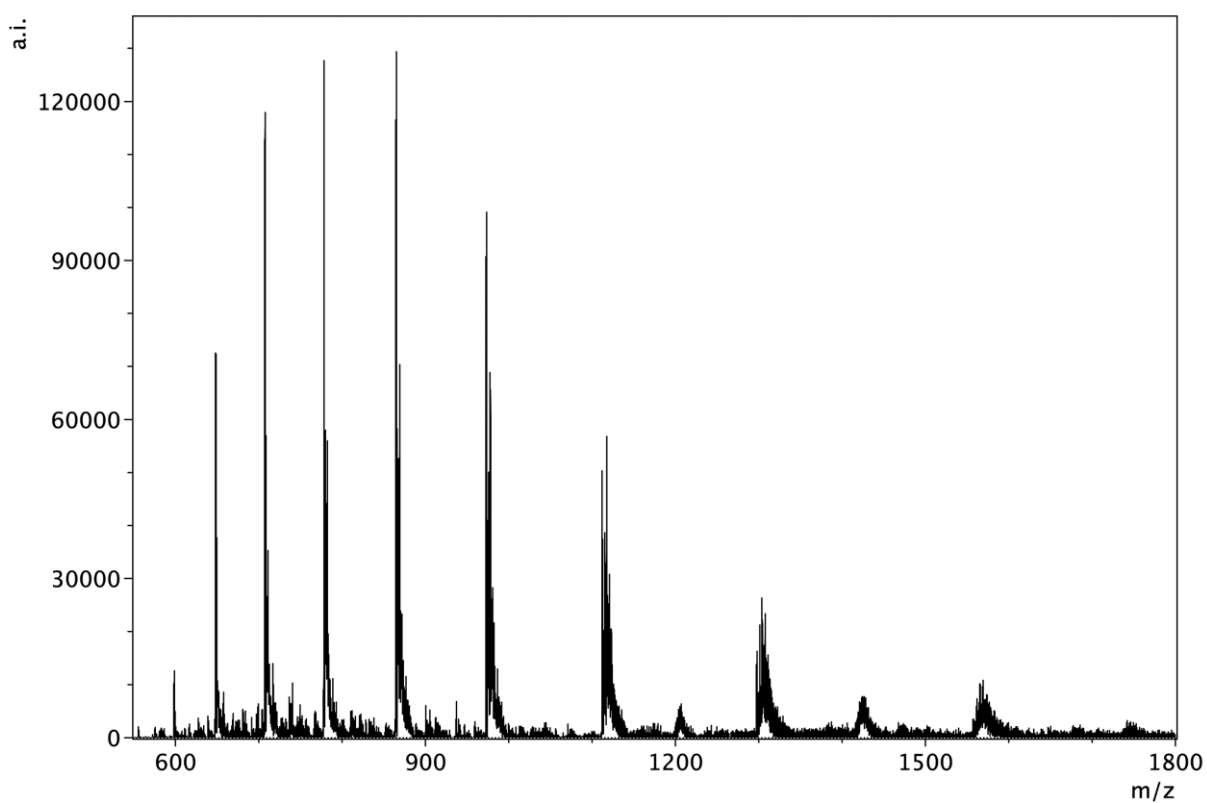


Figure S102. Negative ion mode ESI-MS following the addition of Ag^+ (1 equiv.) to the oligonucleotide $\text{C}_{12}\text{-(T)}_3\text{-C}_{12}$, $^{13}\text{C}_{12}$.

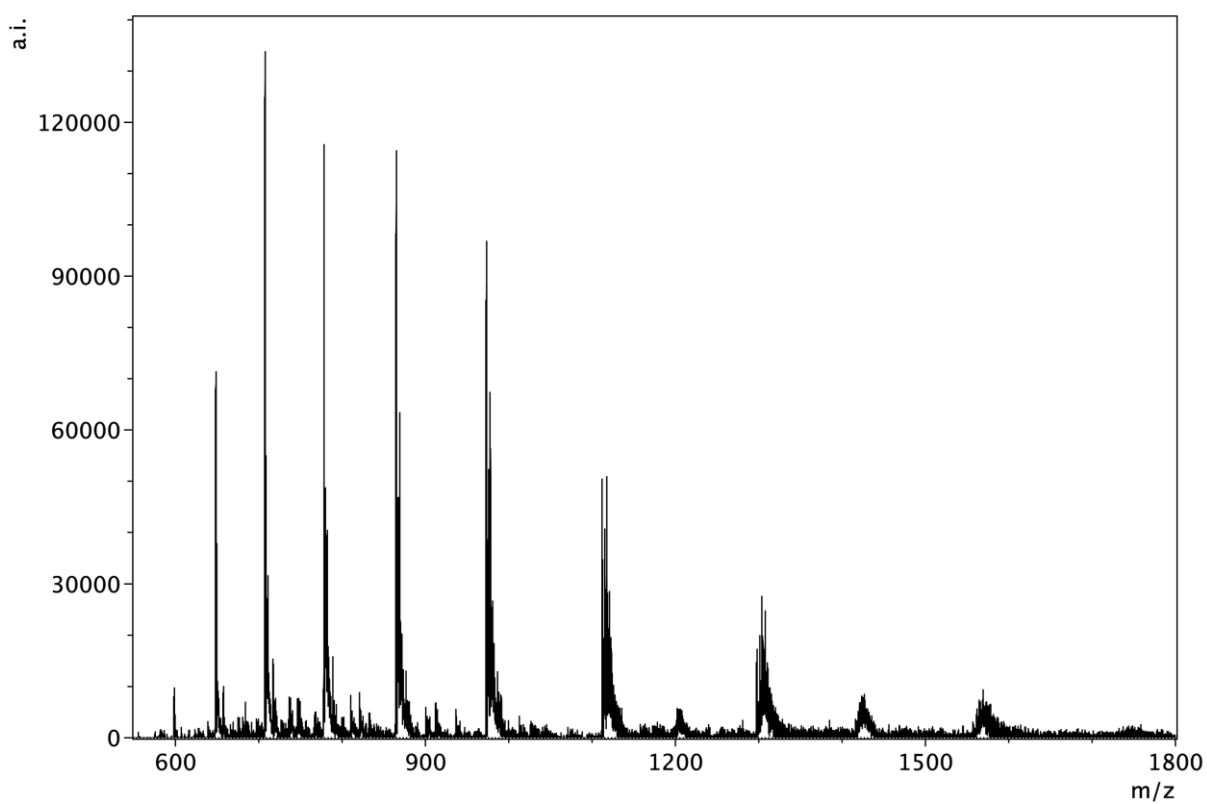


Figure S103. Negative ion mode ESI-MS following the addition of Ag^+ (2 equiv.) to the oligonucleotide $\text{C}_{12}\text{-(T)}_3\text{-C}_{12}$, $^{13}\text{C}_{12}$.

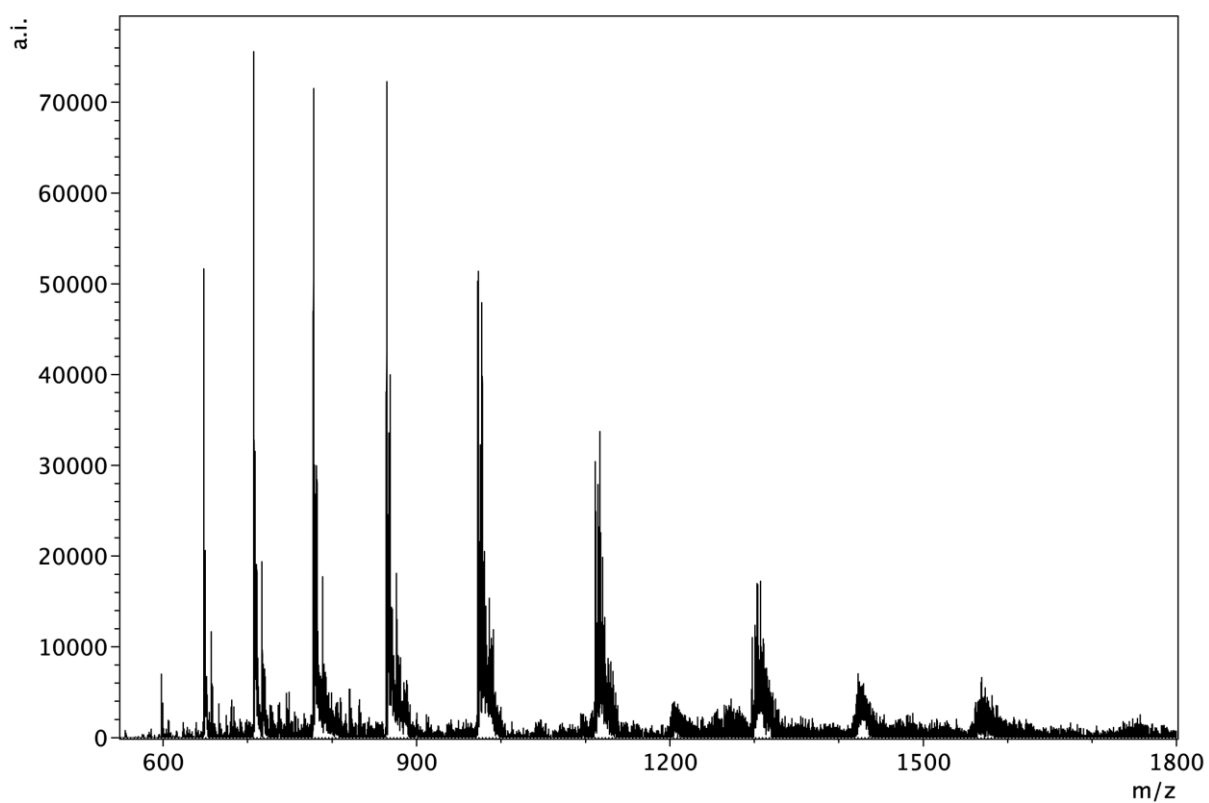


Figure S104. Negative ion mode ESI-MS following the addition of Ag^+ (4 equiv.) to the oligonucleotide $\text{C}_{12}-(\text{T})_3-\text{C}_{12}$, $^{13}\text{C}_{12}$.

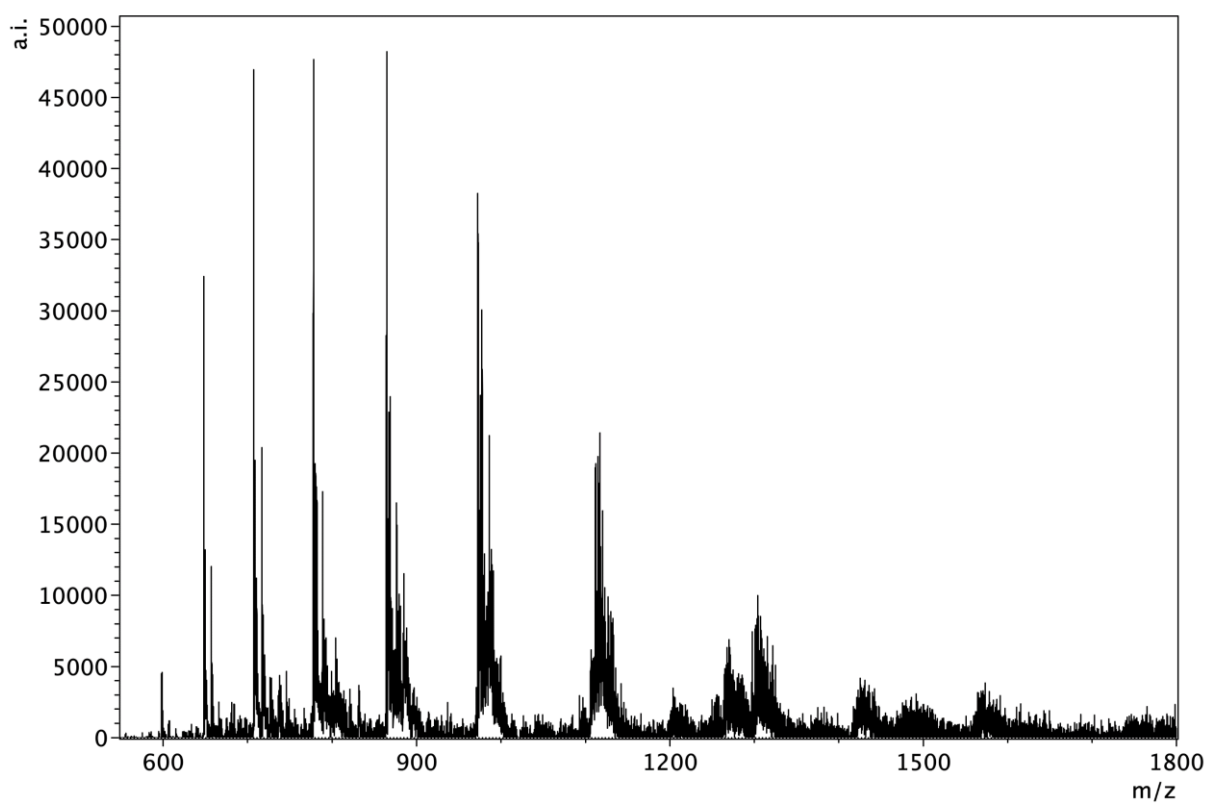


Figure S105. Negative ion mode ESI-MS following the addition of Ag^+ (6 equiv.) to the oligonucleotide $\text{C}_{12}-(\text{T})_3-\text{C}_{12}$, $^{13}\text{C}_{12}$.

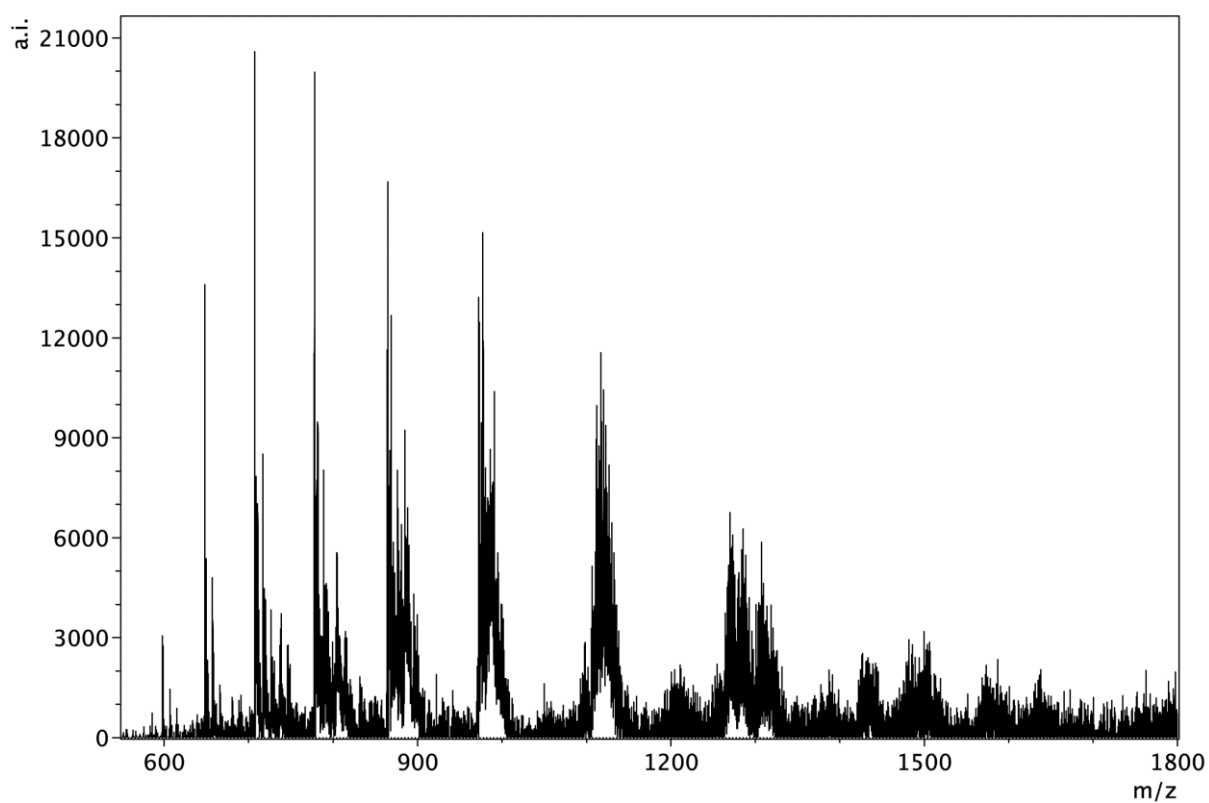


Figure S106. Negative ion mode ESI-MS following the addition of Ag^+ (8 equiv.) to the oligonucleotide $\text{C}_{12}\text{-(T)}_3\text{-C}_{12}$, T^3C_{12} .

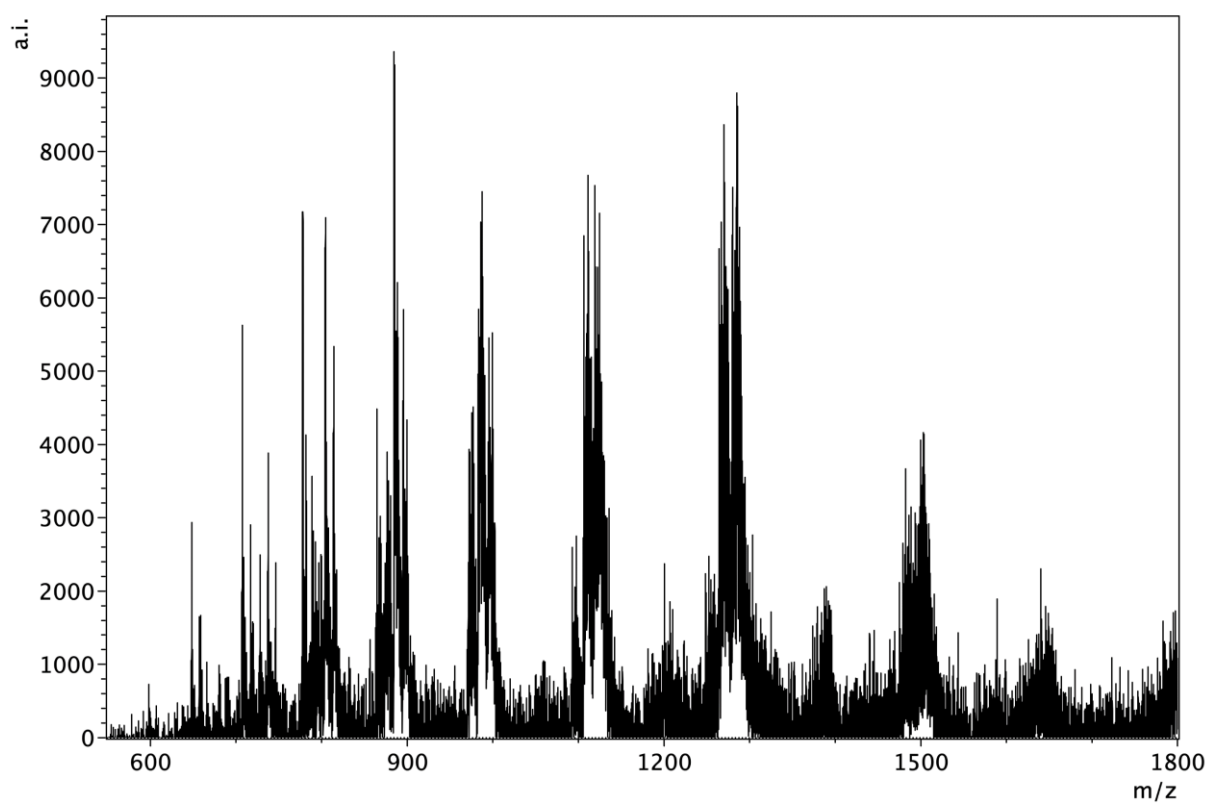


Figure S107. Negative ion mode ESI-MS following the addition of Ag^+ (12 equiv.) to the oligonucleotide $\text{C}_{12}\text{-(T)}_3\text{-C}_{12}$, T^3C_{12} .

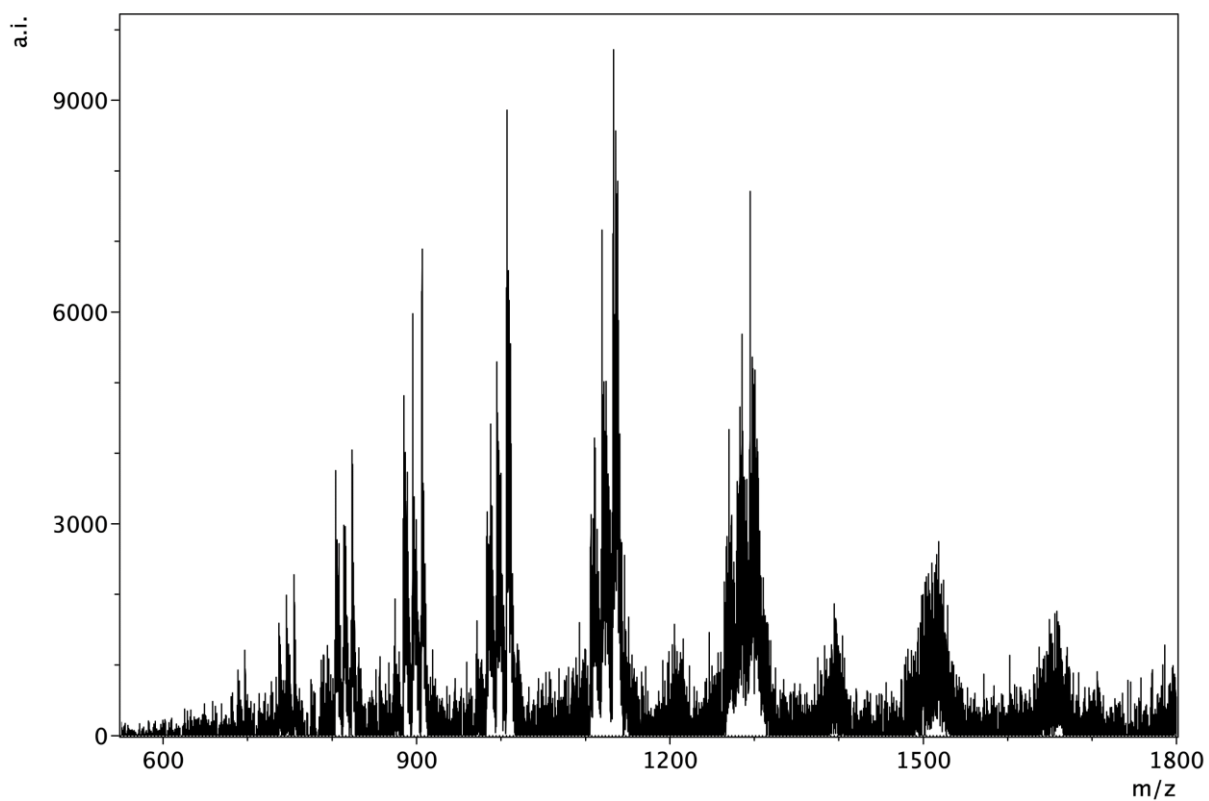


Figure S108. Negative ion mode ESI-MS following the addition of excess Ag^+ (20 equiv.) to the oligonucleotide $\text{C}_{12}\text{-(T)}_3\text{-C}_{12}$, T_3C_{12} .

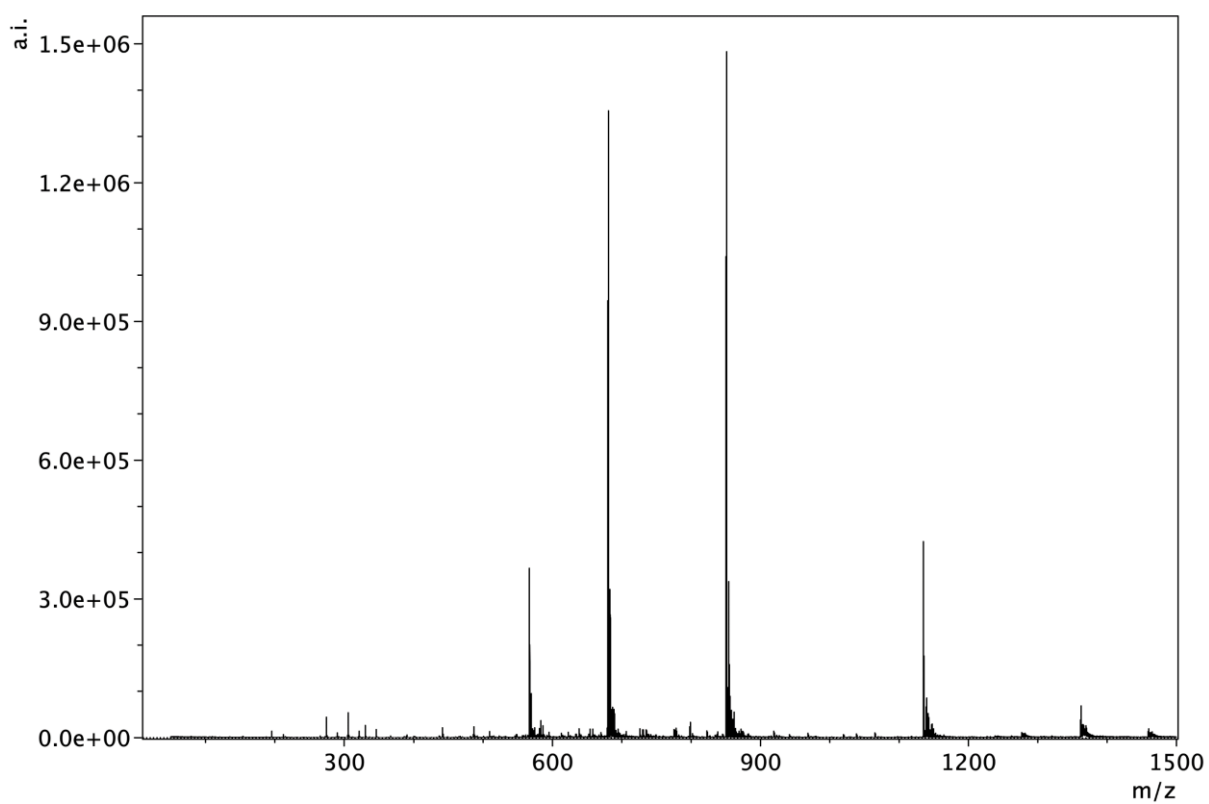


Figure S109. Negative ion mode ESI-MS of the oligonucleotide $d\text{C}_{12}$.

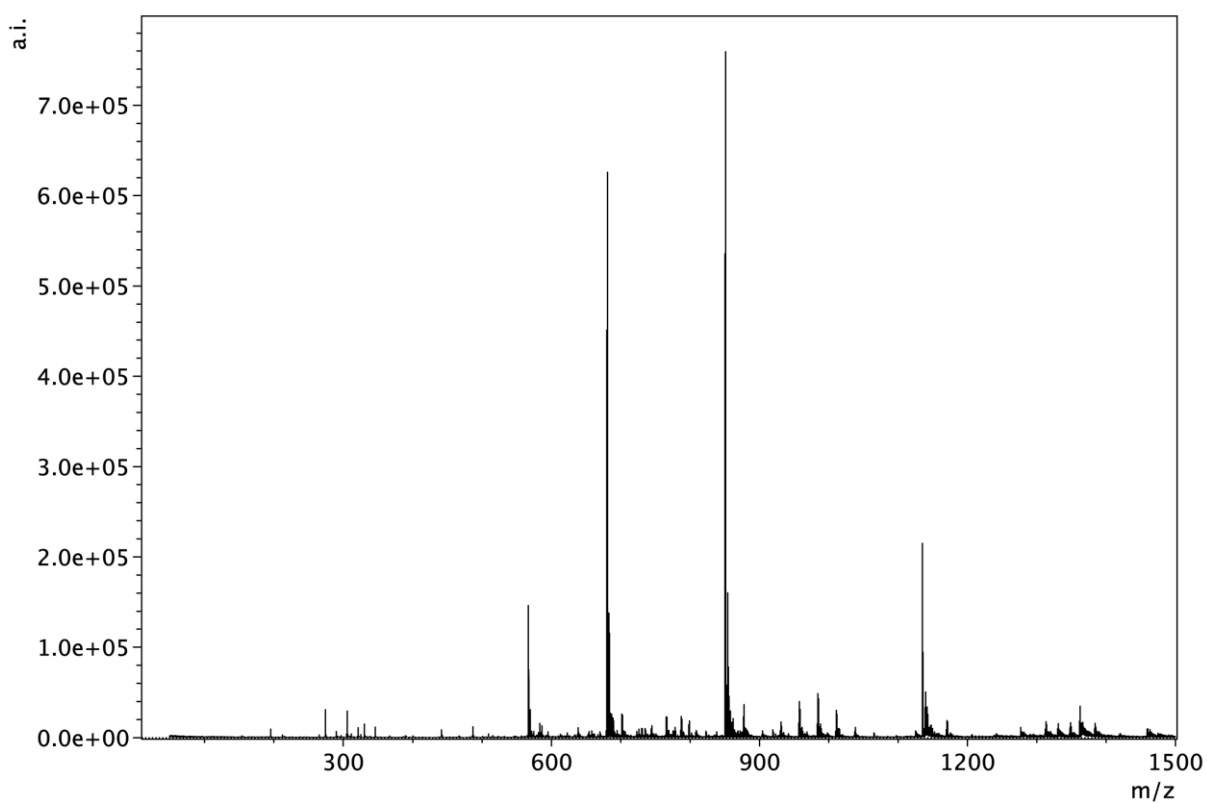


Figure S110. Negative ion mode ESI-MS following the addition of Ag^+ (12 equiv.) to the oligonucleotide $d\text{C}_{12}$.

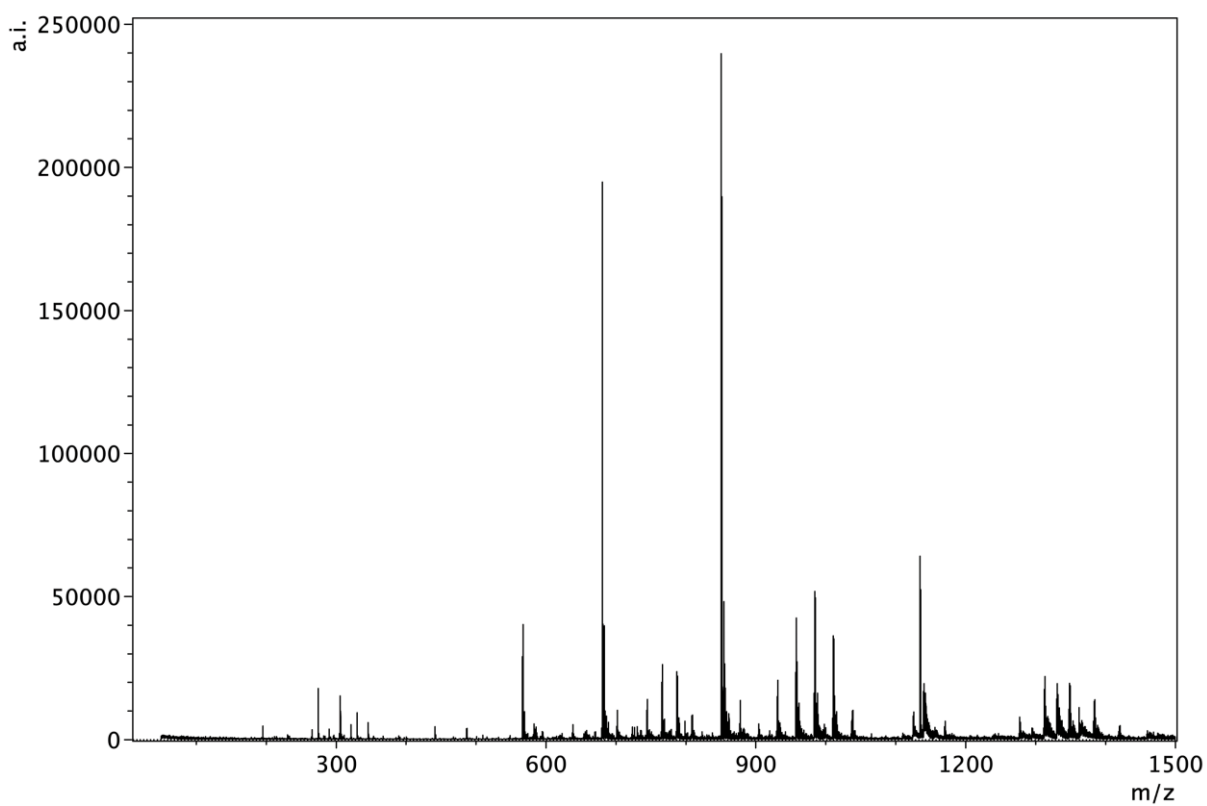


Figure S111. Negative ion mode ESI-MS following the addition of excess Ag^+ (20 equiv.) to the oligonucleotide $d\text{C}_{12}$.

S.3.3. ΔG ; Gibbs Energy Calculations using MS peak intensity data.

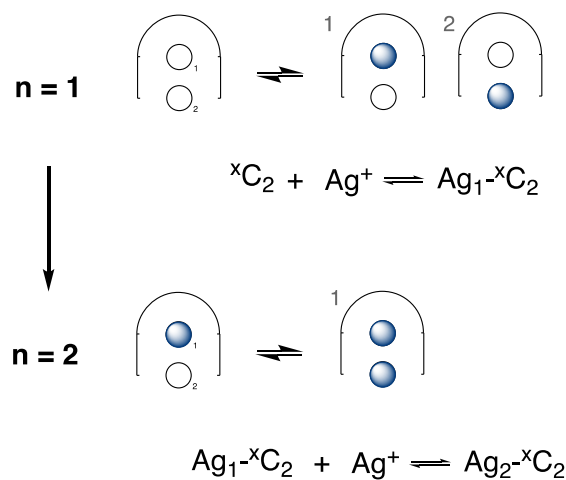


Figure 112. Site occupation analysis during the titration of silver ions into a hairpin with two (xC_2) possible mediation sites.

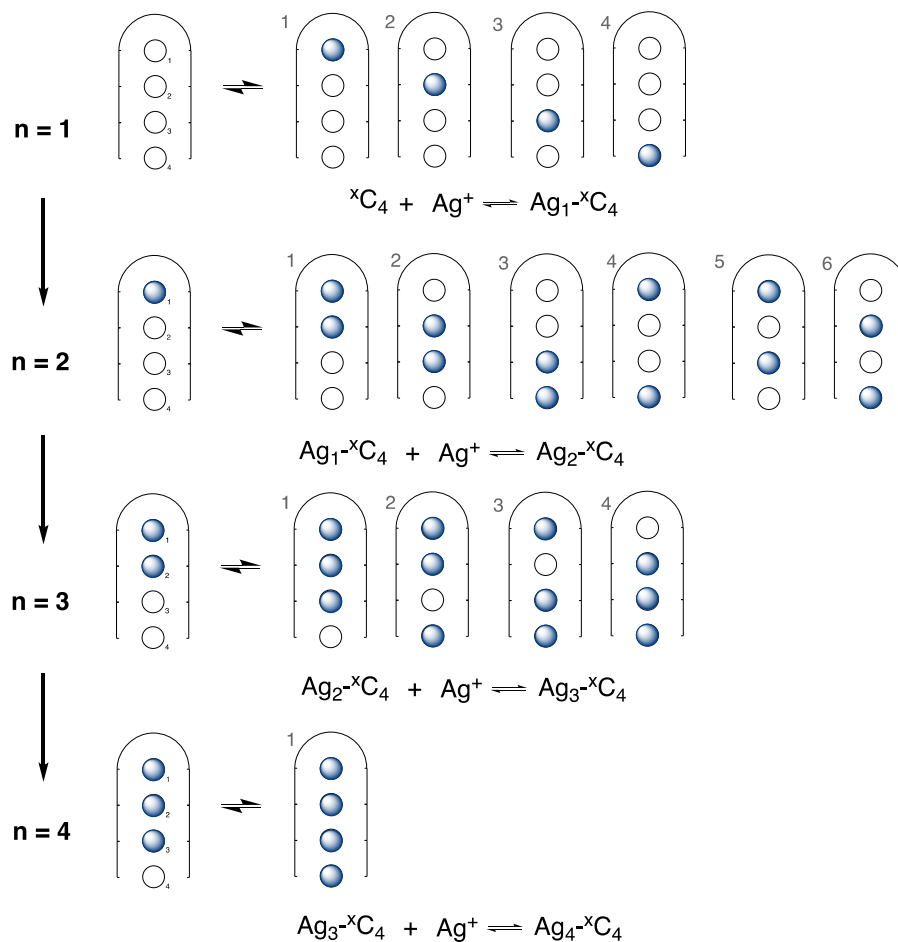


Figure 113. Site occupation analysis during the titration of silver ions into a hairpin with four (xC_4) possible mediation sites.

Calculations:

T (Kelvin) = 298 K

R (ideal gas constant) = 8.314 K/mol-K

RT / kJmol⁻¹ = 2.477572

Statistical factor for site occupation;

Corrections using a statistical factor was used to account for multiple site occupancy using the binomial coefficient (ⁿC_r):

$${}^nC_r = \frac{n!}{(n-r)! \cdot r!}$$

(where *n* = number of sites available and *r* = number of bound silver ions).

Number of Ag ^(I)	Loop Capacity (^x C _n)			
	2	4	6	12
1	2	4	6	12
2	1	6	15	66
3	-	4	20	220
4	-	1	15	495
5	-	-	6	792
6	-	-	1	924
7	-	-	-	792
8	-	-	-	495
9	-	-	-	220
10	-	-	-	66
11	-	-	-	12
12	-	-	-	1